

MARCH 2018

AJNR

VOLUME 39 • PP 405–604

AJNR

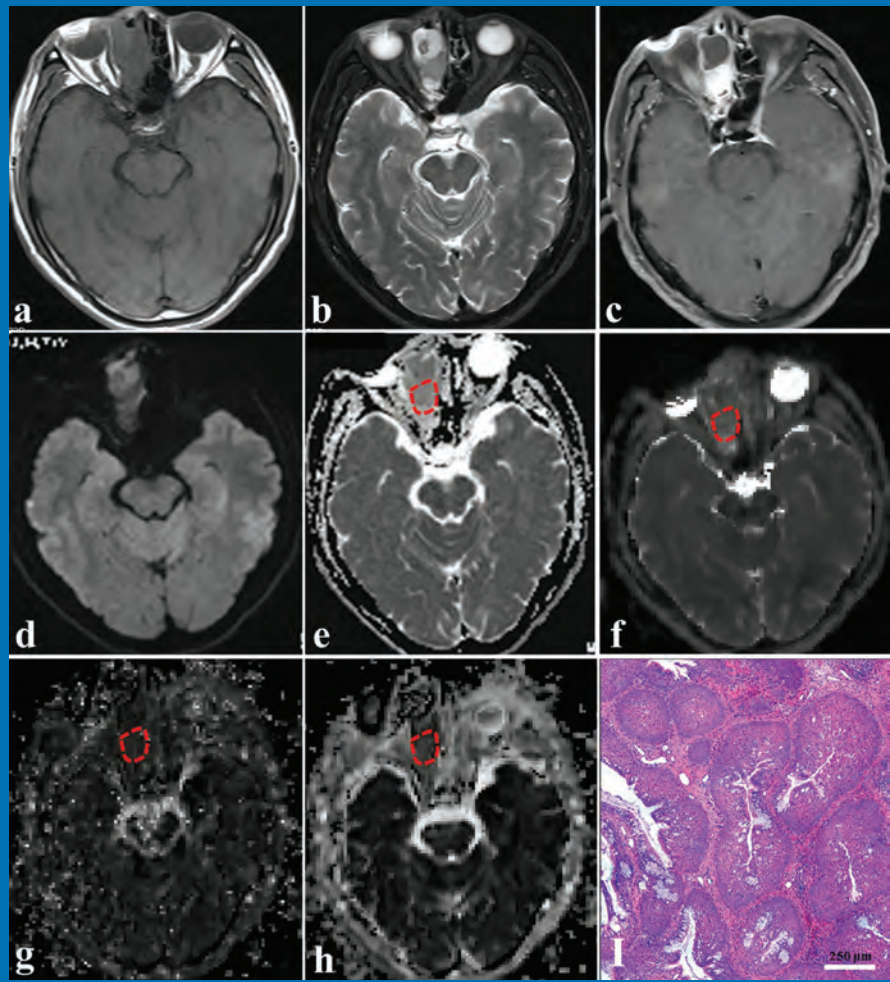
AMERICAN JOURNAL OF NEURORADIOLOGY

MARCH 2018
VOLUME 39
NUMBER 3
WWW.AJNR.ORG

THE JOURNAL OF DIAGNOSTIC AND
INTERVENTIONAL NEURORADIOLOGY

Blunt cerebrovascular injuries
Iodine extravasation quantification to predict thrombectomy
hemorrhagic complications
3T compressed sensing accelerated 3D-FLAIR for MS plaques

Official Journal ASNR • ASFNR • ASHNR • ASPNR • ASSR



A Complete Coil Portfolio

MicroVention's comprehensive portfolio features clinically proven Hydrogel coils, which can be used exclusively or in combination with our trusted Platinum coils to treat a wide range of aneurysms and neurovascular lesions.



Aneurysm
Therapy
Solutions

Breakthrough Hydrogel Technology

- Less Recurrence
- Less Retreatment
- More Progressive Occlusion

Compared to platinum coils with comparable safety¹

REFERENCES:

1. Taschner et al. Second-Generation Hydrogel Coils for the Endovascular Treatment of Intracranial Aneurysm; A Randomized Controlled Trial. 2018;49:00-00. DOI:10.1161/STROKEAHA.117.018707



INDICATIONS FOR USE:

The HydroCoil® Embolic System (HES) and MicroPlex® Coil System (MCS) are intended for the endovascular embolization of intracranial aneurysms and other neurovascular abnormalities such as arteriovenous malformations and arteriovenous fistulae. The HES and MCS are also intended for vascular occlusion of blood vessels within the neurovascular system to permanently obstruct blood flow to an aneurysm or other vascular malformation and for arterial and venous embolizations in the peripheral vasculature.

The device should only be used by physicians who have undergone pre-clinical training in all aspects of HES/MCS procedures as prescribed by MicroVention.



**For more information or a product demonstration,
contact your local MicroVention representative:**



**MicroVention Worldwide
Innovation Center**
35 Enterprise
Aliso Viejo, CA 92656 USA
MicroVention UK Limited
MicroVention Europe, S.A.R.L.
MicroVention Deutschland GmbH
microvention.com

PH +1.714.247.8000

PH +44 (0) 191 258 6777

PH +33 (1) 39 21 77 46

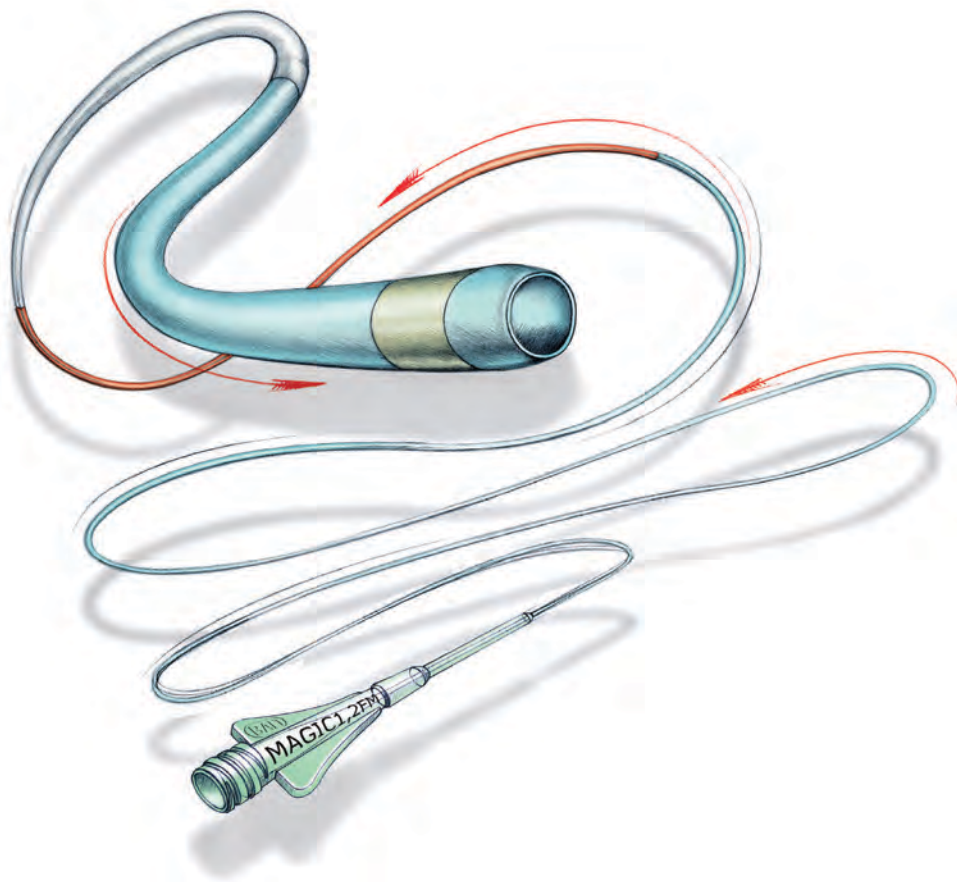
PH +49 211 210 798-0

Magic[®]



FLOW-DEPENDENT MICROCATHETER SERIES

Now available through Balt USA



ordermagics@balt-usa.com

MAGIC catheters are designed for general intravascular use. They may be used for the controlled, selective regional infusion of therapeutic agents or embolic materials into vessels.¹

Federal (USA) law restricts this device to sale, distribution by or on the order of a physician. Indications, contraindications, warnings and instructions for use can be found in the product labeling supplied with each device.

1. Magic Catheters IFU - Ind 19



BALT USA
18 Technology Drive #169, Irvine, CA 92618
P 949.788.1443 F 949.788.1444

© 2017 BALT USA MKTG-068 Rev. B



Bending expectations of conformability and stability.

Enhanced conformability – The hybrid cell structure is designed to enhance stent opening and conformability in bifurcations and tight curves.

Ease of use – All sizes of the Neuroform Atlas Stent are deliverable through Excelsior® SL-10® and Excelsior XT-17™ Microcatheters.

Higher deployment accuracy – The Neuroform Atlas Stent is designed to have very low foreshortening, which enables very high deployment accuracy.



Neuroform Atlas™ STENT SYSTEM

ASNR 56th Annual Meeting & The Foundation of the ASNR Symposium 2018

June 2 - 7, 2018 | Vancouver Convention Centre East | Vancouver, B.C., CANADA



ASNR 2018 KEYNOTE PRESENTATION *by Andy DeLaO*

The Radiology Renaissance: Shaping the Future of Healthcare

Monday, June 4, 2018 - 8:00am - 9:00am Hall A - Vancouver Convention Centre East

This keynote will highlight the changing world of radiology inside of healthcare. Radiologists at one point were referred to as the "doctor's doctor." Radiologists were the trusted advisors to help physicians from primary care to specialists such as surgeons and oncologists make clinical decisions based on imaging. As technology evolves, the role of the radiologist undergoes transformation. Today we are seeing the emergence of another technology evolution in healthcare. It presents an opportunity for radiologists to transition once again, but the choices they face today will determine the future role of radiology.



The Vancouver Convention Centre East © 2013 Vancouver Convention Centre

Welcome and Greetings

Please join us in Vancouver, CANADA for the **56th Annual Meeting of the American Society of Neuroradiology** on June 2-7, 2018 at the Vancouver Convention Centre East. Surrounded by the coastal mountains and located on the waterfront, you can enjoy these spectacular views in the heart of downtown Vancouver. With its undeniable charm and friendly atmosphere, Vancouver is known around the world as both a popular tourist attraction and one of the best places to live. ASNR enthusiastically presents **Neuroradiology: Adding Value and Improving Healthcare** at the Symposium of the Foundation of the ASNR, as well as the common thread throughout the Annual Meeting. Implementing a value-based strategy in imaging has grasped the attention of nearly every healthcare provider; in particular with Radiologists understanding that the future will demand their imaging practices deliver better value. Value in healthcare is typically defined as those imaging strategies that yield improved outcomes, lower costs, or both. As payment transitions from a fee-for-service to a value-based system, thus creating a fundamentally different marketplace dynamic, measuring good outcomes are at the center of this changeover. At this time of uncertainty what little remains clear is that without a well-defined knowledge of their outcomes, no medical specialty will be able to succeed in the future value-based system. The Symposium will feature how Neuroradiology, in its many subspecialty areas, adds value to clinical care pathways by directing healthcare practice towards better outcomes. The annual meeting programming will continue on this theme emphasizing imaging that improves health outcomes, while considering costs, thus adding value. Our discussions will incorporate many innovative approaches to how neuroimaging currently does and will continue to improve overall healthcare performance.

As the Program Chair for ASNR 2018, it is my pleasure and honor to welcome you to Vancouver, CANADA for our annual meeting! Vancouver is known for being a very walkable city with a compact downtown core hosting many places to enjoy. So pack your comfortable walking shoes and let's tour together with our colleagues and friends!

Pina Sanelli

Pina C. Sanelli, MD, MPH, FACR
ASNR 2018 Program Chair/President-Elect



ASNR 2018 ■ VANCOUVER

ASFNR ASHNR ASPNR ASSR SNIS

THE FOUNDATION OF THE ASNR



Pina C. Sanelli, MD, MPH, FACR

ASNR 2018 Program Chair/President-Elect

Programming developed in cooperation with the...

American Society of Functional Neuroradiology (ASFNR)

Max Wintermark, MD

American Society of Head and Neck Radiology (ASHNR)

Deborah R. Shatzkes, MD

American Society of Pediatric Neuroradiology (ASPNR)

Ashok Panigrahy, MD

American Society of Spine Radiology (ASSR)

John D. Barr, MD, FACR, FSIR, FAHA

Society of NeuroInterventional Surgery (SNIS)

Mahesh V. Jayaraman, MD

ASNR Health Policy (HPC) Committee

William D. Donovan, MD, MPH, FACR | Gregory N. Nicola, MD, FACR

ASNR Computer Sciences & Informatics (CSI) Committee

John L. Go, MD, FACR

ASNR Research Scientist Programming Committee

Dikoma C. Shungu, PhD | Timothy P.L. Roberts, PhD

The International Hydrocephalus Imaging Working Group (IHIWG) / CSF Flow Group

Ari M Blitz, MD | Harold L. Reigate, MD | Bryn A. Martin, PhD

Check out Meeting Registration/Housing!

Please visit 2018.asnr.org for more information

ASNR 56th Annual Meeting

c/o American Society of Neuroradiology

800 Enterprise Drive, Suite 205

Oak Brook, Illinois 60523-4216

Phone: 630-574-0220 Fax: 630 574-0661

2018.asnr.org





52nd Annual Meeting | American Society of

Head & Neck Radiology

**The Westin Savannah Harbor Golf Resort & Spa
Savannah, GA**

September 26 - 30, 2018

Please contact Educational Symposia at 813-806-1000 or ASHNR@edusymp.com or visit www.ASHNR.org for additional information.

We're Inside Every Great Neuroradiologist!

ASNR MEMBERS RECEIVE

American Journal of Neuroradiology (AJNR)

The leading neuroradiology research journal, published monthly

Neurographics

Bimonthly educational journal with CME for members

ASNR Annual Meeting

Discounts for members on the field's premier conference

eCME

Online collection of lectures and articles with SA-CME and Category 1 credit

Advocacy

Coding/reimbursement, quality standards and practice guidelines; demonstrating neuroradiology's value!

Networking

Access to 5,000 peers

... And More!

Join the leaders in neuroradiology today!

Learn more at www.asnr.org/join

ASNR

American Society of Neuroradiology

800 Enterprise Dr., Suite 205, Oak Brook, IL 60523 • (630)574-0220 • membership@asnr.org • www.asnr.org



SAVE THE DATE 2018



12th Annual Meeting of the
American Society of

Functional Neuroradiology

October 15-17, 2018

Hotel del Coronado, San Diego, CA

October 14, 2018

Optional Hands-on BOLD fMRI Workshop

For More Information, Visit www.asfnr.org

Neuroform Atlas™ Stent System

See package insert for complete indications, contraindications, warnings and instructions for use.

Humanitarian Device Authorized by Federal law for use with neurovascular embolic coils in patients who are ≥ 18 years of age for the treatment of wide neck, intracranial, saccular aneurysms arising from a parent vessel with a diameter of ≥ 2 mm and ≤ 4.5 mm that are not amenable to treatment with surgical clipping. Wide neck aneurysms are defined as having a neck > 4 mm or a dome-to-neck ratio < 2. The effectiveness of this device for this use has not been demonstrated.

INDICATIONS FOR USE

The Neuroform Atlas™ Stent System is indicated for use with neurovascular embolic coils in patients who are ≥ 18 years of age for the treatment of wide neck, intracranial, saccular aneurysms arising from a parent vessel with a diameter of ≥ 2 mm and ≤ 4.5 mm that are not amenable to treatment with surgical clipping. Wide neck aneurysms are defined as having a neck > 4 mm or a dome-to-neck ratio of < 2.

CONTRAINDICATIONS

Patients in whom antiplatelet and/or anticoagulation therapy is contraindicated.

POTENTIAL ADVERSE EVENTS

The potential adverse events listed below, as well as others, may be associated with the use of the Neuroform Atlas™ Stent System or with the procedure:

Allergic reaction to nital metal and medications, Aneurysm perforation or rupture, Coil herniation through stent into parent vessel, Death, Embolus, Headache, Hemorrhage, In-stent stenosis, Infection, Ischemia, Neurological deficit/intracranial sequelae, Pseudoaneurysm, Stent fracture, Stent migration/embolization, Stent misplacement, Stent thrombosis, Stroke, Transient ischemic attack, Vasospasm, Vessel occlusion or closure, Vessel perforation/rupture, Vessel dissection, Vessel trauma or damage, Vessel thrombosis, Visual impairment, and other procedural complications including but not limited to anesthetic and contrast media risks, hypotension, hypertension, access site complications.

WARNINGS

- Contents supplied STERILE using an ethylene oxide (EO) process. Do not use if sterile barrier is damaged. If damage is found, call your Stryker Neurovascular representative.
- For single use only. Do not reuse, reprocess or resterilize. Reuse, reprocessing or resterilization may compromise the structural integrity of the device and/or lead to device failure which, in turn, may result in patient injury, illness or death. Reuse, reprocessing or resterilization may also create a risk of contamination of the device and/or cause patient infection or cross-infection, including, but not limited to, the transmission of infectious disease(s) from one patient to another. Contamination of the device may lead to injury, illness or death of the patient.
- After use, dispose of product and packaging in accordance with hospital, administrative and/or local government policy.
- This device should only be used by physicians who have received appropriate training in interventional neuroradiology or interventional radiology and preclinical training on the use of this device as established by Stryker Neurovascular.
- Select a stent size (length) to maintain a minimum of 4 mm on each side of the aneurysm neck along the parent vessel. An incorrectly sized stent may result in damage to the vessel or stent migration. Therefore, the stent is not designed to treat an aneurysm with a neck greater than 22 mm in length.
- If excessive resistance is encountered during the use of the Neuroform Atlas™ Stent System or any of its components at any time during the procedure, discontinue use of the stent system. Continuing to move the stent system against resistance may result in damage to the vessel or a system component.
- Persons allergic to nickel titanium (Nitinol) may suffer an allergic response to this stent implant.
- Purge the system carefully to avoid the accidental introduction of air into the stent system.
- Confirm there are no air bubbles trapped anywhere in the stent system.

CAUTIONS / PRECAUTIONS

- Federal Law (USA) restricts this device to sale by or on the order of a physician.
- Use the Neuroform Atlas Stent System prior to the "Use By" date printed on the package.
- Carefully inspect the sterile package and Neuroform Atlas Stent System prior to use to verify that neither has been damaged during shipment. Do not use kinked or damaged components; contact your Stryker Neurovascular representative.
- The stent delivery microcatheter and the Neuroform Atlas Stent delivery wire should not be used to recapture the stent.
- Exercise caution when crossing the deployed stent with adjunctive devices.
- After deployment, the stent may foreshorten from up to 6.3%.
- The max OD of the coiling microcatheter should not exceed the max OD of the stent delivery microcatheter.

- Standard interventional devices with distal tips > 1.8 F may not be able to pass through the interstices of the stent.
- Safety of the Neuroform Atlas Stent System in patients below the age of 18 has not been established.
- In cases where multiple aneurysms are to be treated, start at the most distal aneurysm first.

MAGNETIC RESONANCE IMAGING (MRI)

Specific Information Magnetic Resonance Conditional

Non-clinical testing and analysis have demonstrated that the Neuroform Atlas Stent is MR Conditional alone, or when overlapped with a second stent, and adjacent to a Stryker Neurovascular coil mass. A patient with the Neuroform Atlas Stent can be safely scanned immediately after placement of this implant, under the following conditions:

- Static magnetic field of 1.5 and 3.0 Tesla
- Maximum spatial gradient field up to 2500 Gauss/cm (25 Tesla/m)
- Maximum MRI system reported whole body averaged specific absorption rate of 2 W/kg (Normal Operating Mode) and head averaged specific absorption rate of 3.2 W/kg.

Under the scan conditions defined above, the Neuroform Atlas Stent is expected to produce a maximum temperature rise of 4°C after 15 minutes of continuous scanning. The Neuroform Atlas Stent should not migrate in this MRI environment.

In non-clinical testing, the image artifact caused by the device extends approximately 2 mm from the Neuroform Atlas Stent when imaged with a spin echo pulse sequence and 3 Tesla MRI System. The artifact may obscure the device lumen. It may be necessary to optimize MRI imaging parameters for the presence of this implant.

Excelsior® XT-17™ Microcatheter

See package insert for complete indications, contraindications, warnings and instructions for use.

INTENDED USE / INDICATIONS FOR USE

Stryker Neurovascular's Excelsior XT-17 Microcatheters are intended to assist in the delivery of diagnostic agents, such as contrast media, and therapeutic agents, such as occlusion coils, into the peripheral, coronary and neuro vasculature.

CONTRAINDICATIONS

None known.

POTENTIAL ADVERSE EVENTS

Potential adverse events associated with the use of microcatheters or with the endovascular procedures include, but are not limited to: access site complications, allergic reaction, aneurysm perforation, aneurysm rupture, death, embolism (air, foreign body, plaque, thrombus), hematoma, hemorrhage, infection, ischemia, neurological deficits, pseudoaneurysm, stroke, transient ischemic attack, vasospasm, vessel dissection, vessel occlusion, vessel perforation, vessel rupture, vessel thrombosis

WARNINGS

- The accessories are not intended for use inside the human body.
- Limited testing has been performed with solutions such as contrast media, saline and suspended embolic particles. The use of these microcatheters for delivery of solutions other than the types that have been tested for compatibility is not recommended. Do not use with glue or glue mixtures.
- Carefully inspect all devices prior to use. Verify shape, size and condition are suitable for the specific procedure.
- Exchange microcatheters frequently during lengthy procedures that require extensive guidewire manipulation or multiple guidewire exchanges.
- Never advance or withdraw an intravascular device against resistance until the cause of the resistance is determined by fluoroscopy. Movement of the microcatheter or guidewire against resistance could dislodge a clot, perforate a vessel wall, or damage microcatheter and guidewire. In severe cases, tip separation of the microcatheter or guidewire may occur.
- Contents supplied STERILE using an ethylene oxide (EO) process. Do not use if sterile barrier is damaged. If damage is found, call your Stryker Neurovascular representative.
- For single use only. Do not reuse, reprocess or resterilize. Reuse, reprocessing or resterilization may compromise the structural integrity of the device and/or lead to device failure which, in turn, may result in patient injury, illness or death. Reuse, reprocessing or resterilization may also create a risk of contamination of the device and/or cause patient infection or cross-infection, including, but not limited to, the transmission of infectious disease(s) from one patient to another. Contamination of the device may lead to injury, illness or death of the patient.
- After use, dispose of product and packaging in accordance with hospital, administrative and/or local government policy.
- These devices are intended for use only by physicians trained in performing endovascular procedures.
- Inspect product before use for any bends, kinks or damage. Do not use a microcatheter that has been damaged. Damaged microcatheters may rupture causing vessel trauma or tip detachment during steering maneuvers.
- The shaping mandrel is not intended for use inside the human body.

- Discontinue use of microcatheter for infusion if increased resistance is noted. Resistance indicates possible blockage. Remove and replace blocked microcatheter immediately. DO NOT attempt to clear blockage by over-pressure. Doing so may cause the microcatheter to rupture, resulting in vascular damage or patient injury.
- Do not exceed 2,070 kPa (300 psi) infusion pressure. Excessive pressure could dislodge a clot, causing thromboemboli, or could result in a ruptured microcatheter or severed tip, causing vessel injury.

CAUTIONS / PRECAUTIONS

- To reduce the probability of coating damage in tortuous vasculature, use a guide catheter with a minimum internal diameter as specified in Table 1 above, and is recommended for use with Stryker Neurovascular hydrophilically coated microcatheters.
- To control the proper introduction, movement, positioning and removal of the microcatheter within the vascular system, users should employ standard clinical angiographic and fluoroscopic practices and techniques throughout the interventional procedure.
- Exercise care in handling of the microcatheter during a procedure to reduce the possibility of accidental breakage, bending or kinking.
- Use the product prior to the "Use By" date printed on the label.
- Limited testing indicates that Excelsior XT-17 Microcatheter is compatible with Dimethyl Sulfoxide (DMSO). The compatibility of Excelsior XT-17 Microcatheter with individual agents suspended in DMSO has not been established.
- Federal Law (USA) restricts this device to sale by or on the order of a physician.
- Wet dispenser coil or packaging tray and hydrophilically coated outer shaft of microcatheters prior to removal from packaging tray. Once the microcatheter has been wetted, do not allow to dry.
- The packaging mandrel is not intended for reuse. The packaging mandrel is not intended for use inside the human body.
- Check that all fittings are secure so that air is not introduced into guide catheter or microcatheter during continuous flush.
- In order to achieve optimal performance of Stryker Neurovascular Microcatheters and to maintain the lubricity of the Hydrolene® Coating surface, it is critical that a continuous flow of appropriate flush solution be maintained between the Stryker Neurovascular Microcatheter and guide catheter, and the microcatheter and any intraluminal device. In addition, flushing aids in preventing contrast crystal formation and/or clotting on both the intraluminal device and inside the guide catheter and/or the microcatheter lumen.
- Do not position microcatheter closer than 2.54 cm (1 in) from the steam source. Damage to the microcatheter may result.
- Excessive tightening of a hemostatic valve onto the microcatheter shaft may result in damage to the microcatheter. Removing the peel away introducer with a guidewire inserted in the crystal formation lumen might result in damage to the microcatheter shaft.
- To facilitate microcatheter handling, the proximal portion of the microcatheter does not have the hydrophilic surface. Greater resistance may be encountered when this section of the microcatheter is advanced into the RHV.

Excelsior® SL-10™ Microcatheter

See package insert for complete indications, contraindications, warnings and instructions for use.

INTENDED USE / INDICATIONS FOR USE

Stryker Neurovascular Excelsior SL-10 Microcatheter is intended to assist in the delivery of diagnostic agents, such as contrast media, and therapeutic agents, such as occlusion coils, into the peripheral, coronary, and neurovasculature.

CONTRAINDICATIONS

None known.

POTENTIAL ADVERSE EVENTS

Potential adverse events associated with the use of microcatheters or with the endovascular procedures include, but are not limited to: access site complications, allergic reaction, aneurysm perforation, aneurysm rupture, death, embolism (air, foreign body, plaque, thrombus), hematoma, hemorrhage, infection, ischemia, neurological deficits, pseudoaneurysm, stroke, transient ischemic attack, vasospasm, vessel dissection, vessel perforation, vessel rupture, vessel thrombosis.

WARNINGS

- Contents supplied STERILE using an ethylene oxide (EO) process. Do not use if sterile barrier is damaged. If damage is found, call your Stryker Neurovascular representative.
- For single patient use only. Do not reuse, reprocess or resterilize. Reuse, reprocessing or resterilization may compromise the structural integrity of the device and/or lead to device failure which, in turn, may result in patient injury, illness or death. Reuse, reprocessing or resterilization may also create a risk of contamination of the device and/or cause patient infection or cross-infection, including, but not limited to, the transmission of infectious disease(s) from one patient to another. Contamination of the device may lead to injury, illness or death of the patient.
- After use, dispose of product and packaging in accordance with hospital, administrative and/or local government policy.
- These devices are intended for use only by physicians trained in performing endovascular procedures.
- Inspect product before use for any bends, kinks or damage. Do not use a microcatheter that has been damaged. Damaged microcatheters may rupture causing vessel trauma or tip detachment during steering maneuvers.
- The shaping mandrel is not intended for use inside the human body.

- beyond the alignment marker when the fluoro-saver marker reaches the microcatheter hub.
- If the fluoro-saver marker is not visible, do not advance the coil without fluoroscopy.
- Do not rotate delivery wire during or after delivery of the coil. Rotating the Target Detachable Coil delivery wire may result in a stretched coil or premature detachment of the coil from the delivery wire, which could result in coil migration.
- Verify there is no coil loop protrusion into the parent vessel after coil placement and prior to coil detachment. Coil loop protrusion after coil placement may result in thromboembolic events if the coil is detached.
- Verify there is no movement of the coil after coil placement and prior to coil detachment. Movement of the coil after coil placement may indicate that the coil could migrate once it is detached.
- Failure to properly close the RHV compression fitting over the delivery wire before attaching the InZone® Detachment System could result in coil movement, aneurysm rupture or vessel perforation.
- Verify repeatedly that the distal shaft of the catheter is not under stress before detaching the Target Detachable Coil. Axial compression or tension forces could be stored in the 2-tip microcatheter causing the tip to move during coil delivery. Microcatheter tip movement could cause the aneurysm or vessel to rupture.
- Advancing the delivery wire beyond the microcatheter tip once the coil has been detached involves risk of aneurysm or vessel perforation.
- The long term effect of this product on extravascular tissues has not been established so care should be taken to retain this device in the intravascular space.

CAUTIONS / PRECAUTIONS

- Federal Law (USA) restricts this device to sale by or on the order of a physician.
- Besides the number of InZone Detachment System units needed to complete the case, there must be an extra InZone Detachment System unit as backup.
- Removing the delivery wire without grasping the introducer sheath and delivery wire together may result in the detachable coil sliding out of the introducer sheath.
- Failure to remove the introducer sheath after inserting the delivery wire into the RHV the microcatheter will interrupt normal infusion of flush solution and allow back flow of blood into the microcatheter.
- Some low level overhead light near or adjacent to the patient is required to

- to injury, illness or death of the patient.
- After use, dispose of product and packaging in accordance with hospital, administrative and/or local government policy.
- **These devices are intended for use only by physicians trained in performing endovascular procedures.**
- Limited testing has been performed with solutions such as contrast media, saline and suspended embolic particles. The use of these catheters for delivery of solutions other than the types that have been tested for compatibility is not recommended. Do not use with glue or glue mixtures.
- The accessories are not intended for use inside the human body.
- Carefully inspect all devices prior to use. Verify shape, size and condition are suitable for the specific procedure.
- Exchange microcatheters frequently during lengthy procedures that require extensive guidewire manipulation or multiple guidewire exchanges.
- Never advance or withdraw an intravascular device against resistance until the cause of the resistance is determined by fluoroscopy. Movement of the microcatheter or guidewire against resistance could dislodge a clot, perforate a vessel wall, or damage microcatheter and guidewire. In severe cases, tip separation of the microcatheter or guidewire may occur.
- Inspect product before use for any bends, kinks or damage. Do not use a microcatheter that has been damaged. Damaged microcatheters may rupture causing vessel trauma or tip detachment during steering maneuvers.
- Shaping mandrel is not intended for use inside the human body.
- Discontinue use of microcatheter for infusion if increased resistance is noted. Resistance indicates possible blockage. Remove and replace blocked microcatheter immediately. DO NOT attempt to clear blockage by over-pressure. Doing so may cause the microcatheter to rupture, resulting in vascular damage or patient injury.
- Do not exceed 2,070 kPa (300 psi) infusion pressure. Excessive pressure could dislodge a clot, causing thromboemboli, or could result in a ruptured microcatheter or severed tip, causing vessel injury.

CAUTIONS / PRECAUTIONS

- Federal Law (USA) restricts this device to sale by or on the order of a physician.
- To facilitate microcatheter handling, the proximal portion of the microcatheter does not have the hydrophilic surface. Greater resistance may be encountered when this section of the microcatheter is advanced into the RHV.
- Exercise care in handling of the microcatheter during a procedure to reduce the possibility of accidental breakage, bending or kinking.
- To reduce the probability of coating damage in tortuous vasculature, use a guide catheter with a minimum internal diameter as specified in Table 1 above, and is recommended for use with Stryker Neurovascular hydrophilically coated microcatheters.
- To control the proper introduction, movement, positioning and removal of the microcatheter within the vascular system, users should employ standard clinical angiographic and fluoroscopic practices and techniques throughout the interventional procedure.
- Flush dispenser coil of hydrophilically coated microcatheters prior to removal from dispenser coil. Once the microcatheter has been wetted, do not allow to dry. Do not reinsert the microcatheter into dispenser coil.
- Do not position microcatheter closer than 2.54 cm (1 in) from the steam source. Damage to the microcatheter may result.
- Check that all fittings are secure so that air is not introduced into guide catheter or microcatheter during continuous flush.
- In order to achieve optimal performance of Stryker Neurovascular Microcatheters and to maintain the lubricity of the Hydrolene® Coating surface, it is critical that a continuous flow of appropriate flush solution be maintained between the Stryker Neurovascular Microcatheter and guide catheter, and the microcatheter and any intraluminal device. In addition, flushing aids in preventing contrast crystal formation and/or clotting on both the intraluminal device and inside the guide catheter and/or the microcatheter lumen.
- Excessive tightening of a hemostatic valve onto the microcatheter shaft may result in damage to the microcatheter.



Stryker Neurovascular
47900 Bayside Parkway
Fremont, CA 94538

strykerneurovascular.com

Date of Release: NOV/2017

EX_EN_US

Copyright © 2017 Stryker

AP001839 v1.0 | Page 2 of 2

Target® Detachable Coil

See package insert for complete indications, contraindications, warnings and instructions for use.

INTENDED USE / INDICATIONS FOR USE

Target Detachable Coils are intended to endovascularly obstruct or occlude blood flow in vascular abnormalities of the neurovascular and peripheral vessels.

Target Detachable Coils are indicated for endovascular embolization of:

- Intracranial aneurysms
- Other neurovascular abnormalities such as arteriovenous malformations and arteriovenous fistulae
- Arterial and venous embolizations in the peripheral vasculature

CONTRAINDICATIONS

None known.

POTENTIAL ADVERSE EVENTS

Potential complications include, but are not limited to: allergic reaction, aneurysm perforation and rupture, arrhythmia, death, edema, embolus, headache, hemorrhage, infection, ischemia, neurological/intracranial sequelae, post-embolization syndrome (fever, increased white blood cell count, discomfort), TIA/stroke, vasospasm, vessel occlusion or closure, vessel perforation, dissection, trauma, vessel rupture, vessel thrombosis. Other procedural complications including but not limited to: anesthetic and contrast media risks, hypotension, hypertension, access site complications.

WARNINGS

- Contents supplied STERILE using an ethylene oxide (EO) process. Do not use if sterile barrier is damaged. If damage is found, call your Stryker Neurovascular representative.
- For single use only. Do not reuse, reprocess or resterilize. Reuse, reprocessing or resterilization may compromise the structural integrity of the device and/or lead to device failure which, in turn, may result in patient injury, illness or death. Reuse, reprocessing or resterilization may also create a risk of contamination of the device and/or cause patient infection or cross-infection, including, but not limited to, the transmission of infectious disease(s) from one patient to another. Contamination of the device may lead to injury, illness or death of the patient.
- After use, dispose of product and packaging in accordance with hospital, administrative and/or local government policy.

This device should only be used by physicians who have received appropriate training in interventional neuroradiology or interventional radiology and preclinical training on the use of this device as established by Stryker Neurovascular.

- Patients with hypersensitivity to 316LVM stainless steel may suffer an allergic reaction to this implant.
- MRI temperature testing was not conducted in arteriovenous malformations or fistulae and performance characteristics of the Target Detachable Coil System (Target Detachable Coils, InZone Detachment Systems, delivery systems and accessories) have not been demonstrated with other manufacturer's devices (whether coils, coil delivery devices, coil detachment systems, catheters, guidewires, and/or other accessories). Due to the potential incompatibility of non Stryker Neurovascular devices with the Target Detachable Coil System, the use of other manufacturer's devices with the Target Detachable Coil System is not recommended.
- To reduce risk of coil migration, the diameter of the first and second coil should never be less than the width of the ostium.
- In order to achieve optimal performance of the Target Detachable Coil System and to reduce the risk of thromboembolic complications, it is critical that a continuous infusion of appropriate flush solution be maintained between a) the femoral sheath and guiding catheter, b) the 2-tip microcatheter and guiding catheter, and c) the 2-tip microcatheter and Stryker Neurovascular guidewire and delivery wire. Continuous flush also reduces the potential for thrombus formation on, and crystallization of infusate around, the detachment zone of the Target Detachable Coil.
- Do not use the product after the "Use By" date specified on the package.
- Reuse of the packaging hoop or use with any coil other than the original coil may result in contamination of, or damage to, the coil.

Damaged delivery wires may cause detachment failures, vessel injury or unpredictable distal tip response during coil deployment. If a delivery wire is damaged at any point during the procedure, do not attempt to straighten or otherwise repair it. Do not proceed with deployment or detachment. Remove the entire coil and replace with undamaged product.

- Utilization of damaged coils may affect coil delivery to, and stability inside, the vessel or aneurysm, possibly resulting in coil migration and/or stretching.
- The fluoro-saver marker is designed for use with a Rotating Hemostatic Valve (RHV). If used without an RHV, the distal end of the coil may be

Copyright © 2017 Stryker

NV00018669 v2.0 | Page 2 of 2



Stryker Neurovascular
47900 Bayside Parkway
Fremont, CA 94538

strykerneurovascular.com

Date of Release: NOV/2017

EX_EN_US



LVIS®

Intraluminal Support Device

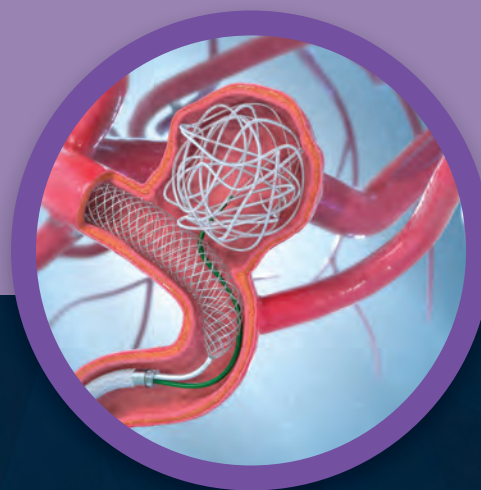
Low-profile Visualized Intرالuminal Support

Stent Deployment. Refined.

Braided Coil Assist Stents with
High Neck Coverage, Excellent Visibility
and Improved Conformability*



Aneurysm
Therapy
Solutions



For more information or a product demonstration,
contact your local MicroVention representative:

MicroVention Worldwide
Innovation Center
35 Enterprise

Aliso Viejo, CA 92656 USA

MicroVention UK Limited

MicroVention Europe, S.A.R.L.

MicroVention Deutschland GmbH

microvention.com

PH +1.714.247.8000

PH +44 (0) 191 258 6777

PH +33 (1) 39 21 77 46

PH +49 211 210 798-0

**Humanitarian Device: Authorized by Federal Law for use with bare platinum embolic coils for the treatment of unruptured, wide neck (neck \geq 4 mm or dome to neck ratio $<$ 2), intracranial, saccular aneurysms arising from a parent vessel with a diameter \geq 2.5 mm and \leq 4.5 mm. The effectiveness of this device for this use has not been demonstrated.*



Smooth and stable.

Target Detachable Coils deliver consistently smooth deployment and exceptional microcatheter stability. Designed to work seamlessly together for framing, filling and finishing. Target Coils deliver the high performance you demand.

For more information, please visit www.strykerneurovascular.com/Target or contact your local Stryker sales representative.



Target[®]
DETACHABLE COILS



Not for sale within the territory of the United States

UNIQUE FLEXIBILITY

ACCLINO[®] flex plus Stent

Highly flexible closed-cell stent with enhanced visibility allowing sequential stent and coil placement using the same microcatheter for the treatment of intracranial aneurysms.

FLEXIBLE. VISIBLE. SMOOTH.

www.acandis.com

acandis[®]

ENGINEERING STROKE SOLUTIONS

AJNR

AMERICAN JOURNAL OF NEURORADIOLOGY

MARCH 2018
VOLUME 39
NUMBER 3
WWW.AJNR.ORG

Publication Preview at www.ajnr.org features articles released in advance of print. Visit www.ajnrblog.org to comment on AJNR content and chat with colleagues and AJNR's News Digest at <http://ajnrdigest.org> to read the stories behind the latest research in neuroimaging.

405 **PERSPECTIVES** *H. Pendharkar*

REVIEW ARTICLE

-    406 **Blunt Cerebrovascular Injuries: Advances in Screening, Imaging, and Management Trends** *P. Nagpal, et al.*

GENERAL CONTENTS

-  415 **Development of High Signal Intensity within the Globus Pallidus and Dentate Nucleus following Multiple Administrations of Gadobenate Dimeglumine** *G.M. Bolles, et al.* **ADULT BRAIN PATIENT SAFETY**
-  421 **High Signal Intensity in the Dentate Nucleus and Globus Pallidus on Unenhanced T1-Weighted MR Images: Comparison between Gadobutrol and Linear Gadolinium-Based Contrast Agents** *F.G. Moser, et al.* **ADULT BRAIN PATIENT SAFETY**
-    427 **Cerebral Mitochondrial Microangiopathy Leads to Leukoencephalopathy in Mitochondrial Neurogastrointestinal Encephalopathy** *L.L. Gramegna, et al.* **ADULT BRAIN**
-  435 **Cerebellar Hypoperfusion in Migraine Attack: Incidence and Significance** *F. Kellner-Weldon, et al.* **ADULT BRAIN**
-  441 **Iodine Extravasation Quantification on Dual-Energy CT of the Brain Performed after Mechanical Thrombectomy for Acute Ischemic Stroke Can Predict Hemorrhagic Complications** *M. Bonatti, et al.* **ADULT BRAIN INTERVENTIONAL**
-   448 **Comparison of Blood Oxygenation Level-Dependent fMRI and Provocative DSC Perfusion MR Imaging for Monitoring Cerebrovascular Reserve in Intracranial Chronic Cerebrovascular Disease** *K.R. Thulborn, et al.* **ADULT BRAIN**
-  454 **Accuracy of the Compressed Sensing Accelerated 3D-FLAIR Sequence for the Detection of MS Plaques at 3T** *S. Toledano-Massiah, et al.* **ADULT BRAIN**
-    459 **Improved Visualization of Cortical Lesions in Multiple Sclerosis Using 7T MP2RAGE** *E.S. Beck, et al.* **ADULT BRAIN**
-  467 **Quantitative Susceptibility Mapping of the Thalamus: Relationships with Thalamic Volume, Total Gray Matter Volume, and T2 Lesion Burden** *G.C. Chiang, et al.* **ADULT BRAIN**
-   473 **Optimization of DARTEL Settings for the Detection of Alzheimer Disease** *J. Komatsu, et al.* **ADULT BRAIN**
-  479 **Substantia Nigra Free Water Increases Longitudinally in Parkinson Disease** *T. Guttuso Jr, et al.* **ADULT BRAIN**

AJNR (Am J Neuroradiol ISSN 0195-6108) is a journal published monthly, owned and published by the American Society of Neuroradiology (ASNR), 800 Enterprise Drive, Suite 205, Oak Brook, IL 60523. Annual dues for the ASNR include \$170.00 for journal subscription. The journal is printed by Cadmus Journal Services, 5457 Twin Knolls Road, Suite 200, Columbia, MD 21045; Periodicals postage paid at Oak Brook, IL and additional mailing offices. Printed in the U.S.A. POSTMASTER: Please send address changes to American Journal of Neuroradiology, P.O. Box 3000, Denville, NJ 07834, U.S.A. Subscription rates: nonmember \$400 (\$470 foreign) print and online, \$320 online only; institutions \$460 (\$530 foreign) print and basic online, \$915 (\$980 foreign) print and extended online, \$380 online only (basic), extended online \$825; single copies are \$35 each (\$40 foreign). Indexed by PubMed/Medline, BIOSIS Previews, Current Contents (Clinical Medicine and Life Sciences), EMBASE, Google Scholar, HighWire Press, Q-Sensei, RefSeek, Science Citation Index, and SCI Expanded. Copyright © American Society of Neuroradiology.

  	485	Pressure Mapping and Hemodynamic Assessment of Intracranial Dural Sinuses and Dural Arteriovenous Fistulas with 4D Flow MRI <i>L.A. Rivera-Rivera, et al.</i>	ADULT BRAIN
	488	Quantitative Analysis of Conebeam CT for Delineating Stents in Stent-Assisted Coil Embolization <i>T. Kuriyama, et al.</i>	INTERVENTIONAL
  	494	Endovascular Thrombectomy in Wake-Up Stroke and Stroke with Unknown Symptom Onset <i>P. Bücke, et al.</i>	INTERVENTIONAL
	500	Nonsphericity Index and Size Ratio Identify Morphologic Differences between Growing and Stable Aneurysms in a Longitudinal Study of 93 Cases <i>A. Chien, et al.</i>	INTERVENTIONAL
 	507	Local Glioma Cells Are Associated with Vascular Dysregulation <i>S.G. Bowden, et al.</i>	FUNCTIONAL ADULT BRAIN
 	515	MR Imaging Criteria for the Detection of Nasopharyngeal Carcinoma: Discrimination of Early-Stage Primary Tumors from Benign Hyperplasia <i>A.D. King, et al.</i>	HEAD & NECK
 	524	Comparison of MR Imaging and Dual-Energy CT for the Evaluation of Cartilage Invasion by Laryngeal and Hypopharyngeal Squamous Cell Carcinoma <i>H. Kuno, et al.</i>	HEAD & NECK
	532	MR Imaging–Based Evaluations of Olfactory Bulb Atrophy in Patients with Olfactory Dysfunction <i>M.S. Chung, et al.</i>	HEAD & NECK
 	538	Intravoxel Incoherent Motion MR Imaging in the Differentiation of Benign and Malignant Sinonasal Lesions: Comparison with Conventional Diffusion-Weighted MR Imaging <i>Z. Xiao, et al.</i>	HEAD & NECK
	547	Imaging of Anaplastic Thyroid Carcinoma <i>S. Ahmed, et al.</i>	HEAD & NECK
	552	Multiparametric Analysis of Permeability and ADC Histogram Metrics for Classification of Pediatric Brain Tumors by Tumor Grade <i>S. Vajapeyam, et al.</i>	PEDIATRICS
	558	Prenatal Factors Associated with Postnatal Brain Injury in Infants with Congenital Diaphragmatic Hernia <i>R. Radhakrishnan, et al.</i>	PEDIATRICS
	563	T2 Relaxometry MRI Predicts Cerebral Palsy in Preterm Infants <i>L.-W. Chen, et al.</i>	PEDIATRICS
	569	Expression Changes in Lactate and Glucose Metabolism and Associated Transporters in Basal Ganglia following Hypoxic-Ischemic Reperfusion Injury in Piglets <i>Y. Zheng, et al.</i>	PEDIATRICS
	577	Using Correlative Properties of Neighboring Pixels to Improve Gray-White Differentiation in Pediatric Head CT Images <i>T.P. Madaelil, et al.</i>	PEDIATRICS
 	583	Looking Deep into the Eye-of-the-Tiger in Pantothenate Kinase–Associated Neurodegeneration <i>J.-H. Lee, et al.</i>	PEDIATRICS
	589	Sonographic Development of the Pericallosal Vascularization in the First and Early Second Trimester of Pregnancy <i>B. De Keersmaecker, et al.</i>	PEDIATRICS
	597	Spinal Arteriovenous Vascular Malformations in Patients with Neural Tube Defects <i>E. Giordan, et al.</i>	SPINE
	604	35 YEARS AGO IN AJNR	

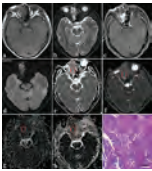
ONLINE FEATURES

LETTERS

- E38** Concerns about a New Preterm MR Imaging Scoring System *L.S. de Vries, et al.*
- E40** Reply *J.M. George, et al.*
-  **E41** Spinal Angiogram: A Treacherous Criterion Standard... *F. Clarençon, et al.*
- E45** Beware of Multiphase CTA Interpretation *E. Raz, et al.*
- E46** Reply *D. Byrne, et al.*

BOOK REVIEWS *R.M. Quencer, Section Editor*

Please visit www.ajnrblog.org to read and comment on Book Reviews.



Inverted papilloma in a 71-year-old man.

A mass in the right ethmoid sinus with involvement of the right nasal cavity demonstrates heterogeneous hypo- (necrosis) to isointensity (tumor cells) on T1WI (A), iso- (tumor cells) to hyperintensity (necrosis) on T2WI (B), and heterogeneously intense enhancement on contrast-enhanced T1WI (C), compared with normal-appearing gray matter. The mass shows isointensity on the DWI (D) compared with normal-appearing gray matter. On the ADC map (E), it shows slightly increased signal with an ADC value of $1.425 \times 10^{-3} \text{ mm}^2/\text{s}$. On IVIM images, the mass appeared obviously iso- to hyperintense on the D map (F) with a D value of $0.871 \times 10^{-3} \text{ mm}^2/\text{s}$ and appeared isointense on the D* (G) and f maps (H) with D* and f values of $61.048 \times 10^{-3} \text{ mm}^2/\text{s}$ and 25.651%, respectively. H&E staining confirmed the mass as an inverted papilloma.

 Indicates Editor's Choices selection

 Indicates Fellows' Journal Club selection

 Indicates open access to non-subscribers at www.ajnr.org

 Indicates article with supplemental on-line table

 Indicates article with supplemental on-line photo

 Indicates article with supplemental on-line video

 Evidence-Based Medicine Level 1

 Evidence-Based Medicine Level 2

Official Journal:

American Society of Neuroradiology
American Society of Functional Neuroradiology
American Society of Head and Neck Radiology
American Society of Pediatric Neuroradiology
American Society of Spine Radiology

EDITOR-IN-CHIEF

Jeffrey S. Ross, MD

Professor of Radiology, Department of Radiology,
Mayo Clinic College of Medicine, Phoenix, AZ

SENIOR EDITORS

Harry J. Cloft, MD, PhD

Professor of Radiology and Neurosurgery,
Department of Radiology, Mayo Clinic College of
Medicine, Rochester, MN

Thierry A.G.M. Huisman, MD

Professor of Radiology, Pediatrics, Neurology, and
Neurosurgery, Chairman, Department of Imaging
and Imaging Science, Johns Hopkins Bayview,
Director, Pediatric Radiology and Pediatric
Neuroradiology, Johns Hopkins Hospital,
Baltimore, MD

Yvonne W. Lui, MD

Associate Professor of Radiology,
Chief of Neuroradiology,
New York University School of Medicine,
New York, NY

C.D. Phillips, MD, FACR

Professor of Radiology, Weill Cornell Medical
College, Director of Head and Neck Imaging,
New York-Presbyterian Hospital, New York, NY

Pamela W. Schaefer, MD

Clinical Director of MRI and Associate Director of
Neuroradiology, Massachusetts General Hospital,
Boston, Massachusetts, Associate Professor,
Radiology, Harvard Medical School, Cambridge, MA

Charles M. Strother, MD

Professor of Radiology, Emeritus, University of
Wisconsin, Madison, WI

STATISTICAL SENIOR EDITOR

Bryan A. Comstock, MS

Senior Biostatistician,
Department of Biostatistics,
University of Washington, Seattle, WA

EDITORIAL BOARD

Ashley H. Aiken, *Atlanta, GA*
Lea M. Alhilali, *Phoenix, AZ*
John D. Barr, *Dallas, TX*
Ari Blitz, *Baltimore, MD*
Barton F. Branstetter IV, *Pittsburgh, PA*
Jonathan L. Brisman, *Lake Success, NY*
Julie Bykowski, *San Diego, CA*
Keith Cauley, *Danville, PA*
Asim F. Choudhri, *Memphis, TN*
Alessandro Cianfoni, *Lugano, Switzerland*
J. Matthew Debnam, *Houston, TX*
Seena Dehkharghani, *New York, NY*
Colin Derdeyn, *Iowa City, IA*
Rahul S. Desikan, *San Francisco, CA*
Yonghong Ding, *Rochester, MN*
Clifford J. Eskey, *Hanover, NH*
Saeed Fakhraan, *Phoenix, AZ*
Massimo Filippi, *Milan, Italy*
Allan J. Fox, *Toronto, Ontario, Canada*
Wende N. Gibbs, *Los Angeles, CA*
Christine M. Glastonbury, *San Francisco, CA*
John L. Go, *Los Angeles, CA*
Allison Grayev, *Madison, WI*
Brent Griffith, *Detroit, MI*
Wan-Yuo Guo, *Taipei, Taiwan*
Ajay Gupta, *New York, NY*
Rakesh K. Gupta, *Lucknow, India*
Lotfi Hachein-Bey, *Sacramento, CA*
Christopher P. Hess, *San Francisco, CA*
Andrei Holodny, *New York, NY*
Benjamin Huang, *Chapel Hill, NC*
George J. Hunter, *Boston, MA*
Mahesh V. Jayaraman, *Providence, RI*
Valerie Jewells, *Chapel Hill, NC*
Christof Karmonik, *Houston, TX*
Timothy J. Kaufmann, *Rochester, MN*
Hillary R. Kelly, *Boston, MA*
Toshibumi Kinoshita, *Akita, Japan*
Kenneth F. Layton, *Dallas, TX*
Michael M. Lell, *Nürnberg, Germany*
Michael Lev, *Boston, MA*
Karl-Olof Lovblad, *Geneva, Switzerland*
Franklin A. Marden, *Chicago, IL*
M. Gisele Matheus, *Charleston, SC*
Joseph C. McGowan, *Merion Station, PA*
Stephan Meckel, *Freiburg, Germany*
Christopher J. Moran, *St. Louis, MO*
Takahisa Mori, *Kamakura City, Japan*
Suresh Mukherji, *Ann Arbor, MI*
Amanda Murphy, *Toronto, Ontario, Canada*
Alexander J. Nemeth, *Chicago, IL*
Sasan Partovi, *Cleveland, OH*
Laurent Pierot, *Reims, France*
Jay J. Pillai, *Baltimore, MD*

Whitney B. Pope, *Los Angeles, CA*
M. Judith Donovan Post, *Miami, FL*
Tina Young Poussaint, *Boston, MA*
Joana Ramalho, *Lisbon, Portugal*
Otto Rapalino, *Boston, MA*
Álex Rovira-Cañellas, *Barcelona, Spain*
Paul M. Ruggieri, *Cleveland, OH*
Zoran Rumboldt, *Rovinj-Rovigno, Croatia*
Amit M. Saindane, *Atlanta, GA*
Erin Simon Schwartz, *Philadelphia, PA*
Lubdha M. Shah, *Salt Lake City, UT*
Aseem Sharma, *St. Louis, MO*
J. Keith Smith, *Chapel Hill, NC*
Maria Vittoria Spampinato, *Charleston, SC*
Gordon K. Sze, *New Haven, CT*
Krishnamoorthy Thamburaj, *Hershey, PA*
Cheng Hong Toh, *Taipei, Taiwan*
Thomas A. Tomsick, *Cincinnati, OH*
Aquila S. Turk, *Charleston, SC*
Willem Jan van Rooij, *Tilburg, Netherlands*
Arastoo Vossough, *Philadelphia, PA*
Elysa Widjaja, *Toronto, Ontario, Canada*
Max Wintermark, *Stanford, CA*
Ronald L. Wolf, *Philadelphia, PA*
Kei Yamada, *Kyoto, Japan*
Carlos Zamora, *Chapel Hill, NC*

EDITORIAL FELLOW

Vahe Zohrabian, *New Haven, CT*

SPECIAL CONSULTANTS TO THE EDITOR

AJNR Blog Editor

Neil Lall, *Denver, CO*

Case of the Month Editor

Nicholas Stence, *Aurora, CO*

Case of the Week Editors

Juan Pablo Cruz, *Santiago, Chile*
Sapna Rawal, *Toronto, Ontario, Canada*

Classic Case Editor

Sandy Cheng-Yu Chen, *Taipei, Taiwan*

Facebook Editor

Peter Yi Shen, *Sacramento, CA*

Health Care and Socioeconomics Editor

Pina C. Sanelli, *New York, NY*

Physics Editor

Greg Zaharchuk, *Stanford, CA*

Podcast Editor

Wende N. Gibbs, *Los Angeles, CA*

Twitter Editor

Jennifer McCarty, *Atlanta, Georgia*

YOUNG PROFESSIONALS ADVISORY COMMITTEE

Asim K. Bag, *Birmingham, AL*
Anna E. Nidecker, *Sacramento, CA*
Peter Yi Shen, *Sacramento, CA*

Founding Editor
Juan M. Taveras

Editors Emeriti
Mauricio Castillo, Robert I. Grossman,
Michael S. Huckman, Robert M. Quencer

Managing Editor
Karen Halm

Assistant Managing Editor
Laura Wilhelm

Digital Publications and Social Media Coordinator
Kylie Mason

Executive Director, ASN
Mary Beth Hepp



Title: KR Wholesale Flower Market on Eve of Diwali. Flowers have a unique sociocultural significance in India. These garlands of chrysanthemum alternating with rose are classically seen in Bangalore in southern India at every flower vendor. Commonly used to decorate doors, windows, and staircases on festive occasions such as Ugadi, Dussera, and Diwali, they may be used any day to express the happiness of a household.

Hima Pendharkar, DMRD, DNB, DM (Neuroradiology), Additional Professor, Department of Neuroimaging & Interventional Radiology, National Institute of Mental Health & Neurosciences, Bangalore, Karnataka, India

Blunt Cerebrovascular Injuries: Advances in Screening, Imaging, and Management Trends

 P. Nagpal,  B.A. Policeni,  G. Bathla,  A. Khandelwal,  C. Derdeyn, and  D. Skeete



ABSTRACT

SUMMARY: Blunt cerebrovascular injury is a relatively uncommon but sometimes life-threatening injury, particularly in patients presenting with ischemic symptoms in that vascular territory. The decision to pursue vascular imaging (generally CT angiography) is based on clinical and imaging findings. Several grading scales or screening criteria have been developed to guide the decision to pursue vascular imaging, as well as to recommend different treatment options for various injuries. The data supporting many of these guidelines and options are limited however. The purpose of this article is to review and compare these scales and criteria and the data supporting clinical efficacy and to make recommendations for future research in this area.

ABBREVIATIONS: ATT = antithrombotic therapy; BCVI = blunt cerebrovascular injury; EAST = Eastern Association for the Surgery of Trauma

Blunt injury of the carotid and vertebral arteries (collectively termed blunt cerebrovascular injury [BCVI]) is an injury in patients caused by blunt trauma. Early studies (in the absence of screening) showed an incidence as low as 0.08%,¹ but with the increased screening and use of CT angiography as the diagnostic test, the incidence is now estimated to be between 1.2% and 2.99% of trauma admissions.²⁻⁴ These injuries can have high morbidity and mortality. Many patients with BCVI ultimately die from other injuries; nonetheless, earlier studies (in which BCVI diagnosis was based on symptoms and not on screening) showed that isolated BCVI-related death could be as high as 38%,^{5,6} with permanent neurologic deficits in most patients.⁷ Stroke is one of the most feared outcomes of BCVI, with a reported overall incidence of 10%–13% in recent literature.^{4,8} Nearly half of the patients with stroke have symptoms before reaching the hospital.^{4,8} Among asymptomatic patients with BCVI, aggressive screening and timely treatment have been shown to decrease the incidence of stroke to <1%.^{9,10}

Initially, digital subtraction angiography was used for diagnosis, but with advances in technology, CTA is considered the im-

aging technique of choice, with a sensitivity and specificity of nearly 98% and 100%, respectively.^{11,12} Various screening criteria have been proposed for patients with blunt trauma, with the Modified Denver Criteria being the most accepted¹³⁻¹⁵; however, other criteria (such as the Memphis Criteria¹⁶ and Boston Criteria¹⁷) may make implementation of protocol confusing and challenging for practitioners. Also, there are no specific guidelines for screening these injuries in the pediatric population. Studies have postulated that the relatively low incidence of BCVI in children with trauma (0.03%–0.9% reported incidence¹⁸⁻²⁰) may be due to poor understanding of risk factors.^{21,22} Although scientific evidence may be lacking, commonly used BCVI screening criteria, which are based on studies in the adult population, may not be appropriate for children and may be leading to increased use of CTA, and hence more radiation to children.²²

In addition to the identification of high-risk patients for screening, BCVI diagnosis may also be impacted by the appropriate use of imaging techniques and the familiarity of the radiologist with the imaging findings. The need for greater awareness of BCVI was also highlighted in a recent survey²³ of radiologists based in large academic institutes, which showed that only 14.2% (5/35) of respondents identified commonly used screening criteria and none of them used injury grading in their reports. This review describes the injury mechanisms, various screening criteria and associations, imaging protocols, CT appearance and grading, and management of BCVI.

BCVI Mechanism and Pathophysiology

The major mechanisms of injury causing BCVI are extreme rotation and hyperextension, with contralateral head rotation, direct

From the Department of Radiology (P.N., B.A.P., G.B., C.D.) and Trauma Services (D.S.), Department of Surgery, University of Iowa Hospitals and Clinics, Iowa City, Iowa; and Department of Radiology (A.K.), Mayo Clinic, Rochester, Minnesota.

Please address correspondence to Bruno A. Policeni, MD, MBA, Department of Radiology, University of Iowa Hospitals and Clinics, Iowa City, IA 52242; e-mail: bruno-policeni@uiowa.edu; @bpoliceni, @pnagpalMD

 Indicates open access to non-subscribers at www.ajnr.org

 Indicates article with supplemental on-line tables.

 Indicates article with supplemental on-line photo.

<http://dx.doi.org/10.3174/ajnr.A5412>

Table 1: Published screening criteria for BCVI

Name of Screening Criteria	Patients to Be Screened	
	Signs/Symptoms of BCVI	Risk Factors of BCVI
Modified ^a Denver Criteria ¹⁴	Arterial hemorrhage (from neck, nose, or mouth) Cervical bruit (in younger than 50 yr of age) Expanding cervical hematoma Focal neurologic defect: TIA, hemiparesis, vertebrobasilar symptoms, Horner syndrome Stroke on CT or MRI Neurologic deficit inconsistent with head CT	High-energy transfer mechanism with the following: LeFort II or III fracture Basilar skull fracture involving carotid canal Cervical vertebral body or transverse foramen fracture, subluxation, or ligamentous injury at any level; any fracture at C1–C3 Closed head injury consistent with DAI and GCS <6 Near-hanging with anoxia Clothesline-type injury or seat belt abrasion with significant swelling, pain, or altered mental status
Memphis Criteria ¹⁶	Cervical spine fracture Neurologic exam not explained by brain imaging Horner syndrome LeFort II or III facial fractures Skull base fractures involving the foramen lacerum Neck soft-tissue injury (eg, seat belt injury or hanging)	

Note:—DAI indicates diffuse axonal injury; GCS, Glasgow Coma Scale.

^aSuggested expansion: occipital condyle fractures, mandibular fractures, traumatic brain injuries with thoracic injuries, scalp degloving, thoracic vascular injuries, and blunt cardiac rupture.⁹

Table 2: Boston Criteria¹⁷ for BCVI

First Tier ^a	Second Tier ^b
Skull base fractures: petrous and basilar fractures Any cervical spine fractures Cervical spine injury (cord, vertebral body, or ligaments) Soft-tissue injury to anterior neck with swelling/ecchymosis/hematoma/or bruit Significant neurologic deficit: lateralizing neurologic deficit, TIA, Horner syndrome Evidence of brain infarct on CT	DAI Complex facial fractures with midface instability Combined significant head and chest trauma Near-hanging Seat belt abrasions on neck Other unexplained neurologic deficits: vertigo, tinnitus, or GCS ≤6

Note:—DAI indicates diffuse axonal injury; GCS, Glasgow Coma Scale.

^aFirst tier criteria: CTA screening on presentation.

^bSecond tier criteria: CTA screening within 24–48 hours of presentation.

blunt injury to the vessel, injury from the fracture fragment, and direct intraoral trauma.^{24,25} BCVI may occur anywhere along the vessel, with the cervical carotid vessel near the skull base and the vertebral artery segments along the transverse foramina being the most common locations. The extracranial segments are more vulnerable to injury because they are more superficial and mobile and run near bony structures. Carotid artery injuries are most common at the distal extracranial segment, with injuries relating to stretching over the lateral masses of the C1–C3 vertebrae from hyperextension and contralateral head rotation.^{15,24,26,27} The vertebral artery is most commonly injured in the pars transversaria (V2) or the atlas loop (V3) due to laceration from fracture fragments or stretching.^{24,28} The BCVI typically begins at the intima or media as an intimal tear or intramural hematoma. Postmortem series have shown complete arterial transection in approximately one-third of cases,²⁹ but this is not as common in clinical practice.^{6,30,31} If the blood from arterial transection is contained by periarterial soft tissue or decompresses into the adjacent injured vein, it forms a pseudoaneurysm or arteriovenous fistula, respectively.⁶

The eventual neurologic damage is most commonly from thromboembolism of platelet aggregates that form at the site of intimal injury. Platelet aggregates or intramural hematoma can also lead to luminal narrowing or occlusion that can cause low-flow infarcts.^{32,33} Typically, these ischemic infarcts occur

Table 3: Utah Score²² for probability of BCVI in the pediatric population

Variable	Score ^a
GCS score ≤8	1
Focal neurologic deficit	2
Carotid canal fracture	2
Petrous temporal bone fracture	3
Cerebral infarct on CT	3
All	11

^aScore ≤2 = low risk (7.9% risk per initial study²² and 2.7% per validation study⁴⁰). Score ≥3 = high risk (score of 3 had a 39.3% risk of BCVI per initial study²² and 18.1% risk per validation study⁴⁰).

between 10 and 72 hours after the injury.^{7,34} Arterial transection can cause exsanguination and AVF. Patients with AVFs can have symptoms related to increased venous pressure or steal phenomenon.

BCVI Screening

As with any entity, the utility of screening for BCVI is based on early diagnosis and treatment in a relatively asymptomatic stage, possibly preventing adverse outcomes. If injuries are not recognized and treated early, patients can have irreversible neurologic symptoms. Many screening criteria have been proposed to identify patients at risk of BCVI. Initial studies on BCVI were performed at the Denver Health Medical Center and the University of Tennessee Health Science Center, and the criteria proposed by them were named the Denver Criteria^{31,35} and the Memphis Cri-

Table 4: Denver grading system, corresponding CTA findings, and grade-based stroke incidence

Grade of Injury	Denver Grading System ³¹	CTA Findings	Stroke Incidence (%) ^{9,48} (CAI/VAI)
I	Irregularity of vessel wall Dissection or IMH with <25% narrowing	Nonstenotic luminal irregularity Intimal flap or wall thickening with <25% stenosis	3/6
II	Intraluminal thrombus Dissection or IMH with >25% narrowing	Luminal hypodensity Intimal flap or wall thickening with >25% stenosis	14/38
III	Pseudoaneurysm	Eccentric contrast-filled outpouching limited by periarterial tissue	26/27
IV	Occlusion	Lack of any intraluminal enhancement Carotid occlusions: abrupt or tapered Vertebral occlusion: usually abrupt	50/28
V	Transection	Irregular extravascular collection of contrast, not limited by periarterial tissue Increases in density on delayed images, if obtained	100/100

Note:—CAI indicates carotid artery injury; VAI, vertebral artery injury; IMH, intramural hematoma.

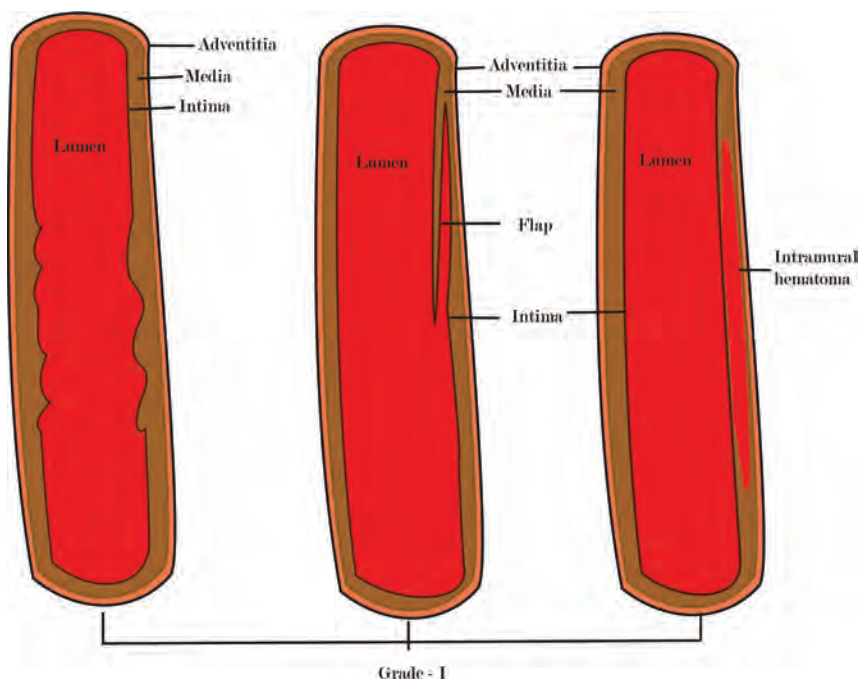


FIG 1. A diagram showing grade I injury patterns.



FIG 2. A 42-year-old man with a fall from a height. CTA shows a C2 transverse foramina fracture (black arrow in A) and type 3 dens fracture (black arrows in B) with irregularity of the left vertebral artery (white arrows), grade I injury.

teria (Tables 1 and 2), respectively.^{16,36} Among the cervical spine injuries, the Denver Criteria initially suggested screening in severe cervical hyperextension/rotation or hyperflexion (particularly if

associated with a displaced midface or complex mandibular fracture) or with cervical body fractures,³⁵ while the Memphis Criteria suggested screening in all cervical spine fractures.¹⁶ In 2007, the Denver group¹⁵ suggested a modification to include only specific cervical spine fracture patterns (complex cervical spine fractures such as subluxation, extension into the foramen transversarium, or upper C1–C3 fractures) for prompt screening.

Both the Western Trauma Association¹⁴ and the Eastern Association for the Surgery of Trauma¹³ (EAST) published their most recent guidelines in 2009 and 2010, respectively, and suggested that though scientific evidence may be lacking (level III recommendation), it may be most justifiable to screen asymptomatic patients based on the Modified Denver Criteria. Later studies showed that nearly 20% of cases of BCVI were missed if the pa-

tients were screened on the basis of the Modified Denver Criteria.^{10,37,38} These “missed” injuries were revisited, and in 2012, the Denver group suggested including mandible fractures, complex skull fractures, traumatic brain injury with thoracic injuries, scalp degloving, and thoracic vascular injuries in addition to previously described screening criteria.⁹ In 2016, the Denver group⁴ showed that the expanded Denver Criteria (On-line Figure) are effective in the detection of previously missed injuries and should now be used for screening. In their study, they found that the overall incidence of BCVI increased to 2.99% from 2.36% with expansion of screening criteria. At the same time, the BCVI-related neurologic event incidence decreased from 12% (18/150 patients) to 9.3% (22/236 patients). Adding to the number of screening criteria, additional Boston Criteria (Tables 1 and 2) have been recently proposed for detection of BCVI, based on a study at Boston Medical Center.¹⁷ The Modified Denver Criteria are most studied, are endorsed by the EAST and Western Trauma Association, and

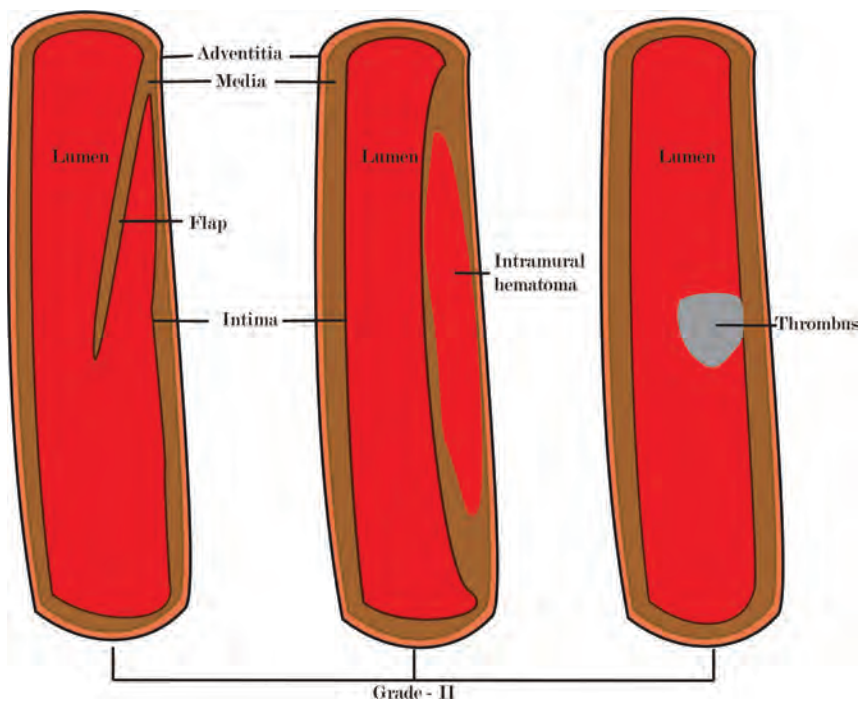


FIG 3. A diagram showing grade II injury patterns.

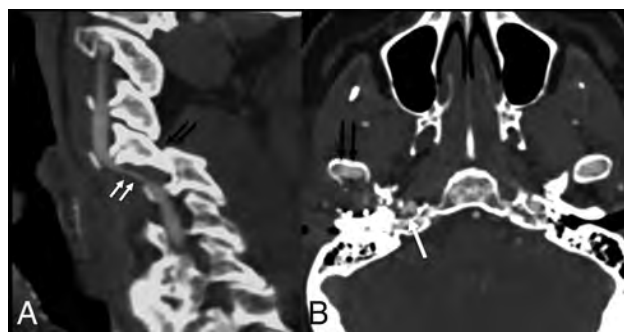


FIG 4. Two patients after motor vehicle collisions and grade II injuries. Sagittal CTA (A) shows locked C5–6 facets (black arrows), with intramural hematoma of the left vertebral artery causing >50% narrowing (white arrows). Axial CTA (B) shows a right mandibular condyle fracture (black arrows) with nonocclusive thrombus (white arrow) in the right internal carotid artery.

are most commonly used. Because the current literature suggests that BCVI may be missed on the Modified Denver Criteria, further expansion as suggested by the Denver group may be appropriate. However, additional multicenter validation studies are needed to identify the best screening criteria.

BCVI in the Pediatric Population

The EAST guidelines recommend that the adult screening guidelines be applied to the pediatric population.¹³ A study by Kopelman et al¹⁹ in 2011 also supported this recommendation; however, in 2012, a study by Jones et al²¹ showed that more than two-thirds of pediatric patients with BCVI and stroke-like symptoms did not have the adult screening risk indications. Overall, the incidence of BCVI is less in the pediatric population compared with adults, which could, in part, be due to less screening in children, as highlighted in the multicenter Arizona-Texas-Oklahoma-Memphis-Arkansas Consortium study.¹⁸ Also,

the pattern of intracranial injury in the pediatric population may be different from that in adults.³⁹ BCVI in pediatric patients was retrospectively analyzed by Ravindra et al²² from the University of Utah School of Medicine in 2015, and they suggested the Utah Score (Table 3) for estimated risk of BCVI in children. A recent multicenter validation study of the Utah Score also showed that compared with the Denver Criteria, the Utah Score correlated better with the risk of BCVI in the pediatric population and the Denver Criteria would have led to overscreening and unnecessary radiation exposure.⁴⁰ The initial study showed that a score of ≤ 2 had a 7.9%²² risk of BCVI, whereas the validation study showed an even lower number of 2.7%⁴⁰ BCVI risk. A score of ≥ 3 had a BCVI risk of 39.3% per the initial study²² and 18.1% per the validation study.⁴⁰ For high-risk patients, CTA is the imaging test of choice. For low-risk (Utah Score ≤ 2), the authors suggested that delayed MR angiography should be considered if there is clinical

suspicion. This may be an area of further research because currently no pediatric population studies exist to support MRA in low-risk patients.

Imaging Modalities for BCVI

Evaluation of the BCVI may be performed with CTA, MR imaging/MRA, or DSA. Despite its portable nature and bedside availability, duplex sonography assessment of BCVI is not preferred because about 90% of lesions are in sonographically nonaccessible segments. Additionally, duplex sonography is operator-dependent, with higher chances of missing dissecting aneurysms²⁴ and lower sensitivity (38.6% for both the carotid and vertebral injuries, 86% for carotid injuries alone).¹³ The EAST guidelines¹³ recommend against the use of duplex sonography for screening. CTA, on the other hand, is fast, noninvasive, readily available, and has high spatial resolution, which is preferred for diagnosing injuries in smaller vessels. It also evaluates coexisting bony and soft-tissue injuries. The initial studies on single- and 4-section scanners showed a sensitivity of 45%–70% for BCVI compared with DSA.^{16,41} However, subsequent studies with 16-section or higher CT scanners have shown that the sensitivity and specificity of BCVI diagnosis approaches 100%.^{5,12,13} Hence, CTA is considered the screening technique of choice for BCVI.^{6,13,24,42} The EAST guidelines¹³ recommend against the use of ≤ 4 -section multidetector array CTA for BCVI screening. With newer generation CT technology (enabling ultrafast imaging with even higher spatial resolution, metal artifact reduction, and low contrast dose), the role of CT continues to expand.⁴³

DSA is regarded as the criterion standard for the diagnosis of BCVI but has certain limitations. It is not readily available and may not be feasible to perform in a critically injured patient. Transportation of the patient to the angiography suite and the

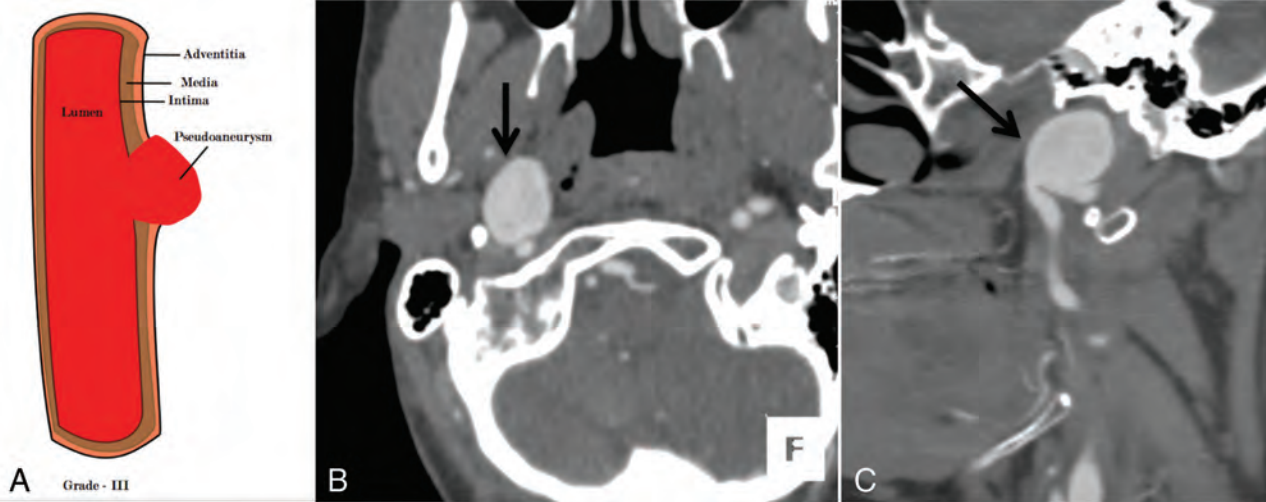


FIG 5. A 36-year-old man with a fall from a height and a C6 fracture (not shown). An illustrative diagram (A) shows grade III injury. CTA axial (B) and sagittal (C) images show a focal outpouching of the anterior wall of the distal cervical right ICA (black arrow), suggesting a pseudoaneurysm, grade III injury. Case courtesy Sachin S. Saboo, MD, UT Southwestern Medical Center, Dallas, Texas.

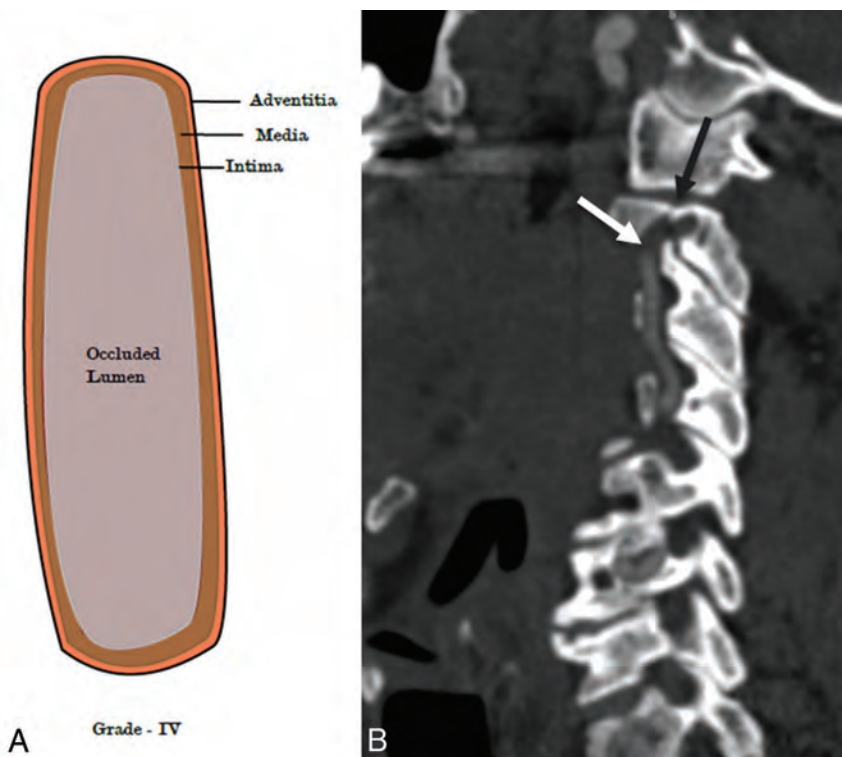


FIG 6. A 64-year-old man with blunt trauma to the neck. An illustrative diagram (A) shows grade IV injury. CTA sagittal image (B) shows a fracture of the C2 transverse foramina (black arrow) with abrupt occlusion of the right vertebral artery (white arrow), grade IV injury.

procedural time add to the delay in diagnosis. Also, it is invasive and has a complication rate of 1%–3%, which includes vascular dissection and thromboembolism. Furthermore, DSA provides no information about the vessel wall and is therefore limited in characterizing vessel wall hematomas.^{24,42} With the universal use of CT for diagnosis, DSA is mostly performed only when an intervention is planned.

MRA also offers comprehensive vessel imaging with the added benefit of non-nephrotoxic contrast, concurrent assessment of ligamentous/spinal injuries, and simultaneous detection of in-

farction. However, the current literature is limited on the use of MR imaging for BCVI, with a reported sensitivity of approximately 50%.¹⁶ As per the EAST guidelines,¹³ it is not recommended as a single technique for diagnosis. MR imaging has a complementary role, with improved differentiation of intramural hematoma, atherosclerotic plaques, and intraluminal thrombus in carotid or vertebral dissections.^{44,45} The limitations of MR imaging include longer scanning times, lack of widespread availability, the need for MR imaging-compatible lines and tubes in an acutely injured patient, inferior spatial resolution, and low sensitivity in characterizing acute intramural hematoma (that is isointense in the acute stage).^{24,42} MRA is mostly used complementary to CTA in selected cases and for follow-up (in children or patients with kidney disease).

CT and MR Imaging Protocol for BCVI Screening

Almost universally, nearly all patients with suspected BCVI are screened by CTA. The trauma imaging protocol pan

scan starts as noncontrast CT of the head and cervical spine, which are reviewed by the trauma surgery team or the radiologist at the CT scanner before the administration of IV contrast. If any injury necessitating BCVI screening is noted, CTA of the head and neck is also performed along with contrast-enhanced CT of the chest, abdomen, and pelvis (and reconstructions of the thoracolumbar spine) with a single intravenous contrast injection. If the injury requiring BCVI screening is noted later, CTA is performed within 24–36 hours of the injury. MR imaging is rarely used for screening. If used, it is mostly in pediatric patients or in patients

with absolute contraindications to CT contrast. The CTA and MRA protocol at our institution is highlighted in On-line Tables 1 and 2, respectively. Multiplanar reconstructions and 3D postprocessing are always done. The images are reconstructed as volume-rendered images, which are helpful for better detection of stenosis and the relation of the abnormality to the adjacent bony and soft-tissue structures.⁴⁶ Low-grade BCVIs are also better detected on MPR and volume-rendered images.⁶ The 3D images are always interpreted in conjunction with the primary dataset and are never interpreted alone.

Imaging Findings and Grading of BCVI

On the basis of the appearance of these injuries, Biffel et al³¹ from the Denver Health Medical Center proposed an injury grading scale in 1999, with increasing risk of stroke and worse prognosis with increasing grade. This grading system was based on carotid injuries visualized with DSA, but it has been adopted for CTA and

MRA with the same grading system for both carotid and vertebral injuries.^{14,30,31} The Denver grading scale, corresponding CTA findings, and grade-based stroke risk are highlighted in Table 4. In 2015, a study by Crawford et al⁴⁷ reported that many of the injuries on CTA could not be initially graded per the Denver grading scale and were labeled as “indeterminate BCVI.” Follow-up of these injuries in 48 hours was suggested to rule in a true BCVI. Approximately 25% of these injuries were reclassified as true injuries, and 5% of patients with indeterminate BCVI developed cerebrovascular symptoms. In our experience, BCVI can always be graded on the Denver scale.

Grade I injury (luminal irregularity with <25% narrowing, Figs 1 and 2) is often subtle, non-flow-limiting, and better appreciated with multiplanar or volume-rendered images.^{6,24} CTA in patients with grade II injury (intraluminal thrombus, raised intimal flap, or dissection/intramural hematoma with >25% narrowing, Figs 3 and 4) may reveal crescentic wall thickening of variable length, luminal narrowing, or the presence of a dissection flap. On MR imaging, the visualization of an intramural hematoma depends on the stage of hemoglobin degradation, most apparent in the subacute stage when it has high signal on T1 images. Because the hematomas may be isointense in the acute (<7 days) and chronic (>2 months) phase, they may be missed.²⁴ Grade III injury (pseudoaneurysm, Fig 5) is seen as saccular outpouchings of variable size. The imaging appearance of grade IV injury (occlusion of the vessel) may vary. Occlusion is often abrupt in the vertebral circulation (Fig 6), whereas they are often long segments with gradual tapering in the carotid arteries (Fig 7).^{6,42} Patients with grade V injury (vessel transection, Fig 8) may have contrast extravasation into the surrounding soft tissues or adjacent vein (giving rise to an arteriovenous fistula). Although the exact site of the fistula may not be apparent on imaging, the presence of early draining veins or an increase in the size of the draining veins is useful for detecting its presence.⁶

The potential mimics of BCVI on imaging include atherosclerosis (seen as wall thickening and/or stenosis), fibromuscular dysplasia (seen as wall irregularity), a hypoplastic vertebral artery (seen as long-segment narrowing), an acutely looped cervical internal carotid artery (mimics a pseudoaneurysm), or early venous enhancement (may mimic an AVF).

Management and Follow-Up of BCVI

There is a dearth of controlled trials to help guide treatment of BCVI, but current guidelines (EAST and Western Trauma Association)^{13,14} suggest observation, surgical repair, antithrombotic therapy (ATT), and endovascular therapy as acceptable management strategies, based on injury location and grade and patient symptoms. If there is no contraindication (such as active bleeding), ATT is indicated for all patients because it lowers the chance of stroke to

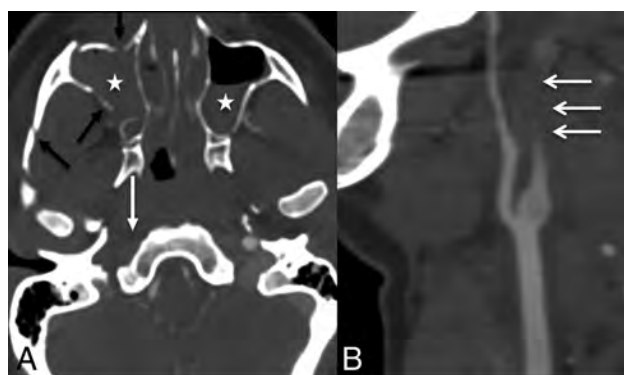


FIG 7. A 36-year-old woman after a motor vehicle collision with facial fractures. CTA axial (A) and sagittal (B) images show fractures of the zygomatic arch and maxilla (black arrows) with hemo sinus (stars) and tapered occlusion of the right ICA (white arrows), grade IV injury.

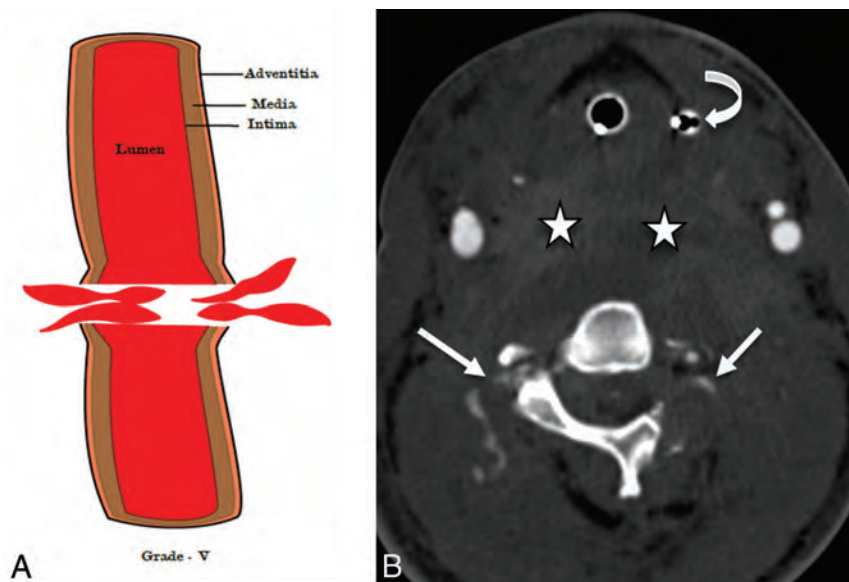


FIG 8. A 28-year-old man after a motor vehicle collision. An illustrative diagram (A) shows a grade V injury. CTA axial image (B) shows transection of the bilateral vertebral arteries with active contrast extravasation (white arrows), grade V injury. Also, note the large prevertebral neck hematoma (stars) displacing the orogastric tube (curved arrow) anteriorly. The patient also sustained C1 and C2 fractures (not shown).

Table 5: Grade-based treatment, follow-up, and suggested management of BCVI

Injury Grade	Initial Treatment	Surgical or Endovascular Treatment	Follow-Up ^a	Long-Term Treatment
I	Antithrombotic therapy ^b (preferably unfractionated heparin) or observation (rarely used)	Not needed	7–10 days, then 3–6 mo until healed	Antiplatelet therapy until healing
II	Antithrombotic therapy ^b	Needed if neurologic symptoms or progression of dissection	7–10 days, then 3–6 mo (until healed or definitive management)	Long-term antiplatelet therapy until healing or definitive interventional or surgical treatment
III		Needed if symptomatic or size >1 cm	7–10 days and then 3–6 mo or based on symptoms	Long-term antiplatelet therapy until healing or definitive treatment
IV		Typically not beneficial	Based on symptoms	Life-long antiplatelets
V	Direct pressure on actively bleeding area	Emergent intervention/surgery	Based on symptoms	No data (symptomatic)

^a Follow-up for asymptomatic carotid cavernous injury is 3–4 weeks.

^b Unless contraindicated.

<1%.^{4,10,14,48} The guidelines^{13,14} recommend the use of weight-based unfractionated heparin (10 U/Kg/h without a bolus and a low activated partial thromboplastin time goal of 40–50 seconds) because it is reversible compared with antiplatelets. The antiplatelet agents (clopidogrel, 75 mg daily, or aspirin, 325 mg daily) are equally as efficacious as heparin for stroke prevention^{10,49} and can be used in the acute setting if the patient has contraindications for heparin. The use of dual antiplatelets is not indicated and may increase the chance of bleeding. Earlier studies suggested that heparin could be transitioned to warfarin, but more recent studies have preferred antiplatelets for the long term due to a better safety profile, equivalent efficiency, and lower cost.^{10,14} Nearly one-third of patients have an initial contraindication to ATT, with concomitant traumatic brain or solid organ injury being the most common.³⁷ A recent study⁵⁰ showed that initiation of ATT at a median hospital day 3 in 119 patients with BCVI did not worsen traumatic brain or solid organ injury above baseline. A multidisciplinary team is valuable for open communication and discussion on antiplatelet and anticoagulant treatment in these patients, because these decisions can also be complex due to frequently associated intracranial and extracranial injuries.

While the ATT may suffice for grade I injuries because there is no flow-limiting potential, patients with grade II may need surgical or endovascular management if there is progression at follow-up (typically at 7–10 days). Grade III–V injuries are preferably repaired surgically or treated endovascularly (more common because most injuries are not surgically accessible). In grade V injuries (active bleeding), the guidelines^{13,14} suggest immediate attempts to control bleeding (direct pressure and emergent intervention/surgery). The management and follow-up of BCVI, depending on the injury grade, suggested by the Denver group⁴ is highlighted in Table 5. A recent multicenter study on the treatment and outcome of BCVI in the pediatric population showed a benefit of ATT with treatment approach similar to adults.⁵¹ The study, however, highlighted the lack of consensus for treatment among different institutions.

The Denver group⁴ and the current guidelines^{13,14} suggest follow-up of medically managed injuries (grades I, II, and sometimes III) at 7–10 days. If repeat imaging at this time reveals resolution of imaging findings, the therapy may be discontinued. If findings persist, the ATT may be further continued for 3–6 months, and the

patients reimaged to determine a further course of action. In case of worsening symptomatology or worsening imaging findings at 7–10 days, patients may be treated with an endovascular approach. The follow-up of patients managed by surgical or endovascular treatment is symptom-based and is usually decided on a case-by-case basis. The most recent expanded Denver BCVI screening criteria and management guideline⁴ are highlighted in the On-line Figure.

CONCLUSIONS

BCVIs are rare, but the incidence is increasing due to increasing high-velocity trauma, screening, and universal availability of CT. If undiagnosed, these can cause adverse neurologic outcome or death. Hence, the adoption of institutional screening criteria is suggested. Multiple screening criteria are available; however, the Modified Denver Criteria are the most well-studied. The Utah Score has been suggested for the pediatric population and was recently validated in a multicenter study; however, current trauma guidelines (the most recent being the EAST guidelines published in 2010) recommend the use of adult screening criteria. There is a need for randomized trials for establishment of screening criteria and treatment for adults and the pediatric population. Also, a radiologist should be aware of not only the imaging appearance but also the high-risk injury patterns because in these cases, the recommendation for evaluation with CTA should come from the radiologist. Familiarity with the injury grading scale is also needed for standardized reporting, to help trauma teams provide uniform definitive treatment based on the current standard of care.

Disclosures: Colin Derdeyn—UNRELATED: Stock/Stock Options: Pulse Therapeutics, Comments: novel stroke treatment device*; Travel/Accommodations/Meeting Expenses Unrelated to Activities Listed: Bayer AG, Comments: stroke lectures in Japan.* Dionne Skeete—UNRELATED: Other: Iowa Department of Public Health, American College of Surgeons, Comments: trauma center reviewer for the State of Iowa and the American College of Surgeons. There is a contract with the University of Iowa with the above entities. Compensation is given directly to the University of Iowa.* *Money paid to the institution.

REFERENCES

1. Davis JW, Holbrook TL, Hoyt DB, et al. **Blunt carotid artery dissection: incidence, associated injuries, screening, and treatment.** *J Trauma* 1990;30:1514–17 CrossRef Medline
2. Mutze S, Rademacher G, Matthes G, et al. **Blunt cerebrovascular**

- injury in patients with blunt multiple trauma: diagnostic accuracy of duplex Doppler US and early CT angiography. *Radiology* 2005; 237:884–92 CrossRef Medline
3. Berne JD, Reuland KS, Villarreal DH, et al. **Sixteen-slice multi-detector computed tomographic angiography improves the accuracy of screening for blunt cerebrovascular injury.** *J Trauma* 2006;60:1204–09; discussion 1209–10 CrossRef Medline
 4. Geddes AE, Burlew CC, Wagenaar AE, et al. **Expanded screening criteria for blunt cerebrovascular injury: a bigger impact than anticipated.** *Am J Surg* 2016;212:1167–74 CrossRef Medline
 5. Schneiderei NP, Simons R, Nicolaou S, et al. **Utility of screening for blunt vascular neck injuries with computed tomographic angiography.** *J Trauma* 2006;60:209–15; discussion 215–16 CrossRef Medline
 6. Sliker CW. **Blunt cerebrovascular injuries: imaging with multidetector CT angiography.** *Radiographics* 2008;28:1689–708; discussion 1709–10 CrossRef Medline
 7. Biffi WL, Moore EE, Ryu RK, et al. **The unrecognized epidemic of blunt carotid arterial injuries: early diagnosis improves neurologic outcome.** *Ann Surg* 1998;228:462–70 CrossRef Medline
 8. DiCocco JM, Fabian TC, Emmett KP, et al. **Functional outcomes following blunt cerebrovascular injury.** *J Trauma Acute Care Surg* 2013;74:955–60 CrossRef Medline
 9. Burlew CC, Biffi WL, Moore EE, et al. **Blunt cerebrovascular injuries: redefining screening criteria in the era of noninvasive diagnosis.** *J Trauma Acute Care Surg* 2012;72:330–35; discussion 336–37, quiz 539 CrossRef Medline
 10. Cothren CC, Biffi WL, Moore EE, et al. **Treatment for blunt cerebrovascular injuries: equivalence of anticoagulation and antiplatelet agents.** *Arch Surg* 2009;144:685–90 CrossRef Medline
 11. Bruns BR, Tesoriero R, Kufera J, et al. **Blunt cerebrovascular injury screening guidelines: what are we willing to miss?** *J Trauma Acute Care Surg* 2014;76:691–95 CrossRef Medline
 12. Eastman AL, Chason DP, Perez CL, et al. **Computed tomographic angiography for the diagnosis of blunt cervical vascular injury: is it ready for primetime?** *J Trauma* 2006;60:925–29; discussion 929 CrossRef Medline
 13. Bromberg WJ, Collier BC, Diebel LN, et al. **Blunt cerebrovascular injury practice management guidelines: the Eastern Association for the Surgery of Trauma.** *J Trauma* 2010;68:471–77 CrossRef Medline
 14. Biffi WL, Cothren CC, Moore EE, et al. **Western Trauma Association critical decisions in trauma: screening for and treatment of blunt cerebrovascular injuries.** *J Trauma* 2009;67:1150–53 CrossRef Medline
 15. Cothren CC, Moore EE, Ray CE Jr, et al. **Cervical spine fracture patterns mandating screening to rule out blunt cerebrovascular injury.** *Surgery* 2007;141:76–82 CrossRef Medline
 16. Miller PR, Fabian TC, Croce MA, et al. **Prospective screening for blunt cerebrovascular injuries: analysis of diagnostic modalities and outcomes.** *Ann Surg* 2002;236:386–93; discussion 393–95 CrossRef Medline
 17. Buch K, Nguyen T, Mahoney E, et al. **Association between cervical spine and skull-base fractures and blunt cerebrovascular injury.** *Eur Radiol* 2016;26:524–31 CrossRef Medline
 18. Azarakhsh N, Grimes S, Notrica DM, et al. **Blunt cerebrovascular injury in children: underreported or underrecognized?: a multicenter ATOMAC study.** *J Trauma Acute Care Surg* 2013;75:1006–11; discussion 1011–12 CrossRef Medline
 19. Kopelman TR, Berardini NE, O’Neill PJ, et al. **Risk factors for blunt cerebrovascular injury in children: do they mimic those seen in adults?** *J Trauma* 2011;71:559–64; discussion 564 CrossRef Medline
 20. Lew SM, Frumiento C, Wald SL. **Pediatric blunt carotid injury: a review of the National Pediatric Trauma Registry.** *Pediatr Neurosurg* 1999;30:239–44 CrossRef Medline
 21. Jones TS, Burlew CC, Kornblith LZ, et al. **Blunt cerebrovascular injuries in the child.** *Am J Surg* 2012;204:7–10 CrossRef Medline
 22. Ravindra VM, Riva-Cambria J, Sivakumar W, et al. **Risk factors for traumatic blunt cerebrovascular injury diagnosed by computed tomography angiography in the pediatric population: a retrospective cohort study.** *J Neurosurg Pediatr* 2015;15:599–606 CrossRef Medline
 23. Wu X, Malhotra A, Forman HP, et al. **The use of high-risk criteria in screening patients for blunt cerebrovascular injury: a survey.** *Acad Radiol* 2017;24:456–61 CrossRef Medline
 24. Nace SR, Gentry LR. **Cerebrovascular trauma.** *Neuroimaging Clin N Am* 2014;24:487–511, viii CrossRef Medline
 25. Crissey MM, Bernstein EF. **Delayed presentation of carotid intimal tear following blunt craniocervical trauma.** *Surgery* 1974;75:543–49 Medline
 26. Arthurs ZM, Starnes BW. **Blunt carotid and vertebral artery injuries.** *Injury* 2008;39:1232–41 CrossRef Medline
 27. Kang SY, Lin EM, Marentette LJ. **Importance of complete pterygo-maxillary separation in the Le Fort I osteotomy: an anatomic report.** *Skull Base* 2009;19:273–77 CrossRef Medline
 28. Arnold M, Bousser MG, Fahrni G, et al. **Vertebral artery dissection: presenting findings and predictors of outcome.** *Stroke* 2006;37:2499–503 CrossRef Medline
 29. Moar JJ. **Traumatic rupture of the cervical carotid arteries: an autopsy and histopathological study of 200 cases.** *Forensic Sci Int* 1987; 34:227–44 CrossRef Medline
 30. Biffi WL, Moore EE, Elliott JP, et al. **The devastating potential of blunt vertebral arterial injuries.** *Ann Surg* 2000;231:672–81 CrossRef Medline
 31. Biffi WL, Moore EE, Offner PJ, et al. **Blunt carotid arterial injuries: implications of a new grading scale.** *J Trauma* 1999;47:845–53 CrossRef Medline
 32. Biffi WL, Moore EE, Offner PJ, et al. **Blunt carotid and vertebral arterial injuries.** *World J Surg* 2001;25:1036–43 CrossRef Medline
 33. DeBette S, Leys D. **Cervical-artery dissections: predisposing factors, diagnosis, and outcome.** *Lancet Neurol* 2009;8:668–78 CrossRef Medline
 34. Esnault P, Cardinale M, Boret H, et al. **Blunt cerebrovascular injuries in severe traumatic brain injury: incidence, risk factors, and evolution.** *J Neurosurg* 2017;127:16–22 CrossRef Medline
 35. Biffi WL, Moore EE, Offner PJ, et al. **Optimizing screening for blunt cerebrovascular injuries.** *Am J Surg* 1999;178:517–22 CrossRef Medline
 36. Miller PR, Fabian TC, Bee TK, et al. **Blunt cerebrovascular injuries: diagnosis and treatment.** *J Trauma* 2001;51:279–85; discussion 85–86 CrossRef Medline
 37. Stein DM, Boswell S, Sliker CW, et al. **Blunt cerebrovascular injuries: does treatment always matter?** *J Trauma* 2009;66:132–43; discussion 143–44 CrossRef Medline
 38. Emmett KP, Fabian TC, DiCocco JM, et al. **Improving the screening criteria for blunt cerebrovascular injury: the appropriate role for computed tomography angiography.** *J Trauma* 2011;70:1058–63; discussion 1063–65 CrossRef Medline
 39. Sarkar K, Keachie K, Nguyen U, et al. **Computed tomography characteristics in pediatric versus adult traumatic brain injury.** *J Neurosurg Pediatr* 2014;13:307–14 CrossRef Medline
 40. Ravindra VM, Bollo RJ, Sivakumar W, et al. **Predicting blunt cerebrovascular injury in pediatric trauma: validation of the “Utah Score.”** *J Neurotrauma* 2017;34:391–99 CrossRef Medline
 41. Biffi WL, Ray CE Jr, Moore EE, et al. **Noninvasive diagnosis of blunt cerebrovascular injuries: a preliminary report.** *J Trauma* 2002;53:850–56 CrossRef Medline
 42. Liang T, Plaa N, Tashakkor AY, et al. **Imaging of blunt cerebrovascular injuries.** *Semin Roentgenol* 2012;47:306–19 CrossRef Medline
 43. Nagpal P, Mullan BF, Sen I, et al. **Advances in imaging and management trends of traumatic aortic injuries.** *Cardiovasc Intervent Radiol* 2017;40:643–54 CrossRef Medline
 44. Sakurai K, Miura T, Sagisaka T, et al. **Evaluation of luminal and vessel wall abnormalities in subacute and other stages of intracranial vertebral artery dissections using the volume isotropic turbo-spin-echo acquisition (VISTA) sequence: a preliminary study.** *J Neuroradiol* 2013;40:19–28 CrossRef Medline
 45. Hunter MA, Santosh C, Teasdale E, et al. **High-resolution double inversion recovery black-blood imaging of cervical artery dissection using 3T MR imaging.** *AJNR Am J Neuroradiol* 2012;33:E133–37 CrossRef Medline
 46. Nagpal P, Khandelwal A, Saboo SS, et al. **Modern imaging**

- techniques: applications in the management of acute aortic pathologies.** *Postgrad Med J* 2015;91:449–62 CrossRef Medline
47. Crawford JD, Allan KM, Patel KU, et al. **The natural history of indeterminate blunt cerebrovascular injury.** *JAMA Surg* 2015;150:841–47 CrossRef Medline
48. Biffl WL, Ray CE Jr, Moore EE, et al. **Treatment-related outcomes from blunt cerebrovascular injuries: importance of routine follow-up arteriography.** *Ann Surg* 2002;235:699–706; discussion 706–07 CrossRef Medline
49. Edwards NM, Fabian TC, Claridge JA, et al. **Antithrombotic therapy and endovascular stents are effective treatment for blunt carotid injuries: results from longterm followup.** *J Am Coll Surg* 2007;204:1007–13; discussion 1014–15 CrossRef Medline
50. Shahan CP, Magnotti LJ, McBeth PB, et al. **Early antithrombotic therapy is safe and effective in patients with blunt cerebrovascular injury and solid organ injury or traumatic brain injury.** *J Trauma Acute Care Surg* 2016;81:173–77 CrossRef Medline
51. Dewan MC, Ravindra VM, Gannon S, et al. **Treatment practices and outcomes after blunt cerebrovascular injury in children.** *Neurosurgery* 2016;79:872–78 CrossRef Medline

Development of High Signal Intensity within the Globus Pallidus and Dentate Nucleus following Multiple Administrations of Gadobenate Dimeglumine

G.M. Bolles, M. Yazdani, S.T. Stalcup, S.G. Creeden, H.R. Collins, P.J. Nietert, and D.R. Roberts



ABSTRACT

BACKGROUND AND PURPOSE: Previous studies have evaluated various gadolinium based contrast agents and their association with gadolinium retention, however, there is a discrepancy in the literature concerning the linear agent gadobenate dimeglumine. Our aim was to determine whether an association exists between the administration of gadobenate dimeglumine and the development of intrinsic T1-weighted signal in the dentate nucleus and globus pallidus.

MATERIALS AND METHODS: In this single-center, retrospective study, the signal intensity of the globus pallidus, dentate nucleus, thalamus, and middle cerebellar peduncle was measured on unenhanced T1-weighted images in 29 adult patients who had undergone multiple contrast MRIs using exclusively gadobenate dimeglumine (mean, 10.1 ± 3.23 doses; range, 6–18 doses). Two neuroradiologists, blinded to the number of prior gadolinium-based contrast agent administrations, separately placed ROIs within the globi pallidi, thalami, dentate nuclei, and middle cerebellar peduncles on the last MR imaging examinations. The correlations between the globus pallidus:thalamus and the dentate nucleus:middle cerebellar peduncle signal intensity ratios with the number of gadolinium-based contrast agent administrations and cumulative dose were tested with either 1-tailed Pearson or Spearman correlations. A priori, $P < .05$ was considered statistically significant.

RESULTS: Both the globus pallidus:thalamus and dentate nucleus:middle cerebellar peduncle ratios showed significant correlation with the number of gadolinium-based contrast agent administrations ($r = 0.39$, $P = .017$, and $r = 0.58$, $P = .001$, respectively). Additionally, the globus pallidus:thalamus and dentate nucleus:middle cerebellar peduncle ratios showed significant correlation with the cumulative dose of gadobenate dimeglumine ($r = 0.48$, $P = .004$, and $r = 0.43$, $P = .009$, respectively). Dentate nucleus hyperintensity was qualitatively present on the last MR imaging in 79.3%–86.2% of patients and in all patients who had received >10 doses.

CONCLUSIONS: At high cumulative doses (commonly experienced by patients, for example, with neoplastic disease), gadobenate dimeglumine is associated with an increase in the globus pallidus:thalamus and dentate nucleus:middle cerebellar peduncles signal intensity ratios.

ABBREVIATIONS: DN = dentate nucleus; GBCA = gadolinium-based contrast agent; GP = globus pallidus; MCP = middle cerebellar peduncle; TH = thalamus

Gadolinium-based contrast agents (GBCAs) are extensively used in evaluating both central nervous system and non-CNS pathologies with MR imaging and provide critical diagnostic

and treatment-guiding information. All GBCAs are composed of gadolinium and a chelating agent. Because gadolinium is an extremely toxic substance, chelating agents are designed to prevent release of gadolinium in the body before renal excretion.

In 2014, Kanda et al¹ first reported the development of progressively increasing signal intensity in the globus pallidus (GP) and dentate nucleus (DN) on unenhanced T1-weighted imaging in patients who had undergone multiple contrast MRIs with the administration of gadopentetate dimeglumine or gadodiamide. At postmortem examination, the cause of this high T1-weighted signal intensity in the GP and DN was shown to be retained gadolinium.^{2,3}

Subsequently, several studies evaluated various GBCAs and

Received August 29, 2017; accepted after revision October 30.

From the Department of Radiology and Radiological Sciences (G.M.B., M.Y., S.T.S., S.G.C., H.R.C., D.R.R.), Department of Neuroradiology, and Department of Public Health Sciences (P.J.N.), Medical University of South Carolina, Charleston, South Carolina.

Paper previously presented at: Annual Meeting of the American Society of Neuroradiology and the Foundation of the ASNR Symposium, April 22–27, 2017; Long Beach, California.

Dr Nietert's time on this project was funded, in part, by the National Institutes of Health National Center for Advancing Translational Science (grant No. UL1-TR001450) and the National Institute of General Medical Sciences (grant No. U54-GM104941).

Please address correspondence to Donna R. Roberts, MD, Department of Radiology and Radiological Sciences, 6 Jonathan Lucas St, MSC 323, Medical University of South Carolina, Charleston, SC 29425-3230; e-mail: robertdr@muscc.edu

Indicates open access to non-subscribers at www.ajnr.org

<http://dx.doi.org/10.3174/ajnr.A5510>

their association with gadolinium retention in both the adult⁴⁻¹¹ and pediatric populations.¹²⁻¹⁹ The general consensus is that linear, but not macrocyclic, GBCAs are associated with the development of hyperintense signal in the GP and DN on unenhanced T1-weighted images as demonstrated by most of these studies, though controversial findings remain.²⁰⁻²³ There is, however, discrepancy in the literature concerning the linear agent gadobenate dimeglumine.²⁴⁻²⁶ Ramalho et al²⁴ evaluated the signal intensity of the DN and GP in patients who received either gadodiamide, a linear nonionic GBCA, or gadobenate dimeglumine, a linear ionic contrast agent. While the administration of multiple doses of gadodiamide was associated with a significant increase in DN and GP T1-weighted signal intensity, the authors found only a significant trend toward an increase in relative percentage change in signal intensity for the DN in patients receiving multiple doses of gadobenate dimeglumine. However, the patients in this study received a mean of 4.6 ± 2.2 doses (range, 3–11 doses), whereas most studies have found the development of high T1-weighted signal in the DN only after >5 GBCA administrations.²⁷

Likewise, Schneider et al²⁶ reported no increase in the T1-weighted signal intensity of the DN in pediatric patients who had been exposed to a mean of 7.8 injections of gadobenate dimeglumine; however, the agent was administered at half dose (0.05 mmol/kg). On the other hand, a study by Weberling et al,²⁵ found a significant increase in the T1-weighted signal intensity in the DN after serial injections of gadobenate dimeglumine but not a significant correlation between the DN-to-pons ratio and the accumulated dose. The patient population in this study was predominantly those with melanoma (47/50 patients), and 14 patients had undergone radiation therapy, which may have confounded the results.

Given the discrepancies in the literature, the purpose of this study was to provide further evaluation of gadobenate dimeglumine by assessing a group of patients with various pathologies and no prior radiation exposure to the posterior fossa who had received at least 7 cumulative injections of exclusively gadobenate dimeglumine administered at the full FDA-approved dose of 0.1 mmol/kg.

MATERIALS AND METHODS

This single-center, retrospective, cohort study was performed after institutional review board approval, with a waiver of informed consent, in compliance with the Health Insurance Portability and Accountability Act. The biostatistician's time was covered by several National Institutes of Health grants. Otherwise, the study was unsponsored.

Patients

All patients at our institution who had undergone MR imaging of the brain with contrast administration from January 2013 until July 2016 were screened for inclusion in the study with the following criteria: 1) adult patients 18 years of age and older, 2) a minimum of 7 gadolinium-enhanced MR imaging scans (which included the last MR imaging for reference), and 3) all contrast MR imaging examinations performed exclusively with gadobenate dimeglumine. During this time, 11,669 MRIs of the brain with

and without gadobenate dimeglumine were performed, and 222 patients had received at least 7 doses of gadobenate dimeglumine.

Using both the local PACS and the electronic medical record, we excluded all patients who had undergone a contrast MR imaging outside our facility at any time to ensure documentation of all GBCA administrations. Additionally, to avoid possible confounding variables, we excluded patients with the following: 1) posterior fossa disease obscuring the dentate nucleus or middle cerebellar peduncle, 2) radiation exposure to the posterior fossa, 3) multiple sclerosis or other disease processes associated with intracranial intrinsic T1-shortening, 4) unsatisfactory images due to MR imaging or motion artifacts affecting the evaluation of the posterior fossa, and 5) any history of abnormal renal (estimated glomerular filtration rate at the time of imaging of <30 mL/min per 1.73 m²) or hepatic function as evaluated by routine laboratory tests.

Imaging Protocols

MR imaging was performed on either a 3T scanner (Skyra and/or Verio; Siemens, Erlangen, Germany) or a 1.5T scanner (Aera and/or Avanto; Siemens). The standard 1.5T MR imaging protocol included either axial T1-weighted spin-echo (TR, 500–588 ms; TE, 7.7–12 ms; slice thickness, 5-mm; gap 1.0) or 3D MPRAGE (TR, 1780–2200 ms; TE, 2.91–3.37 ms; slice thickness, 1.0 mm; gap, 0.5; FOV, 250 mm) before and after GBCA administration. The standard 3T MR imaging protocol included either axial T1-weighted spin-echo (TR, 500–550 ms; TE, 6.4–8.9 ms; slice thickness, 5 mm; gap, 1.0) or 3D MPRAGE (TR, 1690–2300 ms; TE, 2.3–3.2 ms; slice thickness, 1.0 mm; gap, 0.5; FOV, 250 mm) before and after GBCA administration. Gadobenate dimeglumine was administered as an intravenous bolus using body weight-adjusted dosing at 0.1 mmol/kg per departmental protocol.

Image and Data Analysis

Two neuroradiologists (M.Y. and S.T.S.), with 3 and 4 years of experience respectively, evaluated the images. Each reader was independently presented with the initial and final MR imaging of each patient in a randomized, blinded fashion on the PACS workstation and asked to qualitatively determine whether the DN demonstrated T1-weighted hyperintensity on the unenhanced T1-weighted images. The readers were blinded to the number of prior GBCA administrations.

In addition, each reader was asked to place ROIs by visual analysis within the GP, thalamus (TH), DN, and middle cerebellar peduncle (MCP) bilaterally, as described by Kanda et al,¹ on the last MR imaging scan. The mean signal intensity of each ROI was obtained and used to calculate the DN-to-MCP signal intensity ratio (DN:MCP) and the GP-to-TH signal intensity ratio (GP:TH) for each subject.

Statistical Analysis

To test the concordance between the 2 readers concerning the GP, TH, DN, and MCP mean signal intensity measurements, we calculated the Lin concordance correlation coefficient using on-line software (<https://www.niwa.co.nz/node/104318/concordance>).

The Shapiro-Wilk test was used to assess the normality of the data. For the GP:TH ratios, the *P* value was = .005, indicating that

Patient characteristics^a

Characteristic	
Total No. of patients	29
Age (yr)	52.1 ± 17.1 (18–84)
Sex (male/female)	20:9
No. of enhanced MRI scans ^b	10.1 ± 3.2 (6–18)
Cumulative dose (mL) ^b	175.2 ± 59.1 (76–316)
Interval (days) between 1st and final MRI	658.5 ± 250.5 (154–1154)
Diagnoses	Intracranial metastases (<i>n</i> = 10), primary brain neoplasm (<i>n</i> = 11), meningioma (<i>n</i> = 3), melanomas (<i>n</i> = 3), unknown lesion (<i>n</i> = 2)

^a Data are mean ± SD, with the range in parentheses.

^b Does not include the last MRI used for measurement.

the data were not normally distributed; therefore, a Spearman correlation was used to investigate the relationship between the GP:TH ratios on the final MR imaging examination and the number of administered GBCA doses as well as the total cumulative dose. For the DN:MCP ratios, the *P* value was 0.786, indicating a normal distribution; therefore, a Pearson correlation was used to assess the relationship between the DN:MCP ratios on the final MR imaging examination and the number of administered GBCA doses and the total cumulative dose. Statistical significance was considered at the $\alpha = .05$ threshold, and 1-tailed *P* values are reported (SPSS, Version 23; IBM, Armonk, New York).

Interrater reliability concerning the presence or absence of hyperintense T1-weighted signal within the dentate nucleus was assessed using the Cohen κ to determine the level of agreement between the 2 readers with the magnitude interpreted using common guidelines.^{28,29}

RESULTS

Twenty-nine patients met the inclusion/exclusion criteria during the study period, and the patient characteristics are described in the Table. The mean age of the patients was 52.1 ± 17.1 years. There were 20 men and 9 women. Most patients underwent imaging for the diagnosis of neoplasm. The mean number of prior GBCA administrations was 10.1 ± 3.23 doses (range, 6–18 doses). Note that 2 patients received only 7 GBCA administrations; therefore, at the time of the last enhanced MR imaging used for measurement, these 2 patients had previously received 6 GBCA doses. Cumulative doses of gadobenate dimeglumine ranged from 76 to 316 mL, with a mean of 175.2 ± 59.05 mL.

Concerning ROI measurements within the GP, TH, DN, and MCP, the value of the Lin correlation coefficient between readers ranged from 0.97 to 0.99, indicating substantial-to-near-perfect reader concordance. Therefore, the measurements from both readers were averaged.

The GP:TH and DN:MCP ratios on the last MR imaging both showed a significant correlation with the number of previous GBCA administrations: $r = 0.39$, $P = .017$, and $r = 0.58$, $P = .001$, respectively (Fig 1). There was also a significant correlation between the cumulative doses of gadobenate dimeglumine and the last GP:TH ratios ($r = 0.48$, $P = .004$) and the last DN:MCP ratios ($r = 0.43$, $P = .009$).

Higher doses of gadobenate dimeglumine resulted in qualitatively visible hyperintensity of the dentate nucleus on the

final MR imaging examination as reported by readers 1 and 2 in 79.3% and 86.2% of the patients, respectively (Fig 2). Both readers reported dentate nucleus hyperintensity in all patients who had received >10 doses of gadobenate dimeglumine. Concerning agreement between the 2 readers on the qualitative presence or absence of T1-weighted hyperintensity within the dentate nucleus on the final MR imaging, $\kappa = 0.77$, $P < .0005$ indicated substantial interobserver agreement.

DISCUSSION

In this study, we demonstrate significant positive correlations between the GP:TH and the DN:MCP ratios and the number of previous GBCA administrations and the total cumulative dose. Our findings are in agreement with the study of Weberling et al²⁵ and extend those results to patients with various intracranial pathologies without the potential confounding effect of radiation therapy.

In our study, hyperintensity within the GP and DN was demonstrated following the administration of a mean of 10.1 ± 3.2 doses. On the other hand, no significant increase in T1 signal on unenhanced images was seen in the GP or DN in the study of Ramalho et al,²⁴ following the administration of a mean of 4.6 ± 2.2 doses of gadobenate dimeglumine, but it was present following gadodiamide administered at a mean of 5.0 ± 2.4 doses. The larger mean dose of gadobenate dimeglumine in our study likely explains this discrepancy. Whether the mean dose required to produce T1 shortening on MR imaging is reflective of the rate or the amount of gadolinium deposition associated with a specific agent is unclear because several confounding factors influence the appearance of gadolinium on MR imaging, including the specific molecular species present. Animal and human postmortem studies will be helpful in comparing the various agents and quantifying their propensity for gadolinium deposition.

As a GBCA, gadobenate dimeglumine has several unique properties. Due to weak, transient interactions with serum albumin,^{30,31} gadobenate dimeglumine has high R1 relaxivity in vivo,^{32,33} resulting in greater signal intensity enhancement on T1-weighted images. In addition to renal excretion, a small percentage of gadobenate dimeglumine is excreted by the hepatobiliary system.³⁴ While gadobenate dimeglumine is a linear GBCA, it has not been associated with a high risk for nephrogenic systemic fibrosis.^{35–37} However, in animal^{38,39} and human serum⁴⁰ studies, gadobenate dimeglumine behaves as would be expected for a linear agent. Therefore, considering the unique properties of gadobenate dimeglumine, it is important to determine whether the agent is associated with T1-hyperintensities within specific regions of the brain. This knowledge is important for performing a clinical risk-versus-benefit analysis.

There were several limitations to this study. Patients could have received GBCA administrations at an outside institution without reporting this information to their clinicians; however, in addition to searching the PACS system for imported outside imaging, the medical records were thoroughly screened for any doc-

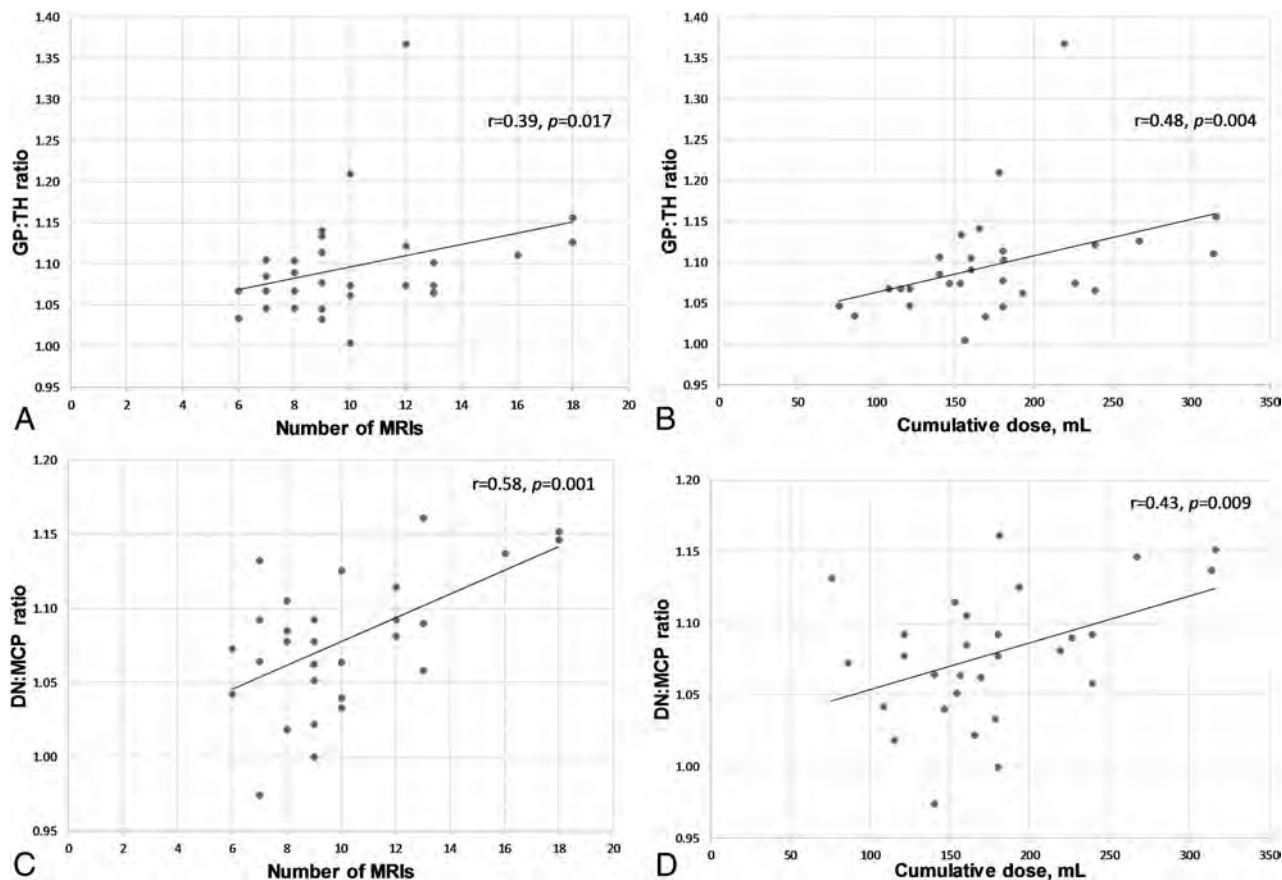


FIG 1. Graphs of the GP:TH and DN:MCP ratios plotted against the number of GBCA enhanced MR imaging scans (A and C) and the cumulative dose of gadobenate dimeglumine (B and D).

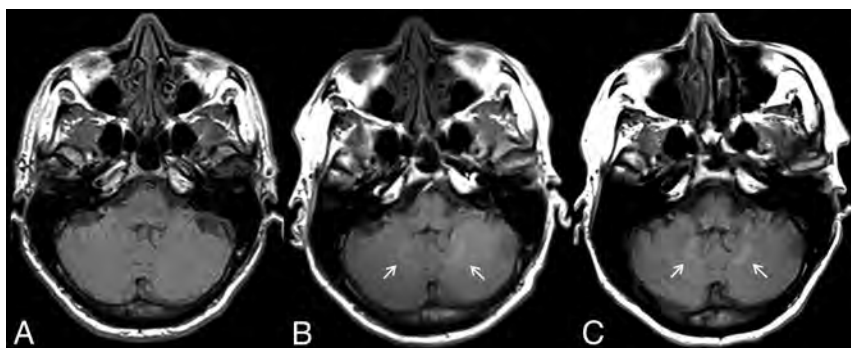


FIG 2. Unenhanced, axial T1-weighted MR images through the dentate nucleus in a 54-year-old man with metastatic renal cell carcinoma after the administration of 1 (A), 8 (B), and 18 (C) doses of gadobenate dimeglumine. There is a progressive increase in the T1 signal intensity in the dentate nucleus (arrows).

umentation of imaging before presentation to our institution. Varying field strengths and MR imaging parameters were used and precluded the calculation of relative percentage change. Finally, as in all studies of this nature, ROI placement is somewhat subjective and therefore subject to reader bias; however, the readers were blinded to the number of prior GBCA administrations; thus, this subjectivity is not likely to have confounded our study findings.

As mentioned in prior articles on the same topic, further studies, particularly those using tissue analysis, should continue to evaluate specific GBCAs and their propensity to deposit within

the human body. Furthermore, research evaluating any potential clinical sequelae from gadolinium deposition, both within the brain and other body tissues, should be performed. Continued prudence in selecting patients who should receive contrast-enhanced MRIs is recommended.

CONCLUSIONS

At higher cumulative doses, as can be experienced by patient groups, such as those with tumors, gadobenate dimeglumine is associated with a significant increase in the GP:TH and DN:MCP ratios on unenhanced T1-weighted images. These data should be incorporated into a risk-versus-benefit analysis when determining the need for GBCA administration in individual patients. While any potential clinical significance is unknown, the iatrogenic deposition of gadolinium within sensitive tissues such as the brain should be minimized in situations where alternative agents with similar clinical efficacy are available.

Disclosures: Paul J. Nietert—*RELATED: Grant:* National Institutes of Health.* Donna R. Roberts—*UNRELATED: Consultancy:* Guerbet, *Comments:* advisory board member; *Grants/Grants Pending:* Guerbet, *Comments:* investigator-initiated award site Principal Investigator, clinical trial*; *Travel/Accommodations/Meeting Expenses Unrelated to Activities Listed:* Guerbet. *Money paid to the institution.

REFERENCES

1. Kanda T, Ishii K, Kawaguchi H, et al. **High signal intensity in the dentate nucleus and globus pallidus on unenhanced T1-weighted MR images: relationship with increasing cumulative dose of a gadolinium-based contrast material.** *Radiology* 2014; 270:834–41 CrossRef Medline
2. Kanda T, Fukusato T, Matsuda M, et al. **Gadolinium-based contrast agent accumulates in the brain even in subjects without severe renal dysfunction: evaluation of autopsy brain specimens with inductively coupled plasma mass spectroscopy.** *Radiology* 2015;276: 228–32 CrossRef Medline
3. McDonald RJ, McDonald JS, Kallmes DF, et al. **Intracranial gadolinium deposition after contrast-enhanced MR imaging.** *Radiology* 2015;275:772–82 CrossRef Medline
4. Errante Y, Cirimele V, Mallio CA, et al. **Progressive increase of T1 signal intensity of the dentate nucleus on unenhanced magnetic resonance images is associated with cumulative doses of intravenously administered gadodiamide in patients with normal renal function, suggesting dechelation.** *Invest Radiol* 2014;49:685–90 CrossRef Medline
5. Quattrocchi CC, Mallio CA, Errante Y, et al. **Gadodiamide and dentate nucleus T1 hyperintensity in patients with meningioma evaluated by multiple follow-up contrast-enhanced magnetic resonance examinations with no systemic interval therapy.** *Invest Radiol* 2015; 50:470–72 CrossRef Medline
6. Radbruch A, Weberling LD, Kieslich PJ, et al. **High-signal intensity in the dentate nucleus and globus pallidus on unenhanced T1-weighted images: evaluation of the macrocyclic gadolinium-based contrast agent gadobutrol.** *Invest Radiol* 2015;50:805–10 CrossRef Medline
7. Cao Y, Huang DQ, Shih G, et al. **Signal change in the dentate nucleus on T1-weighted MR images after multiple administrations of gadopentetate dimeglumine versus gadobutrol.** *AJR Am J Roentgenol* 2016;206:414–19 CrossRef Medline
8. Stojanov DA, Aracki-Trenkic A, Vojinovic S, et al. **Increasing signal intensity within the dentate nucleus and globus pallidus on unenhanced T1W magnetic resonance images in patients with relapsing-remitting multiple sclerosis: correlation with cumulative dose of a macrocyclic gadolinium-based contrast agent, gadobutrol.** *Eur Radiol* 2016;26:807–15 CrossRef Medline
9. Bjørnerud A, Vatnehol SA, Larsson C, et al. **Signal enhancement of the dentate nucleus at unenhanced MR imaging after very high cumulative doses of the macrocyclic gadolinium-based contrast agent gadobutrol: an observational study.** *Radiology* 2017;285:434–44 CrossRef Medline
10. Radbruch A, Haase R, Kieslich PJ, et al. **No signal intensity increase in the dentate nucleus on unenhanced T1-weighted MR images after more than 20 serial injections of macrocyclic gadolinium-based contrast agents.** *Radiology* 2017;282:699–707 CrossRef Medline
11. Splendiani A, Perri M, Marsecano C, et al. **Effects of serial macrocyclic-based contrast materials gadoterate meglumine and gadobutrol administrations on gadolinium-related dentate nuclei signal increases in unenhanced T1-weighted brain: a retrospective study in 158 multiple sclerosis (MS) patients.** *Radiol Med* 2017 Sep 27. [Epub ahead of print] CrossRef Medline
12. Miller JH, Hu HH, Pokorney A, et al. **MRI brain signal intensity changes of a child during the course of 35 gadolinium contrast examinations.** *Pediatrics* 2015;136:e1637–40 CrossRef Medline
13. Roberts DR, Chatterjee AR, Yazdani M, et al. **Pediatric patients demonstrate progressive T1-weighted hyperintensity in the dentate nucleus following multiple doses of gadolinium-based contrast agent.** *AJNR Am J Neuroradiol* 2016;37:2340–47 CrossRef Medline
14. Roberts DR, Holden KR. **Progressive increase of T1 signal intensity in the dentate nucleus and globus pallidus on unenhanced T1-weighted MR images in the pediatric brain exposed to multiple doses of gadolinium contrast.** *Brain Dev* 2016;38:331–36 CrossRef Medline
15. Hu HH, Pokorney A, Towbin RB, et al. **Increased signal intensities in the dentate nucleus and globus pallidus on unenhanced T1-weighted images: evidence in children undergoing multiple gadolinium MRI exams.** *Pediatr Radiol* 2016;46:1590–98 CrossRef Medline
16. Flood TF, Stence NV, Maloney JA, et al. **Pediatric brain: repeated exposure to linear gadolinium-based contrast material is associated with increased signal intensity at unenhanced T1-weighted MR imaging.** *Radiology* 2017;282:222–28 CrossRef Medline
17. Radbruch A, Haase R, Kickingereder P, et al. **Pediatric brain: no increased signal intensity in the dentate nucleus on unenhanced T1-weighted MR images after consecutive exposure to a macrocyclic gadolinium-based contrast agent.** *Radiology* 2017;283:828–36 CrossRef Medline
18. Tibussek D, Rademacher C, Caspers J, et al. **Gadolinium brain deposition after macrocyclic gadolinium administration: a pediatric case-control study.** *Radiology* 2017;285:223–230 CrossRef Medline
19. Rossi Espagnet MC, Bernardi B, Pasquini L, et al. **Signal intensity at unenhanced T1-weighted magnetic resonance in the globus pallidus and dentate nucleus after serial administrations of a macrocyclic gadolinium-based contrast agent in children.** *Pediatr Radiol* 2017;47:1345–52 CrossRef Medline
20. Kanda T, Osawa M, Oba H, et al. **High signal intensity in dentate nucleus on unenhanced T1-weighted MR images: association with linear versus macrocyclic gadolinium chelate administration.** *Radiology* 2015;275:803–09 CrossRef Medline
21. Radbruch A, Quattrocchi CC. **Interpreting signal-intensity ratios without visible T1 hyperintensities in clinical gadolinium retention studies.** *Pediatr Radiol* 2017;47:1688–89 CrossRef Medline
22. Radbruch A, Weberling LD, Kieslich PJ, et al. **Gadolinium retention in the dentate nucleus and globus pallidus is dependent on the class of contrast agent.** *Radiology* 2015;275:783–91 CrossRef Medline
23. Radbruch A, Weberling LD, Kieslich PJ, et al. **Intraindividual analysis of signal intensity changes in the dentate nucleus after consecutive serial applications of linear and macrocyclic gadolinium-based contrast agents.** *Invest Radiol* 2016;51:683–90 CrossRef Medline
24. Ramalho J, Castillo M, AlObaidy M, et al. **High signal intensity in globus pallidus and dentate nucleus on unenhanced T1-weighted MR images: evaluation of two linear gadolinium-based contrast agents.** *Radiology* 2015;276:836–44 CrossRef Medline
25. Weberling LD, Kieslich PJ, Kickingereder P, et al. **Increased signal intensity in the dentate nucleus on unenhanced T1-weighted images after gadobenate dimeglumine administration.** *Invest Radiol* 2015;50:743–48 CrossRef Medline
26. Schneider GK, Stroeder J, Roditi G, et al. **T1 signal measurements in pediatric brain: findings after multiple exposures to gadobenate dimeglumine for imaging of nonneurologic disease.** *AJNR Am J Neuroradiol* 2017;38:1799–1806 CrossRef Medline
27. Kanda T, Oba H, Toyoda K, et al. **Brain gadolinium deposition after administration of gadolinium-based contrast agents.** *Jpn J Radiol* 2016;34:3–9 CrossRef Medline
28. Cohen J. **Weighted kappa: nominal scale agreement with provision for scaled disagreement or partial credit.** *Psychol Bull* 1968;70: 213–20 CrossRef Medline
29. Landis JR, Koch GG. **The measurement of observer agreement for categorical data.** *Biometrics* 1977;33:159–74 CrossRef Medline
30. Cavagna FM, Maggioni F, Castelli PM, et al. **Gadolinium chelates with weak binding to serum proteins: a new class of high-efficiency, general purpose contrast agents for magnetic resonance imaging.** *Invest Radiol* 1997;32:780–96 CrossRef Medline
31. de Haën C, Cabrini M, Akhnana L, et al. **Gadobenate dimeglumine 0.5 M solution for injection (MultiHance) pharmaceutical formulation and physicochemical properties of a new magnetic resonance imaging contrast medium.** *J Comput Assist Tomogr* 1999;23(Suppl 1):S161–68 CrossRef Medline
32. Pintaske J, Martirosian P, Graf H, et al. **Relaxivity of gadopentetate dimeglumine (Magnevist), gadobutrol (Gadovist), and gadobenate dimeglumine (MultiHance) in human blood plasma at 0.2, 1.5, and 3 Tesla.** *Invest Radiol* 2006;41:213–21 CrossRef Medline

33. Shen Y, Goerner FL, Snyder C, et al. **T1 relaxivities of gadolinium-based magnetic resonance contrast agents in human whole blood at 1.5, 3, and 7 T.** *Invest Radiol* 2015;50:330–38 CrossRef Medline
34. Kirchin MA, Pirovano GP, Spinazzi A. **Gadobenate dimeglumine (Gd-BOPTA): an overview.** *Invest Radiol* 1998;33:798–809 CrossRef Medline
35. Bruce R, Wentland AL, Haemel AK, et al. **Incidence of nephrogenic systemic fibrosis using gadobenate dimeglumine in 1423 patients with renal insufficiency compared with gadodiamide.** *Invest Radiol* 2016;51:701–05 CrossRef Medline
36. Nandwana SB, Moreno CC, Osipow MT, et al. **Gadobenate dimeglumine administration and nephrogenic systemic fibrosis: is there a real risk in patients with impaired renal function?** *Radiology* 2015; 276:741–47 CrossRef Medline
37. Martin DR, Kalb B, Mittal A, et al. **No Incidence of nephrogenic systemic fibrosis after gadobenate dimeglumine administration in patients undergoing dialysis or those with severe chronic kidney disease.** *Radiology* 2017 Jul 21. [Epub ahead of print] CrossRef Medline
38. Frenzel T, Apte C, Jost G, et al. **Quantification and assessment of the chemical form of residual gadolinium in the brain after repeated administration of gadolinium-based contrast agents: comparative study in rats.** *Invest Radiol* 2017;52:396–404 CrossRef Medline
39. McDonald RJ, McDonald JS, Dai D, et al. **Comparison of gadolinium concentrations within multiple rat organs after intravenous administration of linear versus macrocyclic gadolinium chelates.** *Radiology* 2017;285:536–45 CrossRef Medline
40. Frenzel T, Lengsfeld P, Schirmer H, et al. **Stability of gadolinium-based magnetic resonance imaging contrast agents in human serum at 37 degrees C.** *Invest Radiol* 2008;43:817–28 CrossRef Medline

High Signal Intensity in the Dentate Nucleus and Globus Pallidus on Unenhanced T1-Weighted MR Images: Comparison between Gadobutrol and Linear Gadolinium-Based Contrast Agents

F.G. Moser, C.T. Watterson, S. Weiss, M. Austin, J. Mirocha, R. Prasad, and J. Wang



ABSTRACT

BACKGROUND AND PURPOSE: In view of the recent observations that gadolinium deposits in brain tissue after intravenous injection, our aim of this study was to compare signal changes in the globus pallidus and dentate nucleus on unenhanced T1-weighted MR images in patients receiving serial doses of gadobutrol, a macrocyclic gadolinium-based contrast agent, with those seen in patients receiving linear gadolinium-based contrast agents.

MATERIALS AND METHODS: This was a retrospective analysis of on-site patients with brain tumors. Fifty-nine patients received only gadobutrol, and 60 patients received only linear gadolinium-based contrast agents. Linear gadolinium-based contrast agents included gadoversetamide, gadobenate dimeglumine, and gadodiamide. T1 signal intensity in the globus pallidus, dentate nucleus, and pons was measured on the precontrast portions of patients' first and seventh brain MRIs. Ratios of signal intensity comparing the globus pallidus with the pons (globus pallidus/pons) and dentate nucleus with the pons (dentate nucleus/pons) were calculated. Changes in the above signal intensity ratios were compared within the gadobutrol and linear agent groups, as well as between groups.

RESULTS: The dentate nucleus/pons signal ratio increased in the linear gadolinium-based contrast agent group ($t = 4.215, P < .001$), while no significant increase was seen in the gadobutrol group ($t = -1.422, P = .08$). The globus pallidus/pons ratios followed similarly, with an increase in the linear gadolinium-based contrast agent group ($t = 2.931, P < .0001$) and no significant change in those receiving gadobutrol ($t = 0.684, P = .25$).

CONCLUSIONS: Successive doses of gadobutrol do not result in T1 shortening compared with changes seen in linear gadolinium-based contrast agents.

ABBREVIATIONS: DN = dentate nucleus; GBCA = gadolinium-based contrast agent; GP = globus pallidus

The use of gadolinium-based contrast agents (GBCAs) has become an important adjunct for MR imaging examinations. Although GBCAs are considered extremely safe in patients without renal failure, it is known that free gadolinium (Gd^{3+}) is toxic to humans. The ability of a chelating agent to retain the gadolinium and therefore maintain its safety profile has been shown to correlate with the structure and stability of the chelating molecule.¹ As demonstrated by both in vivo and in vitro studies, macrocyclic chelating

agents are generally more stable than linear ones, bind Gd^{3+} more tightly, and have lower dissociation rates.¹⁻⁵

Recent data indicate that patients exposed to multiple administrations of certain GBCAs may exhibit dose-related T1 shortening in the globus pallidus (GP) and dentate nucleus (DN).⁶⁻¹² Moreover, these imaging findings have correlated with gadolinium deposition in the GP and DN on postmortem examinations, even in patients with relatively normal renal function.^{13,14} Increased signal intensity in the GP and DN on unenhanced T1-weighted MR images has been positively correlated with prior exposure to both ionic and nonionic linear GBCAs in patients.⁶

Results regarding macrocyclic agents have been more varied. In 2015, Kanda et al¹⁰ found that hyperintensity in the DN was associated with past administration of the linear GBCA gadopentate dimeglumine (Magnevist; Bayer HealthCare Pharmaceuticals, Wayne, New Jersey) but not with the macrocyclic GBCA gadoteridol (ProHance; Bracco Diagnostics, Princeton, New Jersey). While Radbruch et al⁹ did not find a significant signal inten-

Received June 26, 2017; accepted after revision November 15.

From the Department of Imaging (F.G.M., C.T.W., S.W., R.P.), S. Mark Taper Foundation Imaging Center, and Samuel Oschin Comprehensive Cancer Institute (J.M.), Cedars Sinai Medical Center, Los Angeles, California; Department of Radiology (M.A.), Lahey Clinic, Burlington, Massachusetts; and Bayer Healthcare (J.W.), Whippany, New Jersey.

This work was supported by Bayer Healthcare, Project No. 00042369.

Please address correspondence to Franklin G. Moser, MD, MMM, Department of Imaging, S. Mark Taper Foundation Imaging Center, Cedars Sinai Medical Center, 8700 Beverly Blvd, Los Angeles, CA 90048; e-mail: Franklin.Moser@cshs.org; @fgmosermd

<http://dx.doi.org/10.3174/ajnr.A5538>

sity increase in the DN and GP after progressive applications of the macrocyclic GBCA gadoterate meglumine (Dotarem; Guerbet, Aulnay-sous-Bois, France), Stojanov et al¹² found a significant increase in signal intensity within the DN and GP in patients with relapsing-remitting multiple sclerosis after multiple doses of the macrocyclic GBCA gadobutrol (Gadavist; Bayer Schering Pharma, Berlin, Germany). The study of Stojanov et al suggests that deposition of gadolinium within the brain may occur not solely as the result of linear GBCA administration but also with some types of macrocyclic agents. To confuse matters, the reports of Stojanov et al were quickly disputed by multiple contradicting studies showing no T1 signal change following the administration of the widely used macrocyclic agent gadobutrol.^{15,16}

Additionally, direct comparison between linear and macrocyclic GBCAs still must be explored. For example, while Stojanov et al¹² have demonstrated T1 shortening in the GP and DN following repeat administration of gadobutrol, the relative degree of these changes compared with those seen in linear-based agents has not been determined, and the results have been since challenged by a number of follow-up studies.¹⁶⁻¹⁸ The purpose of this study was to compare possible gadobutrol-related T1 signal intensity changes with those of linear agents in a similar population. Prior studies evaluating such T1 changes following the use of gadobutrol have resulted in limited power or cumulative dose per patient.^{15,16}

MATERIALS AND METHODS

Whole-brain MR imaging was performed using 1.5T (Symphony; Siemens, Erlangen, Germany) or 3T (Verio; Siemens) MR imaging units. Unenhanced T1-weighted MR images (3D MPRAGE) were obtained with the following parameters on 1.5T systems: TR = 1330 ms; TE = 4.8 ms; TI = 800 ms; flip angle = 15°; section thickness = 12.5 mm; matrix size = 256 × 192; echo-train length = 1. T1-weighting parameters on 3T systems were the following: TR = 2100 ms; TE = 3.0 ms; TI = 900 ms; flip angle = 9°; section thickness = 11 mm; matrix size = 256 × 256; echo-train length = 1.

Following institutional review board approval, patients were retrospectively selected from among neuroimaging patients at Cedars-Sinai Medical Center. Informed consent was waived given the retrospective nature of the study. The population selected for study consisted of patients who had undergone at least 7 prior contrast-enhanced MR imaging examinations. Due to the relative frequency of contrast-enhanced examinations associated with standard care, all patients had intra-axial malignancy, most commonly anaplastic astrocytoma or glioblastoma multiforme. All patients receiving gadolinium contrast agents had been screened for renal failure with serum creatinine levels.

As a result of an institution-wide contrast formulary policy change, it was simple to determine which contrast agents patients received. Before 2011, our institution had exclusively used linear, nonionic contrast agents, gadoversetamide (OptiMARK; Covidien, Irvine, California) and, to a lesser extent, gadodiamide (Omniscan; GE Healthcare, Piscataway, New Jersey). Between 2011 and February 2012, gadobenate dimeglumine (MultiHance; Bracco Diagnostics), a linear, ionic GBCA, became the primary

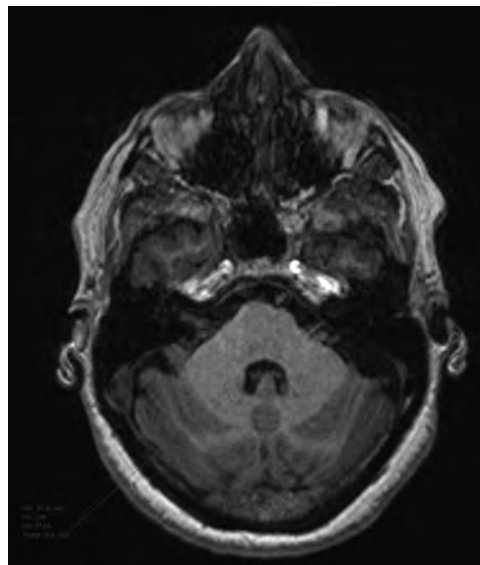


FIG 1. Dentate nucleus ROI selection.

contrast agent. After February 2012, we began to exclusively use gadobutrol (Gadavist), a macrocyclic GBCA, for all neuroimaging. This allowed us to have a population of patients who had received only the macrocyclic agent gadobutrol to compare against an earlier population who had received only linear GBCAs.

We used the following inclusion criteria: 1) Patients must have undergone at least 7 consecutive studies with gadobutrol or at least 7 scans with only linear contrast agents (OptiMARK, MultiHance, and Omniscan); 2) initial and final MRIs had both pre- and postcontrast T1-weighted images; 3) one class of contrast agent was exclusively used for all 7 examinations, either macrocyclic (exclusively gadobutrol) or linear (any combination of those mentioned above); 4) at least 1 basal ganglion and the posterior fossa were spared tumor or radiation effects; 5) subjects had normal renal function, defined as a glomerular filtration rate of >30; and 6) the seventh examination occurred at least 2 weeks following the sixth. Patients were excluded on the basis of the following: 1) tumor- or treatment-related change in the posterior fossa or bilateral globi pallidi; and 2) abnormal baseline T1 signal intensity ratio of >1:1 when comparing the DN with the pons.

The study population was divided into 2 groups: Group 1 included patients who received only gadobutrol, and group 2 included patients who received only linear contrast agents (OptiMARK, MultiHance, Omniscan). Following exclusion, group 1 contained 59 patients while group 2 contained 60. Anonymized data for each group were collected using Excel (Microsoft, Redmond, Washington) and were stored on-site in an encrypted fashion.

Two radiologists conducted a quantitative analysis of unenhanced T1-weighted images using ROI measurements. Measurements were made on the baseline scan and the seventh scan. In keeping with previously described techniques, ROIs were drawn over the left globus pallidus, dentate nucleus, lateral ventricle, and pons, and average signal intensity was recorded.^{12,19} Examples of ROI selection are presented as Figs 1–3. We compared DN and GP signal intensities with T1 measurements of the pons and calcu-

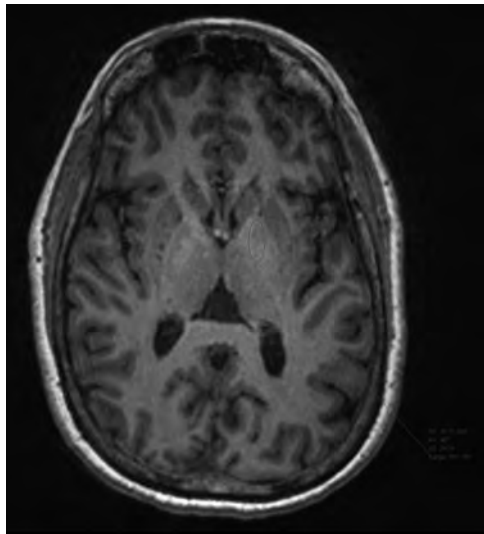


FIG 2. Globus pallidus ROI selection.

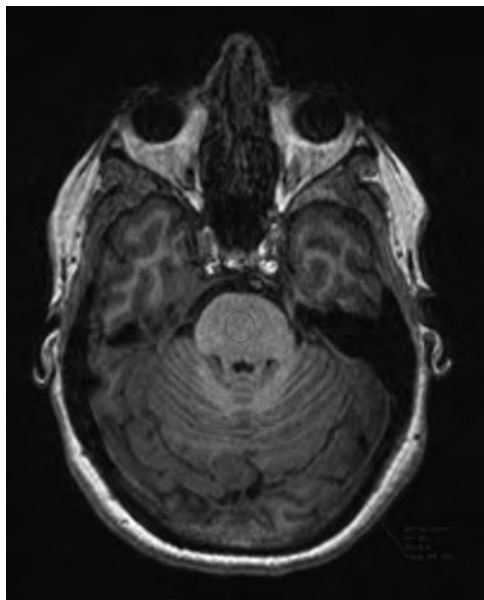


FIG 3. Pons ROI selection.

lated the ratios of these intensities: dentate nucleus/pons (DN/pons) and globus pallidus/pons (GP/pons).¹² If the left side could not be evaluated due to artifacts or pathology, the right side was used.

Statistical Analysis

In keeping with other authors' methods, it was decided that it would be best to compare ratios between the GP and pons as well as the DN and pons. Paired *t* tests were used to compare changes within a given group (ie, the gadobutrol group or the linear agent group) between the first and seventh examinations. Wilcoxon rank sum tests were used for between-group comparisons of the percentage change in the signal intensity ratio (either DN/pons or GP/pons) seen during the patients' 7 examinations. All statistical analysis was performed with Statistical Analysis Software, Version 9.2 (SAS Institute, Cary, North Carolina).

Table 1: Paired *t* test comparing DN/pons and GP/pons at time 1 versus 7 within groups

	DN/Pons		GP/Pons	
	Group 1: Gadobutrol	Group 2: Linear Agents	Group 1: Gadobutrol	Group 2: Linear Agents
No.	59	60	59	60
Mean change	-0.01	0.03	-0.01	0.03
SD	<0.005	<0.005	<0.005	0.01
<i>t</i>	-1.422	4.215	-0.684	2.931
<i>P</i>	.08	<.001	.25	.002

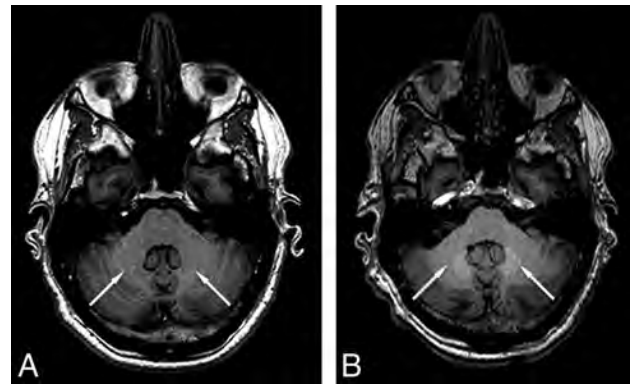


FIG 4. Sample images showing obvious signal increase, indicated by arrows, after 6 injections of linear GBCAs (B) compared with the baseline scan (A).

RESULTS

Consistent with expectations, a significant signal intensity increase was detected in the DN/pons ratio by the seventh examination in the linear agent group ($t = 4.215$, $P < .001$; Table 1). A sample pair of images showing the signal increase is shown in Fig 4. No significant change was demonstrated in the group receiving gadobutrol ($t = -1.422$, $P = .08$; Table 1). The difference between the signal changes seen in these 2 groups was also significant (+3.10% for those receiving linear GBCA; -0.8% for patients receiving gadobutrol; $P < .0001$; Fig 5 and Table 2).

Similarly, a significant increase was seen in the GP/pons ratio in the linear agent group between the first and seventh examinations ($t = 2.931$, $P = .002$; Table 1), while no such increase was seen in the group receiving gadobutrol ($t = 0.684$, $P = .25$; Table 1). Again, the difference in the percentage change between these groups was significant (+2.47% for the linear GBCA group; -0.30% in the gadobutrol group, $P = .033$; Fig 6 and Table 2).

DISCUSSION

The demonstration of a stable DN/pons T1 signal intensity ratio over subsequent administrations of gadobutrol supports the growing preponderance of evidence suggesting that macrocyclic GBCAs, as a class, are less likely to deposit gadolinium in the brain. As with previous examinations, the use of linear GBCAs was found to result in increased T1 signal in the globus pallidus and dentate nucleus.

There are several limitations to our study. Patient age was not controlled for, in favor of improving sample size. While all patients were seen for malignancy, nearly all with anaplastic astrocytoma or glioblastoma multiforme, the distributions of these

Table 2: Wilcoxon test comparing percentage change in DN/pons and GP/pons ratios from study 1 to study 7 between the gadobutrol and linear groups

Group	No.	Percentage Change (Mean)	SD	Median	Lower Quartile	Upper Quartile
DN/Pons						
Gadobutrol (group 1)	59	-0.80	4.78	-0.66	-4.24	2.21
Linear GBCAs (group 2)	60	3.10	5.56	3.70	-0.52	6.76
GP/Pons						
Gadobutrol (group 1)	59	-0.30	5.44	0.72	-3.56	2.26
Linear GBCAs (group 2)	60	2.47	6.53	2.05	-2.56	6.48

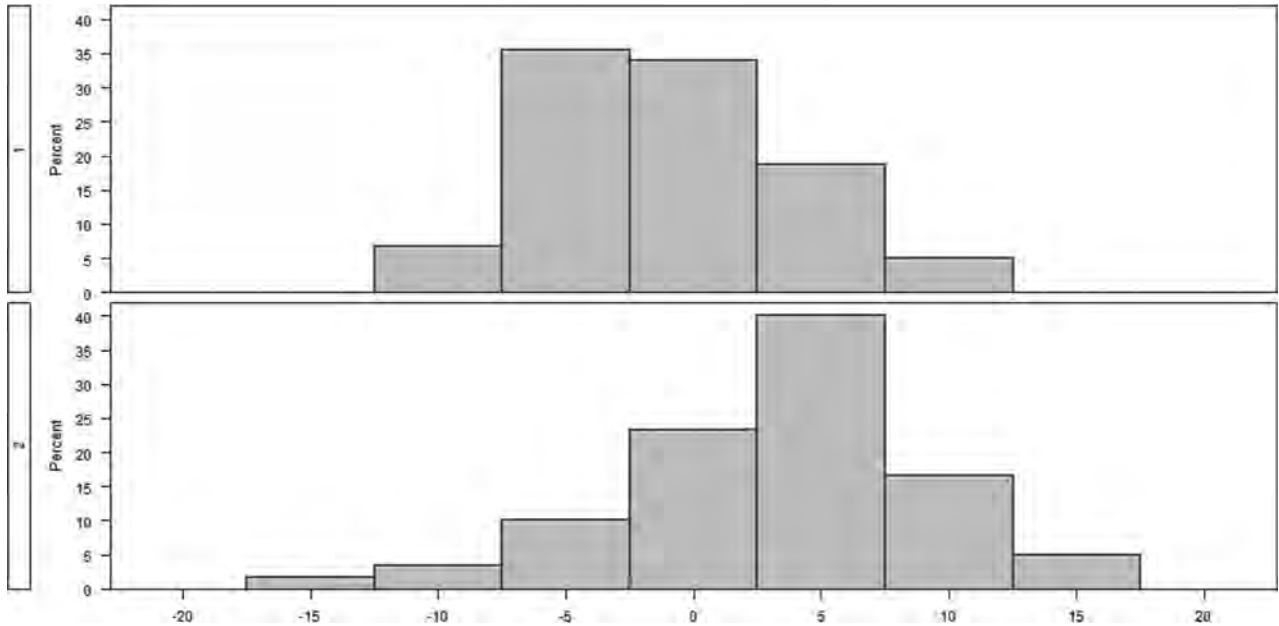


FIG 5. Group histograms for the relative percentage change in the DN/pons ratio from 1 to 7.

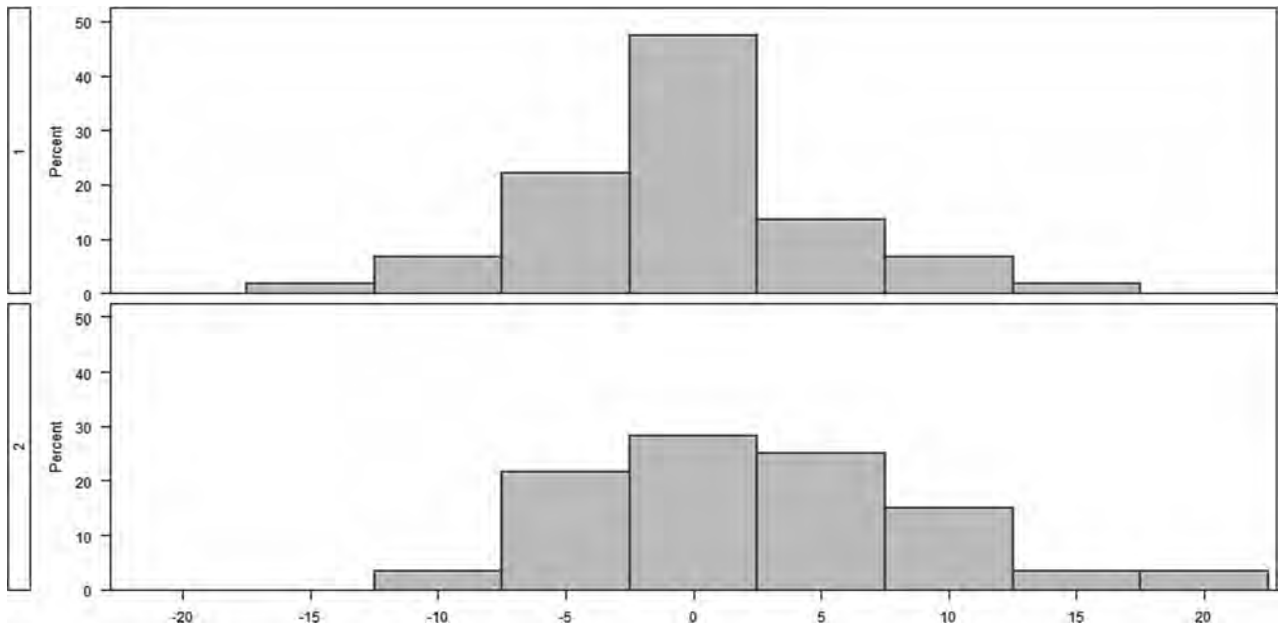


FIG 6. Group histograms for the relative percentage change in the GP/pons ratio from 1 to 7.

malignancies and relative chemotherapy effects were not controlled for. The damage to the BBB caused by disease processes, treatment, or both is also a potential confounding variable because most patients undergoing repeat brain MRIs have a known

intracranial malignancy. Both 1.5T and 3T systems were used. While most examinations were performed at 1.5T, differences in equipment may have resulted in slight variations on measurements. There was also no intra-/interobserver agreement separately

before this study because the average signal intensity measurement is normally less sensitive to intra-/interobserver variations.

Our study has only explored the contribution of gadobutrol to signal intensity change in up to 7 injections, so the possibility of observing a signal intensity increase cannot be excluded in patients with even higher cumulative gadobutrol injection doses. Even though we tried to ensure the completeness of all participants' medical records, the possibility of any unknown prior GBCA usage cannot be excluded for all patients.

Although most studies in the literature on the gadolinium deposition topic are MR imaging–based, inductively coupled plasma mass spectrometry–based postmortem tissue sampling studies, which have much higher sensitivity to the existence of gadolinium atoms, have also been conducted in both preclinical and clinical studies. Because of the higher sensitivity of inductively coupled plasma mass spectrometry techniques, deposits from both linear and macrocyclic agents have been reported,^{20–23} though the amount of deposition from macrocyclic agents was found to be much lower than from linear counterparts. Presumably, they are not as easily detected by standard T1-weighted MR imaging because of the lower deposition rate of macrocyclic agents.

Most interesting, while not statistically significant, patients receiving gadobutrol showed an unexpected decrease in signal intensity in both the DN and GP between the first and seventh studies. The decrease in the DN/pons ratio was found to be nearly significant at $P = .08$. Because linear GBCA administration before 2012 was not controlled for in the gadobutrol group, it is possible that this decrease reflects the results of clearance of previously deposited gadolinium from prior administrations, which may corroborate developing research on clearance and the efficacy of a “gadolinium holiday.”²⁴ Alternatively, this nonsignificant signal decrease could also be caused by the bias in patient sampling and in signal measurement inherent in ROI-based analysis.

CONCLUSIONS

Patients exposed to gadobutrol, a macrocyclic agent, failed to show a demonstrable change in T1 signal intensity in the regions of the brain classically susceptible to gadolinium deposition. This finding corroborates evidence suggesting that macrocyclic agents are less likely to cause signal increase on nonenhanced T1WI MR images than linear GBCAs.

Disclosures: Franklin G. Moser—RELATED: Grant: Bayer Healthcare, Comments: grant to conduct research.* Christopher T. Watterson—RELATED: Grant: Bayer Healthcare, Comments: educational grant.* Sasha Weiss—RELATED: Grant: Bayer Healthcare.* James Mirocha—RELATED: Grant: Bayer Healthcare.* Jinnan Wang—UNRELATED: Employment: Bayer Healthcare; Stock/Stock Options: Bayer Healthcare. *Money paid to the institution.

REFERENCES

1. Frenzel T, Lengsfeld P, Schirmer H, et al. **Stability of gadolinium-based magnetic resonance imaging contrast agents in human serum at 37 degrees C.** *Invest Radiol* 2008;43:817–28 CrossRef Medline
2. Morcos SK. **Extracellular gadolinium contrast agents: differences in stability.** *Eur J Radiol* 2008;66:175–79 CrossRef Medline
3. Kanal E, Maravilla K, Rowley HA. **Gadolinium contrast agents for CNS imaging: current concepts and clinical evidence.** *AJNR Am J Neuroradiol* 2014;35:2215–26 CrossRef Medline
4. Maravilla KR, Smith MP, Vymazal J, et al. **Are there differences between macrocyclic gadolinium contrast agents for brain tumor imaging? Results of a multicenter intraindividual crossover comparison of gadobutrol with gadoteridol (the TRUTH study).** *AJNR Am J Neuroradiol* 2015;36:14–23 CrossRef Medline
5. Lin SP, Brown JJ. **MR contrast agents: physical and pharmacologic basics.** *J Magn Reson Imaging* 2007;25:884–99 CrossRef Medline
6. Kanda T, Ishii K, Kawaguchi H, et al. **High signal intensity in the dentate nucleus and globus pallidus on unenhanced T1-weighted MR images: relationship with increasing cumulative dose of a gadolinium-based contrast material.** *Radiology* 2014;270:834–41 CrossRef Medline
7. Errante Y, Cirimele V, Mallio CA, et al. **Progressive increase of T1 signal intensity of the dentate nucleus on unenhanced magnetic resonance images is associated with cumulative doses of intravenously administered gadodiamide in patients with normal renal function, suggesting dechelation.** *Invest Radiol* 2014;49:685–90 CrossRef Medline
8. Quattrocchi CC, Mallio CA, Errante Y, et al. **Gadodiamide and dentate nucleus T1 hyperintensity in patients with meningioma evaluated by multiple follow-up contrast-enhanced magnetic resonance examinations with no systemic interval therapy.** *Invest Radiol* 2015;50:470–72 CrossRef Medline
9. Radbruch A, Weberling LD, Kieslich PJ, et al. **Gadolinium retention in the dentate nucleus and globus pallidus is dependent on the class of contrast agent.** *Radiology* 2015;275:783–91 CrossRef Medline
10. Kanda T, Osawa M, Oba H, et al. **High signal intensity in dentate nucleus on unenhanced T1-weighted MR images: association with linear versus macrocyclic gadolinium chelate administration.** *Radiology* 2015;275:803–09 CrossRef Medline
11. Ramalho J, Castillo M, AlObaidy M, et al. **High signal intensity in globus pallidus and dentate nucleus on unenhanced T1-weighted MR images: evaluation of two linear gadolinium-based contrast agents.** *Radiology* 2015;276:836–44 CrossRef Medline
12. Stojanov DA, Aracki-Trenkic A, Vojinovic S, et al. **Increasing signal intensity within the dentate nucleus and globus pallidus on unenhanced T1W magnetic resonance images in patients with relapsing-remitting multiple sclerosis: correlation with cumulative dose of a macrocyclic gadolinium-based contrast agent, gadobutrol.** *Eur Radiol* 2016;26:807–15 CrossRef Medline
13. McDonald RJ, McDonald JS, Kallmes DF, et al. **Intracranial gadolinium deposition after contrast-enhanced MR imaging.** *Radiology* 2015;275:772–82 CrossRef Medline
14. Kanda T, Fukusato T, Matsuda M, et al. **Gadolinium-based contrast agent accumulates in the brain even in subjects without severe renal dysfunction: evaluation of autopsy brain specimens with inductively coupled plasma mass spectroscopy.** *Radiology* 2015;276:228–32 CrossRef Medline
15. Kromrey ML, Liedtke KR, Ittermann T, et al. **Intravenous injection of gadobutrol in an epidemiological study group did not lead to a difference in relative signal intensities of certain brain structures after 5 years.** *Eur Radiol* 2017;27:772–77 CrossRef Medline
16. Radbruch A, Weberling LD, Kieslich PJ, et al. **High-signal intensity in the dentate nucleus and globus pallidus on unenhanced T1-weighted images: evaluation of the macrocyclic gadolinium-based contrast agent gadobutrol.** *Invest Radiol* 2015;50:805–10 CrossRef Medline
17. Cao Y, Huang DQ, Shih G, et al. **Signal change in the dentate nucleus on T1-weighted MR images after multiple administrations of gadopentetate dimeglumine versus gadobutrol.** *AJR Am J Roentgenol* 2016;206:414–19 CrossRef Medline
18. Schlemm L, Chien C, Bellmann-Strobl J, et al. **Gadopentetate but not gadobutrol accumulates in the dentate nucleus of multiple sclerosis patients.** *Mult Scler* 2017;23:963–72 CrossRef Medline
19. Moser FG, Hilal SK, Abrams G, et al. **MR imaging of pseudotumor cerebri.** *AJR Am J Roentgenol* 1988;150:903–09 CrossRef Medline
20. Robert P, Violas X, Grand S, et al. **Linear gadolinium-based contrast agents are associated with brain gadolinium retention in healthy rats.** *Invest Radiol* 2016;51:73–82 CrossRef Medline
21. Lohrke J, Frisk AL, Frenzel T, et al. **Histology and gadolinium distribution in the rodent brain after the administration of cumulative**

- high doses of linear and macrocyclic gadolinium-based contrast agents.** *Invest Radiol* 2017;52:324–33 CrossRef Medline
22. McDonald RJ, McDonald JS, Dai D, et al. **Comparison of gadolinium concentrations within multiple rat organs after intravenous administration of linear versus macrocyclic gadolinium chelates.** *Radiology* 2017;285:536–45 CrossRef Medline
23. Bussi S, Coppo A, Botteron C, et al. **Differences in gadolinium retention after repeated injections of macrocyclic MR contrast agents to rats.** *J Magn Reson Imaging* 2017 Jul 21. [Epub ahead of print] CrossRef Medline
24. Smith AP, Marino M, Roberts J, et al. **Clearance of gadolinium from the brain with no pathologic effect after repeated administration of gadodiamide in healthy rats: an analytical and histologic study.** *Radiology* 2017;282:743–51 CrossRef Medline

Cerebral Mitochondrial Microangiopathy Leads to Leukoencephalopathy in Mitochondrial Neurogastrointestinal Encephalopathy

L.L. Gramegna, A. Pisano, C. Testa, D.N. Manners, R. D'Angelo, E. Boschetti, F. Giancola, L. Pironi, L. Caporali, M. Capristo, M.L. Valentino, G. Plazzi, C. Casali, M.T. Dotti, G. Cenacchi, M. Hirano, C. Giordano, P. Parchi, R. Rinaldi, R. De Giorgio, R. Lodi, V. Carelli, and C. Tonon



ABSTRACT

BACKGROUND AND PURPOSE: Mitochondrial neurogastrointestinal encephalopathy is a rare disorder due to recessive mutations in the *thymidine phosphorylase* gene, encoding thymidine phosphorylase protein required for mitochondrial DNA replication. Clinical manifestations include gastrointestinal dysmotility and diffuse asymptomatic leukoencephalopathy. This study aimed to elucidate the mechanisms underlying brain leukoencephalopathy in patients with mitochondrial neurogastrointestinal encephalopathy by correlating multimodal neuroradiologic features to postmortem pathology.

MATERIALS AND METHODS: Seven patients underwent brain MR imaging, including single-voxel proton MR spectroscopy and diffusion imaging. Absolute concentrations of metabolites calculated by acquiring unsuppressed water spectra at multiple TEs, along with diffusion metrics based on the tensor model, were compared with those of healthy controls using unpaired *t* tests in multiple white matters regions. Brain postmortem histologic, immunohistochemical, and molecular analyses were performed in 1 patient.

RESULTS: All patients showed bilateral and nearly symmetric cerebral white matter hyperintensities on T2-weighted images, extending to the cerebellar white matter and brain stem in 4. White matter, *N*-acetylaspartate, creatine, and choline concentrations were significantly reduced compared with those in controls, with a prominent increase in the radial water diffusivity component. At postmortem examination, severe fibrosis of brain vessel smooth muscle was evident, along with mitochondrial DNA replication depletion in brain and vascular smooth-muscle and endothelial cells, without neuronal loss, myelin damage, or gliosis. Prominent periependymal cytochrome *C* oxidase deficiency was also observed.

CONCLUSIONS: Vascular functional and histologic alterations account for leukoencephalopathy in mitochondrial neurogastrointestinal encephalopathy. Thymidine toxicity and mitochondrial DNA replication depletion may induce microangiopathy and blood-brain-barrier dysfunction, leading to increased water content in the white matter. Periependymal cytochrome *C* oxidase deficiency could explain prominent periventricular impairment.

ABBREVIATIONS: AD = axial diffusivity; BW = brain water; FA = fractional anisotropy; MNGIE = mitochondrial neurogastrointestinal encephalopathy; mtDNA = mitochondrial DNA replication; MD = mean diffusivity; PLIC = posterior limbs of the internal capsule; PO-WM = parieto-occipital white matter; RD = radial diffusivity

Mitochondrial neurogastrointestinal encephalopathy (MNGIE) is a rare autosomal recessive disorder due to mutations in the *TYMP*¹ gene that result in thymidine phosphorylase deficiency. This causes toxic systemic elevation of thymidine and deoxyuridine levels,

deoxynucleotide pool imbalance, and secondary mitochondrial DNA replication (mtDNA) abnormalities.²⁻⁵

Disease onset, typically in young adulthood, is characterized by a slowly progressive multisystemic involvement, which includes ptosis, chronic progressive external ophthalmoplegia with mitochondrial myopathy, demyelinating neuropathy, hearing

Received July 23, 2017; accepted after revision October 30.

From the Functional MR Unit (L.L.G., C.T., D.N.M., R.L., C.T.) and Neurology Unit (R.D., R.R.), S.Orsola-Malpighi Hospital, Bologna, Italy; Departments of Biomedical and Neuro-motor Sciences (L.L.G., C.T., D.N.M., L.C., M.C., M.L.V., G.P., G.C., P.P., R.L., V.C., C.T.) and Surgical and Medical Sciences (E.B., F.G., L.P., R.D.G.), University of Bologna, Bologna, Italy; Departments of Radiology, Oncology, and Pathology (A.P., C.G.) and Medico-Surgical Sciences and Biotechnologies (C.C.), Sapienza, University of Rome, Rome, Italy; Istituto di Ricovero e Cura a Carattere Scientifico Institute of Neurological Sciences (L.C., M.C., M.L.V., G.P., P.P., V.C.), Bologna, Italy; Department of Medicine, Surgery, and Neuroscience (M.T.D.), University of Siena, Siena, Italy; and Department of Neurology (M.H.), Columbia University Medical Centre, New York, New York.

Preliminary data for this study were previously presented at: Annual Meeting of the International Society of Magnetic Resonance in Medicine, Italian Chapter, October 24–25, 2013; Perugia, Italy.

This study was supported by the Italian Ministry of Health with the grant RF-2009-1492481 ITA-MNGIE (to R.D.G.) to clarify main pathophysiological, clinical, and therapeutic aspects of MNGIE.

Please address correspondence to Raffaele Lodi, MD, PhD, Functional MR Unit, S.Orsola-Malpighi Hospital, Via Massarenti 9, 40138 Bologna, Italy; e-mail: raffaele.lodi@unibo.it

Indicates open access to non-subscribers at www.ajnr.org

Indicates article with supplemental on-line appendix and table.

Indicates article with supplemental on-line photos.

<http://dx.doi.org/10.3174/ajnr.A5507>

loss, and, most important, severe gastrointestinal dysmotility, leading to cachexia and diverticulosis of the small bowel.^{3,6}

Severe mtDNA depletion is the most striking molecular defect affecting several tissues (ie, smooth muscle of the gastrointestinal wall and vasculature [small vessels]), suggesting that microvascular dysfunction may play a role in the pathogenesis.^{7,8} Although the skeletal muscle does not express thymidine phosphorylase, the toxic nucleoside accumulation results in a typical mitochondrial myopathy due to both depletion and accumulation of multiple deletions of mtDNA.² Central nervous system involvement in MNGIE remains undercharacterized and puzzling. The brain neuroradiologic hallmark is leukoencephalopathy, with bilateral and symmetrically severe MR imaging signal alterations involving mostly cerebral hemispheric white matter.^{9,10} Remarkably, despite the extensive MR imaging alterations, most patients with MNGIE remain asymptomatic⁶; brain proton MR spectroscopy (¹H-MR spectroscopy) studies of patients with MNGIE have shown white matter biochemical alterations suggesting either neuronal loss/dysfunction^{11,12} or a normal metabolic profile.¹³ Furthermore, a previous study reported increased water diffusivity, evaluated by diffusion-weighted MR imaging, in 4 patients with MNGIE.¹² The neuropathologic study of 2 patients with genetically confirmed MNGIE did not show neuronal loss, demyelination, or glial proliferation, despite a striking loss of thymidine phosphorylase expression in capillaries of the white matter and an increased intracellular albumin staining, consistent with altered blood-brain barrier permeability.¹⁴

The purpose of this study was to elucidate the mechanisms underlying brain leukoencephalopathy in patients with MNGIE using a multimodal neuroradiologic and pathologic approach.

MATERIALS AND METHODS

Patients

Seven unrelated patients with a molecular diagnosis of MNGIE (3 men; age range, 23–38 years) were included in this study.

Patients were scanned on a 1.5T MR imaging system (Signa Horizon LX; GE Healthcare, Milwaukee, Wisconsin). Quantitative MR imaging parameters were compared with those obtained from 9 healthy volunteers (4 men; age range, 20–35 years) who underwent white matter ¹H-MR spectroscopy and from 14 healthy volunteers (7 men; age range, 21–43 years) who underwent diffusion tensor imaging. Patients were clinically assessed by neurologic, gastroenterologic, and nutritional evaluations. Four patients died, and in 1 patient (case 7), a postmortem examination was performed.

The Ethics Committee of S.Orsola-Malpighi Hospital approved the study, and written informed consent was obtained.

Biochemical and Genetic Characterization

Thymidine phosphorylase activity was assessed and quantified as previously reported. The *TYMP* gene was Sanger-sequenced.¹⁵

Brain MR Imaging

Conventional Brain MR Imaging Protocol Acquisition. Brain MR imaging was performed using a quadrature birdcage head coil. The conventional MR imaging protocol included an axial and coronal FLAIR T2 sequence, sagittal FSE T2, and axial FSE T1-weighted imaging.

Proton MR Spectroscopy Protocol Acquisition. A volume of interest of 8 cm³ was selected in the left parieto-occipital white matter (PO-WM). Water-suppressed proton MR spectra were acquired using the point-resolved spectroscopy single-voxel localization sequence (PROBE) at TE = 35, 70, 100, 144, and 288 ms (TR = 4000 ms, number of acquisitions = 64) to estimate the T2 of *N*-acetylaspartate, creatine plus phosphocreatine, and choline-containing compounds¹⁶ for the group of healthy controls and for 3 of 7 patients.

For the remaining 4 patients, the left PO-WM spectrum was acquired only at TE = 35 ms to limit the acquisition time to 4 minutes 16 seconds. In all subjects, unsuppressed water spectra were also acquired at TE = 25, 30, 40, 50, 60, 80, 100, 300, 600, 900, and 1000 ms; with TR = 15,000 ms, as previously described,¹⁶ to evaluate the water signal and T2 water relaxation time.

Diffusion Tensor Imaging Protocol Acquisition. DTI was performed by a single-shot echo-planar imaging sequence using 6 noncollinear directions of the diffusion gradients with the following parameters: TR = 10,000 ms, TE = 107 ms, slice thickness = 4 mm with a 2-mm gap, voxel size = 1.25 × 1.25 × 6 mm³, b-value = 900 s/mm².

Proton MR Spectroscopy Data Analysis. Both suppressed and unsuppressed water spectra were processed with the fitting program LCModel (Version 6.3; <http://www.lcmode.com/>).¹⁷ The exclusion criterion for ¹H-MR spectroscopy metabolite evaluation was an LCModel estimated fitting error of >20%. The absolute concentrations of NAA and Cho were obtained using the T2 times of the metabolites calculated by fitting the monoexponential decay of their signal in the water-suppressed PROBE spectra at different TEs¹⁸ and estimating the intracellular water content by the biexponential fit of water signal amplitude of the unsuppressed water spectra as detailed in the On-line Appendix. We considered a T2 relaxation value reported in the literature for mIns (150 ms)¹⁹ because TE values used for water-suppressed spectra acquisitions are not sufficiently short to obtain an accurate signal T2-decay of this metabolite.

Diffusion Tensor Imaging Data Analysis. DTI processing was performed by using the FMRIB software library (FSL; <http://www.fmrib.ox.ac.uk/fsl>). DTI-EPI images were coregistered and corrected for eddy current and head movement effects using the FMRIB Linear Image Registration Tool (FLIRT; <https://fsl.fmrib.ox.ac.uk/fsl/fslwiki/FLIRT>). Parameter maps for mean diffusivity (MD), fractional anisotropy (FA), axial diffusivity (AD, λ_1), and radial diffusivity [RD, $(\lambda_2 + \lambda_3)/2$] were determined voxelwise using the program DTIFit (<https://fsl.fmrib.ox.ac.uk/fsl/fslwiki/FDT/UserGuide#DTIFIT>). The EPI images were registered to the T1-weighted images using FSL tools.

To correlate the DTI-derived parameters with the biochemical profile, we defined an ROI on the DTI using the spatial coordinates of the spectroscopy volume of interest localized in the left PO-WM. Because in this ROI, WM fibers do not have a single predominant orientation, additional ROIs were defined on MD map images within white matter regions with high fiber directionality to assess changes in AD and RD with greater accuracy, namely the optic radiations, the posterior limbs of the internal

Table 1: Demographic, genetic, and clinical features of patients with MNGIE

Case No.	Age at MRI (yr)/Sex	TYMP Mutation ^a	Mutation Type	TP Activity	Age at Neurologic Onset	Age at Gastroenterologic ^b Onset
1	23/F	c.1249 dupC	Frame shift	Undetectable	20 yr (ptosis/CPEO)	Childhood
2	29/F	c.1160-2A>G and c.1382_1383insC	Splice defect Frame shift	Undetectable	Childhood (CPEO)	Childhood
3	28/M	c.215-1G>A and c.328C>T	Splice defect p. Q110X	Undetectable	24 yr (ptosis/CPEO)	20 yr
4	27/F	c.1160-1G>A	Splice defect	Very low	20 yr (ptosis/CPEO)	Childhood
5	38/M	c.522T>A	Splice defect	Undetectable	37 yr (ptosis/CPEO)	30 yr
6	25/M	c.1160-1G>A	Splice defect	Very low	25 yr (peripheral neuropathy)	19 yr
7	36/M	c.457G>A	p. G153S	Undetectable	Childhood (ptosis)	25 yr

Note:—CPEO indicates chronic progressive external ophthalmoplegia; TP, thymidine phosphorylase.

^a All homozygote.

^b Main gastroenterologic symptoms included irritable bowel and/or functional dyspepsia-like symptoms.

capsule (PLIC), and the splenium of the corpus callosum (On-line Fig 1). The mean values of MD, FA, AD, and RD were calculated for each ROI.

Statistical Analysis

We first evaluated differences in demographic data between patients and controls, using a *t* test or a Spearman χ^2 test as appropriate. We performed a *t* test for unpaired data to evaluate differences between patients and controls in quantitative MR imaging values, namely metabolite concentrations, water signals, $T_{2\text{brain water (BW)}}$ and $T_{2\text{CSF}}$ water relaxation times and DTI parameters. Moreover, in the patient group, we performed a Spearman test to evaluate the correlation between MR spectroscopy metabolite values and DTI parameters. The threshold for significance for all analyses was set at $P < .05$.

Postmortem Study

The postmortem study was performed in patient 7, eight months after the MR imaging. Whole-body postmortem examination was performed within 24 hours of death. The brain was removed and fixed in 4% buffered formalin for neuropathologic examination.

Histologic, Histochemical, and Immunohistochemical Analyses

Tissue specimens including frontal, temporal, parietal, occipital, insular, and cingulate cortices; basal ganglia; thalamus; hippocampus; amygdala, brain stem (midbrain, pons, medulla oblongata); and several blocks of cerebellar hemispheres, including the dentate nucleus, and vermis, were obtained from formalin-fixed brain tissue and used for histologic, histochemical, and immunohistochemical analyses. Six-micrometer-thick sections were stained with hematoxylin-eosin, periodic acid-Schiff, and periodic acid-Schiff plus diastase, Luxol fast blue, congo red, and PicroSirius Red. Immunohistochemical staining was performed using a large panel of antibodies (On-line Appendix).

Molecular Analysis on Postmortem Brain Samples

Paraffin brain sections from patient 7 and 3 age-matched controls (subjects who underwent postmortem examination for diagnostic purposes without clinical/pathologic evidence of central nervous system diseases) were subjected to laser capture microdissection with the MMI Nikon UV-CUT System (Molecular Ma-

chines & Industries, Glattbrugg, Switzerland), as previously described²⁰ (also see the On-line Appendix).

RESULTS

Genetic diagnosis and biochemical features of patients with MNGIE are reported in Table 1.

MR Imaging: Bilateral Altered White Matter Signal

Brain MR imaging revealed a bilateral and nearly symmetric white matter involvement characterized by hyperintensity on FLAIR T2 and FSE T2 and hypointensity on T1-weighted sequences in all patients (Fig 1, On-line Fig 2, and On-line Table). Mild-to-severe frontal and parieto-occipital white matter involvement was detected in each patient. The temporal lobe white matter and basal ganglia were affected in 5 patients, and the cerebellar white matter and brain stem, in 4. Three patients (cases 1, 2, and 3) with milder brain involvement showed signal intensity changes exclusively localized in the deep periventricular cerebral white matter with normal signal intensity of the infratentorial structures.

¹H-MR Spectroscopy: Reduced Cerebral White Matter Metabolite Concentrations

In PO-WM, patients showed a significant decrease of NAA, Cr, and Cho concentrations. mIns, which had the highest metabolite variability in patients with MNGIE, showed a trend toward reduced concentration (Fig 2). Metabolite ratios such as NAA/Cr, Cho/Cr, and mIns/Cr were similar in patients and controls (Table 2).

$T_{2\text{BW}}$ values, calculated from the fast decay component of the signal from unsuppressed water acquisitions and attributable to both the intracellular and intramyelin water compartments, were significantly higher in patients compared with controls (Table 3 and On-line Fig 3).

DTI: Prominent Increase of White Matter Radial Diffusivity

In the same PO-WM region selected for the MR spectroscopy acquisition, patients with MNGIE showed significantly higher MD, RD, and AD as well as significantly lower FA values compared with controls. The RD increase, relative to mean control values, was more prominent than the AD increase (RD, +52%; AD, +23%). Similar results were obtained in the optic radiations.

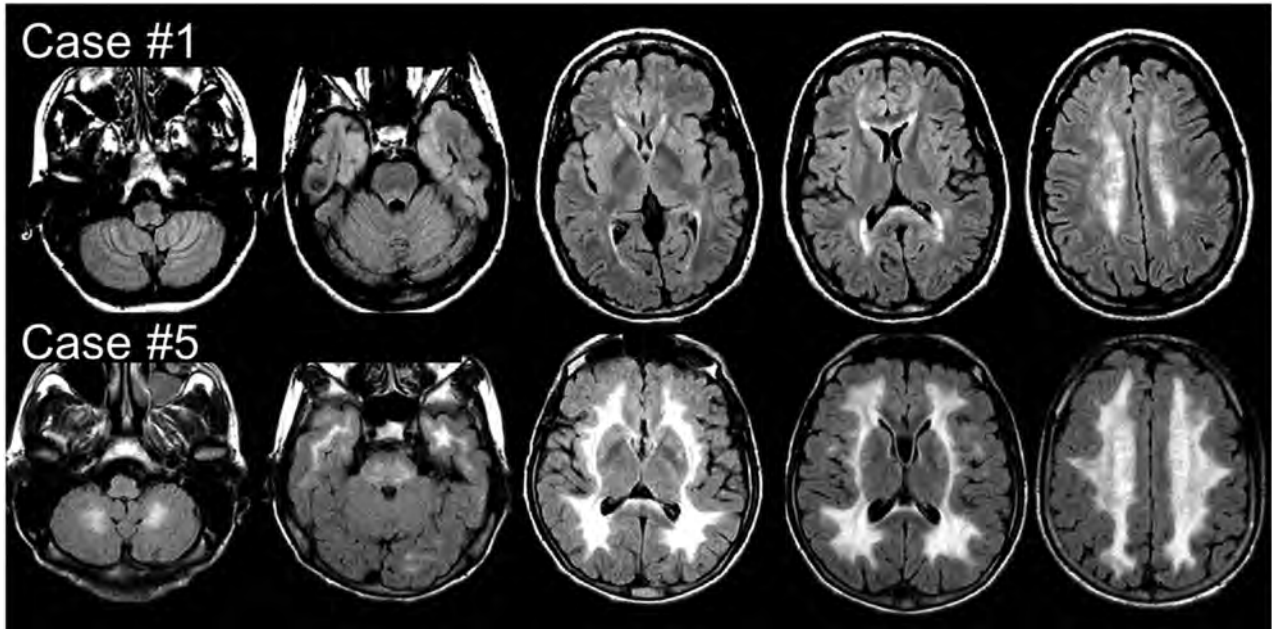


FIG 1. MR imaging. Axial FLAIR T2 images from 2 of the 7 patients with MNGIE at the supra- and infratentorial levels. Case 1 does not show any infratentorial involvement, while a more diffuse supra- and infratentorial signal intensity increase can be seen in case 5.

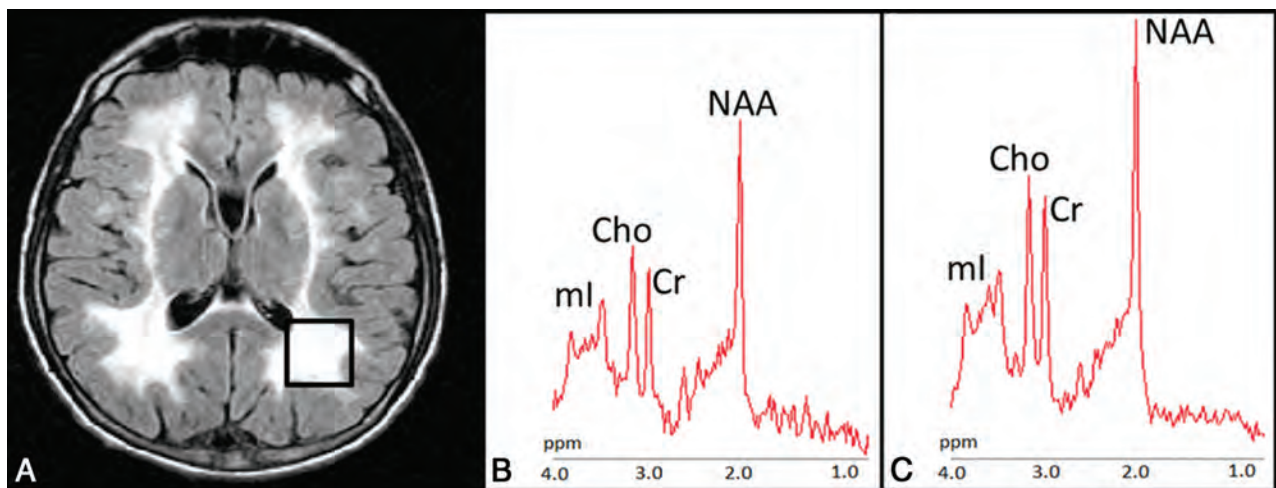


FIG 2. Proton MR spectroscopy. A, Axial FLAIR T2-weighted image shows the localization of the 8-cm³ ¹H-MR spectroscopy volume of interest in the left parieto-occipital white matter in case 5. Proton MR spectra from the VOI in case 5 (B) and in a healthy control (C). The relative content of metabolites is similar in the patient and healthy subject. Note the higher level of noise in the patient and smaller metabolite peaks.

In patients with MNGIE, the difference between RD and AD changes was even more evident in the PLIC and splenium of the corpus callosum, where a significant increase in RD values was associated with unchanged AD in both ROIs (Table 3).

Correlation analysis between metabolite concentrations and DTI metrics from the same PO-WM voxel in patients with MNGIE disclosed a negative correlation between NAA absolute concentration and MD ($r = -0.82$, $P = .023$), RD ($r = -0.82$, $P = .02$), and AD values ($r = -0.89$, $P = .007$).

Neuropathology: Fibrosis of Small-Vessel Walls and Microbleeding

Gross examination findings of the brain and vessels of the circle of Willis were unremarkable. Microscopic examination revealed a moderate pallor of the deep cerebral white matter extending fo-

cally into the internal capsule and thalamic white matter, while sparing the arcuate fibers and the corpus callosum. These changes, however, were not associated with a significant gliosis, neuronal loss, or axonal degeneration. The gray matter was also unremarkable.

The most striking feature was observed at the level of small perforating arterioles, which showed a replacement of smooth-muscle cells of the tunica media by dense fibrous tissue (Fig 3A–C). Loss of smooth-muscle cells was more evident in the external layers of the tunica media (Fig 3B), though a total fibrous replacement was observed in some vessels (Fig 3C). These features were particularly frequent in the white matter of the frontal lobe, the basal ganglia, and the midbrain, but absent in pial arteries (not shown). Fibrosis was occasionally associated with concentric wall thickening and luminal narrowing (Fig 3D). In addition, hemo-

Table 2: ¹H-MRS white matter parieto-occipital metabolite absolute concentrations, ratios, and water signal intensity, and T2 values in patients with MNGIE and healthy controls

	Patients with MNGIE (n = 7) (mean ± SD)	Healthy Controls (n = 9) (mean ± SD)	P Value ^a
Metabolite concentrations (mM)			
NAA	6.98 ± 0.79	9.81 ± 0.94	<.001 ^{a,c}
Cr	4.15 ± 0.48	5.97 ± 0.55	<.001 ^{a,c}
Cho	1.53 ± 0.23	1.89 ± 0.24	.01 ^a
mIns	4.46 ± 1.14	5.44 ± 0.76	.06 ^a
Metabolite ratios			
NAA/Cr	1.85 ± 0.18	1.80 ± 0.11	.57 ^b
Cho/Cr	0.39 ± 0.06	0.33 ± 0.04	.04 ^b
mIns/Cr	0.99 ± 0.27	0.85 ± 0.08	.16 ^b
Water signal (a.u.)			
S _{BW} (0)	(14.0 ± 9.0) × 10 ¹⁰	(10.8 ± 2.0) × 10 ¹⁰	.370
S _{CSF} (0)	(4.0 ± 7.5) × 10 ¹⁰	(1.3 ± 0.6) × 10 ¹⁰	.23 ^a
T2 water			
T _{2BW} (ms)	112 ± 24	75 ± 8	.001 ^{a,c}
T _{2CSF} (ms)	520 ± 185	776 ± 344	.098 ^a

Note:—a.u. indicates arbitrary units; S_{BW} (0) and S_{CSF} (0), water signals corresponding to brain and cerebrospinal water, respectively; T_{2BW} and T_{2CSF}, water relaxation times corresponding to brain and cerebrospinal water, respectively.

^a Statistical significance was set at P < .0125 after Bonferroni correction for multiple comparisons.

^b Statistical significance was set at P < .0167 after Bonferroni correction for multiple comparisons.

^c Significant.

Table 3: DTI derivate metrics in patients with MNGIE and healthy controls

ROI	MD (Mean ± SD)	FA (Mean ± SD)	AD (Mean ± SD)	RD (Mean ± SD)
PO-WM				
MNGIE	1.09 ± 0.16	0.27 ± 0.05	1.40 ± 0.16	0.93 ± 0.16
Controls	0.79 ± 0.05	0.40 ± 0.02	1.14 ± 0.07	0.61 ± 0.05
P Value ^a	<.0001 ^b	<.0001 ^b	.0001 ^b	<.0001 ^b
OR				
MNGIE	1.15 ± 0.20	0.41 ± 0.07	1.69 ± 0.19	0.88 ± 0.21
Controls	0.81 ± 0.05	0.59 ± 0.09	1.35 ± 0.12	0.54 ± 0.06
P Value ^a	<.0001 ^b	.0003 ^b	.0002 ^b	<.0001 ^b
PLIC				
MNGIE	0.78 ± 0.06	0.61 ± 0.07	1.40 ± 0.06	0.47 ± 0.08
Controls	0.69 ± 0.05	0.70 ± 0.04	1.36 ± 0.11	0.35 ± 0.05
P Value ^a	.0019 ^b	.0008 ^b	0.36	.0003 ^b
CC				
MNGIE	0.88 ± 0.08	0.66 ± 0.06	1.64 ± 0.11	0.49 ± 0.10
Controls	0.81 ± 0.09	0.76 ± 0.06	1.72 ± 0.19	.35 ± 0.08
P Value ^a	.12	.0012 ^b	0.37	.0028 ^b

Note:—OR indicates optic radiation; CC, corpus callosum.

^a Statistical significance was set at P < .003 after Bonferroni correction for multiple comparisons.

^b Significant.

siderin-laden macrophages, consistent with previous microbleeding aspects, were observed close to fibrotic small vessels and capillaries (Fig 3E). Immunohistochemical stains revealed increased deposition of collagen IV in the basal lamina of several vessels (not shown) and a slight perivascular gliosis (Fig 3F). The endothelial layer, as observed by CD31 immunostaining, was unremarkable (not shown). Immunostaining for amyloid was negative (not shown).

Consistent with the mitochondrial etiology of the disease, scattered neurons showed decreased expression of the mtDNA-encoded COX I subunit. This feature was particularly evident in the subependymal region of the lateral ventricles (not shown) and was paralleled by mtDNA depletion in different regions of the brain (frontal gray and white matter, and substantia nigra) and, most important, in microdissected vascular smooth-muscle and endothelial cells (Fig 4).

DISCUSSION

We documented that leukoencephalopathy, the hallmark of brain MR imaging in MNGIE, is characterized by dilution of all metabolites associated with a prominent increase of the radial component of water diffusion in multiple white matter regions. These results, obtained in 7 patients, combined with the post-mortem findings in the brain of one of them, support the hypothesis that neuroradiologic abnormalities in MNGIE result from microvascular damage. Indeed, we found a diffuse replacement of the vascular wall by dense fibrous tissue and multiple perivascular microbleeds in the white matter of the frontal lobe, in the basal ganglia, and in the midbrain.

Pathologic features of vessels are reminiscent of those described in cerebral microvessel disease²¹⁻²³ and point to impaired intracerebral blood flow regulation and blood-brain barrier permeability as synergic mechanisms leading to increased intracellular and intramyelin water content. The fibrosis of vascular smooth-muscle cells is in line with that observed in the external layer of the muscularis propria of the gastrointestinal tract,⁸ which is the main factor responsible for the severe dysmotility occurring in most patients with MNGIE. Analogous to observations in the muscularis propria and small vessels of the gastrointestinal wall, brain angiopathy is also characterized by a severe mtDNA depletion and COX deficiency, triggered by the toxic effects of high circulating levels of nucleosides.⁸ A previous brain neuropathologic study of 2 patients with MNGIE showed an increase of albumin

immunoreactivity in the cytoplasm of reactive astrocytes compared with controls.¹⁴ This finding was interpreted as a result of a functional blood-brain barrier alteration, as suggested by the embryonic role played by *TYMP* in glial proliferation.²⁴

In all our patients, brain MR imaging demonstrated a typical, diffuse (mild-to-severe) leukoencephalopathy, in striking contrast to the absence of clinical central nervous system involvement, as observed in previously reported patients.⁶ In particular, in mildly affected patients, MR imaging signal alterations were confined to the subependymal deep cerebral white matter, while in the severely affected patients, these changes extended to the subcortical white matter, deep gray matter, and subtentorial structures. This gradient of MR imaging white matter abnormalities parallels the prominent COX deficiency seen in case 7 in the periependymal tissue, which may be damaged first by high CSF levels of thymidine.

¹H-MR spectroscopy of the cerebral white matter of patients

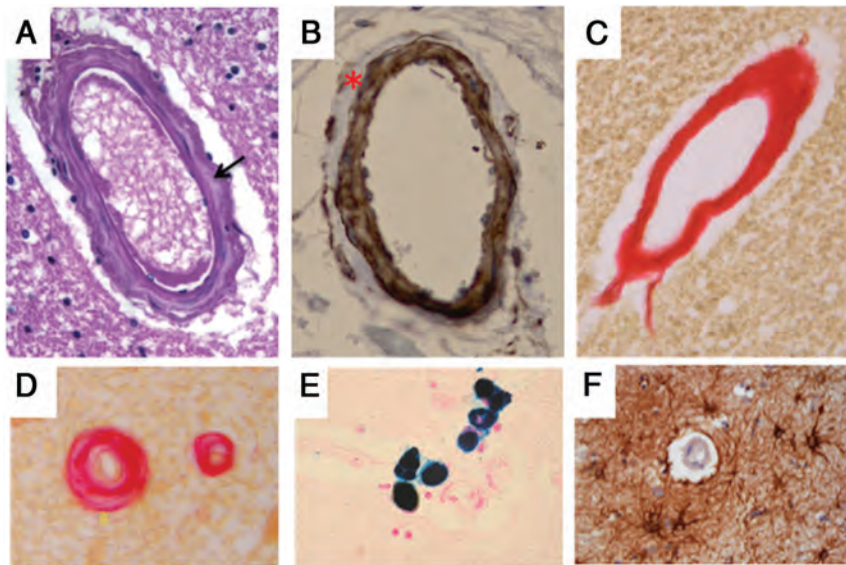


FIG 3. Histologic features of brain vessels in patient 7 with MNGIE. *A*, Representative image of a penetrating arteriole showing increased collagen deposition in the tunica media (arrow) (H&E, original magnification $\times 40$). *B*, Loss of smooth-muscle cells of the tunica media in a penetrating vessel, especially evident at the outermost layer (smooth-muscle actin, original magnification $\times 40$). *C*, A thick fibrous coat completely replaces the 3-layer structure of a penetrating vessel (PicroSirius Red, original magnification $\times 40$). *D*, Fibrous replacement is associated with luminal narrowing in a small brain vessel (PicroSirius Red, original magnification $\times 40$). *E*, Perl iron stain consistent with hemosiderin deposits close to a brain capillary (Perls stain, original magnification $\times 40$). *F*, Perivascular gliosis (glial fibrillary acidic protein, original magnification $\times 40$).

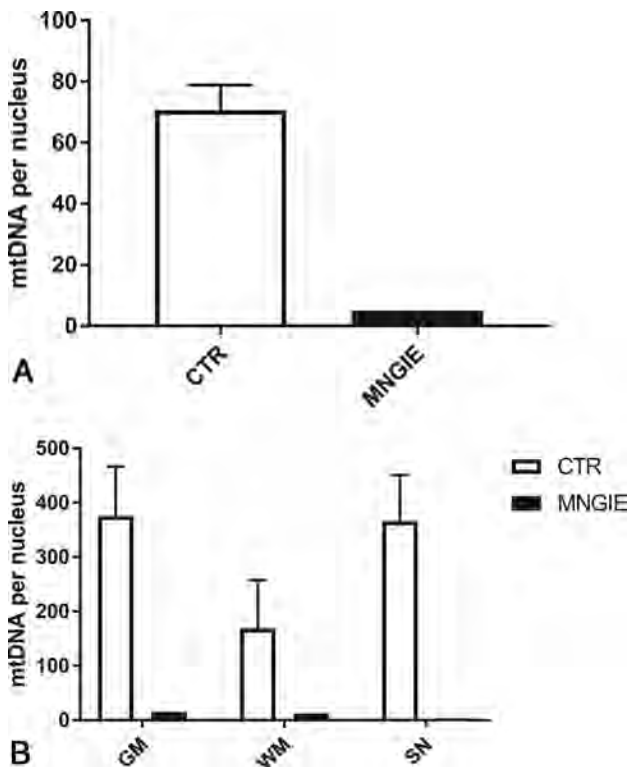


FIG 4. The mtDNA amount in the brain of patient 7 with MNGIE. *A*, mtDNA amount in smooth-muscle and endothelial cells microdissected by laser capture from an MNGIE brain and controls ($n = 3$) (expressed as mtDNA copy per nucleus). *B*, The mtDNA amount in different cerebral regions microdissected by laser capture from MNGIE and controls ($n = 3$) (expressed as mtDNA copy per nucleus). SN indicates substantia nigra; CTR, controls.

with MNGIE showed significant reductions of NAA, Cho, and Cr concentrations. The increase of the T2 of the water signals, derived from a slower decay of the unsuppressed water signal at a short TE (26–300 ms), may be attributed to both intramyelinic and intracellular water.²⁵ The significant increase in T2 of intracellular water of patients compared with controls suggests the enlargement of the intracellular compartment and consequently supports the hypothesis of a dilution effect underpinning the decreased metabolite concentrations. Previous ¹H-MR spectroscopy studies performed on 7 patients with MNGIE suggested unchanged metabolite ratios in the cerebral white matter.^{11–13} For the first time, we provide absolute metabolite quantification by acquiring unsuppressed water spectra at multiple TEs, to distinguish intra- from extracellular water.¹⁸

In our patients with MNGIE, the DTI metrics in the same parieto-occipital voxel of the ¹H-MR spectroscopy study showed an increase of mean diffusivity and a decrease of fractional anisotropy values, with a more prominent involvement of the radial than longitudinal diffusivity.

To better estimate variations in axial and radial diffusivity, considering the abundance of white matter crossing fibers in the parieto-occipital voxel, we also evaluated DTI metrics in WM tracts with high fiber directionality, such as the optic radiations, PLIC, and splenium of corpus callosum. In all these structures, a prominent increase of radial diffusivity was confirmed (Table 3). ROIs of the splenium of the corpus callosum and PLIC showed a selective increase in radial diffusivity with unchanged axial diffusivity. Radial diffusivity is considered a measure of myelin integrity,²⁶ as demonstrated by its selective increase in the corpus callosum of animal models with cuprizone-induced demyelination^{27,28} and in the optic nerves of mice with demyelination resulting from retinal ischemia.²⁹ Similarly, in patients with relapsing-remitting multiple sclerosis, tract-specific DTI analysis of the optic radiations showed selective increases in RD only within the T2 lesions and, therefore, related to local myelin disruption.³⁰

The absence of demyelination at postmortem examination in one of our patients with MNGIE as well as in the other 2 previously reported cases¹⁴ points to increased intramyelin water content as the most likely explanation for prominent or selective radial diffusivity found in brain white matter structures in our patients. A negative correlation between *N*-acetylaspartate concentration and mean diffusivity values within the same white matter volume was demonstrated, supporting the hypothesis of a dilution effect as the basis of the metabolite concentration reduction, possibly affecting neuronal cells, because no correlation was observed between any other metabolite concentration expressed in either neural or glial cells and any DTI metrics.

In addition to fibrous replacement of the vascular wall, the neuropathologic study revealed multiple microbleeds in the white matter of the frontal lobe, basal ganglia, and midbrain. None of the MNGIE T2-weighted images revealed foci of local signal loss consistent with the presence of hemosiderin deposits,³¹ though sequences such as gradient-echo T2*-weighted susceptibility-weighted imaging, the most sensitive MR imaging for the detection of hemosiderin deposits,³² were not acquired. However, the neuroradiologic and clinical features characterizing small-vessel disease, such as lacunar strokes and progressive cognitive decline,³³ were absent in all our patients, suggesting key differences of small-vessel involvement in MNGIE compared with other conditions.

CONCLUSIONS

White matter metabolic and microstructural alterations detected in patients with MNGIE can be related to microangiopathy in the deep white matter and an energy metabolism deficit in the subependymal cells. Leukoencephalopathy in MNGIE may be the result of endothelial failure due to thymidine toxicity and mtDNA depletion, which may induce blood-brain barrier dysfunction and microangiopathy, leading to increased white matter water content. The question of whether leukoencephalopathy is a reversible feature cannot be solved at present. Long-term follow-up of patients with bone marrow^{34,35} and liver transplantation³⁶ will likely provide an answer.

Disclosures: Giuseppe Plazzi—UNRELATED: Board Membership: Jazz Pharmaceuticals, UCB, BioProject. Roberto De Giorgio—RELATED: Grant: RF-2009-1492481 ITA MNGIE*. Valerio Carelli—UNRELATED: Consultancy: GenSight, Santhera Pharmaceuticals; Other: GenSight and Santhera Pharmaceuticals, Comments: clinical trial on Leber Hereditary Optic Neuropathy*. Michio Hirano—UNRELATED: Grant: National Institutes of Health*, Comments: for a Phase I safety study of bone marrow transplant for MNGIE. *Money paid to the institution.

REFERENCES

- Nishino I, Spinazzola A, Hirano M. **Thymidine phosphorylase gene mutations in MNGIE, a human mitochondrial disorder.** *Science* 1999;283:689–92 CrossRef Medline
- Nishigaki Y, Marti R, Copeland WC, et al. **Site-specific somatic mitochondrial DNA point mutations in patients with thymidine phosphorylase deficiency.** *J Clin Invest* 2003;111:1913–21 CrossRef Medline
- Hirano M, Nishigaki Y, Marti R. **Mitochondrial neurogastrointestinal encephalomyopathy (MNGIE): a disease of two genomes.** *Neurologist* 2004;10:8–17 CrossRef Medline
- Spinazzola A, Marti R, Nishino I, et al. **Altered thymidine metabolism due to defects of thymidine phosphorylase.** *J Biol Chem* 2002;277:4128–33 CrossRef Medline
- Marti R, Nishigaki Y, Hirano M. **Elevated plasma deoxyuridine in patients with thymidine phosphorylase deficiency.** *Biochem Biophys Res Commun* 2003;303:14–18 CrossRef Medline
- Garone C, Tadesse S, Hirano M. **Clinical and genetic spectrum of mitochondrial neurogastrointestinal encephalomyopathy.** *Brain* 2011;134(Pt 11):3326–32 CrossRef Medline
- Giordano C, Sebastiani M, Plazzi G, et al. **Mitochondrial neurogastrointestinal encephalomyopathy: evidence of mitochondrial DNA depletion in the small intestine.** *Gastroenterology* 2006;130:893–901 CrossRef Medline
- Giordano C, Sebastiani M, De Giorgio R, et al. **Gastrointestinal dysmotility in mitochondrial neurogastrointestinal encephalomyopathy is caused by mitochondrial DNA depletion.** *Am J Pathol* 2008;173:1120–28 CrossRef Medline
- Nishino I, Spinazzola A, Hirano M. **MNGIE: from nuclear DNA to mitochondrial DNA.** *Neuromuscul Disord* 2001;11:7–10 CrossRef Medline
- Millar WS, Lignelli A, Hirano M. **MRI of five patients with mitochondrial neurogastrointestinal encephalomyopathy.** *Am J Roentgenol* 2004;182:1537–41 CrossRef Medline
- Schüpbach WM, Vadday KM, Schaller A, et al. **Mitochondrial neurogastrointestinal encephalomyopathy in three siblings: clinical, genetic and neuroradiological features.** *J Neurol* 2007;254:146–53 CrossRef Medline
- Scarpelli M, Ricciardi GK, Beltramello A, et al. **The role of brain MRI in mitochondrial neurogastrointestinal encephalomyopathy.** *Neuroradiol J* 2013;26:520–30 CrossRef Medline
- Roussel P, Elmaleh-Bergès M, Ogier de Baulny H, et al. **Mitochondrial neurogastrointestinal encephalomyopathy [in French].** *J Neuroradiol* 2008;35:121–24 CrossRef Medline
- Szigeti K, Sule N, Adesina AM, et al. **Increased blood-brain barrier permeability with thymidine phosphorylase deficiency.** *Ann Neurol* 2004;56:881–86 CrossRef Medline
- Mohamed S, Caporali L, De Giorgio R, et al. **HPLC-UV analysis of thymidine and deoxyuridine in plasma of patients with thymidine phosphorylase deficiency.** *J Chromatogr B Analyt Technol Biomed Life Sci* 2014;949–950:58–62 CrossRef Medline
- Malucelli E, Manners DN, Testa C, et al. **Pitfalls and advantages of different strategies for the absolute quantification of N-acetyl aspartate, creatine and choline in white and grey matter by 1H-MRS.** *NMR Biomed* 2009;22:1003–13 Medline
- Provencher SW. **Automatic quantitation of localized in vivo 1H spectra with LCModel.** *NMR Biomed* 2001;14:260–64 CrossRef Medline
- Kreis R, Ernst T, Ross BD. **Development of the human brain: in vivo quantification of metabolite and water content with proton magnetic resonance spectroscopy.** *Magn Reson Med* 1993;30:424–37 CrossRef Medline
- Kreis R, Slotboom J, Hofmann L, et al. **Integrated data acquisition and processing to determine metabolite contents, relaxation times, and macromolecule baseline in single examinations of individual subjects.** *Magn Reson Med* 2005;54:761–68 CrossRef Medline
- Giordano C, d'Amati G. **Evaluation of gastrointestinal mtDNA depletion in mitochondrial neurogastrointestinal encephalomyopathy (MNGIE).** *Methods Mol Biol* 2011;755:223–32 CrossRef Medline
- Wardlaw JM, Smith C, Dichgans M. **Mechanisms of sporadic cerebral small vessel disease: insights from neuroimaging.** *Lancet Neurol* 2013;12:483–97 CrossRef Medline
- Pantoni L. **Cerebral small vessel disease: from pathogenesis and clinical characteristics to therapeutic challenges.** *Lancet Neurol* 2010;9:689–701 CrossRef Medline
- Wardlaw JM. **Blood-brain barrier and cerebral small vessel disease.** *J Neurol Sci* 2010;299:66–71 CrossRef Medline
- Wolburg H, Lippoldt A. **Tight junctions of the blood-brain barrier: development, composition and regulation.** *Vascul Pharmacol* 2002;38:323–37 CrossRef Medline
- MacKay A, Laule C, Vavasour I, et al. **Insights into brain microstructure from the T2 distribution.** *Magn Reson Imaging* 2006;24:515–25 CrossRef Medline
- Aung WY, Mar S, Benzinger TL. **Diffusion tensor MRI as a biomarker in axonal and myelin damage.** *Imaging Med* 2013;5:427–40 CrossRef Medline
- Song SK, Yoshino J, Le TQ, et al. **Demyelination increases radial diffusivity in corpus callosum of mouse brain.** *Neuroimage* 2005;26:132–40 CrossRef Medline
- Xie M, Tobin JE, Budde MD, et al. **Rostrocaudal analysis of corpus callosum demyelination and axon damage across disease stages refines diffusion tensor imaging correlations with pathological features.** *J Neuropathol Exp Neurol* 2010;69:704–16 CrossRef Medline
- Sun SW, Liang HF, Le TQ, et al. **Differential sensitivity of in vivo and ex vivo diffusion tensor imaging to evolving optic nerve injury in**

- mice with retinal ischemia. *Neuroimage* 2006;32:1195–204 CrossRef Medline
30. Klistorner A, Vootakuru N, Wang C, et al. **Decoding diffusivity in multiple sclerosis: analysis of optic radiation lesional and non-lesional white matter.** *PLoS One* 2015;10:e0122114 CrossRef Medline
31. Greenberg SM, Vernooij MW, Cordonnier C, et al; Microbleed Study Group. **Cerebral microbleeds: a guide to detection and interpretation.** *Lancet Neurol* 2009;8:165–74 CrossRef Medline
32. Fazekas F, Kleinert R, Roob G, et al. **Histopathologic analysis of foci of signal loss on gradient-echo T2*-weighted MR images in patients with spontaneous intracerebral hemorrhage: evidence of microangiopathy-related microbleeds.** *AJNR Am J Neuroradiol* 1999;20:637–42 Medline
33. Inzitari D, Pracucci G, Poggesi A, et al; LADIS Study Group. **Changes in white matter as determinant of global functional decline in older independent outpatients: three-year follow-up of LADIS (leukoaraiosis and disability) study cohort.** *BMJ* 2009;339:b2477 CrossRef Medline
34. Filosto M, Scarpelli M, Tonin P, et al. **Course and management of allogeneic stem cell transplantation in patients with mitochondrial neurogastrointestinal encephalomyopathy.** *J Neurol* 2012;259:2699–706 CrossRef Medline
35. Halter JP, Michael W, Schüpbach M, et al. **Allogeneic haematopoietic stem cell transplantation for mitochondrial neurogastrointestinal encephalomyopathy.** *Brain* 2015;138:2847–58 CrossRef Medline
36. De Giorgio R, Pironi L, Rinaldi R, et al. **Liver transplantation for mitochondrial neurogastrointestinal encephalomyopathy.** *Ann Neurol* 2016;80:448–55 CrossRef Medline

Cerebellar Hypoperfusion in Migraine Attack: Incidence and Significance

F. Kellner-Weldon, M. El-Koussy, S. Jung, M. Jossen, P.P. Klinger-Gratz, and R. Wiest



ABSTRACT

BACKGROUND AND PURPOSE: Patients diagnosed with migraine with aura have an increased lifetime risk of ischemic stroke. It is not yet clear whether prolonged cortical hypoperfusion during an aura increases the immediate risk of cerebellar infarction because it may induce crossed cerebellar diaschisis and subsequent tissue damage. To address this question, we retrospectively analyzed potential relationships between cortical oligemia and cerebellar hypoperfusion in patients with migraine with aura and their potential relation to small infarct-like cerebellar lesions.

MATERIALS AND METHODS: One hundred six migraineurs who underwent MR imaging, including DSC perfusion, were included in the study. In patients with apparent perfusion asymmetry, we used ROI analysis encompassing 18 infra- and supratentorial ROIs to account for differences in regional cerebral blood flow and volume. The presence of cerebellar hypoperfusion was calculated using an asymmetry index, with values of >10% being considered significant.

RESULTS: We observed perfusion asymmetries in 23/106 patients, 22 in patients with migraine with aura (20.8%). Cerebellar hypoperfusion was observed in 12/23 patients (52.2%), and crossed cerebellar diaschisis, in 9/23 patients (39.1%) with abnormal perfusion. In none of the 106 patients were DWI restrictions observed during migraine with aura.

CONCLUSIONS: Cerebellar hypoperfusion and crossed cerebellar diaschisis are common in patients with migraine with aura and cortical perfusion abnormalities. Crossed cerebellar diaschisis in migraine with aura may be considered a benign phenomenon because we observed no association with DWI restriction or manifest cerebellar infarctions, even in patients with prolonged symptom-related perfusion abnormalities persisting for up to 24 hours.

ABBREVIATIONS: AI = asymmetry index; CCD = crossed cerebellar diaschisis; HCH = hypoperfused cerebellar hemisphere; MwA = migraine with aura; rCBF = regional CBF; rCBV = regional CBV

Migraine is the most frequent primary headache and affects up to 12% of the general population,¹ causing disabling symptoms during attacks. Migraine without aura is defined as a recurrent headache with attacks lasting between 4 and 72 hours, typically unilateral, of pulsatile quality, with moderate severity that is aggravated by routine physical activity and associated with nausea and/or photo- and phonophobia.² In contrast, migraine

with aura (MwA) presents with transient focal neurologic symptoms that may mimic acute ischemic stroke, particularly if not immediately followed by a typical headache.¹ Patients who have MwA have an increased lifetime risk of latent cerebellar infarctions that is twice as high as that in the unaffected population.³ In patients with MwA, most WM lesions (80%) are observed in the posterior cerebral artery territory, most pronounced along vascular borderzones. Spreading oligemia associated with neuronal depression—a condition induced by a slowly propagating wave of neuronal and glial depolarization within the cerebral cortex—has been postulated as the most likely cause.⁴ Hemodynamic responses because of spreading depression may, like ictal and postictal neuronal activation and deactivation, induce regional brain perfusion changes that are sensitive to MR perfusion imaging. Variant patterns of perfusion changes have been observed during onset, spread, and termination of migraine attacks.⁵⁻⁸

Cortical hypoperfusion may also be associated with crossed cerebellar diaschisis (CCD), a depression of CBF and metabolism

Received June 28, 2016; accepted after revision November 5, 2017.

From the Support Center for Advanced Neuroimaging (F.K.-W., M.E.-K., M.J., P.P.K.-G., R.W.), Institute for Diagnostic and Interventional Neuroradiology, and Department of Neurology (S.J.), University Hospital Inselspital, Bern, Switzerland; and Department of Radiology (P.P.K.-G.), University of Basel, Basel, Switzerland.

This study was partially supported by Bayer (Swiss) AG, Zurich, Switzerland.

Please address correspondence to Frauke Kellner-Weldon, MD, Institute for Diagnostic and Interventional Neuroradiology, University Hospital Inselspital, 3010 Bern, Switzerland; e-mail: frauke.kellner-weldon@insel.ch

Indicates open access to non-subscribers at www.ajnr.org

<http://dx.doi.org/10.3174/ajnr.A5508>

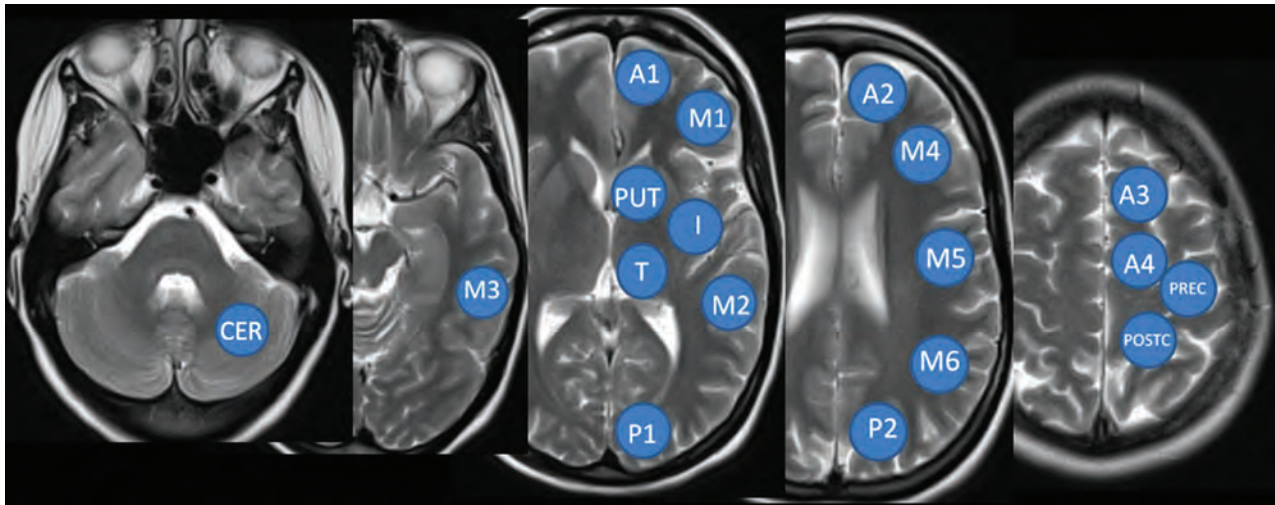


FIG 1. ROI analysis for perfusion parameters: CER indicates cerebellum; Put, putamen; I, insula; T, thalamus; A, arterial territory of the anterior cerebral artery; M, arterial territory of the middle cerebral artery; P, arterial territory of the posterior cerebral artery; PREC, precentral gyrus; POSTC, postcentral gyrus.

in the cerebellar hemisphere contralateral to a supratentorial neuronal deactivation. CCD is observed in several disorders that result in neuronal damage or depletion, such as acute ischemic motor stroke,^{9,10} hemorrhage,^{11,12} and epilepsy with disturbance of the motor network.¹³ So far, CCD in migraine has only been described anecdotally^{14,15} as posing a risk of subsequent brain infarctions for patients with CCD. The aim of our study was to investigate the association between cortical oligemia and cerebellar hypoperfusion in patients with MWA and their potential relation to small infarct-like cerebellar lesions.

MATERIALS AND METHODS

Study Population

We retrospectively identified patients with a proved history of migraine, admitted to our tertiary care stroke center between October 2010 and October 2013 who were referred for MR imaging within 24 hours of onset of symptoms of suspected stroke. Patients were diagnosed with migraine if they fulfilled the criteria specified in the International Classification of Headache Disorders.² The diagnosis was confirmed by a board-certified neurologist either at discharge or, in cases of a first episode, after confirmation during follow-up visits. The demographic characteristics and clinical history were obtained from the case records. The study was approved by the local ethics committee. Inclusion criteria were the following: 1) confirmed migraine according to the International Headache Society¹; 2) MR imaging within 24 hours of the onset of symptoms according to the standardized stroke protocol, which included perfusion imaging. Exclusion criteria were any cause of secondary headache (eg, cerebral vascular ischemia, sinus venous thrombosis, tumor, hemorrhage, dissection, or encephalitis). Due to the retrospective nature of this study, we did not exclude patients who were taking medication.

Image Acquisition

The imaging studies were performed with either a 1.5T or 3T scanner (Magnetom Avanto, Magnetom Aera, or Magnetom Verio; Siemens, Erlangen, Germany) using a standard 12-channel

head coil. Gadobutrol (Gadovist; Bayer Schering Pharma, Berlin, Germany) at 0.1 mL/kg body weight was injected before the perfusion sequence. Perfusion parameters were as follows: 1.5T: TR, 1410 ms; TE, 30 ms; averages, 1; FOV read, 230 mm; FOV phase, 100%; voxel size, 1.8 × 1.8 × 5.0 mm; flip angle, 90°; 80 repetitions; acquisition time, 1:59 minutes; 3T: TR, 1400 ms; TE, 29 ms; averages, 1; FOV read, 230 mm; FOV phase, 100%; voxel size, 1.8 × 1.8 × 5.0 mm; flip angle, 90°; 80 repetitions; acquisition time, 1:59 minutes. Nineteen parallel images were acquired with a slice thickness of 5.0 mm. Time-of-flight axial 3D MR angiography was performed with the following parameters for 1.5T: TR, 23 ms; TE, 7 ms; flip angle, 25°; FOV read, 230 mm; FOV phase, 94%; voxel size, 1.3 × 1.2 × 1.0 mm; number of slices, 78; number of averages, 1; for 3T: TR, 22 ms; TE, 3.6 ms; flip angle, 18°; FOV read, 181 mm; FOV phase, 90%; voxel size, 1.2 × 1.2 × 0.5 mm; number of slices, 78; number of averages, 1.

Image Analysis

Perfusion Analysis. Postprocessing for perfusion image analysis was performed with an FDA-approved postprocessing software package Olea Sphere 2.0 (Olea Medical, La Ciotat, France). The arterial input function was selected automatically using a cluster analysis algorithm,¹⁶ and the deconvoluted perfusion parameters were calculated using the oscillation index-type extension of the block-circulant singular value decomposition technique.¹⁷ Two radiologists with >15 years of experience qualitatively analyzed the perfusion data of all patients with the intention of depicting perfusion disturbances in any supratentorial area of the brain parenchyma on TTP, CBF, or CBV maps once consensus had been reached. The window width was manually adjusted to maximize visual contrast. The imaging data of patients with perfusion asymmetries were further analyzed in a semiquantitative fashion.

Semiquantitative Imaging Analysis. To account for focal changes of perfusion, ROI positioning followed the ASPECTS

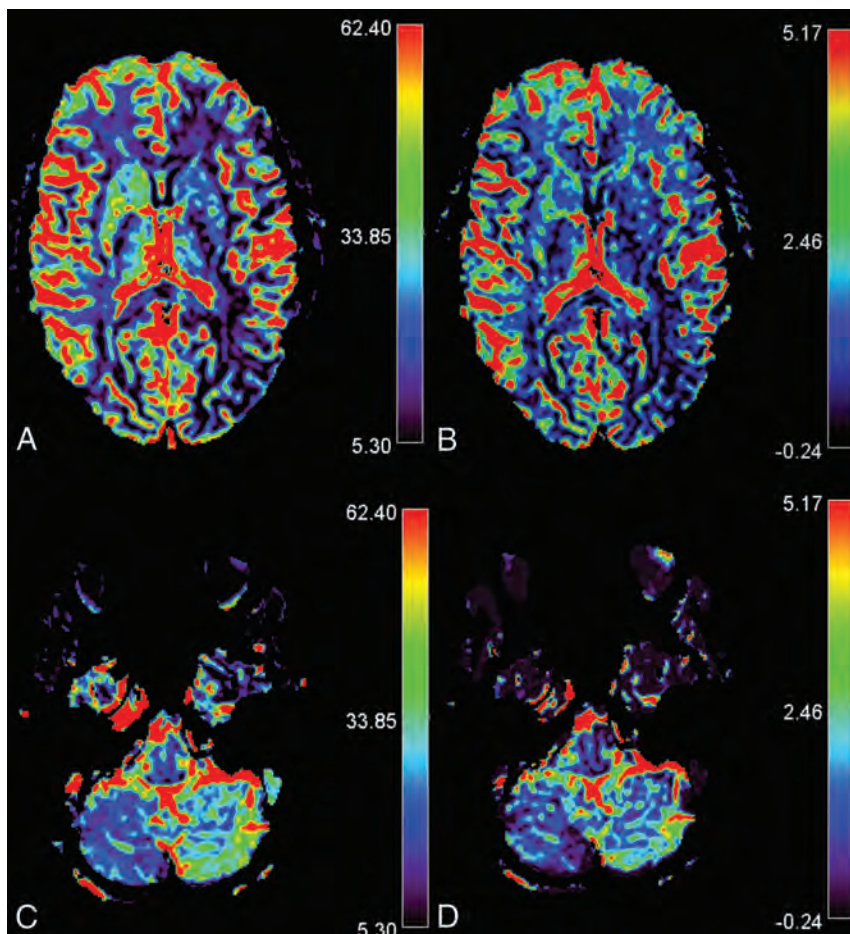


FIG 2. CCD in a 14-year-old girl presenting with MwA and CCD. Slices A and C show rCBF images of the infra- and supratentorial brain, and slices B and D, rCBV images respectively. The patient presented with HCH in the right cerebellum with overt hemispheric perfusion asymmetry. Fourteen of 17 supratentorial ROIs in the left supratentorial hemisphere exceeded the AI threshold with lateralization of hyperperfusion contralateral to the cerebellum. Bars indicate relative values for CBV and CBF.

score^{18,19} with 1 additional slice covering the sensory and motor cortex and frontal superior gyrus. ROIs were semiautomatically positioned on the postprocessed parameter maps, and the numeric values were extracted for TTP, MTT, regional CBF (rCBF), regional CBV (rCBV), and time-to-maximum of the tissue residue function time-to-maximum.¹⁶ For each hemisphere, 18 ROIs were placed as in Fig 1.

Because DSC MR perfusion imaging must be considered a semiquantitative method, we calculated an asymmetry index (AI) for the paired ROIs of the parameters rCBF and rCBV.^{20,21} The apparently more severely hypoperfused hemisphere was identified by experts. The AI was calculated using the following formula: $AI = 200 \times (ROI_{normal} - ROI_{hypoperfused}) / (ROI_{normal} + ROI_{contralateral})$.²² We heuristically set the cutoff at >10% for asymmetric perfusion, in line with previous work on perfusion imaging in patients with epilepsy.^{23,24}

CCD was defined as involving 2 conditions: 1) an AI value of >10% within 1 hypoperfused cerebellar hemisphere (HCH), and 2) an asymmetry in the contralateral hemisphere with an AI value of >10% in a majority of any of the supratentorial ROIs.

A sample description is provided in Fig 2.

Vertebral Artery Configuration

The vertebral arteries were analyzed on TOF angiograms to look for patency or hypoplasia to exclude perfusion abnormalities in the PICA territory related to an occluded or hypoplastic vessel. Vertebral artery hypoplasia was defined as a diameter of the vertebral artery of <1 mm.

Statistics

We used SPSS (Version 21; IBM, Armonk, New York) for statistical analysis. Descriptive data are presented as mean and SD or median. We used the Student *t* test for normally distributed supratentorial data and the Mann-Whitney *U* test for not normally distributed infratentorial data to compare numbers of ROIs with AI > 10% and mean values of AI (%) between groups. A *P* value < .05 was considered significant.

RESULTS

We identified 191 patients with migraine from our data base. Of these, 106 patients underwent a dedicated stroke protocol within 24 hours of onset of symptoms and 98 were finally diagnosed with MwA. In 23/106 patients (21.69%) patients, we identified focal cortical hypoperfusion. None of the patients presented with a DWI restriction. Fifteen of the 23 were female. Mean age was 28.8 years (range, 13–77 years). The laterality of the clinical symptoms was left-sided

in 8 patients and right-sided in 11. Alternating clinical patterns were observed in 2, and nonspecific symptoms, in 2 patients. MwA was the predominant final diagnosis in the patients with perfusion asymmetry, 22/23 patients.

For 13 of these 23 patients, the time between onset of symptoms and imaging was precisely documented (mean, 212 minutes; range, 95–429 minutes; median, 180 minutes). For the remaining 10 patients, the records documented MR imaging being performed within 12 hours of symptom onset. Of the 83 patients who had no perfusion alterations, the time between the onset of symptoms and MR imaging was precisely documented for 45 patients (mean, 384 minutes; range 55–1400 minutes; median, 315 minutes). For the remaining 38 patients, the onset of symptoms occurred up to 24 hours before the MR imaging. See Table 1 for clinical information on all patients and Table 2 for information on the subgroup of patients with and without CCD. Patients with cortical oligemia presented more often with aura symptoms than patients with normal perfusion. In patients with cortical oligemia, language and sensory symptoms were reported more frequently than visual and motor symptoms. Patients with HCH and the subgroup with CCD had a slightly lower frequency of

sensory symptoms than the non-HCH group, but other aura symptoms were equally distributed between the groups (Tables 1 and 2). Aura symptoms were not a predictor of HCH or CCD (Table 2).

Semiquantitative Evaluation

Overall, we included 18 paired ROIs in the analysis. The size of each ROI was kept uniform for all patients but varied among regions to account for regional anatomy (mean, $291 \pm 100 \text{ mm}^2$; range, 132–471 mm^2). All 23 patients presented with at least 1 supratentorial ROI with an AI value of $>10\%$ rCBF and rCBV.

Twelve patients had HCH. Nine of these patients presented

with reduced rCBF contralateral to the ill-perfused cerebellar hemisphere (CCD-positive); in 3 patients, we detected cortical rCBF reduction ipsilateral to the cerebellum. All patients with HCH presented with clinical symptoms attributable to a region of cortical hypoperfusion in the contralateral hemisphere (Table 3).

When HCH was present, the number of ROIs with an AI $>10\%$ found contralateral to the hypoperfused cerebellar hemisphere (103 for rCBF and 101 for rCBV) was nearly twice the number of ROIs which exceeded the threshold of 10% in the ipsilateral hemisphere (51 for rCBF and 54 for rCBV).

We observed no significant differences between HCH and non-HCH groups for mean AI values of rCBF and rCBV in the supratentorial hemisphere (Table 4).

Table 1: Clinical characteristics

Predominant Symptom	Abnormal Perfusion		Normal Perfusion	
	n = 23	%	n = 83	%
Headache	21	91.3	69	57.3
Aura symptoms	22	95.7	76	63.1
Visual	10	43.5	44	36.5
Sensory	17	73.9	37	30.7
Motor	8	34.8	22	18.3
Language	11	47.8	16	13.3

Vertebral Artery Configuration

In 22/23 patients, the vertebral artery appeared normal. One patient with CCD-positive MWA had a hypoplastic vertebral artery, which tapered into the PICA on the side of the hypoperfused cerebellum.

DISCUSSION

In this retrospective single-center study, we aimed to investigate the association between oligemia and HCH in patients with

migraine and its potential relation to small infarct-like cerebellar lesions. We observed cortical oligemia in 23/106 (21.69%) patients who underwent MR imaging to rule out ischemic stroke. Fifty-two percent of patients with oligemia presented with abnormal cerebellar perfusion, and 39.1% fulfilled the criteria for CCD, rendering it a frequent consequence of cortical spreading depression unrelated to vertebral artery hypoplasia.²⁵

Cerebellar hypoperfusion in patients with stroke is associated with a worse clinical outcome than if it was not present, related to deafferentation and transneuronal metabolic depression.²⁶ In seizure-related CCD, the outcome is variable, ranging from complete neurologic recovery to permanent disability depending on the duration of prolonged excitatory synaptic activity affecting cortico-ponto-cerebellar pathways.²⁷⁻³¹ While diffusion restriction is a common consequence of perfusion changes and related metabolic depletion in patients with stroke and epilepsy, this should be considered an exceptional phenomenon in migraine. In our cohort, none of the 106 patients had restricted diffusion or preexisting cerebellar infarct-like lesions. Although CCD was frequent, none of our patients with migraine experienced permanent deficits. We conclude that unlike in stroke- and seizure-

Table 2: Predominant clinical symptoms in patients with abnormal cortical perfusion

Predominant Symptom	Patients with Oligemia		HCH (CCD Subgroup)		Non-HCH	
	n = 23	%	n = 12 (9)	%	n = 11	%
Headache	21	91.3	10 (7)	43.5 (30.4)	11	47.8
Aura symptoms	22	95.7	12 (9)	52.2 (39.1)	10	43.5
Visual	10	43.5	5 (2)	21.7 (8.7)	5	21.7
Sensory	17	73.9	7 (5)	30.4 (21.7)	10	43.5
Motor	8	34.8	4 (4)	17.4 (17.4)	4	17.4
Language	11	47.8	6 (6)	26.1 (26.1)	5	21.7

Table 3: The number of ROIs with an AI of $>10\%$ in supratentorial oligemia (maximum, 17 per patient), in the group with hemispheric cerebellar hypoperfusion (154/204) and in the group with symmetric cerebellar perfusion (145/187)

	Abnormal ROIs (AI $>10\%$)	
	Patients with Hemispheric Cerebellar Hypoperfusion (n = 12)	Patients with Symmetric Cerebellar Perfusion (n = 11)
rCBF (No.)		
Total No. (%)	154 (75.5)	145 (77.5)
Contralateral	103	
Ipsilateral	51	
rCBV (No.)		
Total No. (%)	155 (75.5)	139 (74.3)
Contralateral	101	
Ipsilateral	54	

Table 4: Mean AI for hypoperfused cerebellar hemisphere and non-HCH (rCBF and rCBV)^a

	AI Absolute Values (%)				P Value
	Group HCH (n = 12)		Group Non-HCH (n = 11)		
	Mean	SD	Mean	SD	
rCBF supratentorial	27.60	6.85	26.30	6.66	.51
rCBV supratentorial	26.75	6.66	24.64	6.27	.48
rCBF infratentorial	30.56	16.77	4.24	3.23	$<.001$
rCBV infratentorial	25.69	16.00	4.02	2.53	$<.001$

^a Significant differences were noted only for infratentorial ROIs.

related CCD, CCD in MwA may be considered a benign phenomenon.

Cerebellar hypoperfusion has been addressed as a potential cause of cerebellar infarct-like lesions in MwA in previous studies.³ The findings of our retrospective study do not support the hypothesis of an increased risk of episode-triggered and oligemia-related hypoxic cerebellar infarctions. In our series, none of the patients with oligemia reached the ischemic threshold. In patients with MwA, the severity of cortical oligemia, expressed as increasing AI, was not directly associated with HCH or CCD, in contrast to observations in patients with ischemic stroke.³⁰ The size of the supratentorial oligemic area, expressed by the number of supratentorial ROIs beyond the threshold AI of >10%, also did not predict the likelihood of HCH or CCD. From a methodologic point of view, we excluded the transition parameters (TTP and MTT) from our perfusion analysis. Our findings were in line with those of Förster et al,³² who demonstrated that perfusion abnormalities in patients with MwA are predominantly substantiated by CBF and CBV changes. TTP analysis of the cerebellar hemispheres is hampered by variant vertebral artery configurations that directly influence the TTP and MTT maps, while no such detrimental effects have been reported for CBF analysis.²⁴

Furthermore, it is not yet known whether the development of infarct-like lesions is facilitated by multifactorial interactions of severe oligemia with other impeding factors that are not detected by perfusion MR imaging (eg, increased vulnerability to blood flow reduction). An increased susceptibility to acute ischemic injury has been demonstrated in patients with migraine, due to an unstable penumbra, especially in those with MwA.³³ Greater susceptibility to spreading depolarization in migraine-susceptible brains may be another potential mechanism for increased cerebral vulnerability to ischemia and stroke. Similar findings have been reported in an animal study.³⁴ Thus, typical episodes with regularly experienced aura symptoms may reflect benign oligemia not related to tissue damage, while prolonged and severe hypoxic episodes may ultimately induce parenchymal damage, which was not observed in our cohort.

This study has some limitations. Due to its retrospective design, there was no healthy control group. Because expert analysis was performed to select apparent perfusion deficits in patients with migraine, a rater-dependent bias cannot be fully excluded. However, in healthy volunteers, interhemispheric asymmetry is minimal (1.01%–3.14%) and symmetric rCBF distribution can be assumed between homologous regions, independent of age.³⁵ Thus, our ROI-based semiquantitative analysis with the rather strict threshold of >10%, as commonly used in stroke or epilepsy studies, may be considered appropriate to balance measurements of random asymmetry and spreading oligemia.^{22–24} Finally, all patients were symptom-free during follow-up. However, we cannot fully exclude the possibility that asymptomatic parenchymal damage may have remained undetected. Further studies would be required to answer this question.

CONCLUSIONS

HCH and CCD are frequently observed in patients presenting with acute MwA. Cerebellar hypoperfusion in patients with migraine appears, in contrast to stroke- and seizure-related CCD, to

be a benign phenomenon. Our study could not provide evidence for a link between cerebellar hypoperfusion and cortical hypoperfusion in the pathogenesis of cerebellar infarctions but encourages future investigations that pay special attention to factors other than hypoperfusion alone to better understand the cause of infarct-like lesions in the cerebellum of patients who have MwA.

Disclosures: Roland Wiest—UNRELATED: Grants/Grants Pending: Swiss National Foundation, Swiss Heart Foundation.

REFERENCES

1. Lipton RB, Stewart WF, Diamond S, et al. **Prevalence and burden of migraine in the United States: data from the American Migraine Study II.** *Headache* 2001;41:646–57 CrossRef Medline
2. Headache Classification Subcommittee of the International Headache Society. **The International Classification of Headache Disorders: 2nd ed.** *Cephalalgia* 2004;24(Suppl 1):9–160 CrossRef Medline
3. Kruit MC, van Buchem MA, Hofman PA, et al. **Migraine as a risk factor for subclinical brain lesions.** *JAMA* 2004;291:427–34 CrossRef Medline
4. Kruit MC, Launer LJ, Ferrari MD, et al. **Infarcts in the posterior circulation territory in migraine: the population-based MRI CAMERA study.** *Brain* 2005;128(Pt 9):2068–77 CrossRef Medline
5. Olesen J, Larsen B, Lauritzen M. **Focal hyperemia followed by spreading oligemia and impaired activation of rCBF in classic migraine.** *Ann Neurol* 1981;9:344–52 CrossRef Medline
6. Kapinos G, Fischbein NJ, Zaharchuk G, et al. **Migraine-like headache with visual deficit and perfusion abnormality on MRI.** *Neurology* 2010;25;74:1743–45 CrossRef Medline
7. Fernandes PM, Whiteley WN, Hart SR, et al. **Strokes: mimics and chameleons.** *Pract Neurol* 2013;21–28 CrossRef Medline
8. Magauran BG Jr, Nitka M. **Stroke mimics.** *Emerg Med Clin North Am* 2012;30:795–804 CrossRef Medline
9. Yamauchi H, Fukuyama H, Nagahama Y, et al. **Uncoupling of oxygen and glucose metabolism in persistent crossed cerebellar diaschisis.** *Stroke* 1999;30:1424–28 CrossRef Medline
10. Yamauchi H, Fukuyama H, Kimura J, **Hemodynamic and metabolic changes in crossed cerebellar hypoperfusion.** *Stroke* 1992; 23:855–60 CrossRef Medline
11. Noguchi T, Nishihara M, Egashira Y, et al. **Arterial spin-labeling MR imaging of cerebral hemorrhages.** *Neuroradiology* 2015;57:1135–44 CrossRef Medline
12. Fu J, Chen WJ, Wu GY, et al. **Whole-brain 320-detector row dynamic volume CT perfusion detected crossed cerebellar diaschisis after spontaneous intracerebral hemorrhage.** *Neuroradiology* 2015; 57:179–87 CrossRef Medline
13. Nakae S, Inamasu J, Ohmi T, et al. **Relative vasodilatory change in seizure-induced crossed cerebellar diaschisis.** *Intern Med* 2016;55: 713–14 CrossRef Medline
14. Dodick DW, Roarke MC. **Crossed cerebellar diaschisis during migraine with prolonged aura: a possible mechanism for cerebellar infarctions.** *Cephalalgia* 2008;28:83–86 CrossRef Medline
15. Crawford JS, Konkol RJ. **Familial hemiplegic migraine with crossed cerebellar diaschisis and unilateral meningeal enhancement.** *Headache* 1997;37:590–93 CrossRef Medline
16. Mouridsen K, Christensen S, Gyldensted L, et al. **Automatic selection of arterial input function using cluster analysis.** *Magn Reson Med* 2006;55:524–31 CrossRef Medline
17. Wu O, Østergaard L, Weisskoff RM, et al. **Tracer arrival timing-insensitive technique for estimating flow in MR perfusion-weighted imaging using singular value decomposition with a block-circulant deconvolution matrix.** *Magn Reson Med* 2003;50: 164–74 CrossRef Medline
18. Aviv RI, Mandelcorn J, Chakraborty S, et al. **Alberta Stroke Program Early CT Scoring of CT perfusion in early stroke visualization and**

- assessment. *AJNR Am J Neuroradiol* 2007;28:1975–80 CrossRef Medline
19. Puetz V, Khomenko A, Hill MD, et al. **Basilar Artery International Cooperation Study (BASICS) Group: extent of hypoattenuation on CT angiography source images in basilar artery occlusion—prognostic value in the Basilar Artery International Cooperation Study.** *Stroke* 2011;42:3454–59 CrossRef Medline
 20. Strother MK, Buckingham C, Faraco CC, et al. **Crossed cerebellar diaschisis after stroke identified noninvasively with cerebral blood flow-weighted arterial spin labeling MRI.** *Eur J Radiol* 2016;85:136–42 CrossRef Medline
 21. Madai VI, Altaner A, Stengl KL, et al. **Crossed cerebellar diaschisis after stroke: can perfusion-weighted MRI show functional inactivation?** *J Cereb Blood Flow Metab* 2011;31:1493–500 CrossRef Medline
 22. Takano A, Shiga T, Kobayashi J, et al. **Thalamic asymmetry on interictal SPECT in patients with frontal lobe epilepsy.** *Nucl Med Commun* 2001;22:319–24 CrossRef Medline
 23. Wiest R, von Bredow F, Schindler K, et al. **Detection of regional blood perfusion changes in epileptic seizures with dynamic brain perfusion CT: a pilot study.** *Epilepsy Res* 2006;72:102–10 CrossRef Medline
 24. Hauf M, Slotboom J, Nirkko A, et al. **Cortical regional hyperperfusion in nonconvulsive status epilepticus measured by dynamic brain perfusion CT.** *AJNR Am J Neuroradiol* 2009;30:693–98 CrossRef Medline
 25. Thierfelder KM, Baumann AB, Sommer WH, et al. **Vertebral artery hypoplasia: frequency and effect on cerebellar blood flow characteristics.** *Stroke* 2014;45:1363–68 CrossRef Medline
 26. Takasawa M, Watanabe M, Yamamoto S, et al. **Prognostic value of subacute crossed cerebellar diaschisis: single-photon emission CT study in patients with middle cerebral artery territory infarct.** *AJNR Am J Neuroradiol* 2002;23:189–93 Medline
 27. Graffeo CS, Snyder KA, Nasr DM, et al. **Prognostic and mechanistic factors characterizing seizure-associated crossed cerebellar diaschisis.** *Neurocrit Care* 2016;24:258–63 CrossRef Medline
 28. Kato T, Okumura A, Hayakawa F, et al. **Transient reduced diffusion in the cortex in a child with prolonged febrile seizures.** *Brain Dev* 2012;34:773–75 CrossRef Medline
 29. Massaro AM. **Teaching neuroimages: crossed cerebellar diaschisis in hemispheric status epilepticus.** *Neurology* 2012;79:e182 CrossRef Medline
 30. Zaidi SA, Haq MA, Bindman D, et al. **Crossed cerebellar diaschisis: a radiological finding in status epilepticus not to miss.** *BMJ Case Rep* 2013;2013. pii: bcr2013200478 CrossRef Medline
 31. Ohe Y, Hayashi T, Deguchi I, et al. **A case of nonconvulsive status epilepticus with a reversible contralateral cerebellar lesion: temporal changes in magnetic resonance imaging and single-photon emission computed tomography finding.** *J Stroke Cerebrovasc Dis* 2013;22:e639–42 CrossRef Medline
 32. Förster A, Wenz H, Kerl HU, et al. **Perfusion patterns in migraine with aura.** *Cephalalgia* 2014;34:870–76 CrossRef Medline
 33. Mawet J, Eikermann-Haerter K, Park KY, et al. **Sensitivity to acute cerebral ischemic injury in migraineurs: a retrospective case-control study.** *Neurology* 2015;85:1945–49 CrossRef Medline
 34. Eikermann-Haerter K, Lee JH, Yalcin N, et al. **Migraine prophylaxis, ischemic depolarizations, and stroke outcomes in mice.** *Stroke* 2015;46:229–36 CrossRef Medline
 35. Catafau AM, Lomeña FJ, Pavia J, et al. **Regional cerebral blood flow pattern in normal young and aged volunteers: a 99mTc-HMPAO SPET study.** *Eur J Nucl Med* 1996;23:1329–37 CrossRef Medline

Iodine Extravasation Quantification on Dual-Energy CT of the Brain Performed after Mechanical Thrombectomy for Acute Ischemic Stroke Can Predict Hemorrhagic Complications

M. Bonatti, F. Lombardo, G.A. Zamboni, F. Vittadello, R. Currò Dossi, B. Bonetti, R. Pozzi Mucelli, and G. Bonatti



ABSTRACT

BACKGROUND AND PURPOSE: Intracerebral hemorrhage represents a potentially severe complication of revascularization of acute ischemic stroke. The aim of our study was to assess the capability of iodine extravasation quantification on dual-energy CT performed immediately after mechanical thrombectomy to predict hemorrhagic complications.

MATERIALS AND METHODS: Because this was a retrospective study, the need for informed consent was waived. Eighty-five consecutive patients who underwent brain dual-energy CT immediately after mechanical thrombectomy for acute ischemic stroke between August 2013 and January 2017 were included. Two radiologists independently evaluated dual-energy CT images for the presence of parenchymal hyperdensity, iodine extravasation, and hemorrhage. Maximum iodine concentration was measured. Follow-up CT examinations performed until patient discharge were reviewed for intracerebral hemorrhage development. The correlation between dual-energy CT parameters and intracerebral hemorrhage development was analyzed by the Mann-Whitney *U* test and Fisher exact test. Receiver operating characteristic curves were generated for continuous variables.

RESULTS: Thirteen of 85 patients (15.3%) developed hemorrhage. On postoperative dual-energy CT, parenchymal hyperdensities and iodine extravasation were present in 100% of the patients who developed intracerebral hemorrhage and in 56.3% of the patients who did not ($P = .002$ for both). Signs of bleeding were present in 35.7% of the patients who developed intracerebral hemorrhage and in none of the patients who did not ($P < .001$). Median maximum iodine concentration was 2.63 mg/mL in the patients who developed intracerebral hemorrhage and 1.4 mg/mL in the patients who did not ($P < .001$). Maximum iodine concentration showed an area under the curve of 0.89 for identifying patients developing intracerebral hemorrhage.

CONCLUSIONS: The presence of parenchymal hyperdensity with a maximum iodine concentration of >1.35 mg/mL may identify patients developing intracerebral hemorrhage with 100% sensitivity and 67.6% specificity.

ABBREVIATIONS: DECT = dual-energy CT; ICH = intracerebral hemorrhage; PH = parenchymal hematoma; VNC = virtual unenhanced reconstructions

Mechanical thrombectomy in addition to intravenous tissue plasminogen activator administration has become the treatment of choice for patients with ischemic stroke secondary to a large-vessel occlusion.^{1,2} Despite the advances in patient selection, intracerebral hemorrhage (ICH) still represents a relevant complication of both mechanical thrombectomy and intravenous

thrombolysis, with a prevalence ranging from 4.3% to 43%.^{3,4} ICHs following revascularization for acute ischemic stroke comprise hemorrhagic infarction and parenchymal hematoma (PH); hemorrhagic infarction is often asymptomatic, whereas PH is associated with high mortality rates and significantly worsened patient prognosis.⁵⁻⁷ Unenhanced CT is commonly performed within 24 hours after the treatment to rule out ICH.⁸ Areas of increased attenuation can be observed in 33%–86% of the patients immediately after mechanical thrombectomy, mainly as a consequence of iodinated contrast material extravasation secondary to blood-brain barrier disruption, but the differential diagnosis with intracerebral hemorrhage can be challenging on single-energy CT acquisitions.⁹⁻¹²

Dual-energy CT (DECT) has already proved to be helpful in differentiating contrast material extravasation and hemorrhage by subtracting the iodine component from the hyperdense area

Received July 21, 2017; accepted after revision November 5.

From the Departments of Radiology (M.B., F.L., G.B.) and Neurology (R.C.D., B.B.), Bolzano Central Hospital, Bolzano, Italy; Department of Radiology (G.A.Z., R.P.M.), University of Verona, Verona, Italy; and Explora-Research and Statistical Analysis (F.V.), Vigodarzere, Italy.

Preliminary data for this work were previously presented at: Annual Meeting of the European Congress of Radiology, March 1–5, 2017; Vienna, Austria.

Please address correspondence to Matteo Bonatti, MD, Department of Radiology, Bolzano Central Hospital, 5 Boehler St, 39100 Bolzano, Italy; e-mail: matteobonatti@hotmail.com

<http://dx.doi.org/10.3174/ajnr.A5513>

on virtual unenhanced reconstructions (VNC).^{9-11,13-16} However, late hemorrhagic complications may also occur in patients without bleeding signs on 24-hour CT. Given the impact of ICH on patient medical management (eg, platelet antiaggregants should be avoided in patients thought to have high bleeding risk), many algorithms have been developed to attempt to identify patients at higher risk for ICH development.^{4,5,17-21}

The aim of our study was to assess the capability of iodine extravasation quantification on dual-energy CT performed immediately after mechanical thrombectomy to predict hemorrhagic complications.

MATERIALS AND METHODS

Patient Population

This was a retrospective study approved by our institutional review board; the need for informed consent was waived. We considered for inclusion 114 consecutive patients who underwent mechanical thrombectomy at Bolzano Central Hospital between August 2013 and January 2017 because of acute ischemic stroke secondary to a large-vessel occlusion with a National Institutes of Health Stroke Scale score of >6 and symptom onset <6 hours for anterior circulation and <12 hours for posterior circulation. All patients underwent preprocedural unenhanced brain CT and CT angiography. Since 2007 in our institution, unenhanced brain CT is performed immediately after mechanical thrombectomy to rule out hemorrhagic complications; since August 2013, we acquire it with a dual-energy protocol to more confidently differentiate iodine extravasation from hemorrhage.¹⁴ The inclusion criterion was performance of unenhanced DECT of the brain within 1 hour after mechanical thrombectomy (91/114 patients). Exclusion criteria were unsatisfactory image quality because of motion artifacts (5/91 patients) and loss of DECT data (1/91 patients). Therefore, our study population included 85 patients, 52 men and 33 women, with a median age of 70 years (range, 31–87 years). All patients underwent follow-up CT 24 hours after the procedure unless earlier due to clinical worsening; further follow-up CTs were performed according to clinical status.

Imaging Protocols

Endovascular procedures were performed on a biplane x-ray system (Allura Xper FD20/20; Philips Healthcare, Best, the Netherlands) by 1 of a pool of 4 radiologists with 3–25 years of experience in interventional neuroradiology. All patients were treated according to a sequential approach that consisted of first-line aspiration using a 5MAX/4MAX reperfusion catheter (Penumbra, Alameda, California) followed by mechanical thrombectomy with a Solitaire Flow-Restoration stent retriever (Covidien, Irvine, California)²²⁻²⁵ if aspiration was unsuccessful.

CT examinations were performed on a second-generation dual-source CT scanner (Somatom Definition Flash; Siemens, Erlangen, Germany) equipped with a tin filter. Immediate postoperative examinations were performed using a dual-energy technique (80/Sn140 kV[peak]), whereas preoperative and follow-up examinations were performed using a single-energy technique (120 kVp). All patients were positioned supine on the table with their arms along the body. Scanning parameters are reported in Table 1.

Table 1: Scanning parameters for postoperative unenhanced dual-energy brain CT and follow-up unenhanced brain CT

	DECT	SECT
Scanning technique	Spiral	Spiral
Scan direction	Caudocranial	Caudocranial
kVp	80/140	120
mAs ref	310/155	390
Collimation (mm)	40 × 0.6	128 × 0.6
Rotation time (sec)	0.5	1
Pitch	0.7	0.55
CARE Dose 4D ^a	On	On
CARE-kV ^a	Not available	Off
X-CARE ^a	Not available	On
Kernel	D34f	H40s

Note:—SECT indicates single-energy CT; ref, reference.

^a Siemens.

Image Analysis

Postoperative DECT images were independently and randomly evaluated by 2 radiologists with 8 and 5 years of experience in diagnostic neuroradiology, blinded to clinical data, using 3-mm-thick multiplanar reconstructions. Window levels were set as suggested by the manufacturer and adjusted as needed. For each patient, simulated 120-kV images, VNC images, and iodine map images were generated using commercially available software (syngo.via, Dual-Energy CT Brain Hemorrhage application, Version VA30A; Siemens). Simulated 120-kV images represent a weighted average of the original low-kilovolt and high-kilovolt images, whereas VNC images and iodine map images are generated using a 3-material decomposition algorithm. For qualitative image analysis, the presence (yes/no), distribution (deep white matter, cortical-subcortical, or both), and homogeneity (homogeneous/inhomogeneous) of parenchymal hyperdensities were assessed on simulated 120-kV images; the presence of iodine extravasation (yes/no) was assessed on iodine map images, and the presence of ICH (yes/no) was assessed on VNC images. Inter-reader discrepancies were solved by consensus. For quantitative image analysis, the average attenuation value (Hounsfield unit) at the site of maximum apparent attenuation (further reported as “maximum hyperdensity attenuation”) was measured on simulated 120-kV images by drawing a 0.3-cm² round ROI, and the average iodine concentration (milligrams/milliliter) at the site of maximum apparent iodine extravasation (further reported as “maximum iodine concentration”) was measured on iodine map images by drawing a 0.3-cm² dual-energy ROI circle. The mean of the values obtained by the 2 readers was used for further analyses.

The Alberta Stroke Program Early CT Score was assessed on preoperative unenhanced CT of each patient by the 2 radiologists in consensus.

Finally, the 2 readers in consensus reviewed all the follow-up CTs, specifically looking for ICH development. ICH was defined by the presence of parenchymal hyperdensity persisting/increasing >48 hours after the procedure and/or by the appearance of new hyperdense lesions²⁶; ICH on follow-up CTs was considered the reference standard for our study. ICHs were further subdivided according to the European Cooperative Acute Stroke Study classification³ into hemorrhagic infarction and parenchymal hematoma.

Table 2: Results of postoperative DECT image analysis with interreader concordance and subsequent consensus

	Reader 1	Reader 2	Interreader Concordance	Consensus
Presence of parenchymal hyperdensity				
Yes	53/85 (62.4%)	53/85 (62.4%)	$\kappa = 0.95$; 95% CI, 0.882–1.000	54/85 (63.5%)
No	32/85 (37.6%)	32/85 (37.6%)		
Hyperdensity location				
DWM	26/53 (49.1%)	31/53 (58.5%)	$\kappa = 0.745$; 95% CI, 0.588–0.903	29/54 (53.7%)
DWM+cortical/subcortical	21/53 (39.6%)	16/53 (30.2%)		
Cortical/subcortical	6/53 (11.3%)	6/53 (11.3%)		
Hyperdensity homogeneity				
Homogeneous	29/53 (54.7%)	31/53 (58.5%)	$\kappa = 0.799$; 95% CI, 0.632–0.966	30/54 (55.6%)
Inhomogeneous	24/53 (45.3%)	22/53 (41.5%)		
Mean maximum attenuation (HU)	100 (median 77, range 45–701)	103 (median 76, range 47–789)	$P = .999$	74 (range, 47–745)
Presence of iodine extravasation				
Yes	53/85 (62.4%)	53/85 (62.4%)	$\kappa = 0.976$; 95% CI, 0.929–1.000	54/85 (63.5%)
No	32/85 (37.6%)	32/85 (37.6%)		
Mean maximum iodine concentration (mg/dL)	3.0 (median, 1.8; range 0.5–28.4)	2.9 (median, 1.6; range 0.6–27.7)	$P = .926$	1.8 (range, 0.5–28.1)
Hemorrhage on VNC images				
Yes	5/85 (5.9%)	5/85 (5.9%)	$\kappa = 1.000$; 95% CI, 1.000–1.000	5/85 (5.9%)
No	80/85 (94.1%)	80/85 (94.1%)		

Note:—DWM indicates deep white matter.

Clinical-Radiologic Data Collection

A third physician, not involved in image analysis, retrieved, from our institutional data base, the following data for each patient: sex, age, time of symptom onset, National Institutes of Health Stroke Scale score at admission, site of vessel occlusion at preoperative CTA, preoperative intravenous tissue plasminogen activator administration (Actilyse; Boehringer Ingelheim, Ingelheim, Germany), general anesthesia during the interventional procedure, number of aspiration and thrombectomy attempts, arterial stent delivery, puncture-to-recanalization time, time to recanalization, and the postoperative Thrombolysis in Cerebral Infarction angiographic score.

Statistical Analysis

Continuous variables are reported as mean and/or median values and range (minimum and maximum); categorical variables, as numbers and percentages. Interobserver agreement was calculated according to weighted κ statistics; agreement was considered very good if $\kappa = 0.81$ –1.00, good if $\kappa = 0.61$ –0.80, moderate if $\kappa = 0.41$ –0.60, fair if $\kappa = 0.21$ –0.40, and poor if $\kappa < 0.20$. Interreader discrepancies for quantitative image analysis were evaluated using the Wilcoxon test for paired data. The comparison between subgroups (ICH versus non-ICH) was performed with the Mann-Whitney U test for continuous variables, whereas qualitative data were compared using the χ^2 or Fisher exact tests (Fisher-Freeman-Halton test for $R \times C$ tables) when necessary. Receiver operating characteristic curves were calculated for continuous variables significantly associated with ICH. Multivariate logistic regression analyses (Wald statistic criteria, using the backward elimination method), adjusted for variables with a $P < .05$ on univariate analysis, were built to assess the value of these parameters to predict the risk of bleeding using a conditional forward procedure. Correlation between maximum iodine density and maximum attenuation was evaluated using the Spearman rank correlation coefficient. All tests were 2-sided; P values $< .05$ were considered statistically significant. Statistical analysis was performed using SPSS, Version 18.0 (IBM, Armonk, New York).

RESULTS

Pre- and Perioperative Data

Patients showed a mean NIHSS score of 20 (median, 20; range, 7–40) at admission. The mean ASPECTS at preoperative unenhanced brain CT was 8.9 (median, 10; range, 6–10). Seventy-six of 85 (89.4%) patients had an anterior circulation stroke, whereas 9/85 (10.6%) had a posterior circulation stroke. “Tandem” occlusion was present in 15/85 (17.6%) cases. Tissue plasminogen activator was administered to 40/85 (47.1%) patients. Fifty of 85 (58.8%) procedures were performed with the patient under general anesthesia, and 35/85 (41.2%), with the patient under conscious sedation. Fifty-eight of 85 (68.2%) patients were treated with aspiration only, and 27/85 (31.8%), with aspiration followed by stent-retriever thrombectomy. The median number of aspiration attempts was 2 (range, 0–8). The median number of retrieval attempts in the 27/85 patients who underwent stent-retriever thrombectomy was 2 (range, 1–4). A carotid artery stent was positioned in 6/85 (7%) patients. The mean time to recanalization was 4 hours 43 minutes (range, 1 hour 25 minutes to 9 hours 40 minutes), and the mean puncture-to-recanalization time was 68 minutes (range, 15–167 minutes). The TICI score was 0 in 10/85 (11.8%) patients; 1 in 5/85 (5.9%); 2a in 15/85 (17.6%); 2b in 16/85 (18.8%); and 3 in 39/85 (45.9%); therefore, revascularization was considered successful in 55/85 (64.7%) cases.

Image Analysis

The results of postoperative DECT image analysis with interreader concordance and subsequent consensus are reported in Table 2.

The 2 readers in consensus reviewed a median of 3 follow-up CTs per patient (range, 2–9). ICH was detected in 14/85 (16.5%) patients: Six patients (7.1%) showed hemorrhagic infarction, and 8 (9.4%), PH. In 7/14 (50.0%) patients, ICH was present 24 hours after the procedure; in 3/14 (21.4%), it appeared 24–48 hours after the procedure; in 2/14 (14.3%), 48–72 hours after the procedure; and in 2/14 (14.3%), >72 hours after the procedure.



FIG 1. A, Postoperative DECT with an iodine map overlay shows a cortical-subcortical hyperdensity secondary to iodine extravasation with a maximum iodine concentration of 3.0 mg/mL; no hyperdensity was visible on virtual unenhanced images (not included). B, A follow-up CT performed 48 hours later because of sudden clinical worsening shows a large parenchymal hematoma with a contralateral shift of the midline structures.

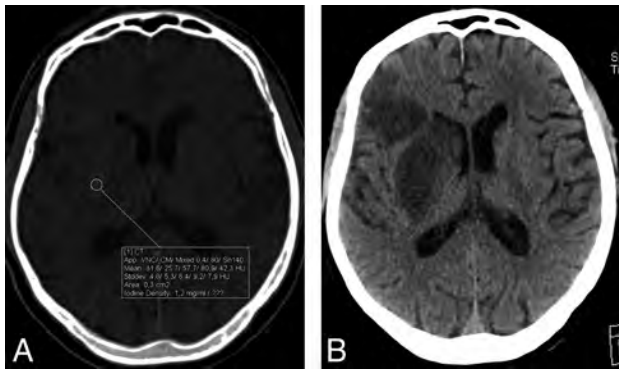


FIG 2. A, Postoperative DECT with an iodine map overlay shows a cortical-subcortical and deep white matter hyperdensity secondary to iodine extravasation with a maximum iodine concentration of 1.2 mg/mL; no hyperdensity was visible on virtual unenhanced images (not included). B, The follow-up CT performed before discharge, 4 days later, shows ischemic lesions at the sites of iodine extravasation but no hemorrhage.

Imaging Findings: ICH Development Correlation

On simulated 120-kV images, parenchymal hyperdensity was present in 14/14 (100%) patients who developed ICH and in 40/71 (56.3%) patients who did not ($P = .002$). Hyperdensity was inhomogeneous in 10/14 (71.4%) patients who developed ICH and in 14/40 (35.0%) patients who did not ($P = .028$). Median maximum hyperdensity attenuation was 85 HU (range, 63–745 HU) in the group of patients who developed ICH and 68 HU (range, 47–171 HU) in the group who did not ($P = .010$). On iodine map images, iodine extravasation was present in 14/14 (100%) patients who developed ICH and in 40/71 (56.3%) patients who did not ($P = .002$). Median maximum iodine concentration was 2.63 mg/mL (range, 1.4–28.1 mg/mL) in the group of patients who developed ICH and 1.40 mg/mL (0.5–4.2 mg/mL) in the group who did not ($P < .001$). A cutoff value of 1.35 mg/mL enabled identifying patients developing ICH with 100% sensitivity (95% CI, 76.8%–100%) and 47.5% specificity (95% CI, 31.5%–63.9%), with a likelihood ratio of 1.905 (Figs 1 and 2).

On VNC images, signs of bleeding were present in 5/14 (35.7%) patients who developed ICH. Complete data about the

correlation between DECT findings and ICH development are reported in Table 3. Maximum hyperdensity attenuation showed an area under the curve of 0.73 (95% CI, 0.60–0.87) for identifying patients developing ICH (Fig 3); a cutoff value of 67 HU enabled identifying patients developing ICH with 92.9% sensitivity (95% CI, 66.1%–99.8%) and 47.5% specificity (95% CI, 31.5%–63.9%), with a likelihood ratio of 1.77. Maximum iodine concentration showed an area under the curve of 0.89 (95% CI, 0.68–0.92) for identifying patients developing ICH (Fig 4); a cutoff value of 1.3 mg/mL enabled identifying patients developing ICH with 100% sensitivity (95% CI, 76.8%–100%) and 47.5% specificity (95% CI, 31.5%–63.9%), with a likelihood ratio of 1.90. A significant correlation between maximum iodine concentration on iodine map images and maximum attenuation on simulated 120-kV images was observed, with the Spearman $r = 0.901$ (95% CI, 0.832–0.943) ($P < .001$). The 2 parameters showed a linear regression correlation with a slope of 20.27 (95% CI, 18.39–22.15) (Fig 5).

Clinical Parameters: ICH Development Correlation

At preoperative CT, the median ASPECTS was 8 in the patients who developed ICH and 10 in the patients who did not ($P = .008$). ASPECTS showed an area under the curve of 0.71 (95% CI, 0.57–0.84) for identifying patients developing ICH; a cutoff value of 8 enabled identification of patients developing ICH with 57.1% sensitivity (95% CI, 28.9%–82.3%) and 71.8% specificity (95% CI, 59.9%–81.9%), with a likelihood ratio of 2.03. Patient sex and age, NIHSS score at admission, site of vessel occlusion, tPA administration, general anesthesia, revascularization technique, number of aspiration attempts, number of stent retriever thrombectomy attempts, stent delivery, puncture-to-recanalization time, time to recanalization, and TICI score did not show any significant correlation with ICH development ($P > .05$).

Multivariate Analysis

On multivariate analysis, it was impossible to elaborate a predictive model for the identification of patients developing ICH. However, in our series, a diagnostic algorithm that subsequently evaluates the presence of parenchymal hyperdensity and maximum iodine concentration (Fig 6) enables identifying patients developing ICH with 100% sensitivity and 67.5% specificity.

DISCUSSION

The aim of our study was to assess the capability of iodine extravasation quantification on dual-energy CT performed immediately after mechanical thrombectomy to predict hemorrhagic complications.

Intracranial hemorrhage represents a well-known complication of acute ischemic stroke revascularization treatment, determining relevant changes in patient medical treatment and often worsening their outcome. In line with the data published in the literature,^{3,4,27} hemorrhagic complications were detected in 16.5% of the patients in our series; 7.1% of the patients showed a hemorrhagic infarction, which was asymptomatic in 83.3% of patients, whereas 9.4% developed a parenchymal hematoma, which always correlated with severe worsening of neurologic status and required decompressive craniectomy in 75% of the cases.

Table 3: Univariate analysis—association between postoperative dual-energy CT parameters and subsequent intracerebral hemorrhage development^a

	Non-ICH Group (n = 71) No. (%)	ICH Group (n = 14) No. (%)	P Value
Hyperdensity on simulated 120-kV images			.002 ^b
Yes	40/71 (56.3%)	14/14 (100%)	
No	31/71 (43.7%)	0/14 (0%)	
Hyperdensity site			.342
DWM	23/40 (57.5%)	6/14 (42.9%)	
DWM + cortical	11/40 (27.5%)	7/14 (50.0%)	
Cortical	6/40 (15.0%)	1/14 (7.1%)	
Hyperdensity homogeneity			.028 ^b
Homogeneous	26/40 (65.0%)	4/14 (28.6%)	
Inhomogeneous	14/40 (35.0%)	10/14 (71.4%)	
Hyperdensity maximum attenuation Median (HU)	68	85	.010 ^b
Iodine extravasation on iodine map images			.002 ^b
Yes	40/71 (56.3%)	14/14 (100%)	
No	31/71 (43.7%)	0/14 (0%)	
Maximum iodine concentration Median (mg/mL)	1.40	2.63	<.001 ^b
Hemorrhage on VNC images			<.001 ^b
Yes	0/71 (0%)	5/14 (35.7%)	
No	71/71 (100%)	9/14 (64.3%)	

Note:—DWM indicates deep white matter.

^a The strength of the association is quantified by the P value (significant if P < .05).

^b Significant.

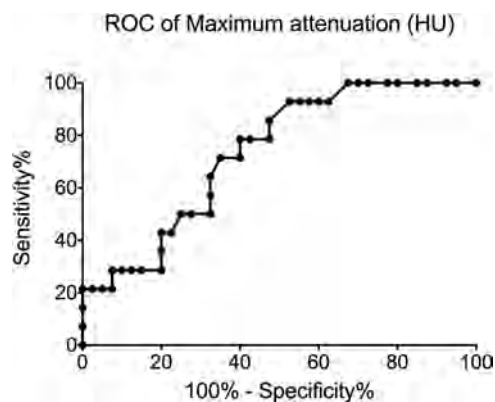


FIG 3. Receiver operator characteristic (ROC) curve showing sensitivity and specificity of maximum hyperdensity attenuation in identifying patients developing ICH.

Although ICH typically appears within the first 24 hours after treatment, delayed bleeding may also occur; in our series, 50% of the ICHs appeared >24 hours after the procedure. The identification of patients with high bleeding risk is crucial to improving their clinical management and potential outcome; for example, antiaggregation should be delayed in these patients and arterial pressure should be strictly monitored to avoid hypertensive peaks. Therefore, many attempts have been made to identify patients at risk for ICH development, with variable results.^{5,17-19} In our series, ASPECTS \leq 8 at preoperative CT and the presence of parenchymal hyperdensity, hyperdensity inhomogeneity, hyperdensity attenuation of >67 HU; iodine extravasation; maximum iodine concentration of >1.35 mg/mL; and bleeding signs on postoperative DECT were significantly correlated with ICH development. Our study also confirmed the reproducibility of DECT in the evaluation of patients after mechanical thrombec-

tomy: All the evaluated parameters showed an interreader agreement ranging from “good” to “very good.”

The integrity of the blood-brain barrier is governed by the tight junctions between endothelial cells, which regulate small molecule diffusion, and the basal lamina, a structural barrier preventing cellular extravasation.²⁸ To our knowledge, only 1 article focused on the relationship between contrast extravasation and hemorrhage development. Yoon et al²⁹ divided parenchymal hyperdensities after revascularization into contrast enhancement, defined as a hyperdense lesion without mass effect that disappeared on a 24-hour follow-up CT scan, and contrast extravasation, defined as a hyperdense lesion with a maximum measurement of >90 HU that persisted on a 24-hour follow-up CT scan. In their work, they found that the latter was associated with a higher rate of parenchymal hematomas; therefore, they postulated that contrast extravasation might be due to basal lamina disruption.

Unlike the work of Yoon et al, our study was based on dual-energy CT acquisitions, which allowed a quantification of iodine extravasation; therefore, we focused on the possible relationship between iodine concentration and subsequent hemorrhage development. Moreover, the study by Yoon et al was based on patients who underwent intra-arterial thrombolysis, whereas the patients included in our study underwent mechanical thrombectomy, a procedure that might incur some degree of endothelial damage.

In our series, there was a significant correlation between the maximum concentration of extravasated iodinated contrast material and subsequent hemorrhage development: Receiver operating characteristic analysis showed that the presence of hyperattenuating areas with maximum iodine concentration of >1.35 mg I/mL on postoperative DECT identified patients developing ICH with 100% sensitivity and 67.6% specificity. We chose the 1.35-mg I/mL cutoff value because the main aim in postoperative patient management is to minimize hemorrhagic complications; therefore, a moderate specificity can be tolerated to obtain excellent sensitivity. According to our results, patients showing iodine extravasation with iodine concentration of >1.35 mg I/mL should not undergo postoperative antiaggregation/anticoagulation and should be more closely monitored to prevent hypertensive peaks.

We found a linear correlation between maximum iodine concentration and maximum hyperdensity attenuation, with a significant association between higher attenuation values and hemorrhage development, substantially confirming the results obtained by Yoon et al with single energy acquisitions. High attenuation may be a consequence of both bleeding and increased iodine extravasation, with the latter being a biomarker of blood-barrier damage, which predisposes to hemorrhage development. Simi-

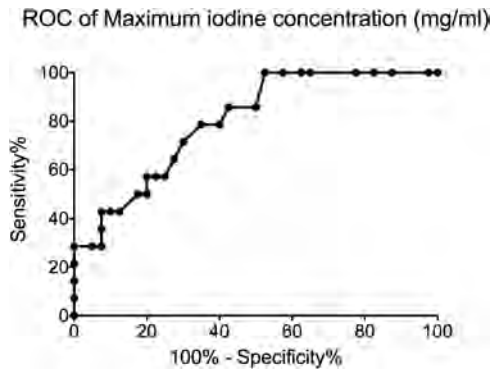


FIG 4. Receiver operator characteristic (ROC) curve showing sensitivity and specificity of maximum iodine concentration in identifying patients developing ICH.

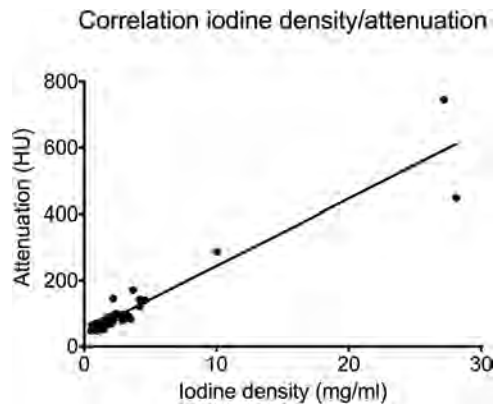


FIG 5. Graph showing the linear correlation existing between maximum hyperdensity attenuation and maximum iodine concentration.

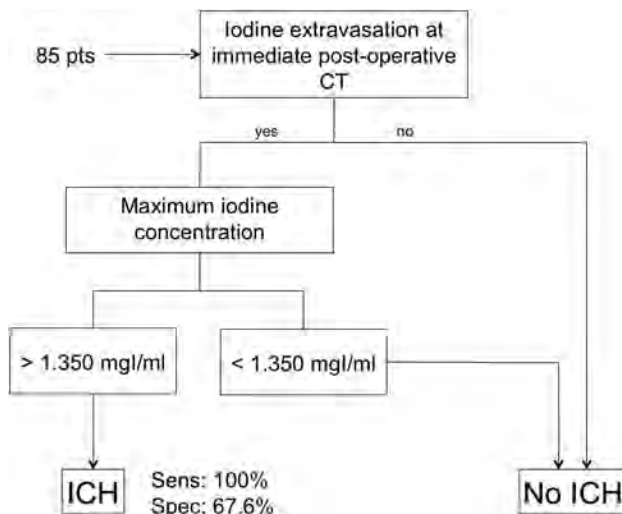


FIG 6. Diagnostic algorithm that enables identifying patients developing ICH with 100% sensitivity and 67.6% specificity.

lary, Nakano et al³⁰ demonstrated that the absence of hyperdense areas at posttreatment CT represents a reliable negative predictor for symptomatic hemorrhage. In agreement with their results, none of the patients in our series without hyperattenuating areas on CT developed ICH.

In our series, we were not able to develop a predictive model to identify patients developing ICH on multivariate analysis, prob-

ably because maximum iodine concentration was a strong predictor of subsequent hemorrhage development and no other factor helped in this prediction. Moreover, this failure might be a consequence of the low number of cases with positive findings (14/85); therefore, further studies with larger patient populations should be performed to confirm our findings.

Our study had several limitations, mainly correlated to its retrospective design. First, we used follow-up CT as the reference standard for identifying patients developing ICH because only a minority of the included patients underwent MR imaging. We are aware that some patients with no signs of bleeding on follow-up CT might have shown small hemosiderin deposits within the ischemic core at MR imaging, but we are also aware that the clinical relevance of these findings is at least questionable. Second, although all patients underwent a routine follow-up CT 24 hours after the procedure, further follow-up examinations were performed only according to clinical status. Therefore, it is possible that some patients who developed asymptomatic hemorrhagic infarction remained undiagnosed. However, these eventually missed hemorrhages were clinically irrelevant and did not affect patient outcome. Another limitation was that the 2 readers measured maximum iodine concentration at the site of maximum apparent iodine extravasation; therefore, the ROIs were subjectively drawn and might not reflect the real maximum iodine concentration in the affected area. However, we found high concordance in the measures performed by the 2 readers.

CONCLUSIONS

Iodine extravasation quantification on dual-energy CT performed immediately after mechanical thrombectomy for acute ischemic stroke may help identify patients with a higher risk of ICH development with excellent sensitivity and moderate specificity. This information might be useful for better tailoring the postoperative management to minimize hemorrhagic complications.

REFERENCES

1. Brinjikji W, Rabinstein A, Cloft HJ, et al. **Recently published stroke trials: what the radiologist needs to know.** *Radiology* 2015;276:8–11 CrossRef Medline
2. Yang P, Zhang Y, Liu J. **LAST2 CH2ANCE: a summary of selection criteria for thrombectomy in acute ischemic stroke.** *AJNR Am J Neuroradiol* 2017;38:E58–59 CrossRef Medline
3. Fiorelli M, Bastianello S, von Kummer R, et al. **Hemorrhagic transformation within 36 hours of a cerebral infarct: relationships with early clinical deterioration and 3-month outcome in the European Cooperative Acute Stroke Study I (ECASS I) cohort.** *Stroke* 1999;30:2280–84 Medline
4. Khatri P, Wechsler LR, Broderick JP. **Intracranial hemorrhage associated with revascularization therapies.** *Stroke* 2007;38:431–40 CrossRef Medline
5. Paciaroni M, Agnelli G, Corea F, et al. **Early hemorrhagic transformation of brain infarction: rate, predictive factors, and influence on clinical outcome: results of a prospective multicenter study.** *Stroke* 2008;39:2249–56 CrossRef Medline
6. Wolpert SM, Bruckmann H, Greenlee R, et al. **Neuroradiologic evaluation of patients with acute stroke treated with recombinant tissue plasminogen activator: the rt-PA Acute Stroke Study Group.** *AJNR Am J Neuroradiol* 1993;14:3–13 Medline
7. Rao NM, Levine SR, Gornbein JA, et al. **Defining clinically relevant cerebral hemorrhage after thrombolytic therapy for stroke: analysis of the National Institute of Neurological Disorders and Stroke**

- tissue-type plasminogen activator trials. *Stroke* 2014;45:2728–33 CrossRef Medline
8. Higashida R, Furlan A, Roberts H, et al; Technology Assessment Committees of the American Society of Interventional and Therapeutic Neuroradiology and the Society of Interventional Radiology. **Trial design and reporting standards for intraarterial cerebral thrombolysis for acute ischemic stroke.** *J Vasc Interv Radiol* 2003;14(9 Pt 2): S493–94 Medline
 9. Jang YM, Lee DH, Kim HS, et al. **The fate of high-density lesions on the non-contrast CT obtained immediately after intra-arterial thrombolysis in ischemic stroke patients.** *Korean J Radiol* 2006;7: 221–28 CrossRef Medline
 10. Tijssen MP, Hofman PA, Stadler AA, et al. **The role of dual energy CT in differentiating between brain haemorrhage and contrast medium after mechanical revascularisation in acute ischaemic stroke.** *Eur Radiol* 2014;24:834–40 CrossRef Medline
 11. Payabvash S, Qureshi MH, Khan SM, et al. **Differentiating intraparenchymal hemorrhage from contrast extravasation on post-procedural noncontrast CT scan in acute ischemic stroke patients undergoing endovascular treatment.** *Neuroradiology* 2014; 56:737–44 CrossRef Medline
 12. Renú A, Amaro S, Laredo C, et al. **Relevance of blood-brain barrier disruption after endovascular treatment of ischemic stroke: dual-energy computed tomographic study.** *Stroke* 2015;46:673–79 CrossRef Medline
 13. Kim JT, Heo SH, Cho BH, et al. **Hyperdensity on non-contrast CT immediately after intra-arterial revascularization.** *J Neurol* 2012; 259:936–43 CrossRef Medline
 14. Gupta R, Phan CM, Leidecker C, et al. **Evaluation of dual-energy CT for differentiating intracerebral hemorrhage from iodinated contrast material staining.** *Radiology* 2010;257:205–11 CrossRef Medline
 15. Phan CM, Yoo AJ, Hirsch JA, et al. **Differentiation of hemorrhage from iodinated contrast in different intracranial compartments using dual-energy head CT.** *AJNR Am J Neuroradiol* 2012;33:1088–94 CrossRef Medline
 16. Bonatti M, Lombardo F, Zamboni GA, et al. **Dual-energy CT of the brain: comparison between DECT angiography-derived virtual unenhanced images and true unenhanced images in the detection of intracranial haemorrhage.** *Eur Radiol* 2017;27:2690–97 CrossRef Medline
 17. Aviv RI, d'Esterre CD, Murphy BD, et al. **Hemorrhagic transformation of ischemic stroke: prediction with CT perfusion.** *Radiology* 2009;250:867–77 CrossRef Medline
 18. Dorado L, Millan M, de la Ossa NP, et al. **Influence of antiplatelet pre-treatment on the risk of intracranial haemorrhage in acute ischaemic stroke after intravenous thrombolysis.** *Eur J Neurol* 2010; 17:301–06 CrossRef Medline
 19. Sugiura Y, Yamagami H, Sakai N, et al; Committee of Recovery by Endovascular Salvage for Cerebral Ultra-acute Embolism (RESCUE)-Japan Study Group. **Predictors of symptomatic intracranial hemorrhage after endovascular therapy in acute ischemic stroke with large vessel occlusion.** *J Stroke Cerebrovasc Dis* 2017;26:766–71 CrossRef Medline
 20. Vandelli L, Marietta M, Gambini M, et al. **Fibrinogen decrease after intravenous thrombolysis in ischemic stroke patients is a risk factor for intracerebral hemorrhage.** *J Stroke Cerebrovasc Dis* 2015;24: 394–400 CrossRef Medline
 21. Watson-Fargie T, Dai D, MacLeod MJ, et al. **Comparison of predictive scores of symptomatic intracerebral haemorrhage after stroke thrombolysis in a single centre.** *J R Coll Physicians Edinb* 2015;45: 127–32 CrossRef Medline
 22. Lapergue B, Blanc R, Guedin P, et al. **A Direct Aspiration, First Pass Technique (ADAPT) versus stent retrievers for acute stroke therapy: an observational comparative study.** *AJNR Am J Neuroradiol* 2016;37:1860–65 CrossRef Medline
 23. Massari F, Henninger N, Lozano JD, et al. **ARTS (Aspiration-Retriever Technique for Stroke): initial clinical experience.** *Interv Neuroradiol* 2016;22:325–32 CrossRef Medline
 24. Romano DG, Cioni S, Leonini S, et al. **Manual thromboaspiration technique as a first approach for endovascular stroke treatment: a single-center experience.** *Interv Neuroradiol* 2016;22:529–34 CrossRef Medline
 25. Romano DG, Cioni S, Vinci SL, et al. **Thromboaspiration technique as first approach for endovascular treatment of acute ischemic stroke: initial experience at nine Italian stroke centers.** *J Neurointerv Surg* 2017;9:6–10 CrossRef Medline
 26. Khalilzadeh O, Sabel B, Sung Y, et al. **Temporal evolution of intraparenchymal hyperdensity after intra-arterial therapy in patients with ischemic stroke: optimal discrimination between hemorrhage and iodinated contrast.** *Clin Neuroradiol* 2014;24:365–71 CrossRef Medline
 27. Elgendy IY, Kumbhani DJ, Mahmoud A, et al. **Mechanical thrombectomy for acute ischemic stroke: a meta-analysis of randomized trials.** *J Am Coll Cardiol* 2015;66:2498–505 CrossRef Medline
 28. Hamann GF, Okada Y, del Zoppo GJ. **Hemorrhagic transformation and microvascular integrity during focal cerebral ischemia/reperfusion.** *J Cereb Blood Flow Metab* 1996;16:1373–78 CrossRef Medline
 29. Yoon W, Seo JJ, Kim JK, et al. **Contrast enhancement and contrast extravasation on computed tomography after intra-arterial thrombolysis in patients with acute ischemic stroke.** *Stroke* 2004;35: 876–81 CrossRef Medline
 30. Nakano S, Iseda T, Kawano H, et al. **Parenchymal hyperdensity on computed tomography after intra-arterial reperfusion therapy for acute middle cerebral artery occlusion: incidence and clinical significance.** *Stroke* 2001;32:2042–48 CrossRef Medline

Comparison of Blood Oxygenation Level–Dependent fMRI and Provocative DSC Perfusion MR Imaging for Monitoring Cerebrovascular Reserve in Intracranial Chronic Cerebrovascular Disease

 K.R. Thulborn,  I.C. Atkinson,  A. Alexander,  M. Singal,  S. Amin-Hanjani,  X. Du,  A. Alaraj, and  F.T. Charbel



ABSTRACT

BACKGROUND AND PURPOSE: Loss of hemodynamic reserve in intracranial cerebrovascular disease reduces blood oxygenation level–dependent activation by fMRI and increases asymmetry in MTT measured by provocative DSC perfusion MR imaging before and after vasodilation with intravenous acetazolamide. The concordance for detecting hemodynamic reserve integrity has been compared.

MATERIALS AND METHODS: Patients ($n = 40$) with intracranial cerebrovascular disease and technically adequate DSA, fMRI and provocative DSC perfusion studies were retrospectively grouped into single vessels proximal to and distal from the circle of Willis, multiple vessels, and Moyamoya disease. The vascular territories were classified as having compromised hemodynamic reserve if the expected fMRI blood oxygenation level–dependent activation was absent or if MTT showed increased asymmetry following vasodilation. Concordance was examined in compromised and uncompromised vascular territories of each group with the Fischer exact test and proportions of agreement.

RESULTS: Extensive leptomeningeal collateral circulation was present in all cases. Decreased concordance between the methods was found in vascular territories with stenosis distal to but not proximal to the circle of Willis. Multivessel and Moyamoya diseases also showed low concordance. A model of multiple temporally displaced arterial inputs from leptomeningeal collateral flow demonstrated that the resultant lengthening MTT mimicked compromised hemodynamic reserve despite being sufficient to support blood oxygenation level–dependent contrast.

CONCLUSIONS: Decreased concordance between the 2 methods for assessment of hemodynamic reserve for vascular disease distal to the circle of Willis is posited to be due to well-developed leptomeningeal collateral circulation providing multiple temporally displaced arterial input functions that bias the perfusion analysis toward hemodynamic reserve compromise while blood oxygenation level–dependent activation remains detectable.

ABBREVIATIONS: ACA = anterior cerebral artery; AIF = arterial input function; BOLD = blood oxygenation level–dependent; CVD = cerebrovascular disease; HR = hemodynamic reserve; LCC = leptomeningeal collateral circulation; MMD = Moyamoya disease; MVD = multivessel disease; PCA = posterior cerebral artery; poa = proportions of agreement; sMCA = superior division of middle cerebral artery; SVDD = single-vessel disease distal to the circle of Willis; SVDP = single-vessel disease proximal to the circle of Willis

Clinical management of patients with chronic cerebrovascular disease (CVD) includes risk assessment for future stroke. Loss of hemodynamic reserve (HR) is one indicator of increased

risk, supporting more aggressive medical treatment and perhaps neurosurgical or neurovascular interventions.^{1–4} HR is assessed with many imaging modalities by the patterns of perfusion redistribution after vasodilation. While a perfusion study may or may not show asymmetry in baseline perfusion, vasodilation induced with acetazolamide may unmask perfusion asymmetries indicative of loss of HR.²

Blood oxygenation level–dependent (BOLD) contrast in fMRI arises from the increased local signal intensity from increased regional blood flow that occurs when neurons perform work.⁵ The role of fMRI for the evaluation of CVD has been reviewed.⁶ Because BOLD contrast requires an intact HR, a paradigm that interrogates cortical areas in all vascular territories simultaneously can be used to detect regional HR in each vascular territory.

We have assessed the concordance between BOLD fMRI and

Received May 29, 2017; accepted after revision November 7.

From the Center for Magnetic Resonance Research (K.R.T., I.C.A., A.Alexander, M.S.) and Department of Neurological Surgery (S.A.-H., X.D., A.Alaraj, F.T.C.), University of Illinois Medical Center, Chicago, Illinois.

The authors acknowledge National Institutes of Health grants RO1 NS059745-01A1, RO1 NS3867601A1, and RO1 CA1295531A1, which provided partial salary support for K.R.T.

Please address correspondence to Keith R. Thulborn, MD, PhD, Center for Magnetic Resonance Research, Room 1307, OCC, M/C 707, University of Illinois at Chicago, 1801 West Taylor St, Chicago, IL 60612; e-mail: kthulbor@uic.edu

 Indicates open access to non-subscribers at www.ajnr.org

 Indicates article with supplemental on-line tables.

<http://dx.doi.org/10.3174/ajnr.A5515>

provocative DSC perfusion MR imaging for assessing HR in a cohort of patients with CVD. A model of the multiple temporally displaced arterial input functions (AIFs) from well-developed leptomeningeal collateral circulation in chronic CVD is posited to explain the observed low concordance between these methods for detecting compromised HR.

MATERIALS AND METHODS

Population

This institutional review board–approved retrospective study comprised patients ($n = 40$; mean age, 48 ± 17 years; 24 women and 16 men) who underwent extensive evaluation for atherosclerotic CVD or Moyamoya disease, including DSA, MR imaging using DSC perfusion before and after vasodilation with acetazolamide, and fMRI with a customized HR assessment paradigm. Symptoms included ≥ 1 instance of weakness ($n = 23$), paresthesia ($n = 11$), difficulty speaking ($n = 10$), atypical headache ($n = 7$), dizziness ($n = 4$), visual disturbance ($n = 3$), and cognitive compromise ($n = 2$). Multiple risk factors for vascular disease were present in most subjects, including hypertension ($n = 26$), hyperlipidemia ($n = 19$), diabetes mellitus ($n = 10$), and smoking ($n = 23$). Patients were selected from >300 cases reviewed in weekly clinical case review conferences attended by treating physicians across a 6-year period (June 2006 to June 2012). Although all patients were diagnosed as having CVD of varying severity, the cohort was selected with technically sound DSA, fMRI, and perfusion studies. Specifically, absence of head motion (<1 -mm translational head motion in 3 orthogonal directions) was stipulated for all functional and perfusion studies. Only the first technically adequate examination was used for patients with multiple studies.

Four groups were formed on the basis of CVD distribution: single-vessel disease distal to the circle of Willis (SVDd, $n = 7$; 56 ± 12 years of age; 2 women and 5 men, including 2 bypasses); single-vessel disease proximal to the circle of Willis with an intact posterior communicating artery ipsilateral to the stenotic internal carotid artery (SVDp, $n = 9$; 53 ± 16 years of age; 4 women and 5 men, including 1 bypass); multivessel intracranial disease not including Moyamoya disease (MVD, $n = 10$; 53 ± 15 years of age; 8 women and 2 men, including 3 bypasses); and Moyamoya disease (MMD) ($n = 14$; 38 ± 16 years of age; 10 women and 4 men, including 3 bypasses). Bypass grafts used anastomoses of the distal superficial temporal artery to the distal middle cerebral artery.

Anatomic MR Imaging

All MR imaging was performed at 3T (Signa; GE Healthcare, Milwaukee, Wisconsin) using routine axial high-resolution T2-weighted FLAIR and gradient-echo imaging and 3D T1-weighted imaging before and after intravenous gadolinium contrast enhancement to exclude vascular territories with hemorrhage or encephalomalacic changes from previous infarctions. Acute stroke was excluded by diffusion-weighted imaging.

Functional MR Imaging

Whole-brain fMRI studies were performed using a published imaging protocol and customized paradigm performed in duplicate.⁷ The HR assessment paradigm was a 2-condition block de-

sign paradigm (30 seconds, 12 volumes/condition, 4.5 cycle). The active condition was hand clasp paced (0.3 Hz) by simultaneous binaural commands (open, close) and central visual commands (OPEN, CLOSE) with peripheral flashing checkerboards (black and white, alternating checkerboard, 10 Hz). The fixation condition was a static central white cross on a black background. Patients were trained with this paradigm immediately before the examination. Head alignment and eye movement were monitored during imaging.

BOLD activation was detected with a voxelwise 2-tailed t test as the difference in image signal intensities between the 2 conditions averaged across the 4 cycles at multiple t thresholds with and without a small Gaussian filter (full width at half maximum = 3 mm). The threshold value (t value = 3.0) was empirically selected to show $<5\%$ active voxels outside the gray matter. BOLD activation was superimposed over coregistered high-resolution T1-weighted anatomic images for localization of activation in each vascular territory.

The expected activation areas were the supplementary motor areas supplied by the anterior cerebral arteries (ACAs) along the medial frontal lobes; primary sensorimotor areas supplied by the superior middle cerebral artery (sMCA) along the pre- and post-central gyri; the primary auditory cortex supplied by the inferior MCA along the superior temporal gyri; and the primary and associative visual cortices supplied by the posterior cerebral artery (PCA) along the calcarine fissures of the occipital lobes. Each territory was labeled in a binary fashion as positive or negative for BOLD contrast without regard for asymmetry in activation at the common threshold, indicating intact (+BOLD) or deficient (−BOLD) HR, respectively.

DSC Perfusion MR Imaging

The DSC perfusion imaging was performed at 3T using the previously published DSC perfusion protocol⁷ with a standard body weight–based dose (0.1 mmol/kg) of intravenous gadolinium-based contrast (Omniscan; GE Healthcare, Piscataway, New Jersey) followed by a saline flush (20 mL) delivered by a mechanical injector (5 mL/s, delay 10 seconds, 20-ga access; Medrad, Indianapolis, Pennsylvania) through a large vein in the antecubital fossa of either arm.⁷ After an initial perfusion study (pre-acetazolamide), vasodilation was induced using intravenous administration of acetazolamide (Diamox, 1 g administered intravenously over 5 minutes). The repeat DSC perfusion imaging was performed after a further delay of 10 minutes to allow full vasodilation.

Time course data were analyzed by a voxelwise fitting of a γ variate function to the contrast agent concentration–time-series using a multivariate nonlinear least-squares fitting algorithm as described in detail elsewhere.^{8,9} The fitted points were limited to the initial baseline, leading edge, and the initial portion of the trailing edge after the peak (<4 points) to avoid contamination from contrast recirculation. Although other methods may be used,¹⁰ this γ variate method avoids bias from the choice of the arterial input function in the setting of CVD.^{11,12} The MTT was defined as the first moment of the γ variate function fitted to the contrast agent concentration–time-series. The relative CBV was the integral of the γ variate function. Only the results for MTT are

shown because the CBV replicated the same responses. The perfusion parameters (MTT, CBV) were obtained pre- and postvasodilation from ROIs placed in the expected gray matter of fMRI activation in the vascular territory of each cerebral artery using the aligned high-resolution anatomic image (Fig 1). Each ROI contained at least 15 voxels and had a minimum contrast-to-noise ratio of 5. The means and SDs of each perfusion parameter were compared across vascular territories both before and after vasodilation. For SVDD and SVDp, the mean perfusion parameters were compared between cerebral hemispheres (4 left-right comparisons). For patients with MMD, the anterior vascular territories (ACA, sMCA, inferior division of the MCA) were compared with the ipsilateral PCA territories (6 anteroposterior comparisons). Depending on the complexity and distribution of disease in patients with MVD, either left-right or anterior-posterior comparisons were used between vascular territories with and without proximal disease.

Two-tailed Student *t* tests were used to detect statistically significant differences ($P < .05$) in perfusion parameters in each pair of vascular territories in each patient, both before and after acetazolamide. The differences in perfusion parameters from pre-acetazolamide to post-acetazolamide in the paired vascular territories were then examined for statistical significance using a second 2-tailed Student *t* test ($P < .05$).

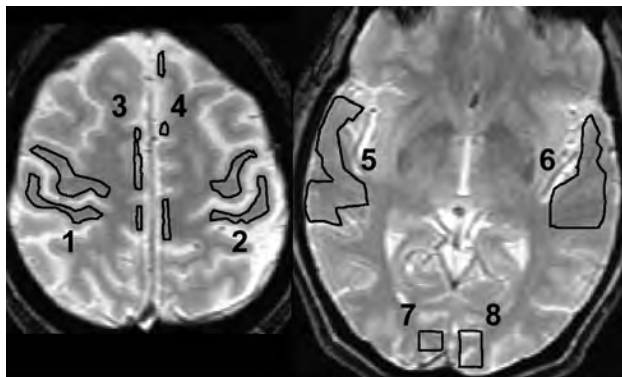


FIG 1. ROIs were drawn manually on anatomic T2-weighted images coregistered with the perfusion images in each of the vascular territories in which regional BOLD activation is expected anatomically (1 and 2: right and left primary sensorimotor areas; 3 and 4: right and left supplementary motor areas; 5 and 6: right and left primary auditory areas; and 7 and 8: right and left primary visual areas). Voxels were included in the ROI if they were >50% within the boundary.

Digital Subtraction Angiography

DSA was used to define the group (SVDD, SVDp, MVD, MMD) for each patient. Vascular narrowing in any vessel was sufficient for consideration to enter this study. These DSA studies were used in all patients to classify the extent of collateral circulation in the region distal to the compromised vessel on a 0–3 scale by an experienced neurointerventionalist using a previously described grading scale,¹³ in which 3 represents extensive leptomeningeal collateral circulation.

Concordance Analysis

The perfusion analysis was performed between paired vascular territories with normal and stenotic supply vessels. Territories labeled + Δ MTT showed an increasing difference in MTT between paired territories after vasodilation, conventionally implying loss of HR. In contrast, $-\Delta$ MTT meant intact HR without statistically significant increases in the difference in MTT following vasodilation. BOLD fMRI used $-$ BOLD to indicate loss of BOLD contrast, implying insufficient HR to support BOLD contrast at the global threshold in a given vascular territory. Intact HR sufficient to support BOLD contrast was indicated by +BOLD. The resultant contingency tables were examined for concordance between the 2 methods by the Fisher exact probability test (Table). This test provided a *P* value ($P < .05$) to indicate the risk of being wrong for rejecting the null hypothesis that the 2 methods were equivalent. Concordance was also examined for 2 subgroups of the MMD group showing different scores for leptomeningeal collateral circulation (LCC score ≤ 2 and LCC score 3). Other groups had scores of 3 in most vascular territories. The alternative parameter, proportions of agreement (poa), was used to indicate fractional agreement between methods.

Modeling

The γ variate function is the functional form of the shape of the contrast agent concentration–time curve at the capillary bed. A voxel in tissue with no proximal vascular disease has a single AIF, and there is no pressure differential to establish collateral circulation among the different vascular territories (Fig 2, left). If critical stenosis develops proximally in 1 vessel, its distal capillary bed dilates to generate a pressure differential to adjacent vascular territories to open flow through existing leptomeningeal collateral vessels (Fig 2, right). The AIFs from these adjacent vessels are displaced in time by the increased lengths of the collateral pathways. The total perfusion of the voxel distal to the stenosis is now

Concordance for BOLD fMRI and DSC perfusion in determining loss of HR in the 4 CVD groups^a

CVD Group	Number of Cases	Territories Distal to Disease	Number of Territories	Null Hypothesis, Fisher Exact	Proportions of Agreement ($\pm 95\%$ CI)
SVDD	7	No	14	Accept ($P = 1$)	0.93 (0.64–0.99)
		Yes	10	Accept ($P = 1$)	0.70 (0.35–0.89)
SVDp	9	No	9	Accept ($P = 1$)	0.89 (0.51–0.99)
		Yes	23	Accept ($P = .96$)	0.91 (0.71–0.99)
MVD	10	No	20	Accept ($P = 1$)	0.90 (0.67–0.98)
		Yes	35	Reject ($P < .004$)	0.77 (0.51–0.86)
MMD (LCC ≤ 2)	8	Yes	46	Accept ($P = .41$)	0.46 (0.31–0.61)
MMD (LCC = 3)	6	Yes	36	Reject ($P < .004$)	0.72 (0.24–0.57)

^a Vascular territories with stroke were excluded from comparisons.

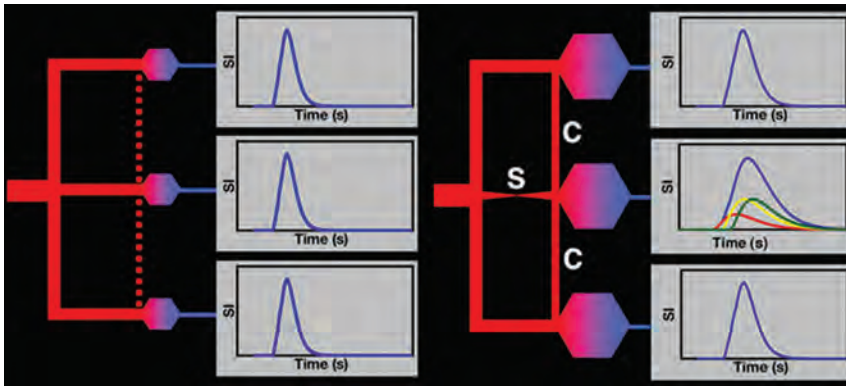


FIG 2. Left: Contrast agent concentration–time curves (blue curves) for 3 vascular territories (upper, middle, lower) are similar for normal vessels. No pressure differential exists between vascular territories to open potential leptomeningeal collateral vessels (dotted red line). Right: Stenosis (S) of the middle territory causes distal dilation, producing a pressure differential that opens leptomeningeal collateral vessels (C) from neighboring vascular territories (upper, lower). The contrast agent concentration–time curve of the compromised territory (middle blue curve) becomes the sum of 3 unresolved inputs (red, yellow, and green curves) temporally displaced due to the increased vascular path lengths from the other territories. MTT lengths in the compromised territory (temporally displaced middle blue curve compared with the upper and lower blue curves). Pharmacologic vasodilation dilates all capillary beds, thereby decreasing the pressure difference between normal and compromised territories to further delay collateral leptomeningeal flow and increase the temporal separations of the multiple AIFs to lengthen MTT but not necessarily reflecting inadequate flow.

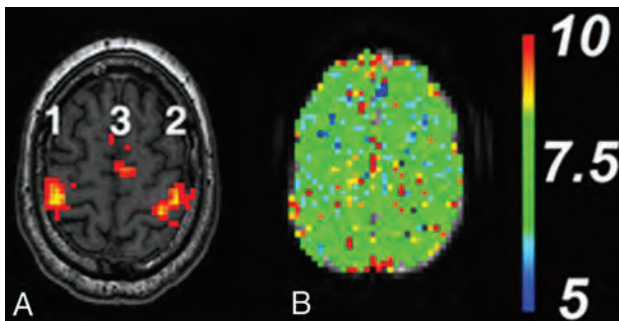


FIG 3. A, Normal sensorimotor activation pattern for BOLD fMRI with the HR assessment paradigm. Areas of activation are the following: 1) right primary sensorimotor cortex (right sMCA), 2) left primary sensorimotor cortex (left sMCA), and 3) left and right supplementary motor area (left and right ACA, respectively). The color scale reflects the continuous t value (threshold $t = 3$ red, $t > 3$ yellow) of the activation-detection statistics. B, Normal quantitative perfusion map of MTT at the same level as A remains symmetric before and after vasodilation. The color scale is in seconds.

the sum of 3 AIFs. This combined AIF also has the form of a γ variate function but with a longer MTT due to the temporal displacements of the collateral AIF. When the capillary beds are dilated pharmacologically, more blood flow enters the 2 normal vessels because their capillary beds now have decreased resistance. If the cardiac output is sufficient, the collateral leptomeningeal circulation remains intact but with reduced flow due to the reduced pressure differential between the normal and compromised vascular territories. The result is an even longer MTT in the territory distal to the stenotic vessel. The temporal spacing and change in magnitudes of the delayed collateral AIF further lengthen the MTT. This pattern may be better termed “redistribution” than “steal” because the tissue in the compromised territory may still receive adequate total flow to maintain metabolism.

RESULTS

Representative patterns of BOLD activation for the HR assessment paradigm and for normal perfusion MTT pre- and postvasodilation in the primary sensorimotor cortex for subjects without CVD are shown in Fig 3. The BOLD pattern shows activation in the supplementary motor and primary sensorimotor areas. The primary auditory and primary visual and visual association areas (not shown) are equally robust. The perfusion maps without vascular disease are reproducible pre- and postvasodilation and symmetric in both left-right and anteroposterior comparisons.

All CVD cases showed prominent collateral circulation (grade 2 or 3) documented by DSA ($n = 40$) and tabulated as LCC scores in On-line Tables 1 and 2. The MTT values for all vascular territories for every subject in all groups are provided in On-line Tables 3 and 4. Rep-

representative examples of concordant and nonconcordant patterns for BOLD fMRI and provocative DSC perfusion are shown in Figs 4 and 5, respectively. The statistical parameters and confidence intervals for concordance between the 2 methods across the 4 CVD categories in vascular territories with normal and diseased supply vessels are shown in the Table. For the SVDd and SVDp, the Fisher exact probability test indicated that the null hypothesis of the 2 methods being in agreement must be accepted in both normal and poststenotic vascular territories. However, this null hypothesis should be rejected for the MVD and MMD (LCC score = 3) with extensive leptomeningeal collateral circulation. For vascular territories without stenosis in the MVD group and for MMD (LCC score ≤ 2) with less extensive leptomeningeal collateral circulation, the null hypothesis also cannot be rejected.

However, the proportions of agreement parameter offers additional insight into these methods for assessing HR, indicating that they are more often in agreement in vascular territories without vascular disease distal to the circle of Willis (SVDd, $poa = 0.93$; SVDp, $poa = 0.89$, MVD, $poa = 0.90$) than when vascular stenosis distal to the circle of Willis is present (SVDd, $poa = 0.70$; MVD, $poa = 0.77$). The presence of vascular disease produces a greater number of territories with compromised HR by DSC perfusion MR imaging than by fMRI. When the vascular disease is limited to a unilateral internal carotid artery proximal to the circle of Willis (SVDp), no difference in the 2 methods is detected (territories contralateral to stenotic ICA, $poa = 0.89$; territories ipsilateral to stenotic ICA, $poa = 0.91$). Although the null hypothesis cannot be rejected for the MMD group with less extensive leptomeningeal disease (LCC scores ≤ 2), agreement between the 2 methods was low ($poa = 0.46$), again with perfusion showing increasing MTT differences in the presence of BOLD activation.

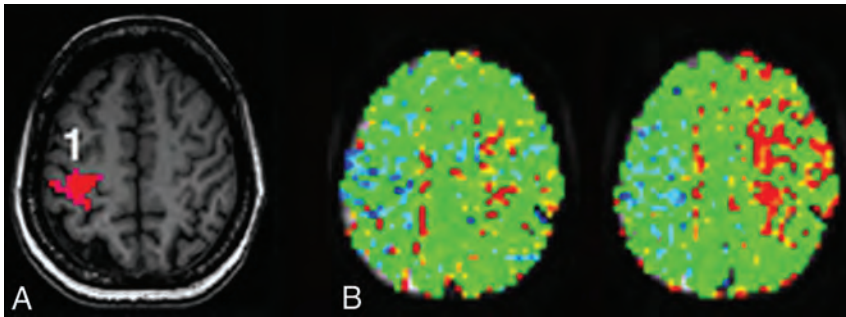


FIG 4. Representative patient with MMD showing concordance. *A*, BOLD fMRI shows activation in the right (1) but not the left primary sensorimotor area or supplementary motor areas bilaterally. The task was performed correctly because bilateral cerebellar motor and visual activations were present (not shown). *B*, Quantitative MTT maps through the same level as in *A* before (left) and after (right) vasodilation. The lengthening of the MTT values after vasodilation would normally be interpreted as loss of HR. The color scale is same as in Fig 3.

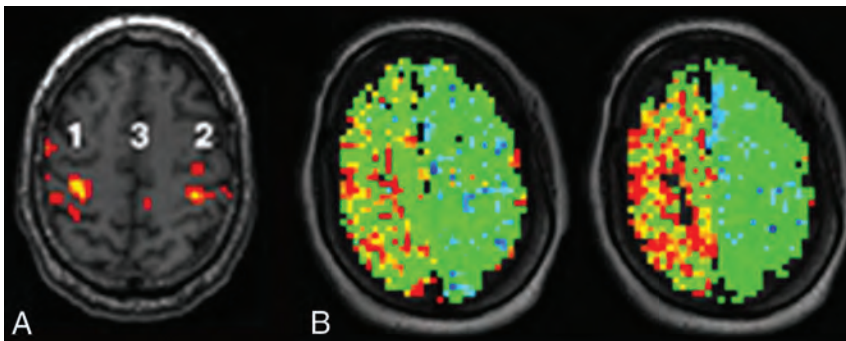


FIG 5. Representative patient with single-vessel disease with unilateral intracranial right internal carotid artery stenosis showing lack of concordance. *A*, BOLD fMRI activation is intact bilaterally in the primary sensorimotor cortex (1 and 2) and supplementary motor cortex (3) as were auditory and visual cortex activations (not shown). *B*, MTT maps through the sensorimotor cortex show increasing MTT asymmetry from before (left) to after vasodilation (right), conventionally interpreted as loss of HR. The color scale is same as in Fig 3.

DISCUSSION

The management of chronic CVD to avoid future stroke involves selecting from multiple interventions that progress from lifestyle changes to more aggressive medical management and ultimately to neurosurgical approaches of angioplasty, stents, and vascular reconstruction. The choice depends on the risk of future stroke because each treatment has financial costs, compliance issues, and potential complications.

Our clinical experience of low concordance between the 2 methods in patients with chronic CVD reflects the results of this retrospective study using technically adequate imaging studies (Table). Extensive collateral leptomeningeal circulation was present anatomically in all patients, but the adequacy of such collateral circulation in the distal tissue cannot be readily assessed angiographically. Perfusion, in which greater asymmetries in MTT following vasodilation would conventionally be interpreted as “steal” or loss of HR, frequently did not agree with intact BOLD fMRI activation in the same vascular territories. Because the perfusion method alone is being advocated as a means for making surgical decisions for intervention in Moyamoya disease,¹⁴ this discrepancy must be understood.

The results summarized in the Table indicate that both methods are concordant in the absence of disease and even in the setting of disease in which the circle of Willis can provide collateral

flow through short large diameter vessels into the proximal cerebral arteries (SVDp). Concordance decreases when the cerebral arteries are compromised distal to the circle of Willis (SCDd) when leptomeningeal vessels must compensate for reduced flow through the stenotic vessel, albeit with temporally displaced arterial inputs, to supply the vascular territory (MMD, MVD). Increasing leptomeningeal circulation in MMD implies decreasing flow from central vessels. The increased concordance for the higher LCC-scored MMD cohort may be attributed to less temporal displacement of AIF when most flow is leptomeningeal rather than from central vessels.

The model for analysis of nondiffusible contrast agents in DSC perfusion assumes that all voxels have a common global arterial input function.¹⁰⁻¹² In CVD, the substantial collateral pathways are longer and smaller, so the AIF can be displaced temporally from that of the stenotic cerebral arteries. The multiple temporally displaced arterial inputs from both primary and collateral leptomeningeal vessels may become more exaggerated with vasodilation. Fig 2 illustrates how multiple temporally displaced arterial inputs produce prolonged MTT, possibly unrelated to the adequacy of supply. Such increasing asymmetry compared

with the normal flow pattern represents redistribution—that is, a change in the perfusion pattern not necessarily reflecting the adequacy of oxygen delivery to the tissue and still having sufficient HR to support BOLD activation.

Conversely, the perfusion parameters may be sufficiently perturbed at baseline to decrease sensitivity to further changes following vasodilation. The complexity of collateral circulation in severe intracranial disease may make the perfusion parameters insensitive to the metabolic demands of the tissue. This substantial collateral circulation would rationalize the lower concordance with the BOLD technique in chronic intracranial CVD.

The limitations of this study are the small number of subjects in each group because of the strict selection criteria. Patients with CVD do not appear to tolerate extended MR imaging studies without head motion. Although the fMRI paradigm robustly produces BOLD contrast in well-established cortical locations of each cerebral artery, it remains sensitive to head motion easily recognized as falsely positive BOLD activation along high-contrast CSF-tissue margins of the image rather than at expected locations. This problem was eliminated from this study cohort by the selection criteria. Vascular territories with areas of encephalomalacic changes from previous strokes or hemorrhage do not show activation, but such vascular territories were excluded from this anal-

ysis by the selection criteria. The statistical threshold for activation was arbitrarily selected to minimize such false-positive activation in white matter. Activation was considered present only when colocalized to the specific cortical pattern established in healthy subjects. Any asymmetry in activation was ignored. The BOLD technique has the additional disadvantage of being a regional measure that may miss smaller regions of compromised perfusion away from the areas of activation. This limitation did not affect these results because concordance was measured in the same areas of eloquent cortex. The role of global neurovascular reactivity with a hypercapnia challenge may be a means to generalize the task-based fMRI regional response into a global response.¹⁵

CONCLUSIONS

The low concordance between BOLD fMRI and provocative perfusion MR imaging for detecting HR compromise in potentially compromised vascular territories of patients with chronic CVD can be rationalized by the complex arterial supply provided by the leptomeningeal collateral circulation that results in temporally displaced multiple arterial inputs. Care is advised when using the perfusion methodology alone to manage patients with complex CVD.

Disclosures: Keith R. Thulborn—*RELATED: Grant:* National Institutes of Health, *Comments:* RO1 NS059745-01A1, RO1 NS386760-1A1, and RO1 CA129553-1A1*. Ian C. Atkinson—*UNRELATED: Consultancy:* Thulborn Associates. Ali Alaraj—*UNRELATED: Consultancy:* Cordis-Codman, Fady T. Charbel—*UNRELATED: Board Membership:* Vassol, *Comments:* noncompensated position; *Grants/Grants Pending:* National Institute of Neurological Disorders and Stroke*; *Patents (Planned, Pending or Issued):* Vassol*; *Royalties:* Vassol*; *Stock/Stock Options:* Vassol. *Money paid to the institution.

REFERENCES

- Gupta A, Chazen JL, Hartman M, et al. **Cerebrovascular reserve and stroke risk in patients with carotid stenosis or occlusion: a systematic review and meta-analysis.** *Stroke* 2012;43:2884–91 CrossRef Medline
- Vagal AS, Leach JL, Fernandez-Ulloa M, et al. **The acetazolamide challenge: techniques and applications in the evaluation of chronic cerebral ischemia.** *AJNR Am J Neuroradiol* 2009;30:876–84 CrossRef Medline
- Mandell DM, Han JS, Poulblanc J, et al. **Mapping cerebrovascular reactivity using blood oxygen level-dependent MRI in patients with arterial steno-occlusive disease: comparison with arterial spin labeling MRI.** *Stroke* 2008;39:2021–28 CrossRef Medline
- Derdeyn CP, Videen TO, Yundt KD, et al. **Variability of cerebral blood volume and oxygen extraction: stages of cerebral haemodynamic impairment revisited.** *Brain* 2002;125:595–607 CrossRef Medline
- Huettel SA, Song AW, McCarthy G. *Functional Magnetic Resonance Imaging.* Sunderland: Sinauer Associates, Inc; 2004:128–214
- Christen T, Bolar DS, Zaharchuk G. **Imaging brain oxygenation with MRI using blood oxygenation approaches: methods, validation, and clinical applications.** *AJNR Am J Neuroradiol* 2013;34:1113–23 CrossRef Medline
- Thulborn KR. **Magnetic resonance imaging in the management of cerebrovascular disease to prevent stroke.** *Neurol Clin* 2008;26:897–921, vii–viii CrossRef Medline
- Ostergaard L, Weisskoff RM, Chesler DA, et al. **High resolution measurement of cerebral blood flow using intravascular tracer bolus passages, Part I: mathematical approach and statistical analysis.** *Magn Reson Med* 1996;36:715–25 CrossRef Medline
- Ostergaard L, Sorensen AG, Kwong KK, et al. **High resolution measurement of cerebral blood flow using intravascular tracer bolus passages, part II: experimental comparison and preliminary results.** *Magn Reson Med* 1996;36:726–36 CrossRef Medline
- Calamante F. **Bolus dispersion issues related to the quantification of perfusion MRI data.** *J Magn Reson Imaging* 2005;22:718–22 CrossRef Medline
- Axel L. **Cerebral blood flow determination by rapid-sequence computed tomography: theoretical analysis.** *Radiology* 1980;137:679–86 CrossRef Medline
- Patil V, Johnson G. **An improved model for describing the contrast bolus in perfusion MRI.** *Med Phys* 2011;38:6380–83 CrossRef Medline
- Kim JJ, Fischbein NJ, Lu Y, et al. **Regional angiographic grading system for collateral flow: correlation with cerebral infarction in patients with middle cerebral artery occlusion.** *Stroke* 2004;35:1340–44 CrossRef Medline
- Ishii Y, Nariai T, Tanaka Y, et al. **Practical clinical use of dynamic susceptibility contrast magnetic resonance imaging (DSC-MRI) for the surgical treatment of moyamoya disease.** *Neurosurgery* 2014;74:302–09 CrossRef Medline
- Prisman E, Slessarev M, Han J, et al. **Comparison of the effects of independently-controlled end-tidal PCO(2) and PO(2) on blood oxygen level-dependent (BOLD) MRI.** *J Magn Reson Imaging* 2008;27:185–91 CrossRef Medline

Accuracy of the Compressed Sensing Accelerated 3D-FLAIR Sequence for the Detection of MS Plaques at 3T

 S. Toledano-Massiah,  A. Sayadi,  R. de Boer,  J. Gelderblom,  R. Mahdjoub,  S. Gerber,  M. Zuber,  M. Zins, and  J. Hodel



ABSTRACT

BACKGROUND AND PURPOSE: The use of 3D FLAIR improves the detection of brain lesions in MS patients, but requires long acquisition times. Compressed sensing reduces acquisition time by using the sparsity of MR images to randomly undersample the k -space. Our aim was to compare the image quality and diagnostic performance of 3D-FLAIR with and without compressed sensing for the detection of multiple sclerosis lesions at 3T.

MATERIALS AND METHODS: Twenty-three patients with relapsing-remitting MS underwent both conventional 3D-FLAIR and compressed sensing 3D-FLAIR on a 3T scanner (reduction in scan time 1 minute 25 seconds, 27%; compressed sensing factor of 1.3). Two blinded readers independently evaluated both conventional and compressed sensing FLAIR for image quality (SNR and contrast-to-noise ratio) and the number of MS lesions visible in the periventricular, intra-juxtacortical, infratentorial, and optic nerve regions. The volume of white matter lesions was measured with automatic postprocessing segmentation software for each FLAIR sequence.

RESULTS: Image quality and the number of MS lesions detected by the readers were similar between the 2 FLAIR acquisitions ($P = .74$ and $P = .094$, respectively). Almost perfect agreement was found between both FLAIR acquisitions for total MS lesion count (Lin concordance correlation coefficient = 0.99). Agreement between conventional and compressed sensing FLAIR was almost perfect for periventricular and infratentorial lesions and substantial for intrajuxtacortical and optic nerve lesions. Postprocessing with the segmentation software did not reveal a significant difference between conventional and compressed sensing FLAIR in total MS lesion volume ($P = .63$) or the number of MS lesions ($P = .15$).

CONCLUSIONS: With a compressed sensing factor of 1.3, 3D-FLAIR is 27% faster and preserves diagnostic performance for the detection of MS plaques at 3T.

ABBREVIATIONS: CNR = contrast-to-noise ratio; CS = compressed sensing; MAGNIMS = Magnetic Resonance Imaging in Multiple Sclerosis; PI = parallel imaging

The diagnosis of MS relies on the demonstration of the dissemination of white matter hyperintensities in space and time with MR imaging.¹ The FLAIR sequence plays a pivotal role in patients with MS because it shows white matter lesions in specific locations (subtentorial, optic nerve,² juxtacortical, periventricular).^{1,3} In its 3D implementation, FLAIR also improves the detection of small demyelinating lesions, resulting in better clinical-radiologic correlation.⁴

Despite the proved diagnostic advantage of 3D-FLAIR versus

2D-FLAIR, the longer scan time of the 3D version has so far hindered its adoption.

Compressed sensing (CS) is an acceleration technique newly available in MR imaging clinical routine. It uses the sparsity of MR images to randomly undersample the k -space, thus saving scan time.⁵⁻⁹ Contrary to parallel imaging (PI), CS is insensitive to the coil configuration. Because each acceleration technique imposes independent constraints on the image reconstruction, CS and PI can be used concurrently.¹⁰ The combination of PI and CS we use is serial. This feature makes the 2 acceleration techniques independent of one another; therefore, the PI sensitivity to coil configuration does not impact CS.¹¹

There is no study yet regarding the effect of CS on diagnostic performance when applied to accelerate 3D-FLAIR acquisitions in patients with MS, to our knowledge. The aim of this study was to compare both image quality and diagnostic performance of 3D-FLAIR with and without CS in the clinical setting of MS.

Received September 3, 2017; accepted after revision November 3.

From the Departments of Radiology (S.T.-M., A.S., S.G., M.Zins) and Neurology (M.Zuber), Fondation Hôpital Saint-Joseph, Paris, France; Quantib B.V. (R.d.B., J.G.), Rotterdam, the Netherlands; GE Healthcare (R.M.), Buc, France; and Department of Neuro-radiology (J.H.), AP-HP, Hôpitaux Universitaires Henri Mondor, Université Paris est, Créteil, France.

Please address correspondence to Sarah Toledano-Massiah, MD, Department of Radiology, Fondation Hôpital Saint-Joseph, 185 rue Raymond Losserand, 75014 Paris, France; e-mail: stoledano@hpsj.fr

<http://dx.doi.org/10.3174/ajnr.A5517>

Table 1: Imaging parameters for the CS and conventional 3D-FLAIR^a

Parameters		
CS 3D-FLAIR		
TE/TI/TR (ms)	140/2064/8000	
ETL	220	
FOV (frequency × phase) (mm)	260 × 221	
Slice thickness (mm)	1.2 mm	
Matrix (frequency × phase)	288 × 256	
NEX	1	
Bandwidth (Hz/pixel)	347.2	
ARC factor (phase × slice)	2.0 × 2.0	
CS 3D-FLAIR/conventional 3D-FLAIR		
CS factor	1.3	NA
Scan time (min:sec)	3:50 (−27%)	5:15

Note:—ETL indicates echo-train length; ARC, auto-calibrating reconstruction for Cartesian imaging (acceleration using parallel imaging technique); NA, not applicable. ^a CS allowed a 27% reduction in scan time of the 3D-FLAIR sequence.

MATERIALS AND METHODS

Patients and MR Imaging

This study was approved by our institutional review board, at Fondation Hôpital Saint Joseph. Informed consent was obtained from all patients. From January 2017 to April 2017, twenty-three consecutive patients with relapsing-remitting MS according to the revised McDonald criteria¹ (14 women; mean age, 47 years; range, 21–77 years) underwent MR imaging for their routine follow-up (3T Discovery MR750; GE Healthcare, Milwaukee, Wisconsin) using a 32-channel head coil.

MR imaging protocol included DWI, 3D gradient-echo magnetization-prepared T1-weighted BRAVO (GE Healthcare; isotropic voxel, 0.9 mm), T2WI, and 3D-FLAIR imaging, without administration of contrast agent. The 3D-FLAIR sequence was performed twice with and without the addition of CS. A CS acceleration factor of 1.3 was used, leading to a 27% reduction in scan time (1 minute 25 seconds). Both FLAIR sequences were strictly identical except for the addition of CS. All 3D-FLAIR, with and without CS, were acquired in the sagittal plane with a PI acceleration auto-calibrating reconstruction for Cartesian imaging factor of 2.

Imaging parameters are summarized in Table 1.

Preliminary Study in Healthy Volunteers

To identify the most suitable CS acceleration factor, we performed 3D-FLAIR acquisitions, 1 without CS, and 4 with different CS factors (1.2, 1.3, 1.4, 1.5) on 5 healthy volunteers.

The FLAIR acquisitions were all identical except for the CS acceleration factor and the related scan time.

For each FLAIR acquisition, image quality was rated on a 3-point scale: 1, “poor” (image quality insufficient for diagnostic purposes); 2, “good” (minor artifacts not impairing diagnosis); and 3, “excellent” (no artifacts). We based the image-quality rating on 3 criteria: delineation of deep brain nuclei and the cortical gray-white matter junction, suppression of CSF, and blurring.

The purpose of this preliminary study in healthy volunteers was to identify the highest scan time reduction of 3D-FLAIR with CS compatible with an image quality score of at least 2 for all 3 criteria.

Table 2: Qualitative analysis^a

	JC	PV	IT	ON
Reader 1				
Conventional FLAIR	131	316	64	8
CS FLAIR	131	326	65	8
Reader 2				
Conventional FLAIR	140	373	76	10
CS FLAIR	129	377	75	10
Consensus reading				
Conventional FLAIR	130	314	64	8
CS FLAIR	131	327	65	8

Note:—JC indicates juxtacortical; PV, periventricular; IT, infratentorial; ON, optic nerve.

^a No. of MS lesions per localization, on conventional FLAIR and CS FLAIR, according to both readers, and after consensus with a third reader.

Image Analysis

Qualitative Analysis in Patients with MS. All FLAIR images were first anonymized and randomly interpreted. Then, all images were blindly and independently assessed by 2 neuroradiologists (S.T.-M. and A.S., with 9 and 4 years of experience, respectively) on the available workstation (Advantage Workstation 4.6; GE Healthcare). Each patient was analyzed only once per session, with either conventional FLAIR or CS FLAIR. The 2 independent blinded readings took place 2 weeks apart to avoid recall bias. Image quality was rated on the same 3-level scale used in the preliminary study. We also evaluated CSF suppression, delineation of deep brain nuclei, and the gray-white matter junction on the same scale.

For each FLAIR acquisition, the readers counted the number of visible MS lesions involving periventricular, intra-juxtacortical, infratentorial, and optic nerve regions (as used to assess spatial dissemination using the McDonald revised or Magnetic Resonance Imaging in Multiple Sclerosis criteria [MAGNIMS]³). A lesion was defined as a focal T2-weighted hyperintensity surrounded by normal isointense white matter. Only lesions of >3 mm along the longest axis were considered. Confluent lesions without precise delineation were considered a single lesion.

Finally, discrepancies between the reviewers as to whether a lesion was present were resolved in consensus with a third rater with 15 years of experience (J.H.). Statistical analysis was based on postconsensus lesion counts (consensus reading in Table 2).

Quantitative Analysis in Patients with MS. Contrast-to-noise ratio (CNR) and SNR analyses were performed by 1 neuroradiologist (S.T.-M.). For each patient and each FLAIR acquisition, ROIs were drawn on axial reformatted views, within the following: 1) an MS lesion, 2) normal-appearing white matter, and 3) background noise. Care was taken to avoid lesion borders. SNR and CNR were calculated as follows: $SNR = SI/SD_{noise}$ and $CNR = (SI_{lesion} - SI_{WM})/SD_{noise}$, where SI is the average signal intensity of the lesion or the WM and SD_{noise} is the SD of the noise.

An automatic postprocessing was additionally performed with Quantib Brain 1.2 software (Quantib, Rotterdam, Netherlands) based on de Boer et al.¹² We analyzed 2 sets of series: 1) the BRAVO T1-weighted scan in combination with the conventional FLAIR scan, and 2) the BRAVO T1-weighted scan in combination with CS FLAIR scan. We used Quantib Brain to quantify the volume and the total number of brain MS lesions visible on both FLAIR sequences, based on the automatic segmentation of white

matter hyperintensities. Using such postprocessing, we took all the MS lesions into account, including those involving the deep white matter.

Statistical Analysis

The Lin concordance correlation coefficient was used to assess interrater agreement and intrareader agreement for total MS lesion count and was interpreted as follows: poor agreement (<0.90), moderate agreement (0.90 to <0.95), substantial agreement (0.95 to <0.99), and almost perfect agreement (≥ 0.99).¹³ The Student *t* test was used to compare image-quality scores between conventional and CS FLAIR. The Wilcoxon signed rank test was performed to test the null hypothesis that there was no significant difference in the total number of MS lesions between conventional and CS FLAIR, based on the radiologists' count. The level of significance was set to $P < .05$. The Lin concordance correlation coefficient was also used to evaluate the agreement between conventional and CS FLAIR in terms of the number of lesions detected in each region. Statistical analysis was based on postconsensus lesion counts.

The Student *t* test was used to compare SNR and CNR values between conventional and CS FLAIR. The total volume of MS lesions between the 2 FLAIR scans, as measured by automatic white-matter hyperintensity segmentation, was compared using the Wilcoxon signed rank test.

RESULTS

Qualitative data are shown in Table 2.

Preliminary Study in Healthy Volunteers

Scan times of the different FLAIR acquisitions, without CS and with a CS factor of 1.2, 1.3, 1.4, and 1.5, were 5 minutes 15 seconds, 4 minutes 10 seconds, 3 minutes 50 seconds, 3 minutes 30 seconds, and 3 minutes 22 seconds, respectively. CS acceleration factor values of 1.4 and 1.5 were disqualified due to a poor delineation (rated 1) of the cortical gray matter junction. A CS factor of 1.3 provided the highest scan time reduction with good (mean score, 2.5) image quality. The CS factor 1.2 yielded only marginally improved image quality (mean score, 2.6) compared with the CS factor 1.3 and was 20 seconds shorter. As a result, the CS factor 1.3 was retained for the patient study.

Qualitative Analysis in Patients with MS

Interrater agreement as measured by the Lin concordance correlation coefficient was substantial (score of 0.95), and intrareader agreement was almost perfect (score, 0.99).

Image-quality scores did not differ between conventional and CS FLAIR ($P = .74$). Mean image-quality scores were 2.78 ± 0.42 for conventional FLAIR, and 2.73 ± 0.44 for CS FLAIR. All FLAIR images were rated at least good. CSF suppression, delineation of the deep brain nuclei, and junction delineation were identical between every set of FLAIR images and rated as excellent. Of the 23 CS FLAIR acquisitions, 6 acquisitions were rated good instead of excellent due to a slight image blurring that did not impair diagnosis.

The total number of MS lesions detected by readers was similar between conventional and CS FLAIR (542 versus 557, $P = .094$).

The correlation coefficient between conventional and CS

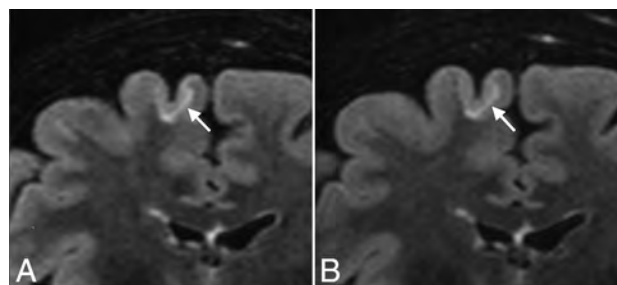


FIG 1. Coronal reformatted views of 3D-FLAIR with (A) and without (B) CS, showing a juxtacortical lesion involving the right frontal superior gyrus (arrows) in a 50-year-old female patient with relapsing-remitting MS. Note the similar delineation of the gray-white matter junction between conventional and CS FLAIR.

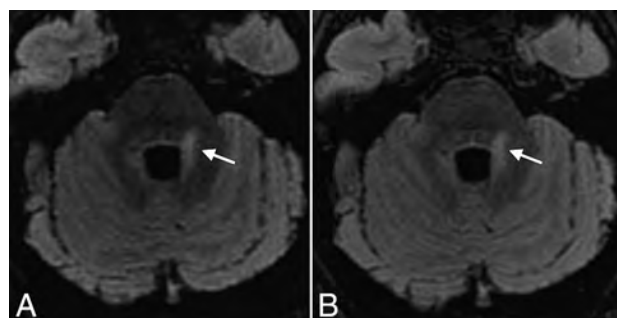


FIG 2. Axial reformatted views of 3D-FLAIR with (A) and without (B) CS, showing a periventricular MS lesion also involving the left middle cerebellar peduncle (arrows) in a 31-year-old female patient with relapsing-remitting MS. Note the excellent and similar suppression of CSF obtained with both sequences.

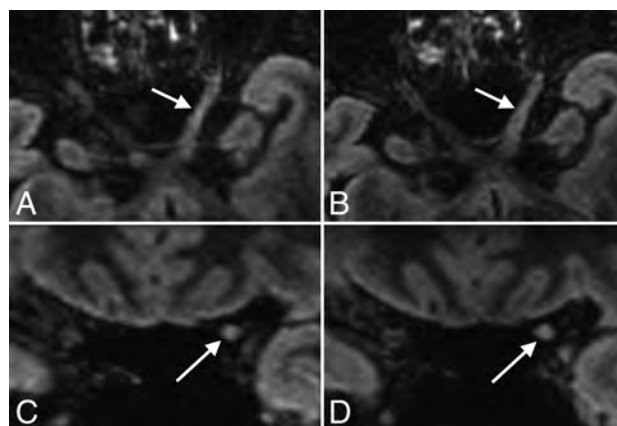


FIG 3. Axial and coronal reformatted views of 3D-FLAIR with (A and C) and without (B and D) CS, showing an MS lesion involving the cisternal and canicular portions of the left optic nerve (arrows) in a 48-year-old female patient with relapsing-remitting MS.

FLAIR for the total MS lesion count after consensus was almost perfect (score, 0.99). Agreement between conventional and CS FLAIR was almost perfect for periventricular and infratentorial lesions (score, 0.99; Fig 2) and substantial for intra-juxtacortical and optic nerve lesions (score, 0.98; Figs 1 and 3).

Quantitative Analysis in Patients with MS

There was no statistical difference between the 2 FLAIR sequences in the SNR of normal-appearing white matter ($P = .57$), the SNR

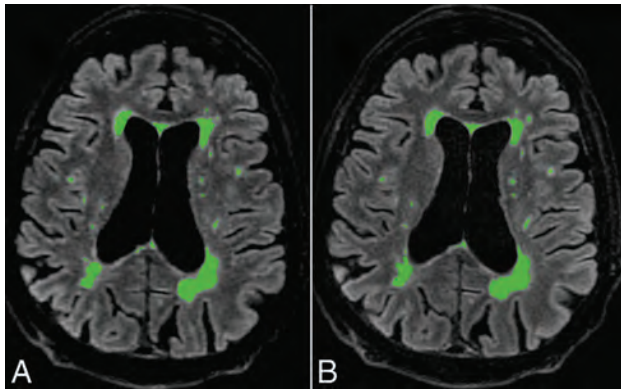


FIG 4. Automatic postprocessing performed with Quantib Brain 1.2 software allowing the assessment of MS lesion volumes using CS (A) and conventional FLAIR (B). With such a quantitative approach, FLAIR hyperintensities of the whole brain were taken into account. There was no significant difference between both FLAIR acquisitions in the total MS lesion volume ($P = .63$) and number (0.15).

of MS lesions ($P = .49$), and the CNR of MS lesions to normal-appearing white matter ($P = .52$).

Postprocessing with Quantib Brain 1.2 software did not reveal any significant difference between conventional and CS FLAIR in total MS lesion volume ($P = .63$) or in the number of MS lesions ($P = .15$) automatically measured (Fig 4).

DISCUSSION

Reducing the MR imaging scan time may improve patient comfort, cost-effectiveness, motion-related artifacts, and thus reproducibility. This improvement may be particularly useful for 3D FSE sequences, such as FLAIR, that usually require long acquisition times. In this study, we found that by adding CS to standard PI acceleration strategies, we can reduce the scan time of 3D-FLAIR by 27% (1 minute 25 seconds) while preserving the accuracy of the detection of MS plaques. This result appears clinically relevant, considering the widespread use of 3D-FLAIR in MR imaging protocols dedicated to MS.⁴ Additionally, the agreement of results produced automatically by postprocessing further strengthens our conclusion, providing an unbiased analysis and taking into account all the visible MS lesions, including those involving the deep white matter.

To our knowledge, the combination of PI and CS to achieve FLAIR imaging has never been evaluated in patients with MS. The use of CS in neuroimaging has been evaluated in healthy volunteers with diffusion imaging¹⁴ and in patients with intracranial aneurysms using TOF-MRA.¹⁵ Our results are also fully concordant with recent studies evaluating CS in cardiac, abdominal, or knee imaging.¹⁶⁻¹⁹ Indeed, these studies have shown comparable image quality and lesion conspicuity between accelerated and nonaccelerated sequences. Admittedly, higher CS factors and scan time reductions can be achieved in MR sequences producing high contrast images with high data sparsity such as TOF-MRA, but such analysis is beyond the scope of the present study.

We observed image blurring in some of the CS FLAIR acquisitions. Such findings appear inherent to the CS technique that uses a variable random undersampling of the k -space, more pronounced at the periphery, thus leading to blurred images. While the quality of CSF suppression was identical in

CS FLAIR and conventional FLAIR, a slight difference in deep brain nuclei and gray-white matter junction delineation was observed due to minor motion-related blurring that did not affect the diagnostic performance. We used a simplified 3-point scale to evaluate image quality. A more detailed scale may have exposed these minor differences, even though they have no impact on diagnostic performance. We performed accelerated FLAIR with a CS factor of 1.3 after testing a wide range of acceleration factors (detailed in the preliminary study) because this value appeared to us as a good compromise among blurring, reduced scan time, and accuracy.

In this study, we aimed at reducing the scan time of the 3D-FLAIR sequence with CS and evaluated its diagnostic performance. However, CS could also be used to further improve image quality in the same acquisition time of the conventional sequence by, for example, increasing the spatial resolution and/or contrast. Such an approach could be particularly useful to reduce partial volume effects and improve delineation of the cortical ribbon.

Of note, the diagnostic performance of both conventional and CS FLAIR appeared similar regardless of the topography of the inflammatory lesions, including those involving the optic nerves. Such findings may be particularly relevant in patients suspected of having MS and for whom spatial dissemination is customarily evaluated on the basis of FLAIR images.¹

This study has some limitations. First, we did not include healthy controls since SNR values were also measured within the normal-appearing white matter of patients. Second, the number of MS lesions detected tended to differ between the 2 blinded readers (particularly for periventricular lesions). Such differences may be related to the small size of some lesions. However, both readers found no significant difference between conventional and CS FLAIR, whatever the lesion topography. We did not evaluate the impact of the acceleration factor value on diagnostic performance because we systematically applied a previously determined (by a preliminary study) CS factor of 1.3. Such a study design would have led to an important increase in protocol duration, which was not acceptable in a clinical setting. Further studies may investigate the optimal combination of acceleration factors of PI and CS according to the artifacts observed. Because we only included follow-up MRIs of patients with relapsing-remitting MS, we did not evaluate the performance of CS FLAIR in other types of MS, such as clinically isolated syndrome. However, it is reasonable to expect that the detectability of MS plaques using FLAIR may not differ according to MS types.

CONCLUSIONS

3D-FLAIR with a CS acceleration factor of 1.3 appeared to be the best compromise between scan time reduction and diagnostic performance in the detection of MS lesions.

Disclosures: Renske de Boer—UNRELATED: Employment: Quantib B.V., Comments: Quantib B.V. developed Quantib Brain; Royalties: GE Healthcare, Comments: Quantib B.V. receives royalties from GE Healthcare for Quantib Brain sales.* Jaap Gelderblom—UNRELATED: Employment: Quantib B.V., Comments: Quantib B.V. developed Quantib Brain; Royalties: GE Healthcare, Comments: Quantib B.V. receives royalties from GE Healthcare for Quantib Brain sales*. Rachid Mahdjoub—UNRELATED: Employment: GE Healthcare, Comments: I am the neuroclinical leader; thus, I provide support and collaborate with research activities of our customers. *Money paid to the institution.

REFERENCES

1. Polman CH, Reingold SC, Banwell B, et al. **Diagnostic criteria for multiple sclerosis: 2010 revisions to the McDonald criteria.** *Ann Neurol* 2011;69:292–302 CrossRef Medline
2. Aiken AH, Mukherjee P, Green AJ, et al. **MR imaging of optic neuropathy with extended echo-train acquisition fluid-attenuated inversion recovery.** *AJNR Am J Neuroradiol* 2011;32:301–05 CrossRef Medline
3. Filippi M, Rocca MA, Ciccarelli O, et al; MAGNIMS Study Group. **MRI criteria for the diagnosis of multiple sclerosis: MAGNIMS consensus guidelines.** *Lancet Neurol* 2016;15:292–303 CrossRef Medline
4. Moraal B, Roosendaal SD, Pouwels PJW, et al. **Multi-contrast, isotropic, single-slab 3D MR imaging in multiple sclerosis.** *Eur Radiol* 2008;18:2311–20 CrossRef Medline
5. Donoho DL. **Compressed sensing.** *IEEE Transactions on Information Theory* 2006;52:1289–306 CrossRef
6. Kayvanrad M, Lin A, Joshi R, et al. **Diagnostic quality assessment of compressed sensing accelerated magnetic resonance neuroimaging.** *J Magn Reson Imaging* 2016;44:433–44 CrossRef Medline
7. Geethanath S, Reddy R, Konar AS, et al. **Compressed sensing MRI: a review.** *Crit Rev Biomed Eng* 2013;41:183–204 CrossRef Medline
8. Lustig M, Donoho D, Pauly JM. **Sparse MRI: the application of compressed sensing for rapid MR imaging.** *Magn Reson Med* 2007;58:1182–95 CrossRef Medline
9. Vasanaawala SS, Alley MT, Hargreaves BA, et al. **Improved pediatric MR imaging with compressed sensing.** *Radiology* 2010;256:607–16 CrossRef Medline
10. Lustig M, Pauly JM. **SPIRiT: iterative self-consistent parallel imaging reconstruction from arbitrary k-space.** *Magn Reson Med* 2010;64:457–71 CrossRef Medline
11. King K, Xu D, Brau AC, et al. **A new combination of compressed sensing and data driven parallel imaging.** In: *Proceedings of the Annual Meeting of the International Society for Magnetic Resonance in Medicine*, Stockholm, Sweden. May 1–7, 2010:4881
12. de Boer R, Vrooman HA, van der Lijn F, et al. **White matter lesion extension to automatic brain tissue segmentation on MRI.** *Neuroimage* 2009;45:1151–61 CrossRef Medline
13. Lin LI. **A concordance correlation coefficient to evaluate reproducibility.** *Biometrics* 1989;45:255–68 CrossRef Medline
14. Menzel MI, Tan ET, Khare K, et al. **Accelerated diffusion spectrum imaging in the human brain using compressed sensing.** *Magn Reson Med* 2011;66:1226–33 CrossRef Medline
15. Fushimi Y, Fujimoto K, Okada T, et al. **Compressed sensing 3-dimensional time-of-flight magnetic resonance angiography for cerebral aneurysms: optimization and evaluation.** *Invest Radiol* 2016;51:228–35 CrossRef Medline
16. Basha TA, Akçakaya M, Liew C, et al. **Clinical performance of high-resolution late gadolinium enhancement imaging with compressed sensing.** *J Magn Reson Imaging* 2017;46:1829–38 CrossRef Medline
17. Feng L, Benkert T, Block KT, et al. **Compressed sensing for body MRI.** *J Magn Reson Imaging* 2016;45:966–87 CrossRef Medline
18. Seo N, Park MS, Han K, et al. **Feasibility of 3D navigator-triggered magnetic resonance cholangiopancreatography with combined parallel imaging and compressed sensing reconstruction at 3T.** *J Magn Reson Imaging* 2017;46:1289–97 CrossRef Medline
19. Kijowski R, Rosas H, Samsonov A, et al. **Knee imaging: rapid three-dimensional fast spin-echo using compressed sensing.** *J Magn Reson Imaging* 2017;45:1712–22 CrossRef Medline

Improved Visualization of Cortical Lesions in Multiple Sclerosis Using 7T MP2RAGE

 E.S. Beck,  P. Sati,  V. Sethi,  T. Kober,  B. Dewey,  P. Bhargava,  G. Nair,  I.C. Cortese, and  D.S. Reich



ABSTRACT

BACKGROUND AND PURPOSE: Cortical lesions are common and often extensive in multiple sclerosis but are difficult to visualize by MRI, leaving important questions about their clinical implications and response to therapy unanswered. Our aim was to determine whether cortical lesions are better visualized using magnetization prepared 2 rapid acquisition gradient echoes (MP2RAGE) than T2*-weighted imaging on 7T MR imaging.

MATERIALS AND METHODS: Brain MR imaging using T1-weighted MP2RAGE at 500- μ m isotropic resolution, T2*-weighted gradient-echo, and T2*-weighted segmented echo-planar imaging sequences were collected for 13 patients with MS and 5 age-matched neurologically healthy controls on a 7T research system. One MS case underwent postmortem MR imaging including gradient-echo and MP2RAGE sequences, after which cortical lesions seen on MR imaging were assessed with immunohistochemistry.

RESULTS: MP2RAGE detected 203 cortical lesions (median, 16 lesions/case; interquartile range, 15), compared to 92 with T2*gradient-echo (median, 7; interquartile range, 8; $P < .001$) and 81 with T2*EPI (median, 7; interquartile range, 5; $P < .001$). This increase in lesion number detected on MP2RAGE versus T2* was observed for juxtacortical, leukocortical, and intracortical lesions. Forty-three percent of all cortical lesions were identified only on MP2RAGE. White matter lesion volume correlated with total juxtacortical ($r = 0.86$, $P < .001$) and leukocortical lesion volume ($r = 0.70$, $P < .01$) but not intracortical lesion volume, suggesting that pathophysiology may differ by lesion type. Of 4 suspected lesions seen on postmortem imaging, 3 were found to be true cortical lesions while 1 represented postmortem tissue damage.

CONCLUSIONS: A combination of MP2RAGE and T2*-weighted imaging at 7T improved detection of cortical lesions and should enable longitudinal studies to elucidate their spatiotemporal dynamics and clinical implications.

ABBREVIATIONS: GRE = gradient recalled-echo; IQR = interquartile range; MP2RAGE = magnetization prepared 2 rapid acquisition gradient echoes

MS is a demyelinating disorder affecting both white and gray matter.¹⁻³ In some individuals, cortical demyelination exceeds white matter demyelination,² and cortical lesions may be more strongly associated with disability and disability progression than white matter lesions.⁴⁻⁸ Cortical and white matter lesions

have potentially distinct origins and levels of inflammation,^{3,9-13} suggesting that they may have different clinical significance and response to treatment. Finally, the clinical course of MS is often not fully explained by volume and accumulation of white matter lesions,¹⁴ making better understanding of other types of MS pathology, including cortical lesions, imperative.

Although MR imaging is essential for MS diagnosis and disease monitoring, our limited understanding of cortical lesions stems from difficulties in imaging these lesions due to their size, myelin content, level of inflammation, and partial volume aver-

Received August 10, 2017; accepted after revision November 15.

From the Translational Neuroradiology Section (E.S.B., P.S., V.S., B.D., G.N., D.S.R.) and Neuroimmunology Clinic (I.C.C.), National Institute of Neurological Disorders and Stroke, National Institutes of Health, Bethesda, Maryland; Advanced Clinical Imaging Technology Group (T.K.), Siemens Healthcare Switzerland, Lausanne, Switzerland; Department of Radiology (T.K.), Centre Hospitalier Universitaire Vaudois, Lausanne, Switzerland; LT55, Ecole Polytechnique Fédérale de Lausanne (T.K.), Lausanne, Switzerland; and Department of Neurology (P.B.), Johns Hopkins University, Baltimore, Maryland.

This work was supported by the Intramural Research Program of the National Institute of Neurological Disorders and Stroke, National Institutes of Health. E.S.B. is further supported by a Clinician Scientist Development Award from the National Multiple Sclerosis Society. P.B. is supported by a career transition award from the National Multiple Sclerosis Society, a Young Investigator Award from Race to Erase MS, and a John F. Kurtzke Clinician Scientist Development Award from the American Academy of Neurology.

Please address correspondence to Daniel S. Reich, MD, PhD, Translational Neuroradiology Section, National Institute of Neurological Disorders and Stroke, National Institutes of Health, Building 10, Room 5C103, 10 Center Drive, Bethesda, MD 20892; e-mail: reichds@ninds.nih.gov

 Indicates open access to non-subscribers at www.ajnr.org

 Indicates article with supplemental on-line appendix and tables.

 Indicates article with supplemental on-line photos.

<http://dx.doi.org/10.3174/ajnr.A5534>

Table 1: MRI acquisition parameters for the 3 sequences acquired at 7T

	3D-MP2RAGE	2D-T2*GRE	3D-Segmented T2*EPI
Orientation	Axial	Axial	Axial
Voxel dimensions (μm)	500 \times 500	215 \times 215	500 \times 500
Slice thickness (μm)	500	1000	500
FOV (mm)	224 (AP) \times 168 (RL) \times 112 (SI)	220 (AP) \times 165 (RL) \times 25 (SI)	220 (AP) \times 180 (RL) \times 88 (SI)
TI (ms)	800/2700	NA	NA
TR (ms)	6000	1300	52
TE (ms)	5	32	23
Flip angle	4°/5°	50°	10°
EPI factor	NA	NA	15
Scan time (min:sec)	10:32	8:36	3:40
No. of repetitions	4	1	1

Note:—AP indicates anterior-posterior axis; RL, right-left axis; SI, superior-inferior axis; NA, not applicable.

aging with CSF. Double inversion recovery and phase-sensitive inversion recovery sequences at 1.5T and 3T and T2*-weighted sequences at 7T have been used to visualize cortical lesions.¹⁵⁻¹⁸ 7T MR imaging allows much higher spatial resolution, which is particularly important for the visualization of small cortical lesions, and T2*-weighted sequences at 7T have been shown to more sensitively and reliably detect cortical lesions than double inversion recovery at 3T.¹⁹ However, small intracortical lesions remain difficult to visualize using all 3 of these techniques, and overall sensitivity remains low.²⁰⁻²²

Here, we aimed to develop an approach that could be used to investigate the natural history of cortical lesions in future studies, rather than develop an imaging sequence for routine clinical use. Recent studies in humans and nonhuman primates have demonstrated the value of T1-based MR imaging for visualizing the myeloarchitecture of the cortex.²³⁻²⁵ Among the different T1 MR imaging techniques, magnetization prepared 2 rapid acquisition gradient echoes (MP2RAGE) provides the best tissue contrast at high spatial resolution while minimizing field inhomogeneities that affect other techniques at 7T.^{26,27} We achieved high resolution while preserving image quality by combining multiple repetitions of the same 3D MP2RAGE acquisition. We also compared visualization of cortical lesions on MP2RAGE with 2 different T2*-weighted acquisitions.

MATERIALS AND METHODS

In Vivo MR Imaging

Thirteen participants in our MS natural history study and 5 neurologically healthy, age-matched controls (On-line Table 1) underwent brain MR imaging on a 7T whole-body research system (Siemens, Erlangen, Germany) equipped with a single-channel transmit, 32-channel phased array receive head coil. To maximize cortical lesion count, we included patients with MS with prior high-quality 7T scans and longstanding disease. The MP2RAGE sequence used previously optimized parameters (Table 1),²⁸ covered the entire cerebrum, was acquired at 500- μm isotropic resolution, and was repeated 4 times to improve image quality (total scan time: \sim 40 minutes; On-line Fig 1). A 2D T2* gradient recalled-echo (GRE) sequence (215 \times 215 \times 1000 μm), like one previously demonstrated to visualize cortical lesions,¹⁸ was acquired in 3 partially overlapping volumes to cover most of the cerebrum (total scan time, \sim 25 minutes). A novel 3D segmented T2*EPI prototype sequence^{29,30} was acquired in 2 partially overlapping volumes at the same resolution as MP2RAGE

(total scan time, \sim 7 minutes) (Table 1). In 2 patients with MS, the T2* sequences were acquired during the same session as MP2RAGE; in the other 11, one or both T2* sequences were acquired on a separate day. The interval between MP2RAGE and GRE or EPI ranged from -8 to $+18$ months; in 10 of the patients with MS, MP2RAGE was acquired first. All patients with MS were also scanned on a 3T Magnetom Skyra scanner (Siemens) equipped with a 32-channel head coil (On-line Table 2).

Image Processing

Initial MP2RAGE processing to generate uniform images and T1 maps was performed on the scanner as part of the Siemens research sequence package (Work-in-Progress Package #900B).²⁶ The 4 repetitions were coregistered, and the voxelwise median was used for all analyses. T2*GRE and T2*EPI were aligned to the MP2RAGE using linear coregistration. See the On-line Appendix for further details.

Lesion Identification and Characterization

Image analysis was conducted using a freely available image analysis software (Medical Image Processing, Analysis, and Visualization; National Institutes of Health; <https://mipav.cit.nih.gov/>). Images were magnified using bilinear interpolation as needed, and raters could manipulate window and level settings. Lesions were identified in the axial plane, with the option to confirm them on sagittal and coronal images. Lesions had to be hypointense on MP2RAGE images and/or hyperintense on T2* images and visible on at least 2 contiguous axial slices. Lesions were classified as intracortical (no white matter involvement; includes subpial lesions), leukocortical (involving both white matter and cortex), or juxtacortical (white matter lesions abutting but not clearly involving the cortex). Data were then compared across sequences. Comparison revealed that some cortical lesions were artifacts or white matter lesions that did not directly contact the cortex; these were excluded from further analyses.

E.S.B. (neurologist with 5 years' experience) marked cortical lesions on each sequence independently for all patients and controls, with at least 1 day between analyses of different sequences for the same individual. D.S.R. (neurologist/neuroradiologist with 14 years' experience) verified all lesions. Locations corresponding to lesions identified on only 1 or 2 sequences were examined on the remaining sequences to determine whether these lesions could be identified retrospectively. All lesions identified by E.S.B. and verified by D.S.R. (total 309) were included in lesion

volume, count, and T1 relaxation time analyses. Lesions within the FOV for all 3 sequences (total 220) were used for sequence-comparison analyses. In 1 patient, T2*GRE images were too motion-degraded to analyze, and lesions identified on MP2RAGE and T2*EPI for this patient were included in all analyses except for sequence comparisons.

To determine interrater agreement, P.B. (neurologist with 7 years' experience) marked cortical lesions on each sequence independently for 5 of the 13 patients with MS and all controls, with verification of all lesions by D.S.R. These ratings were then compared with those of E.S.B. for the same patients and controls. To determine intrarater agreement, E.S.B. re-analyzed the same 5 patients with MS several months after the first set of ratings.

To compute lesion volume, a single rater (E.S.B.) delineated ROIs manually, along the border of each lesion on all slices in which the lesion appeared on MP2RAGE. Total white matter lesion volume was also estimated using 3T FLAIR and MP2RAGE images. Images were registered to a brain atlas,³¹ and lesions were then segmented with LesionTOADS software (<https://www.nitrc.org/projects/toads-cruise>).³² Segmentation results were manually reviewed and corrected as necessary.

T1 relaxation times were obtained for each lesion using the median MP2RAGE T1 map. To obtain T1 values for normal-appearing tissue and control tissue, we randomly chose 1 intracortical, 1 leukocortical, and 1 juxtacortical lesion for each case. For normal-appearing cortex and white matter, a contralateral ROI on a single slice was selected for each lesion. For control cortex and white matter, an ROI on a single slice matching each of the chosen lesions was selected in a control brain; ROIs were distributed evenly among the 5 control brains.

Statistics

The Kruskal-Wallis test with correction for multiple comparisons allowed cross-sequence comparison of lesion counts as well as lesion subtype count and volume analyses. One-way analysis of variance with correction for multiple comparisons allowed comparison of T1 relaxation times. Spearman correlation coefficients linked the volume of the cortical lesion subtypes with that of white matter lesions.

Standard Protocol Approvals, Registrations, and Consents

The study received approval from the NIH institutional review board, where the study was performed. All participants provided written informed consent. The next of kin for the person whose brain was evaluated postmortem provided written informed consent for the brain postmortem examination and use of material and clinical information for research purposes.

RESULTS

More Cortical Lesions were Identified on MP2RAGE than on T2*-Weighted Images In Vivo at 7T

7T images from 13 patients with MS and 5 neurologically healthy controls were analyzed (demographics in On-line Table 1). Three hundred nine cortical lesions were identified in the patients with MS (median, 24; range, 3–62; interquartile range [IQR], 15), including 85 juxtacortical (median, 5; range, 0–29; IQR, 5), 164

leukocortical (median, 14; range, 1–30; IQR, 12), and 60 intracortical (median, 3; range, 0–13; IQR, 3) lesions. Figure 1 shows representative examples of lesion appearance across sequences. Small intracortical lesions identified on MP2RAGE were often visible in retrospect on T2*GRE and/or T2*EPI (Fig 1G–I); the same was true on MP2RAGE for several lesions initially identified only on T2* (see below). Some lesions initially classified as white matter or juxtacortical on T2* were reclassified after comparison with MP2RAGE (Fig 1P–R), where the gray-white junction was better defined. Cortical involvement of some leukocortical lesions, in particular U-shaped lesions at the depths of the sulci, was more obvious on T2* than on MP2RAGE, where cortical (particularly subpial) involvement was sometimes subtler (Fig 1J–L).

Almost twice as many cortical lesions were detected on MP2RAGE as on T2* (Fig 2 and Table 2), independent of lesion subtype. A single cortical lesion was identified in 1 of the 5 healthy controls; this lesion was leukocortical and seen only on MP2RAGE (On-line Fig 2).

Forty-nine percent (108/220) of cortical lesions were identified on both MP2RAGE and at least 1 of the T2* sequences, and 43% (95/220) were identified only on MP2RAGE. Only 8% (17/220) were identified on at least 1 of the T2* sequences but not on MP2RAGE. These numbers were similar for juxtacortical and leukocortical lesions (Fig 2). For intracortical lesions, 39% (17/44) were identified on both MP2RAGE and at least 1 T2* sequence, whereas 36% (16/44) were identified on MP2RAGE only and 25% (11/44) were identified only on T2*.

The number of total cortical lesions identified on the 2 T2* sequences did not differ, nor did the number of any of the 3 cortical lesion subtypes (Fig 2 and Table 2). Lesion subtype and size did not differ between lesions identified on T2*EPI but not GRE and lesions identified on T2*GRE but not EPI (On-line Table 4).

Lesions initially identified only on 1 or 2 sequences were evaluated retrospectively on the remaining sequences. Eighty-eight percent (84/95) of lesions identified prospectively on MP2RAGE only were seen in retrospect on at least 1 of the T2* sequences. Forty-six of the 84 lesions were small or had only subtle signal change on T2* images, likely explaining the lack of prospective identification, while 36 of the 84 lesions were visible but did not have clear cortical involvement on the T2* images; only 2 of the 84 lesions had obvious cortical involvement on T2* images, which had been missed in the initial analysis. All 17 lesions prospectively identified on T2* sequences but not on MP2RAGE were seen retrospectively on MP2RAGE images. Eleven of the 17 lesions were small or had only subtle signal changes on MP2RAGE, 2 lesions did not appear to involve the cortex on MP2RAGE, and 4 lesions had obvious cortical involvement on MP2RAGE but had been missed in the initial analysis. Ninety-eight percent (43/44) of the lesions identified on T2*GRE but not T2*EPI were visible in retrospect on T2*EPI, and 94% (31/33) of the lesions identified on T2*EPI but not T2*GRE were visible in retrospect on T2*GRE.

Inter- and Intrarater Variability is Higher for T2* than for MP2RAGE

For the 5 patients with MS in whom cortical lesions were identified on all 3 sequences by 2 raters, 44% of verified lesions were

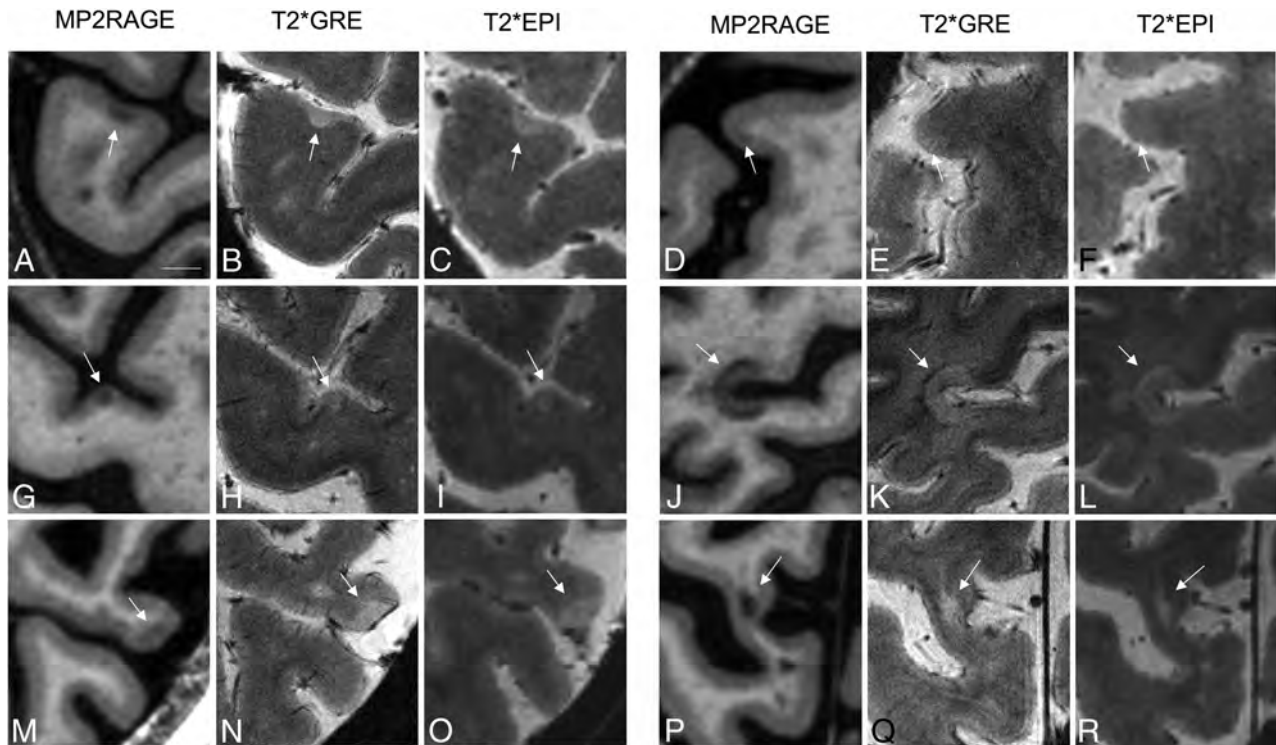


FIG 1. Comparison of cortical lesion detection with MP2RAGE and T2* weighted sequences at 7T. Intracortical (A–I), leukocortical (J–O), and juxtacortical (P–R) lesions (arrows) are seen to different degrees on T1 MP2RAGE (A, D, G, J, M, and P), T2*GRE (B, E, H, K, N, and Q), and T2*EPI (C, F, I, L, O, and R) sequences. A–C, An example of an intracortical lesion identified prospectively on all 3 sequences. D–F, An example of an intracortical lesion identified prospectively only on MP2RAGE but not visible even in retrospect on T2*GRE or T2*EPI. G–I, An example of an intracortical lesion identified prospectively only on MP2RAGE but visible in retrospect on T2*GRE and T2*EPI. J–L, An example of a leukocortical lesion, spanning the full cortical thickness and identified on all 3 sequences. M–O, An example of a leukocortical lesion, spanning the full cortical thickness and identified on T2*GRE and T2*EPI prospectively but only in retrospect on MP2RAGE. P–R, An example of a juxtacortical lesion identified as juxtacortical on MP2RAGE but initially incorrectly classified as a white matter lesion on GRE and EPI. Scale bar = 5 mm.

identified on at least 1 sequence by both raters, whereas 56% of lesions were identified by only 1 rater. This discrepancy was greatest for intracortical lesions, of which only 26% were identified by both raters, compared with 51% for leukocortical and 52% for juxtacortical lesions. On MP2RAGE, 48% of lesions were identified by both raters; more than twice as many as were identified by both raters on T2*GRE (23%) or T2*EPI (22%).

Intrarater variability for the same 5 cases was similar to interrater variability, with 47% of lesions identified on at least 1 sequence by both raters and 53% of lesions identified only once. Fifty-two percent of lesions identified on MP2RAGE were identified both times, compared with 40% on T2*GRE and 24% on T2*EPI.

Number and Volume of Cortical Lesion Subtypes Vary Widely across Patients

Across the 13 patients with MS, there were more leukocortical (164) than intracortical (60) or juxtacortical (85) lesions. For each individual, however, the relative number of lesions of each type was highly variable, as was cortical lesion volume (On-line Fig 3 and On-line Table 5). Total white matter lesion volume did not correlate with intracortical lesion volume ($P = .44$), but leukocortical lesion volume ($r = 0.71, P = .009$) and juxtacortical lesion volume ($r = 0.86, P < .001$) each correlated with total white matter lesion volume (Fig 3A–C).

When stratified by volume, 72% of the largest third of lesions (range, 55–2854 μL ; mean, 200 μL) were identified on MP2RAGE

and at least 1 T2* sequence, whereas 26% were identified only on MP2RAGE and 3% were identified only on T2*. In contrast, for lesions with volumes in the middle third (range, 26–55 μL ; mean, 40 μL), 46% were identified on both sequence types, whereas 41% were identified on MP2RAGE only and 14% on T2* only. For the smallest third of lesions (range, 5–26 μL ; mean, 15 μL), 30% were identified on both sequence types; 63%, on MP2RAGE only; and 7%, on T2* only. Thus, larger lesions are more likely to be identified on both MP2RAGE and T2* sequences, whereas smaller lesions are more likely to be identified on only MP2RAGE.

T1 Relaxation Times Differ across Cortical Lesion Types

The mean T1 relaxation times were calculated for each cortical lesion, for normal-appearing gray and white matter in patients with MS, and for control cortex and white matter (Fig 3D). The mean T1 was higher in juxtacortical (2062 ± 230 ms) than in leukocortical (1961 ± 182 ms, $P < .001$) or intracortical (1871 ± 96 ms, $P < .001$) lesions. Leukocortical lesions also had higher T1 than intracortical lesions ($P < .001$). The mean T1 relaxation time for each lesion type was higher ($P < .001$) than for the corresponding normal-appearing and control tissue. There was no difference between normal-appearing (1703 ± 90 ms) and control (1685 ± 88 ms) gray matter or between normal-appearing (1261 ± 92 ms) and control (1207 ± 86 ms) white matter. T1 of lesions identified on both MP2RAGE and at least 1 T2* sequence

(2012 ± 213 ms) was higher than that of lesions identified only on MP2RAGE (1923 ± 182 ms, $P < .01$) and those identified only on T2* sequences (1893 ± 87 ms, $P < .05$). The T1 of lesions identified on MP2RAGE only was not significantly different from that of lesions identified on T2* only.

Most Cortical Lesions Visualized by MP2RAGE on Postmortem 7T MR Imaging Can Be Verified Pathologically

One postmortem MS brain was imaged at 7T with MP2RAGE and T2*GRE (On-line Appendix). The areas of tissue corresponding to 4 suspected leukocortical lesions, all with predominantly cortical involvement, were isolated and stained for myelin proteolipid protein. Three of the suspected lesions, all of which were identified prospectively on MP2RAGE and T2*GRE, were clearly demyelinated lesions (On-line Fig 4). The fourth, which was identified on T2*GRE prospectively and only seen in retrospect on MP2RAGE, was a small tear in the cortex that likely occurred during postmortem handling.

DISCUSSION

In this study, we show that acquisition of high-resolution MP2RAGE at 7T dramatically increases the detection of cortical lesions compared with state-of-the-art T2*GRE or our prototype T2*EPI sequence. Reasons for the superior sensitivity of MP2RAGE over T2* include more homogeneous signal intensity, better gray-white junction delineation, and decreased image artifacts. Importantly, we found that MP2RAGE allowed identification of smaller and more subtle lesions while generally preserving visualization of lesions identifiable on T2*.

Our comparison of MP2RAGE images acquired in patients with MS and controls, our postmortem verification of several cortical lesions seen on MP2RAGE, and our retrospective identification of most lesions seen on MP2RAGE on T2* images together suggest that most identified cortical lesions are true demyelinated lesions. Although we cannot rule out that some cortical lesions identified in MS are due to other types of tissue damage or artifacts (also the case for white matter lesions), the number of such lesions is likely low.

Despite the advantages of MP2RAGE, some cortical lesions were seen better on T2* images, whereas others appeared to have different degrees of cortical involvement on MP2RAGE versus T2*. Some cortical lesions appeared subpial on T2* but not on MP2RAGE (eg, Fig 1M–O). One potential explanation is that there are pathologic differences in lesions close to the pial surface versus deeper in the cortex, leading to differences in visualization on MR imaging. T2* sequences may also be particularly sensitive to cortical pathology due to differences in magnetic susceptibility between cortical layers. A more definitive answer to this question will require detailed postmortem MR imaging–histopathologic correlation.

Although we hypothesize that the ability of MP2RAGE and T2* to detect cortical lesions differs in part due to specific pathologic features of different lesions, most lesions identified on 1 or 2 sequences were visible on the remainder of the sequences in retrospect. When evaluated retrospectively, many lesions missed initially on T2* were small or had

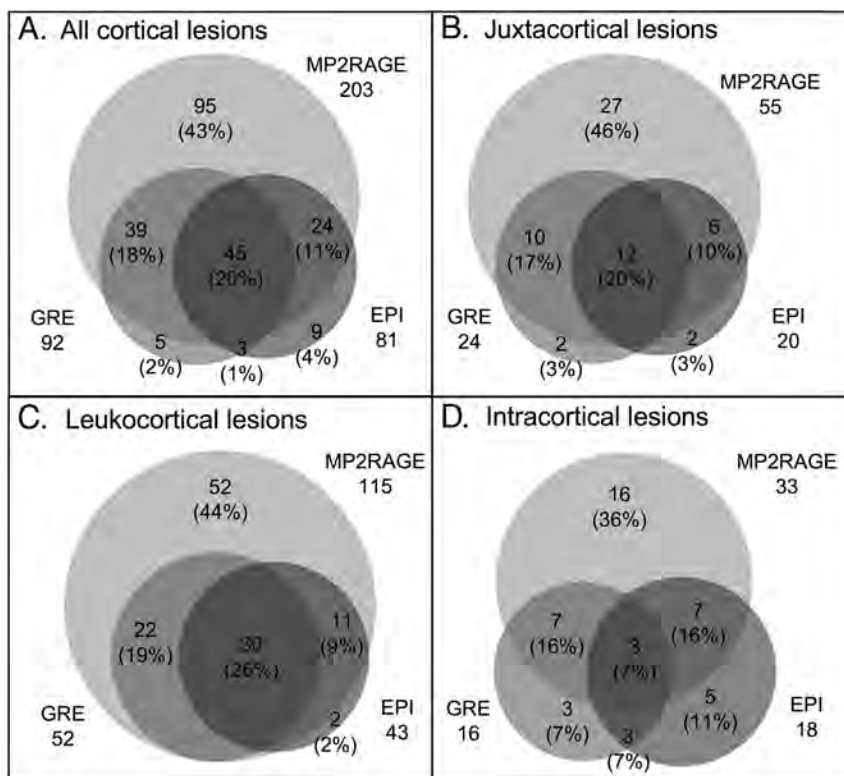


FIG 2. Increased cortical lesion detection with MP2RAGE. Venn diagrams show comparison of prospective lesion identification with MP2RAGE, T2*GRE, and T2*EPI for all cortical lesions and for each cortical lesion subtype.

Table 2. Comparison of lesion identification on MP2RAGE, T2*GRE, and T2*EPI images

	MP2RAGE			T2* GRE			T2* EPI			Significance		
	Per Patient			Per Patient			Per Patient			MP2RAGE vs GRE	MP2RAGE vs EPI	GRE vs EPI
	Total	Median	Range, IQR	Total	Median	Range, IQR	Total	Median	Range, IQR			
All	203	16	3–35, 15	92	8	0–21, 8	81	7	0–15, 5	***	***	NS
Juxtacortical	55	4	0–13, 4	24	2	0–18, 2	20	2	0–6, 4	*	*	NS
Leukocortical	115	11	1–21, 10	52	4	0–11, 4	43	4	0–8, 5	**	***	NS
Intracortical	33	2	0–8, 3	16	1	0–5, 2	18	1	0–6, 2	*	NS	NS

Note:—NS indicates not significant; asterisk, $P < .05$; double asterisks, $P < .01$; triple asterisks, $P < .001$.

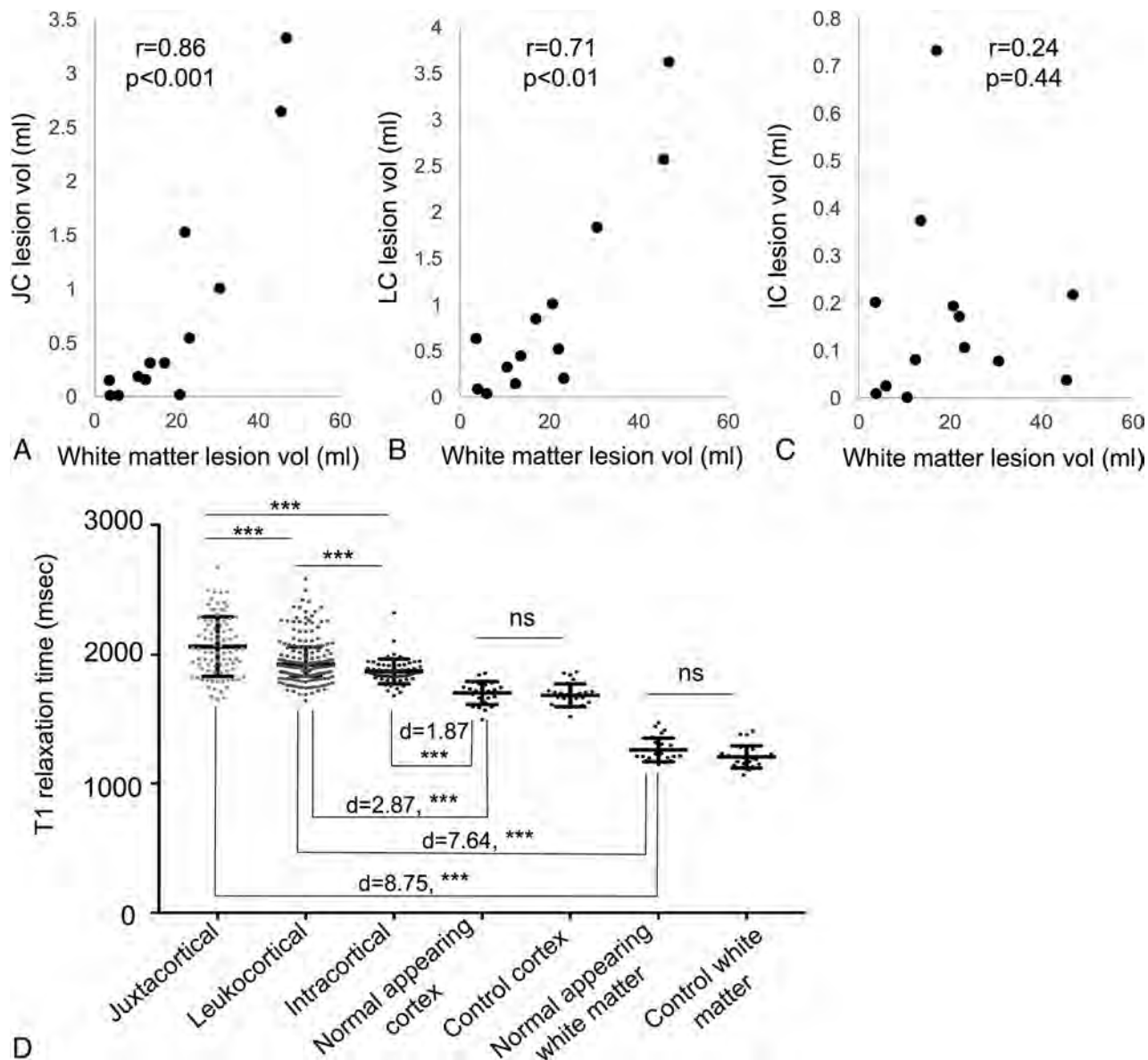


FIG 3. Cortical lesion volume and T1 relaxation times. A–C, Total white matter lesion volume correlates with total juxtacortical lesion volume and leukocortical lesion volume but not with intracortical lesion volume. D, T1 relaxation time is highest for juxtacortical lesions, followed by leukocortical and intracortical lesions. The T1 for all cortical lesion types exceeds that of normal-appearing and control tissues, though this difference is more dramatic for juxtacortical and leukocortical lesions compared with normal-appearing white matter versus leukocortical and intracortical lesions compared with normal-appearing gray matter. Normal-appearing tissue and control tissue did not differ in T1 value. *d* indicates effect size. Error bars represent SD. Three asterisks indicate, $P < .001$.

only a subtle signal change, which was compounded by the higher prevalence of motion artifacts on T2* images and the increased slice thickness on T2*GRE. In addition, likely due to their small size and sometimes subtle nature, many cortical lesions are missed when a single rater evaluates an image, a particular problem with T2*. Thus, going forward, multiple raters, each using MP2RAGE and T2* images, will likely allow the most sensitive and accurate detection of cortical lesions. A computational method for identifying potential cortical lesions on the basis of T1 values that differ from those of the surrounding cortex may also be useful in the future for more comprehensive lesion detection.

One limitation to the sequence comparison performed here is that the MP2RAGE images used were derived from averaging 4 acquisitions and had a longer total acquisition time than the T2*

sequences. Our goal was to identify as many cortical lesions as possible using sequences with optimal image quality; while this goal required averaging for MP2RAGE to achieve image quality similar to that of single acquisitions for the T2* sequences, we believe that the comparison of sequences performed here is valid.

In this study, we subcategorized cortical lesions as intracortical, leukocortical, and juxtacortical but did not further subclassify intracortical lesions; even at high resolution, it was often difficult to distinguish intracortical lesions elsewhere categorized as types II, III, and IV.³³ We also chose not to distinguish between leukocortical lesions that mostly affect the cortex versus those that mostly affect white matter because relative cortical and white matter involvement appears to be a continuum; however, it will be

interesting to study cortical lesion evolution longitudinally to distinguish lesions that originate in the cortex versus white matter. The T2*EPI sequence appeared to be as good as T2*GRE for the identification of cortical lesions, despite the larger voxel volume and substantially shorter imaging time. We therefore propose using T2*EPI as a second sequence for cortical lesion identification, to confirm lesions identified on MP2RAGE and assess their subpial involvement.

Previous work correlating different types and severity of MS with cortical lesion number has been, for the most part, performed at low field strength using double and phase-sensitive inversion recovery^{34–38}; it is likely that cortical lesions identified in those studies were heavily skewed toward juxtacortical and leukocortical lesions, underestimating the number of intracortical lesions.³⁹ With the increased sensitivity to small cortical lesions provided by MP2RAGE, we were able to more accurately determine the correlation between cortical and white matter lesions. We found that total juxtacortical and leukocortical but not intracortical lesion volume correlated with white matter lesion volume and that even this correlation may be driven by high-lesion-load cases, providing evidence that the pathophysiologic processes leading to cortical and white matter lesion formation and/or growth are distinct. Thus, it seems likely to us that following white matter lesion evolution may not yield a complete picture of the disease, and treatments that are effective in stopping new white matter lesions may not stop cortical lesion formation. We did not find any correlation between cortical lesion number or volume and clinical characteristics, but this may be due to the small sample size and our participant-selection method, which favored individuals with long-standing MS and known cortical lesions. Larger prospective studies using the methodology described here are therefore necessary.

MP2RAGE also provides T1 maps, which could further help quantitatively characterize lesions⁴⁰ and tease out pathologic differences among lesion types. We show that T1 differs across cortical lesion subtypes. Differences between the T1 of lesions and their corresponding control tissue are smallest for intracortical lesions; these small differences make them harder to detect. Changes in cortical lesion T1 may prove useful as a marker for tissue destruction and recovery.

Although our combination of MR imaging sequences at 7T improves detection of cortical lesions, one major limitation is the long acquisition time required (approximately 70 minutes for all 3 sequences), restricting the use of this approach to the research setting. However, it may be possible to decrease the number of MP2RAGE scan repetitions for clinical use, decreasing sensitivity but still likely representing an improvement over the current standard. Future advances in phased array coil designs and parallel imaging methods may also allow reduction in scan time without substantial loss in lesion identification. Another limitation of our study is that MP2RAGE and T2* sequences were sometimes acquired several months apart, and we cannot fully discount the possibility that differences in lesion identification were due to lesion formation or evolution between MRIs. However, in almost all cases, T2* images were acquired after MP2RAGE images, so the increased lesion identification on MP2RAGE cannot be attributed to new lesion formation between scans.

CONCLUSIONS

We demonstrate here that improved cortical lesion detection can be achieved in vivo by using a unique combination of MR imaging sequences at 7T. This advance may allow assessment of whether cortical lesions account for some of the clinical heterogeneity in MS that is not explained by white matter lesion load and could help better predict the course of disease and guide treatment.

ACKNOWLEDGMENTS

We thank Martina Absinta, Matthew Schindler, Souheil Inati, and the staff of the National Institutes of Health functional MRI Facility for help with MR imaging acquisitions. We also thank Joan Ohayon, Frances Andrada, and the staff of the National Institute of Neurological Disorders and Stroke Neuroimmunology Clinic for care of and collection of clinical data from the study participants. The National Cancer Institute Laboratory of Pathology and Seung Kwon Ha assisted in acquiring and processing the pathologic material. Gina Norato of the National Institute of Neurological Disorders and Stroke Clinical Trials Unit helped with statistical analyses.

Disclosures: Erin S. Beck—RELATED: Grant: National Multiple Sclerosis Society, Comments: I am the recipient of a Clinician Scientist Development Award from the National Multiple Sclerosis Society*. Tobias Kober—RELATED: Employment: Siemens, Switzerland. Daniel S. Reich—RELATED: Grant: National Multiple Sclerosis Society, Comments: Fellowship Grant to Erin S. Beck*; UNRELATED: Other: Vertex Pharmaceuticals, Myelin Repair Foundation, Comments: Funds for research were transferred to my institution as part of Cooperative Research and Development Agreements*. *Money paid to the institution.

REFERENCES

1. Brownell B, Hughes JT. **The distribution of plaques in the cerebrum in multiple sclerosis.** *J Neurol Neurosurg Psychiatry* 1962;25:315–20 CrossRef Medline
2. Bø L, Vedeler CA, Nyland HI, et al. **Subpial demyelination in the cerebral cortex of multiple sclerosis patients.** *J Neuropathol Exp Neurol* 2003;62:723–32 CrossRef Medline
3. Lucchinetti CF, Popescu BF, Bunyan RF, et al. **Inflammatory cortical demyelination in early multiple sclerosis.** *N Engl J Med* 2011;365:2188–97 CrossRef Medline
4. Calabrese M, Agosta F, Rinaldi F, et al. **Cortical lesions and atrophy associated with cognitive impairment in relapsing-remitting multiple sclerosis.** *Arch Neurol* 2009;66:1144–50 Medline
5. Calabrese M, Poretto V, Favaretto A, et al. **Cortical lesion load associates with progression of disability in multiple sclerosis.** *Brain* 2012;135:2952–61 CrossRef Medline
6. Harrison DM, Roy S, Oh J, et al. **Association of cortical lesion burden on 7-T magnetic resonance imaging with cognition and disability in multiple sclerosis.** *JAMA Neurol* 2015;72:1004–12 CrossRef Medline
7. Kutzelnigg A, Lucchinetti CF, Stadelmann C, et al. **Cortical demyelination and diffuse white matter injury in multiple sclerosis.** *Brain* 2005;128:2705–12 CrossRef Medline
8. Calabrese M, Romualdi C, Poretto V, et al. **The changing clinical course of multiple sclerosis: a matter of gray matter.** *Ann Neurol* 2013;74:76–83 CrossRef Medline
9. Magliozzi R, Howell O, Vora A, et al. **Meningeal B-cell follicles in secondary progressive multiple sclerosis associate with early onset of disease and severe cortical pathology.** *Brain* 2007;130:1089–104 Medline
10. Magliozzi R, Howell OW, Reeves C, et al. **A gradient of neuronal loss and meningeal inflammation in multiple sclerosis.** *Ann Neurol* 2010;68:477–93 CrossRef Medline
11. Howell OW, Reeves CA, Nicholas R, et al. **Meningeal inflammation**

- is widespread and linked to cortical pathology in multiple sclerosis. *Brain* 2011;134:2755–71 CrossRef Medline
12. Choi SR, Howell OW, Carassiti D, et al. **Meningeal inflammation plays a role in the pathology of primary progressive multiple sclerosis.** *Brain* 2012;135:2925–37 CrossRef Medline
 13. Absinta M, Vuolo L, Rao A, et al. **Gadolinium-based MRI characterization of leptomeningeal inflammation in multiple sclerosis.** *Neurology* 2015;85:18–28 CrossRef Medline
 14. Filippi M, Charil A, Rovaris M, et al. **Insights from magnetic resonance imaging.** *Handb Clin Neurol* 2014;122:115–49 CrossRef Medline
 15. Geurts JJ, Pouwels PJ, Uitdehaag BM, et al. **Intracortical lesions in multiple sclerosis: improved detection with 3D double inversion-recovery MR imaging.** *Radiology* 2005;236:254–60 CrossRef Medline
 16. Calabrese M, De Stefano N, Atzori M, et al. **Detection of cortical inflammatory lesions by double inversion recovery magnetic resonance imaging in patients with multiple sclerosis.** *Arch Neurol* 2007;64:1416–22 CrossRef Medline
 17. Nelson F, Poonawalla AH, Hou P, et al. **Improved identification of intracortical lesions in multiple sclerosis with phase-sensitive inversion recovery in combination with fast double inversion recovery MR imaging.** *AJNR Am J Neuroradiol* 2007;28:1645–49 CrossRef Medline
 18. Mainero C, Benner T, Radding A, et al. **In vivo imaging of cortical pathology in multiple sclerosis using ultra-high field MRI.** *Neurology* 2009;73:941–48 CrossRef Medline
 19. Nielsen AS, Kinkel RP, Tinelli E, et al. **Focal cortical lesion detection in multiple sclerosis: 3 Tesla DIR versus 7 Tesla FLASH-T2.** *J Magn Reson Imaging* 2012;35:537–42 CrossRef Medline
 20. Geurts JJ, Bö L, Pouwels PJ, et al. **Cortical lesions in multiple sclerosis: combined postmortem MR imaging and histopathology.** *AJNR Am J Neuroradiol* 2005;26:572–77 Medline
 21. Pitt D, Boster A, Pei W, et al. **Imaging cortical lesions in multiple sclerosis with ultra-high-field magnetic resonance imaging.** *Arch Neurol* 2010;67:812–18 CrossRef Medline
 22. Jonkman LE, Klaver R, Fleysher L, et al. **Ultra-high-field MRI visualization of cortical multiple sclerosis lesions with T2 and T2*: a postmortem MRI and histopathology study.** *AJNR Am J Neuroradiol* 2015;36:2062–67 CrossRef Medline
 23. Haast RA, Ivanov D, Formisano E, et al. **Reproducibility and reliability of quantitative and weighted T1 and T2* mapping for myelin-based cortical parcellation at 7 Tesla.** *Front Neuroanat* 2016;10:112 CrossRef Medline
 24. Geyer S, Weiss M, Reimann K, et al. **Microstructural parcellation of the human cerebral cortex: from Brodmann's post-mortem map to in vivo mapping with high-field magnetic resonance imaging.** *Front Hum Neurosci* 2011;5:19 CrossRef Medline
 25. Bock NA, Hashim E, Kocharyan A, et al. **Visualizing myeloarchitecture with magnetic resonance imaging in primates.** *Ann N Y Acad Sci* 2011;1225(suppl 1):E171–81 CrossRef Medline
 26. Marques JP, Kober T, Krueger G, et al. **MP2RAGE, a self bias-field corrected sequence for improved segmentation and T1-mapping at high field.** *Neuroimage* 2010;49:1271–81 CrossRef Medline
 27. O'Brien KR, Kober T, Hagmann P, et al. **Robust T1-weighted structural brain imaging and morphometry at 7T using MP2RAGE.** *PLoS One* 2014;9:e99676 CrossRef Medline
 28. Marques JP, Gruetter R. **New developments and applications of the MP2RAGE sequence: focusing the contrast and high spatial resolution R1 mapping.** *PLoS One* 2013;8:e69294 CrossRef Medline
 29. Sati P, Thomasson DM, Li N, et al. **Rapid, high-resolution, whole-brain, susceptibility-based MRI of multiple sclerosis.** *Mult Scler* 2014;20:1464–70 CrossRef Medline
 30. Sati P, Patil S, Inati S, et al. **Rapid MR susceptibility imaging of the brain using segmented 3D echo-planar imaging (3D EPI) and its clinical applications.** *Magnetom FLASH* 2017;68:26–32
 31. Fonov V, Evans AC, Botteron K, et al; Brain Development Cooperative Group. **Unbiased average age-appropriate atlases for pediatric studies.** *Neuroimage* 2011;54:313–27 CrossRef Medline
 32. Shiee N, Bazin PL, Ozturk A, et al. **A topology-preserving approach to the segmentation of brain images with multiple sclerosis lesions.** *Neuroimage* 2010;49:1524–35 CrossRef Medline
 33. Peterson JW, Bö L, Mörk S, et al. **Transected neurites, apoptotic neurons, and reduced inflammation in cortical multiple sclerosis lesions.** *Ann Neurol* 2001;50:389–400 CrossRef Medline
 34. Calabrese M, Filippi M, Rovaris M, et al. **Evidence for relative cortical sparing in benign multiple sclerosis: a longitudinal magnetic resonance imaging study.** *Mult Scler* 2009;15:36–41 Medline
 35. Diker S, Has AC, Kurne A, et al. **The association of cognitive impairment with gray matter atrophy and cortical lesion load in clinically isolated syndrome.** *Mult Scler Relat Disord* 2016;10:14–21 CrossRef Medline
 36. Absinta M, Rocca MA, Moiola L, et al. **Cortical lesions in children with multiple sclerosis.** *Neurology* 2011;76:910–13 CrossRef Medline
 37. Papadopoulou A, Müller-Lenke N, Naegelin Y, et al. **Contribution of cortical and white matter lesions to cognitive impairment in multiple sclerosis.** *Mult Scler* 2013;19:1290–96 CrossRef Medline
 38. Nelson F, Datta S, Garcia N, et al. **Intracortical lesions by 3T magnetic resonance imaging and correlation with cognitive impairment in multiple sclerosis.** *Mult Scler* 2011;17:1122–29 CrossRef Medline
 39. Seewann A, Kooi EJ, Roosendaal SD, et al. **Postmortem verification of MS cortical lesion detection with 3D DIR.** *Neurology* 2012;78:302–08 CrossRef Medline
 40. Kober T, Granziera C, Ribes D, et al. **MP2RAGE multiple sclerosis magnetic resonance imaging at 3 T.** *Invest Radiol* 2012;47:346–52 CrossRef Medline

Quantitative Susceptibility Mapping of the Thalamus: Relationships with Thalamic Volume, Total Gray Matter Volume, and T2 Lesion Burden

G.C. Chiang, J. Hu, E. Morris, Y. Wang, and S.A. Gauthier



ABSTRACT

BACKGROUND AND PURPOSE: Both thalamic iron deposition and atrophy have been reported in patients with multiple sclerosis compared with healthy controls, but how they are related is unclear. The purpose of this study was to understand the pathophysiologic basis for this iron deposition.

MATERIALS AND METHODS: Ninety-five patients with relapsing-remitting multiple sclerosis underwent 3T MR imaging with a standardized protocol that included quantitative susceptibility mapping to measure iron concentration and a 3D T1 echo-spoiled gradient-echo sequence to obtain thalamic volumes. Volumes of interest were manually delineated on the quantitative susceptibility map to encompass both thalami. Multivariate regression analyses were performed to identify the association between thalamic susceptibility and volume. Associations between thalamic susceptibility and total gray matter volume, cortical thickness, and T2 lesion volume were also assessed.

RESULTS: The relative susceptibility of the thalamus was associated with T2 lesion volume ($P = .015$) and was higher in the presence of enhancing lesions ($P = .013$). The relative susceptibility of the thalami was not associated with thalamic volumes, total gray matter volumes, or cortical thickness ($P > .05$).

CONCLUSIONS: Iron levels in the thalami are associated with T2 lesion burden and the presence of enhancing lesions, but not with thalamic or gray matter volumes, suggesting that iron accumulation is associated with white matter inflammation rather than gray matter neurodegeneration.

ABBREVIATION: QSM = quantitative susceptibility mapping

Thalamic atrophy has been reported to be an early finding in patients with multiple sclerosis¹⁻⁷ and may result from growth factor depletion after lesional transection of thalamo-cortical fibers⁸⁻¹⁰ or nonlesional microstructural degeneration.¹¹ Iron accumulation in the thalamus has also been widely

reported,^{1,3,4,12-18} but it is unclear how it relates to the observed thalamic degeneration.

One possibility is that iron may be an epiphenomenon of thalamic neurodegeneration,¹⁹ as has been described in several neurodegenerative disorders, including amyotrophic lateral sclerosis,²⁰ Alzheimer disease,²¹ and Parkinson disease.²¹ Alternatively, iron may accumulate as a result of inflammation along tracts that connect with the thalamus, with activated microglia along these tracts expressing high levels of ferritin²²⁻²⁵ and iron being released by degenerating oligodendrocytes and myelin fibers. As iron imaging becomes more recognized as a marker of disease in multiple sclerosis,²⁶ it will become increasingly important to understand the pathophysiologic basis for changes in iron relative to existing markers of atrophy and lesion burden.

The primary aim of our study was therefore to determine the relationship between iron levels in the thalami and thalamic atrophy, using quantitative susceptibility mapping (QSM), an MR imaging technique used to quantify tissue iron concentrations.²⁷ Second, we evaluated whether iron levels in the thalami are associated with T2 lesion burden and the presence of enhancing le-

Received July 24, 2017; accepted after revision November 15.

From the Departments of Radiology (G.C.C., J.H., Y.W.) and Neurology (E.M., S.A.G.), Weill Cornell Medical College, New York-Presbyterian Hospital, New York, New York.

This work was supported, in part, by the National Institutes of Health National Center for Advancing Translational Sciences/Clinical and Translational Science Center grant (UL1 TR000457-06), the National Institutes of Health/National Institute of Neurological Disorders and Stroke grant (R01NS090464), and the Weill Cornell Medicine-Qatar Medical Student Research Award.

Paper previously presented, in part, at: Annual Meeting of the American Society of Neuroradiology, May 21-26, 2016; Washington, DC.

Please address correspondence to Gloria C. Chiang, MD, Department of Radiology, Division of Neuroradiology, Weill Cornell Medical College, New York-Presbyterian Hospital, 525 East 68th St, Starr Pavilion, Box 141, New York, NY 10065; e-mail: gcc9004@med.cornell.edu

Indicates open access to non-subscribers at www.ajnr.org

<http://dx.doi.org/10.3174/ajnr.A5537>

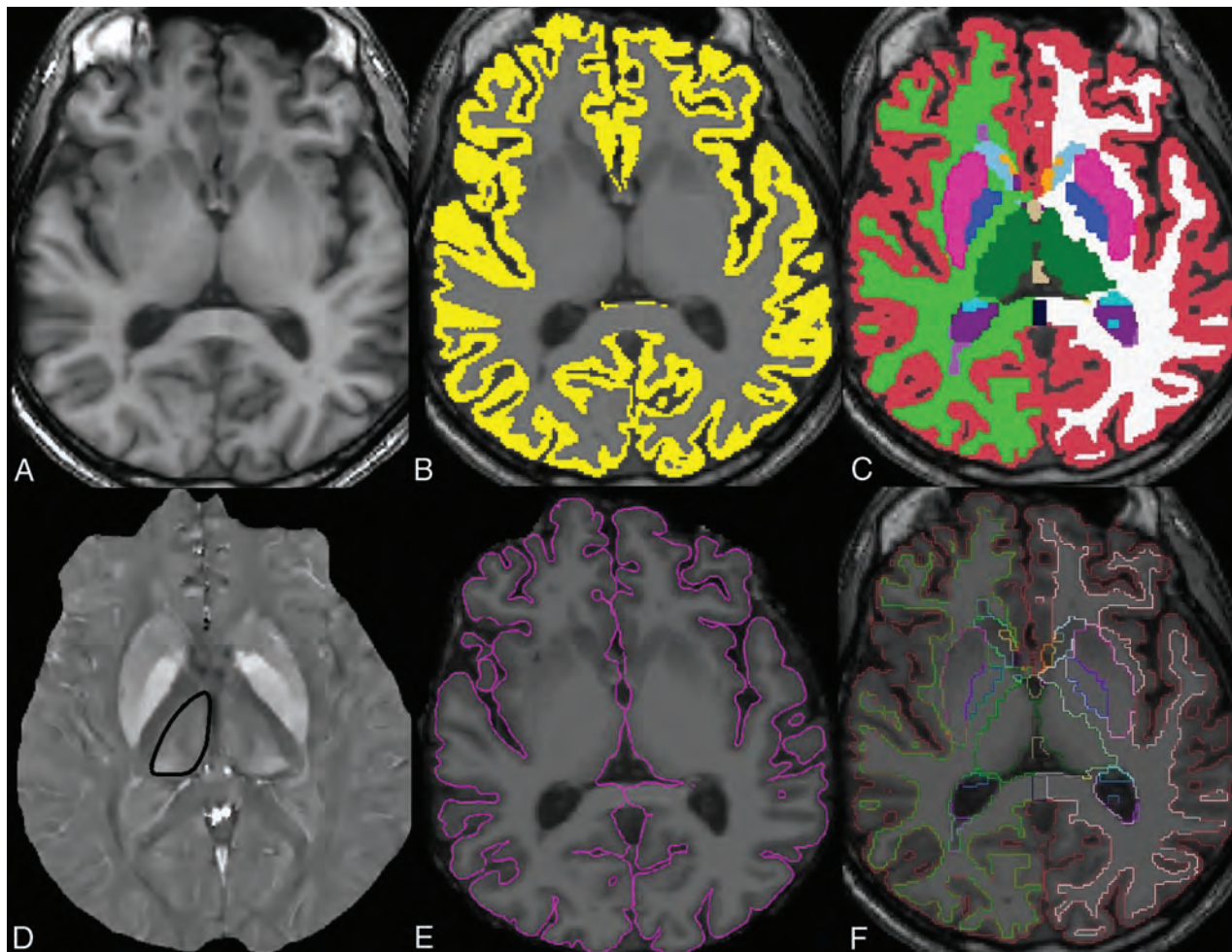


FIG 1. Axial images through the thalami from the 3D T1 MPRAGE sequence (A), with an overlaid gray matter mask (B) and volumetric segmentation (C) from FreeSurfer. Thalamic volumes of interest are shown in green. The quantitative susceptibility map image from the same axial level (D) shows the contoured right thalamus (*black outline*). The pial boundary (E) is used for cortical thickness estimation, and the segmentation outline (F) is overlaid on the axial T1-weighted image.

sions, reflective of white matter inflammation. Finally, we evaluated whether iron levels in the thalami are associated with markers of global gray matter neurodegeneration, including total gray matter volume and cortical thickness.

MATERIALS AND METHODS

Subjects

One hundred patients with relapsing-remitting multiple sclerosis from an ongoing, prospective cohort of patients, followed at our Multiple Sclerosis Center from August 2013 through March 2015, were initially included in this retrospective analysis. For homogeneity of the cohort, patients with primary-progressive multiple sclerosis were not included. Five patients were excluded due to poor imaging quality of the QSM or the T1-weighted anatomic sequence, leaving 95 patients in our final analysis. All subjects gave written informed consent for participation in this study, which was approved by our institutional review board. Patient age, sex, use of disease-modifying therapies at the time of the MR imaging, and disease duration since the first clinical symptom were obtained from the medical record.

MR Imaging Data Acquisition and Analysis

All patients underwent our standardized multiple sclerosis research protocol on a 3T scanner (Signa HDxt; GE Healthcare, Milwaukee, Wisconsin) with an 8-channel phased array head coil. The imaging protocol included the following: 1) a 3D T2*-weighted spoiled multiecho gradient recalled-echo sequence (TR/TE = 57/4.3 ms, flip angle = 20°, 416 × 320 matrix, 0.5 × 0.5 × 2 mm³ resolution); 2) a T2-weighted fast spin-echo sequence (TR/TE = 5250/86 ms, flip angle = 90°, 3-mm sections, 416 × 256 matrix); 3) a 3D T2 FLAIR sequence (TR/TE = 6050/140 ms, 0.6 × 0.6 × 1.2 mm³ resolution); and 4) a pre- and postgadolinium 3D inversion recovery-prepared T1-weighted fast echo-spoiled gradient-echo sequence (TR/TE = 8.8/3.4 ms, flip angle = 15°, 256 × 256 matrix, 0.45 × 0.45 × 1.2 mm³ resolution). QSM was reconstructed from the gradient recalled-echo sequence using the morphology-enabled dipole inversion method.²⁸

The volumetric 3D T1-weighted images were aligned, skull-stripped, and segmented by using FreeSurfer software, Version 5.1 (<http://surfer.nmr.mgh.harvard.edu>) to obtain thalamic volumes (Fig 1).²⁹ The left and right thalamic volumes were summed to obtain the total thalamic volume in cubic millimeters. Free-

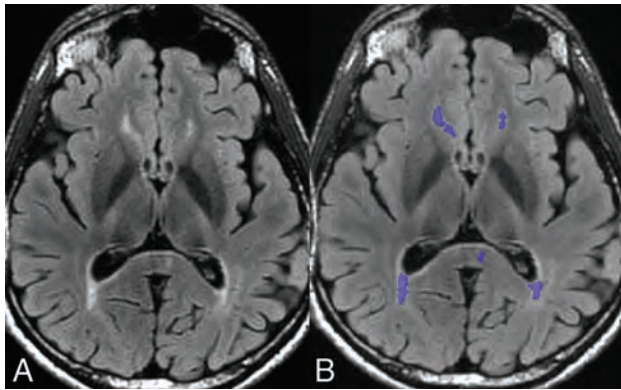


FIG 2. Axial image from the 3D T2 FLAIR sequence (A) with overlaid volumetric segmentation of T2 lesions (purple) (B) from Olea software processing in the same patient as in Fig 1.

Surfer was also used to obtain total gray matter volume and cortical thickness. 3D T1-weighted images were first segmented into gray matter masks, which were visually checked and manually edited for misclassification. The cortical thickness measurement was then calculated as the shortest distance between each point on the pial surface and the gray/white surface, measured in millimeters. All FreeSurfer analyses were performed by a trained senior research aide with 3 years of experience (E.M.) and visually checked for anatomic accuracy by both the aide and a board-certified neurologist (S.A.G.).

The volume of T2-hyperintense white matter lesion load was calculated using FDA-approved software (Olea Sphere 2.3; Olea Medical, La Ciotat, France) (Fig 2). Briefly, 3D volumes of the white matter lesions were created by selecting a seed voxel at the center of the lesions and expanding the volumes of interest to include surrounding voxels of similar signal intensities across all slices. Manual editing was then performed to include or exclude voxels as necessary on the basis of visual inspection.

Iron concentrations of the thalami were determined by using syngo.via software (Siemens, Erlangen, Germany). First, QSM maps were fused to the 3D T2 FLAIR images for improved anatomic delineation. Then, with the Volume-of-Interest tool, the upper and lower borders of the thalami were manually delineated by a board-certified radiologist with subspecialty certification in neuroradiology (G.C.C.) (Fig 1). The Contour tool then identified the appropriate margins for the thalami on the intervening slices in semiautomated fashion, and the Nudge tool was used to exclude major veins that could confound the QSM values, particularly the internal cerebral veins and basal veins of Rosenthal. As a zero reference, a small circular ROI was also placed in the CSF in the atrium of each lateral ventricle, adjacent to the thalamus. The relative susceptibility within the thalami was calculated by subtracting the mean susceptibility in the thalami from that in the CSF ROI.

Statistical Analysis

All statistical analyses were performed in STATA, Version 13 (StataCorp, College Station, Texas). A sample size of 95 was determined to have 80% power to detect a correlation coefficient of 0.28 between variables with a 2-sided α of .05.³⁰

Multivariate regression analyses were used to determine

whether the relative susceptibility of the thalami was associated with thalamic atrophy, T2 white matter lesion volumes, the presence of enhancing lesions, total gray matter volume, and cortical thickness. Ladder-of-powers quantile-normal plots were assessed to determine the normality of the outcome variables. White matter lesion volume was log-transformed for normalization. Age, sex, disease duration, and use of disease-modifying therapies were included as covariates.

To exclude the potential confounder of age-related T2 white matter lesions on lesion volume, we also repeated the analysis excluding all patients older than 50 years of age.

RESULTS

The mean age of the patients included in this study was 42 ± 10 years, with a range of 25–71 years. Two-thirds of the cohort was female, and one-third, male, reflecting the higher disease prevalence in women. The mean Expanded Disability Status Scale score was 2.2 ± 2.2 , with a range of 0–8.5. Fifty-seven of the 95 patients were on disease-modifying agents. Nine had enhancing lesions at the time of the scan. The mean duration of disease since the patient's first reported symptom was 8.9 ± 7.8 years, with a range of 0.3–33.7 years. The mean volume of white matter lesions was 11.0 ± 15.8 mL, with a range of 0.1–122.4 mL. The mean total thalamic volume was 14.0 ± 2.1 mL, with a range of 8.4–20.0 mL. The mean relative susceptibility of the thalami was -29.0 ± 11.7 parts per billion, with a range of -61.5 to 6.4 parts per billion. The mean total gray matter volume was 607 ± 67 mL, with a range of 411–784 mL. The mean cortical thickness was 2.40 ± 0.16 mm, with a range of 1.92–2.68 mm.

The results of the regression analyses are shown in Tables 1 and 2. The relative susceptibility of the thalami was associated with T2 lesion volume both before ($P = .037$) and after adjusting for covariates ($P = .015$), with higher thalamic susceptibility associated with a greater T2 lesion burden. Repeating the analysis with patients younger than 50 years of age did not change the results ($P = .036$), suggesting that age-related white matter lesions were not a significant confounder. Longer disease duration was also associated with greater T2 lesion burden ($P < .001$), whereas age ($P = .25$), sex ($P = .90$), and use of disease-modifying agents ($P = .81$) were not.

The presence of enhancing lesions was also associated with higher iron levels before ($P = .04$) and after ($P = .013$) adjustment for covariates. Older age was associated with higher iron levels only after adjustment ($P = .028$).

The relative susceptibility of the thalami was not associated with thalamic volumes, total gray matter volume, or cortical thickness ($P = .63$, 0.16, and 0.94, respectively).

DISCUSSION

Both thalamic atrophy³⁻⁷ and iron deposition^{1,3,4,12-18} have been reported in patients with multiple sclerosis, but whether these 2 processes are interrelated is unclear. Using QSM to quantify tissue susceptibility, which correlates with iron concentrations in post-mortem specimens^{27,31,32} and is less sensitive to local changes in water content than $R2^*$,³³⁻³⁶ we found no association between thalamic susceptibility and volume. On the other hand, we found

Table 1: Results of the regression analyses evaluating associations between thalamic susceptibility and thalamic volume, total gray matter volume, cortical thickness, and T2 lesion volume

	Before Adjustment for Covariates			After Adjustment for Covariates		
	Coefficient	95% CI	P Value	Coefficient	95% CI	P Value
Thalamic volume	9.0	−28.0–46.1	.63	9.4	−28.9–47.7	.63
Total gray matter volume	−860	−2026–305	.15	−720	−1731–291	.16
Cortical thickness	−0.0007	−0.003–0.002	.62	−0.00008	−0.003–0.002	.95
White matter T2 lesion volumes	0.026	0.0016–0.051	.037 ^a	0.029	0.0057–0.053	.015 ^a

^a $P < .05$.

Table 2: Results of the regression analyses evaluating whether thalamic susceptibility is associated with baseline characteristics

	Before Adjustment for Covariates			After Adjustment for Covariates		
	Coefficient	95% CI	P Value	Coefficient	95% CI	P Value
Presence of enhancing lesions	8.40	0.41–16.40	.04 ^a	10.68	2.28–19.09	.013 ^a
Age	0.19	−0.037–0.42	.099	0.27	0.031–0.52	.02 ^a
Sex	0.75	−4.36–5.85	.77	1.45	−3.69–6.58	.58
Use of disease-modifying therapies	−0.57	−5.46–4.32	.82	0.44	−4.43–5.32	.86
Disease duration	−0.023	−0.33–0.28	.88	−0.066	−0.39–0.26	.69

^a $P < .05$.

that thalamic susceptibility was associated with overall T2 lesion burden and the presence of enhancing lesions.

Several prior studies have described increased thalamic iron levels among patients with multiple sclerosis or clinically isolated syndrome compared with healthy controls.^{3,4,13,14,17,18} One explanation for this increased iron could be that iron accumulates because of thalamic neurodegeneration. Studies have shown that as neurodegeneration occurs, activated microglia and tissue macrophages that arrive to clear out the iron-rich cellular debris express high levels of ferritin,^{23–25} perpetuating ongoing oxidative stress, neurodegeneration, and iron accumulation.^{37–39} A post-mortem study of patients with amyotrophic lateral sclerosis confirmed this link between neurodegeneration and iron accumulation, with the susceptibility detected on MR imaging corresponding to iron-rich microglia in the motor cortex.²⁰ Another study described iron accumulation as an epiphenomenon of neuronal damage because iron levels in the basal ganglia of patients with multiple sclerosis were closely associated with the degree of gray matter atrophy and were not elevated early in the disease course in patients with clinically isolated syndrome.¹⁹

However, in our cohort, we found no association between iron levels in the thalamic nuclei and thalamic atrophy, suggesting that these may be disparate processes. Our finding is consistent with a prior longitudinal study that reported that short-term changes in iron levels in the deep gray matter of patients with multiple sclerosis appear to occur independent of changes in volume.¹ We further found no association between thalamic iron levels and markers of gray matter neurodegeneration, including total gray matter volume and cortical thickness, suggesting that iron accumulation and gray matter neurodegeneration are likely independent processes.

On the other hand, we found that thalamic iron levels were associated with markers of white matter inflammation, including overall T2 lesion burden and the presence of enhancing lesions. Several prior studies have shown that proinflammatory cytokines seen in patients with multiple sclerosis, such as tumor necrosis factor α , interleukin-1, and interferon γ , lead to increases in ferritin^{40–42} and iron accumulation in the deep gray matter.^{42,43} Demyelinating lesions disrupting tracts that connect with the thalamus

may also result in inflammation, microglial activation, and iron accumulation in the thalamus. Studies in animal models have shown that a chemical injection in the region of the striatum results in iron accumulation, not just locally, but also in distant interconnected regions.^{44,45} In patients, activated microglia expressing ferritin have also been detected along tracts affected by acute subcortical ischemia as an indicator of poststroke inflammation.⁴⁶ We hypothesize that white matter lesions and inflammation taken together lead to axonal transection and white matter degeneration in tracts that connect to the thalamus, resulting in thalamic iron accumulation. Although age-related iron accumulation was also noted in our cohort, as has been described in the literature,⁴⁷ adjusting for age did not weaken the association between the presence of enhancing lesions and thalamic iron accumulation.

This study has several limitations. First, we used manual segmentation of the thalamus, which limits reproducibility and use in larger cohorts but better avoids venous contamination of QSM parameters. Second, we did not acquire diffusion tensor imaging data to determine the burden of lesions along specific thalamocortical tracts, which may contribute to iron accumulation. Third, we did not include patients with primary-progressive multiple sclerosis; iron in these patients may accumulate via a different pathophysiologic mechanism. Finally, further confirmation of these findings in larger cohorts is necessary.

CONCLUSIONS

Using QSM, we found that iron concentrations in the thalamus are associated with T2 lesion burden and the presence of enhancing lesions, both imaging markers of white matter inflammation. Iron concentrations were not found to be associated with local thalamic or global gray matter neurodegeneration.

Disclosures: James Hu—RELATED: Support for Travel to Meetings for the Study or Other Purposes: Weill Cornell, Comments: research award. Yi Wang—RELATED: Grant: National Institutes of Health, Comments: R01NS090464*; UNRELATED: Grant: National Institutes of Health, Comments: R01NS095562, S10OD021782*; Patents (Planned, Pending or Issued): QSM patents*; Stock/Stock Options: Medimagetric, Comments: Medimagetric is working with Cornell on commercialization of QSM technology. Susan A. Gauthier—UNRELATED: Grants/Grants Pending: Novartis, Genzyme, Mallinckrodt.* *Money paid to the institution.

REFERENCES

- Khalil M, Langkammer C, Pichler A, et al. **Dynamics of brain iron levels in multiple sclerosis: a longitudinal 3T MRI study.** *Neurology* 2015;84:2396–402 CrossRef Medline
- Cifelli A, Arridge M, Jezzard P, et al. **Thalamic neurodegeneration in multiple sclerosis.** *Ann Neurol* 2002;52:650–53 CrossRef Medline
- Hagemer J, Yeh EA, Brown MH, et al. **Iron content of the pulvinar nucleus of the thalamus is increased in adolescent multiple sclerosis.** *Mult Scler* 2013;19:567–76 CrossRef Medline
- Zivadinov R, Heininen-Brown M, Schirda CV, et al. **Abnormal subcortical deep-gray matter susceptibility-weighted imaging filtered phase measurements in patients with multiple sclerosis: a case-control study.** *Neuroimage* 2012;59:331–39 CrossRef Medline
- Bergsland N, Zivadinov R, Dwyer MG, et al. **Localized atrophy of the thalamus and slowed cognitive processing speed in MS patients.** *Mult Scler* 2016;22:1327–36 CrossRef Medline
- Schoonheim MM, Hulst HE, Brandt RB, et al. **Thalamus structure and function determine severity of cognitive impairment in multiple sclerosis.** *Neurology* 2015;84:776–83 CrossRef Medline
- Ramasamy DP, Benedict RH, Cox JL, et al. **Extent of cerebellum, subcortical and cortical atrophy in patients with MS: a case-control study.** *J Neurol Sci* 2009;282:47–54 CrossRef Medline
- Mosca TJ, Hong W, Dani VS, et al. **Trans-synaptic Teneurin signaling in neuromuscular synapse or organization and target choice.** *Nature* 2012;484:237–41 CrossRef Medline
- Nikoltopoulou V, Lickert H, Frade JM, et al. **Neurotrophin receptors TrkA and TrkC cause neuronal death whereas TrkB does not.** *Nature* 2010;467:59–63 CrossRef Medline
- Rocca MA, Mesaros S, Pagani E, et al. **Thalamic damage and long-term progression of disability in multiple sclerosis.** *Radiology* 2010;257:463–69 CrossRef Medline
- Deppe M, Krämer J, Tenberge JG, et al. **Early silent microstructural degeneration and atrophy of the thalamocortical network in multiple sclerosis.** *Hum Brain Mapp* 2016;37:1866–79 CrossRef Medline
- Modica CM, Zivadinov R, Dwyer MG, et al. **Iron and volume in the deep gray matter: association with cognitive impairment in multiple sclerosis.** *AJNR Am J Neuroradiol* 2015;36:57–62 CrossRef Medline
- Al-Radaideh AM, Wharton SJ, Lim SY, et al. **Increased iron accumulation occurs in the earliest stages of demyelinating disease: an ultra-high field susceptibility mapping study in clinically isolated syndrome.** *Mult Scler* 2013;19:896–903 CrossRef Medline
- Hagemer J, Weinstock-Guttman B, Bergsland N, et al. **Iron deposition on SWI-filtered phase in the subcortical deep gray matter of patients with clinically isolated syndrome may precede structure-specific atrophy.** *AJNR Am J Neuroradiol* 2012;33:1596–601 CrossRef Medline
- Cobzas D, Sun H, Walsh AJ, et al. **Subcortical gray matter segmentation and voxel-based analysis using transverse relaxation and quantitative susceptibility mapping with application to multiple sclerosis.** *J Magn Reson Imaging* 2015;42:1601–10 CrossRef Medline
- Ge Y, Jensen JH, Lu H, et al. **Quantitative assessment of iron accumulation in the deep gray matter of multiple sclerosis by magnetic field correlation imaging.** *AJNR Am J Neuroradiol* 2007;28:1639–44 CrossRef Medline
- Lebel RM, Eissa A, Seres P, et al. **Quantitative high-field imaging of sub-cortical gray matter in multiple sclerosis.** *Mult Scler* 2012;18:433–41 CrossRef Medline
- Quinn MP, Gati JS, Klassen ML, et al. **Increased deep gray matter iron is present in clinically isolated syndromes.** *Mult Scler Relat Disord* 2014;3:194–202 CrossRef Medline
- Khalil M, Langkammer C, Ropele S, et al. **Determinants of brain iron in multiple sclerosis: a quantitative 3T MRI study.** *Neurology* 2011;77:1691–97 CrossRef Medline
- Kwan JY, Jeong SY, Van Gelderen P, et al. **Iron accumulation in deep cortical layers account for MRI signal abnormalities in ALS: correlating 7 Tesla MRI and pathology.** *PLoS One* 2012;7:e35241 CrossRef Medline
- Zecca L, Youdim MB, Riederer P, et al. **Iron, brain ageing and neurodegenerative disorders.** *Nat Rev Neurosci* 2004;5:863–73 CrossRef Medline
- Haider L, Simeonidou C, Steinberger G, et al. **Multiple sclerosis deep grey matter: the relation between demyelination, neurodegeneration, inflammation and iron.** *J Neurol Neurosurg Psychiatry* 2014;85:1386–95 CrossRef Medline
- Garden GA, Möller T. **Microglia biology in health and disease.** *J Neuroimmune Pharmacol* 2006;1:127–37 CrossRef Medline
- Cheepsunthorn P, Radov L, Menzies S, et al. **Characterization of a novel brain-derived microglial cell line isolated from neonatal rat brain.** *Glia* 2001;35:53–62 CrossRef Medline
- Andersen HH, Johnsen KB, Moos T. **Iron deposits in the chronically inflamed central nervous system and contributes to neurodegeneration.** *Cell Mol Life Sci* 2014;71:1607–22 CrossRef Medline
- Walsh AJ, Blevins G, Lebel RM, et al. **Longitudinal MR imaging of iron in multiple sclerosis: an imaging marker of disease.** *Radiology* 2014;270:186–96 CrossRef Medline
- Langkammer C, Schweser F, Krebs N, et al. **Quantitative susceptibility mapping (QSM) as a means to measure brain iron? A post mortem validation study.** *Neuroimage* 2012;62:1593–99 CrossRef Medline
- Liu J, Liu T, de Rochefort L, et al. **Morphology enabled dipole inversion for quantitative susceptibility mapping using structural consistency between the magnitude image and the susceptibility map.** *Neuroimage* 2012;59:2560–68 CrossRef Medline
- Fischl B, Salat DH, Busa E, et al. **Whole brain segmentation: automated labeling of neuroanatomical structures in the human brain.** *Neuron* 2002;33:341–55 CrossRef Medline
- Mukaka MM. **Statistics corner: a guide to appropriate use of correlation coefficient in medical research.** *Malawi Med J* 2012;24:69–71 Medline
- Wisnieff C, Ramanan S, Olesik J, et al. **Quantitative susceptibility mapping (QSM) of white matter multiple sclerosis lesions: interpreting positive susceptibility and the presence of iron.** *Magn Reson Med* 2015;74:564–70 CrossRef Medline
- Sun H, Walsh AJ, Lebel RM, et al. **Validation of quantitative susceptibility mapping with Perls' iron staining for subcortical gray matter.** *Neuroimage* 2015;105:486–92 CrossRef Medline
- Schmalbrock P, Prakash RS, Schirda B, et al. **Basal ganglia iron in patients with multiple sclerosis measured with 7T quantitative susceptibility mapping correlates with inhibitory control.** *AJNR Am J Neuroradiol* 2016;37:439–46 CrossRef Medline
- Wang Y, Liu T. **Quantitative susceptibility mapping (QSM): decoding MRI data for a tissue magnetic biomarker.** *Magn Reson Med* 2015;73:82–101 CrossRef Medline
- Schweser F, Deistung A, Lehr BW, et al. **Differentiation between diamagnetic and paramagnetic cerebral lesions based on magnetic susceptibility mapping.** *Med Phys* 2010;37:5165–78 CrossRef Medline
- Haacke EM, Miao Y, Liu M, et al. **Correlation of putative iron content as represented by changes in R2* and phase with age in deep gray matter of healthy adults.** *J Magn Reson Imaging* 2010;32:561–76 CrossRef Medline
- Barbeito AG, Garringer HJ, Baraibar MA, et al. **Abnormal iron metabolism and oxidative stress in mice expressing a mutant form of the ferritin light polypeptide gene.** *J Neurochem* 2009;109:1067–78 CrossRef Medline
- Deng X, Vidal R, Englander EW. **Accumulation of oxidative DNA damage in brain mitochondria in mouse model of hereditary ferritinopathy.** *Neurosci Lett* 2010;479:44–48 CrossRef Medline
- Pelizzoni I, Macco R, Morini MF, et al. **Iron handling in hippocampal neurons: activity-dependent iron entry and mitochondria-mediated neurotoxicity.** *Aging Cell* 2011;10:172–83 CrossRef Medline
- Rogers JT, Bridges KR, Durmowicz GP, et al. **Translational control during the acute phase response: ferritin synthesis in response to interleukin-1.** *J Biol Chem* 1990;265:14572–78 Medline

41. Tsuji Y, Miller LL, Miller SC, et al. **Tumor necrosis factor-alpha and interleukin 1-alpha regulate transferrin receptor in human diploid fibroblasts. Relationship to the induction of ferritin heavy chain.** *J Biol Chem* 1991;266:7257–61 Medline
42. Smirnov IM, Bailey K, Flowers CH, et al. **Effects of TNF-alpha and IL-1beta on iron metabolism by A549 cells and influence on cytotoxicity.** *Am J Physiol* 1999;277:L257–63 Medline
43. Williams R, Rohr AM, Wang WT, et al. **Iron deposition is independent of cellular inflammation in a cerebral model of multiple sclerosis.** *BMC Neurosci* 2011;12:59 CrossRef Medline
44. Shoham S, Werman E, Ebstein RP. **Iron accumulation in the rat basal ganglia after excitatory amino acid injections: dissociation from neuronal loss.** *Exp Neurol* 1992;118:227–41 CrossRef Medline
45. Sastry S, Arendash GW. **Time-dependent changes in iron levels and associated neuronal loss within the substantia nigra following lesions within the neostriatum/globus pallidus complex.** *Neuroscience* 1995;67:649–66 CrossRef Medline
46. Radlinska BA, Ghinani SA, Lyon P, et al. **Multimodal microglia imaging of fiber tracts in acute subcortical stroke.** *Ann Neurol* 2009;66:825–32 CrossRef Medline
47. Aquino D, Bizzi A, Grisoli M, et al. **Age-related iron deposition in the basal ganglia: quantitative analysis in healthy subjects.** *Radiology* 2009;252:165–72 CrossRef Medline

Optimization of DARTEL Settings for the Detection of Alzheimer Disease

J. Komatsu, I. Matsunari, M. Samuraki, K. Shima, M. Noguchi-Shinohara, K. Sakai, T. Hamaguchi, K. Ono, H. Matsuda, and M. Yamada



ABSTRACT

BACKGROUND AND PURPOSE: Although Diffeomorphic Anatomical Registration Through Exponentiated Lie Algebra (DARTEL) has been introduced as an alternative to conventional voxel-based morphometry, there are scant data available regarding the optimal image-processing settings. The aim of this study was to optimize image-processing and ROI settings for the diagnosis of Alzheimer disease using DARTEL.

MATERIALS AND METHODS: Between May 2002 and August 2014, we selected 158 patients with Alzheimer disease and 198 age-matched healthy subjects; 158 healthy subjects served as the control group against the patients with Alzheimer disease, and the remaining 40 served as the healthy data base. Structural MR images were obtained in all the participants and were processed using DARTEL-based voxel-based morphometry with a variety of settings. These included modulated or nonmodulated, nonsmoothed or smoothed settings with a 4-, 8-, 12-, 16-, or 20-mm kernel size. A z score was calculated for each ROI, and univariate and multivariate logistic regression analyses were performed to determine the optimal ROI settings for each dataset. The optimal settings were defined as those demonstrating the highest χ^2 test statistics in the multivariate logistic regression analyses. Finally, using the optimal settings, we obtained receiver operating characteristic curves. The models were verified using 10-fold cross-validation.

RESULTS: The optimal settings were obtained using the hippocampus and precuneus as ROIs without modulation and smoothing. The average area under the curve was 0.845 (95% confidence interval, 0.788–0.902).

CONCLUSIONS: We recommend using the precuneus and hippocampus as ROIs without modulation and smoothing for DARTEL-based voxel-based morphometry as a tool for diagnosing Alzheimer disease.

ABBREVIATIONS: AD = Alzheimer disease; AUC = area under the curve; CDR = Clinical Dementia Rating; DARTEL = Diffeomorphic Anatomical Registration Through Exponentiated Lie Algebra; HS = healthy subjects; MMSE = Mini-Mental State Examination; ROC = receiver operating characteristic; VBM = voxel-based morphometry

Statistical neuroimaging analysis techniques such as voxel-based morphometry (VBM) have been widely used to evaluate structural MR imaging data, but in recent years, such methods have been suggested as a diagnostic aid for the early detection of

Alzheimer disease (AD).^{1,2} However, conventional VBM has often been criticized due to its imperfect registration of individual images of the standard brain.³ Diffeomorphic Anatomical Registration Through Exponentiated Lie Algebra (DARTEL) has been introduced as an alternative method to conventional VBM due to novel abilities allowing precise segmentation and normalization of images.⁴ Some studies have reported that DARTEL-based VBM provides a greater diagnostic accuracy for the detection of AD than conventional VBM methods.⁵ Modulation, which involves the scaling of images depending on the extent of expansion or contraction, is considered an important processing step for

Received September 4, 2016; accepted after revision October 30, 2017.

From the Department of Neurology and Neurobiology of Aging (J.K., M.S., K. Shima, M.N.-S., K. Sakai, T.H., K.O., M.Y.), Kanazawa University Graduate School of Medical Sciences, Takara-machi, Ishikawa, Japan; Department of Clinical Research (I.M.), Medical and Pharmacological Research Center Foundation, Hakui, Ishikawa, Japan; Division of Nuclear Medicine (I.M.), Department of Radiology, Saitama Medical University Hospital, Iruma-gun, Saitama, Japan; Department of Neurology (K.O.), Showa University School of Medicine, Tokyo, Japan; and Integrative Brain Imaging Center (H.M.), National Center of Neurology and Psychiatry, Kodaira, Tokyo, Japan.

This work was supported, in part, by a grant for Development of Advanced Technology for Measurement and Evaluation of Brain Functions, Ishikawa Prefecture Collaboration of Regional Entities for the Advancement of Technological Excellence (to M.Y.), from the Japan Science and Technology Corporation, Japan, and by a grant for the Knowledge Cluster Initiative (High-Tech Sensing and Knowledge Handling Technology [Brain Technology]) (to M.Y.) from the Japanese Ministry of Education, Culture, Sports, Science and Technology, Japan, and by the Ishikawa Prefectural Government (to I.M.).

Please address correspondence to Ichiro Matsunari, MD, PhD, Division of Nuclear Medicine, Department of Radiology, Saitama Medical University Hospital, 38 Morohongo, Moroyama, Iruma-gun, Saitama 350-0495, Japan; e-mail: m_ichiro@saitama-med.ac.jp

Indicates open access to non-subscribers at www.ajnr.org

Indicates article with supplemental on-line tables.

<http://dx.doi.org/10.3174/ajnr.A5509>

DARTEL-based VBM. The smoothing before statistical image analysis is also an important factor that can affect VBM results. However, there are scant data available regarding the optimal image-processing settings for DARTEL-based VBM.

Shima et al⁶ previously demonstrated that a subset of patients with AD demonstrate atrophy in neocortical areas such as the posterior cingulate gyri and parietal lobe rather than in traditional areas such as the hippocampus, which is particularly true in early-onset AD. Therefore, it would be conceivable to hypothesize that optimal ROI settings for the detection of AD might vary according to age.

The purpose of this study was to optimize image-processing and ROI settings for the discrimination of patients with AD from age-matched healthy subjects using DARTEL-based VBM.

MATERIALS AND METHODS

Subjects

This prospective study was performed as a part of the Ishikawa Brain Imaging Study, which included any research to seek and develop imaging biomarkers for early and objective assessment of AD and other forms of neurodegenerative diseases using PET and MR imaging.^{7,8} The study protocol was approved by the Medical and Pharmacological Research Center Foundation ethics committee, and written informed consent was obtained from all subjects before participation in the study. Of the 594 consecutive patients who were examined by neurologists and who underwent MR imaging (3D-T1-weighted, T2-weighted, MR angiography) at our memory clinic between May 2002 and August 2014, we selected 240 patients with a clinical diagnosis of probable AD at an early stage. Of the MR imaging scans, 3D-T1-weighted scans were used for both screening and analysis, whereas T2-weighted MR imaging and MR angiography were used for screening. Diagnosis of AD was based on the criteria of the National Institute of Neurologic and Communicative Disorders and Stroke and the Alzheimer's Disease and Related Disorders Association.⁹ Forty-three patients were excluded from the study on the following grounds: 1) evidence of moderate-to-severe cognitive disturbance: grade 2 or more on the Clinical Dementia Rating (CDR),¹⁰ with evidence of severe language, attentional, or behavioral disturbances that might complicate neurologic assessment; 2) uncontrolled major systemic disease or other neurologic disorders; and 3) evidence of focal brain lesions determined by MR imaging. We also excluded 39 patients with AD older than 80 years of age because it was impossible to find suitable age-matched healthy controls. Finally, 158 patients with AD were enrolled for analysis.

Regarding the generation of a control group for the construction of a healthy data base and for comparison against patients with AD, healthy subjects (HS) were recruited in response to advertisements. The following criteria were used to define healthy: 1) no history of brain trauma, psychiatric or neurologic disorders, or uncontrolled major systemic diseases and no current use of centrally acting drugs; 2) no abnormalities following general and neurologic examination; 3) a Mini-Mental State Examination (MMSE)¹¹ score of ≥ 28 and no clinical evidence of dementia; and 4) no evidence of asymptomatic cerebral infarction or brain vessel abnormalities on MR imaging. From the

criteria, 704 subjects were determined to be HS among the 1369 recruited volunteers. From the 704 subjects, 198 age-matched subjects were selected; of these, 158 served as the control group against the patients with AD and the remaining 40 served as the healthy database.

Imaging Procedure

Both patients with AD and HS underwent structural MR imaging analysis. The structural MR imaging studies were performed using a 1.5T system (Signa Horizon; GE Healthcare, Milwaukee, Wisconsin). A 3D volumetric acquisition of a T1-weighted gradient-echo sequence produced a gapless series of thin transaxial sections using a magnetization-prepared rapid acquisition of gradient-echo sequence (TE/TR, 2.0/9.2 ms; flip angle, 20°; acquisition matrix, 256 × 192; number of slices, 124; pixel size, 0.78 × 1.04; slice thickness, 1.4 mm).

Image Processing

MR imaging data were analyzed with DARTEL-based spatial normalization with SPM8 software (<http://www.fil.ion.ucl.ac.uk/spm/software/spm12>).⁴ MR images from 158 patients with AD and 198 HS were used to create templates for the DARTEL-based normalization technique. During spatial normalization, brain regions are expanded or contracted. Modulation involves scaling by the amount of expansion or contraction, so that the total amount of gray matter intensity in the modulated gray matter remains the same as it would be in the original images. Thus, gray matter intensity on modulated images should represent tissue volume rather than tissue concentration on nonmodulated images. During processing, both modulated and nonmodulated gray matter images were obtained for DARTEL-based VBM analysis. Modulated and nonmodulated gray matter images were nonsmoothed or smoothed, which is an image blurring using a function with a 4-, 8-, 12-, 16-, or 20-mm full width at half maximum Gaussian kernel, respectively, to investigate the effect of smoothing kernel size on DARTEL-based VBM. Twelve image datasets for each subject were generated.

Tomographic Z Score Mapping

After the preprocessing of MR imaging data, gray matter MR images were compared with the mean and SD of normal database gray matter images using a voxel-by-voxel z score analysis with a software program developed by Matsuda et al¹²: $Z \text{ Score} = ([\text{Control Mean}] - [\text{Individual Value}]) / (\text{Control SD})$. This comparison was performed so that a positive z score value would represent reduced gray matter concentration or volume. These z score maps were displayed by overlay on tomographic sections. In each z score map, WFU Pick atlas-based ROIs (Department of Radiology of Wake Forest University School of Medicine, Winston-Salem, North Carolina; fmri.wfubmc.edu)¹³ were drawn on the amygdala, hippocampus, parahippocampus, posterior cingulate gyrus, precuneus, frontal lobe, occipital lobe, parietal lobe, and temporal lobe.

Analysis

For each dataset, we investigated the diagnostic ability of each technique to discriminate patients with AD from HS. We per-

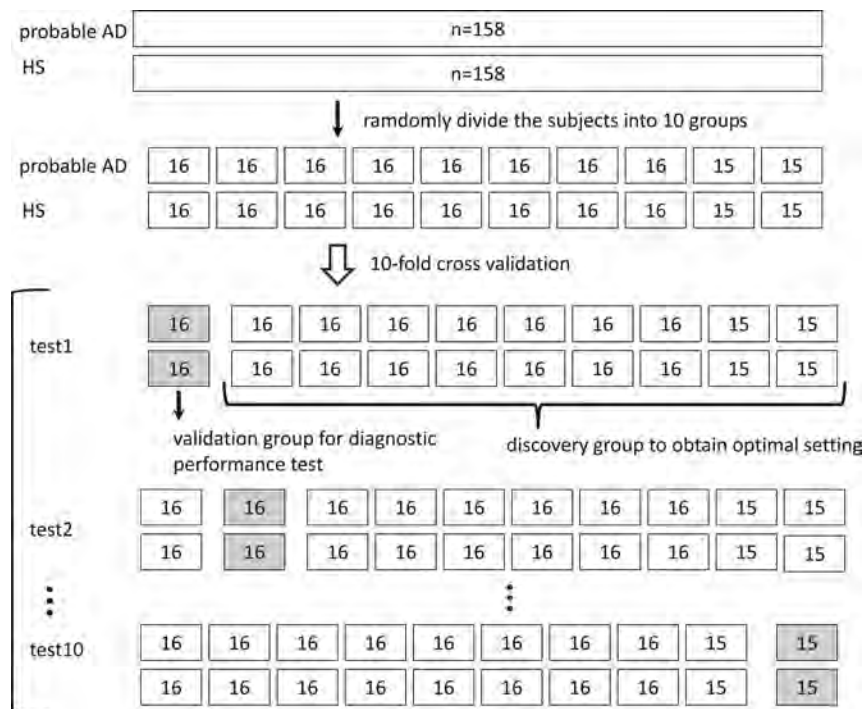


FIG 1. The scheme of 10-fold cross-validation. One hundred fifty-eight subjects with AD and 158 HS were randomly divided into 10 folds, with the same number of subjects with AD and HS in each fold. In each iteration, 9 of the folds were used for discovery (optimal setting determination) and 1 fold was used for validation (diagnostic performance test).

Table 1: Clinical characteristics of AD group and HS group

	AD (n = 158)	HS (n = 158)	NDB (n = 40)	P Value
Age (yr)	69 ± 8	68 ± 8	69 ± 6	.881 ^a
Onset age (yr)	67 ± 8	—	—	—
Sex (M/F)	80:78	87:71	20:20	.692 ^b
MMSE	22.7 ± 3.6	29.0 ± 0.7	29.6 ± 0.6	<.001 ^a
CDR (0.5/1)	20/138	—	—	—
Term of education (yr)	11.7 ± 2.6	12.2 ± 2.9	12.1 ± 2.3	.196 ^c

Note:—NDB indicates normal data base.

^a ANOVA.

^b χ^2 test.

^c Kruskal-Wallis test.

formed 10-fold cross-validation to optimize image-processing and ROI settings and test the diagnostic performance. The subjects were randomly divided into 10 folds, with the same number of patients with AD and HS in each fold. In each iteration, 9 of the folds were used for discovery (optimal setting determination) and the remaining one was used for validation (diagnostic performance test). The scheme of 10-fold cross-validation is illustrated in Fig 1.

On the basis of the z score, the optimal ROIs for the discrimination of AD under each processing condition were determined using univariate and multivariate logistic regression analyses referring likelihood ratio χ^2 test statistic. Although our patients with AD and healthy subjects were matched for age and number as a whole, they were not individually matched. Therefore, we used regular logistic regression rather than the conditional logistic regression to analyze our datasets. The optimal settings were defined as the settings demonstrating the highest χ^2 test statistics in the multivariate logistic regression analyses. Multivariate logistic regression analyses

were performed using a stepwise backward elimination procedure. To assess the aging effect, age was entered as a variable for both univariate and multivariate analysis.

The validation group was used to estimate the diagnostic performance of the optimal setting with receiver operating characteristic (ROC) analysis. Diagnostic accuracy was assessed by the area under the curve (AUC). Data were expressed as mean ± SD. Comparisons of mean values were performed with ANOVA. When assumptions required for the ANOVA were not met, the non-parametric 2-sided Kruskal-Wallis test was used. The proportional difference among the groups was assessed using a χ^2 test. Statistical significance was defined as $P < .05$ (2-sided). All the statistical analyses were performed using a statistical software package (JMP 10; SAS Institute. Cary, North Carolina).

RESULTS

Clinical characteristics of patients with AD, HS, and the healthy database are summarized in Table 1. Clinical characteristics of the discovery and validation groups in the tests 1–10 are shown in On-line Tables 1A–10A. The results of univariate and multivariate analyses for the discrimination of patients with AD from HS in the tests 1–10 are shown in On-line Tables 1B–1G, 2B–2G, 3B–3G, 4B–4G, 5B–5G, 6B–6G, 7B–7G, 8B–8G, 9B–9G, and 10B–10G. The summaries of the optimal ROIs and diagnostic performance expressed as

AUCs for each image-processing setting are shown in On-line Tables 1H–10H. Finally, the summary of 10-fold cross-validation is shown in Table 2.

Determination of Optimal Image-Processing and ROI Settings

When the smoothing kernel size was set to 8–20 mm, the amygdala and parietal lobe ROIs mainly contributed to the discrimination of AD regardless of the use of modulation (On-line Tables). When images were modulated and the smoothing kernel size was set to 0–4 mm, the amygdala and posterior cingulate gyrus ROIs were the main contributor. When images were nonmodulated and the smoothing kernel size was set to 0–4 mm, the hippocampus and precuneus ROIs were the predominant contributor (On-line Tables).

The results of multivariate analysis are summarized in Table 2. In 8 of 10 tests, the highest χ^2 statistic was obtained when images were nonmodulated and nonsmoothed. Furthermore,

Table 2: Summary of 10-fold cross-validation^a

	Optimized Image-Processing Condition		Optimal ROI	Likelihood Ratio χ^2 Test Statistic	P Value	AUC
	Modulation	Smoothing Kernel Size (mm)				
Test 1	–	Nonsmoothed	Hippocampus	111.92	<.001	0.830
Test 2	–	Nonsmoothed	Hippocampus Precuneus	113.55	<.001	0.945
Test 3	–	Nonsmoothed	Hippocampus Precuneus	120.76	<.001	0.869
Test 4	–	Nonsmoothed	Hippocampus Precuneus	126.04	<.001	0.756
Test 5	–	4	Hippocampus Precuneus	123.10	<.001	0.871
Test 6	+	8	Parahippocampus Amygdala Frontal lobe Parietal lobe	118.83	<.001	0.738
Test 7	–	Nonsmoothed	Hippocampus Precuneus	124.73	<.001	0.836
Test 8	–	Nonsmoothed	Hippocampus Precuneus	119.94	<.001	0.871
Test 9	–	Nonsmoothed	Hippocampus Precuneus	126.26	<.001	0.851
Test 10	–	Nonsmoothed	Hippocampus Precuneus	127.45	<.001	0.787

^aLikelihood ratio χ^2 test statistic and P values were determined by multivariate logistic regression analyses. Optimal image-processing condition and ROI and diagnostic performance are expressed as area under the curve for each validation group.

the optimal ROIs for the above settings mostly included the hippocampus and precuneus. Age did not survive as a variate to discriminate patients with AD from HS in any test. Thus, the optimal settings for the discrimination of patients with AD from HS were obtained when ROIs were set to the hippocampus and precuneus without modulation and smoothing in 7 of the 10 tests.

Most interesting, following modulation, the z score of the amygdala was increased, and conversely, that of the hippocampus was reduced. Examples are presented in Fig 2.

Diagnostic Performance of DARTEL-Based VBM Using the Optimal Image-Processing Settings and ROIs

Using the optimal image-processing and ROI settings determined by multivariate analyses of the training groups, we performed ROC analyses in each test group to assess the diagnostic ability as shown in Table 2. The AUC ranged from 0.738 to 0.945. When only the results of the ROI settings of the hippocampus and precuneus without modulation and smoothing (tests 2, 3, 4, 7, 8, 9, and 10) were summarized, the average of the AUC was 0.845 (95% confidence interval, 0.788–0.902). Additionally, there was a general trend for the ROC results to get worse along with smaller χ^2 statistics as the smooth function kernel size increased, particularly in nonmodulation settings (On-line Tables).

DISCUSSION

The major finding of this study was that the diagnostic ability of DARTEL-based VBM was highest when MR images were non-modulated and nonsmoothed with ROIs set to the hippocampus and precuneus.

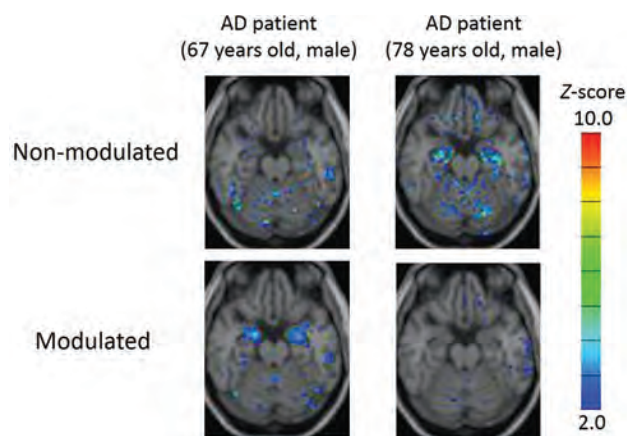


FIG 2. Two sample cases of z score maps with and without modulation from patients with AD. Automated voxel-by-voxel z score analysis was performed by comparison of the relative gray matter concentration of patients with the mean and SD of HS. Color-scaled z score maps were displayed by overlaying them on the spatially normalized transaxial MR imaging. Smoothing was not applied. The modulated MR image of the patient with AD (67-year-old man; MMSE score, 19; CDR, 1) showed a high z score in the amygdala. The finding became obscure when the MR image was nonmodulated. Meanwhile, the nonmodulated MR image of another patient with AD (78-year-old man; MMSE score, 21; CDR, 1) showed a high z score in the hippocampus. The finding disappeared when the MR image was modulated.

Impact of Modulation on the Discrimination of AD in DARTEL-Based VBM

In the present study, modulation significantly influenced the diagnostic performance of DARTEL-based VBM for AD. Following modulation, volumetric differences in the amygdala became increasingly visible, and conversely, those of the hippocampus became more obscure. In theory, perfect spatial normalization

would result in no detectable differences between the individual gray matter images unless modulated.

The negative effect of modulation on the hippocampus might suggest that the detected differences between patients with AD and healthy subjects are likely to reflect imperfect registration between images rather than true volume differences. By contrast, the positive effect of modulation on the amygdala might suggest that spatial normalization was successful. These findings indicate that the effects of modulation influence each brain region differently, likely dependent on the structural complexity of each area.

Optimal Smoothing Kernel Size for the Discrimination of AD by DARTEL-Based VBM

In statistical image analysis, smoothing is routinely applied to reduce noise, normalize the distribution, and compensate for imperfect image registration.¹⁴ A previous modulated DARTEL-based VBM study reported that optimal kernel size varied according to the group size.¹⁵ The present study indicated that optimal kernel size varied depending on the use of modulation and variation in the ROI. If we took into account the above settings, the optimal setting was without smoothing the images. This result could be due to an increased ability to detect localized abnormalities by not smoothing. However, this anatomic difference between patients with AD and HS would be lost with smoothing, resulting in a smaller χ^2 and AUC, particularly in nonmodulation settings. Like the modulation effects as aforementioned, the effects of smoothing could also be region-dependent. Furthermore, our observation might be related to the specific programs used in this study during data processing. Therefore, one should interpret our results with caution, taking these circumstances into account.

Optimal ROI for the Discrimination of VAD by DARTEL-Based VBM

To determine a suitable ROI for the diagnosis of AD, previous VBM studies analyzed corresponding areas of gray matter volume for patients with AD and HS using group comparison analyses.^{1,2,4,5,16,17} In the present study, we extracted areas of significant correlation for the discrimination of AD using multivariate logistic regression analysis and determined such areas as ROIs. As a result, in addition to medial temporal structures, the precuneus was designated as an optimal ROI for the detection of AD. This is in line with a previous study by Shima et al⁶ demonstrating that some patients with AD show atrophy in neocortical areas such as the posterior cingulate gyrus and precuneus rather than in the medial temporal structures, particularly in young patients. Thus, the diagnostic performance of VBM for the discrimination of AD could be improved by combining the neocortical areas with medial temporal structures as ROIs.

Effects of Age on the Diagnostic Accuracy of AD with DARTEL-Based VBM

We did not find aging effects on the choice of VBM parameters when age was included as a predictor to discriminate AD from HS in our regression model. This was perhaps because most of our patients had late-onset AD as reflected by the mean onset age (67 ± 8 years) and the age range not being wide enough to show

significant effects. This needs to be addressed in further studies focusing on young patients with AD.

Limitations

There are limitations to the study. First, the diagnosis of probable AD was made on the basis of clinical examinations and therefore may differ from that obtained with final pathologic verification, a limitation present in many such studies. However, it has been reported that diagnostic accuracy can exceed 90% in an academic memory disorders clinic setting.¹⁸ Second, we investigated the optimal settings of DARTEL-based VBM to only discriminate between patients with AD and healthy subjects. Therefore, our data cannot be applied to other types of dementia. Finally, the data would be more robust if we could use our optimized model parameters applied on outside AD datasets such as the Alzheimer's Disease Neuroimaging Initiative data (<http://adni.loni.usc.edu/>). However, this proposal is beyond the scope of the current study and should be addressed in future.

CONCLUSIONS

For the discrimination of VAD from HS using DARTEL-based VBM, we recommend using the precuneus and hippocampus as ROIs without modulation and smoothing. The use of optimized ROIs and image-processing settings can provide a high level of diagnostic accuracy in the discrimination of AD.

Disclosures: Ichiro Matsunari—*RELATED: Grant:* This study was supported, in part, by a grant for Development of Advanced Technology for Measurement and Evaluation of Brain Functions, Ishikawa Prefecture Collaboration of Regional Entities for the Advancement of Technological Excellence (to M.Y.), from Japan Science and Technology Corporation, Japan, and by a grant for the Knowledge Cluster Initiative (High-Tech Sensing and Knowledge Handling Technology [Brain Technology]) (to M.Y.) from the Japanese Ministry of Education, Culture, Sports, Science and Technology, Japan, and by Ishikawa Prefectural Government (to I.M.)*. Moeko Noguchi-Shinohara—*UNRELATED: Grants/Grants Pending:* Japan Agency for Medical Research and Development.* Masahito Yamada—*RELATED: Grant:* Japanese Ministry of Education, Culture, Sports, Science and Technology, Japan Science and Technology Corporation*; *UNRELATED: Grants/Grants Pending:* Japan Agency for Medical Research and Development*. *Money paid to the institution.

REFERENCES

1. Hirata Y, Matsuda H, Nemoto K, et al. **Voxel-based morphometry to discriminate early Alzheimer's disease from controls.** *Neurosci Lett* 2005;382:269–74 [CrossRef Medline](#)
2. Kawachi T, Ishii K, Sakamoto S, et al. **Comparison of the diagnostic performance of FDG-PET and VBM-MRI in very mild Alzheimer's disease.** *Eur J Nucl Med Mol Imaging* 2006;33:801–09 [CrossRef Medline](#)
3. Bookstein FL. **"Voxel-based morphometry" should not be used with imperfectly registered images.** *Neuroimage* 2001;14:1454–62 [CrossRef Medline](#)
4. Ashburner J. **A fast diffeomorphic image registration algorithm.** *Neuroimage* 2007;38:95–113 [CrossRef Medline](#)
5. Matsuda H, Mizumura S, Nemoto K, et al. **Automatic voxel-based morphometry of structural MRI by SPM8 plus diffeomorphic anatomic registration through exponentiated lie algebra improves the diagnosis of probable Alzheimer disease.** *AJNR Am J Neuroradiol* 2012;33:1109–14 [CrossRef Medline](#)
6. Shima K, Matsunari I, Samuraki M, et al. **Posterior cingulate atrophy and metabolic decline in early stage Alzheimer's disease.** *Neurobiol Aging* 2012;33:2006–17 [CrossRef Medline](#)
7. Chen WP, Samuraki M, Shima K, et al. **Effect of an age-mismatched and sex-mismatched normal database on the diagnostic performance of ¹⁸F-FDG PET for Alzheimer's disease: the Ishikawa Brain**

- Imaging Study.** *Nucl Med Commun* 2011;32:1128–33 CrossRef Medline
8. Samuraki M, Matsunari I, Chen WP, et al. **Glucose metabolism and gray-matter concentration in apolipoprotein E ε4 positive normal subjects.** *Neurobiol Aging* 2012;33:2321–23 CrossRef Medline
 9. McKhann G, Drachman D, Folstein M, et al. **Clinical diagnosis of Alzheimer's disease: report of the NINCDS-ADRDA Work Group under the auspices of Department of Health and Human Services Task Force on Alzheimer's Disease.** *Neurology* 1984;34:939–44 CrossRef Medline
 10. Hughes CP, Berg L, Danziger WL, et al. **A new clinical scale for the staging of dementia.** *Br J Psychiatry* 1982;140:566–72 CrossRef Medline
 11. Folstein MF, Folstein SE, McHugh PR. **"Mini-mental state": a practical method for grading the cognitive state of patients for the clinician.** *J Psychiatr Res* 1975;12:189–98 CrossRef Medline
 12. Matsuda H, Mizumura S, Nagao T, et al. **Automated discrimination between very early Alzheimer disease and controls using an easy Z-score imaging system for multicenter brain perfusion single-photon emission tomography.** *AJNR Am J Neuroradiol* 2007;28:731–36 Medline
 13. Maldjian JA, Laurienti PJ, Kraft RA, et al. **An automated method for neuroanatomic and cytoarchitectonic atlas-based interrogation of fMRI data sets.** *Neuroimage* 2003;19:1233–39 CrossRef Medline
 14. Jones DK, Symms MR, Cercignani M, et al. **The effect of filter size on VBM analyses of DT-MRI data.** *Neuroimage* 2005;26:546–54 CrossRef Medline
 15. Shen S, Sterr A. **Is DARTEL-based voxel-based morphometry affected by width of smoothing kernel and group size? A study using simulated atrophy.** *J Magn Reson Imaging* 2013;37:1468–75 CrossRef Medline
 16. Frisoni GB, Testa C, Zorzan A, et al. **Detection of grey matter loss in mild Alzheimer's disease with voxel based morphometry.** *J Neurol Neurosurg Psychiatry* 2002;73:657–64 CrossRef Medline
 17. Matsunari I, Samuraki M, Chen WP, et al. **Comparison of 18F-FDG PET and optimized voxel-based morphometry for detection of Alzheimer's disease: aging effect on diagnostic performance.** *J Nucl Med* 2007;48:1961–70 CrossRef Medline
 18. Rasmusson DX, Brandt J, Steele C, et al. **Accuracy of clinical diagnosis of Alzheimer disease and clinical features of patients with non-Alzheimer disease neuropathology.** *Alzheimer Dis Assoc Disord* 1996; 10:180–88 CrossRef Medline

Substantia Nigra Free Water Increases Longitudinally in Parkinson Disease

T. Guttuso Jr, N. Bergsland, J. Hagemeyer, D.G. Lichter, O. Pasternak, and R. Zivadinov



ABSTRACT

BACKGROUND AND PURPOSE: Free water in the posterior substantia nigra obtained from a bi-tensor diffusion MR imaging model has been shown to significantly increase over 1- and 4-year periods in patients with early-stage idiopathic Parkinson disease compared with healthy controls, which suggests that posterior substantia nigra free water may be an idiopathic Parkinson disease progression biomarker. Due to the known temporal posterior-to-anterior substantia nigra degeneration in idiopathic Parkinson disease, we assessed longitudinal changes in free water in both the posterior and anterior substantia nigra in patients with later-stage idiopathic Parkinson disease and age-matched healthy controls for comparison.

MATERIALS AND METHODS: Nineteen subjects with idiopathic Parkinson disease and 19 age-matched healthy control subjects were assessed on the same 3T MR imaging scanner at baseline and after approximately 3 years.

RESULTS: Baseline mean idiopathic Parkinson disease duration was 7.1 years. Both anterior and posterior substantia nigra free water showed significant intergroup differences at baseline ($P < .001$ and $P = .014$, respectively, idiopathic Parkinson disease versus healthy controls); however, only anterior substantia nigra free water showed significant longitudinal group \times time interaction increases ($P = .021$, idiopathic Parkinson disease versus healthy controls). There were no significant longitudinal group \times time interaction differences found for conventional diffusion tensor imaging or free water–corrected DTI assessments in either the anterior or posterior substantia nigra.

CONCLUSIONS: Results from this study provide further evidence supporting substantia nigra free water as a promising disease-progression biomarker in idiopathic Parkinson disease that may help to identify disease-modifying therapies if used in future clinical trials. Our novel finding of longitudinal increases in anterior but not posterior substantia nigra free water is potentially a result of the much longer disease duration of our cohort compared with previously studied cohorts and the known posterior-to-anterior substantia nigra degeneration that occurs over time in idiopathic Parkinson disease.

ABBREVIATIONS: aSN = anterior substantia nigra; FW = free water; HC = healthy control; IPD = idiopathic Parkinson disease; IPD-NM = subjects with IPD not receiving any MAOI at baseline; IPD-R = subjects with IPD receiving rasagiline at baseline; MAOI = monoamine oxidase inhibitor; MMSE = Mini-Mental State Examination; MoCA = Montreal Cognitive Assessment; MNI = Montreal Neurological Institute; NODDI = neurite orientation dispersion and density imaging; pSN = posterior substantia nigra; SN = substantia nigra pars compacta

At the time of diagnosis of idiopathic Parkinson disease (IPD) about 30%–50% of the dopaminergic neurons in the sub-

stantia nigra pars compacta (SN) have degenerated, resulting in dopamine deficiency and motor symptoms.^{1–3} This degeneration is initially focused in the ventrolateral tier, which is grossly in the posterior SN, with the more anterior regions of the SN affected relatively later in the disease.³ Thus, the pattern of SN neuronal loss in IPD is heterogeneous and progresses from a posterior-to-anterior direction with over time.

Diffusion tensor imaging is a diffusion MR imaging–derived assessment that reflects tissue microstructural integrity.⁴ As a result, multiple groups have sought to determine whether SN DTI can distinguish subjects with IPD from healthy controls (HCs). Results of these studies have been conflicting.⁵ These conflicting results have been theorized to be due to inconsistent methodologies used to de-

Received July 3, 2017; accepted after revision November 19.

From the Movement Disorder Center (T.G., D.G.L.) and Buffalo Neuroimaging Analysis Center (N.B., J.H., R.Z.), Department of Neurology, and MR Imaging Clinical and Translational Research Center (R.Z.), Jacobs School of Medicine and Biomedical Sciences, University at Buffalo, State University of New York, Buffalo, New York; and Departments of Psychiatry and Radiology (O.P.), Brigham and Women's Hospital, Harvard Medical School, Boston, Massachusetts.

This work was supported by an investigator-initiated award from Teva Neurosciences and from the National Center for Advancing Translational Sciences of the National Institutes of Health, UL1TR001412, and National Institutes of Health awards R01MH108574 and P41EB015902.

Please address correspondence to Thomas Guttuso Jr, MD, 3435 Main St, 97 Farber Hall, Buffalo, NY 14214; e-mail: tguttuso@buffalo.edu

Indicates open access to non-subscribers at www.ajnr.org

<http://dx.doi.org/10.3174/ajnr.A5545>

lineate the SN or unpredictable contamination of DTI assessments from free water (FW), which is extracellular water.⁵⁻⁷ FW mapping obtained from a bi-tensor diffusion MR imaging model was developed, which allows separating out the contribution of FW to DTI assessments (FW-corrected DTI) and for determining the fraction of FW itself, to control for FW contamination.⁷ Most interesting, subsequent studies have shown that FW itself in the posterior (p) SN distinguishes patients with IPD from HCs better than conventional DTI as well as FW-corrected DTI assessments.^{8,9} Furthermore, 2 studies by the Vaillancourt group have shown pSN FW to significantly increase longitudinally over 1 and 4 years in patients with early-stage IPD compared with HCs, suggesting that pSN FW may be a disease-progression biomarker in early IPD.^{10,11}

Due to the known temporal posterior-to-anterior SN degeneration in IPD,³ we assessed longitudinal changes in FW and explored changes in FW-corrected DTI and conventional DTI in both the posterior and anterior (a) SN in patients with later-stage IPD and age-matched HCs over approximately 3 years. Additional exploratory outcomes included assessment for associations between longitudinal changes in clinical outcomes (motor and cognitive) and longitudinal changes in DTI/FW in the SN and multiple other regions of interest. We were particularly interested in identifying ROIs that may reflect longitudinal worsening of cognition because dementia eventually occurs in 80% of patients with IPD, is likely unrelated to SN pathology, and is one of the most disabling long-term sequela of IPD.¹² Finally, we also explored differences in these outcomes between the subjects with IPD receiving the monoamine oxidase inhibitor (MAOI) rasagiline at baseline and IPD subjects not receiving any MAOI at baseline to examine the potential disease-modifying actions of rasagiline.¹³

MATERIALS AND METHODS

The institutional review board at the University at Buffalo provided ethics approval for this study before subject enrollment. From March 2011 to March 2013, thirty-two subjects with IPD and 25 age- and sex-matched HC subjects provided written informed consent and underwent MR imaging and clinical assessment, including 'on' state Unified Parkinson's Disease Rating Scale Part III,¹⁴ the Montreal Cognitive Assessment (MoCA),¹⁵ and the Mini-Mental State Examination (MMSE).¹⁶ Subsequently, from January to October 2015, after again providing written informed consent, available subjects were re-assessed with the same clinical and MR imaging measures (follow-up assessments). All subjects with IPD satisfied the UK Parkinson's Disease Society Brain Bank criteria for diagnosis¹⁷ and were assessed clinically by the same movement disorder neurologist (T.G. or D.G.L.) at both time points. Healthy controls consisted primarily of spouses and friends of the participants with IPD. A small number of healthy controls in this study had participated in previous research studies at the University at Buffalo and had consented to be contacted for future studies.

Using the same 3T-MR imaging scanner Signa Excite HD 12.0 Twin Speed 8-channel; (GE Healthcare, Milwaukee, Wisconsin) and a multichannel head and neck coil at both time points, we performed diffusion MR imaging with a voxel size of $2 \times 2 \times 4$ mm³ and a 0.5-mm gap. The sequence used 2 averages with 25 noncollinear directions, $b=900$ s/mm² and 1 volume without directional weighting ($b=0$ s/mm²). A high-resolution 3D T1-

weighted volume with $1 \times 1 \times 1$ mm³ isotropic voxels was also acquired. Image analyses were performed in the Buffalo Neuroimaging Analysis Center by an evaluator (N.B.) blinded to subjects' clinical and treatment characteristics. DTI image analyses were performed with the FSL 5.0 Toolbox (www.fmrib.ox.ac.uk/fsl). We used code implemented in Matlab (MathWorks, Natick, Massachusetts) to fit a regularized bi-tensor model and to generate FW maps and FW-corrected maps of the 4 standard DTI assessments.⁷ To eliminate all non-neural tissue, we extracted the original $b=0$ images (with no diffusion-weighting) and de-skulled them in FSL using the Brain Extraction Tool (<http://fsl.fmrib.ox.ac.uk/fsl/fslwiki/BET>). Susceptibility-induced geometric distortions were corrected for using nonlinear registration of the $b=0$ s/mm² image to the T1WI volume, while eddy currents were corrected using the FSL eddy tool (<https://fsl.fmrib.ox.ac.uk/fsl/fslwiki/eddy>).¹⁸

FW, FW-corrected DTI, and conventional DTI measures of fractional anisotropy, mean diffusivity, axial diffusivity, and radial diffusivity were assessed in the anterior and pSN as well as several regions likely to reflect cognitive status¹⁹⁻²³: the anterior and posterior cingulate, anterior thalamus, fornix, genu and splenium of the corpus callosum, and major lobar white matter tracts. All ROIs were drawn manually except for those in the lobar white matter. The former ROIs were derived by nonlinear registration of the 3D T1WI volume Montreal Neurological Institute (MNI) space. MNI-defined lobar masks were warped into native space using the corresponding inverse warp. Finally, the ROIs were then restricted to voxels having a partial volume estimate of >0.85 for white matter, as derived from tissue segmentation of the 3D T1WI volume.²⁴

SN ROIs were drawn by one of the blinded authors (N.B.) as previously described.¹¹ Briefly, the $b=0$ image was linearly registered with 12 *df* to a T2-weighted MNI space image with 2-mm³ isotropic voxels.²⁵ Next, left and right hemisphere anterior and posterior SN ROIs were drawn separately on each $b=0$ image after transformation into MNI space. Each ROI consisted of a 2×2 mm square placed on 2 consecutive slices, for a total of eight $2 \times 2 \times 2$ mm³ voxels. The superior slice for the SN ROI placement was chosen just inferior to the red nucleus where the red nucleus was either barely or no longer visible. Anterior and pSN ROIs were placed in the area of hypointense signal on the $b=0$ image corresponding to the SN (Fig 1). Such SN ROI placement is also consistent with placement guided by neuromelanin-sensitive imaging.⁵ Finally, the DTI-derived maps were resampled into MNI space with trilinear interpolation using the $b=0$ transformation matrix, and quantitative measures were extracted from the SN ROIs. Other exploratory ROIs were delineated as previously described.^{19,21,23} The MR imaging scanner underwent no hardware or software upgrades during the study.

Statistical analyses were conducted using SPSS for Windows, Version 24.0 (IBM, Armonk, New York). Intergroup differences in baseline characteristics were analyzed using the χ^2 test, Student *t* test, and nonparametric Mann-Whitney *U* test when appropriate. The repeated measures ANCOVA general linear model framework with age and sex as covariates was used for longitudinal and cross-sectional assessments. The ROI main effects of group and time as well as the interaction effect of group \times time were considered significant at $P < .05$. There were no corrections for multiple comparisons in non-SN ROIs due to the exploratory nature of these outcomes and the limited sample size of the study.

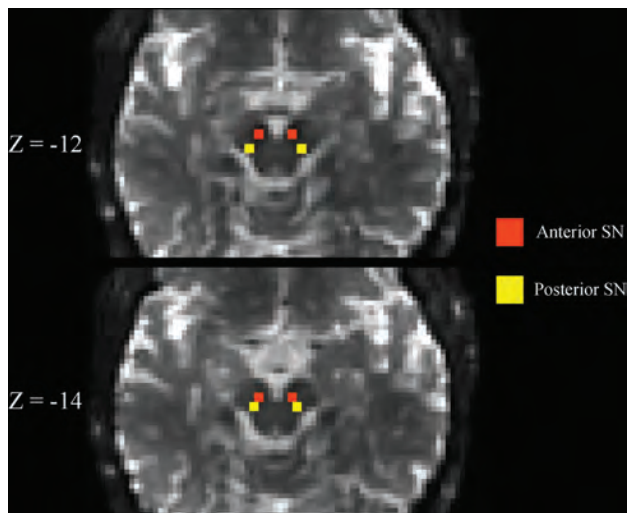


FIG 1. Substantia nigra ROIs. Representative $b=0$ s/mm^2 images linearly registered to the MNI atlas are shown demonstrating the placement of the substantia nigra ROIs. Z-coordinates refer to the slice shown in MNI space. See the “Materials and Methods” section for a more detailed description of how ROIs were placed.

Within-Parkinson-disease-group associations between longitudinal changes in imaging measures and longitudinal changes in clinical outcomes were assessed using age-, sex- and disease duration-adjusted forward-selection models ($P < .05$ selection criterion), in which change in clinical outcomes was considered the dependent measure. Post hoc analyses for differences at baseline between the subjects with IPD receiving rasagiline at baseline (IPD-R) and subjects with IPD not receiving any MAOI at baseline (IPD-NM) were performed using the Fisher least significant difference and Fisher exact test (categorical) and for longitudinal differences using the repeated measures ANCOVA general linear model framework with disease duration as a covariate. For reproducibility analysis of the manually drawn ROIs, 2-way absolute agreement, single-measure intraclass correlation coefficient was used. A random sample of data from 5 healthy controls and 5 patients with IPD was analyzed and re-analyzed after 1 month to minimize recall bias. The order of the analyses was also randomized.

RESULTS

Of the original 57 subjects enrolled at baseline, 18 were unable to be reassessed at the 3-year follow-up visit due to death ($n = 4$), a deep brain stimulation operation ($n = 2$), change in residence ($n = 3$), decision not to participate ($n = 6$), or loss to follow-up ($n = 3$). Another subject was removed from the analyses after a frontal lobe astrocytoma was found on the 3-year follow-up MR imaging. Therefore, 38 subjects with available data at both time points were included in the analyses. The characteristics of these 38 subjects are summarized in Table 1. There were no significant intergroup differences in subjects' ages, but the IPD group had significantly more men and a longer time to follow-up compared with the HC group.

Anterior SN FW demonstrated both significant intergroup differences at baseline and group \times time longitudinal interaction differences over the 3-year follow-up period, while pSN FW only demonstrated significant intergroup differences at baseline (Fig 2 and Table 2). No other SN DTI or FW-corrected DTI assessment showed both significant intergroup and group \times time interaction differences.

Comparisons of longitudinal changes in MR imaging assessments with longitudinal changes in clinical outcomes showed increasing bitemporal white matter FW-corrected mean diffusivity to be associated with decreasing (worsening) MMSE and MoCA scores (Fig 3; standardized coefficient, P values; respectively: -0.909 , $P = .001$; -0.534 , $P = .037$). In addition, left aSN FW and total pSN FW changes were associated with worsening MMSE but not MoCA scores (standardized coefficient, P values; respectively: -0.781 , $P = .002$; 0.563 , $P = .011$). Only increasing left parietal white matter FW-corrected axial diffusivity was associated with increasing (worsening) Unified Parkinson's Disease Rating Scale Part III motor scores (standardized coefficient, P value: 0.654 , $P = .033$).

There were no significant baseline or longitudinal differences between the IPD-R ($n = 11$) and IPD-NM ($n = 8$) groups for any ROI assessment after correction for disease duration (5.1 years for subjects with IPD-R and 9.8 years for those with IPD-NM at baseline). The subjects with IPD-R had been receiving rasagiline for a mean of 35.6 ± 40.3 months before baseline.

For the left anterior SN, left posterior SN, right anterior SN, and right posterior SN, the intraclass correlation coefficient values were 0.93, 0.85, 0.91, and 0.83, respectively. Intraclass correlation coefficient results of the non-SN ROIs ranged between 0.75 (for the anterior thalamus) to 0.96 (for the genu of the corpus callosum).

DISCUSSION

In our later-stage IPD cohort, we found significant longitudinal intergroup differences in aSN FW, with more rapid increases in subjects with IPD compared with HCs over approximately 3 years of follow-up (Fig 2). This represents the first, independent replication of previously observed longitudinal increases in SN FW in IPD,^{10,11} though in the aSN segment and not the pSN. These data, in total, support SN FW as a promising disease-progression biomarker in IPD.

As noted, previous studies have shown conflicting results regarding cross-sectional, conventional DTI assessments of the SN in subjects with IPD compared with HCs.^{5,26} These inconsistencies may, in part, be due to FW contamination of the conventional DTI measures^{7-9,27} or to discrepancies in SN ROI delineation.⁵ Both cross-sectional and longitudinal studies, including ours, have shown SN FW to distinguish those with IPD from HCs better and to be more sensitive to SN changes over time than conventional DTI or FW-corrected DTI SN assessments.⁸⁻¹¹ Another recent longitudinal DTI study by Loane et al²⁸ did not find any cross-sectional differences in SN fractional anisotropy or mean diffusivity at baseline between subjects with IPD and HCs but did find significant longitudinal changes in both assessments in IPD over about 1.5 years of follow-up. However, the Loane et al study found that SN fractional anisotropy values in HCs at baseline fell between SN fractional anisotropy values in subjects with IPD at baseline and those with IPD 1.5 years later. Such a finding would not be consistent with a valid IPD disease state biomarker. On the other hand, when using SN FW assessments, which were not used by Loane et al, our study and previous studies have shown baseline intergroup differences consistent with a disease state biomarker and showed SN FW to significantly increase longitudinally.^{10,11}

It also appears that SN ROI delineation may affect DTI study results in IPD. For example, Langley et al⁵ showed robust cross-sectional differences in SN fractional anisotropy using neu-

Table 1: Subject demographic and clinical information^a

	HC (n = 19)		IPD (n = 19)		Between Groups	
	BL	F/U	BL	F/U	P Value within BL	P Value within F/U
Age (yr)	56.5 (10.1)	59.6 (10.3)	59.8 (8.4)	63.2 (8.4)	.276	.251
Male sex (No.) (%)	5 (26)	—	12 (63)	—	.022	—
Disease duration (yr)	—	—	7.1 (5.1)	10.4 (5.3)	—	—
Time to F/U (mo)	—	36.2 (5.4)	—	43.8 (7.8)	—	.001
MMSE score	29.4 (0.9)	29.5 (0.9)	29.4 (1.0)	27.6 (4.8)	.586	.862
MoCA score	27.3 (2.4)	27.9 (2.1)	24.4 (4.2)	24.3 (6.9)	.095	.046
CDR score (mean, median) (IQR)	0, 0 (0–0)	0.1, 0 (0–0)	0.2, 0 (0–0.5)	0.3, 0 (0–0.5)	.053	.317
UPDRS-III score	0.8 (1.2)	1.3 (2.3)	18.8 (7.3)	22.1 (9.2)	<.001	<.001
H&Y (mean, median) (IQR)	0, 0 (0–0)	0, 0 (0)	1.9, 2 (1–2.5)	2.4, 2.5 (2–3)	<.001	<.001
S&E score	100 (0)	100 (0)	91.3 (9.3)	79.5 (21.8)	.001	.001
GDS score	1.9 (2.9)	1.2 (1.9)	2.3 (2.1)	5.2 (7.9)	.615	.044

Note:—H&Y indicates Hoehn and Yahr scale; S&E, Schwab and England Activities of Daily Living Scale; GDS, Geriatric Depression Scale; IQR, interquartile range; BL, baseline; F/U, follow up; CDR, Clinical Dementia Rating; UPDRS III, Unified Parkinson's Disease Rating Scale, Part III.

^a Results are presented as mean (SD), unless otherwise noted.

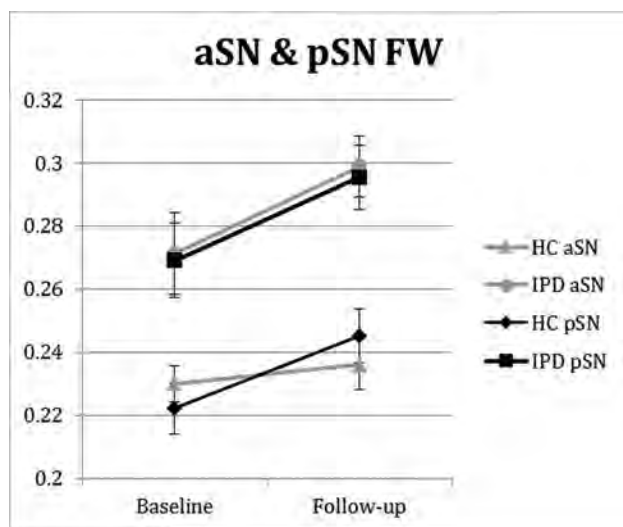


FIG 2. Longitudinal changes in SN FW in patients with later-stage IPD and HCs. aSN and pSN FW group and group \times time interaction intergroup differences were $P < .001$, $P = 0.021$, and $P = .014$, $P = 0.651$, respectively. Follow-up was approximately 3 years from baseline. Error bars are ± 1 standard error of mean.

romelanin-sensitive MR imaging to delineate the SN ROI in a location mostly inferior to the red nucleus but found no significant cross-sectional differences in SN fractional anisotropy when the SN ROI was delineated at the level of the red nucleus in the same IPD and HC cohorts. Therefore, using FW assessments and delineating the SN ROI just inferior to the red nucleus, as was done by Langley et al, by the Vaillancourt group, and by us in the present study (Fig 1),^{5,8–11,29} may provide more consistent results in future cross-sectional and longitudinal IPD studies.

The main novel finding in our study was that aSN and not pSN showed significant longitudinal increases in FW. Whether one observes FW longitudinal increases in the pSN and/or aSN may be a reflection of IPD disease duration, with the pSN first showing increased FW followed by the aSN, which would be in keeping with the known spatial profile of SN degeneration over time in IPD.³ This possibility is supported by the fact that the 2 IPD cohorts previously studied had mean disease durations at baseline of 0.6 and 3.0 years and showed longitudinal increases in pSN FW, while our IPD cohort had a mean disease duration of 7.1 years at baseline and showed significant longitudinal increases in aSN

FW.^{10,11} Indeed, another IPD cohort with a mean disease duration of 5.2 years showed significant cross-sectional increases in both aSN and pSN FW compared with HCs, similar to findings in our cohort (Fig 2 and Table 2).⁹ Although these data support SN FW to potentially reflect the known posterior-to-anterior pattern of SN degeneration with time in IPD,³ further work is needed to better clarify cross-sectional and longitudinal FW differences at both SN sites based on disease duration in IPD.

Identification of disease-progression biomarkers that are not influenced by IPD symptomatic therapies will be of great value in identifying disease-modifying therapies for IPD.³⁰ SN FW represents a logical biomarker toward this end. Free water is water molecules within a voxel that are not hindered or restricted by the cellular environment and therefore originate from extracellular water.⁷ Free water has been shown to reflect pathologic processes, including tissue atrophy and inflammation,³¹ both of which are known to occur in the SN of IPD. In addition, SN FW is not significantly affected by acute levodopa administration in subjects with IPD.³² Thus, SN FW assessments may help to distinguish the disease-modifying effect of a therapy, such as a reduction in SN degeneration and atrophy, from its symptomatic action, which has been difficult to achieve on the basis of clinical outcome assessment alone.³⁰ In addition, 3T MR imaging is widely available and relatively inexpensive to perform compared with radioligand-based imaging modalities. Such features make SN FW assessed by MR imaging an attractive imaging outcome to incorporate into future disease-modifying clinical trials.

It would also be interesting to explore how SN assessments using newer multicompartamental diffusion imaging modalities, such as neurite orientation dispersion and density imaging (NODDI) or restriction spectrum imaging, compare with SN FW both cross-sectionally and longitudinally in IPD.^{33,34} With different algorithms than we used to assess FW, both NODDI and restriction spectrum imaging also provide estimations of isotropic FW as well as neurite density disentangled from orientation dispersion.^{33,34} Thus, NODDI and restriction spectrum imaging may prove to be more sensitive modalities to assess SN pathology in IPD than the FW assessment technique we have used. In fact, SN NODDI has recently been shown to robustly distinguish those with IPD from HCs in a cross-sectional fashion; however, neither NODDI nor restriction spectrum imaging have been used to assess longitudinal SN changes in IPD, to date.³⁵ Also, these techniques require more ad-

Table 2: SN FW outcomes over 3 years of follow-up in HC and IPD groups^a

	HC (n = 19)		IPD (n = 19)		Group Effect	Time Effect	Interaction
	Baseline	Follow-Up	Baseline	Follow-Up			
aSN FW	.2301 (.0243)	.2361 (.0351)	.2713 (.0535)	.2989 (.0364)	<.001	.112	.021
pSN FW	.2221 (.0349)	.2452 (.0367)	.2691 (.0513)	.2955 (.0441)	.014	.246	.651

^a Values are mean (SD). Group, time, and group × time interaction effect values are *P* values.

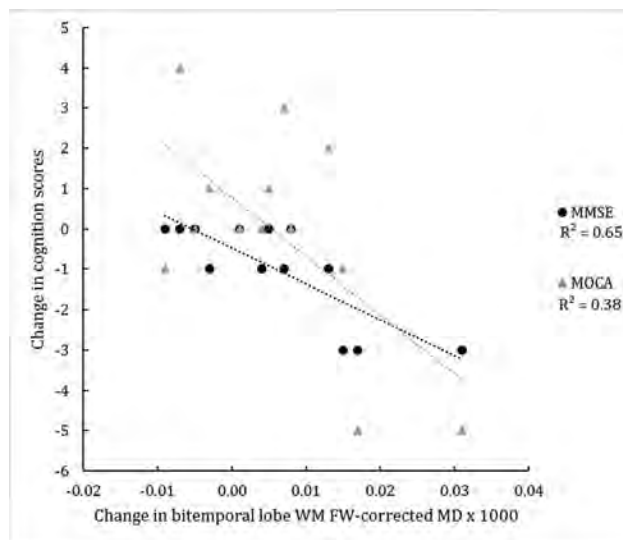


FIG 3. Change in the in bi-temporal lobe white matter FW-corrected mean diffusivity of subjects with IPD and corresponding changes in the MMSE and MoCA scores over 3 years. R^2 indicates coefficient of determination.

vanced acquisition schemes, whereas the bi-tensor model used in the current study can be applied to any DTI-based protocol.

Besides the significant longitudinal changes in aSN FW, we also found that longitudinal increases in bitemporal white matter FW-corrected mean diffusivity were associated with longitudinal worsening of cognition in IPD as measured by both the MMSE and MoCA (Fig 3). Previous cross-sectional studies have also found significant lobar white matter DTI changes associated with worsened cognition in IPD.^{19,20,22} Meaningful clinical outcomes not responsive to levodopa, such as cognition, will likely be critical to the interpretation of long-term disease-modifying trials because the nonmotor symptom of dementia is typically far more disabling than the IPD motor symptoms.³⁰ Because it takes approximately 10 years on average after IPD diagnosis for dementia to occur,³⁶ the use of biomarkers that are sensitive to cognitive decline in IPD would help to identify cognitive-protecting disease-modifying therapies during a shorter time period is more realistic for the duration of a randomized controlled trial. Our findings suggest that longitudinal assessment of temporal lobe white matter FW-corrected mean diffusivity may represent a cognitive biomarker to complement a disease-modifying trial design. However, because this is the first longitudinal study showing this association and our non-SN ROI outcomes were not corrected for multiple comparisons, these results should be considered preliminary until further data are available.

We did not find any significant longitudinal or post hoc cross-sectional differences at baseline between the IPD-R and IPD-NM groups for any ROI assessment after correction for the intergroup differences in disease durations. In contrast, a recent study did find significantly reduced pSN FW in subjects with IPD-R with a

mean disease duration of 2.3 years compared with subjects with IPD-NM.³⁷ The differences in these findings may be due to differences in sample sizes, IPD cohort disease duration, or MR imaging acquisition techniques. A prospective, randomized longitudinal study addressing the effects of rasagiline on pSN FW is currently in progress.³⁸

The main weakness of our study was the high rate of subject attrition. This may have been due to the original 57 subjects needing to give consent to a new study after a prolonged, 3-year period and due to the more advanced disease duration of our IPD cohort (7.1 years at baseline). The loss of >30% of our original cohort likely diminished our power to detect intergroup differences. The Ofori et al¹⁰ and Loane et al²⁸ longitudinal IPD imaging studies used 1- and 1.5-year follow-up periods and IPD cohorts with disease durations at baseline of 3.0 and 3.9 years, respectively, and had no subject attrition, suggesting these to be preferable follow-up periods and IPD disease durations for maximizing subject retention.^{10,28}

Another weakness of our study was the use of a 4-mm slice thickness for the DTI-based MR imaging sequence with 0.5-mm gaps between slices and only 25 gradient directions. Most of the previously referenced DTI and FW studies used a 2-mm slice thickness without any gaps and 64 gradient directions.^{5,9,10,20,28} The coarser image and angular resolutions from our MR imaging protocol compared with MR imaging protocols of the previous studies likely decreased our sensitivity to detect intergroup differences. Also, the larger MR imaging slice thickness used in our study most likely accounts for the much higher SN FW values, even in HCs, compared with those found in previous studies.^{9,10} Future studies assessing SN FW and/or DTI in IPD would likely benefit from the use of an MR imaging slice thickness close to 2 mm without gaps between slices and a larger number of gradient directions.

CONCLUSIONS

This study supports SN FW assessed by MR imaging as a promising disease-progression biomarker in IPD. Now that 2 independent groups have reported significant increases in SN FW over time in 3 different IPD cohorts, further research is justified on longitudinal SN FW changes in IPD and on longitudinal effects of potential disease-modifying therapies on this neuroimaging outcome.

ACKNOWLEDGMENTS

We thank David E. Vaillancourt for providing example SN ROIs. We also thank all the research participants.

Disclosures: Thomas Guttuso Jr—RELATED: Grant: Teva Neuroscience, Comments: An investigator-initiated grant supported some of this research*; UNRELATED: Consultancy: Teva Neurosciences, US Worldmeds; Payment for Lectures Including Service on Speakers Bureaus: Teva Neurosciences. David G. Lichten—RELATED: Grant: Teva Neuroscience, Comments: investigator-initiated award to T. Guttuso Jr; UNRELATED: Consultancy: US Worldmeds, Comments: Xadago launch; Payment for Lectures Including Service on Speakers Bureaus: Teva Neuroscience, University of

Oklahoma Foundation, *Comments*: Neurology Grand Rounds, University of Oklahoma, Speaker's Bureau, Teva Neuroscience. Ofer Pasternak—*RELATED*: Grant: National Institutes of Health, *Comments*: R01MH108574 and P41EB015902*; *UNRELATED*: *Consulting Fee or Honorarium*: University of Florida. Robert Zivadinov—*RELATED*: Grant: Teva Neuroscience*; *UNRELATED*: Grants/Grants Pending: Sanofi-Genzyme, Novartis, Roche*; *Payment for Lectures Including Service on Speakers Bureau*: Sanofi-Genzyme, Novartis, Roche, Celgene. *Money paid to the institution.

REFERENCES

- Ma SY, Roytta M, Rinne JO, et al. **Correlation between neuromorphometry in the substantia nigra and clinical features in Parkinson's disease using disector counts.** *J Neurol Sci* 1997;151:83–87 CrossRef Medline
- Greffard S, Verny M, Bonnet AM, et al. **Motor score of the Unified Parkinson Disease Rating Scale as a good predictor of Lewy body-associated neuronal loss in the substantia nigra.** *Arch Neurol* 2006; 63:584–88 CrossRef Medline
- Kordower JH, Olanow CW, Dodiya HB, et al. **Disease duration and the integrity of the nigrostriatal system in Parkinson's disease.** *Brain* 2013;136:2419–31 CrossRef Medline
- Alexander AL, Lee JE, Lazar M, et al. **Diffusion tensor imaging of the brain.** *Neurotherapeutics* 2007;4:316–29 CrossRef Medline
- Langley J, Huddleston DE, Merritt M, et al. **Diffusion tensor imaging of the substantia nigra in Parkinson's disease revisited.** *Hum Brain Mapp* 2016;37:2547–56 CrossRef Medline
- Vaillancourt DE, Spraker MB, Prodoehl J, et al. **High-resolution diffusion tensor imaging in the substantia nigra of de novo Parkinson disease.** *Neurology* 2009;72:1378–84 CrossRef Medline
- Pasternak O, Sochen N, Gur Y, et al. **Free water elimination and mapping from diffusion MRI.** *Magn Reson Med* 2009;62:717–30 CrossRef Medline
- Ofori E, Pasternak O, Planetta PJ, et al. **Increased free water in the substantia nigra of Parkinson's disease: a single-site and multi-site study.** *Neurobiol Aging* 2015;36:1097–104 CrossRef Medline
- Planetta PJ, Ofori E, Pasternak O, et al. **Free-water imaging in Parkinson's disease and atypical parkinsonism.** *Brain* 2016;139:495–508 CrossRef Medline
- Ofori E, Pasternak O, Planetta PJ, et al. **Longitudinal changes in free-water within the substantia nigra of Parkinson's disease.** *Brain* 2015;138:2322–31 CrossRef Medline
- Burciu RG, Ofori E, Archer DB, et al. **Progression marker of Parkinson's disease: a 4-year multisite imaging study.** *Brain* 2017;140: 2183–92 CrossRef Medline
- Hely MA, Reid WG, Adena MA, et al. **The Sydney multicenter study of Parkinson's disease: the inevitability of dementia at 20 years.** *Mov Disord* 2008;23:837–44 CrossRef Medline
- Olanow CW, Rascol O, Hauser R, et al; ADAGIO Study Investigators. **A double-blind, delayed-start trial of rasagiline in Parkinson's disease.** *N Engl J Med* 2009;361:1268–78 CrossRef Medline
- Fahn S, Elton RL; UPDRS Development Committee. **The Unified Parkinson's Disease Rating Scale.** In: Fahn S, Marsden CD, Calne DB, et al, eds. *Recent Developments in Parkinson's Disease*. Vol 2. Florham Park: Macmillan Healthcare Information; 1987:153–63
- Gill DJ, Freshman A, Blinder JA, et al. **The Montreal cognitive assessment as a screening tool for cognitive impairment in Parkinson's disease.** *Mov Disord* 2008;23:1043–46 CrossRef Medline
- Folstein MF, Folstein SE, McHugh PR. **"Mini-mental state": a practical method for grading the cognitive state of patients for the clinician.** *J Psychiatr Res* 1975;12:189–98 CrossRef Medline
- Gibb WR, Lees AJ. **The relevance of the Lewy body to the pathogenesis of idiopathic Parkinson's disease.** *J Neurol Neurosurg Psychiatry* 1988;51:745–52 CrossRef Medline
- Andersson JL, Sotiropoulos SN. **An integrated approach to correction for off-resonance effects and subject movement in diffusion MR imaging.** *Neuroimage* 2016;125:1063–78 CrossRef Medline
- Deng B, Zhang Y, Wang L, et al. **Diffusion tensor imaging reveals white matter changes associated with cognitive status in patients with Parkinson's disease.** *Am J Alzheimers Dis Other Demen* 2013;28: 154–64 CrossRef Medline
- Duncan GW, Firbank MJ, Yarnall AJ, et al. **Gray and white matter imaging: a biomarker for cognitive impairment in early Parkinson's disease?** *Mov Disord* 2016;31:103–10 CrossRef Medline
- Fletcher E, Raman M, Huebner P, et al. **Loss of fornix white matter volume as a predictor of cognitive impairment in cognitively normal elderly individuals.** *JAMA Neurol* 2013;70:1389–95 CrossRef Medline
- Melzer TR, Watts R, MacAskill MR, et al. **White matter microstructure deteriorates across cognitive stages in Parkinson disease.** *Neurology* 2013;80:1841–49 CrossRef Medline
- Planetta PJ, Schulze ET, Geary EK, et al. **Thalamic projection fiber integrity in de novo Parkinson disease.** *AJNR Am J Neuroradiol* 2013;34:74–79 CrossRef Medline
- Zhang Y, Brady M, Smith S. **Segmentation of brain MR images through a hidden Markov random field model and the expectation-maximization algorithm.** *IEEE Trans Med Imaging* 2001;20:45–57 CrossRef Medline
- Fonov V, Evans AC, Botteron K, et al; Brain Development Cooperative Group. **Unbiased average age-appropriate atlases for pediatric studies.** *Neuroimage* 2011;54:313–27 CrossRef Medline
- Schuff N, Wu IW, Buckley S, et al. **Diffusion imaging of nigral alterations in early Parkinson's disease with dopaminergic deficits.** *Mov Disord* 2015;30:1885–92 CrossRef Medline
- Metzler-Baddeley C, O'Sullivan MJ, Bells S, et al. **How and how not to correct for CSF-contamination in diffusion MRI.** *Neuroimage* 2012; 59:1394–403 CrossRef Medline
- Loane C, Politis M, Kefalopoulou Z, et al. **Aberrant nigral diffusion in Parkinson's disease: a longitudinal diffusion tensor imaging study.** *Mov Disord* 2016;31:1020–26 CrossRef Medline
- Vaillancourt DE, Spraker MB, Prodoehl J, et al. **Effects of aging on the ventral and dorsal substantia nigra using diffusion tensor imaging.** *Neurobiol Aging* 2012;33:35–42 CrossRef Medline
- Olanow CW, Kieburtz K. **Defining disease-modifying therapies for PD—a road map for moving forward.** *Mov Disord* 2010;25:1774–79 CrossRef Medline
- Pasternak O, Shenton ME, Westin CF. **Estimation of extracellular volume from regularized multi-shell diffusion MRI.** *Med Image Comput Assist Interv* 2012;15(Pt 2):305–12 Medline
- Chung JW, Burciu RG, Ofori E, et al. **Parkinson's disease diffusion MRI is not affected by acute antiparkinsonian medication.** *Neuroimage Clin* 2017;14:417–21 CrossRef Medline
- Reas ET, Hagler DJ Jr, White NS, et al. **Sensitivity of restriction spectrum imaging to memory and neuropathology in Alzheimer's disease.** *Alzheimers Res Ther* 2017;9:55 CrossRef Medline
- Zhang H, Schneider T, Wheeler-Kingshott CA, et al. **NODDI: practical in vivo neurite orientation dispersion and density imaging of the human brain.** *Neuroimage* 2012;61:1000–16 CrossRef Medline
- Kamagata K, Hatano T, Okuzumi A, et al. **Neurite orientation dispersion and density imaging in the substantia nigra in idiopathic Parkinson disease.** *Eur Radiol* 2016;26:2567–77 CrossRef Medline
- Buter TC, van den Hout A, Matthews FE, et al. **Dementia and survival in Parkinson disease: a 12-year population study.** *Neurology* 2008;70:1017–22 CrossRef Medline
- Burciu RG, Ofori E, Shukla P, et al. **Free-water and BOLD imaging changes in Parkinson's disease patients chronically treated with a MAO-B inhibitor.** *Hum Brain Mapp* 2016;37:2894–903 CrossRef Medline
- Vaillancourt DE. **Image Parkinson's Disease Progression Study.** <https://clinicaltrials.gov/ct2/show/NCT02789020?term=vaillancourt&rank=9> Accessed November 24, 2016

Pressure Mapping and Hemodynamic Assessment of Intracranial Dural Sinuses and Dural Arteriovenous Fistulas with 4D Flow MRI

L.A. Rivera-Rivera, K.M. Johnson, P.A. Turski, and O. Wieben



ABSTRACT

SUMMARY: The feasibility of 4D flow MR imaging to visualize flow patterns and generate relative pressure maps in the dural venous sinus in healthy subjects ($n = 60$) and patients with dural arteriovenous fistulas ($n = 7$) was investigated. Dural venous drainage was classified based on torcular Herophili anatomy by using 4D flow MR imaging–derived angiograms and magnitude images. Subjects were scanned in a 3T clinical MR imaging system. 4D flow MR imaging enabled noninvasive characterization of dural sinus anatomy and mapping of relative pressure differences.

ABBREVIATIONS: DAVF = dural arteriovenous fistula; TS = transverse sinus

Venous hypertension is thought to be implicated in dural arteriovenous fistulas (DAVFs) with aggressive presentation.^{1,2} We investigated the use of 4D flow MR imaging for the noninvasive assessment of DAVFs³ through measuring the vascular velocity vector field. These data can be processed for the analysis of the spatial and temporal distributions of flow and pressure gradients,^{4–6} including dural venous sinus pressure and flow patterns. The purpose of this study was to compare 4D flow MR imaging–derived hemodynamics and relative pressure maps in the dural venous drainage of patients with DAVF and healthy subjects. In addition, we report on the anatomic variations found in the dural venous drainage.

MATERIALS AND METHODS

Seven patients (age range, 33–72 years; mean age, 52 years; 2 women) diagnosed with unilateral DAVFs affecting the transverse/sigmoid sinus and 60 healthy subjects (age range, 45–75 years; mean age, 64 years; 32 women) were scanned by using a 3T clinical MR imaging system (MR750; GE Healthcare, Milwaukee, Wisconsin) with an 8-channel head coil. Phase-contrast MR imaging data with 3-directional velocity encoding were acquired with a radially undersampled 4D flow MR imaging sequence, phase contrast with vastly undersampled isotropic projection (PC-VIPR),^{7,8} and the following imaging parameters: velocity encoding = 80 cm/s for control patients (TR, 7.4 ms; TE, 2.7 ms) and 100 cm/s for patients with DAVFs (TR, 7.8 ms; TE, 2.5 ms); FOV = $22 \times 22 \times 16$ cm³; 0.7 mm isotropic resolution; 14,000 projection angles; scan time = ~ 7 minutes; flip angle $\alpha = 10^\circ$; and receiver bandwidth = ± 83 kHz. Magnitude, velocity data, and PC angiograms were all generated with off-line reconstruction. Background phase correction of velocities was performed in Matlab (MathWorks, Natick, Massachusetts), and vessel segmentation was performed semiautomatically (Mimics; Materialise, Leuven, Belgium) from the phase-contrast angiograms. Pressure maps were also calculated in Matlab by using previously validated methods.^{5,6} This approach solves the Navier-Stokes equation by assuming blood is an incompressible Newtonian fluid (density = 1060 kg/m³; viscosity = 3.2 cP). Visualization of pressure differences and flow quantification were carried out in EnSight (CEI, Apex, North Carolina). Flow and area were quantified from cut planes in each transverse sinus (TS), left and right, placed 25 mm from the torcular Herophili, and pressure gradients were quantified as the pressure difference at 25 mm and 50 mm from the torcular Herophili. These measurements were per-

Received July 7, 2017; accepted after revision October 26.

From the Departments of Medical Physics (L.A.R.-R., K.M.J., P.A.T., O.W.) and Radiology (K.M.J., P.A.T., O.W.), University of Wisconsin School of Medicine and Public Health, Madison, Wisconsin.

This work was supported by National Institute on Aging grant P50-AG033514, National Institute of Neurological Disorders and Stroke grant R01NS066982, National Heart, Lung, and Blood Institute grant R01HL072260, National Institute of General Medical Sciences grant R25GM083252, the American Society of Neuroradiology Alzheimer's Grant Award, and GE Healthcare.

Paper previously presented at: Annual Meeting and Exhibition of the International Society for Magnetic Resonance in Medicine, April 22–27, 2017; Honolulu, Hawaii, and Annual Meeting of the American Society of Neuroradiology, April 22–27, 2017; Long Beach, California.

Please address correspondence to Oliver Wieben, PhD, University of Wisconsin-Madison, Room 1127, Wisconsin Institutes for Medical Research, 1111 Highland Ave, Madison, WI 53705-2275; e-mail: owieben@wisc.edu

Indicates open access to non-subscribers at www.ajnr.org

Indicates article with supplemental on-line tables.

Indicates article with supplemental on-line photos.

<http://dx.doi.org/10.3174/ajnr.A5494>

formed by a Ph.D. candidate with 5 years of MR imaging postprocessing experience (L.A.R.-R.). The anatomy of the dural sinuses was classified according to Gökçe et al⁹ based on torcular Herophili anatomy. A senior neuroradiologist (P.A.T., >30 years of experience) inspected the images to determine anatomic classification.

Statistics were assessed by using ANOVA followed by post hoc analysis with the Tukey-Kramer method. Data normality was assessed with quantile-quantile plots. Analysis was performed in Matlab. $P < .05$ was set as the threshold for statistical significance.

RESULTS

Representative color pressure maps in a healthy subject and a patient with DAVF are shown in Fig 1. For the healthy subject (Fig 1A, -D), blood pressure decreased downstream with lower pressure in the TS than in the superior sagittal sinus. However, the

patient with DAVF (Fig 1C, -F) shows a pressure increase in the TS affected by the fistula and a decrease on the TS contralateral to the DAVF. Another patient pressure map and flow streamlines can be found in On-line Figs 1 and 2. The streamlines move retrograde from the site affected by the fistula into the right TS.

The anatomic variations in the dural sinus drainage were catalogued as follows: for healthy subjects, there were 10 type I, 35 type II, and 15 type III variations (On-line Fig 3 and On-line Table 1). For patients with DAVF, there were 5 type I and 2 type II variations. Flow and cross-sectional area measurements in healthy subjects are summarized in On-line Table 2.

Flow and pressure drops in the TS for all subjects are shown in Fig 2. For patients with DAVF, pressure increased along the TS ipsilateral to the fistula with a median of 0.055 ± 0.130 mm Hg, whereas pressure decreased in the TS contralateral to the fistula with a median of -0.367 ± 0.205 mm Hg ($P = .109$). In healthy subjects, the pressure decreased very similarly in both TSs, with values of -0.105 ± 0.033 mm Hg and -0.101 ± 0.043 mm Hg, respectively ($P = .994$). In patients with DAVF, flow in the TS affected by the fistula was 40 ± 129 mL/min, and flow in the TS contralateral to the fistula was 328 ± 134 mL/min ($P = .046$). In healthy subjects, independent of anatomy type, flow was significantly larger in the right TS (262 ± 83 mL/min) compared with the left TS (121 ± 56 mL/min; $P < .001$).

DISCUSSION

Initially, we characterized dural venous sinus pressure in a population of 60 healthy subjects, establishing a reference frame for the interpretation of dural sinus pathology. The main findings of this study are an increase in pressure in the TS ipsilateral to the DAVF compared

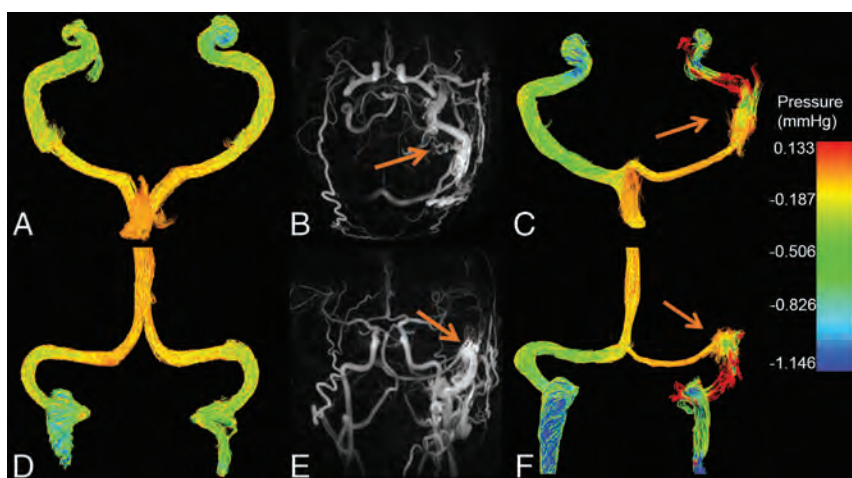


FIG 1. Color pressure maps (mm Hg) in a healthy subject in the axial (A) and coronal (D) planes as well as for a patient (C and F) with a type IIa DAVF affecting the left transverse and sigmoid sinus (arrows). MIP images in the axial (B) and coronal (E) plane show the site of arteriovenous shunting (arrows) where there is increased pressure seen on the axial (C) and coronal (F) pressure maps.

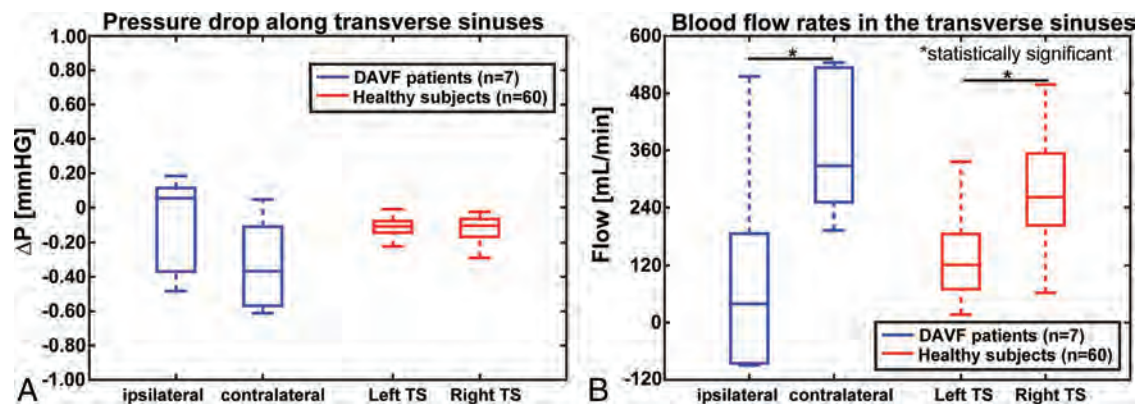


FIG 2. Boxplots showing the pressure change (A) and blood flow rates (B) along the TS in the patients with DAVF ($n = 7$) and healthy subjects ($n = 60$). The pressure drops were computed from the difference in pressure in 2 cut planes placed on each TS. The cut planes were placed 25 mm and 50 mm from the torcular Herophili. The median pressure drop in the ipsilateral and contralateral TS to the DAVF were 0.055 ± 0.130 mm Hg and -0.367 ± 0.205 mm Hg, respectively ($P = .109$). In the healthy subjects, the pressure drops were -0.105 ± 0.033 mm Hg in the left TS and -0.101 ± 0.043 mm Hg in the right TS ($P = .994$). The median blood flow rates in the patients with DAVF show a value of 40 ± 129 mL/min in the TS affected by the fistula and, in the TS contralateral to the fistula, equal to 328 ± 134 mL/min ($P = .046$). The median flow in healthy subjects including all anatomy types was significantly larger in the right TS compared with the left TS, with values of 262 ± 83 mL/min and 121 ± 56 mL/min, respectively ($P < .001$).

with a pressure drop in the contralateral TS. In healthy subjects, the pressure dropped similarly in the left and right TS. These findings suggest asymmetric pressure drops can potentially be used to identify patients with DAVFs, in whom the TS displaying an increase in pressure or smaller pressure drop represents the site affected by the DAVF. During conventional angiography, dural sinus pressure gradients are frequently measured invasively by navigating a coaxial microcatheter to the draining dural sinus. This preliminary study demonstrates that it is feasible to characterize relative pressure in DAVFs noninvasively by using 4D flow MR imaging.

Retrograde dural/cortical venous drainage is a risk factor for intracranial hemorrhage in patients with DAVFs.¹ Consequently, hemodynamic assessment of DAVFs is important for an accurate characterization of severity. Blood flow directionality was successfully assessed for both patients with DAVF and healthy subjects. During this study, 1 patient DAVF classification was changed. Initially, the fistula was classified as type I; after demonstrating retrograde flow in the 4D flow MR imaging, the fistula was reclassified as Type IIa in the Cognard system. The technique described in this study can be implemented to explore other pathologies such as venous stenosis, which is often associated with idiopathic intracranial hypertension and pulsatile tinnitus.¹⁰

There are a number of limitations in this study. First, for group comparisons, we used time-average data because cardiac data were not recorded for all but 1 patient with DAVF. Second, the MR imaging technique we used has some potential inaccuracies in pressure mapping in the presence of turbulent flow, which requires more advanced pressure solvers.¹¹ The pressure maps have not been validated against a criterion standard, which will be addressed in a follow-up study with invasive conventional angiography measures that navigate a coaxial microcatheter to the draining dural sinus. This study will also contain more patients with DAVFs.

CONCLUSIONS

Noninvasive pressure mapping in the dural sinuses is feasible with 4D flow MR imaging. In addition, 4D flow MR imaging allows blood flow directionality assessment along the dural sinuses, which can help clinicians detect retrograde flow in DAVFs.

ACKNOWLEDGMENTS

One of the main contributors to this publication, Zachary J. Clark, MD, passed away suddenly and tragically before this manuscript

was completed. Due to ICJME (international committee of medical journal editors) authorship requirements that all authors have the opportunity to review revisions and proofs prior to publication, Dr. Clark could not be included in the authors list. Zach greatly contributed to this work and will be dearly missed.

Disclosures: Kevin M. Johnson—RELATED: Grants/Grants Pending: National Institutes of Health*; UNRELATED: Consultancy: Vertex Pharmaceuticals; Other: GE Healthcare, Comments: the University of Wisconsin-Madison receives research support from GE Healthcare*. Patrick A. Turski—RELATED: Grants/Grants Pending: National Institutes of Health, Comments: ROI Accelerated Neurovascular MRA*. Oliver Wieben—UNRELATED: Other: GE Healthcare, Comments: research agreement*. *Money paid to the institution.

REFERENCES

1. Gandhi D, Chen J, Pearl M, et al. **Intracranial dural arteriovenous fistulas: classification, imaging findings, and treatment.** *AJNR Am J Neuroradiol* 2012;33:1007–13 CrossRef Medline
2. Bernstein RA, Gress DR. **Dural arteriovenous fistulas and the neurology of venous hypertension.** *Semin Cerebrovasc Dis Stroke* 2004;4:168–75 CrossRef
3. Markl M, Frydrychowicz A, Kozerke S, et al. **4D flow MRI.** *J Magn Reson Imaging* 2012;36:1015–36 CrossRef Medline
4. Tyszka JM, Laidlaw DH, Asa JW, et al. **Three-dimensional, time-resolved (4D) relative pressure mapping using magnetic resonance imaging.** *J Magn Reson Imaging* 2000;12:321–29 CrossRef Medline
5. Moftakhar R, Aagaard-Kienitz B, Johnson K, et al. **Noninvasive measurement of intra-aneurysmal pressure and flow pattern using phase contrast with vastly undersampled isotropic projection imaging.** *AJNR Am J Neuroradiol* 2007;28:1710–14 CrossRef Medline
6. Bley TA, Johnson KM, François CJ, et al. **Noninvasive assessment of transstenotic pressure gradients in porcine renal artery stenoses by using vastly undersampled phase-contrast MR angiography.** *Radiology* 2011;261:266–73 CrossRef Medline
7. Gu T, Korosec FR, Block WF, et al. **PC VIPR: a high-speed 3D phase-contrast method for flow quantification and high-resolution angiography.** *AJNR Am J Neuroradiol* 2005;26:743–49 Medline
8. Johnson KM, Lum DP, Turski PA, et al. **Improved 3D phase contrast MRI with off-resonance corrected dual echo VIPR.** *Magn Reson Med* 2008;60:1329–36 CrossRef Medline
9. Gökçe E, Pınarbaşı T, Acu B, et al. **Torcular Herophili classification and evaluation of dural venous sinus variations using digital subtraction angiography and magnetic resonance venographies.** *Surg Radiol Anat* 2014;36:527–36 CrossRef Medline
10. Lansley JA, Tucker W, Eriksen MR, et al. **Sigmoid sinus diverticulum, dehiscence, and venous sinus stenosis: potential causes of pulsatile tinnitus in patients with idiopathic intracranial hypertension?** *AJNR Am J Neuroradiol* 2017;38:1783–88 CrossRef Medline
11. Ha H, Lantz J, Ziegler M, et al. **Estimating the irreversible pressure drop across a stenosis by quantifying turbulence production using 4D flow MRI.** *Sci Rep* 2017;7:46618 CrossRef Medline

Quantitative Analysis of Conebeam CT for Delineating Stents in Stent-Assisted Coil Embolization

T. Kuriyama, N. Sakai, M. Beppu, C. Sakai, H. Imamura, K. Masago, N. Katakami, and H. Isoda

ABSTRACT

BACKGROUND AND PURPOSE: Innovative techniques and device-related advances have improved the outcomes of neuroendovascular treatment. 3D imaging has previously used 2×2 binning, but 1×1 binning has recently been made available. The aim of this study was to evaluate the quantitative ability of conebeam CT for stent delineation and to investigate its effectiveness in the clinical environment.

MATERIALS AND METHODS: Four acquisition groups of 3D MIP images acquired using conebeam CT with varying conditions (acquisition time, 10 or 20 seconds and binning, 1×1 or 2×2) were compared. Two methods of analysis were performed, a phantom study and an analysis of 28 randomly selected patients. The phantom study assessed the contrast-to-noise ratio and full width at half maximum values in conebeam CT images of intracranial stent struts. In the clinical subjects, we assessed contrast-to-noise ratio, full width at half maximum, and dose-area product.

RESULTS: In the phantom study, the contrast-to-noise ratio was not considerably different between 10- and 20-second acquisition times at equivalent binning settings. Additionally, the contrast-to-noise ratio at equivalent acquisition times did not differ considerably by binning setting. For the full width at half maximum results, equivalent acquisition times differed significantly by binning setting. In the clinical analyses, the 10-second/ 1×1 group (versus 20 second/ 2×2) showed a higher contrast-to-noise ratio ($P < .05$) and a dose-area product reduced by approximately 70% ($P < .05$), but the difference in full width at half maximum was not significant ($P = .20$).

CONCLUSIONS: For stent-assisted coil embolization, quantitative assessment of conebeam CT showed that 10 second/ 1×1 was equivalent to 20 second/ 2×2 for imaging deployed intracranial stents. Furthermore, the 10-second/ 1×1 settings resulted in a much smaller DAP.

ABBREVIATIONS: CBCT = conebeam CT; CNR = contrast-to-noise ratio; FWHM = full width at half maximum; DAP = dose-area product

Outcomes of neuroendovascular treatment have improved because of innovative interventional techniques and advances in medical equipment.¹⁻⁶ There are a variety of coil embolization methods,¹⁻⁴ such as the balloon technique and the stent-assisted techniques, but their purpose is to create thrombosis in the aneurysm sac.^{7,8}

Stent-assisted coil embolization involves complete saccular filling with platinum coils.⁹ Conebeam CT (CBCT) is used to verify the placement of the deployed stent,⁹ stent and vessel wall connections, proper sizing of the stent, and the necessity of re-implantation. Therefore, it is necessary to obtain high-quality 3D images in a timely manner following stent-assisted coil embolization. Stent struts are visible in 3D-MIP images^{10,11} and are generally visible using flat panel detector systems through 2×2 binning. Recently, the development of advanced flat panel detector technology has allowed 1×1 binning of CBCT data to improve the contrast-to-noise ratio (CNR) of CBCT images⁶ and to thus render high-quality 3D vascular images. Because the performance of angiographic systems has improved, conventional CBCT acquisition now has an image resolution equal to that of 3D-DSA images. When the CBCT acquisition time is short, the radiation dose is reduced. The aim of this study was to evaluate the delineation of deployed stents using different combinations of acquisition times and binning settings.

Received August 31, 2017; accepted after revision November 13.

From the Department of Radiological and Medical Laboratory Sciences (T.K., H. Isoda), Nagoya University Graduate School of Medicine, Nagoya, Japan; Divisions of Radiological Technology (T.K.), Neuroendovascular Therapy (N.S., C.S.), and Integrated Oncology (N.K.), Institute of Biomedical Research and Innovation, Kobe, Japan; Division of Neurosurgery (N.S., M.B., H. Imamura), Kobe City Medical Center General Hospital, Kobe, Japan; Department of Pathology and Molecular Diagnostics (K.M.), Aichi Cancer Center, Nagoya, Japan; and Brain & Mind Research Center (H. Isoda), Nagoya University, Nagoya, Japan.

Paper previously presented at: Annual Meeting of The Japanese Society for Neuroendovascular Therapy, November 19–21, 2015; Okayama, Japan.

Please address correspondence to Mr Takumi Kuriyama, 1-1-20, Daikochou, Higashi-ku, Nagoya, 461-8673, Japan; e-mail: t.kuriyama@nagoya-u.jp

<http://dx.doi.org/10.3174/ajnr.A5533>

Table 1: Imaging parameters and conditions for CBCT

	10-Second CBCT	20-Second CBCT
Exposure parameters		
Tube voltage	70 kV	70 kV
Pulse width	12.5 ms	12.5 ms
Radiation exposure	1.20 μ Gy/pulse	1.20 μ Gy/pulse
Binning/focus size/FOV	1 \times 1/0.4 mm/22 cm 2 \times 2/0.6 mm/42 cm	
Acquisition parameters		
Angle step	0.8°/frame	0.4°/frame
Angle	200°	200°
Total frame	250	500
Matrix size/binning	960 ² /2 \times 2 1024 ² /1 \times 1	
Injection condition		
Injection rate	1.0 mL/s	1.0 mL/s
Concentration of contrast medium	14%	14%
X-ray delay time	4.5 seconds	4.5 seconds
Injection time of contrast medium	14.5 seconds	24.5 seconds

MATERIALS AND METHODS

Acquisition Time and Binning in the Phantom Study

A phantom was made with a 10-mL syringe and a stent filled with saline. The phantom stent was a newest generation, self-expandable, closed-cell device (Enterprise vascular reconstruction device; Codman & Shurtleff, Raynham, Massachusetts). The phantom was then placed onto a cradle in the air. All CBCT images were acquired with a biplane flat panel detector (30 \times 40 cm) angiographic system (Artis Q BA Twin; Siemens, Erlangen, Germany). Table 1 shows the conditions of the CBCT imaging. We used 4 combinations of acquisition times and binning settings: a 10-second acquisition time with 1 \times 1 binning (10 second/1 \times 1), a 10-second acquisition time with 2 \times 2 binning (10 second/2 \times 2), a 20-second acquisition time with 1 \times 1 binning (20 second/1 \times 1), and a 20-second acquisition time with 2 \times 2 binning (20 second/2 \times 2). The data generated were transferred to a commercially available workstation (syngo X Workplace; Siemens) for postprocessing of 3D-MIP images. The following settings were applied to reconstruct the MIP image dataset: kernel, Hounsfield unit; image characteristics, sharp. The postprocessing was performed with a volume of approximately 7.5 \times 7.5 \times 7.5 cm and a 512 \times 512 matrix, which yielded an isotropic voxel size of 0.15 mm. The 3D-MIP reconstructions of each aneurysm were generated in an oblique orientation with a 1.5-mm section thickness. All reconstructed CBCT data were then downloaded to a personal computer using the DICOM format.

The image-processing software is freely available on-line (ImageJ, Version 1.43; National Institutes of Health; <https://imagej.nih.gov/ij/>). The CNR was measured for the stent strut and the background using an ROI (0.5 \times 0.5 mm) in a phantom filled with diluted contrast media (iopamidol, Iopamiron 300; Bayer Yakuhin, Osaka, Japan). The concentrations of contrast media used were 10%, 15%, 20%, and 25% diluted with saline. The CNR was measured at 5 ROIs expressed as mean \pm SD. An experienced (>15 years) radiologic technologist determined the full width at half maximum (FWHM) and CNR values and calculated the mean, SD, median, and 95% confidence interval values.

Image processing was performed manually by drawing lines perpendicular to the stent strut to create a plot profile curve and then measuring the FWHM. However, we observed that the FWHM was susceptible to underestimation within the contrast

medium. Thus, we chose not to use contrast medium. The FWHM was then measured at 5 points, expressed as mean \pm SD.

Acquisition Time and Binning in Clinical Subsets

This retrospective study was approved by the ethics committees at our institutions (Nagoya University Graduate School of Medicine, Nagoya, Japan; and Institute of Biomedical Research and Innovation, Kobe, Japan). Twenty-eight patients (18 women, 10 men; 64 \pm 12 years of age; range, 36–78 years of age) were included in this study. Each patient had been treated for a single cerebral aneurysm by stent-assisted coil embolization. Twenty

patients (71%) had been treated for anterior circulation aneurysms, while the remaining 8 patients (29%) had been treated for posterior circulation aneurysms. Subjects were divided into 2 acquisition groups of 14 patients each: group A, 20-second acquisition time and 2 \times 2 binning (May 2015 to June 2015), and group B, 10-second acquisition time and 1 \times 1 binning (July 2015 to August 2015). Two syringes were prepared for a dual head injector (Press Duo; Nemoto Kyorindo, Tokyo, Japan), one with a 15% concentration of contrast medium delivered to delineate the stent and another with a 100% concentration of contrast medium delivered to delineate the vessel and aneurysm. We did not analyze the delineation images that were obtained with the 100% contrast medium. In all patients, stent deployments were safely achieved at the desired sites.

All reconstructed CBCT data were downloaded to a personal computer using the DICOM format. Both patient subsets (groups A and B) were analyzed with FWHM of the stent strut and by CNR of the stent in the phantom study. To determine the CNR and FWHM values of the implanted stents, we used an ROI-based method equivalent to that described for the phantom study (Fig 1, upper row). The units for the contrast values are Hounsfield unit_{CBCT} and were determined from the CBCT images. Dose-area product (DAP; microgray \times square centimeter) values of both groups were then investigated to determine radiation exposure.

Data Analysis

All statistical analyses were performed in Excel, Version 14.6.4 for Mac (Microsoft, Redmond, Washington). In the phantom study, a 2-sided *t* test was used to analyze correlations within the 4 groups of different combinations of acquisition times and binning. Statistical significance was set at a corrected *P* < .01 using the Bonferroni correction for the phantom experiments.¹² For the patient subsets, the nonparametric *U* test was applied to analyze correlations. Statistical significance was set at *P* < .05 for analysis of the patient experiments.

RESULTS

Acquisition Time and Binning in the Phantom Study

Figure 1 shows 3D-MIP images of the phantom stent at various concentrations of contrast medium. We measured contrast values

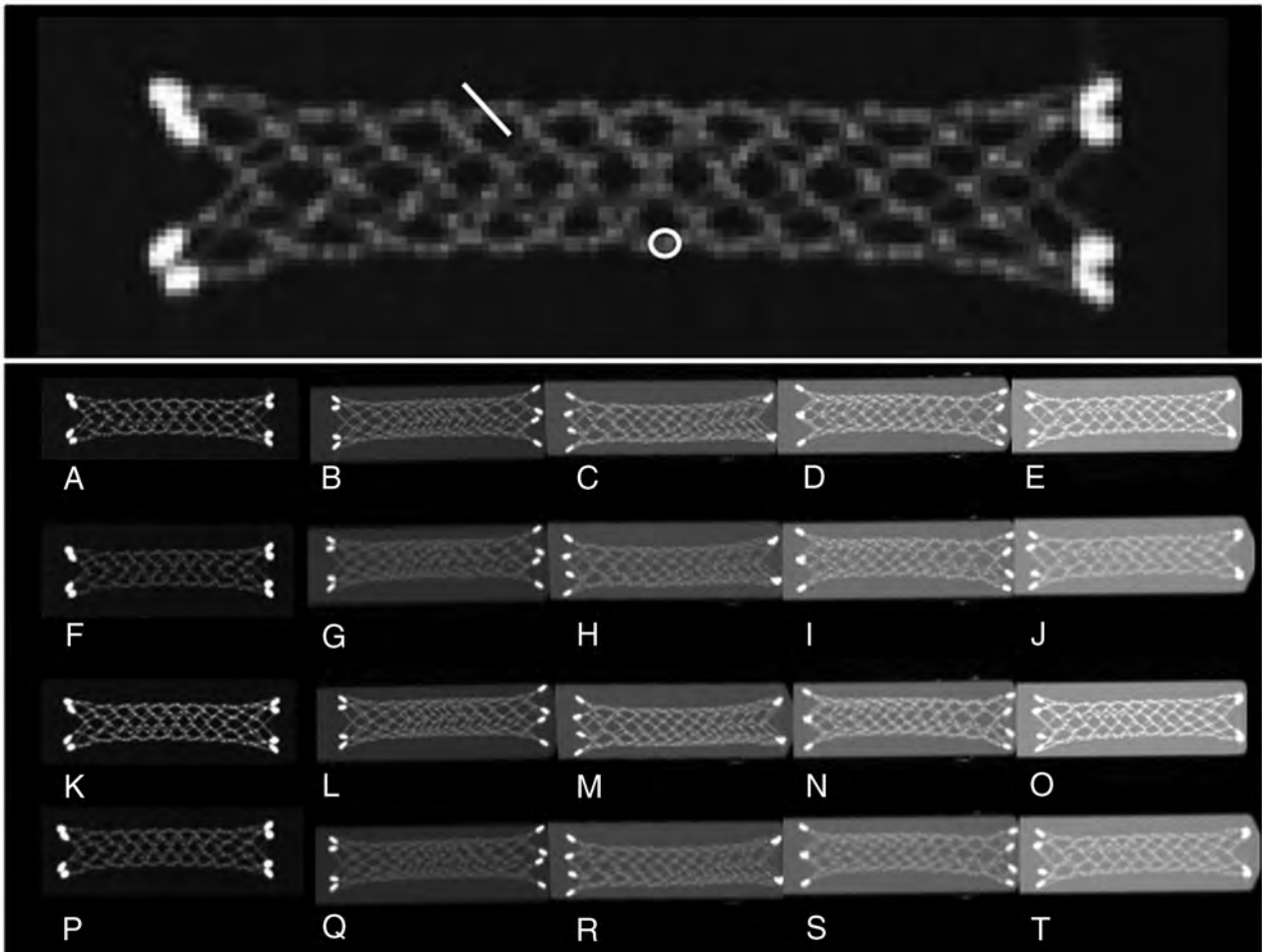


FIG 1. 3D-MIP images of phantom stents at various concentrations of contrast medium.

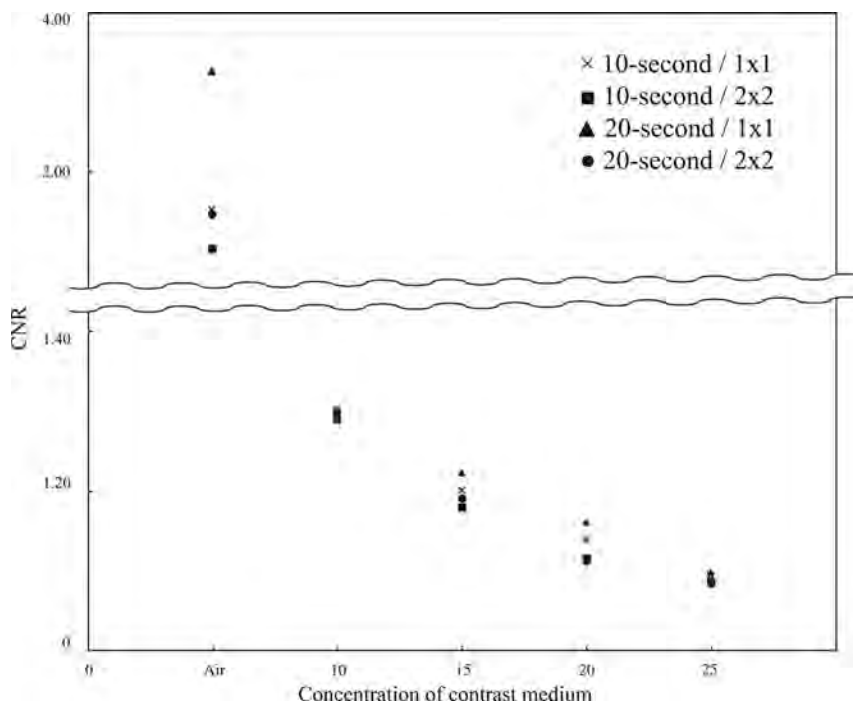


FIG 2. CNR of a phantom stent imaged at various settings (10- or 20-second acquisition time, 1×1 or 2×2 binning) plotted against increasing concentrations of contrast medium.

using contrast medium concentrations ranging from 10% to 25%. The phantom was filled with contrast medium to confirm that the contrast of the stent did not decrease in the contrast medium. The contrast value was the difference between the contrast value of the stent and that of the contrast medium. The contrast values in the MIP images of the stents increased when contrast medium was added. In Fig 2, the CNR of the stent is plotted at various settings (10- or 20-second acquisition; 1×1 or 2×2 binning) against the concentration of contrast medium (0% [saline], 10%, 15%, 20%, and 25%). *P* values for differences in CNR values of the phantom stent strut images by acquisition time/binning settings and contrast medium concentration are presented in Table 2.

At 10% concentration of the contrast medium, we observed that the stent strut was delineated and enhancement was marginal for the phantom. At 25% concentration of the contrast medium,

Table 2: P values for differences in contrast-to-noise ratios of phantom stent struts by acquisition time/binning level at various contrast medium concentrations

Acquisition Combination (Sec/Binning vs Sec/Binning)	Concentration of Contrast Medium			
	Just Saline	10%	15%	20%
10/1 × 1 vs 10/2 × 2	.9328	.5888	.2733	.2734
10/1 × 1 vs 20/1 × 1	.9419	.9828	.2595	.4224
10/1 × 1 vs 20/2 × 2	.0019	.9413	.6592	.2044
10/2 × 2 vs 20/1 × 1	.0257	.1573	.0088	.0145
10/2 × 2 vs 20/2 × 2	.9985	.8009	.2948	.5754
20/1 × 1 vs 20/2 × 2	.0568	.9481	.092	.0113

All numbers represent P values.

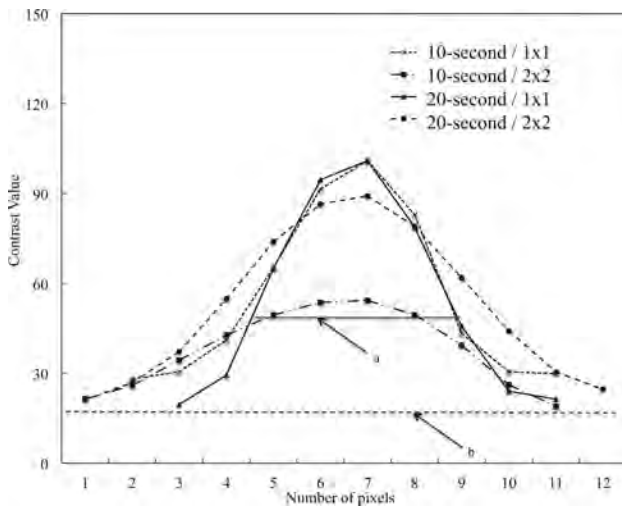


FIG 3. FWHM values of the phantom stent images obtained in saline at various settings (10- or 20-second acquisition time; 1 × 1 or 2 × 2 binning).

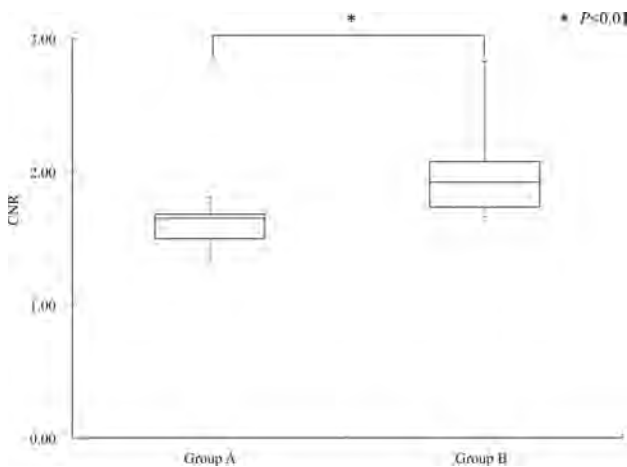


FIG 4. CNR of stent struts imaged with CBCT with a 15% concentration of contrast medium in groups A and B.

stent visualization was difficult and enhancement was high for the phantom (Fig 1). There was not a significant difference in CNR between the 10- and 20-second acquisition times at equivalent binning settings.

Figure 3 shows a plot of FWHM results for the phantom stent strut imaged at various settings (10- or 20-second acquisition; 1 × 1 or 2 × 2 binning) while set in a cradle in air. FWHM values of the stent strut were as follows: 10 second/1 × 1, 0.37 ± 0.04 mm; 10 second/2 × 2, 0.59 ± 0.09 mm; 20 second/1 × 1, 0.35 ± 0.04 mm;

and 20 second/2 × 2, 0.51 ± 0.12 mm. There was no significant difference between 10-second and 20-second acquisition times at equivalent binning settings (10 second/1 × 1 versus 20 second/1 × 1, $P = .5796$; 10 second/2 × 2 versus 20 second/2 × 2, $P = .2725$). However, FWHM with equivalent acquisition times differed significantly by binning settings (10 second/1 × 1 versus 10 second/2 × 2, $P = .0011$; 20 second/1 × 1 versus 20 second/2 × 2, $P = .0242$). The

results for comparisons of different acquisition times and different binning settings were as follows: 10 second/1 × 1 versus 20 second/2 × 2, $P = .0371$; 10 second/2 × 2 versus 20 second/1 × 1, $P = .0007$.

Acquisition Time and Binning in Clinical Subsets A versus B

Figure 4 shows the CNR values from CBCT images of the stent struts. The CBCT images were obtained with a 15% concentration of contrast medium in both groups. The nonparametric analysis comparing CNR values between clinical subjects in group A (20 second/2 × 2) (median, 1.65; 95% CI, 1.50–1.68) and those in group B (10 second/1 × 1) (median, 1.92; 95% CI, 1.73–2.08) showed that the 2 groups differed significantly ($P < .05$).

Figure 5 presents FWHM results for the stent strut on CBCT images obtained with a 15% concentration of contrast medium in both groups A and B. There were no significant differences in the nonparametric analysis of FWHM between the clinical subjects in group A (median, 0.73 mm; 95% CI, 0.63–0.83 mm) and those in group B (median, 0.65 mm; 95% CI, 0.62–0.80 mm; $P = .1985$).

Figure 6 shows the DAP results of the clinical subjects in groups A and B. The DAP values differed significantly between group A (median, 3574 $\mu\text{Gy} \cdot \text{cm}^2$; 95% CI, 3123–4061 $\mu\text{Gy} \cdot \text{cm}^2$) and group B (median, 1035 $\mu\text{Gy} \cdot \text{cm}^2$; 95% CI, 999–1109 $\mu\text{Gy} \cdot \text{cm}^2$; $P < .05$).

Figure 7 shows 3D-MIP images of 2 representative patients. The images were obtained with a 15% concentration of contrast medium. The degree of stent delineation in images obtained with 10 second/1 × 1 (group B, Fig 7B) was statistically like that in images obtained with 20 second/2 × 2 (group A, Fig 7A).

DISCUSSION

Acquisition Time and Binning in the Phantom Study

We confirmed that the CNR resulting from 1 × 1 binning was approximately the same as that obtained from 2 × 2 binning (Fig 2). Ultimately, CBCT performed with 10 second/1 × 1 and a 15% concentration of contrast medium produced images that were satisfactory for viewing the deployed stent position and vessels (Fig 1).

In terms of binning, projection images^{13–16} were converted using the algorithm of Veldkamp et al,¹³ which corrects the offset and sensitivity of the flat panel detector while allowing geometric distortion of the subject's FOV. On processing values for all angles, a convolution was performed with a Shepp & Logan filter. The action of 2 × 2 binning causes 4 pixels to be likened to 1 pixel.

With nonlinear interpolation, the default value of 14 bits per pixel is expanded to 16 bits (Fig 1F–J and P–T). However, 1×1 binning portrays contrast at a 16-bit level, matching each voxel with a

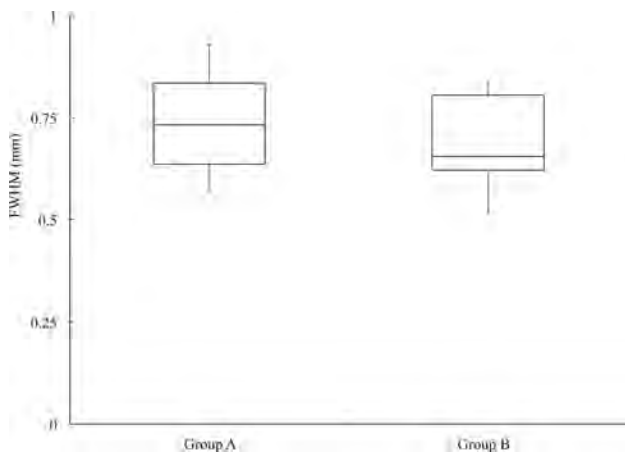


FIG 5. FWHM of the stent strut on CBCT images with a 15% concentration of contrast medium in groups A and B.

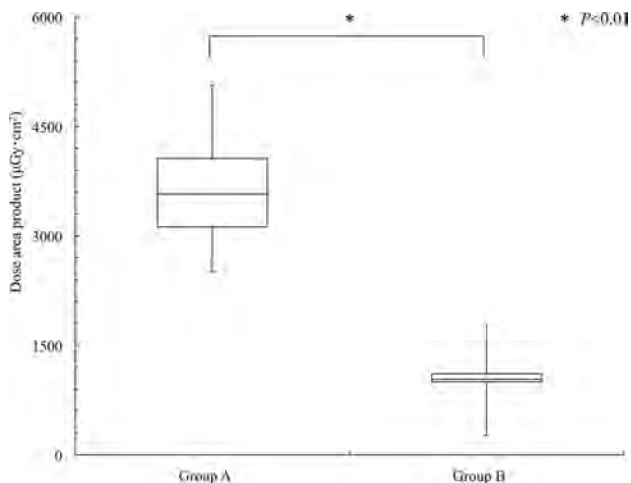


FIG 6. The DAP values in groups A and B.

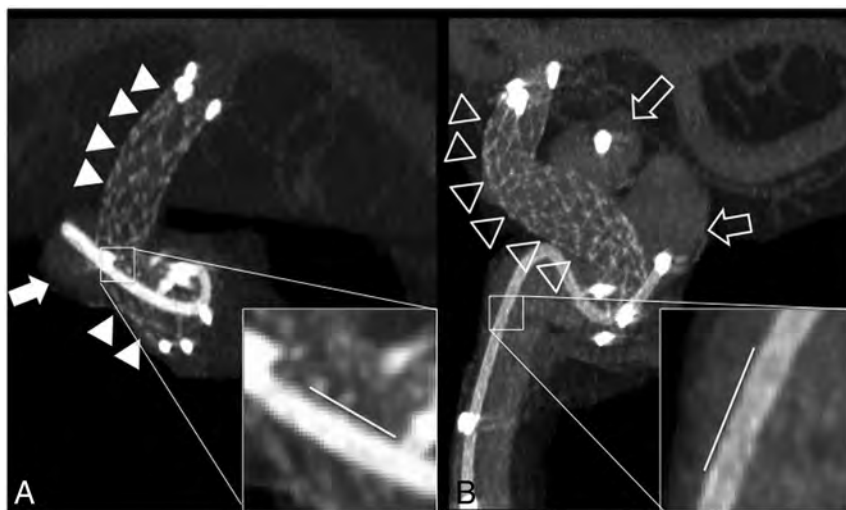


FIG 7. 3D-MIP images of 2 clinical cases imaged with different acquisition times and binning settings and a 15% concentration of contrast medium.

corresponding pixel (Fig 1 A–E and K–O). CBCT imaging with 1×1 binning can therefore produce greater density and spatial resolution. Ultimately, CBCT imaging with a 10-second acquisition time, 1×1 binning, and use of 15% contrast medium can be sufficient to provide satisfactory CBCT images for overview of the deployed stent position and vessels. It is easier to delineate blood vessels if a higher concentration of contrast medium is used in the blood vessels; thus, a higher concentration of contrast medium makes it easier to evaluate the relationship between the deployed stent position and blood vessels.

Acquisition Time and Binning in Clinical Subsets A and B

Our phantom study results suggested that images obtained with 10-second acquisition times and 1×1 binning have better CNR ($P < .01$) and FWHM ($P = .0371$) values compared with those obtained with 20-second acquisition times and 2×2 binning. The reconstructed CBCT images¹³ obtained with 10-second acquisition times had fewer projections; therefore, jagged borders were visible. With the 20-second acquisitions, there were more projections; therefore, borders were displayed more smoothly. Despite a lack of a qualitative advantage in visualization, these features make 10-second acquisition/ 1×1 binning preferable because these settings benefit the patient in the stent-assisted coil embolization technique.

The 28 clinical subjects who underwent stent-assisted coil embolization were divided into 2 groups of 14 patients each. The CBCT images for group A were obtained with 20-second acquisition times and 2×2 binning, while those for group B were obtained with 10-second acquisition times and 1×1 binning. We observed significant differences in CNR values between the groups ($P < .05$, Fig 4), but no significant difference was observed in FWHM values ($P = .1985$, Fig 5). Thus, the CBCT images of the deployed stents were qualitatively similar between the 2 groups. Images obtained in group B had a qualitative disadvantage due to a reduced number of projections, but these images were still sufficient to determine the relationship among the stent, the blood vessels, and the cerebral aneurysm.

The American Association of Physicists in Medicine reported

that the radiation dose from a single rotation of a conebeam around a stationary phantom the size of a human head is approximately equal to the absorbed radiation dose for fan-beam scanning.¹⁷ There have been reports that when the same area is imaged, the DAP in CBCT is similar to the CT dose index in multidetector CT without a moving cradle.^{18–21} The data acquired from group B images were approximately half of the data acquired from group A images. However, the DAP values observed in group B were reduced by approximately 70% compared with the patients in group A. The size of the detector was only 30×40 cm, and the magnification of C-arm CBCT is usually between 1.5 and 2. With 1.5 as an example, the maximal FOV in our study was only $40/1.5 = 27$ cm. An

FOV of 22 cm might be too small to image the head because some structures, such as the nose/ear, might generate truncation artifacts. In this study, the 2-cm FOV was meant to image the implanted stent rather than the whole brain. Not only was the radiation exposure reduced in group B, but the data transfer and reconstruction times were also shorter. These results imply that a 10-second acquisition time with 1×1 binning is beneficial to the patient undergoing a stent-assisted coil embolization technique. We therefore recommend the use of CBCT imaging for patients undergoing stent treatment of cerebral aneurysm to lower radiation exposure. Because DAP does not always indicate a reduction in effective patient dose, further study will be needed to confirm our initial findings.

The primary limitation of this study was the inability to qualitatively evaluate CBCT images of the deployed stents. Additionally, the small size of our patient sample was due, in part, to the difficulty in selecting only subjects who received a certain type of stent implant. As the quality of stents for neuroendovascular treatment continues to improve, the need to delineate stents with low radiation exposure will also increase.

CONCLUSIONS

In our study, CBCT phantom stent strut images with 10-second acquisition times and 1×1 binning showed significantly better CNR and FWHM values compared with images obtained using 20-second acquisition times and 2×2 binning. Clinical results showed that FWHM values did not differ significantly between a 10-second/ 1×1 and a 20-second/ 2×2 group. However, patients in the 10-second/ 1×1 group received approximately 70% less radiation exposure compared with the patients in the 20-second/ 2×2 group. On the basis of our current study, the benefits of 1×1 binning in diagnostic imaging make it a ready successor to standard 2×2 binning for gauging the stability of stents in stent-assisted coil embolization.

Disclosures: Nobuyuki Sakai—UNRELATED: Grants/Grants Pending: Terumo; Payment for Lectures Including Service on Speakers Bureaus: Achieva, BioMedical Solutions, Daiichi Sankyo, Johnson & Johnson, Medtronic, NeuroVasc, Otsuka Pharma, Penumbra, Philips Healthcare, Rebound Therapeutics, Siemens, Terumo, Stryker.

REFERENCES

1. Kwon OK, Kim SH, Kwon BJ, et al. **Endovascular treatment of wide-necked aneurysms by using two microcatheters: techniques and outcomes in 25 patients.** *AJNR Am J Neuroradiol* 2005;26:894–900 Medline
2. Mocco J, Snyder KV, Albuquerque FC, et al. **Treatment of intracranial aneurysm with the Enterprise stent: a multicenter registry.** *J Neurosurg* 2009;110:35–39 CrossRef Medline
3. Yang X, Wu Z, Mu S, et al. **Endovascular treatment of giant and large intracranial aneurysm using the Neuroform stent-assisted coil placement.** *Neurol Res* 2008;30:598–602 CrossRef Medline
4. Yavus K, Geyik S, Saatci I, et al. **WingSpan stent system in the endovascular treatment of intracranial aneurysm: clinical experience with midterm follow-up results.** *J Neurosurg* 2008;109:445–53 CrossRef Medline
5. Imamura H, Sakai N, Adachi H, et al. **Long-term results of endovascular embolization of cerebral aneurysms.** *Journal of Neuroendovascular Therapy* 2010;4:133–9 CrossRef
6. van der Bom IM, Hou SY, Puri AS, et al. **Reduction of coil mass artifacts in high-resolution flat detector conebeam CT of cerebral stent-assisted coiling.** *AJNR Am J Neuroradiol* 2013;34:2163–70 CrossRef Medline
7. Higashida RT, Halbach VV, Dowd CF, et al. **Initial clinical experience with a new self-expanding nitinol stent for the treatment of intracranial cerebral aneurysms: the Cordis Enterprise stent.** *AJNR Am J Neuroradiol* 2005;26:1751–56 Medline
8. Tamatani S, Ito Y, Abe H, et al. **Evaluation of the stability of aneurysms after embolization using detachable coils: correlation between stability of aneurysms and embolized volume of aneurysms.** *AJNR Am J Neuroradiol* 2002;23:762–67 Medline
9. Kuriyama T, Sakai N, Niida N, et al. **Dose reduction in cone-beam CT scanning for intracranial stent deployment before coil embolization of intracranial wide-neck aneurysms.** *Interv Neuroradiol* 2016;22:420–25 CrossRef Medline
10. Patel NV, Gounis MJ, Wakhloo AK, et al. **Contrast-enhanced angiographic cone-beam CT of cerebrovascular stents: experimental optimization and clinical application.** *AJNR Am J Neuroradiol* 2011;32:137–44 CrossRef Medline
11. Benndorf G, Strother CM, Claus B, et al. **Angiographic CT in cerebrovascular stenting.** *AJNR Am J Neuroradiol* 2005;26:1813–18 CrossRef Medline
12. Armstrong RA. **When to use the Bonferroni correction.** *Ophthalmic Physiol Opt* 2014;34:502–08 CrossRef
13. Veldkamp WJ, Joemai RM, van der Molen AJ, et al. **Development and validation of segmentation and interpolation techniques in sonograms for metal artifact suppression in CT.** *Med Phys* 2010;37:620–28 CrossRef Medline
14. Abdoli M, De Jong JR, Pruijm J, et al. **Reduction of artefacts caused by hip implants in CT-based attenuation-corrected PET images using 2-D interpolation of a virtual sinogram on an irregular grid.** *Eur J Nucl Med Mol Imaging* 2011;38:2257–68 CrossRef Medline
15. Zhao S, Robeltson D, Wang G, et al. **X-ray CT metal artifact reduction using wavelets: an application for imaging total hip prostheses.** *IEEE Trans Med Imaging* 2000;19:1238–47 CrossRef Medline
16. Kachelrie M, Watzke O, Kalender WA. **Generalized multi-dimensional adaptive filtering for conventional and spiral single-slice, multi-slice, and cone-beam CT.** *Med Phys* 2001;28:475–90 CrossRef Medline
17. AAPM: Report No. 111: Comprehensive Methodology for the Evaluation of Radiation Dose in X-Ray Computed Tomography (2010). http://www.aapm.org/pubs/reports/RPT_111.pdf. html Accessed October 15, 2017
18. Shope T, Gagne R, Johnson G. **A method for describing the doses delivered by transmission x-ray computed tomography.** *Med Phys* 1981;8:488–95 CrossRef Medline
19. Mori S, Endo M, Nishizawa K, et al. **Enlarged longitudinal dose profiles in cone-beam CT and the need for modified dosimetry.** *Med Phys* 2005;32:1061–69 CrossRef Medline
20. Fahrig R, Dixon RL, Payne T, et al. **Dose and image quality for a cone-beam C-arm CT system.** *Med Phys* 2006;33:4541–50 CrossRef Medline
21. Khan AN, Shuaib W, Nikolic B, et al. **Absorbed radiation dose in radiosensitive organs using 64- and 320-row multidetector computed tomography: a comparative study.** *Scientifica (Cairo)* 2014;2014:305942 CrossRef Medline

Endovascular Thrombectomy in Wake-Up Stroke and Stroke with Unknown Symptom Onset

 P. Bücke,  M. Aguilar Pérez,  V. Hellstern,  M. AlMatter,  H. Bänzner, and  H. Henkes



ABSTRACT

BACKGROUND AND PURPOSE: Mechanical thrombectomy in acute ischemic stroke within 6 hours of symptom onset is effective and safe. However, in many patients, information on the beginning of symptoms is not available. Patients can be divided into those with wake-up stroke and daytime-unwitnessed stroke. Evidence on outcome and complications after mechanical thrombectomy in wake-up stroke and daytime-unwitnessed stroke is rare. A potential beneficial effect of mechanical thrombectomy in selected patients with wake-up stroke or daytime-unwitnessed stroke is suspected.

MATERIALS AND METHODS: We analyzed 1073 patients with anterior circulation stroke undergoing mechanical thrombectomy between 2010 and 2016. Patients with wake-up stroke and daytime-unwitnessed stroke were compared with controls receiving mechanical thrombectomy as the standard of care. We assessed good functional outcome (mRS ≤ 2 at 3 months), mortality rates, and frequencies of symptomatic intracranial hemorrhage. Subgroup analyses tried to detect influences of patient selection via further imaging modalities (MR imaging, CTP; wake-up stroke [advanced], daytime-unwitnessed stroke [advanced]) on outcome and safety.

RESULTS: There was no significant difference in good functional outcome between patients with wake-up stroke and controls (35.9% versus 38.3%, $P = .625$). Outcome in patients with daytime-unwitnessed stroke was inferior compared with controls (27.3%, $P = .007$). Groups did not differ in all-cause mortality at day 90 ($P = .224$) and the rate of symptomatic intracranial hemorrhage ($P = .292$). Advanced imaging improved the frequency of good functional outcome (non-wake-up stroke [advanced] versus wake-up stroke [advanced]: OR, 2.92; 95% CI, 1.32–6.45; non-daytime-unwitnessed stroke [advanced] versus daytime-unwitnessed stroke [advanced]: OR, 2.09; 95% CI, 1.03–4.25) with an additional reduction in all-cause mortality (non-daytime-unwitnessed stroke [advanced] versus daytime-unwitnessed stroke [advanced]: OR, 0.42; 95% CI, 0.20–0.88).

CONCLUSIONS: Mechanical thrombectomy in selected patients with wake-up stroke allows a good functional outcome comparable with that of controls. Outcome after mechanical thrombectomy in daytime-unwitnessed stroke seems to be inferior compared with that in controls. Advanced imaging modalities may increase the frequency of good functional outcome in both patients with wake-up stroke and daytime-unwitnessed stroke.

ABBREVIATIONS: aTE = aspiration thrombectomy; DUS = daytime-unwitnessed stroke; mTE = mechanical thrombectomy; WUS = wake-up stroke

Mechanical thrombectomy (mTE) in acute ischemic stroke due to embolic large-vessel occlusion has been shown to be effective and safe. Several randomized controlled trials have demonstrated the superiority of mTE in combination with intrave-

nous thrombolysis compared with intravenous thrombolysis alone.^{1–5} Subsequently, specific recommendations for patient selection and execution of mTE and/or aspiration thrombectomy (aTE) were implemented (eg, initiation within 6 hours after symptom onset).⁶ However, in many patients, information on the beginning of stroke symptoms is not available. They might therefore be excluded from beneficial endovascular therapy. Evidence on mTE in a prolonged time window is inconsistent, and data on the efficacy and safety of mTE in patients with unknown symptom onset are rare.^{7–9}

Received August 21, 2017; accepted after revision November 13.

From the Psychiatric University Hospital Zurich (P.B.), University of Zurich, Zurich, Switzerland; Neurological Clinic (P.B., H.B.) and Neuroradiological Clinic (M.A.P., V.H., M.A., H.H.), Klinikum Stuttgart, Stuttgart, Germany; and Medical Faculty (H.H.), University Duisburg-Essen, Essen, Germany.

Please address correspondence to Philipp Bücke, MD, Neurological Clinic, Klinikum Stuttgart, Kriegsbergstr 60-62, 70174 Stuttgart, Germany; e-mail: philipp.buecke@gmail.com

 Indicates article with supplemental on-line tables.

 Indicates article with supplemental on-line photos.

<http://dx.doi.org/10.3174/ajnr.A5540>

MATERIALS AND METHODS

From our ongoing prospective single-center stroke registry, consecutive patients treated with mTE/aTE between January 2010 and December 2016 were considered for this retrospective non-

interventional analysis. Patients were either primarily treated in our center (Neurozentrum, Klinikum Stuttgart) or secondarily transferred from hospitals in surrounding cities.¹⁰ Nonetheless, enrollment was based on the initial intention to treat patients via mTE/aTE. There was no secondary triage, selection procedure, or additional imaging before the intervention. The study was approved by the local institutional review board.

Study Population

Patients with an anterior circulation stroke due to an occlusion of the ICA, the intracranial carotid bifurcation, or an M1 or M2 branch of the MCA were included. Patients with an occlusion of an MCA M3 branch, the anterior cerebral artery, or the posterior circulation were excluded. In case of an initial proximal vessel occlusion that was later found recanalized during angiography (spontaneously or after intravenous thrombolysis), datasets were removed from further analysis. We did exclude patients who were not treated according to current recommendations (eg, because of a delayed treatment onset) unless they were classified as having wake-up stroke (WUS) or daytime-unwitnessed stroke (DUS).⁶ Further exclusion criteria were the following: stent angioplasty without mTE/aTE due to high-grade intra- or extracranial stenosis or dissection because of anticipated differences in clinical outcome; the application of older generation stent retrievers and aspiration systems not used in recent randomized controlled trials (the following stent retrievers and aspiration systems were included: Solitaire FR, Medtronic, Minneapolis, Minnesota; pREset, phenox, Bochum, Germany; ACE aspiration catheters, Penumbra, Alameda, California; and Sofia, MicroVention, Tustin, California); and the lack of a 3-month follow-up. Datasets with inconsistent information that could not be verified were excluded.

Patients treated within 6 hours of symptom onset (according to current guidelines) were included in the control group (C). Because of expected differences in pathophysiology and outcome, patients with an unknown symptom onset were divided in the following manner: 1) WUS, occurring out of sleep in the early morning hours; 2) DUS.^{11–13} WUS was defined as stroke symptoms being present during awakening. Patients had to be asymptomatic when going to sleep and during the night. DUS included patients who were asymptomatic while waking up or had recognized symptoms at some point during day or night. Patients without information on “last seen well” who could not be specified as having WUS by the assessing neurologist were subsumed in DUS.

Subgroup analyses were conducted using consecutive steps in patient selection: 1) further imaging modalities with CTP or MR imaging allowing patient selection due to a mismatch concept (CBV versus TTP or MTT in CTP, FLAIR-DWI mismatch in MR imaging; WUS[advanced], DUS[advanced]); and 2) advanced imaging with MR imaging only (WUS[mri], DUS[mri]).^{14–19} Examples of mismatch in both MR imaging and CTP are shown in On-line Figs 1–3. The decision to perform advanced imaging was made by the respective stroke specialist. In patients without CTP or MR imaging, we routinely opted for mTE when there was a proved vessel occlusion (eg, in CTA, hyperdense vessel sign), no major demarcation of infarcted tissue on plain CT, or an ASPECTS score of ≥ 4 . There was no fixed CTP protocol (eg,

quantitative measurement or thresholds defining mismatch). Information on a possible mismatch was reported by the referring hospital or our neuroradiology department. The results were validated by the neurointerventionalist before endovascular therapy. WUS[mri] and DUS[mri] were subsequently compared with a selected control group (C[mri]) with MR imaging as the initial imaging technique. To detect a possible effect of imaging selection on outcome, we compared patients with WUS and DUS in subgroups 1 and 2 with the remaining patients with WUS or DUS not part of the respective group (eg, WUS[mri] versus non-WUS[mri]).

Outcome Measures

Primary outcome measure was mRS at day 90, with mRS 0–2 indicating good functional outcome. Secondary outcome measures were the following: 1) development of a symptomatic intracranial hemorrhage according to the Solitaire with the Intention for Thrombectomy as Primary Endovascular Treatment for Acute Ischemic Stroke (SWIFT PRIME) criteria (parenchymal hemorrhage type 1 or 2, SAH, or intraventricular hemorrhage within 24 hours after mTE with a deterioration in the NIHSS score of ≥ 4 points or leading to death)²⁰; 2) in-hospital mortality; and 3) all-cause mortality at day 90.

Data Collection

Information on age, sex, medical history, stroke onset, NIHSS, imaging technique, mRS score, and stroke etiology was drawn from referral letters, admission notes, or discharge papers. Imaging times were stored in our PACS. Periprocedural information (eg, TICI scores) was documented by the neuroradiology department. Follow-up data were collected by our study nurse via telephone calls.

Statistical Analysis

Numeric baseline characteristics were described in medians (quartiles) or means (SDs). Categorical baseline parameters were described in frequencies. For comparing groups, the Fisher exact test or the χ^2 test was used for categorical parameters. Numeric parameters were analyzed with the Kruskal-Wallis-test or the Mann-Whitney *U* test as appropriate. Dichotomized outcome (head-to-head comparison of groups) was evaluated in a univariate logistic regression model adjusting for possible confounders (based on literature research; baseline-NIHSS, age, ICA occlusion, stroke etiology, imaging-to-groin time, diabetes mellitus, and hypertension). A *P* value $< .05$ was considered statistically significant. STATA/IC 13.1 for Windows (StataCorp, College Station, Texas) was used for statistical analysis.

RESULTS

Between January 2010 and December 2016, one thousand nine hundred sixty-one patients were treated with mTE/aTE, 888 patients (45.2%) did not meet the predefined inclusion criteria (Fig 1), and 1073 patients (54.8%) would eventually be analyzed. Most ($n = 780$, 72.7%) formed the control group. In 293 patients (27.3%), symptom onset was unclear. One hundred twenty-eight patients (11.9%) were categorized as having WUS; and 165 (15.4%), DUS.

The baseline characteristics are shown in On-line Table 1. There was no difference in the frequency of good functional outcome (mRS ≤ 2) between patients with WUS and controls (35.9% versus 38.3%, $P = .625$; Table 1). Good functional outcome was reduced in those with DUS compared with controls (27.3%, $P = .007$). WUS and DUS did not differ significantly ($P = .127$). Figure 2 illustrates the distribution of mRS scores at day 90. In-hospital mortality (C: 18.9%; WUS: 12.6%; DUS: 23.3%; $P = .067$) and all-cause mortality at day 90 (C: 26.5%; WUS: 22.7%; DUS: 31.5%; $P = .224$) did not differ significantly. The rate of symp-

tomatic intracranial hemorrhage was similar in all groups ($P = .292$, Table 1). Results did not change in the head-to-head comparison of groups adjusted for the abovementioned confounders (good functional outcome; WUS versus C: OR, 0.74; 95% CI, 0.48–1.16; $P = .193$; DUS versus C: OR, 0.49; 95% CI, 0.31–0.79; $P = .003$; data not shown).

Sixty-eight of the 128 patients with WUS (53.1%) underwent CTP or MR imaging (DUS: $n = 63$; 38.2%). MR imaging was performed in 36.7% of patients with WUS ($n = 47$) and in 31.5% of those with DUS ($n = 52$). In WUS[advanced], mismatch was present in 52 patients (76.5%; DUS[advanced]: $n = 46$, 73.0%; WUS[mri]: $n = 36$, 76.6%; DUS[mri]: $n = 37$, 71.2%). Subgroup analyses based on imaging selection are summarized in Table 2. When we compared WUS[advanced] and DUS[advanced] with unselected controls, there was no statistically significant difference in good functional outcome (C: 38.3%; WUS[advanced]: 47.1%; DUS[advanced]: 36.5%; $P = .344$). In-house mortality was reduced significantly in WUS[advanced] compared with controls (7.5% versus 18.9%, $P = .019$). Similar results were seen in patients with WUS[mri] and DUS[mri] (Table 2).

When we compared controls with patients in the WUS and DUS subgroups presenting with a verified mismatch only, the results did not change. Mortality rates remained stable with a nonsignificant increase in the percentage of good functional outcome (WUS[advanced]: 51.9%; DUS[advanced]: 39.1%; WUS[mri]: 52.8%; DUS[mri]: 43.2%; On-line Table 2). There was no significant difference in good functional outcome among WUS[mri] (51.1%), DUS[mri] (38.5%), and C[mri] (48.8%; $P = .357$; Table 2). The same was true for all-cause mortality at 3 months (C[mri]: 20.0%; WUS[mri]: 12.8%; DUS[mri]: 23.1%; $P = .385$) and the rate of symptomatic intracranial hemorrhage ($P = .875$).

We did compare WUS[advanced] and WUS[mri] with WUS not part of the respective groups (non-WUS[advanced], non-WUS[mri]; Table 3). Non-WUS[advanced] versus WUS[advanced] showed an increase in the rate of good functional outcome (23.3% versus 47.1%; OR, 2.92; 95% CI, 1.32–6.45; $P = .006$). In non-WUS[mri] versus WUS[mri], good functional outcome increased similarly (27.2% versus 51.1%; OR, 2.80; 95% CI, 1.28–6.10; $P = .008$) with an additional decrease in in-hospital mortality (17.3% versus 4.3%; OR, 0.22; 95% CI, 0.05–1.04; $P = .049$) and all-cause mortality at day 90 (28.4% versus 12.8%; OR, 0.37; 95% CI, 0.14–1.01; $P = .05$). For DUS, advanced imaging provided a significant improvement in the frequency of good functional outcome (non-DUS[advanced] versus DUS[advanced]: 21.6% versus 36.5%; OR, 2.09; 95% CI, 1.03–4.24; $P = .048$; non-DUS[mri] versus DUS[mri]: 22.1% versus 38.5%; OR, 2.20; 95% CI, 1.06–4.55; $P = .038$). A significant reduction of in-hospital mortality (30.0% versus 12.7%; OR, 0.34; 95% CI, 0.14–0.82; $P = .013$) and all-cause mortality at day 90 (38.2% versus 20.6%; OR, 0.42; 95% CI, 0.20–0.88; $P = .025$) was seen in non-DUS[advanced] versus DUS[advanced].

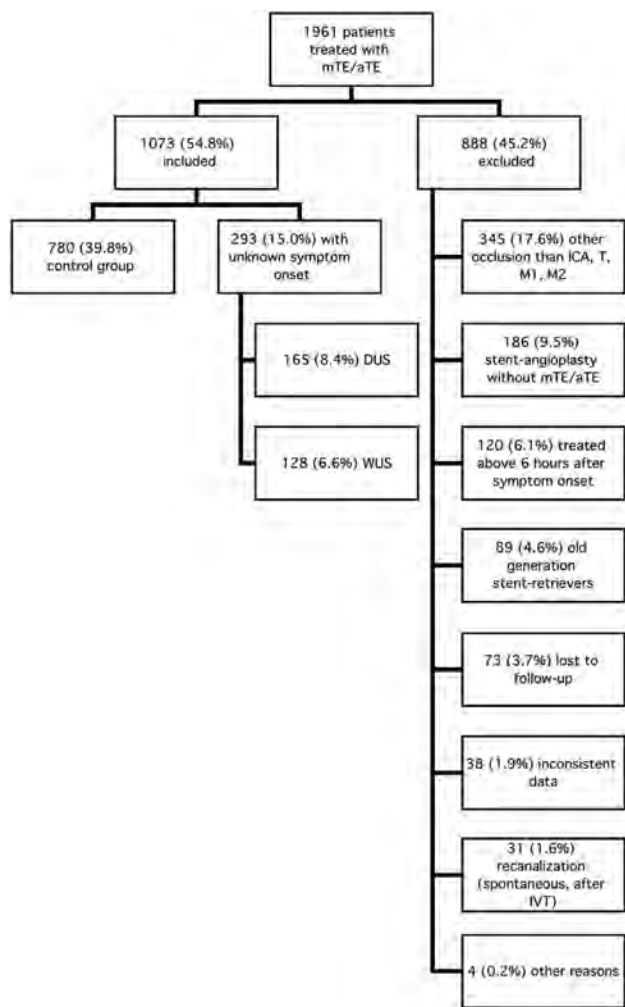


FIG 1. Flowchart depicting patient selection according to predefined inclusion and exclusion criteria. IVT indicates intravenous thrombolysis.

Table 1: Primary and secondary outcome parameters

	Control Group ($n = 780$)	WUS ($n = 128$)	DUS ($n = 165$)	P Value ^a	P Value ^b
mRS 0–2 at 3 mo (No.) (%)	299 (38.3)	46 (35.9)	45 (27.3)	.025	(A) .625 (B) .007 (C) .127
In-hospital mortality (No.) (%)	145 (18.9)	16 (12.6)	38 (23.3)	.067	NA
All-cause mortality at 3 mo (No.) (%)	207 (26.5)	29 (22.7)	52 (31.5)	.224	NA
sICH (No.) (%)	42 (5.5)	3 (2.4)	10 (6.3)	.292	NA

Note:—sICH indicates symptomatic intracranial hemorrhage.

^a P value for group comparison.

^b P value for head-to-head comparison, calculated when the P value for the group comparison was $<.05$: (A), control group vs WUS; (B), control group vs DUS; (C), WUS vs DUS.

DISCUSSION

Stroke with an unknown symptom onset is frequent and accounts for up to 30% of ischemic stroke cases.¹¹⁻¹³ WUS (in which symptoms are realized during awakening) and DUS (unrealized symptom onset during daytime) can be distinguished. Endovascular therapy is currently not approved in those patients.⁶ On the basis of a considerable real-world dataset, we tried to detect differences in outcome among patients with WUS, DUS, and controls (excluding patients with known symptom onset presenting >6 hours after notification of symptoms). In our cohort, outcome in WUS did not differ from that in controls (mRS 0–2: 35.9% versus 38.3%), suggesting a beneficial effect of mTE in WUS. No increase in mortality rates or the frequency of symptomatic intracranial hemorrhage was observed. Functional outcome in DUS overall was significantly inferior compared with that of controls (mRS 0–2: 27.3%).

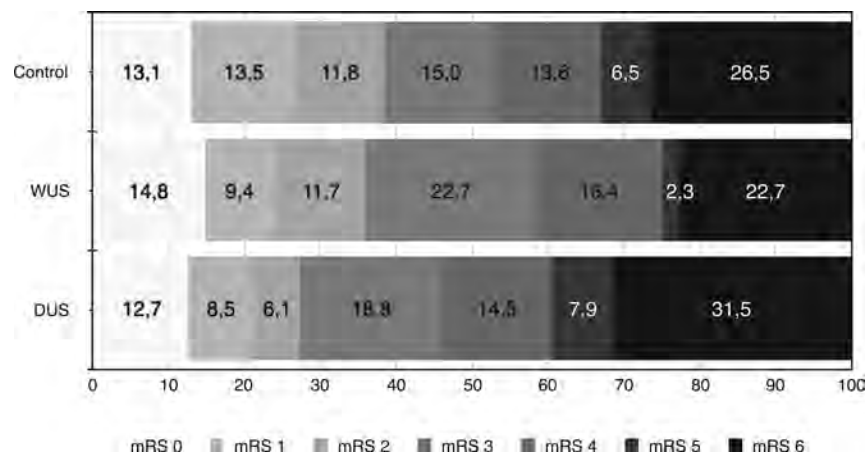


FIG 2. Distribution of mRS scores at 90 days.

Table 2: Subgroup analysis—patient selection via imaging modalities

	Control Group (n = 780)	WUS[advanced] (n = 68)	DUS[advanced] (n = 63)	P Value ^a	P Value ^b
A) CTP or MRI [advanced]					
mRS 0–2 (3 mo) (No.) (%)	299 (38.3)	32 (47.1)	23 (36.5)	.344	NA
In-hospital mortality (No.) (%)	145 (18.9)	5 (7.5)	8 (12.7)	.031	(A) 0.019 (B) .309 (C) .388
All-cause mortality (3 mo) (No.) (%)	207 (26.5)	11 (16.2)	13 (20.6)	.120	NA
sICH (No.) (%)	42 (5.5)	1 (1.5)	2 (3.3)	.380	NA
	Control Group (n = 780)	WUS[mri] (n = 47)	DUS[mri] (n = 52)		
B) MRI [mri]					
mRS 0–2 (3 mo) (No.) (%)	299 (38.3)	24 (51.1)	20 (38.5)	.216	NA
In-hospital mortality (No.) (%)	145 (18.9)	2 (4.3)	8 (15.4)	.024	(A) .009 (B) .713 (C) .204
All-cause mortality (3 mo) (No.) (%)	207 (26.5)	6 (12.8)	12 (23.1)	.093	NA
sICH (No.) (%)	42 (5.5)	1 (2.2)	2 (4.0)	.808	NA
	Control [mri] (n = 170)	WUS[mri] (n = 47)	DUS[mri] (n = 52)		
C) MRI compared with selected controls [mri]					
mRS 0–2 (3 mo) (No.) (%)	83 (48.8)	24 (51.1)	20 (38.5)	.357	NA
In-hospital mortality (No.) (%)	19 (11.5)	2 (4.3)	8 (15.4)	.211	NA
All-cause mortality (3 mo) (No.) (%)	34 (20.0)	6 (12.8)	12 (23.1)	.385	NA
sICH (No.) (%)	5 (3.0)	1 (2.2)	2 (4.0)	.875	NA

Note:—sICH indicates symptomatic intracranial hemorrhage; NA, not applicable.

^a P value for group comparison.

^b P value for head-to-head comparison, calculated when the P value for the group comparison was <.05: (A), control group vs WUS; (B), control group vs DUS; (C), WUS vs DUS.

The first evidence indicating a possible beneficial effect of intravenous thrombolysis in carefully selected patients presenting in a prolonged time-window was published several years ago.^{21,22} Similar results were obtained for endovascular therapy in late-presenting stroke cases.^{23,24} From a present-day perspective, the use of older generation thrombectomy devices and small sample sizes limited generalizability. Subsequent retrospective and observational data suggested a potential beneficial effect of mTE in WUS with unknown symptom onset.^{7,9} However, DUS was not addressed. Recently, preliminary results of the diffusion-weighted imaging or CT perfusion assessment with Clinical Mismatch in the Triage of Wake Up and Late Presenting Strokes Undergoing Neurointervention with Trevo (DAWN) and Endovascular Therapy Following Imaging Evaluation for Ischemic Stroke 3 (DEFUSE 3) trials were presented.²⁵⁻²⁸ DAWN included WUS and patients “last seen well” up to 24 hours prior to endovascular therapy; DEFUSE 3 recruited patients treated between 6 and 16 hours after notification of symptoms. Both randomized controlled trials were terminated after interim analysis demonstrated superiority of the interventional group. It was proved that a strict imaging selection can identify patients eligible for mTE well after the currently approved time window. So far there is still little information on possible differences between WUS and DUS.

In our data, patient selection due to administration of CTP or MR imaging

Table 3: Effect of advanced imaging on outcome and safety

	WUS[advanced] (n = 68)	Non-WUS[advanced] (n = 60)	OR (95% CI), P Value
A) WUS treated after CTP or MRI [advanced] compared with the remaining WUS [non-advanced]			
mRS 0–2 (3 mo) (No.) (%)	32 (47.1)	14 (23.3)	2.92 (1.32–6.45), .006
In-hospital mortality (No.) (%)	5 (7.5)	11 (18.3)	0.36 (0.11–1.12), .106
All-cause mortality (3 mo) (No.) (%)	11 (16.2)	18 (30.0)	0.45 (0.19–1.07), .090
sICH (No.) (%)	1 (1.5)	2 (3.4)	0.43 (0.04–4.95), .599
DUS[advanced] (n = 63) Non-DUS[advanced] (n = 102)			
B) DUS treated after CTP and MRI [advanced] compared with the remaining DUS [non-advanced]			
mRS 0–2 (3 mo) (No.) (%)	23 (36.1)	22 (21.6)	2.09 (1.03–4.25), .048
In-hospital mortality (No.) (%)	8 (12.7)	30 (30.0)	0.34 (0.14–0.82), .013
All-cause mortality (3 mo) (No.) (%)	13 (20.6)	39 (38.2)	0.42 (0.20–0.88), .025
sICH (No.) (%)	2 (3.3)	8 (8.1)	0.39 (0.08–1.90), .320
WUS[mri] (n = 47) Non-WUS[mri] (n = 81)			
C) WUS treated after MRI [mri] compared with the remaining WUS [non-mri]			
mRS 0–2 (3 mo) (No.) (%)	24 (51.1)	22 (27.2)	2.80 (1.28–6.10), .008
In-hospital mortality (No.) (%)	2 (4.3)	14 (17.3)	0.22 (0.05–1.04), .049
All-cause mortality (3 mo) (No.) (%)	6 (12.8)	23 (28.4)	0.37 (0.14–1.01), .050
sICH (No.) (%)	1 (2.2)	2 (2.6)	0.84 (0.07–9.68), 1.000
DUS[mri] (n = 52) Non-DUS[mri] (n = 113)			
D) DUS treated after MRI [mri] compared with the remaining DUS [non-mri]			
mRS 0–2 (3 mo) (No.) (%)	20 (38.5)	25 (22.1)	2.20 (1.06–4.55), .038
In-hospital mortality (No.) (%)	8 (15.4)	30 (27.0)	0.49 (0.21–1.17), .115
All-cause mortality (3 mo) (No.) (%)	12 (23.1)	40 (35.4)	0.55 (0.27–1.17), .149
sICH (No.) (%)	2 (4.0)	8 (7.3)	0.53 (0.11–2.62), .726

Note:—sICH indicates symptomatic intracranial hemorrhage.

likewise led to a significant increase in the frequency of good functional outcome in patients with WUS and DUS. Consecutive steps in patient selection (1, all patients; 2, patients with CTP or MR imaging; 3, patients with MR imaging; 4, patients with documented mismatch in CTP or MR imaging; 5, patients with documented mismatch in MR imaging) increased the frequency of good functional outcome in both WUS and DUS (WUS 1: 35.9%; WUS 2: 47.1%; WUS 3: 51.1%; WUS 4: 51.9%; WUS 5: 52.8%; DUS 1: 27.3%; DUS 2: 36.5%; DUS 3: 38.5%; DUS 4: 39.1%; DUS 5: 43.2%). Outcome in DUS still was reduced. However, with the application of advanced imaging techniques, the statistically significant difference disappeared.

Besides outcome, WUS and DUS also seem to differ in pathophysiologic characteristics. An increase in platelet aggregation as well as a blood pressure surge during awakening are said to be associated with WUS but not DUS.^{29,30} WUS might occur right before awakening and therefore be comparable with a stroke population with documented symptom onset.³¹ Indeed, it was shown that clinical and imaging characteristics in WUS and stroke eligible for intravenous thrombolysis seem to be comparable, whereas DUS—as in our cohort—tends to have a worse prognosis.^{13,32,33} We did not observe significant differences in baseline characteristics. Longer imaging-to-groin times in WUS and DUS can be explained by a higher percentage of MR imaging scans and might indicate a careful patient selection. An average 138 minutes in controls is attributed to many patients being secondarily transferred for mTE/aTE.¹⁰

This study has several limitations. First, due to the retrospective design, selection bias can be suspected because we do not

know in which cases mTE or aTE was not considered. Also, a certain inconsistency in decision-making can be assumed. Second, the definition of WUS and DUS could lead to some overlap of groups. Some of the patients categorized as having DUS by the assessing neurologist (eg, patients arriving late in the evening) could be WUS instead. There was no common CTP protocol or quantitative mismatch measurement, which may reduce comparability. An imbalance in group size might introduce a power problem (especially in subgroup analysis).

CONCLUSIONS

Our data suggest that mTE/aTE in selected patients with WUS allows a good functional outcome comparable with that in patients treated within 6 hours of symptom onset. Patients with DUS seem to be inferior to controls regarding outcome and mortality rates. The application of advanced imaging modalities (MR imaging, CTP) significantly increases the frequency of good functional outcome in both WUS and DUS and seems to reduce mortality.

ACKNOWLEDGMENTS

We were supported by Hiltrud Niggemann in performing the statistical analysis. Casjupea Knispel, stroke and study nurse of the Neuroradiological Clinic, participated in data collection and conducted the follow-up interviews.

Disclosures: Marta Aguilar Pérez—UNRELATED: Consultancy: phenox, Comments: proctor and consultant. Hansjörg Bänzner—UNRELATED: Payment for Lectures Including Service on Speakers Bureaus: Bayer AG, Vital Pharma GmbH, Boehringer

Ingelheim, Bristol-Myers Squibb, Daiichi Sankyo, Hans Henkes—UNRELATED: Board Membership: phenox, Comments: I am Speaker of the Board without payment; phenox compensates travel expenses; Consultancy: phenox, Comments: I am a consultant phenox and receive financial compensation for this effort; Patents (Planned, Pending or Issued): phenox, Medtronic, Comments: I am a coinventor of several intellectual property claims held by Medtronic and phenox; Stock/Stock Options: phenox, Comments: I am cofounder and shareholder of phenox; Travel/Accommodations/Meeting Expenses Unrelated to Activities Listed: phenox, Comments: I receive compensation for travel expenses for activities on behalf of phenox.

REFERENCES

- Berkhemer OA, Fransen PS, Beumer D, et al. **A randomized trial of intraarterial treatment for acute ischemic stroke.** *N Engl J Med* 2015; 372:11–20 CrossRef Medline
- Goyal M, Demchuk AM, Menon BK, et al; ESCAPE Trial Investigators. **Randomized assessment of rapid endovascular treatment of ischemic stroke.** *N Engl J Med* 2015;372:1019–30 CrossRef Medline
- Saver JL, Goyal M, Bonafe A, et al; SWIFT PRIME Investigators. **Stent-retriever thrombectomy after intravenous t-PA vs. t-PA alone in stroke.** *N Engl J Med* 2015;372:2285–95 CrossRef Medline
- Campbell BC, Mitchell PJ, Kleinig TJ, et al; EXTEND-IA Investigators. **Endovascular therapy for ischemic stroke with perfusion-imaging selection.** *N Engl J Med* 2015;372:1009–18 CrossRef Medline
- Jovin TG, Chamorro A, Cobo E, et al; REVASCAT Trial Investigators. **Thrombectomy within 8 hours after symptom onset in ischemic stroke.** *N Engl J Med* 2015;372:2296–306 CrossRef Medline
- Wahlgren N, Moreira T, Michel P, et al; ESO-KSU, ESO, ESMINT, ESNR and EAN. **Mechanical thrombectomy in acute ischemic stroke: consensus statement by ESO-Karolinska Stroke Update 2014/2015, supported by ESO, ESMINT, ESNR and EAN.** *Int J Stroke* 2016;11:134–47 CrossRef Medline
- Mokin M, Kan P, Sivakanthan S, et al. **Endovascular therapy of wake-up strokes in the modern era of stent retriever thrombectomy.** *J Neurointerv Surg* 2016;8:240–43 CrossRef Medline
- Qureshi AI, Miley JT, Chaudhry SA, et al. **Safety and effectiveness of endovascular treatment after 6 hours of symptom onset in patients with anterior circulation ischemic stroke: a matched case control study.** *J Stroke Cerebrovasc Dis* 2013;22:1076–81 CrossRef Medline
- Kuntze Söderqvist Å, Andersson T, Wahlgren N, et al. **Mechanical thrombectomy in acute ischemic stroke: patients with wake-up stroke and the elderly may benefit as well.** *J Stroke Cerebrovasc Dis* 2016;25:2276–83 CrossRef Medline
- Bücke P, Pérez MA, Schmid E, et al. **Endovascular thrombectomy in acute ischemic stroke: outcome in referred versus directly admitted patients.** *Clin Neuroradiol* 2017 Jan 31. [Epub ahead of print] CrossRef Medline
- Kim YJ, Kim BJ, Kwon SU, et al. **Unclear-onset stroke: daytime-unwitnessed stroke vs. wake-up stroke.** *Int J Stroke* 2016;11:212–20 CrossRef Medline
- Wouters A, Lemmens R, Dupont P, et al. **Wake-up stroke and stroke of unknown onset: a critical review.** *Front Neurol* 2014;5:153 CrossRef Medline
- Reid JM, Dai D, Cheripelli B, et al. **Differences in wake-up and unknown onset stroke examined in a stroke registry.** *Int J Stroke* 2015; 10:331–35 CrossRef Medline
- Bouslama M, Haussen DC, Grossberg JA, et al. **Computed tomographic perfusion selection and clinical outcomes after endovascular therapy in large vessel occlusion stroke.** *Stroke* 2017;48:1271–77 CrossRef Medline
- Campbell BC, Yassi N, Ma H, et al. **Imaging selection in ischemic stroke: feasibility of automated CT-perfusion analysis.** *Int J Stroke* 2015;10:51–54 CrossRef Medline
- Thomalla G, Cheng B, Ebinger M, et al; VISTA Imaging Investigators. **DWI-FLAIR mismatch for the identification of patients with acute ischaemic stroke within 4.5 h of symptom onset (PRE-FLAIR): a multicentre observational study.** *Lancet Neurol* 2011;10:978–86 CrossRef Medline
- Thomalla G, Boutitie F, Fiebach JB, et al; WAKE-UP Investigators. **Stroke with unknown time of symptom onset: baseline clinical and magnetic resonance imaging data of the first thousand patients in WAKE-UP (efficacy and safety of MRI-based thrombolysis in wake-up stroke: a randomized, double-blind, placebo-controlled trial).** *Stroke* 2017;48:770–73 CrossRef Medline
- Turk A, Magarik JA, Chaudry I, et al. **CT perfusion-guided patient selection for endovascular treatment of acute ischemic stroke is safe and effective.** *J Neurointerv Surg* 2012;4:261–65 CrossRef Medline
- Michel P, Ntaios G, Reichhart M, et al. **Perfusion-CT guided intravenous thrombolysis in patients with unknown-onset stroke: a randomized, double-blind, placebo-controlled, pilot feasibility trial.** *Neuroradiology* 2012;54:579–88 CrossRef Medline
- Saver JL, Goyal M, Bonafe A, et al; SWIFT PRIME Investigators. **Solitaire™ with the Intention for Thrombectomy as Primary Endovascular Treatment for Acute Ischemic Stroke (SWIFT PRIME) trial: protocol for a randomized, controlled, multicenter study comparing the Solitaire revascularization device with IV tPA with IV tPA alone in acute ischemic stroke.** *Int J Stroke* 2015;10:439–48 CrossRef Medline
- Cho AH, Sohn SI, Han MK, et al. **Safety and efficacy of MRI-based thrombolysis in unclear-onset stroke: a preliminary report.** *Cerebrovasc Dis* 2008;25:572–79 CrossRef Medline
- Schellinger PD, Thomalla G, Fiehler J, et al. **MRI-based and CT-based thrombolytic therapy in acute stroke within and beyond established time windows: an analysis of 1210 patients.** *Stroke* 2007; 38:2640–45 CrossRef Medline
- Abou-Chebl A. **Endovascular treatment of acute ischemic stroke may be safely performed with no time window limit in appropriately selected patients.** *Stroke* 2010;41:1996–2000 CrossRef Medline
- Natarajan SK, Snyder KV, Siddiqui AH, et al. **Safety and effectiveness of endovascular therapy after 8 hours of acute ischemic stroke onset and wake-up strokes.** *Stroke* 2009;40:3269–74 CrossRef Medline
- Third European Stroke Organisation Conference. Prague, Czech Republic. May 16–18, 2017; <https://eso-stroke.org/kategorie-1/data-highlights-opening-plenary-esoc-2017/>. Accessed October 18, 2017
- NeuroNews. DEFUSE 3 terminated early with high likelihood of benefit in the endovascular group. <https://neuronewsinternational.com/defuse-3-terminated-early-high-likelihood-benefit-endovascular-group/>. Accessed October 18, 2017
- Jovin TG, Saver JL, Ribo M, et al. **Diffusion-weighted imaging or computerized tomography perfusion assessment with clinical mismatch in the triage of wake up and late presenting strokes undergoing neurointervention with Trevo (DAWN) trial methods.** *Int J Stroke* 2017;12:641–52 CrossRef Medline
- Albers GW, Lansberg MG, Kemp S, et al. **A multicenter randomized controlled trial of endovascular therapy following imaging evaluation for ischemic stroke (DEFUSE 3).** *Int J Stroke* 2017;12:896–905 CrossRef Medline
- Lundholm MD, Rooney M, Maas MB, et al. **Wake-up stroke is associated with greater nocturnal mean arterial pressure variability.** *Stroke* 2017;48:1668–70 CrossRef Medline
- Kario K, Yano Y, Matsuo T, et al. **Morning blood pressure surge, morning platelet aggregation, and silent cerebral infarction in older Japanese hypertensive patients.** *J Hypertens* 2011;29:2433–39 CrossRef Medline
- Rubin MN, Barrett KM. **What to do with wake-up stroke.** *Neurohospitalist* 2015;5:161–72 CrossRef Medline
- Mackey J, Kleindorfer D, Sucharew H, et al. **Population-based study of wake-up strokes.** *Neurology* 2011;76:1662–67 CrossRef Medline
- Costa R, Pinho J, Alves JN, et al. **Wake-up stroke and stroke within the therapeutic window for thrombolysis have similar clinical severity, imaging characteristics, and outcome.** *J Stroke Cerebrovasc Dis* 2016;25:511–14 CrossRef Medline

Nonsphericity Index and Size Ratio Identify Morphologic Differences between Growing and Stable Aneurysms in a Longitudinal Study of 93 Cases

A. Chien, M. Xu, H. Yokota, F. Scalzo, E. Morimoto, and N. Salamon



ABSTRACT

BACKGROUND AND PURPOSE: Recent studies have strongly associated intracranial aneurysm growth with increased risk of rupture. Identifying aneurysms that are likely to grow would be beneficial to plan more effective monitoring and intervention strategies. Our hypothesis is that for unruptured intracranial aneurysms of similar size, morphologic characteristics differ between aneurysms that continue to grow and those that do not.

MATERIALS AND METHODS: From aneurysms in our medical center with follow-up imaging dates in 2015, ninety-three intracranial aneurysms (23 growing, 70 stable) were selected. All CTA images for the aneurysm diagnosis and follow-up were collected, a total of 348 3D imaging studies. Aneurysm 3D geometry for each imaging study was reconstructed, and morphologic characteristics, including volume, surface area, nonsphericity index, aspect ratio, and size ratio were calculated.

RESULTS: Morphologic characteristics were found to differ between growing and stable groups. For aneurysms of <3 mm, nonsphericity index ($P < .001$); 3–5 mm, nonsphericity index ($P < .001$); 5–7 mm, size ratio ($P = .003$); >7 mm, volume ($P < .001$); surface area ($P < .001$); and nonsphericity index ($P = .002$) were significant. Within the anterior communicating artery, the nonsphericity index ($P = .008$) and, within the posterior communicating artery, size ratio ($P = .004$) were significant. The nonsphericity index receiver operating characteristic area under the curve was 0.721 for discriminating growing and stable cases on the basis of initial images.

CONCLUSIONS: Among aneurysms with similar sizes, morphologic characteristics appear to differ between those that are growing and those that are stable. The nonsphericity index, in particular, was found to be higher among growing aneurysms. The size ratio was found to be the second most significant parameter associated with growth.

ABBREVIATIONS: ACA = anterior communicating artery; BA/VA = basilar artery/vertebral artery; ICH = intracerebral hemorrhage; NSI = nonsphericity index; PcomA = posterior communicating artery

Because part of the population has asymptomatic, unruptured intracranial aneurysms (1%–3%), they are regularly incidentally detected with medical imaging.^{1,2} An appropriate course of monitoring or intervention must then be decided. While this de-

cision is relatively straightforward for larger intracranial aneurysms (>7 mm), the best approach for smaller aneurysms is less clear. Recent studies have found a positive correlation between aneurysm growth and rupture.^{3–6} Therefore, it would seem beneficial to identify small aneurysms likely or unlikely to grow and plan treatment/monitoring strategies accordingly.

An unruptured aneurysm may be detected at any size when it becomes symptomatic or incidentally detected through imaging. Currently, from such a snapshot, it is difficult to guess the natural history of an aneurysm: Is it relatively new and rapidly growing or has it gradually increased in size; is it still growing or relatively stable? At present, there is no clear information to predict whether an aneurysm will continue to grow, while certain factors, such as anatomic location, correlate with significantly increased rupture risk.⁷ The objective of this research was to address whether aneurysm morphologic characteristics, size and shape, may provide an additional means of identifying future growth.

Received August 13, 2017; accepted after revision November 13.

From the Departments of Radiological Science (A.C., M.X., H.Y., E.M., N.S.) and Neurology (F.S.), David Geffen School of Medicine at the University of California, Los Angeles, Los Angeles, California.

This work was supported, in part, by a Brain Aneurysm Foundation Research Grant; a Society of Interventional Radiology Foundation Dr. Ernest J. Ring Academic Development Grant; and a University of California, Los Angeles Radiology Exploratory Research Grant.

Paper previously presented, in part, at: Annual Meeting of the American Society of Neuroradiology, Washington, DC; May 21–26, 2016.

Please address correspondence to Aichi Chien, PhD, Department of Radiological Science, David Geffen School of Medicine at UCLA, 10833 LeConte Ave, Box 957350, Los Angeles, CA 90095; e-mail: aichi@ucla.edu

Indicates article with supplemental on-line table.

<http://dx.doi.org/10.3174/ajnr.A5531>

Table 1: Case information

	Aneurysm Growth		
	Yes	No	Total
Patients			
No. of patients	23	62	85
No. of women	20	49	69
No. of men	3	13	16
Mean age (yr)	63.6 ± 15.5	65.9 ± 11.9	65.2 ± 12.9
Atrial fibrillation	2	3	5
Cancer	3	8	11
Coronary artery disease	1	3	4
Diabetes mellitus	4	9	13
Dyslipidemia	6	32	38
Family history of intracranial aneurysm	0	3	3
History of TIA	2	2	4
History of ICH	1	1	2
History of stroke	0	3	3
Hypertension	12	32	44
Hypothyroid	4	12	16
Previous or current cigarette smoking	3	16	19
Previous SAH	2	2	4
Seizure	2	1	3
Cases			
Aneurysms	23	70	93
Average follow-ups	2.35 ± 1.15	2.93 ± 2.45	2.78 ± 2.21
Follow-up time (mo)	46.4 ± 29.4	51.6 ± 46.2	50.3 ± 42.6
ACA	4	16	20
ICA	8	38	46
MCA	1	8	9
PcomA	9	4	13
BA/VA	1	4	5
Sidewall aneurysm	19	58	77
Bifurcation aneurysm	4	12	16
Imaging studies			
All	73	275	348
<3 mm	21	74	95
3–5 mm	25	135	160
5–7 mm	15	50	65
>7 mm	12	16	28
ACA	15	59	74
ICA	25	152	177
MCA	7	29	36
PcomA	26	9	35
BA/VA	2	24	26

During the past decade, many imaging-derived indices have been proposed for assessing aneurysm risk, primarily focused on identifying differences between ruptured and unruptured aneurysms.^{8–12} These indices include a broad variety of metrics, some of which, like wall shear stress or the pulsatility index, are calculated through computational simulation.^{13–16} However, to date, there have been few studies of aneurysm growth that focus on imaging-derived indices.^{17,18} For this research, we focused on morphologic characteristics, which, as a group, are directly calculated from 2D/3D images without simulation. As a result, these types of indices are simpler to use and more easily applied to larger sample sizes.

The simplest morphologic characteristic describing an aneurysm is its size, typically represented by its maximum diameter.² Indices investigated in this study include volume, surface area, the nonsphericity index (NSI), aspect ratio, and size ratio.^{9,19,20} While these represent a small selection of previously published indices, they all have previously been identified as having some predictive value for discriminating ruptured/unruptured aneurysms; therefore, because

there is an association between aneurysm growth and rupture, these indices were chosen for this study.^{3,5,6} Because this study analyzed longitudinal data, in addition to comparing morphologic indices for aneurysms at diagnosis and grouped by location, aneurysm imaging studies were segregated by size.

MATERIALS AND METHODS

Case Information

This study was performed with approval of the institutional review board. It was a retrospective analysis of intracranial aneurysm cases with follow-up imaging in the data base of our medical center. All the CT angiograms were acquired on the basis of an established clinical imaging protocol for brain aneurysm follow-up, to ensure consistency for clinical aneurysm management.^{21,22} Ninety-three intracranial aneurysms (23 growing, 70 stable) from 2010 to 2015 with at least 1 imaging follow-up were selected. An aneurysm was classified as growing if it exhibited a >0.6-mm increase in diameter measured in all subsequent imaging studies. CTA images at each time point for aneurysm diagnosis and follow-up were collected. A total of 348 CTA volumetric imaging sets were included. Aneurysms were followed for a mean of 50.3 ± 42.6 months, with a mean of 2.78 ± 2.21 follow-up imaging dates, for a mean of 3.35 ± 1.35 imaging studies per aneurysm case. Patient information and aneurysm characteristics, including location, aneurysm type, and imaging study numbers, are summarized in Table 1.

Image Processing and Analysis

For each aneurysm, 3D geometry for each imaging study was reconstructed and basic morphologic characteristics such as volume and surface area were calculated.^{23,24} From these, the NSI was calculated. Aspect ratio and size ratio were based on manual measurements made by a skilled radiologist who was blinded to whether aneurysms were growing or stable. Figure 1 shows the formulas used for calculation of the indices as well as a depiction of where various shapes fall within the range of values, because this is sometimes difficult to decipher from the formula. As mentioned above, for analysis, the imaging studies were divided into 4 categories (<3 mm, 3–5 mm, 5–7 mm, and >7 mm). Growing and stable aneurysms were also grouped for analysis by general anatomic location (anterior communicating artery [ACA], ICA, MCA, posterior communicating artery [PcomA], or basilar artery/vertebral artery [BA/VA]) and type of aneurysm (sidewall or bifurcation).

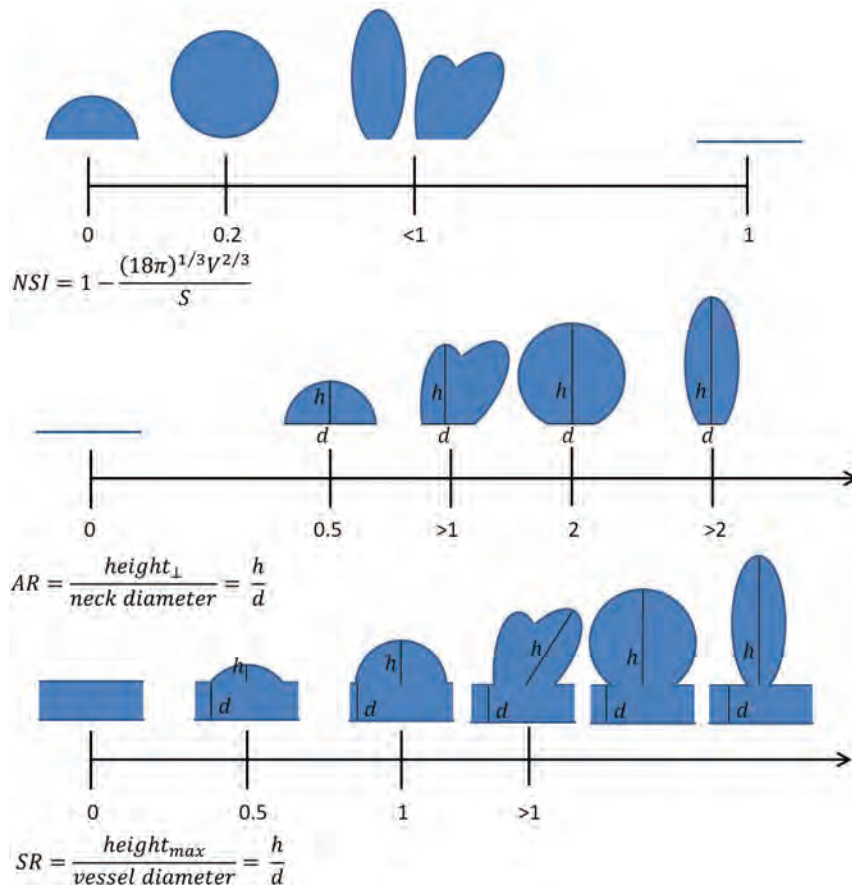


FIG 1. Morphologic indices used in this study, in addition to maximum diameter, volume, and surface area. Formulas for their calculation, along with diagrams illustrating the relative position of various shapes on the different scales are shown. Horizontal lines indicate no aneurysm; AR, aspect ratio; SR, size ratio; max, maximum. The NSI ranges from 0 to 1 and is based on 3D geometry, while the AR and SR start at zero but have no fixed upper limit. Only SR incorporates the size of the parent artery into the calculation.

Statistical Analysis

Statistical comparisons between growing and stable groups were made using a 2-tailed *t* test with an assumption of unequal variance (Welch *t* test). The Pearson χ^2 test was used to compare patient information between groups (Table 1). For all statistical analyses, a significant *P* value was .01. Statistical analysis was performed and figures were prepared in SPSS 24 (IBM, Armonk, New York) and Excel (Microsoft, Redmond, Washington).

RESULTS

Aneurysm Size versus Morphology

No significant differences in patient information were found between growing and stable aneurysm groups (Table 1). Statistical analysis identified different morphologic indices as significant when examining different groups of images. Measurements for growing and stable aneurysm images segregated by size are summarized in Table 2. For very small aneurysms (<3 mm), the NSI ($P < .001$) was significantly different between growing and stable groups. For aneurysms of 3–5 mm, only the NSI was significant as well ($P < .001$). For aneurysms of 5–7 mm, only the size ratio was significant ($P = .003$). For large aneurysms (>7 mm), volume ($P < .001$), surface area ($P < .001$), and NSI ($P = .002$) were significantly different among the groups. When we considered all

diagnoses and follow-up time points together, volume ($P < .001$), surface area ($P < .001$), and the NSI ($P < .001$) were significant. Finally, when considering only the initial imaging study for each aneurysm, effectively examining all aneurysm cases at diagnosis, only the NSI ($P = .003$) was significant for growing versus stable. In all analyses in which the NSI was significant, it was consistently higher in the growing group versus the stable group. Figure 2 presents boxplots of the NSI for the growing and stable groups segregated by size.

Receiver operating characteristic curves were plotted for the various indices for growing versus stable (Fig 3). When all imaging studies for all aneurysms were included, the NSI provided superior discrimination between groups, with the area under the curve of 0.712 versus indices such as surface area (area under the curve = 0.638). When only the initial imaging study from all aneurysms was included, the NSI was again superior to the other indices (area under the curve = 0.721).

Aneurysm Location versus Morphology and Aneurysm Type versus Morphology

Results from comparing growing and stable aneurysms by location are summarized in Table 3. Within the ACA, the NSI ($P = .008$) was significantly different

between growing and stable aneurysms. Although no significant differences were found among ICA aneurysm groups, a trend toward a difference in the NSI ($P = .014$) was observed. The size ratio ($P = .004$) was significantly different between groups of aneurysm images within the PcomA. MCA and BA/VA imaging studies were excluded from the location analysis because of insufficient growing aneurysms. In the analysis of growth in bifurcation and sidewall aneurysms (17% and 83% of total cases, respectively; Table 1 and On-line Table), the NSI was the only significant factor between growing and stable in sidewall aneurysms ($P = .006$) (Table 4).

DISCUSSION

Several common morphologic indices for describing aneurysms are highly dependent on diameter, such as volume, surface area, aspect ratio, and size ratio (aspect ratio and size ratio calculate a ratio on the basis of the aneurysm neck and parent artery diameter, respectively, characteristics typically much less variable than aneurysm height) (Fig 1).^{19,20} Indices such as the NSI are independent of aneurysm diameter and, while slightly more complicated to calculate, in exchange provide more robust shape characterization and, on the basis of this study, appear to provide

Table 2: Index values for growing and stable aneurysms segregated by size^a

	Index					
	<3 mm (n = 95)	3–5 mm (n = 160)	5–7 mm (n = 65)	>7 mm (n = 28)	All ^b (n = 348)	Initial ^c (n = 93)
Maximum diameter						
Growing	2.21 ± 0.66	3.93 ± 0.58	6.09 ± 0.58	8.55 ± 1.28	4.64 ± 2.33	3.98 ± 2.09
Stable	2.22 ± 0.55	3.82 ± 0.52	5.77 ± 0.58	8.78 ± 1.52	4.03 ± 1.78	4.14 ± 1.84
Volume						
Growing	9.41 ± 8.51	49.2 ± 49.7	151 ± 119	572 ± 287 ^{d,e}	145 ± 235 ^{d,e}	110 ± 197
Stable	12.5 ± 6.88	30.4 ± 20.9	108 ± 68.9	150 ± 261 ^d	46.7 ± 81.0 ^d	57.0 ± 106
Surface area						
Growing	28.1 ± 15.9	75.1 ± 49.4	144 ± 85.6	384 ± 165 ^{d,e}	126 ± 146 ^{d,e}	105 ± 133
Stable	30.0 ± 13.2	50.6 ± 26.4	122 ± 60.4	116 ± 140 ^d	61.9 ± 57.4 ^d	70.1 ± 69.5
NSI						
Growing	0.45 ± 0.08 ^{d,e}	0.36 ± 0.10 ^{d,e}	0.26 ± 0.05	0.31 ± 0.08 ^{d,f}	0.36 ± 0.11 ^{d,e}	0.38 ± 0.11 ^{d,f}
Stable	0.31 ± 0.14 ^d	0.27 ± 0.10 ^d	0.29 ± 0.09	0.22 ± 0.03 ^d	0.28 ± 0.11 ^d	0.29 ± 0.12 ^d
Aspect ratio						
Growing	0.89 ± 0.54	0.91 ± 0.33	1.21 ± 0.34	1.21 ± 0.27	1.03 ± 0.43	1.01 ± 0.54
Stable	0.90 ± 0.24	0.99 ± 0.29	1.09 ± 0.33	1.27 ± 0.81	1.00 ± 0.34	1.02 ± 0.40
Size ratio						
Growing	0.56 ± 0.25	0.94 ± 0.31	2.93 ± 1.3 ^{d,f}	2.48 ± 0.71	1.49 ± 1.20	1.21 ± 0.91
Stable	0.70 ± 0.30	1.05 ± 0.34	1.63 ± 0.59 ^d	1.96 ± 1.11	1.11 ± 0.59	1.19 ± 0.68

^a Data are presented as mean ± SD.

^b The "All" column includes all imaging studies for all cases.

^c The "Initial" column includes the first imaging study for all cases.

^d Significant difference between groups.

^e $P < .001$.

^f $P < .01$.

more consistent growth prediction.^{8,9} For all except the smallest aneurysms, volume and surface area were larger for growing aneurysms than stable aneurysms, though this was only significant among large (>7 mm) aneurysms and when all aneurysm imaging studies were considered. These indices not being significant among smaller aneurysms may indicate that differences in aneurysm morphology are more pronounced for larger aneurysms (Table 2).

When the NSI was significantly different between growing and stable groups, it was consistently higher in the growing group. Referring to Fig 1, this higher NSI corresponds to the growing aneurysms having a more irregular shape. If one considers the association previous studies have found between growth and rupture, a higher NSI among growing aneurysms is consistent with previous findings of a higher NSI among ruptured aneurysms.^{9,10,25} When we further considered morphologic differences among aneurysm sizes, aneurysms of 5–7 mm were found, in general, to be less irregular (more spheric) than smaller or larger aneurysms, as indicated by the NSI values. A plausible explanation for this finding is that aneurysms in this size range are close to the treatment threshold and the more irregular cases were treated instead of being followed with imaging. Among the locations, MCA aneurysms were the least irregular, with PcomA aneurysms having the most convoluted and complex shapes (Table 3). This finding might be due to fewer cases in these locations and the influence of treatment preferences. Because bifurcation aneurysms are usually considered to have a high rupture risk, in our study, 83% of the cases were sidewall aneurysms. Previous work by Baharoglu et al¹² showed the NSI to be associated with rupture in bifurcation aneurysms. In this study, we found the NSI to be significantly higher in growing sidewall aneurysms, while it was not significantly different in bifurcation aneurysms, possibly due to the relatively small percentage of bifurcation cases. This finding

may also be because the current study investigated the growth of a low-risk group of aneurysm cases with an average size of 4 mm, while the study of Baharoglu et al¹² was focused on aneurysms with high rupture risk, on average 7 mm. The NSI values recorded in this study were higher than values previously reported by other researchers for intracranial aneurysms.^{9,10,17} The reason is unclear but may be due to the smoothing of reconstructed aneurysm geometry, or a lack thereof, before calculation of aneurysm volume and surface area.

Because aneurysms may be detected at any point during their natural history, when one considers longitudinal data, each imaging study may contribute additional information. From the perspective of natural history, there is not anything special about the initial images of an asymptomatic unruptured aneurysm versus images obtained at follow-up. There may, however, be differences among the longitudinal images, due to growth or simply the details of the image acquisition. In the current research, the rationale for performing most of the statistical analyses at the level of the imaging study instead of the aneurysm case was to better identify predictors that might be applied to evaluate initial diagnostic images in combination with size, currently a major criterion for treatment/follow-up decisions. This research supports aneurysm growth being predicted by the same morphologic characteristics previously shown to be significant for rupture, specifically NSI.

The results of this study contrast with a previous, multicenter prospective study that investigated the ability of various indices to predict subsequent aneurysm growth.¹⁷ Beyond the prospective-versus-retrospective study design and single time point versus multiple time point image analysis, there are several differences that might explain the apparent discrepancy. First and foremost, the criteria for growth were different between the 2 studies, with the current study relying on a fixed size threshold (0.6 mm) confirmed by subsequent images and Ramachandran et al¹⁷ using expert clinician review. Second, the follow-up duration was con-

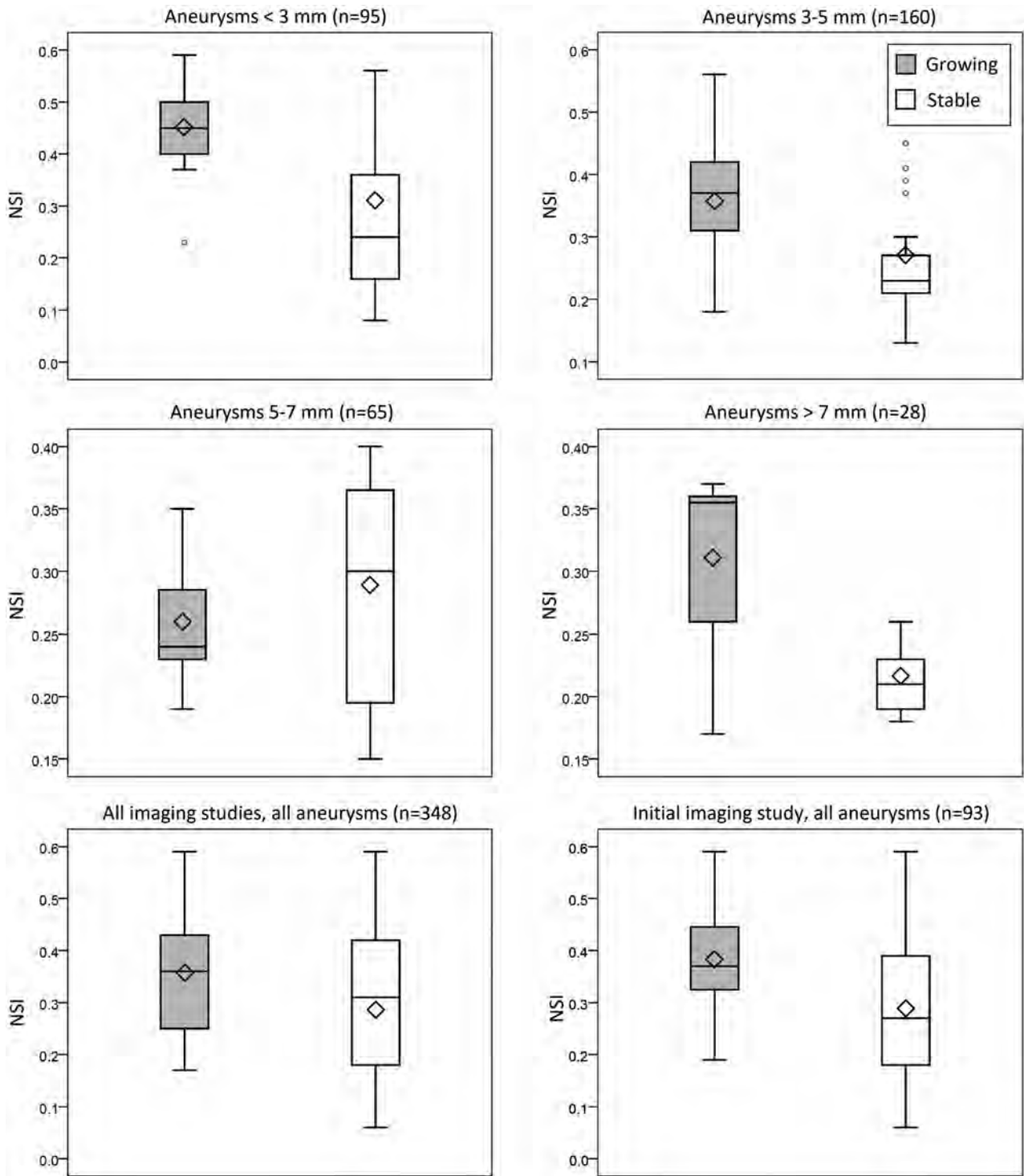


FIG 2. The NSI for imaging studies segregated by size (Tukey boxplots). *Shaded and unshaded bars* represent growing and stable groups, respectively, in each panel. *Diamonds* indicate the mean for each group; and the *small circles*, outliers.

siderably longer in the current study (an average of approximately 4-versus-2 years). Given the growth rates observed in our population sample, many of the aneurysms in the current study would have been incorrectly classified as stable with only a 2-year follow-up. In some combination, these differences in study design may be responsible.

As the receiver operating characteristic curves illustrate (Fig 3), for our population sample, the NSI was able to more

consistently discriminate growing and stable aneurysms on the basis of the initial imaging study than aneurysm diameter or other shape indices. The NSI therefore appears to be a useful metric for identifying aneurysms likely to continue to grow, and we hope to eventually see it incorporated into aneurysm management decisions. Growth studies require longitudinal datasets and consequently require the analysis of many more sets of images. Because morphologic characterization of aneu-

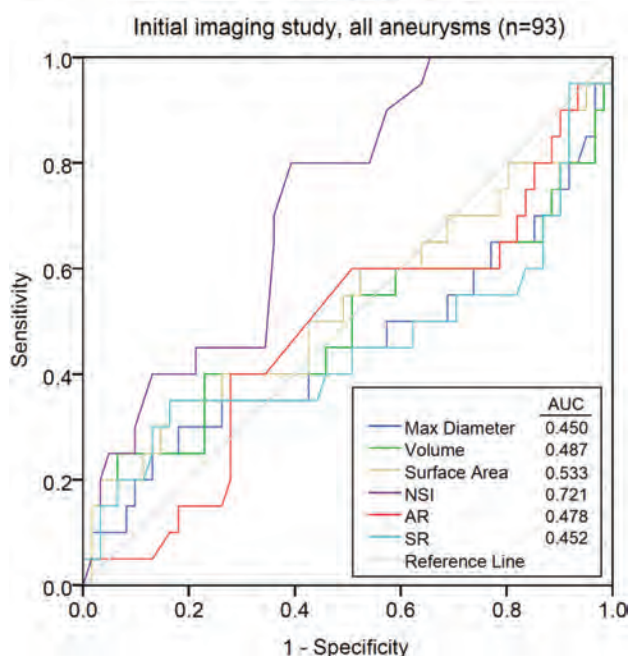
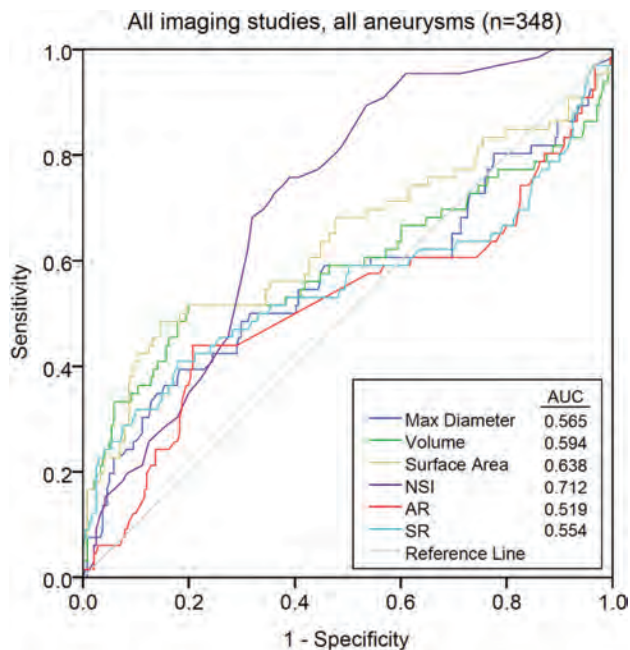


FIG 3. Receiver operating characteristic curves for each of the indices included in the study, for all imaging studies, and the initial imaging study only. Area under the curve values are listed in the legends. The NSI provides the best discrimination between growing and stable aneurysms (area under the curve = 0.712 for all imaging studies, and area under the curve = 0.721 for the initial imaging study). AR indicates aspect ratio; SR, size ratio; max, maximum.

rysms is relatively rapid, such assessments can be scaled for multicenter studies or clinical practice. Future work will combine morphologic indices like the NSI with more detailed epidemiologic analysis.

Limitations

Because this was a single-center retrospective study, it has bias, including existing treatment preferences, such as anatomic location and type, which results in censoring of data. In addition, the

Table 3: Index values for growing and stable aneurysms segregated by location^a

Index	ACA	ICA	PcomA
Maximum diameter			
Growing	4.66 ± 2.63	3.86 ± 1.45	5.20 ± 2.85
Stable	3.76 ± 1.77	4.36 ± 1.88	4.05 ± 1.30
Volume			
Growing	71.8 ± 69.6	85.5 ± 175	260 ± 324
Stable	47.2 ± 45.8	51.9 ± 99.7	82.6 ± 102
Surface area			
Growing	75.2 ± 60.7	87.5 ± 116	202 ± 192
Stable	57.3 ± 38.9	68.5 ± 65.4	105 ± 91.8
NSI			
Growing	0.31 ± 0.11 ^{b,c}	0.38 ± 0.12	0.39 ± 0.08
Stable	0.22 ± 0.07 ^b	0.31 ± 0.12	0.45 ± 0.08
Aspect ratio			
Growing	0.95 ± 0.25	0.90 ± 0.40	0.98 ± 0.29
Stable	1.17 ± 0.39	0.96 ± 0.33	0.73 ± 0.25
Size ratio			
Growing	1.53 ± 1.09	0.93 ± 0.55	1.40 ± 0.86 ^{b,c}
Stable	1.48 ± 0.75	1.03 ± 0.50	0.81 ± 0.33 ^b

^a Data are presented as mean ± SD.

^b Significant difference between groups.

^c $P < .01$.

Table 4: Index values for growing and stable aneurysms segregated by aneurysm type^a

	Bifurcation (n = 16)	Sidewall (n = 77)
Max diameter		
Growing	4.19 ± 1.68	3.93 ± 2.21
Stable	3.96 ± 2.16	4.18 ± 1.79
Volume		
Growing	54.8 ± 52.5	122 ± 214
Stable	51.0 ± 57.1	58.2 ± 114
Surface area		
Growing	68.9 ± 42.9	113 ± 145
Stable	62.7 ± 51.8	71.7 ± 73.0
NSI		
Growing	0.31 ± 0.10	0.39 ± 0.11 ^{b,c}
Stable	0.22 ± 0.07	0.31 ± 0.12 ^b
Aspect ratio		
Growing	1.00 ± 0.33	1.01 ± 0.57
Stable	1.02 ± 0.32	1.02 ± 0.41
Size ratio		
Growing	1.71 ± 1.45	1.11 ± 0.77
Stable	1.37 ± 0.91	1.15 ± 0.62

Note:—Max indicates maximum.

^a Data are presented as mean ± SD.

^b Significant difference between groups.

^c $P < .01$.

sample is likely biased against aneurysms >7 mm and of irregular shape because these are more frequently treated, except in circumstances such as advanced age. Such bias is likely to be present in a prospective study as well, to not endanger patient safety. Regarding the measurement method, as aneurysm size decreases, the accuracy of measurements does as well. Examination of how different CTA imaging protocols affect such measurements would be beneficial.²⁶ Finally, as expected on the basis of the frequency of intracranial aneurysm growth after diagnosis, there are significantly more stable aneurysms than growing aneurysms in the study. This finding is further exacerbated in some of the size/location groups and may make it more challenging to generalize the findings to the broader population. A larger, multicenter retrospective study including several years of data could address most of these issues.

CONCLUSIONS

This study identified a significant relationship between aneurysm morphologic characteristics and growth. Specifically, the NSI was relatively consistently associated with growth in various analyses, in which it tended to be larger for aneurysms that would continue to grow. Additional shape indices such as size ratio were found to be associated with growth for particular size ranges and locations. Morphologic analysis appears to be a powerful means of identifying aneurysms likely to grow as well as a useful tool to investigate aneurysm growth, suitable for studies with many cases.

Disclosures: Aichi Chien—RELATED: Grant: Brain Aneurysm Foundation Research Grant and Society of Interventional Radiology Foundation Dr. Ernest J. Ring Academic Development Grant.* *Money paid to the institution.

REFERENCES

1. Brown RD. **Unruptured intracranial aneurysms.** *Semin Neurol* 2010;30:537–44 CrossRef Medline
2. International Study of Unruptured Intracranial Aneurysms Investigators. **Unruptured intracranial aneurysms: risk of rupture and risks of surgical intervention.** *N Engl J Med* 1998;339:1725–33 CrossRef Medline
3. Villablanca JP, Duckwiler GR, Jahan R, et al. **Natural history of asymptomatic unruptured cerebral aneurysms evaluated at CT angiography: growth and rupture incidence and correlation with epidemiologic risk factors.** *Radiology* 2013;269:258–65 CrossRef Medline
4. Chien A, Liang F, Sayre J, et al. **Enlargement of small, asymptomatic, unruptured intracranial aneurysms in patients with no history of subarachnoid hemorrhage: the different factors related to the growth of single and multiple aneurysms.** *J Neurosurg* 2013;119:190–97 CrossRef Medline
5. Backes D, Rinkel GJ, Laban KG, et al. **Patient- and aneurysm-specific risk factors for intracranial aneurysm growth: a systematic review and meta-analysis.** *Stroke* 2016;47:951–57 CrossRef Medline
6. Brinjikji W, Zhu YQ, Lanzino G, et al. **Risk factors for growth of intracranial aneurysms: a systematic review and meta-analysis.** *AJNR Am J Neuroradiol* 2016;37:615–20 CrossRef Medline
7. Bijlenga P1, Ebeling C, Jaegersberg M, et al; @neurIST Investigators. **Risk of rupture of small anterior communicating artery aneurysms is similar to posterior circulation aneurysms.** *Stroke* 2013;44:3018–26 CrossRef Medline
8. Chien AC, Sayre J, Viñuela F. **Comparative morphological analysis of the geometry of ruptured and unruptured aneurysms.** *Neurosurgery* 2011;69:349–56 CrossRef Medline
9. Raghavan ML, Ma B, Harbaugh RE. **Quantified aneurysm shape and rupture risk.** *J Neurosurg* 2005;102:355–62 CrossRef Medline
10. Dhar S, Tremmel M, Mocco J, et al. **Morphology parameters for intracranial aneurysm rupture risk assessment.** *Neurosurgery* 2008;63:185–96; discussion 196–97 CrossRef Medline
11. Xiang J, Natarajan SK, Tremmel M, et al. **Hemodynamic-morphologic discriminants for intracranial aneurysm rupture.** *Stroke* 2011;42:144–52 CrossRef Medline
12. Baharoglu MI, Lauric A, Gao BL, et al. **Identification of a dichotomy in morphological predictors of rupture status between sidewall- and bifurcation-type intracranial aneurysms.** *J Neurosurg* 2012;116:871–81 CrossRef Medline
13. Cebral JR, Castro MA, Burgess JE, et al. **Characterization of cerebral aneurysms for assessing risk of rupture by using patient-specific computational hemodynamics models.** *AJNR Am J Neuroradiol* 2005;26:2550–59 Medline
14. Patti J, Viñuela F, and Chien AC. **Distinct trends of pulsatility found at the necks of ruptured and unruptured aneurysms.** *J Neurointerv Surg* 2014;6:103–07 CrossRef Medline
15. Chien A, Castro MA, Tateshima S, et al. **Quantitative hemodynamic analysis of brain aneurysms at different locations.** *AJNR Am J Neuroradiol* 2009;30:1507–12 CrossRef Medline
16. Cebral JR, Mut F, Weir J, et al. **Quantitative characterization of the hemodynamic environment in ruptured and unruptured brain aneurysms.** *AJNR Am J Neuroradiol* 2011;32:145–51 CrossRef Medline
17. Ramachandran M, Retarekar R, Raghavan ML, et al. **Assessment of image-derived risk factors for natural course of unruptured cerebral aneurysms.** *J Neurosurg* 2016;124:288–95 CrossRef Medline
18. Chien A, Lau V, Yi Q, et al. **Posterior communicating artery aneurysms demonstrate faster interval growth than other growing aneurysms.** *Neuroradiol J* 2017 Jan 1. [Epub ahead of print] CrossRef Medline
19. Ujiie H, Tachibana H, Hiramatsu O, et al. **Effects of size and shape (aspect ratio) on the hemodynamics of saccular aneurysms: a possible index for surgical treatment of intracranial aneurysms.** *Neurosurgery* 1999;45:119–29; discussion 129–30 Medline
20. Tremmel M, Dhar S, Levy EI, et al. **Influence of intracranial aneurysm-to-parent vessel size ratio on hemodynamics and implication for rupture: results from a virtual experimental study.** *Neurosurgery* 2009;64:622–30; discussion 630–21 CrossRef Medline
21. Villablanca JP, Hooshi P, Martin N, et al. **Three-dimensional helical computerized tomography angiography in the diagnosis, characterization, and management of middle cerebral artery aneurysms: comparison with conventional angiography and intraoperative findings.** *J Neurosurg* 2002;97:1322–32 CrossRef Medline
22. Villablanca JP, Jahan R, Hooshi P, et al. **Detection and characterization of very small cerebral aneurysms by using 2D and 3D helical CT angiography.** *AJNR Am J Neuroradiol* 2002;23:1187–98 Medline
23. Dong B, Chien A, Mao Y, et al. **Level set based surface capturing in 3D medical images.** *Med Image Comput Comput Assist Interv* 2008;11:162–69 Medline
24. Lederman C, Vese L, Chien A. **Registration for 3D morphological comparison of brain aneurysm growth.** In: Bebis G, Boyle B, Parvin D, et al, eds. *Advances in Visual Computing: 7th International Symposium, ISVC 2011, Las Vegas, NV, USA, September 26–28, 2011, Proceedings. Part I.* Berlin: Springer-Verlag; 2011:392–99
25. Chien A, Sayre J. **Morphologic and hemodynamic risk factors in ruptured aneurysms imaged before and after rupture.** *AJNR Am J Neuroradiol* 2014;35:2130–35 CrossRef Medline
26. O'Meara B, Rahal JP, Lauric A, et al. **Benefit of a sharp computed tomography angiography reconstruction kernel for improved characterization of intracranial aneurysms.** *Neurosurgery* 2014;10(Suppl 1):97–105; discussion 105 CrossRef Medline

Local Glioma Cells Are Associated with Vascular Dysregulation

S.G. Bowden,¹ B.J.A. Gill,¹ Z.K. Englander,¹ C.I. Horenstein,¹ G. Zanazzi,¹ P.D. Chang,¹ J. Samanamud,¹ A. Lignelli,¹ J.N. Bruce,¹ P. Canoll, and J. Grinband



ABSTRACT

BACKGROUND AND PURPOSE: Malignant glioma is a highly infiltrative malignancy that causes variable disruptions to the structure and function of the cerebrovasculature. While many of these structural disruptions have known correlative histopathologic alterations, the mechanisms underlying vascular dysfunction identified by resting-state blood oxygen level–dependent imaging are not yet known. The purpose of this study was to characterize the alterations that correlate with a blood oxygen level–dependent biomarker of vascular dysregulation.

MATERIALS AND METHODS: Thirty-two stereotactically localized biopsies were obtained from contrast-enhancing ($n = 16$) and nonenhancing ($n = 16$) regions during open surgical resection of malignant glioma in 17 patients. Preoperative resting-state blood oxygen level–dependent fMRI was used to evaluate the relationships between radiographic and histopathologic characteristics. Signal intensity for a blood oxygen level–dependent biomarker was compared with scores of tumor infiltration and microvascular proliferation as well as total cell and neuronal density.

RESULTS: Biopsies corresponded to a range of blood oxygen level–dependent signals, ranging from relatively normal ($z = -4.79$) to markedly abnormal ($z = 8.84$). Total cell density was directly related to blood oxygen level–dependent signal abnormality ($P = .013$, $R^2 = 0.19$), while the neuronal labeling index was inversely related to blood oxygen level–dependent signal abnormality ($P = .016$, $R^2 = 0.21$). The blood oxygen level–dependent signal abnormality was also related to tumor infiltration ($P = .014$) and microvascular proliferation ($P = .045$).

CONCLUSIONS: The relationship between local, neoplastic characteristics and a blood oxygen level–dependent biomarker of vascular function suggests that local effects of glioma cell infiltration contribute to vascular dysregulation.

ABBREVIATIONS: BOLD = blood oxygen level–dependent; CE = contrast-enhancing; Gd = gadolinium; NE = nonenhancing

Malignant glioma is a highly infiltrative malignancy that causes variable disruptions to the structure and function of the cerebrovasculature.¹ Most prominent among these is a break-

down of the blood-brain barrier, associated with the main tumor mass^{1–3} and clinically evident through the extravasation of gadolinium-conjugated contrast media.⁴ However, other vascular deficits are identifiable in the infiltrative margin of the tumor. Vasogenic edema, represented by T2-FLAIR hyperintensity, is the most frequently used abnormality for directing surgical and radiation treatments in nonenhancing (NE) areas. Recent application of functional imaging has identified additional physiologic consequences of malignant glioma infiltration, with decreased vascular reactivity noted on hypercapnia challenges^{5–7} and reduced cor-

Received February 8, 2017; accepted after revision November 9.

From the Department of Neurological Surgery (S.G.B.), Oregon Health & Science University, Portland, Oregon; The Gabriele Bartoli Brain Tumor Research Laboratory (S.G.B., B.J.A.G., Z.K.E., J.S., J.N.B., P.C.), and Departments of Neurological Surgery (B.J.A.G., Z.K.E., J.N.B., P.C.), Pathology and Cell Biology (G.Z., P.C.), and Radiology (A.L., J.G.), Columbia University Medical Center, New York, New York; Department of Radiology (C.I.H.), North Shore University Hospital, Long Island, New York; and Department of Radiology (P.D.C.), University of California, San Francisco, California.

Preliminary results from this work were presented at: Eastern-Atlantic Medical Student Research Forum, March 3–5, 2016; Miami, Florida. Further results were previously presented at: Society of Neuro-Oncology Annual Meeting and Education Day, November 17–22, 2016; Scottsdale, Arizona.

This project was funded, in part, by the 2015 Research Scientist Award from the American Society of Neuroradiology (J.G.), the James S. McDonnell Foundation, and the Irving Institute for Clinical and Translational Research: Pilot Research Award (P.C.). Support from NVIDIA included 1 TITAN X Graphic Card (12 GB) to run a deep learning code to perform cell counting (P.D.C.). Dr Chang's salary is sup-

ported by the National Institutes of Health (National Institute of Biomedical Imaging and Bioengineering) T32 Training Grant, T32EB001631.

Please address correspondence to Jack Grinband, PhD, Department of Radiology, Columbia University, 710 West 168th St, New York, NY 10032; e-mail: jackgrinband@gmail.com

Indicates open access to non-subscribers at www.ajnr.org

Indicates article with supplemental on-line table.

<http://dx.doi.org/10.3174/ajnr.A5526>

tical activation intensity and volume using task-based fMRI.^{8–11} Tumor vessel angiogenesis is a frequently cited and plausible contributor to such deficits within the contrast-enhancing (CE) tumor mass.^{5,7,9,10} However, areas of decreased vascular reactivity and reduced cortical activation have also been identified in lower grade gliomas, indicating that even sparsely infiltrated regions of brain parenchyma could have similar functional impairment.⁵ Nevertheless, the variable presence, distribution, and degree of these abnormalities leave their relationship to tumor infiltration uncertain.

A recent report by Chow et al¹² identified a biomarker of glioma-related vascular dysregulation using resting-state blood oxygen level-dependent (BOLD) fMRI. The mean BOLD time-series extracted from normal, tumor-free brain of the contralesional hemisphere represents normal cardiac pulsations and respiration-related changes in arterial carbon dioxide (CO₂)^{13–15} and can be used as a temporal signature of normal vascular reactivity.¹⁶ Similarly, the mean BOLD time-series extracted from CE tumor represents abnormal tumor-related vascular function. By combining these temporal signatures, the spatial extent of glioma-related vascular deficits can be illustrated by identifying voxels of NE brain parenchyma that behave more like the CE tumor and less like the normal contralesional brain tissue. This technique demonstrated that vascular dysregulation can extend beyond the CE tumor core into the NE infiltrative margin. Furthermore, the presence of nonoverlapping regions between the BOLD biomarker and T2-FLAIR hyperintensity, or BOLD-FLAIR mismatch, suggests discordance between deficits in neurovascular function and a breakdown of the blood-brain barrier. However, the absence of a histologic correlate in Chow et al¹² leaves substantial uncertainty as to whether this vascular dysregulation is related directly to tumor infiltration or to the indirect effects of the tumor. For example, such dysfunction could be directly related to local tumor effects, such as a disruption in the structural, physical, or ultrastructural properties of the brain by invading glioma cells.¹¹ Alternatively, distal, indirect causes, such as mass effect from the tumor or vasogenic edema; disruption of shared venous drainage; or damage to axons could also explain these BOLD abnormalities.^{8,12,17}

The purpose of this study was to characterize the histopathologic alterations underlying the BOLD biomarker of vascular dysfunction in malignant gliomas. We compared BOLD dynamics from resting-state fMRI with neoplastic characteristics of a set of stereotactically localized biopsies. We hypothesized that the degree of disruption of vascular function measured by the BOLD biomarker is related to the severity of histopathologic abnormalities associated with tumor infiltration.

MATERIALS AND METHODS

Patient Selection

We performed a retrospective review of a database of MRI-localized biopsies obtained during open surgical resection of glioma at Columbia University Medical Center (CUMC). All patients included in the database previously provided consent as part of a CUMC review board-approved study protocol. Seventeen patients with pathology-proved, treatment-naïve glioblastoma ($n = 14$) or grade III, *IDH* wild-type astrocytoma ($n = 3$) and preop-

erative BOLD fMRI were identified. The average age was 63.8 years (range, 48–82 years) with 5 men and 12 women. Thirty-two tissue biopsies were obtained from the CE ($n = 16$) and the NE ($n = 16$) regions of tumor during open surgical resection. Automated cell counting was successfully performed on 31 H&E stains and 28 NeuN stains (MAB377; MilliporeSigma, Darmstadt, Germany).

Image Acquisition

Before tumor resection, patients underwent standard-of-care imaging (including T1-weighted, gadolinium-enhanced [T1+Gd], T2-FLAIR, and DWI) as well as a resting-state BOLD fMRI scans on 1 of 4 hospital scanners (Intera 1.5T, Achieva 3T, Philips Healthcare, Best, the Netherlands; TwinSpeed HDx 1.5T or Excite HDx 3T, GE Healthcare, Milwaukee, Wisconsin). The ranges of scanning parameters for T1 sequences were the following: TR = 10–2000 ms, flip angle = 13°–90°, TE = 2–20 ms. For FLAIR sequences, the ranges were the following: TR = 8000–11,000 ms, flip angle = 90°, TE = 104–337 ms, TI = 2200–2800 ms. BOLD parameters were the following: TR = 1000–2400 ms, flip angle = 72°–90°, TE = 20–34 ms, number of volumes = 150–200. The scanning parameters for each patient are listed in the On-line Table. Contrast-enhanced images were acquired with IV gadobenate dimeglumine (MultiHance; Bracco Diagnostics, Princeton, New Jersey) with a weight-based dose of 0.2 mL/kg. The time between the IV injection and contrast-enhanced imaging was 5 minutes. BOLD images were obtained before contrast-enhanced imaging.

Biopsy Acquisition

All tissue sampling was performed during the normal surgical plan, provided it posed no additional risk to the patient. Samples were taken from the CE tumor core in all cases and NE regions when within the planned surgical trajectory. Biopsies were obtained before surgical debulking to minimize the effects of brain shift and deformation. Frameless stereotactic guidance was provided by a volumetric T1+Gd scan uploaded to a neuronavigation interface (Curve; Brainlab, Feldkirchen, Germany). Biopsy location was recorded by screen captures of the neuronavigation interface, allowing the downstream determination of the Cartesian coordinates of each biopsy. We have recently shown that this method results in spatial accuracy to within ~2 mm.¹⁸ Biopsies that were taken from radiologically defined areas of necrosis or those that were predominantly histologically necrotic (>75% of the tissue sample) were excluded from the analysis.

Histopathologic Analysis

Samples were formalin-fixed and paraffin-embedded for histopathologic analysis. Five-micrometer sections were stained with H&E. Seven-micrometer sections were immunostained with the NeuN antibody. Qualitative histologic characteristics of neoplasms were evaluated by 2 blinded neuropathologists (G.Z., P.C.). H&E-stained sections were reviewed for the degree of tumor infiltration and scored as no tumor present (score = 0), infiltrating tumor (score = 1), or highly cellular tumor (score = 2). The tumor score was a composite of several features, including cytologic atypia and cell density. H&E slides were also reviewed

for the degree of microvascular proliferation, scored as delicate microvasculature (normal vascular architecture; score = 0), simple hyperplastic structures (<3 circumferential layers with patent lumen; score = 1), or complex microvascular hyperplasia (≥ 3 endothelial layers or glomeruloid-type vessels; score = 2).

Total cell density was calculated using an automated cell-counting algorithm.¹⁸ Briefly, the H&E-stained sections were digitized using a Leica scn400 system (Leica Biosystems, Buffalo Grove, Illinois), with hematoxylin-stained nuclei counted in iteratively processed high-power fields. Total cell density was computed as the median number of hematoxylin-stained cells across all high-power fields that contained at least 1 nucleus. Each immunoperoxidase-stained slide was digitized at low-power $\times 10$ magnification, and a semiautomated algorithm was used to determine the overall NeuN index, to calculate the labeling index for NeuN. For each slide, user-defined RGB (3-channel) and size thresholds were determined by visual inspection of 9 randomly generated low-power $\times 10$ fields. On the basis of these statistics, the algorithm subsequently identified all immunoperoxidase-stained cells in each low-power field and computed the neuronal fraction by dividing the surface area of stained cells by the total surface area of all tissue in the low-power field. The NeuN index was defined as the 90% quantile of fractions across all low-power fields that contained at least 1 stained cell.

Screenshot Registration and Coordinate Determination

Screenshots of the neuronavigation interface showing the biopsy location were superimposed onto a coregistered T1+Gd image. Coregistration of the screenshots to the T1+Gd image in 3D space was performed using custom software written in Matlab (MathWorks, Natick, Massachusetts). The registration pipeline first correlated the pixel intensities of the screenshot to the voxel intensities of each volumetric T1 slice, and the slice with peak correlation was identified as the biopsy slice. A correlation between the screenshot and the biopsy slice was then taken at different x and y offsets, and the peak correlation was used to identify the correct x and y offsets. Finally, each biopsy location on the screenshot was labeled with a cross-hair. To identify this location, we correlated a digital cross-hair to the screenshot at different x and y offsets and used the peak correlation to identify the x and y coordinates of the biopsy site. All coregistered screenshots were confirmed by visual inspection.

Tumor Masks

All structural images were coregistered to the T1+Gd image with the highest spatial resolution using rigid-body registration (FMRIB Linear Image Registration Tool, FLIRT; <https://fsl.fmrib.ox.ac.uk/fsl/fslwiki/FLIRT>¹⁹; 6 *df*), and all masks were created in the high-resolution reference image space. 3D masks of the CE tumor were hand drawn on high-resolution T1+Gd images by a board-certified neuroradiologist (C.I.H.). The boundaries of the masks were drawn to be as specific for CE intra-axial tumor as possible. To this end, we excluded the following from the tumor mask: ambiguous voxels at the border of CE tumor and NE brain tissue; ambiguous voxels at the border of CE tumor and necrotic core; areas of linear enhancement determined to represent vessels; and extra-axial spread of tumor along the dura or ventricular

surface. The control masks were generated by coregistering the T1+Gd image to Montreal Neurological Institute 152 space and transforming a contralesional hemisphere mask, created in Montreal Neurological Institute 152 space, to the patient's reference space (ie, the high-resolution T1+Gd image) using nearest-neighbor interpolation. The contralesional control masks were then visually inspected by a board-certified neuroradiologist (C.I.H.) to ensure that no CE tumor or abnormal FLAIR hyperintense tissue was included in the mask. To generate the functional masks, we registered BOLD scans to the high-resolution reference image (FLIRT, 6 *df*) and applied the inverse transform to the high-resolution masks to put them into functional space. Because the BOLD data were collected at a lower spatial resolution than the structural data, the transformation of the masks resulted in partial voluming. To minimize any influence of partial voluming from nonenhancing portions of the surrounding tissue, the CE masks were thresholded so that the fraction of the CE tumor was at least 0.95. Similarly, the control masks were thresholded so that the fraction of NE tissue was at least 0.95. All original and transformed masks were visually inspected by a board-certified radiologist (C.I.H.) to confirm accuracy.

Image Preprocessing of BOLD Data

All functional data were processed with the FMRIB Software Library (FSL, Version 5.0.6; <http://www.fmrib.ox.ac.uk/fsl>)¹⁹ and Matlab (2012b) software. Each functional image was motion-corrected, slice-timing corrected, spatially smoothed (Gaussian filter, full width at half maximum = 5 mm), high-pass filtered (100 seconds), and skull-stripped. We performed independent components analysis (MELODIC; <https://fsl.fmrib.ox.ac.uk/fsl/fslwiki/MELODIC>²⁰), which resulted in ~ 40 – 90 components per scan. The components were visually inspected, and any components related to scanner noise or head movement artifacts were removed. To further minimize the effect of motion on BOLD signal intensity, the motion parameters were regressed out of the data before additional regression was performed with the tumor and control ROI time-series. The 18 motion regressors used in the regression model consisted of 3 translations, 3 rotations, the first derivative of each, and the corresponding quadratic terms. The residual from this model was then used for all subsequent regression analyses.

BOLD Dynamics

To create the BOLD masks, we followed the procedure described in Chow et al.¹² We first made the simplifying assumption that there are 2 functional tissue classes within the brain, tumor and healthy tissue, which are represented by the CE portion of the tumor and the contralesional hemisphere, respectively. Mean time-series were extracted from the masks defined by the CE tumor and from the contralesional control hemisphere, by averaging the BOLD time-series of all voxels within each mask. Multiple linear regression was performed for all brain voxels using the 2-regressor model, the CE tumor mean time-series and the contralesional control mean time-series and their first derivatives, to allow variation in timing. The output of this analysis and the metrics used to make our conclusions consisted of parameter estimates (β weights) and z statistic values (β weights normalized by

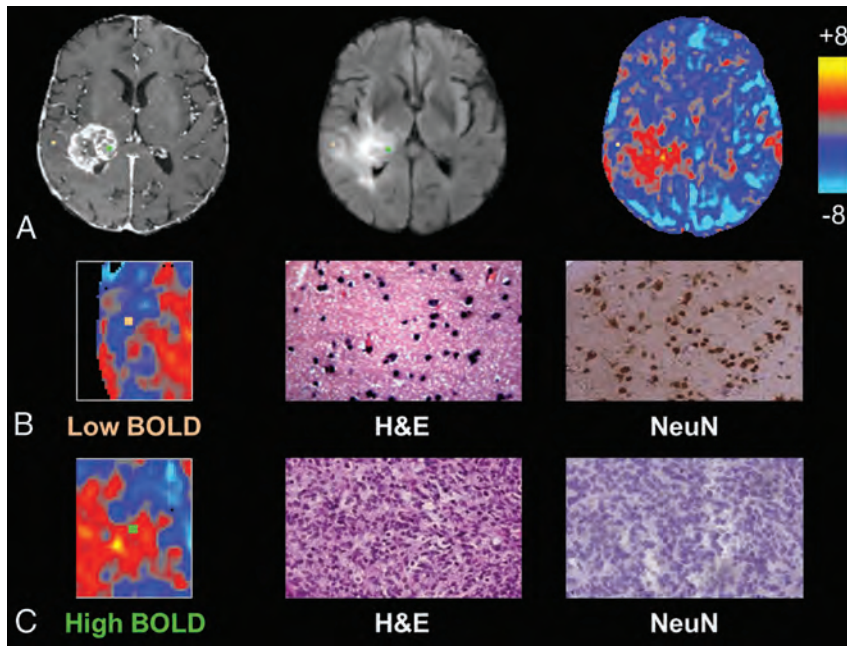


FIG 1. Individual biopsies from areas of intact and disrupted vascular function exhibit distinct histopathologic characteristics. A, Biopsy locations overlaid onto T1 postcontrast, FLAIR, and BOLD images with correlative histopathology in B and C. The sample from relatively normal BOLD signal, representing normal vascular function (orange, B), shows normal cellularity and high NeuN staining, suggestive of noninfiltrated gray matter, whereas the sample from a region of BOLD signal abnormality (green, C) shows tumor tissue and no neuronal staining.

the residual variance) for each voxel. The difference between the 2 z statistic images (ie, $Z_{CE} - Z_{Control}$) was used as the BOLD biomarker representing vascular function, as described in Chow et al.¹² Specifically, strongly negative values (shown in blue on z statistic maps, Fig 1) represent areas of normal vascular function—that is, the voxel time-series is more like the control ROI; strongly positive values (shown in red-yellow on z statistic maps, Fig 1) represent areas of vascular dysregulation—that is, the voxel time-series is more like the CE tumor.

Analysis of Histopathologic and Radiologic Correlation

All statistical tests were performed using the Statistics Toolbox in Matlab (2012b). Linear regression was used to evaluate the relationships between BOLD signal intensity and quantitative histopathologic features (total cell density and NeuN labeling index). The parameter estimate for the CE regressor decreases as a function of distance from the CE mask due to tumor-related vascular dysregulation and nonspecific effects of distance (ie, voxels in close proximity have more similar intensities than voxels that are far apart). To control for nonspecific effects of distance, we included a distance regressor, the measured distance from the biopsy location to the nearest CE voxel, in the regression model of cellularity versus BOLD and NeuN versus BOLD. To assess the relationship between qualitative histologic features (degree of tumor infiltration and microvascular proliferation) and the BOLD signal, we performed a 1-way analysis of variance.

RESULTS

Biopsies demonstrated a range of BOLD signal intensities based on their projection onto z statistic maps, ranging from relatively normal ($z = -4.79$) to markedly abnormal ($z = 8.84$). Differences in the degree of signal abnormality appeared to be related to

certain histopathologic characteristics within individual tissue samples. Representative biopsies from a single patient are shown in Fig 1, which illustrates tissue samples taken from areas of differing BOLD signals (Fig 1A). Tissue corresponding to a negative BOLD value ($z = -1.90$; Fig 1B) demonstrated normal cell density, high NeuN staining, noninfiltrated gray matter, and normal, delicate microvasculature. In contrast, a sample corresponding to a highly positive BOLD signal ($z = 4.44$; Fig 1C) contained hypercellular tissue, little neuronal staining, highly cellular tumor, and complex microvascular hyperplasia.

Among all biopsies, linear regression analysis demonstrated a significant inverse relationship between total cell density and distance from the nearest CE voxel ($P = .003$, $R^2 = 0.27$; Fig 2A) and a positive relationship between neuronal density and distance ($P = .032$, $R^2 = 0.17$; Fig 2B). The BOLD signal also showed an inverse relationship with distance ($P = .004$, $R^2 = 0.25$; Fig 2C). Linear regression between BOLD signal intensity and total cell density, with distance to the nearest CE voxel as a confounding variable, showed a positive relationship ($P = 2 \times 10^{-5}$, $R^2 = 0.48$; Fig 3A). A similar analysis showed that the NeuN labeling index was negatively related to BOLD signal intensity ($P = .001$, $R^2 = 0.35$; Fig 3B). An alternative explanation for this negative relationship could be the greater prevalence of gliomas in white matter, which normally has low neuronal density, rather than the neurotoxic effects of the tumor. To test this hypothesis, we compared the BOLD values in gray (mean, -2.9 ± 0.76) and white (mean, -2.4 ± 0.83) matter on the contralesional control hemisphere. Gray matter voxels were significantly more negative than white matter voxels (t test, $P = .001$, $t = 4.00$); however, the difference in BOLD values due to tissue type (gray-white = -0.54 ± 0.56) cannot explain the very large range of BOLD values

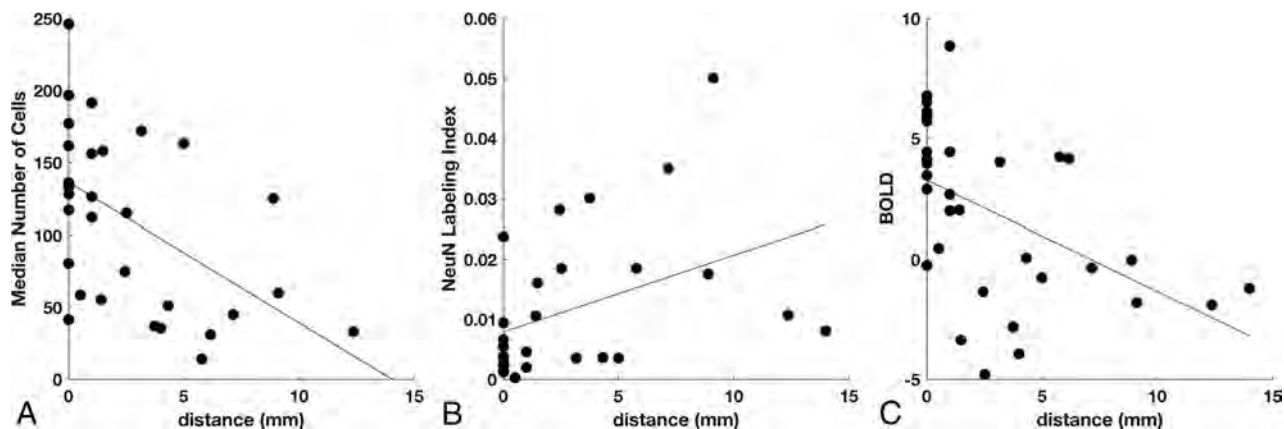


FIG 2. Effect of distance from contrast enhancement on cellularity, neuronal density, and BOLD signal abnormality. *A*, Cell density decreases with the distance to the nearest contrast-enhancing voxel ($n = 31$, $P = .003$). *B*, Neuronal density increases with the distance to contrast enhancement ($n = 27$, $P = .032$). *C*, Intensity of the BOLD biomarker decreases with the distance to contrast enhancement ($n = 32$, $P = .004$).

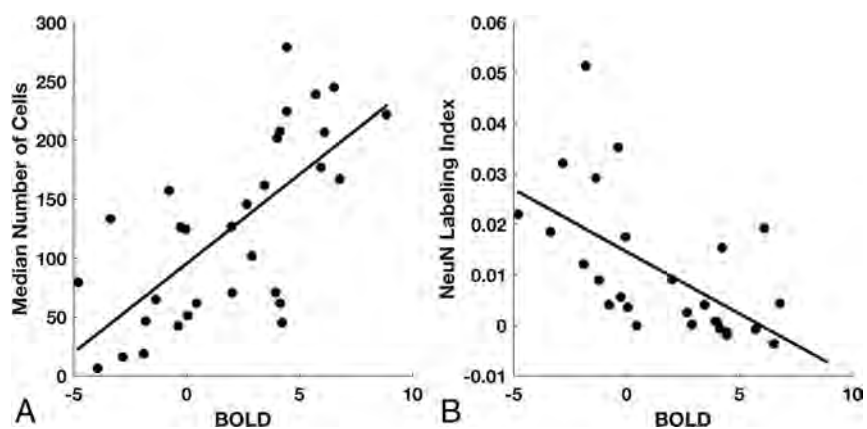


FIG 3. BOLD signal abnormality is related to total cell and neuronal density. *A*, After we controlled for the effect of distance on the BOLD signal, median cell density is positively related to the BOLD z statistic ($n = 31$, $P = 2 \times 10^{-5}$). *B*, The NeuN labeling index is inversely related to the BOLD z statistic ($n = 27$, $P = .001$).

across the biopsy samples (maximum–minimum = 8.85 to –4.79 = 13.64).

The distributions of BOLD signal abnormality related to tumor infiltration and microvascular proliferation are summarized in Fig 4. Across all biopsies, both the tumor infiltration score (ANOVA: $F[2,29] = 4.95$, $P = .014$) (Fig 4A) and the microvascular proliferation score (ANOVA: $F[2,29] = 3.46$, $P = .045$) (Fig 4B) were significantly related to the BOLD signal abnormality. A post hoc Student *t* test showed a significant difference in BOLD signal between the group of samples with no detectable tumor (score = 0) and those with highly cellular tumor (score = 2; $P = .003$) or the combination of infiltrating and highly cellular tumor (score 1 or 2; $P = .029$). Similarly, a *t* test showed a significant difference in BOLD signal between the group of samples with no identifiable microvascular proliferation (score = 0) and those with marked vascular hyperplasia (score = 2; $P = .038$) or the combination of simple and complex vascular hyperplasia (score 1 or 2; $P = .027$).

DISCUSSION

The diffuse infiltration and histologic heterogeneity of malignant gliomas pose a distinct challenge to the identification of the toxic effects of these tumors on the structure and function of the cere-

brovasculature. The integrity of the vasculature in and around the main mass of the tumor is typically assessed with standard-of-care imaging that uses T1-weighted contrast-enhanced and FLAIR sequences.^{1–4} Regions of abnormal contrast enhancement associated with the main tumor mass typically correspond to elevated CBV, CBF, and microvascular permeability on perfusion-weighted imaging.^{21–27} Most interesting, there are few vascular abnormalities in the NE, FLAIR-hyperintense peritumoral regions on perfusion imaging,^{21–27} despite the recognized infiltration of tumor cells into these areas.^{28–31} Additional evidence suggests that edema surrounding the tumor originates directly from the CE tissue, passively diffuses into the NE regions, and may therefore not be associated with blood-brain barrier breakdown in the NE tissue.^{32,33}

Several intriguing studies have, however, identified decreased vascular reactivity outside CE regions of glioma.^{5,7,34} In turn, it has been postulated that infiltrating glioma cells disrupt neurovascular coupling,^{35,36} impairing both normal hypercapnia-induced elevations in CBF and CBV and the vascular reactivity of cortical tissue, particularly within gray matter. However, without any histopathologic correlation to these radiologic findings, it has been unclear whether infiltrating glioma cells contribute directly

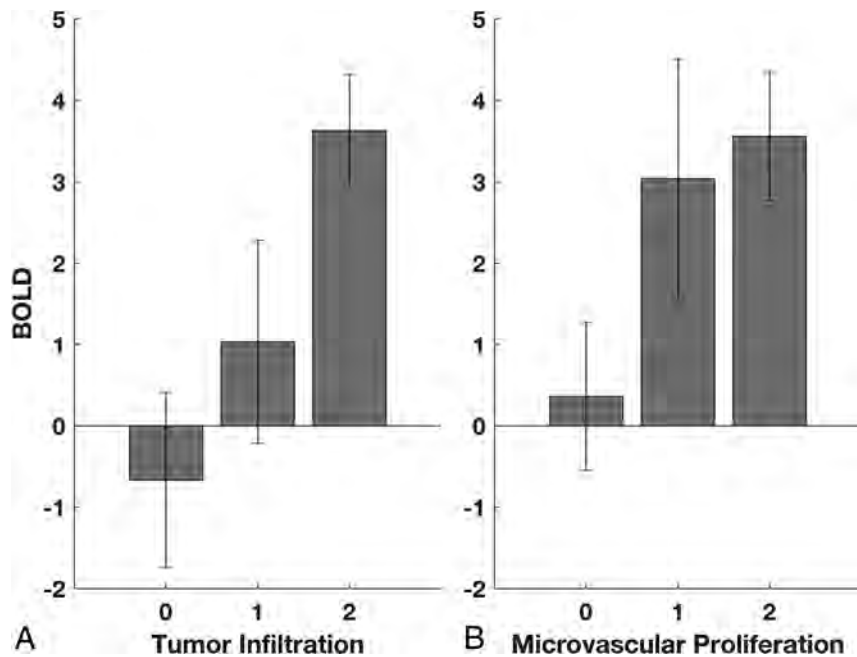


FIG 4. BOLD signal abnormality is related to tumor infiltration and microvascular proliferation. *A*, ANOVA demonstrates a significant relationship between the BOLD z statistic and tumor infiltration ($P = .014$). Scores of 0, 1, and 2 represent no detectable tumor, infiltrating tumor, and highly cellular tumor, respectively. *B*, ANOVA demonstrates a significant relationship between the BOLD z statistic and microvascular proliferation ($P = .045$). Scores of 0, 1, and 2 represent normal vascular architecture, simple hyperplastic structures, and complex microvascular hyperplasia, respectively.

to these abnormalities. The results of the present study, by relating histopathologic and radiologic data, demonstrate that the BOLD biomarker of vascular dysfunction is directly associated with tumor infiltration. We found markedly abnormal tissue in areas of BOLD signal abnormality and relatively unaffected brain tissue in areas of relatively normal BOLD signal. Moreover, the BOLD biomarker is directly related to total cell density and inversely related to neuronal density and is correlated to scores of tumor infiltration and microvascular proliferation.

The spatial distribution of the BOLD biomarker is also consistent with a decreasing cell density gradient with distance from the tumor core.²⁸ The biomarker decreases as a function of distance from the CE tumor core, replicating our previous findings.¹² We found that the effect of distance is similar among BOLD, cellularity, and neuronal density, suggesting that the detectable infiltrating margins of the tumor span approximately 1–2 cm beyond the contrast enhancement, comparable with the commonly used 2- to 3-cm margins for radiation treatment.³⁷ More important, the relationship between the BOLD biomarker and the cell counts (ie, cellularity and neuronal density) remained statistically significant, even after including distance from the CE core as a covariate, indicating that the BOLD data can explain additional variance of tumor heterogeneity unrelated to a simple density gradient.

The mechanisms by which glioma influences vascular function are unknown. Several potential mechanisms have been proposed as broad or long-distance effects of glioma on vascular function. For example, mass effect and consequent venous compression could alter rates of blood flow over large regions of surrounding brain tissue^{8,17}; shared venous drainage could allow signal from blood draining from the tumor core to predominate even in the peritumoral area¹²; the effects of aberrant metabolite

and neurotransmitter production found in gliomas may extend to normal cortical vessels, inducing vascular dysregulation at indeterminate distances from invading tumor cells; and the tumor may affect fibers of passage in its vicinity, inducing necrosis or structural changes with detrimental downstream effects, consistent with findings of multidomain cognitive dysfunction in some patients with glioblastoma that are not easily attributable to local injury from the tumor³⁸ and the disruption of global resting-state networks.^{39–42}

In contrast, local tumor effects may also contribute to the vascular dysfunction seen with the BOLD biomarker. For example, invading glioma cells could perturb the structure of the neurovascular unit by compromising direct contact between vascular endothelial cells and astrocytes.^{1,3,43} Alternatively, astrocytic mediation of the vascular response may be modulated directly by the neurotransmitters of the glioma cells⁴⁴ or by affecting the action of normal signaling molecules.

A BOLD fMRI biomarker of vascular dysfunction has several potential clinical applications that could warrant further investigation. BOLD, with its sensitivity to local effects of infiltrating glioma, could be another useful adjunct in guiding surgery beyond the CE boundary, especially considering the growing body of evidence favoring aggressive resection.^{45,46} For the same reason, it may be useful in targeting adjuvant radiation therapy toward affected areas unamenable to surgical resection. In the same vein, investigating the BOLD dynamics in areas of residual disease may offer insight into the mechanisms of disease recurrence and progression: It is possible that disease recurrence is more attributable to compromised vascular function than residual tumor burden alone. Thus, application of the BOLD biomarker in post-treatment surveillance could offer new insight into patterns of

glioblastoma spread, assess response to new therapies, and segment areas of tumor recurrence.

There are, however, several limitations to our conclusions. There is no way to ensure perfect fidelity between the physical biopsy location and the biopsy site as represented by frameless stereotaxy during an open tumor resection. As per the study protocol, attempts were made to mitigate the effects of intraoperative brain shift within the limits of the surgical plan by minimizing intraoperative use of mannitol, CSF diversion, or hyperventilation before biopsy. Most important, all biopsy sampling was performed before tumor debulking. Nevertheless, it is possible that the BOLD value extracted from the presumed biopsy site could be displaced by ≥ 1 voxel from the true biopsy location. However, we recently showed that our sampling method has registration accuracy to within ~ 2 mm,¹⁸ suggesting that this type of error would have minimal effect on our results.

Additionally, we did not have rigid control of scanning parameters due to the retrospective nature of this study; consequently, contrast-to-noise and signal-to-noise could vary significantly across individuals. However, all structural data were reviewed by a neuroradiologist and assessed to be clearly interpretable for creating tissue masks. Similarly, variability in scanning parameters certainly affected the signal-to-noise properties of the BOLD data. Despite this variability, we showed a significant relationship between BOLD data and histologic features, suggesting that future prospective studies that can hold scanning parameters constant could decrease the variance of this relationship. Finally, masks were constructed by a single neuroradiologist, resulting in some subjectivity in mask boundaries. However, our previous work¹² has demonstrated that the vascular dysregulation maps are not sensitive to small changes in mask variability (eg, using gray matter versus white matter as the contralesional control mask resulted in 2 BOLD maps that had a correlation of 0.96).

CONCLUSIONS

Vascular dysregulation, as represented by a resting-state BOLD biomarker, is seen both within and well beyond the margins of contrast enhancement in malignant gliomas. Many factors likely influence this dysfunction in NE regions. However, the statistically significant correlation between tumor infiltration and the degree of BOLD abnormality suggests that infiltrating glioma cells contribute to vascular dysfunction in both CE and NE regions.

Disclosures: Peter D. Chang—RELATED: Provision of Writing Assistance, Medicines, Equipment, or Administrative Support: NVIDIA Corporation, Comments: donation of graphics-processing unit computing hardware for analysis. Peter Canoll—RELATED: Grant: James S. McDonnell Foundation, Comments: This grant supported the collection and analysis of the localized biopsies*. Jack Grinband—RELATED: Grant: American Society of Neuroradiology*. *Money paid to the institution.

REFERENCES

1. Watkins S, Robel S, Kimbrough IF, et al. **Disruption of astrocyte-vascular coupling and the blood-brain barrier by invading glioma cells.** *Nat Commun* 2014;5:4196 CrossRef Medline
2. Persidsky Y, Ramirez SH, Haorah J, et al. **Blood-brain barrier: structural components and function under physiologic and pathologic conditions.** *J Neuroimmune Pharmacol* 2006;1:223–36 CrossRef Medline
3. Cuddapah VA, Robel S, Watkins S, et al. **A neurocentric perspective on glioma invasion.** *Nat Rev Neurosci* 2014;15:455–65 CrossRef Medline
4. Wen PY, Macdonald DR, Reardon DA, et al. **Updated response assessment criteria for high-grade gliomas: Response Assessment in Neuro-Oncology working group.** *J Clin Oncol* 2010;28:1963–72 CrossRef Medline
5. Pillai JJ, Zacà D. **Comparison of BOLD cerebrovascular reactivity mapping and DSC MR perfusion imaging for prediction of neurovascular uncoupling potential in brain tumors.** *Technol Cancer Res Treat* 2012;11:361–74 CrossRef Medline
6. Hsu YY, Chang CN, Jung SM, et al. **Blood oxygenation level-dependent MRI of cerebral gliomas during breath holding.** *J Magn Reson Imaging* 2004;19:160–67 CrossRef Medline
7. Zacà D, Jovicich J, Nadar SR, et al. **Cerebrovascular reactivity mapping in patients with low grade gliomas undergoing presurgical sensorimotor mapping with BOLD fMRI.** *J Magn Reson Imaging* 2014;40:383–90 CrossRef Medline
8. Holodny AI, Schulder M, Liu WC, et al. **The effect of brain tumors on BOLD functional MR imaging activation in the adjacent motor cortex: implications for image-guided neurosurgery.** *AJNR Am J Neuroradiol* 2000;21:1415–22 Medline
9. Hou BL, Bradbury M, Peck KK, et al. **Effect of brain tumor neovascularity defined by rCBV on BOLD fMRI activation volume in the primary motor cortex.** *Neuroimage* 2006;32:489–97 CrossRef Medline
10. Jiang Z, Krainik A, David O, et al. **Impaired fMRI activation in patients with primary brain tumors.** *Neuroimage* 2010;52:538–48 CrossRef Medline
11. Schreiber A, Hubbe U, Ziyeh S, et al. **The influence of gliomas and nonglial space-occupying lesions on blood-oxygen-level-dependent contrast enhancement.** *AJNR Am J Neuroradiol* 2000;21:1055–63 Medline
12. Chow DS, Horenstein CI, Canoll P, et al. **Glioblastoma induces vascular dysregulation in nonenhancing peritumoral regions in humans.** *AJR Am J Roentgenol* 2016;206:1073–81 CrossRef Medline
13. Shmueli K, van Gelderen P, de Zwart JA, et al. **Low-frequency fluctuations in the cardiac rate as a source of variance in the resting-state fMRI BOLD signal.** *Neuroimage* 2007;38:306–20 CrossRef Medline
14. Murphy K, Birn RM, Handwerker DA, et al. **The impact of global signal regression on resting state correlations: are anti-correlated networks introduced?** *Neuroimage* 2009;44:893–905 CrossRef Medline
15. Birn RM, Murphy K, Bandettini PA. **The effect of respiration variations on independent component analysis results of resting state functional connectivity.** *Hum Brain Mapp* 2008;29:740–50 CrossRef Medline
16. Liu P, Li Y, Pinho M, et al. **Cerebrovascular reactivity mapping without gas challenges.** *Neuroimage* 2017;146:320–26 CrossRef Medline
17. Holodny AI, Schulder M, Liu WC, et al. **Decreased BOLD functional MR activation of the motor and sensory cortices adjacent to a glioblastoma multiforme: implications for image-guided neurosurgery.** *AJNR Am J Neuroradiol* 1999;20:609–12 Medline
18. Chang PD, Malone HR, Bowden S, et al. **A multiparametric model for mapping cellularity in glioblastoma using radiographically localized biopsies.** *AJNR Am J Neuroradiol* 2017;38:890–98 CrossRef Medline
19. Jenkinson M, Beckmann CF, Behrens TE, et al. **FSL.** *Neuroimage* 2012;62:782–90 CrossRef Medline
20. Beckmann CF, Smith SM. **Probabilistic independent component analysis for functional magnetic resonance imaging.** *IEEE Trans Med Imaging* 2004;23:137–52 CrossRef Medline
21. Calli C, Kitis O, Yuntun N, et al. **Perfusion and diffusion MR imaging in enhancing malignant cerebral tumors.** *Eur J Radiol* 2006;58:394–403 CrossRef Medline
22. Hakyemez B, Erdogan C, Bolca N, et al. **Evaluation of different cerebral mass lesions by perfusion-weighted MR imaging.** *J Magn Reson Imaging* 2006;24:817–24 CrossRef Medline

23. Tyler JL, Diksic M, Villemure JG, et al. **Metabolic and hemodynamic evaluation of gliomas using positron emission tomography.** *J Nucl Med* 1987;28:1123–33 Medline
24. Schramm P, Xyda A, Klotz E, et al. **Dynamic CT perfusion imaging of intra-axial brain tumours: differentiation of high-grade gliomas from primary CNS lymphomas.** *Eur Radiol* 2010;20:2482–90 CrossRef Medline
25. Noguchi T, Yoshiura T, Hiwatashi A, et al. **Perfusion imaging of brain tumors using arterial spin-labeling: correlation with histopathologic vascular density.** *AJNR Am J Neuroradiol* 2008;29:688–93 CrossRef Medline
26. Tourdias T, Rodrigo S, Oppenheim C, et al. **Pulsed arterial spin labeling applications in brain tumors: practical review.** *J Neuroradiol* 2008;35:79–89 CrossRef Medline
27. Cha S, Yang L, Johnson G, et al. **Comparison of microvascular permeability measurements, K(trans), determined with conventional steady-state T1-weighted and first-pass T2*-weighted MR imaging methods in gliomas and meningiomas.** *AJNR Am J Neuroradiol* 2006;27:409–17 Medline
28. Kelly PJ. **Computed tomography and histologic limits in glial neoplasms: tumor types and selection for volumetric resection.** *Surg Neurol* 1993;39:458–65 CrossRef Medline
29. Earnest F 4th, Kelly PJ, Scheithauer BW, et al. **Cerebral astrocytomas: histopathologic correlation of MR and CT contrast enhancement with stereotactic biopsy.** *Radiology* 1988;166:823–27 CrossRef Medline
30. Greene GM, Hitchon PW, Schelper RL, et al. **Diagnostic yield in CT-guided stereotactic biopsy of gliomas.** *J Neurosurg* 1989;71:494–97 CrossRef Medline
31. Nagashima G, Suzuki R, Hokaku H, et al. **Graphic analysis of microscopic tumor cell infiltration, proliferative potential, and vascular endothelial growth factor expression in an autopsy brain with glioblastoma.** *Surg Neurol* 1999;51:292–99 CrossRef Medline
32. Pronin IN, Holodny AI, Petraikin AV. **MRI of high-grade glial tumors: correlation between the degree of contrast enhancement and the volume of surrounding edema.** *Neuroradiology* 1997;39:348–50 CrossRef Medline
33. Pronin IN, McManus KA, Holodny AI, et al. **Quantification of dispersion of Gd-DTPA from the initial area of enhancement into the peritumoral zone of edema in brain tumors.** *J Neurooncol* 2009;94:399–408 CrossRef Medline
34. Iranmahboob A, Peck KK, Brennan NP, et al. **Vascular reactivity maps in patients with gliomas using breath-holding BOLD fMRI.** *J Neuroimaging* 2016;26:232–39 CrossRef Medline
35. Agarwal S, Sair HI, Pillai JJ. **The resting-state functional magnetic resonance imaging regional homogeneity metrics, Kendall's coefficient of concordance, regional homogeneity and coherence, regional homogeneity are valid indicators of tumor-related neurovascular uncoupling.** *Brain Connect* 2017;7:228–35 CrossRef Medline
36. Agarwal S, Lu H, Pillai JJ. **Value of frequency domain resting-state functional magnetic resonance imaging metrics amplitude of low-frequency fluctuation and fractional amplitude of low-frequency fluctuation in the assessment of brain tumor-induced neurovascular uncoupling.** *Brain Connect* 2017;7:382–89 CrossRef Medline
37. Choi SH, Kim JW, Chang JS, et al. **Impact of including peritumoral edema in radiotherapy target volume on patterns of failure in glioblastoma following temozolomide-based chemoradiotherapy.** *Sci Rep* 2017;7:42148 CrossRef Medline
38. Bartolomei F, Bosma I, Klein M, et al. **How do brain tumors alter functional connectivity? A magnetoencephalography study.** *Ann Neurol* 2006;59:128–38 CrossRef Medline
39. Maesawa S, Bagarinao E, Fujii M, et al. **Evaluation of resting state networks in patients with gliomas: connectivity changes in the unaffected side and its relation to cognitive function.** *PLoS One* 2015;10:e0118072 CrossRef Medline
40. Esposito R, Mattei PA, Briganti C, et al. **Modifications of default-mode network connectivity in patients with cerebral glioma.** *PLoS One* 2012;7:e40231 CrossRef Medline
41. Harris RJ, Bookheimer SY, Cloughesy TF, et al. **Altered functional connectivity of the default mode network in diffuse gliomas measured with pseudo-resting state fMRI.** *J Neurooncol* 2014;116:373–79 CrossRef Medline
42. Park JE, Kim HS, Kim SJ, et al. **Alteration of long-distance functional connectivity and network topology in patients with supratentorial gliomas.** *Neuroradiology* 2016;58:311–20 CrossRef Medline
43. Hillman EM. **Coupling mechanism and significance of the BOLD signal: a status report.** *Annu Rev Neurosci* 2014;37:161–81 CrossRef Medline
44. Araque A, Parpura V, Sanzgiri RP, et al. **Tripartite synapses: glia, the unacknowledged partner.** *Trends Neurosci* 1999;22:208–15 CrossRef Medline
45. Hervey-Jumper SL, Berger MS. **Maximizing safe resection of low- and high-grade glioma.** *J Neurooncol* 2016;130:269–82 CrossRef Medline
46. Duffau H. **Long-term outcomes after supratotal resection of diffuse low-grade gliomas: a consecutive series with 11-year follow-up.** *Acta Neurochir (Wien)* 2016;158:51–58 CrossRef Medline

MR Imaging Criteria for the Detection of Nasopharyngeal Carcinoma: Discrimination of Early-Stage Primary Tumors from Benign Hyperplasia

A.D. King, L.Y.S. Wong, B.K.H. Law, K.S. Bhatia, J.K.S. Woo, Q.-Y. Ai, T.Y. Tan, J. Goh, K.L. Chuah, F.K.F. Mo, K.C.A. Chan, A.T.C. Chan, and A.C. Vlantis



ABSTRACT

BACKGROUND AND PURPOSE: MR imaging can detect nasopharyngeal carcinoma that is hidden from endoscopic view, but for accurate detection carcinoma confined within the nasopharynx (stage T1) must be distinguished from benign hyperplasia of the nasopharynx. This study aimed to document the MR imaging features of stage T1 nasopharyngeal carcinoma and to attempt to identify features distinguishing it from benign hyperplasia.

MATERIALS AND METHODS: MR images of 189 patients with nasopharyngeal carcinoma confined to the nasopharynx and those of 144 patients with benign hyperplasia were reviewed and compared in this retrospective study. The center, volume, size asymmetry (maximum percentage difference in area between the right and left nasopharyngeal halves), signal intensity asymmetry, deep mucosal white line (greater contrast enhancement along the deep tumor margin), and absence/distortion of the adenoidal septa were evaluated. Differences were assessed with logistic regression and the χ^2 test.

RESULTS: The nasopharyngeal carcinoma center was lateral, central, or diffuse in 134/189 (70.9%), 25/189 (13.2%), and 30/189 (15.9%) cases, respectively. Nasopharyngeal carcinomas involving the walls showed that a deep mucosal white line was present in 180/183 (98.4%), with a focal loss of this line in 153/180 (85%) cases. Adenoidal septa were absent or distorted in 111/111 (100%) nasopharyngeal carcinomas involving the adenoid. Compared with benign hyperplasia, nasopharyngeal carcinoma had a significantly greater volume, size asymmetry, signal asymmetry, focal loss of the deep mucosal white line, and absence/distortion of the adenoidal septa ($P < .001$). Although size asymmetry was the most accurate criterion (89.5%) for nasopharyngeal carcinoma detection, use of this parameter alone would have missed 11.9% of early-stage T1 nasopharyngeal carcinomas.

CONCLUSIONS: MR imaging features can help distinguish stage T1 nasopharyngeal carcinoma from benign hyperplasia in most cases.

ABBREVIATIONS: BH = benign hyperplasia; BH1 = BH type 1; BH2 = BH type 2; % Δ = maximum percentage difference in area; NPC = nasopharyngeal carcinoma

Undifferentiated nasopharyngeal carcinoma (NPC) is highly responsive to radiation therapy and often curable when detected at an early stage. Endoscopy remains the standard investigation of primary tumor detection, followed by endoscopic biopsy for histologic confirmation. However, endoscopic visualization is not possible for all tumors, including small nasopharyngeal tumors

in the lateral nasopharyngeal recess or a submucosal location. Our previous research demonstrated the importance of MR imaging as an adjunct to endoscopy during NPC detection. Overall, MR imaging–based detection of NPC is very accurate (95%); additionally, 10% of MR imaging–detected NPCs are endoscopically occult, and MR imaging can detect slow-growing tumors up to 3 years before endoscopic detection.^{1–3} However, earlier MR imaging research was conducted in a largely symptomatic group of patients with NPC, which included those with advanced local disease in whom NPC detection had been assisted by submucosal tumor spread into the deep tissues surrounding the nasopharynx.

Received April 26, 2017; accepted after revision October 28.

From the Departments of Imaging and Interventional Radiology (A.D.K., L.Y.S.W., B.K.H.L., Q.-Y.A.), Clinical Oncology (F.K.F.M., A.T.C.C.), and Otorhinolaryngology, Head and Neck Surgery (J.K.S.W., A.C.V.); and Department of Chemical Pathology (K.C.A.C.), State Key Laboratory in Oncology in South China, Li Ka Shing Institute of Health Sciences, Faculty of Medicine, The Chinese University of Hong Kong, Prince of Wales Hospital, Hong Kong, S.A.R. China; Imaging Department (K.S.B.), St Mary's Hospital, Imperial College Healthcare, National Health Service Trust, London, UK; Department of Radiology (T.Y.T.), Changi General Hospital, Singapore; and Departments of Diagnostic Radiology (J.G.) and Pathology (K.L.C.), Tan Tock Seng Hospital, Singapore.

This work was supported, in part, by grants from the Research Grants Council of the Hong Kong Special Administrative Region, China (project No. CUHK4457/06, CUHK4656/12, and SEG_CUHK02).

Please address correspondence to A.D. King, FRCR, Department of Imaging and Interventional Radiology, Faculty of Medicine, The Chinese University of Hong Kong, Prince of Wales Hospital, 30-32 Ngan Shing St, Shatin, New Territories, Hong Kong S.A.R. China; e-mail: king2015@cuhk.edu.hk

Indicates open access to non-subscribers at www.ajnr.org

Indicates article with supplemental on-line table.

<http://dx.doi.org/10.3174/ajnr.A5493>

By contrast, the detection of early-stage T1 tumors confined within the nasopharynx, which must also be discriminated from benign hyperplasia (BH) along the nasopharyngeal walls and in the adenoid, presents a greater challenge to MR imaging. Currently, the use of MR imaging as an adjunct for the detection of stage T1 NPC is increasing as more asymptomatic patients with early-stage cancers are detected through screening programs that use plasma markers such as Epstein-Barr virus DNA.⁴⁻⁷

Although size asymmetry between the right and left nasopharyngeal halves and loss of the normal adenoidal septa are among the features used to detect NPC via MR imaging,^{1,2,8} the incidence of each sign has not been assessed. In addition, with a greater focus on early NPC detection through screening programs, we have become more aware of the range of MR imaging features that may be seen in NPC confined to the nasopharynx. These MR imaging features, which include the presence and integrity of a deep mucosal line along the walls of the nasopharynx (ie, a line of greater enhancement along the deep layer of the tumor) and variations in signal intensity and heterogeneity, have received scant attention in the literature. We have also observed that some of these MR imaging features of stage T1 NPC overlap those of BH; thus potentially reducing the accuracy of MR imaging for NPC detection.

In this era of screening programs for early NPC detection, our first aim was to document the MR imaging features of NPC confined to the nasopharynx or early-stage T1 lesions, which are the least obvious of the 4 T-stages on MR images. Our second aim was to compare these MR imaging features with those of BH to determine whether our current MR imaging criteria² require refinement to improve NPC detection.

MATERIALS AND METHODS

Patients

This retrospective study was approved by the Chinese University of Hong Kong institutional review board, and the requirement for written informed consent from the patients was waived. The NPC and non-NPC groups included 28 and 160 patients, respectively, who participated in a previous study² and long-term follow-up analysis³ to compare the diagnostic accuracy of MR imaging with that of endoscopy and endoscopic biopsy.

NPC Group

The nasopharyngeal MR images of 212 consecutive patients with primary NPC tumors confined to nasopharynx (stage T1) who underwent contrast-enhanced MR imaging between January 2005 and June 2014 were reviewed. The post-nasopharyngeal biopsy MR images of 23 patients were degraded, leaving 189 patients for analysis (141 men, 48 women; mean age, 52.5 years; age range, 23–80 years). Among these cases, 188 were undifferentiated carcinoma and one was a poorly differentiated carcinoma.

BH Group

The nasopharyngeal MR images of 206 consecutive patients who were investigated for suspected NPC but had no endoscopic evidence of NPC at the time of contrast-enhanced MR imaging, between July 2005 and June 2014, and after a minimum follow-up of 2 years were reviewed. Of these, 62 (30.1%) patients with a normal nasopharynx, defined as a mucosal thickness of ≤ 3 mm plus an

adenoid that was absent, or vestigial (contrast-enhancing septa with little or no intervening solid tissue) or comprising cysts (including a Tornwaldt cyst) were excluded from the study, leaving 144 patients with benign hyperplasia for analysis (84 men, 60 women; mean age, 48.2 years; age range, 17–83 years). BH presents in 2 main patterns with different MR imaging features and was therefore divided into types 1 (BH1) and 2 (BH2) based on the dominant pattern on T1-weighted postcontrast images, according to previously described criteria.² Essentially, BH1 comprised a mucosal thickness of >3 mm with homogeneous contrast enhancement and/or an adenoid without contrast-enhancing septa and was present in 66/144 cases (45.8%). BH2 comprised a mucosal thickness of >3 mm with a line/band of greater contrast enhancement in the deep layer relative to the superficial layer of the wall (deep mucosal white line) and/or an adenoidal mass with contrast-enhancing septa separated by linear bands of minimally contrast-enhancing tissue (striped appearance) and was present in 78/144 cases (54.2%).

MR Imaging Acquisition

MR imaging of the nasopharynx was performed on a 1.5T or 3T whole-body MR imaging system. The examination targeted the nasopharynx, and approximately 20 minutes were required to perform the following 4 sequences in the MR imaging protocol: an axial fat-suppressed T2-weighted sequence (TR/TE, 2500/100 ms; echo-train length, 15; FOV, 22 cm; section thickness, 4 mm with no intersection gap; matrix, 256×202), an axial T1-weighted spin-echo sequence (TR/TE, 500/20 ms; FOV, 22 cm; section thickness, 4 mm with no intersection gap; matrix, 512×512), and a T1-weighted spin-echo sequence in the axial and coronal planes following a bolus injection of 0.1 mmol of gadoterate meglumine (Dotarem; Guerbet, Aulnay-sous-Bois, France) per kilogram of body weight.

MR Imaging Analysis

The nasopharynx was divided into 2 main sites: the nasopharyngeal walls and the adenoid, which consisted of a focal bulge in the roof/posterior wall. NPC was assessed regarding the following parameters: site (walls, adenoid, subsites, and tumor center), size (volume and size asymmetry), signal intensity (intensity, homogeneity, and asymmetry), deep mucosal white line, and adenoidal septa as defined in Table 1. Cysts were excluded from the analysis of MR imaging features related to signal intensity and asymmetry. BH was assessed regarding the following parameters: site (walls and adenoid), size (volume and size asymmetry), signal intensity (intensity and signal asymmetry), deep mucosal white line (walls), and adenoidal septa (adenoid), as described for NPC. For the investigation of signal intensity, BH was divided into BH1 and BH2, and the representative ROI on each T1-weighted postcontrast image was obtained from either the enhancing wall of a BH1 or from the band of low contrast enhancement in the wall or adenoidal columns of a BH2. By definition, the deep mucosal white line is not present in BH1 and was therefore only assessed in BH2. MR images were assessed by a single radiologist (A.D.K.) with >20 years of experience with the MR imaging of NPC.

Table 1: MR imaging analysis of the nasopharynx

MR Imaging Features of NPC	Method of Analysis
Site	Walls: mucosa plus submucosa, including the lymphoid tissue layers in the mucosal space superficial to the fascia and pharyngeal muscles; wall subsites comprise the following: the pharyngeal recess, roof (above the level of the pharyngeal recess), and posterior/inferior walls (at or below the level of the pharyngeal recess) Adenoid: central mucosal lymphoid tissues in the roof and upper posterior wall where lymphoid tissue within the nasopharynx is abundant Center: lateral, central, or diffuse
Size	Volume (area of nasopharyngeal walls and adenoid on each slice \times slice thickness)
Size asymmetry	Area difference between the right and left halves of the nasopharynx on the slice with the maximum difference, expressed as the $\% \Delta A$ (difference in area between the 2 sides/area on smaller side \times 100)
Signal intensity	Representative ROI is selected on the T1-weighted postcontrast image (T2-weighted signal intensity is measured at the corresponding site); signal intensity is expressed as a ratio of signal intensity/signal intensity of the belly of the lateral pterygoid muscle
Signal intensity asymmetry	Subjective signal intensity asymmetry between the right and left halves of the nasopharynx on T1-weighted postcontrast images
Homogeneity	Subjective assessment of signal intensity on T1-weighted postcontrast images, divided into homogeneous and heterogeneous
Deep mucosal white line	Line/band of greater contrast enhancement in the deep layer relative to the superficial layer of the nasopharyngeal wall at the site of the tumor, divided into absent, present with focal loss, and present and intact; assessment was not made at the adenoid
Adenoidal septa	Contrast-enhancing septa within the adenoid, divided into absent, present and distorted (displacement or partial loss excluding that caused by adenoidal cysts), and present and not distorted (intact and symmetric)

Statistical Analysis

Differences between NPC and BH were compared using logistic regression analyses (odds ratios and corresponding 95% confidence intervals) of volume, the maximum percentage difference in area ($\% \Delta A$), and signal intensity, and the χ^2 test to evaluate signal intensity asymmetry, the deep mucosal white line, and adenoidal septa. Differences in signal intensity among NPC, BH1, and BH2, including a subgroup analysis of signal intensities obtained on the same MR imaging scanner, were compared using the analysis of variance and are depicted with boxplots. A receiver operating characteristic curve analysis and subsequent area under the curve calculation were used to identify the optimal thresholds for volume and $\% \Delta A$ by maximizing the sensitivity and specificity, and the diagnostic performances of these thresholds were calculated. Five-fold cross-validation was performed to examine the accuracy of the volume and size asymmetry. All statistical tests were 2-sided, and a P value of $< .05$ indicated a statistically significant difference. Analyses were performed with SPSS statistical analysis software (Version 23.0; IBM, Armonk, New York).

RESULTS

MR Imaging Features of Early-Stage T1 NPC Confined to the Nasopharynx

NPC involved the adenoid in 111 patients and/or the walls in 183 patients. Affected subsites, including those deep to the adenoid, were the lateral nasopharyngeal recess, the roof, and the posterior/inferior subsites in 157/189 (83.1%), 184/189 (97.4%), and 148/189 patients (78.3%), respectively. Twenty of 189 patients (10.6%) had 1 subsite only, and all subsites were affected bilaterally in 12/189 patients (6.3%). The tumor center was lateral in 134/189 patients (70.9%) (Fig 1), of which 95 crossed the midline; central in 25/189 patients (13.2%) (Fig 2); and diffuse in 30/189 patients (15.9%) (Fig 3). NPCs were enhanced het-

erogeneously in 129/189 patients (68.3%) (Fig 1C). Despite large variations in size, asymmetry, and signal intensity between the 2 halves of the nasopharynx, almost all cases exhibited the deep mucosal white line (180/183, 98.4%) (Figs 1A, -B and 3B), which was interrupted in at least 1 slice in 153/180 patients (85%) (Fig 1B). Furthermore, the adenoidal septa were absent/distorted in 111/111 patients (100%) with an adenoid (Fig 2). Further details are presented in the On-line Table.

MR Imaging Features of BH

BH1 involved the walls in all 66/66 patients (100%) (Fig 4A), and no adenoid without contrast-enhancing septa was observed. BH2 involved the walls, adenoid, and both sites in 17/78 (22%), 5/78 (6%), and 56/78 patients (72%), respectively (Fig 4B, -C). Size (volume and size asymmetry), signal intensity (intensity and signal asymmetry), deep mucosal white line, and adenoidal septa data are listed in the On-line Table.

Comparison of the MR Imaging Features of Early-Stage T1 NPC and BH

The NPC signal intensity fell between those of BH1 and BH2 (T1 postcontrast BH1 $>$ NPC $>$ BH2; T2 BH2 $>$ NPC $>$ BH1), and significant differences were observed among the 3 groups ($P < .001$) (On-line Table and Fig 5). A subgroup analysis of cases performed on the same 1.5T MR imaging scanner (NPC = 31, BH1 = 43, BH2 = 64) revealed the same signal intensity differences among the 3 groups, which remained significant for all T1 postcontrast scans (BH1 versus BH2, $P < .001$; BH1 versus NPC, $P < .001$; BH2 versus NPC, $P = .015$) and T2 comparisons of BH1 versus BH2 ($P < .001$) and BH2 versus NPC ($P = .018$), but not BH1 versus NPC ($P = .183$).

Compared with BH, stage T1 NPC confined to the nasopharynx exhibited a significantly greater volume, size asymmetry, sig-

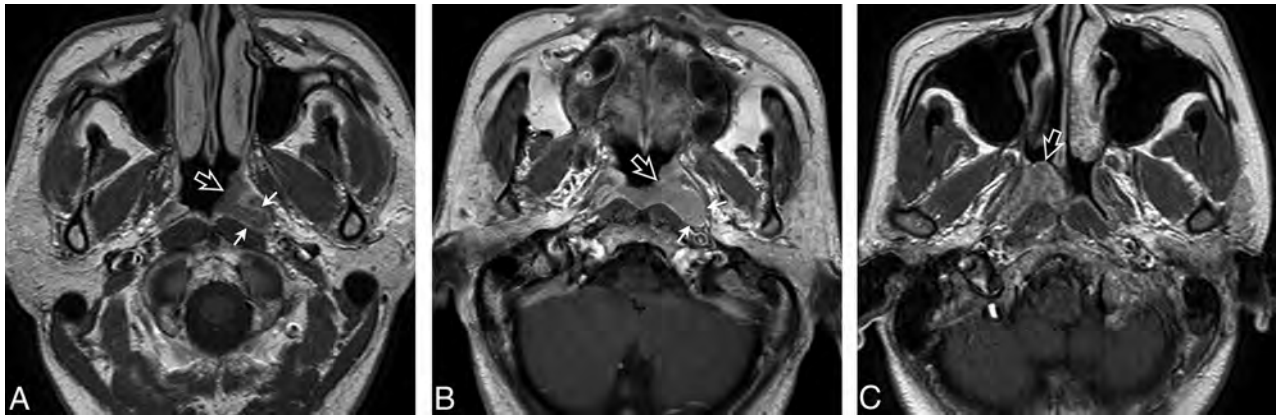


FIG 1. A, Axial T1-weighted postcontrast MR image of the nasopharynx in a 51-year-old man with NPC (*open arrow*). An asymmetric tumor with a lateral center at the level of the left pharyngeal recess is confined to 1 side of the nasopharynx. The tumor exhibits homogeneous low contrast enhancement with an intact deep mucosal white line (*small solid arrows*) along the deep margin. B, Axial T1-weighted postcontrast MR image of the nasopharynx in a 68-year-old man with NPC (*open arrow*). An asymmetric tumor with a lateral center at the level of the left pharyngeal recess is confined to 1 side of the nasopharynx. The tumor exhibits homogeneous moderate contrast enhancement with a focal loss of the deep mucosal white line (*small solid arrows*) along the deep margin. C, Axial T1-weighted postcontrast MR image of the nasopharynx in a 44-year-old woman with NPC (*open arrow*). An asymmetric tumor with a lateral center at the level of the right side of the roof shows heterogeneous contrast enhancement.



FIG 2. Axial T1-weighted postcontrast MR image of the nasopharynx in a 32-year-old woman with NPC (*open arrow*). An asymmetric tumor with a central center in the adenoid exhibits homogeneous contrast enhancement and loss of the normal adenoidal septa.

nal asymmetry, focal loss of the deep mucosal white line, and absence/distortion of the adenoidal septa ($P < .001$) (On-line Table). The optimum NPC detection thresholds were a volume of $\geq 5.01 \text{ cm}^3$ ($P < .001$, area under the receiver operating characteristic curve = 0.676) and a $\% \Delta A$ of $\geq 33.7\%$ ($P < .001$, area under the receiver operating characteristic curve = 0.948) (Fig 6). The diagnostic performance of MR imaging stage T1 NPC detection based on volume, $\% \Delta A$, signal asymmetry, deep mucosal white line absence/focal loss, and adenoidal septa absence/distortion is shown in Table 2. The estimated accuracy of volume and

size asymmetry obtained from 5-fold cross-validation was not overestimated and was within the 95% CI of observed accuracy of volume and size asymmetry. Although a $\% \Delta A$ of $\geq 33.7\%$ was the most accurate criterion for NPC detection, this parameter yielded 22 (11.6%) false-negatives among 189 cases and 13 (9.0%) false-positives among 144 cases. False-negative results arose in NPCs that were diffuse ($n = 12$) (Fig 3), central ($n = 8$), or lateral ($n = 2$) and had a $\% \Delta A$ of 2.4%–31.0% (mean, 15.5%). False-positive results arose in asymmetric BHs with $\% \Delta A$ values of 34.6%–82.3% (mean, 51.9%) (Fig 7). A subgroup analysis of the diagnostic performances of criteria in symmetric ($\% \Delta A < 33.7\%$) NPC and BH showed the highest level of accuracy for a focal loss of the mucosal white line (90.7%), followed by absent/distorted adenoidal septa (89.3%), signal asymmetry (83.0%), and volume (71.2%) (Table 3).

DISCUSSION

Plasma markers are currently used to screen patients at risk of NPC, including asymptomatic subjects from regional populations and family screening programs as well as symptomatic patients with nonspecific symptoms such as epistaxis. In this setting, MR imaging is also used to detect clinically occult early stage NPC in patients with abnormal blood test results but normal endoscopic results. Unfortunately, it is common to encounter patients who have both false-positive NPC plasma markers and BH of the nasopharyngeal walls and adenoid. In these patients, the challenge is not only to detect stage T1 NPC confined to the nasopharynx using MR imaging but also to discriminate these cancers from benign disease and thus reduce the number of unnecessary nasopharyngeal biopsies.

Although detailed MR imaging patterns of the local spread of NPCs have been well-described in the literature,^{9–11} there is a paucity of data related to stage T1 NPC confined to the nasopharynx, despite its importance for NPC screening. In this study, we found that stage T1 NPCs varied considerably in size, from small tumors localized at a single site to large exophytic tumors involv-

ing all sites and filling the nasopharyngeal cavity. Most NPCs arose laterally to cause size and signal asymmetries between the nasopharyngeal halves, whereas less than a third were diffuse or located centrally in the roof or posterior wall. The deep mucosal white line along the deep tumor margin was almost universally present among stage T1 cancers. This deep mucosal white line of greater contrast enhancement in the deep relative to the superficial layer has received scant attention in the literature. We believe that this line represents contrast enhancement in the dense fibrous tissue containing submucosal blood vessels. In most NPCs (84%), the deep mucosal white line exhibited focal discontinuity on at least 1 imaging slice. Although the integrity of this line has not been previously assessed in NPC, we believe that discontinuity might represent the earliest sign of impending extranasopharyngeal

invasion. A loss or distortion of the normal contrast-enhancing adenoidal septa was an additional feature observed in stage T1 NPC. Although this feature has been described in NPC, its incidence has not been reported.^{1,2,8} In the present study, all stage T1 NPCs exhibited this complete absence or distortion of the adenoidal septa, regardless of whether the tumor arose from within the adenoid or spread into the hypertrophied adenoid from adjacent walls.

The MR imaging features of stage T1 NPC differed significantly from those of BH. Compared with all cases of BH, stage T1 NPC confined to the nasopharynx had a greater volume, size asymmetry, and signal asymmetry; of these, size asymmetry was the most accurate criterion for NPC identification. This is not surprising because most stage T1 NPCs were centered laterally, whereas BH is a diffuse process. Although this study quantified differences in size between the 2 sides of the nasopharynx, in routine practice, this feature can usually be easily assessed subjectively. However, although most stage T1 NPCs could be detected via size asymmetry, a minority (11.9%) of early cancers were symmetric, especially those that were diffuse or centrally located. These early cancers were difficult to detect by MR imaging because they were not accompanied by the deep tumor invasion associated with higher T-stage tumors, which was used in previous studies that achieved NPC detection sensitivities of 97%–100%.^{2,12}

Differences in signal intensity (ie, NPC had a lower and higher contrast enhancement relative to BH1 and BH2, respectively) helped to identify focal tumors, though overall signal intensity alone was a poor discriminator. We found that stage

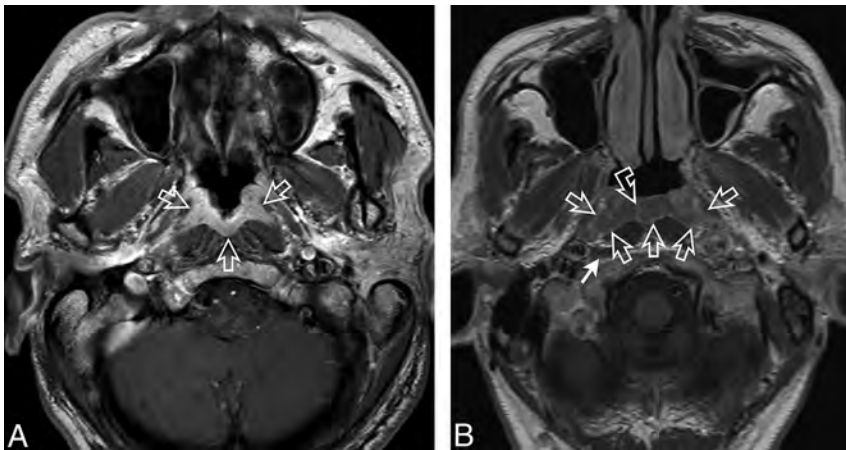


FIG 3. A, Axial T1-weighted postcontrast MR image of the nasopharynx in a 51-year-old man with NPC (*open arrows*). A symmetric tumor with diffuse involvement of all nasopharyngeal walls exhibits homogeneous contrast enhancement without a white line along the deep mucosal margin. B, Axial T1-weighted postcontrast MR image of the nasopharynx in a 59-year-old man with NPC (*open arrows*). A symmetric tumor with diffuse involvement of the nasopharyngeal walls exhibits homogeneous low contrast enhancement and an intact mucosal white line along the deep margin. The adenoid extends along the posterior wall from the roof, with an adenoidal “stripe” on the right (*curved open arrow*) but not on the left side. A small right retropharyngeal node is also indicated (*solid arrow*). The patient had bulky N3-stage metastatic nodes below this level.

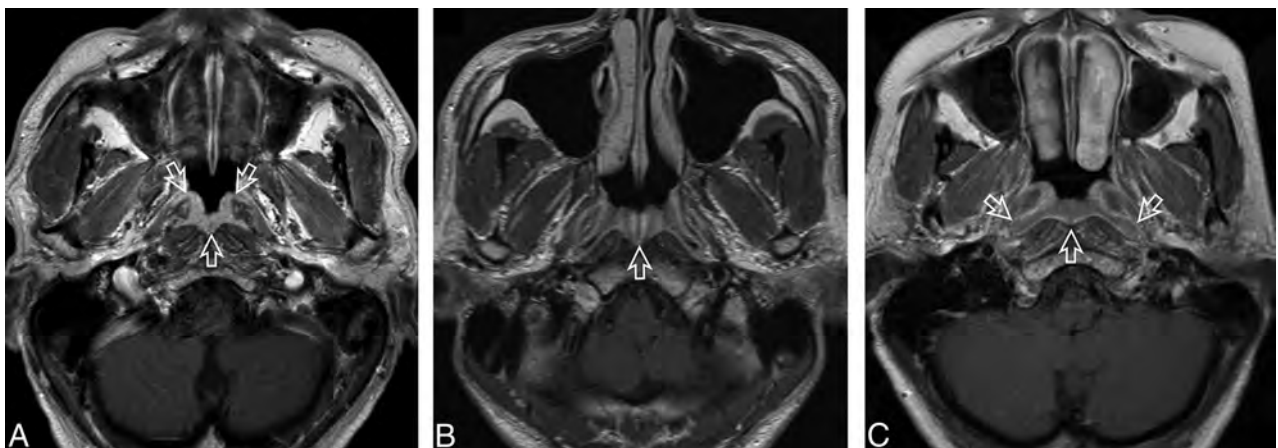


FIG 4. A, Axial T1-weighted postcontrast MR image of the nasopharynx in a 53-year-old man with BH1 (*open arrows*). An area of diffuse symmetric mucosal thickening with homogeneous contrast enhancement is visible. B, Axial T1-weighted postcontrast MR image of the nasopharynx in a 28-year-old man with BH2 of the adenoid (*open arrow*). The symmetric lesion exhibits contrast-enhancing septa that run perpendicular to the nasopharyngeal wall and are separated by columns of low contrast enhancement. C, Axial T1-weighted postcontrast MR image of the nasopharynx in a 48-year-old woman with BH2 along the nasopharyngeal walls (*open arrows*). An area of diffuse, symmetric homogeneous low contrast enhancement and an intact deep mucosal white line along the deep margin are visible.

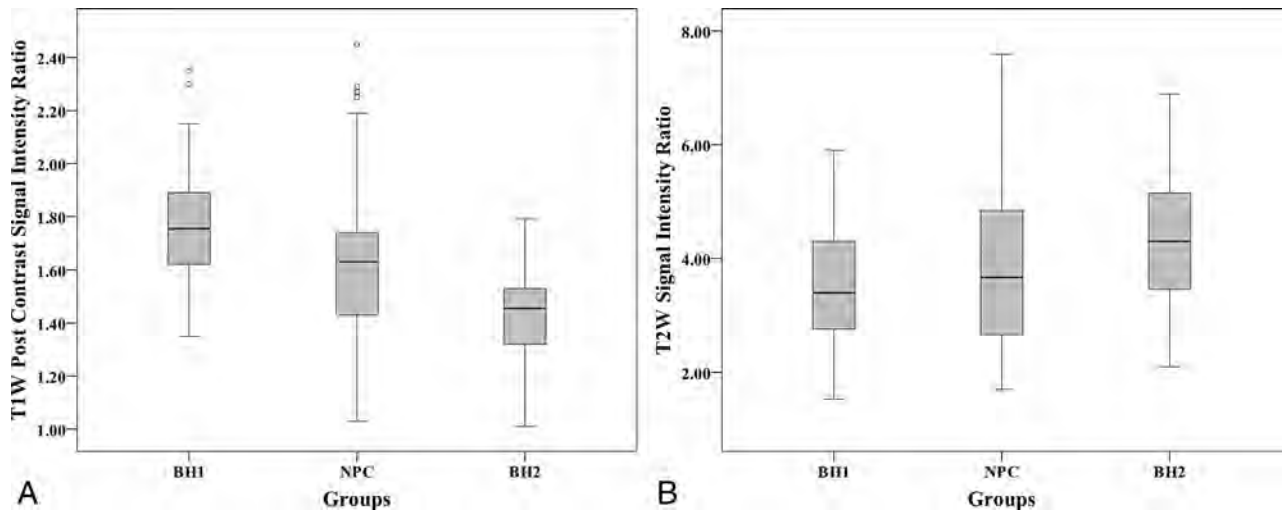


FIG 5. A, Boxplots showing differences in the T1 postcontrast signal intensity ratios (relative to muscle) among NPC, BH1, and BH2. B, Boxplots show differences in the T2 signal intensity ratios (relative to muscle) among NPC, BH1, and BH2.

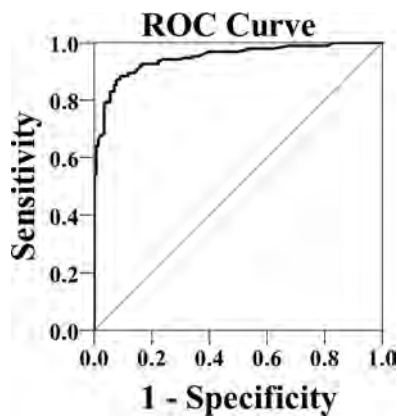


FIG 6. Receiver operating characteristic curve of the percentage difference in area for NPC detection.

T1 NPCs exhibited variable contrast enhancement both within heterogeneous tumors and among different tumors. BH is also known to exhibit a range of MR imaging appearances.^{2,13-17} Notably, there were no differences between NPC and BH in this study when the signal intensities of BH1 and BH2 were combined. The range of NPC contrast-enhancement levels and the overlap with BH are of concern regarding symmetric NPCs, which can exhibit higher contrast enhancement and thus appear like BH1 (Figs 3A and 4A) or lower contrast enhancement and thus appear like BH2 (Figs 3B and 4C). Signal intensity was also assessed on the basis of the asymmetry in signal intensity between the 2 sides of the nasopharynx. Although this criterion was highly accurate for NPC, the positive predictive value was low, especially in symmetric NPCs (positive predictive value, 42%). Volume was the poorest discriminator among all criteria, even for symmetric NPCs, because the volumes of both NPC and BH ranged widely. Therefore, the use of volume to determine NPC would have led to a high number of nasopharyngeal biopsies for benign disease.

The 2 remaining MR imaging criteria related to the adenoidal septa (adenoid) and the deep mucosal white line (walls) exhibited greater promise for NPC detection. These 2 criteria detected NPC

with a high level of accuracy, including symmetric tumors that may otherwise have been missed by MR imaging. Regarding the first criterion, distortion, disruption, or a complete loss of the adenoidal septa was significantly more likely to appear in NPC compared with adenoidal BH. However, the adenoidal septa should be assessed carefully because distortion caused by cysts or a single central column of lymphoid hyperplasia could be mistaken for NPC.¹⁵ Accordingly, vestigial adenoids and those comprising mainly cysts were not assessed in this study. Moreover, some previous MR imaging studies reported a higher rate of absent adenoidal septa in cases of adenoidal BH.¹⁷ Therefore, we suggest that an hypertrophied adenoid with absent or distorted septa should only be biopsied in a patient who is at a high risk of NPC and has undergone an MR imaging examination dedicated to the nasopharynx. However, the previously reported high negative predictive value of this sign suggests that nasopharyngeal biopsy can be avoided if the adenoidal septa are symmetric and separated by hyperplastic columns of low contrast enhancement (ie, striped appearance).² Regarding the second criterion, a focal loss of the deep mucosal white line was found to be significantly more common in NPC than in BH2. However, any assessment of the loss of this deep mucosal white line should be mindful of the fact that this line is not seen in the BH1 pattern. The BH1 and BH2 patterns often coexist in the nasopharynx; therefore, a focal loss of this line should only be determined on a slice through the nasopharynx where the line is present but focally disrupted.

Despite the use of new criteria, the ability of MR imaging to discriminate NPC from BH remains hindered by the false-positive findings of NPC, which are caused by asymmetric BH. The presence of a focal area of BH2 (Fig 7) is of special concern because the deep mucosal white line and superficial band of low contrast enhancement show a striking similarity to some small-stage T1 NPCs (Fig 1A). Accordingly, we have continued to follow these subjects. We believe that the diffuse BH2 pattern might be a response to stimulants such as Epstein-Barr virus infection, which cause a greater abundance of lymphoid cells in the lymphoid stroma and epithelium and may cause the appearance of a band of

Table 2: Diagnostic performance of MR imaging for the discrimination of early NPC from BH

	Volume	Size Asymmetry	Signal Asymmetry	Deep Mucosal White Line	Adenoid
Test positive for NPC	Volume $\geq 5.01 \text{ cm}^3$	$\% \Delta A \geq 33.7\%$	Signal asymmetry present	Focal loss of the deep mucosal white line	Septa absent or distorted (excluding septa distorted by cysts)
	$n = 333$ (NPC = 189, BH = 144)	$n = 333$ (NPC = 189, BH = 144)	$n = 333$ (NPC = 189, BH = 144)	$n = 253$ (NPC = 180, BH2 = 73)	$n = 172$ (NPC = 111, BH2 = 61)
Area under the curve (95% CI)	0.676 (0.618–0.734)	0.948 (0.926–0.971)			
P value	<.001	<.001			
True-positive (No.)	119	167	161	153	111
False-positive (No.)	47	13	26	10	9
True-negative (No.)	97	131	118	63	52
False-negative (No.)	70	22	28	27	0
Sensitivity (%)	63.0	88.4	85.2	85.0	100.0
Specificity (%)	67.4	91.0	81.9	86.3	85.2
Positive predictive value (%)	71.7	92.8	86.1	93.9	92.5
Negative predictive value (%)	58.1	85.6	80.8	70.0	100.0
Accuracy (%)	64.9	89.5	83.8	85.4	94.8

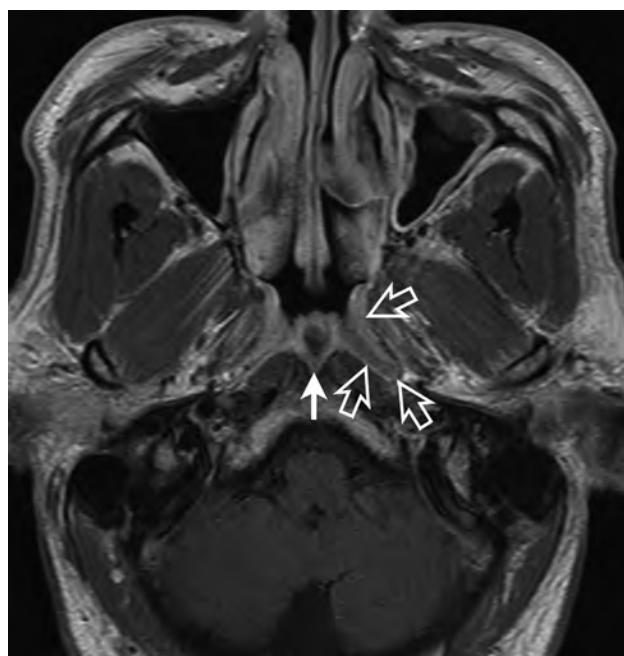


FIG 7. Axial T1-weighted postcontrast MR image of the nasopharynx in a 52-year-old man with asymmetric BH. Greater thickening is observed in the left side of the roof (*open arrows*), where a focal area of mucosal thickening comprises a superficial band of low contrast enhancement overlying an intact deep mucosal white line (BH type 2). A Tornwaldt cyst is also present (*solid arrow*).

low contrast enhancement in the superficial layer of the nasopharyngeal mucosa, as well as in the columns of the hypertrophied adenoid. Differential rates of resolution might explain the asymmetry and why a minority of BH2 cases are focal by the time the MR imaging examination is performed. These focal sites of BH2 might act as a chronic reservoir of infection and become the MR imaging precursors of NPC. Furthermore, recruitment of vessels by the growing tumor might result in areas of greater enhancement like those observed in BH1 and explain the heterogeneous enhancement pattern of early T-stage NPC. Although currently this scenario is only conjecture, the BH2 pattern is interesting and we believe it deserves future study.

Size asymmetry was the best overall criterion for detecting stage T1 NPC; however, size asymmetry included not only subjects with a focal mass but also those with asymmetry in an otherwise diffuse lymphoid hyperplasia pattern. Our previous NPC detection study with long-term follow-up³ showed that asymmetry in a diffuse benign hyperplasia pattern without a focal mass had a low specificity for NPC; therefore, to keep nasopharyngeal biopsies of healthy subjects to a minimum, we did not use this criterion to indicate NPC in a recent population screening study.⁷ Taking into consideration the new criteria in this study and recent research, we have updated our proposed MR imaging grading system (Table 4): The grades for normal (grade 1) and probably benign (grade 2) are unchanged; asymmetry in thickness of an otherwise benign hyperplasia pattern is now graded as indeterminate (grade 3); the new signs (asymmetry in signal, focal loss of the white line, or absence/distortion of adenoidal septa) together with a focal mass are graded as suspicious (grade 4); and extension outside the nasopharynx is graded as probably malignant (grade 5). Future studies are required to validate this proposed MR imaging grading system, but we hope it will provide a framework for further refinement and inclusion of new indicators of malignancy such as the presence of metastatic retropharyngeal nodes.

This study had several limitations. First, the signal intensity in an NPC may be influenced by the subjective choice of the representative ROI and possibly by postbiopsy effects that are not obvious on the images. Differences in magnet strengths and between manufacturers must also be considered as potential limitations when comparing signal ratios. Given these potential limitations, we only used the signal intensity data to illustrate the main differences among the 3 groups (NPC, BH1, and BH2) and not to identify diagnostic thresholds. In addition, a subgroup analysis of cases performed on the same scanner yielded results similar to those of the overall analysis, except for the difference in T2 signal intensity ratios between NPC and BH1, which showed the same trend but no longer reached statistical significance. Second, our results may not be applicable to MR imaging examinations that are not dedicated to the nasopharynx, such as examinations of the brain, which

Table 3: MR imaging criteria subgroup analysis of symmetric (% Δ A < 33.7%) NPC and BH

	Volume	Signal Asymmetry	Deep Mucosal White Line	Adenoid
Test positive for NPC	Volume \geq 5.01 cm ³	Signal asymmetry present	Focal loss of the deep mucosal white line	Septa absent or distorted (excluding septa distorted by cysts)
	<i>n</i> = 153 (NPC = 22, BH = 131)	<i>n</i> = 153 (NPC = 22, BH = 131)	<i>n</i> = 83 (NPC = 20, BH2 = 63)	<i>n</i> = 72 (NPC = 16, BH2 = 56)
True-positive (No.)	20	11	16	16
False-positive (No.)	42	15	8	8
True-negative (No.)	89	116	55	48
False-negative (No.)	2	11	4	0
Sensitivity (%)	90.1	50.0	80.0	100.0
Specificity (%)	67.9	88.5	87.3	85.7
Positive predictive value (%)	32.3	42.3	66.7	66.7
Negative predictive value (%)	97.8	91.3	93.2	100
Accuracy (%)	71.2	83.0	85.5	88.9

Table 4: Proposed MR imaging criteria for primary NPC detection

Grade	Condition	Appearance
1	Normal	Thin mucosa \leq 3 mm; adenoid absent, vestigial or composed almost entirely of cysts
2	Probably benign	Diffusely thickened >3-mm symmetric mucosa either homogeneously enhancing (benign hyperplasia type 1) or with greater contrast enhancement in the deep layer (mucosal white line) compared with the superficial layer (benign hyperplasia type 2); adenoid with intact contrast-enhancing septa (benign hyperplasia type 2)
3	Indeterminate	Diffusely thickened >3-mm mucosa asymmetric in thickness; adenoid asymmetric in thickness
4	Suspicious	1) Diffusely thickened >3-mm mucosa asymmetric in signal intensity; adenoid asymmetric in signal intensity 2) Diffusely thickened mucosa >3 mm with focal loss of the mucosal white line; absence/distortion of the thin contrast-enhancing adenoidal septa (not attributed to cysts) 3) Focal mass confined within the nasopharynx
5	Probably malignant	Superficial extension to the nasal cavity/oropharynx or deep extension to the sites bordering the nasopharynx

often include sections through the nasopharyngeal roof. Finally, we did not examine the role of diffusion-weighted imaging, which remains in the early stages of development for small nasopharyngeal lesions, or the combined performance of MR imaging and nasopharyngeal endoscopy and plasma levels of Epstein-Barr virus DNA.

CONCLUSIONS

In this era of plasma marker screening for NPC, MR imaging is assuming a greater role in the detection of endoscopically occult stage T1 disease confined to the nasopharyngeal mucosa or adenoid. We found that although stage T1 NPCs varied in size, most were centered laterally, thus causing asymmetries in size and signal intensity, and nearly all exhibited a mucosal white line deep in the tumor that was frequently interrupted and absent or distorted adenoidal septa. Compared with BH, stage T1 NPC exhibited significantly greater volume, size, and signal intensity asymmetries; focal losses of the deep mucosal white line; and absence/distortion of the adenoidal septa. The contrast enhancement of stage T1 NPC was weaker than that of BH1 and stronger than that of BH2, though considerable overlap was observed. Although size asymmetry remained the best criterion for identifying stage T1 NPC, the ability of MR imaging to detect stage T1 NPC was reduced for symmetric tumors that were diffuse or centrally located and shared overlapping signal intensities with those of BH. For these cancers, the focal loss of the deep mucosal white line and absent/distorted adenoidal stripes were the best criteria for NPC detection, fol-

lowed by signal asymmetry. Therefore, a range of MR imaging criteria is needed to detect stage T1 NPC, and we have included these in our proposed guidelines. Future studies are needed to validate and refine these criteria.

ACKNOWLEDGMENTS

We would like to acknowledge the assistance of Pak Lai Terry Tsoi, Way Loon Jonathan Chen, Helen Pui Yan Lee, and Man Tung Karen Yuen.

Disclosures: Ann D. King—RELATED: Grant: Research Grants Council of the Hong Kong Special Administrative Region, China, Comments: partially funded by grants (project No. CUHK4457/06, CUHK4656/12, and SEG_CUHK02)*. Benjamin King Hong Law—RELATED: Grant: Research Grants Council of the Hong Kong Special Administrative Region, China, Comments: partially funded by grants (project No. CUHK4457/06, CUHK4656/12, and SEG_CUHK02)*. Khoon Leong Chuah—UNRELATED: Employment: Tan Tock Seng Hospital, Comments: employed as a consultant pathologist. Frankie K.F. Mo—RELATED: Grant: Research Grants Council of the Hong Kong Special Administrative Region, China, Comments: partially funded by grants (project No. CUHK4457/06, CUHK4656/12, and SEG_CUHK02)*. K.C. Allen Chan—RELATED: Grant: Kadoorie Charitable Foundation, Comments: I received funding support from Kadoorie Charitable Foundation for NPC research*; UNRELATED: Board Membership: Cirina, Comments: I am a director of Cirina; Payment for Lectures Including Service on Speakers Bureaus: Bio-Rad, Comments: I received an honorarium from Bio-Rad as an invited speaker in academic lectures; Patents (Planned, Pending or Issued): Cirina, Comments: I hold patents on molecular diagnostics; Royalties: Cirina; Stock/Stock Options: Cirina, Comments: I hold equities in Cirina. Anthony T.C. Chan—RELATED: Grant: Research Grants Council of the Hong Kong Special Administrative Region, China, Comments: partially funded by grants (project No. CUHK4457/06, CUHK4656/12, and SEG_CUHK02)*. Alexander C. Vlantis—RELATED: Grant: Research Grants Council of the Hong Kong Special Administrative Region, China, Comments: partially funded by grants (project

REFERENCES

1. King AD, Vlantis AC, Tsang RK, et al. **Magnetic resonance imaging for the detection of nasopharyngeal carcinoma.** *AJNR Am J Neuroradiol* 2006;27:1288–91 Medline
2. King AD, Vlantis AC, Bhatia KS, et al. **Primary nasopharyngeal carcinoma: diagnostic accuracy of MR imaging versus that of endoscopy and endoscopic biopsy.** *Radiology* 2011;258:531–37 CrossRef Medline
3. King AD, Vlantis AC, Yuen TW, et al. **Detection of nasopharyngeal carcinoma by MR imaging: diagnostic accuracy of MRI compared with endoscopy and endoscopic biopsy based on long-term follow-up.** *AJNR Am J Neuroradiol* 2015;36:2380–85 CrossRef Medline
4. Lo YM, Chan AT, Chan LY, et al. **Molecular prognostication of nasopharyngeal carcinoma by quantitative analysis of circulating Epstein-Barr virus DNA.** *Cancer Res* 2000;60:6878–81 Medline
5. Leung SF, Tam JS, Chan AT, et al. **Improved accuracy of detection of nasopharyngeal carcinoma by combined application of circulating Epstein-Barr virus DNA and anti-Epstein-Barr viral capsid antigen IgA antibody.** *Clin Chem* 2004;50:339–45 CrossRef Medline
6. Chan KC, Hung EC, Woo JK, et al. **Early detection of nasopharyngeal carcinoma by plasma Epstein-Barr virus DNA analysis in a surveillance program.** *Cancer* 2013;119:1838–44 CrossRef Medline
7. Chan KC, Woo JK, King A, et al. **Analysis of plasma Epstein-Barr virus DNA to screen for nasopharyngeal cancer.** *N Engl J Med* 2017;377:513–22 CrossRef Medline
8. Wu YP, Cai PQ, Tian L, et al. **Hypertrophic adenoids in patients with nasopharyngeal carcinoma: appearance at magnetic resonance imaging before and after treatment.** *Chin J Cancer* 2015;34:130–36 CrossRef Medline
9. Ng SH, Chang TC, Ko SF, et al. **Nasopharyngeal carcinoma: MRI and CT assessment.** *Neuroradiology* 1997;39:741–46 CrossRef Medline
10. King AD, Lam WW, Leung SF, et al. **MRI of local disease in nasopharyngeal carcinoma: tumour extent vs tumour stage.** *Br J Radiol* 1999;72:734–41 CrossRef Medline
11. Liang SB, Sun Y, Liu LZ, et al. **Extension of local disease in nasopharyngeal carcinoma detected by magnetic resonance imaging: improvement of clinical target volume delineation.** *Int J Radiat Oncol Biol Phys* 2009;75:742–50 CrossRef Medline
12. Gao Y, Zhu SY, Dai Y, et al. **Diagnostic accuracy of sonography versus magnetic resonance imaging for primary nasopharyngeal carcinoma.** *J Ultrasound Med* 2014;33:827–34 CrossRef Medline
13. Vogler RC, Ii FJ, Pilgram TK. **Age-specific size of the normal adenoid pad on magnetic resonance imaging.** *Clin Otolaryngol Allied Sci* 2000;25:392–95 CrossRef Medline
14. Kösling S, Knipping S, Hofmockel T. **Imaging of nasopharyngeal diseases** [in German]. *Radiologe* 2009;49:17–26 CrossRef Medline
15. Bhatia KS, King AD, Vlantis AC, et al. **Nasopharyngeal mucosa and adenoids: appearance at MR imaging.** *Radiology* 2012;263:437–43 CrossRef Medline
16. Sekiya K, Watanabe M, Nadgir RN, et al. **Nasopharyngeal cystic lesions: Tornwaldt and mucous retention cysts of the nasopharynx: findings on MR imaging.** *J Comput Assist Tomogr* 2014;38:9–13 CrossRef Medline
17. Surov A, Ryl I, Bartel-Friedrich S, et al. **MRI of nasopharyngeal adenoid hypertrophy.** *Neuroradiol J* 2016;29:408–12 CrossRef Medline

Comparison of MR Imaging and Dual-Energy CT for the Evaluation of Cartilage Invasion by Laryngeal and Hypopharyngeal Squamous Cell Carcinoma

H. Kuno, K. Sakamaki, S. Fujii, K. Sekiya, K. Otani, R. Hayashi, T. Yamanaka, O. Sakai, and M. Kusumoto



ABSTRACT

BACKGROUND AND PURPOSE: Dual-energy CT can distinguish iodine-enhanced tumors from nonossified cartilage and has been investigated for evaluating cartilage invasion in patients with laryngeal and hypopharyngeal squamous cell carcinomas. In this study, we compared the diagnostic accuracy of MR imaging and of a combination of weighted-average and iodine overlay dual-energy CT images in detecting cartilage invasion by laryngeal and hypopharyngeal squamous cell carcinomas, in particular thyroid cartilage invasion.

MATERIALS AND METHODS: Fifty-five consecutive patients who underwent 3T MR imaging and 128-slice dual-energy CT for preoperative initial staging of laryngeal or hypopharyngeal squamous cell carcinomas were included. Two blinded observers evaluated laryngeal cartilage invasion on MR imaging and dual-energy CT using a combination of weighted-average and iodine-overlay images. Pathologic findings of surgically resected specimens were used as the reference standard for evaluating sensitivity, specificity, and the areas under the receiver operating characteristic curve of both modalities for cartilage invasion by each type of cartilage and for all cartilages together. Sensitivity and specificity were compared using the McNemar test and generalized linear mixed models.

RESULTS: Dual-energy CT showed higher specificity than MR imaging for diagnosing all cartilage together (84% for MR imaging versus 98% for dual-energy CT, $P < .004$) and for thyroid cartilage (64% versus 100%, $P < .001$), with a similar average area under the curve (0.94 versus 0.95, $P = .70$). The sensitivity did not differ significantly for all cartilages together (97% versus 81%, $P = .16$) and for thyroid cartilage (100% versus 89%, $P = .50$), though there was a trend toward increased sensitivity with MR imaging.

CONCLUSIONS: Dual-energy CT showed higher specificity and acceptable sensitivity in diagnosing laryngeal cartilage invasion compared with MR imaging.

ABBREVIATIONS: AUC = area under the curve; IO = iodine overlay; ROC = receiver operating characteristic; SAFIRE = sinogram-affirmed iterative reconstruction; SCC = squamous cell carcinoma; WA = weighted-average

In patients with laryngeal and hypopharyngeal squamous cell carcinomas (SCCs), diagnosing cartilage invasion is extremely important for making treatment-related decisions. The thyroid cartilage plays a critical role in primary tumor staging because the

extent of thyroid cartilage invasion is a defining factor between T3 and T4a stages.¹ When tumor extends through the thyroid cartilage into the superficial soft tissue of the neck, the patient is staged T4a and may require total laryngectomy.²⁻⁶ In cases in which cartilage invasion is localized without transcartilaginous extension, potentially organ-preserving treatment may still be performed.^{2-5,7,8} Therefore, inappropriate treatment choices secondary to over- or underestimation of thyroid cartilage invasion can have grave implications for a patient's quality of life.⁹

MR imaging and CT are used for staging of laryngeal and hypopharyngeal SCCs. However, there is no clear consensus as to which imaging technique is best-suited for evaluating cartilage invasion. Each institution has its own protocol, depending on the availability of imaging equipment and the radiologists' preference and experience. MR imaging has higher soft-tissue contrast resolution and higher sensitivity than conventional CT in diagnosing laryngeal cartilage invasion by laryngeal or hypopharyngeal SCCs.¹⁰ However, motion artifacts are a serious problem with MR

Received February 13, 2017; accepted after revision November 10.

From the Departments of Diagnostic Radiology (H.K., K.S., M.K.) and Head and Neck Surgery (R.H.), National Cancer Center Hospital East, Kashiwa, Chiba, Japan; Departments of Radiology (H.K., O.S.), Otolaryngology–Head and Neck Surgery (O.S.), and Radiation Oncology (O.S.), Boston Medical Center, Boston University School of Medicine, Boston, Massachusetts; Department of Biostatistics (K.S., T.Y.), Yokohama City University, Yokohama, Kanagawa, Japan; Division of Pathology (S.F.), Exploratory Oncology Research and Clinical Trial Center, National Cancer Center, Kashiwa, Chiba, Japan; and Advanced Therapies Innovation Department (K.O.), Siemens Healthcare K.K., Shinagawa-ku, Tokyo, Japan.

Please address correspondence to Hirofumi Kuno, MD, PhD, Department of Diagnostic Radiology, National Cancer Center Hospital East, 6-5-1, Kashiwanoha, Kashiwa, Chiba 277-8577, Japan; e-mail: hkuno@east.ncc.go.jp

 Indicates article with supplemental on-line table.

 Indicates article with supplemental on-line photo.

<http://dx.doi.org/10.3174/ajnr.A5530>

imaging in patients with laryngeal or hypopharyngeal cancer with difficulty in breathing and swallowing.¹¹ Additionally, edema or inflammatory changes in cartilage may have findings similar or identical to those of tumor invasion on MR imaging.^{10,12} CT has high spatial and temporal resolution and remains the preferred technique for imaging the larynx and hypopharynx. However, nonossified cartilage and tumors may have similar attenuation values,^{2,13} making them almost indistinguishable, especially when the tumor is located adjacent to nonossified thyroid cartilage.

Recently, emerging dual-energy CT techniques have been investigated for head and neck cancer imaging with the potential for improved tumor visualization and characterization.¹⁴⁻²¹ In particular, techniques using iodine overlay (IO) images were found useful for distinguishing iodine-enhanced tumors from nonossified cartilage^{11,14,19,22} and for having higher specificity than conventional CT, without a deterioration of sensitivity, in particular for the evaluation of thyroid cartilage invasion.¹⁴ Furthermore, interobserver agreement is usually poor for conventional CT and was found to be higher for dual-energy CT.^{14,23} These new dual-energy CT techniques have prompted re-evaluations of the diagnostic performance of CT compared with MR imaging in diagnostic fields where MR imaging has been routinely used.²⁴⁻²⁶ The purpose of this study was to compare MR imaging and dual-energy CT in their ability to evaluate cartilage invasion, in particular thyroid cartilage invasion, by laryngeal and hypopharyngeal SCCs.

MATERIALS AND METHODS

Patients

This retrospective study was approved by the institutional review board at National Cancer Center Hospital East. The requirement to obtain written informed consent was waived. Between September 2010 and September 2014, six hundred five consecutive newly diagnosed patients with histologically proved laryngeal or hypopharyngeal SCCs underwent contrast-enhanced dual-energy CT for cancer staging using 128-slice dual-source CT. Among them, 111 patients (18%) also underwent 3T MR imaging before treatment. Fifty-three of the 111 patients (48%) were excluded because they were treated nonsurgically (5 underwent radical radiation therapy and 48 received chemoradiotherapy). We excluded an additional 3 patients: Two were unable to complete the MR imaging examination, and another patient's MR imaging study was nondiagnostic secondary to severe motion artifacts. The remaining 55 patients (50%) were enrolled in this study. All subjects were treated with surgery (16 patients underwent total laryngectomy, and 39 underwent total pharyngolaryngectomy), and pathologic findings of surgical specimens were used as the reference standard. Of 55 patients, 17 patients (31%) had laryngeal SCCs (7 supraglottic, 4 glottic, 6 transglottic) and 38 (69%) had hypopharyngeal SCCs (27 piriform sinus, 4 postcricoid, 7 posterior pharyngeal wall).

MR Imaging Techniques

All MR imaging studies were performed on a 3T MR imaging system (Achieva TX; Philips Healthcare, Best, the Netherlands) with a 16-channel head and neck coil. Axial turbo spin-echo T1-weighted (TR/TE, 559/8.8 ms; flip angle, 90°; FOV, 230 mm; ma-

trix, 288 × 288), T2-weighted (TR/TE, 4481/90 ms; flip angle, 90°; FOV, 230 mm; matrix, 320 × 320), and contrast-enhanced fat-saturated fast-field echo T1-weighted images (TR/TE, 179/3.5 ms; flip angle, 70°; FOV, 230 mm; matrix, 304 × 304) were obtained parallel to the vocal cords with a 3-mm thickness and 1-mm gap. Additionally, 3D imaging using T2-weighted and pre- and post-contrast-enhanced T1-weighted imaging was also performed from 1.0 cm above the hyoid bone to the inferior margin of the cricoid cartilage for all patients. 3D T1-weighted images were acquired in the transverse plane using a 3D turbo-field echo sequence, precontrast (TR/TE, 4.6/2.3 ms; flip angle, 15°; FOV, 230 mm; matrix, 224 × 224) and postcontrast with fat-saturation (TR/TE, 5.9/3.5 ms; flip angle, 15°; FOV, 230 mm; matrix, 224 × 224) with a 1-mm thickness and 0-mm gap.

Dual-Energy CT Techniques

All dual-energy CT studies were performed with 128-slice dual-source CT scanner (Somatom Definition Flash; Siemens, Erlangen, Germany) in the dual-energy CT mode²⁷ with the following parameters: 100 and Sn140-kV tube voltages, 200 and 200 effective mAs, 0.33-second rotation time, 32 × 0.6-mm collimation with a z-flying focal spot, and a pitch of 0.6. The average CT dose index was 14.45 mGy. Patients received 60–150 mL (600 mg I/kg) of iodinated contrast medium (iohexol 300; Ioverin, Teva Pharma Japan, Nagoya, Japan; or iopamidol 370; Oypalomin, Konica Minolta, Tokyo, Japan) intravenously at a rate of 2.5 mL/s. The scan started 70 seconds after the start of the injection and proceeded from the base of the skull to the bottom of the neck.

Two image sets (100 kV and Sn140 kV) were reconstructed with 1-mm slice thickness and a 0.7-mm increment with D30f kernels, and a third linearly blended image set (weighted-average [WA] images) with a B30f kernel was used to obtain a 120-kV equivalent image.¹⁶ WA images are used as diagnostic images because they are equivalent in terms of image quality to single-energy 120-kV CT images. Sinogram-affirmed iterative reconstruction (SAFIRE) was used for WA images (SAFIRE strength 1) and for 100-kV and Sn140-kV images (SAFIRE strength 3). IO images were generated using a 3-material decomposition analysis (syngo Dual Energy, Brain Hemorrhage; Siemens) as proposed in a recent study.¹⁴ The window for color coding of IO images was visually adjusted to maximize enhancement in tumor tissue and minimize noise in muscle tissue per case. Parallel ranges with 2.0-mm-thick sections and a 16-cm FOV were generated from the WA images, the virtual unenhanced images, and the IO images as follows: axial and coronal sections parallel and vertical to the vocal cords, respectively (in soft-tissue and bone windows), from 1.0 cm above the hyoid bone to the inferior margin of the cricoid cartilage.

Image Evaluation

The MR imaging and dual-energy CT diagnostic criteria for cartilage invasion are defined below (summarized in On-line Table).

MR Imaging. Cartilage invasion was “positive” in cases in which the cartilage displayed signals similar to those of the adjacent tumor on all pre- and postcontrast T1- and T2-weighted images in the cortical bone, cartilage, and bone marrow space.¹² When the cartilage had higher signal intensity than the adjacent tumor on

T2-weighted images or when stronger enhancement was present on postcontrast T1-weighted images, the abnormal signal intensity was diagnosed as negative because these changes may represent reactive changes.¹² Interpretation always started with the 2D sequence images, followed by 3D sequence images when 2D sequence images alone were insufficient due to artifacts. When the 2D and 3D sequence findings were mismatched, the diagnosis obtained on higher quality images was used.

Dual-Energy CT. Image interpretation always started with the WA image to evaluate tumor location, extension, and invasion.¹⁴ Cartilage with asymmetric sclerosis (ossification) without erosion or lysis was diagnosed as negative on WA images, because these are usually considered reactive changes.^{28,29} When a lesion had been evaluated as having erosion or lysis of ossified cartilage on WA images, the iodine distribution in the remaining nonossified cartilage was evaluated on IO images for a final diagnosis of either positive or negative for cartilage invasion. Areas of ossified cartilage were thoroughly excluded from evaluation on IO images because the dual-energy algorithms could not distinguish calcium from iodine.^{14,26,30}

Two radiologists (with 9 and 5 years of experience, respectively, in head and neck radiology), blinded to the clinical history and the image from the other technique, independently analyzed the images. The images were presented in random order in 2 sessions, initially with only MR images, followed 5 weeks later with only dual-energy CT images. The invasion of the thyroid, cricoid, and arytenoid cartilages was evaluated using the following 5-point-scale scoring system: 1, definitely negative; 2, probably negative; 3, erosion (possibly positive); 4, lysis (probably positive); and 5, transmural extralaryngeal spread through the cartilage (definitely positive).¹⁴ We arrived at the final diagnosis by consensus. The readers reached consensus in the same manner by discussion when a discrepancy existed for MR imaging and dual-energy CT.

Image-quality in terms of motion artifacts was also evaluated on a 5-point scale: grade 1, nondiagnostic with major artifacts; grade 2, major artifacts with most organs depicted with diagnostic image quality; grade 3, moderate artifacts with low image quality but diagnostic; grade 4, minor artifacts with good image quality; and grade 5, no artifacts with excellent image quality.

Pathologic Evaluation

A pathologist (with 22 years of experience) evaluated the surgical specimens, including all cartilage around tumors of all 55 patients. The specimens were fixed in formalin, decalcified, and then sliced horizontally with a thickness of 5 mm to match the cross-sectional MR and dual-energy CT images. The histopathologic findings served as the reference standard.

Statistical Analysis

The image quality of MR imaging and dual-energy CT was compared by applying the Wilcoxon signed rank test to the image-evaluation grades. For estimating the sensitivity and specificity of both modalities for the detection of cartilage invasion, we used the diagnostic confidence scores with a cutoff point of 3 as a positive diagnosis and generated contingency tables separately for each type of cartilage and for all cartilages together. Because each

patient had only 1 thyroid and only 1 cricoid cartilage, we applied the McNemar test to compare sensitivity and specificity for these cartilages. For comparisons of sensitivity and specificity for the evaluation of arytenoid cartilages and of all cartilages together, generalized linear mixed models were used to take into account correlations between multiple cartilages in the same patient.¹² The overall diagnostic performances were compared using the areas under the curve (AUCs) of the receiver operating characteristic (ROC) curve. For thyroid cartilage, partial AUCs corresponding to a specificity range of 90%–100% were also compared because this specificity range is clinically the most relevant. Inter-reader agreement between the independent evaluations of the 2 readers for the scores based on the MR imaging and the combination of WA and IO images was estimated by weighted κ statistics. We applied weighted κ statistics, taking into account that large differences of >1 point between the scores of the 2 readers were more serious than smaller differences.³¹ We used commercial software (SAS, Version 9.3 for Windows; SAS Institute, Cary, North Carolina) for the generalized linear mixed modeling and Stata (Version 12.1; StataCorp, College Station, Texas) for all other tests. $P < .05$ indicated a significant difference.

RESULTS

Image Quality Assessment

All MR and WA or IO images generated with the dual-energy CT data were considered of diagnostic image quality (grade 2 or more). Motion artifact grading scores are listed in Table 1. The median image-quality grading score was 3 (interquartile range, 0) for MR imaging and 4 (interquartile range, 0) for dual-energy CT ($P < .001$).

Pathologic Findings of Surgically Resected Specimens

We examined 220 cartilages (55 thyroid, 55 cricoid, 110 arytenoid cartilages) of 55 patients. Cartilage invasion was found in 36 of the 220 preparations (16%; 19 thyroid, 8 cricoid, 9 arytenoid cartilages) and on a per-patient basis in 19 of the 55 patients (35%). Invasion of the thyroid cartilage was found in all 19 patients whose specimens tested positive for cartilage invasion. Extralaryngeal extension of tumor cells with or without cartilage invasion was confirmed pathologically in 34 of 55 (62%) patients. The 17 laryngeal tumors were classified as pT3 ($n = 7$) and pT4a ($n = 10$), and the 38 hypopharyngeal tumors were classified as pT2 ($n = 5$), pT3 ($n = 7$), and pT4a ($n = 26$).

Relationship between Imaging Findings and Histopathologic Diagnosis of Surgical Specimens

MR Imaging. Among the 36 cartilage invasions that were histopathologically confirmed, 35 were correctly detected by MR imaging and only one was incorrectly detected as a false-negative finding (0 thyroid, 0 cricoid, and 1 arytenoid cartilage). However, MR imaging also led to 29 false-positive findings (13 thyroid, 6 cricoid, and 10 arytenoid cartilages) seen in areas of ossified cartilages. Inflammatory changes with desmoplastic reaction were found in many ossified cartilages, especially in areas of fatty marrow with calcification for thyroid cartilage (Fig 1), and mimicked cartilage invasion. In addition, the area of

Table 1: Summary of motion artifact grading scores for MRI and dual-energy CT^a

	1	2	3	4	5	Mean Score (SE)	P Value
All patients (n = 55)							<.001 ^b
MRI	0	3	48	4	0	3.02 (0.05)	
Dual-energy CT	0	0	0	46	9	4.16 (0.05)	
T1 or T2 stage (n = 6)							.050
MRI	0	0	3	3	0	3.50 (0.22)	
Dual-energy CT	0	0	0	4	2	4.33 (0.21)	
T3 stage (n = 13)							<.001 ^b
MRI	0	1	11	1	0	3.00 (0.11)	
Dual-energy CT	0	0	0	12	1	4.08 (0.08)	
T4a stage (n = 36)							<.0001 ^b
MRI	0	2	34	0	0	2.94 (0.04)	
Dual-energy CT	0	0	0	30	6	4.17 (0.06)	

Note:—SE indicates standard error.

^a Data are number of patients. The rating grade is as follows: grade 1, nondiagnostic with major artifacts; grade 2, major artifacts with most organs depicted with diagnostic image quality; grade 3, moderate artifacts with image quality low but diagnostic; grade 4, minor artifacts with good image quality; grade 5, no artifacts with excellent image quality.

^b Indicates a significant difference using the Wilcoxon signed rank test ($P < .05$).

tumor extension in cartilage tended to be overestimated by MR imaging (On-line Figure).

Dual-Energy CT. Dual-energy CT correctly detected 29 cartilage invasions. However, 7 invasions were missed (2 thyroid, 2 cricoid, and 3 arytenoid cartilages), among them 3 minor invasions of tumor cells into an ossified part of the cartilage (2 thyroid and 1 cricoid) with an extent of <3-mm diameter in the histopathologic specimens (On-line Figure). There were no false-positive findings of thyroid cartilage invasion, but there were 4 false-positive findings of cricoid ($n = 1$) and arytenoid ($n = 3$) cartilage invasion where erosive changes seemed to be present on dual-energy CT images.

Diagnostic Performance of MR Imaging and Dual-Energy CT

The diagnostic performance of MR imaging and dual-energy CT for patients who underwent surgery is summarized in Table 2.

For analysis of all cartilages together, the specificity of dual-energy CT (98%; 95% CI, 95%–99%) for the detection of cartilage invasion was significantly higher ($P = .004$) than that of MR imaging (84%; 95% CI, 78%–89%). The point estimate of the sensitivity of dual-energy CT (81%; 95% CI, 64%–92%) was lower than that of MR imaging (97%; 95% CI, 85%–100%), but the difference between the sensitivities of the modalities was not statistically significant ($P < .16$). There was no indication of a true difference in the total AUCs (0.97; 95% CI, 0.88–1.00 for MR imaging; and 0.95; 95% CI, 0.89–1.00 for dual-energy CT; $P = .19$).

For thyroid cartilage, the specificity of dual-energy CT was significantly higher ($P < .001$) for the detection of cartilage invasion (100%; 95% CI, 90%–100%) than MR imaging (64%; 95% CI, 46%–79%), while no significant differences ($P = .50$) were found between the sensitivities for the detection of cartilage invasions of MR imaging (100%; 95% CI, 82%–100%) and dual-energy CT (89%; 95% CI, 67%–99%). The ROC curves for thyroid cartilage and the corresponding areas under the curve for diagnoses with MR imaging and dual-energy CT are shown in Fig 2. There was no indication of a difference in the mean areas under ROC curve (0.94; 95% CI, 0.88–1.00 for MR imaging versus 0.95; 95% CI, 0.89–1.00 for dual-energy CT; $P = .700$) for the evaluation of thyroid cartilage. The calculated partial AUC at the low

false-positive ratio area between 0.0 and 0.1 showed that dual-energy CT (0.09; 95% CI, 0.08–1.00) was superior to MR imaging (0.01; 95% CI, 0.00–0.63) for the evaluation of thyroid cartilage ($P = .003$).

Analyses of other cartilages showed the following results: No significant differences were found between the sensitivities for the detection of cartilage invasion of MR imaging and dual-energy CT: cricoid cartilage (100%; 95% CI, 63%–100% for MR imaging versus 75%; 95% CI, 35%–97% for dual-energy CT) and arytenoid cartilage (89%; 95% CI, 52%–100% versus 67%; 95% CI, 30%–93% for dual-energy CT). No significant difference between the specificities of both modalities were found for cricoid cartilage ($P = .06$) and arytenoid cartilage ($P = .09$), where the specificities were estimated as 87% (95% CI, 74%–95%) and 91% (95% CI, 83%–95%) for MR imaging compared with 98% (95% CI, 89%–100%) and 97% (95% CI, 92%–100%), respectively, for dual-energy CT. There was no indication of a true difference in the total AUCs for cricoid cartilage (0.99; 95% CI, 0.97–1.00 for MR imaging versus 0.93; 95% CI, 0.85–1.00 for dual-energy CT; $P = .15$) and arytenoid cartilage (0.95; 95% CI, 0.88–1.00 for MR imaging versus 0.93; 95% CI, 0.87–0.99 for dual-energy CT; $P = .50$).

Interreader Agreement

Interreader agreement of the 2 readers was assessed with quadratic weighted κ statistics for MR imaging and for the combination of WA and IO images with the following results³¹: excellent agreement of 0.80 (95% CI, 0.70–0.89) and almost perfect agreement of 0.84 (95% CI, 0.74–0.93), respectively, for the all cartilage together; almost perfect agreement of 0.88 (95% CI, 0.61–1.00) and 0.90 (95% CI, 0.63–1.00), respectively, for thyroid cartilage; substantial agreement of 0.69 (95% CI, 0.45–0.97) and 0.79 (95% CI, 0.53–1.00), respectively, for cricoid cartilage; and substantial agreement of 0.75 (95% CI, 0.56–0.93) and 0.77 (95% CI, 0.59–0.95), respectively, for arytenoid cartilage. These results indicated that both modalities have similar interreader agreement.

DISCUSSION

In this study, we evaluated the diagnostic performance of MR imaging and the combination of WA and IO dual-energy CT images in the evaluation of cartilage invasion by laryngeal and

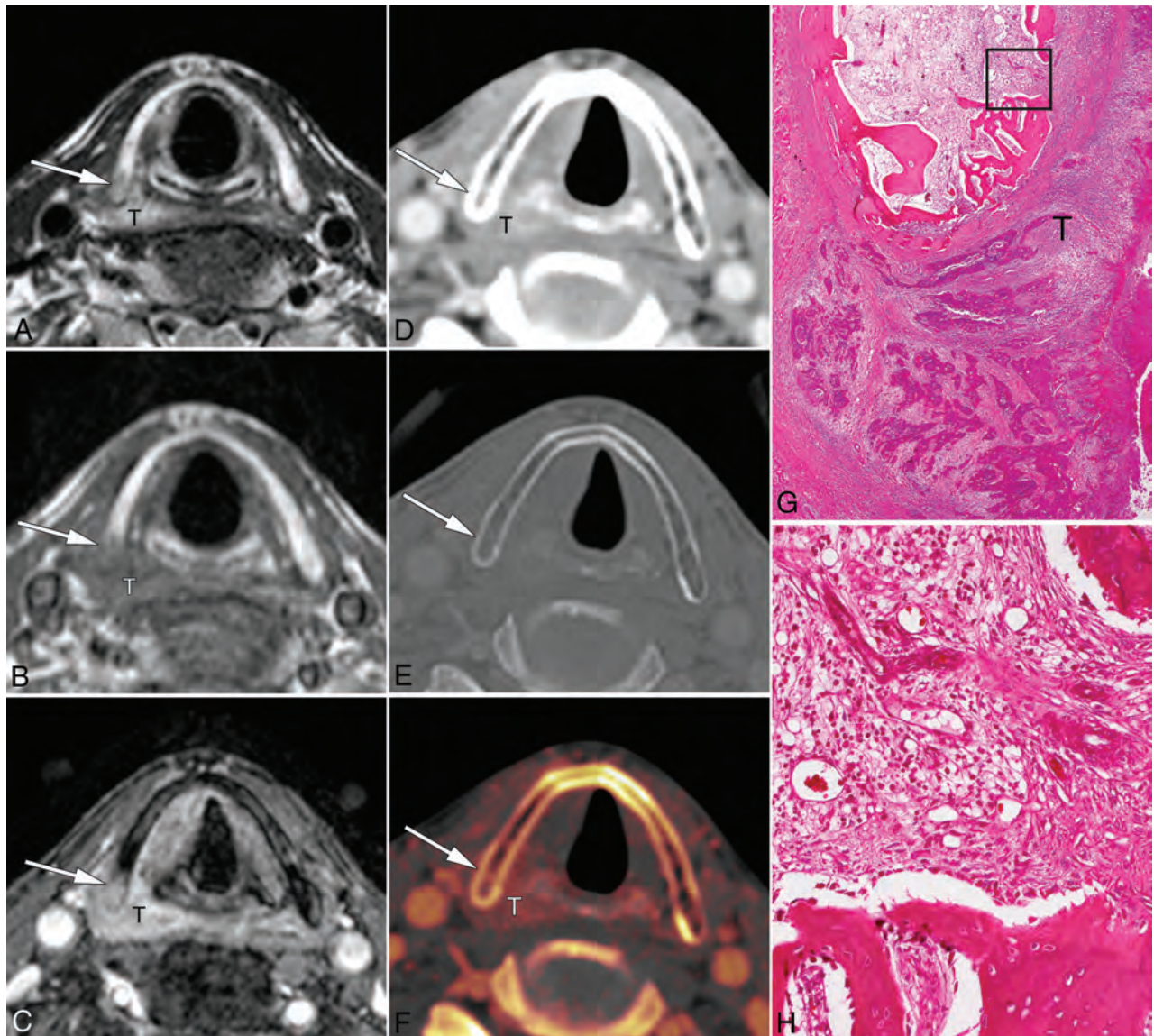


FIG 1. False-positive findings for thyroid cartilage invasion on MR imaging in a 59-year-old man with hypopharyngeal cancer. *A*, T2-weighted MR image obtained at the glottis level shows a tumor (T) arising from the right piriform sinus with intermediate signal intensity. The adjacent posterior right thyroid lamina also shows an area of intermediate signal intensity (*arrow*). *B*, T1-weighted image shows that the tumor (T) has low signal intensity, whereas adjacent thyroid cartilage has similar signal intensity (*arrow*). *C*, Contrast-enhanced fat-suppressed T1-weighted MR image shows similar contrast enhancement of the tumor (T) and adjacent thyroid cartilage (*arrow*). *D*, A weighted-average image does not show erosion or lysis at the same level (*D*, soft-tissue window; *E*, bone window). *F*, Iodine overlay image shows enhancement of tumor (T) more clearly and is not used for the diagnosis of cartilage according to the findings of the WA image. *G*, A micrograph of the corresponding axial slice of the surgical specimen at the same level shows that the squamous cell carcinoma cells do not permeate into the right thyroid cartilage lamina (hematoxylin-eosin stain; original magnification, $\times 5$). *H*, Magnified photograph (*square* in *G*) of the posterior part of the right thyroid cartilage lamina with enhancement on MR imaging shows moderate infiltration of lymphocytes into the medullary space, accompanied by fibrosis and aggregation of macrophages, without tumor (H&E stain; original magnification, $\times 200$).

hypopharyngeal SCCs. The specificity of dual-energy CT was significantly superior to that of MR imaging when evaluating all cartilages combined and when evaluating thyroid cartilage alone. The point estimates of the sensitivity were higher for MR imaging than for dual-energy CT; however, these differences were not significant for all cartilages combined and for thyroid cartilage alone.

There was also no significant difference in the areas under the ROC curve for the detection of thyroid cartilage invasion of both modalities, suggesting that the overall diagnostic performance might be similar for dual-energy CT and MR imaging and the highest specificities of dual-energy CT may have been achieved in

a trade-off against the sensitivity. However, although the total areas under the curve of the ROC curve were identical, the curves showed a crossover at 0.14 and the sensitivity of dual-energy CT at low false-positive ratios ranging between 0.0 and 0.1 was higher than that of MR imaging.³² The histopathologic specimens of the false-negative cases (thyroid and cricoid cartilages) seen on dual-energy CT revealed that most had minimal invasion of tumor cells into an ossified part of the cartilage with an extent of <3 -mm diameter, which was not detectable with dual-energy CT, whereas massive cartilage invasion was misdiagnosed in none of the cases as negative findings. In the era of laryngeal conservation, the re-

Table 2: Relationship between dual-energy CT/MR imaging and histopathologic findings for the detection of cartilage invasion^a

	TP	TN	FN	FP	Sensitivity (%)	Specificity (%)	PPV (%)	NPV (%)
Thyroid cartilage (n = 55)								
MRI	19	23	0	13	100 (82–100)	64 (46–79)	59 (41–76)	100 (85–100)
Dual-energy CT	17	36	2	0	89 (67–99)	100 (90–100)	100 (80–100)	95 (82–99)
P value ^b					.5	<.001		
Cricoid cartilage (n = 55)								
MRI	8	41	0	6	100 (63–100)	87 (74–95)	57 (29–82)	100 (91–100)
Dual-energy CT	6	46	2	1	75 (35–97)	98 (89–100)	86 (42–100)	96 (86–99)
P value ^b					.5	.06		
Arytenoid cartilage (n = 110)								
MRI	8	91	1	10	89 (52–100)	91 (83–95)	44 (22–69)	99 (94–100)
Dual-energy CT	6	98	3	3	67 (30–93)	97 (92–100)	67 (30–93)	97 (92–99)
P value ^c					.43	.09		
All cartilage (n = 220)								
MRI	35	155	1	29	97 (85–100)	84 (78–89)	55 (42–67)	99 (96–100)
Dual-energy CT	29	180	7	4	81 (64–92)	98 (95–99)	88 (72–97)	96 (92–98)
P value ^c					.16	<.004		

Note:—TP indicates true positive; TN, true negative; FP, false positive; FN, false negative; PPV, positive predictive value; NPV, negative predictive value.

^a Numbers in parentheses are 95% confidence intervals. Negative findings for cartilage invasion are scores 1 and 2; positive findings are scores 3–5.

^b As determined with the McNemar test.

^c According to the generalized linear mixed model that accounted for the multiple observations within patients.

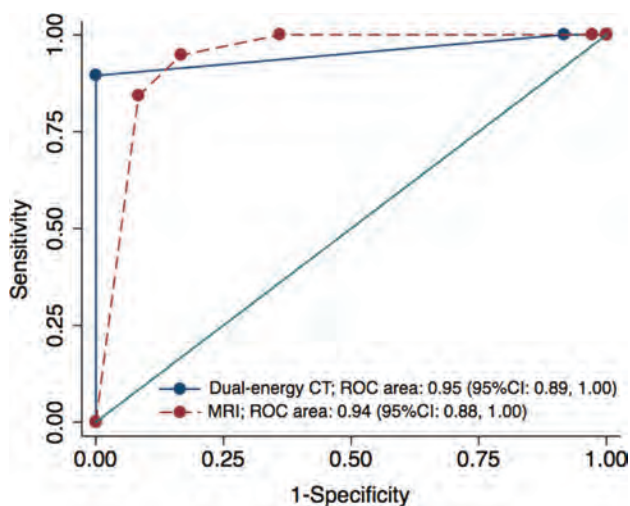


FIG 2. Graph shows 2 crossing ROC curves and corresponding AUCs in the prediction of thyroid cartilage invasion. There was no evidence of differences in the average areas under the ROC curve between MR imaging and dual-energy CT (0.938 versus 0.952, respectively; $P = .70$).

duction of overestimation for thyroid cartilage is particularly important for treatment-related decision-making compared with the reduction of underestimation for cartilage invasion; therefore, we believe that dual-energy CT may potentially assist in patient management.

MR imaging has a high sensitivity and high negative predictive value for detecting cartilage invasion compared with conventional CT.¹⁰ However, inflammatory changes in cartilage often resemble cartilage invasion, and high false-positive rates remain an issue.^{10,12} In our study, MR imaging demonstrated false-positive findings in areas of ossified cartilage with inflammatory change, and the higher sensitivity on MR imaging seems to be at the expense of specificity. Cortical bone and ossified cartilage are difficult to identify on MR imaging because of a lack of signal from bone. Therefore, MR imaging may be challenging for the evaluation of cortical bone changes, such as erosion or lysis. In addition, in patients with advanced SCCs, MR imaging seems to

be prone to motion artifacts because of the relatively long scan times, which can render images nondiagnostic. In our study, the image quality of MR imaging tended to have motion artifacts, especially in patients with locally advanced (T3–T4) SCCs, while dual-energy CT showed no artifacts. Recently, phased array surface coils were applied to the neck for reducing the motion artifacts and increasing the spatial resolution.^{33,34} However, this technique uses a small FOV, restricting the imaged area to the larynx.

Dual-energy CT can provide WA images, which are like conventional 120-kV images, and additional IO images, both with high spatial resolution.^{27,35,36} However, IO images have the technical limitation that lesions in ossified cartilage cannot be clearly identified.¹⁴ In our study, we therefore used combined WA and IO images for the diagnoses of both ossified and nonossified cartilage. The lesions that include calcified structures needed to be evaluated on WA images first because on IO images, iodine distribution could be overestimated due to the presence of calcified structures. When the WA image did not show cartilage destruction, regardless of inflammatory changes in the fatty marrow, cartilage invasion was considered absent in this diagnostic algorithm. High specificity for dual-energy CT could be achieved because the WA and IO images depicted the precise shapes of ossified cartilages and iodine distribution in nonossified thyroid cartilages and bone marrow space at the same time, thus preventing the overestimation of invasion that occurred during diagnoses with MR imaging. Furthermore, there is the potential for misclassification in the presence of artifacts that makes correlation and interpretation in conjunction with WA imperative.

There are limitations in our study. First, the difference between the signal intensities of the tumor adjacent to the cartilage and the nonossified cartilage was assessed visually without quantitative measurement of iodine concentrations. Therefore, the potentially confounding effect of interreader error, including display settings, may be present. In addition, there are other dual-energy CT approaches for evaluation of nonossified thyroid cartilage or head and neck squamous cell carcinoma in general that could potentially increase accuracy. These need to be evaluated in a future study. Second, because of the sample-size limitation, the

statistical analysis was limited to the whole sample and each subgroup of primary tumor could not be analyzed. Besides, the small sample size may mask the lack of statistical difference in the sensitivity. Further studies with a larger number of patients are needed to provide further evidence for clinical relevance. Third, this study included only a small number of early-stage cases with no evaluation of their prognosis. If dual-energy CT promotes a more frequent selection of laryngeal-preserving therapy, it will be essential to evaluate long-term prognosis through collection of data from additional cases and to test the validity of this approach for each subset of tumors in a future prospective study.

CONCLUSIONS

The specificity of dual-energy CT is higher than that of MR imaging for the evaluation of cartilage invasion by laryngeal and hypopharyngeal SCCs for all cartilage combined and for thyroid cartilage alone. Dual-energy CT can prevent the overestimation of cartilage invasion that may occur due to inflammatory changes by using appropriate diagnostic criteria on WA images and IO images for ossified and nonossified cartilage. Although subtle tumor invasion into the ossified cartilage may be missed by dual-energy CT, it may add value by avoiding overestimation of cartilage invasion and may help in promoting laryngeal preservation approaches for laryngeal and hypopharyngeal SCCs.

Disclosures: Hirofumi Kuno—RELATED: Other: Siemens Healthcare K.K., Comments: One of the authors (K.O.) is an employee of Siemens Healthcare K.K., and Siemens Healthcare K.K. provided a license for iterative CT reconstruction (SAFIRE) to the National Cancer Center Hospital East for this study. Authors who are not employees of Siemens Healthcare monitored and had control of inclusion of any data and information submitted for publication*; UNRELATED: Grants/Grants Pending: Grant-in-Aid for Young Scientists (B) KAKEN (#26861033). Katharina Otani—OTHER RELATIONSHIPS: Employee of Siemens Healthcare K.K. Osamu Sakai—UNRELATED: Consultancy: Guerbet, Boston Imaging Core Lab; Payment for Lectures Including Service on Speakers Bureaus: Bracco Diagnostics, Eisai, Masahiko Kusumoto—UNRELATED: Payment for Lectures Including Service on Speakers Bureaus: Ono Pharmacy, MSD, AstraZeneca. *Money paid to the institution.

REFERENCES

- Baugnon KL, Beitler JJ. Pitfalls in the staging of cancer of the laryngeal squamous cell carcinoma. *Neuroimaging Clin N Am* 2013;23:81–105 CrossRef Medline
- Hermans R. Staging of laryngeal and hypopharyngeal cancer: value of imaging studies. *Eur Radiol* 2006;16:2386–400 CrossRef Medline
- Pfister DG, Laurie SA, Weinstein GS, et al; American Society of Clinical Oncology. American Society of Clinical Oncology clinical practice guideline for the use of larynx-preservation strategies in the treatment of laryngeal cancer. *J Clin Oncol* 2006;24:3693–704 CrossRef Medline
- Forastiere AA, Goepfert H, Maor M, et al. Concurrent chemotherapy and radiotherapy for organ preservation in advanced laryngeal cancer. *N Engl J Med* 2003;349:2091–98 CrossRef Medline
- Hoffman HT, Porter K, Karnell LH, et al. Laryngeal cancer in the United States: changes in demographics, patterns of care, and survival. *Laryngoscope* 2006;116:1–13 Medline
- Choi YS, Park SG, Song EK, et al; Korean South West Oncology Group (KSWOG) Investigators. Comparison of the therapeutic effects of total laryngectomy and a larynx-preservation approach in patients with T4a laryngeal cancer and thyroid cartilage invasion: a multicenter retrospective review. *Head Neck* 2016;38:1271–27 CrossRef Medline
- Knab BR, Salama JK, Solanki A, et al. Functional organ preservation with definitive chemoradiotherapy for T4 laryngeal squamous cell carcinoma. *Ann Oncol* 2008;19:1650–54 CrossRef Medline
- Lefebvre JL, Ang KK. Larynx preservation clinical trial design: key issues and recommendations—a consensus panel summary. *Head Neck* 2009;31:429–41 CrossRef Medline
- Li B, Bobinski M, Gandour-Edwards R, et al. Overstaging of cartilage invasion by multidetector CT scan for laryngeal cancer and its potential effect on the use of organ preservation with chemoradiation. *Br J Radiol* 2011;84:64–69 CrossRef Medline
- Becker M, Zbaren P, Laeng H, et al. Neoplastic invasion of the laryngeal cartilage: comparison of MR imaging and CT with histopathologic correlation. *Radiology* 1995;194:661–69 CrossRef Medline
- Kuno H, Onaya H, Fujii S, et al. Primary staging of laryngeal and hypopharyngeal cancer: CT, MR imaging and dual-energy CT. *Eur J Radiol* 2014;83:e23–35 CrossRef Medline
- Becker M, Zbaren P, Casselman JW, et al. Neoplastic invasion of laryngeal cartilage: reassessment of criteria for diagnosis at MR imaging. *Radiology* 2008;249:551–59 CrossRef Medline
- Dadfar N, Seyyedi M, Forghani R, et al. Computed tomography appearance of normal nonossified thyroid cartilage: implication for tumor invasion diagnosis. *J Comput Assist Tomogr* 2015;39:240–43 CrossRef Medline
- Kuno H, Onaya H, Iwata R, et al. Evaluation of cartilage invasion by laryngeal and hypopharyngeal squamous cell carcinoma with dual-energy CT. *Radiology* 2012;265:488–96 CrossRef Medline
- Tawfik AM, Kerl JM, Bauer RW, et al. Dual-energy CT of head and neck cancer: average weighting of low- and high-voltage acquisitions to improve lesion delineation and image quality—initial clinical experience. *Invest Radiol* 2012;47:306–11 CrossRef Medline
- Vogl TJ, Schulz B, Bauer RW, et al. Dual-energy CT applications in head and neck imaging. *AJR Am J Roentgenol* 2012;199:S34–39 CrossRef Medline
- Wichmann JL, Nöske EM, Kraft J, et al. Virtual monoenergetic dual-energy computed tomography: optimization of kiloelectron volt settings in head and neck cancer. *Invest Radiol* 2014;49:735–41 CrossRef Medline
- Albrecht MH, Scholtz JE, Kraft J, et al. Assessment of an advanced monoenergetic reconstruction technique in dual-energy computed tomography of head and neck cancer. *Eur Radiol* 2015;25:2493–501 CrossRef Medline
- Forghani R, Levental M, Gupta R, et al. Different spectral Hounsfield unit curve and high-energy virtual monochromatic image characteristics of squamous cell carcinoma compared with nonossified thyroid cartilage. *AJNR Am J Neuroradiol* 2015;36:1194–200 CrossRef Medline
- Lam S, Gupta R, Levental M, et al. Optimal virtual monochromatic images for evaluation of normal tissues and head and neck cancer using dual-energy CT. *AJNR Am J Neuroradiol* 2015;36:1518–24 CrossRef Medline
- Scholtz JE, Kaup M, Kraft J, et al. Objective and subjective image quality of primary and recurrent squamous cell carcinoma on head and neck low-tube-voltage 80-kVp computed tomography. *Neuroradiology* 2015;57:645–51 CrossRef Medline
- Lam S, Gupta R, Kelly H, et al. Multiparametric evaluation of head and neck squamous cell carcinoma using a single-source dual-energy CT with fast kVp switching: state of the art. *Cancers (Basel)* 2015;7:2201–16 CrossRef Medline
- Hermans R, Vander Goten A, Baert AL. Image interpretation in CT of laryngeal carcinoma: a study on intra- and interobserver reproducibility. *Eur Radiol* 1997;7:1086–90 CrossRef Medline
- Pache G, Krauss B, Strohm P, et al. Dual-energy CT virtual noncalcium technique: detecting posttraumatic bone marrow lesions—feasibility study. *Radiology* 2010;256:617 CrossRef Medline
- Joe E, Kim SH, Lee KB, et al. Feasibility and accuracy of dual-source dual-energy CT for noninvasive determination of hepatic iron accumulation. *Radiology* 2012;262:126–35 CrossRef Medline
- Postma AA, Hofman PA, Stadler AA, et al. Dual-energy CT of the brain and intracranial vessels. *AJR Am J Roentgenol* 2012;199:S26–33 CrossRef Medline
- Flohr TG, McCollough CH, Bruder H, et al. First performance eval-

- uation of a dual-source CT (DSCT) system. *Eur Radiol* 2006;16:256–68 CrossRef Medline
28. Becker M, Zbären P, Delavelle J, et al. **Neoplastic invasion of the laryngeal cartilage: reassessment of criteria for diagnosis at CT.** *Radiology* 1997;203:521–32 CrossRef Medline
 29. Beitler JJ, Muller S, Grist WJ, et al. **Prognostic accuracy of computed tomography findings for patients with laryngeal cancer undergoing laryngectomy.** *J Clin Oncol* 2010;28:2318–22 CrossRef Medline
 30. Gupta R, Phan CM, Leidecker C, et al. **Evaluation of dual-energy CT for differentiating intracerebral hemorrhage from iodinated contrast material staining.** *Radiology* 2010;257:205–11 CrossRef Medline
 31. Sim J, Wright CC. **The kappa statistic in reliability studies: use, interpretation, and sample size requirements.** *Phys Ther* 2005;85:257–68 Medline
 32. Obuchowski NA. **Receiver operating characteristic curves and their use in radiology.** *Radiology* 2003;229:3–8 CrossRef Medline
 33. Allegra E, Ferrise P, Trapasso S, et al. **Early glottic cancer: role of MRI in the preoperative staging.** *Biomed Res Int* 2014;2014:890385 CrossRef Medline
 34. Ravanelli M, Farina D, Rizzardi P, et al. **MR with surface coils in the follow-up after endoscopic laser resection for glottic squamous cell carcinoma: feasibility and diagnostic accuracy.** *Neuroradiology* 2013;55:225–32 CrossRef Medline
 35. Graser A, Johnson TRC, Chandarana H, et al. **Dual energy CT: preliminary observations and potential clinical applications in the abdomen.** *Eur Radiol* 2009;19:13–23 CrossRef Medline
 36. Johnson TR, Krauss B, Sedlmair M, et al. **Material differentiation by dual energy CT: initial experience.** *Eur Radiol* 2007;17:1510–17 CrossRef Medline

MR Imaging–Based Evaluations of Olfactory Bulb Atrophy in Patients with Olfactory Dysfunction

M.S. Chung, W.R. Choi, H.-Y. Jeong, J.H. Lee, and J.H. Kim

ABSTRACT

BACKGROUND AND PURPOSE: Although the olfactory bulb volume as assessed with MR imaging is known to reflect olfactory function, it is not always measured during olfactory pathway assessments in clinical settings. We aimed to evaluate the utility of visual olfactory bulb atrophy and neuropathy analyses using MR imaging in patients with olfactory dysfunction.

MATERIALS AND METHODS: Thirty-four patients who presented with subjective olfactory loss between March 2016 and February 2017 were included. Patients underwent a nasal endoscopic examination, olfactory testing with the Korean Version of the Sniffin' Sticks test, and MR imaging. All patients completed the Sino-Nasal Outcome Test and Questionnaire of Olfactory Disorders. Olfactory bulb atrophy and neuropathy were evaluated on MR images by 2 head and neck radiologists.

RESULTS: The etiology of olfactory loss was chronic rhinosinusitis with/without nasal polyps in 15 (44.1%) patients, respiratory viral infection in 7 (20.6%), trauma in 2 (5.9%), and idiopathic in 10 (29.4%) patients. Although 10 (29.4%) of the 34 patients were normosmic according to the Sniffin' Sticks test, their scores on the other tests were like those of patients who were hyposmic/anosmic according to the Sniffin' Sticks test. However, the detection rate of olfactory bulb atrophy was significantly higher in patients with hyposmia/anosmia than it was in patients with normosmia ($P = .002$). No difference in olfactory bulb neuropathy was identified among patients with normosmia and hyposmia/anosmia ($P = .395$).

CONCLUSIONS: MR imaging evaluations of olfactory bulb atrophy can be used to objectively diagnose olfactory dysfunction in patients with subjective olfactory loss.

ABBREVIATIONS: OB = olfactory bulb; LQ = Life Quality; QOD = Questionnaire of Olfactory Disorders; URI = upper respiratory infection; VISTA = volume isotropic turbo spin-echo acquisition

Symptoms regarding one's sense of smell (olfactory dysfunction) are relatively common, with a prevalence of about 20% in the general population. The etiologies of olfactory loss include postviral upper respiratory infection (URI), sinonasal disease, head trauma, aging, congenital causes, toxins/drugs, miscellaneous, idiopathic, and neurologic diseases such as Parkinson disease, multiple sclerosis, and Alzheimer disease.¹ Olfaction plays a

role in identifying food and hazards and may be involved in social communication; thus, olfactory dysfunction can decrease an individual's quality of life.²⁻⁴

Because treatments for olfaction loss are ineffective in many patients, precise assessments of their olfactory disturbances should be conducted before starting treatment, because these may be helpful for predicting their prognosis and providing proper counseling.⁵ In addition, some patients' olfactory function test scores are normal despite subjectively feeling as though their ability to smell is reduced. In these cases, it is difficult to determine whether one's ability to smell is decreased or whether treatment for hyposmia/anosmia is necessary. Therefore, the use of additional objective diagnostic tools may help confirm olfactory dysfunction in such individuals. Olfactory abilities are generally measured through olfactory function tests such as the University of Pennsylvania Smell Identification Test, the Connecticut Chemosensory Clinical Research Center Threshold Test, or the Sniffin' Sticks test. MR imaging can provide anatomic information on the olfactory pathway. One of the primary parameters for evaluating

Received July 25, 2017; accepted after revision October 26.

From the Department of Radiology (M.S.C.), Chung-Ang University Hospital, Chung-Ang University College of Medicine, Seoul, Republic of Korea; and Departments of Otorhinolaryngology–Head and Neck Surgery (W.R.C., H.-Y.J., J.H.K.), and Radiology and Research Institute of Radiology (J.H.L.), Asan Medical Center, University of Ulsan College of Medicine, Seoul, Republic of Korea.

Paper previously presented, in part, at: International Congress of Otorhinolaryngology–Head and Neck Surgery, April 21–23, 2017; Seoul, Korea.

Please address correspondence to Ji Heui Kim, MD, PhD, Department of Otorhinolaryngology–Head and Neck Surgery, Asan Medical Center, University of Ulsan College of Medicine, 88 Olympic-ro 43-gil, Songpa-gu, Seoul 05505, Republic of Korea; e-mail: jhkim0217@amc.seoul.kr

<http://dx.doi.org/10.3174/ajnr.A5491>

the olfactory pathway with MR imaging is olfactory bulb (OB) volume. Research has shown that OB volume in patients with olfactory loss is significantly decreased, and changes in OB volume are correlated with odor threshold changes.⁵⁻⁷ However, OB volume measurements are not commonly used for evaluating the olfactory pathway in clinical settings because volumetric analysis itself is difficult to routinely measure through planimetric manual contouring of multiple sections compared with visual analysis. Moreover, the cutoff values for diagnosing atrophy of OB volume in individual patients have not been established.⁸⁻¹¹ Therefore, in the present study, we evaluated the relationship between olfactory function tests and visual analyses of OB atrophy or neuropathy on MR images to determine whether such visual analyses could serve as easy and reliable imaging biomarkers of olfactory dysfunction.

MATERIALS AND METHODS

Study Subjects

This study included 34 patients (15 males and 19 females; mean age, 51.4 years; range, 9–72 years) who presented with subjective olfactory loss between March 2016 and March 2017. The mean duration of olfactory loss was 59.2 months (range, 2–552 months). This retrospective study was approved by the institutional review board of Asan Medical Center, exempting the study from requiring patient consent.

Chronic rhinosinusitis was diagnosed according to criteria established by the European Position Paper on Rhinosinusitis and Nasal Polyps (2012) guidelines based on the history, nasal endoscopy, and CT of the paranasal sinuses.¹² A post-URI olfactory deficit was diagnosed when acute loss of olfaction started after URI development and lasted until the consultation without other causes of olfactory loss. A posttraumatic olfactory deficit was diagnosed when the patient experienced a loss of olfaction after cranial trauma without other causes.⁵ If the patients did not have a clear cause of olfactory loss despite an extensive evaluation, their etiology was considered idiopathic.¹³

Olfactory Function Test

Olfactory function was tested by using the Korean Version of the Sniffin' Sticks II test. The odor Threshold, Discrimination, and Identification tests were performed in 3-minute intervals. The Threshold was defined as the concentration at which *n*-butanol (maximum concentration 4%, 16 steps of 1:2 serial dilutions) was accurately identified 4 consecutive times. For the Discrimination test, triplets of odorants (2 identical, 1 different) were presented, and the subject was asked to choose the different odorant. The Identification test was performed using 16 odors familiar to Koreans. The sum of the 3 tests was expressed as the total Threshold-Discrimination-Identification score. Total scores of 0–20 were defined as “anosmia”; 20.25–27, as “hyposmia”; and 27.25–48, as “normosmia,” according to a previous study.¹⁴

Symptom Questionnaires

All patients completed the Sino-Nasal Outcome Test-22 and Questionnaire of Olfactory Disorders (QOD) during a clinic visit. The Sino-Nasal Outcome Test questions were scored from 0 (no problem) to 5 (severe problem), and the maximum total score was 110.¹⁵ The QOD consisted of 3 statements, namely the Life Qual-

ity (LQ), Sincerity, and Parosmia statements, and 5 visual analog scales.^{2,16} The sum of the QOD-LQ scores comprised the LQ raw score (maximum score = 57 points), which was transformed into the LQ by the following formula: $LQ = LQ \text{ Raw Score} / 0.57$ (%). The sum of the QOD Sincerity scores comprised the Sincerity raw score (maximum score = 18), which was converted to the Sincerity score by the following formula: $Sincerity \text{ Score} = Sincerity \text{ Raw Score} / 0.18$ (%). The sum of the QOD Parosmia scores comprised the Parosmia raw score (maximum score = 12), which was converted to the Parosmia score with the following formula: $Parosmia \text{ Score} = Parosmia \text{ Raw Score} / 0.12$ (%). The visual analog scales consisted of 5 olfactory dysfunction problems, which were scored from 0 to 10.

Image Acquisition

The MR images were acquired using a 3T MR imaging system (Ingenia 3T CX; Philips Healthcare, Best, Netherlands) with a 64-channel head and neck coil. Coronal T2WI and precontrast 3D-FLAIR and 3D-T2 volume isotropic turbo spin-echo acquisition (VISTA; Phillips Healthcare) were performed with the following parameters: TR/TE, 300/80 ms; TSE factor, 15; bandwidth, 209 Hz/pixel; section thickness, 1.5 mm; matrix, 512 × 512; FOV, 90 × 190 mm; voxel size, 0.43 × 0.43 × 1.5 mm; and scan time, 3 minutes for T2WI; TR/TE, 8000/244 ms; TSE factor, 80; bandwidth, 510 Hz/pixel; sensitivity encoding factor, 2.5; section thickness, 0.6 mm; matrix, 256 × 256; FOV, 40 × 180 × 180 mm; voxel size, 0.35 × 0.35 × 0.6 mm; and scan time, 6 minutes and 40 seconds for 3D-FLAIR; and TR/TE, 2000/268 ms; TSE factor, 75; bandwidth, 330 Hz/pixel; acceleration factor, 2.5; section thickness, 0.6 mm; matrix, 376 × 374; FOV, 30 × 150 × 150 mm; voxel size, 0.2 × 0.2 × 0.6 mm; and scan time, 7 minutes and 42 seconds for 3D-T2 VISTA. Sections were angled perpendicular to the anterior base of the skull or cribriform plate. The scan coverage was from the frontal sinus to the optic chiasm.

Imaging Data Analyses

Two head and neck radiologists, with 18 and 6 years of experience, respectively, analyzed the MR imaging findings via consensus using the PACS system. The radiologists were blinded to the results of the patients' olfactory function tests. The boundaries of the OB were determined using the surrounding CSF and the anterior cribriform plate as markers. Atrophy of the OB was diagnosed on the basis of the following findings: flattening and thinning of the olfactory bulb with loss of the normal oval or J-shape of the OB,¹⁷ and an asymmetric decrease in the size of the OB compared with the OB on the contralateral side (Fig 1).¹⁸ Neuropathy was defined as neuromalacia of the OB, with focal or diffuse high signal intensity in the OB and increased signal compared with the signal intensity of the adjacent frontal white matter with/without decreased volume on 3D-FLAIR or coronal T2-weighted images (Fig 2).¹⁰

Statistical Analysis

The etiology of olfactory deficits and subjective symptom severity among patients with normosmia and hyposmia/anosmia following olfactory function tests were compared using the nonparametric Mann-Whitney *U* test and χ^2 test. The Mann-Whitney *U*

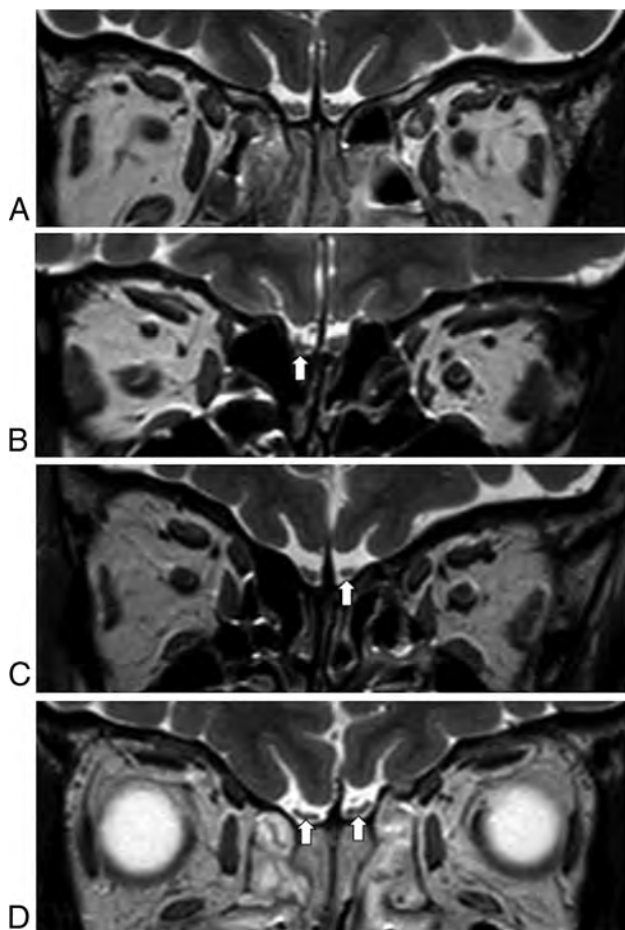


FIG 1. Atrophy of the olfactory bulbs. Compared with a patient with normal olfactory bulbs (A), which have an oval or inverted-J shape, patients with atrophy in the olfactory bulbs show asymmetric decreases in the size of the affected olfactory bulbs (B, right; and C, left, arrow) or flattening of the olfactory bulbs (D, arrows).

test and Fisher exact test were used to compare the results of olfactory function tests between patients with the presence or absence of OB atrophy and neuropathy. The Mann-Whitney *U* test was used for comparison of the presence or absence of OB atrophy following age and olfactory deficit duration. Data were analyzed by using SPSS 21 (IBM, Armonk, New York). Differences were considered significant at $P < .05$.

RESULTS

Etiology and Severity of Patients' Subjective Olfactory Symptoms

The etiology of the olfactory deficits was chronic rhinosinusitis with/without polyps in 15 (44.1%) patients, postviral URI in 7 (20.6%), trauma in 2 (5.9%), and idiopathic in 10 (29.4%) patients. None of the patients had olfactory deficits owing to neurologic disease.

Ten (29.4%) of the 34 patients were normosmic according to the Korean Version of the Sniffin' Sticks II test; the mean total Threshold-Discrimination-Identification score for these 10 patients was 35.5 (range, 27.25–43), and their mean Threshold, Discrimination, and Identification scores were 12.5, 11.4, and 11.6, respectively. Twenty-four (70.6%) of the 34 patients had olfactory dysfunction (hyposmic/anosmic) according to the Korean Version of the Snif-

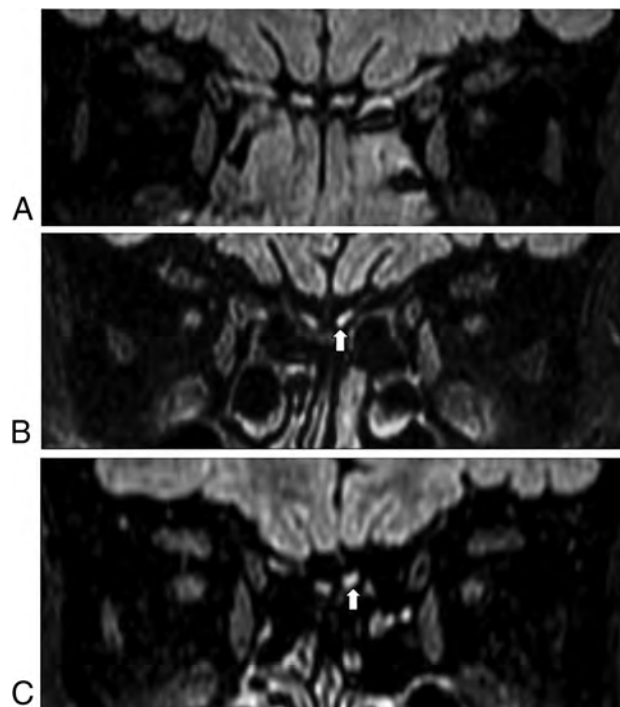


FIG 2. Neuropathy of the olfactory bulbs. Homogeneous signal intensity in both olfactory bulbs is noted in a patient without neuropathy (A); however, focal (B) or diffuse (C) hyperintense areas in left olfactory bulb (arrow) compared with the white matter of the frontal lobe are visible on FLAIR images in patients with neuropathy.

Table 1: Korean Version of the Sniffin' Sticks II test results according to the etiology of olfactory deficits^a

Etiology	Normosmia (n = 10)	Hyposmia/Anosmia (n = 24)	P Value ^b
Chronic rhinosinusitis	4 (40.0)	11 (45.8)	.683
Postviral URI	3 (30.0)	4 (16.7)	
Trauma	0 (0)	2 (8.3)	
Idiopathic	3 (30.0)	7 (29.2)	

^a Data are the number of patients (%).

^b χ^2 test.

fin' Sticks II test; the mean total Threshold-Discrimination-Identification score for these 24 patients was 15.3 (range, 6–27), and their mean Threshold, Discrimination, and Identification scores were 3.1, 6.7, and 5.5, respectively. No differences in olfactory dysfunction were identified among the etiologies ($P = .683$, Table 1) or among the various age groups (0–19, 20–39, 40–59, and 60–72 years; $P = .491$). The Sino-Nasal Outcome Test and QOD scores of patients with normosmia were similar to those of patients with olfactory dysfunction (Table 2).

Relationship between the Olfactory Function Test Scores and OB Atrophy and Neuropathy

Atrophy of the OB on MR images was more frequently identified in patients with olfactory dysfunction (17/24, 70.8%) than in patients with normosmia (1/10, 10.0%) ($P = .002$). Of the patients with atrophy, unilateral atrophy was found in 1 patient with normosmia and 4 patients with olfactory dysfunction, and bilateral atrophy was found in 13 patients with olfactory dysfunction. The mean Threshold, Discrimination, Identification, and total

Table 2: Comparison of subjective symptom severity between patients with normosmia and those with hyposmia/anosmia^a

	Normosmia (n = 10)	Hyposmia/ Anosmia (n = 24)	P Value ^b
SNOT-22 score (mean ± SD)	13.6 ± 9.5	22.83 ± 16.6	.160
QOD (mean ± SD)			
LQ raw score	22.3 ± 10.9	21.4 ± 11.6	.867
LQ (%)	39.1 ± 19.1	37.6 ± 20.3	.867
Sincerity raw score	5.8 ± 2.3	6.4 ± 2.6	.589
Sincerity (%)	32.2 ± 12.8	35.4 ± 14.2	.589
Parosmia raw score	2.3 ± 1.9	2.9 ± 3.3	.838
Parosmia (%)	19.2 ± 15.7	24.7 ± 27.2	.838
Visual analog scales	19.7 ± 10.7	23.8 ± 16.1	.589

Note:—SNOT-22 indicates Sino-Nasal Outcome Test-22.

^a LQ = LQ raw score/0.57 (%); Sincerity = Sincerity raw score/0.18 (%); Parosmia score = Parosmia raw score/0.12 (%).

^b Mann-Whitney U test.

Table 3: Comparison of Korean Version of the Sniffin' Sticks II test scores according to the presence/absence of olfactory bulb atrophy

	Normal	Atrophy	P Value ^a
Threshold	8.1 ± 5.9	3.8 ± 5.1	.030
Discrimination	9.6 ± 2.8	6.7 ± 2.9	.006
Identification	9.1 ± 3.9	5.7 ± 2.5	.006
Total Threshold-Discrimination-Identification score	26.9 ± 11.9	16.2 ± 8.8	.008

^a Mann-Whitney U tests.

Table 4: Atrophy and neuropathy of the olfactory bulb on MR images according to the Korean Version of the Sniffin' Sticks II test results and etiology^a

Etiology	Normosmia	Hyposmia/ Anosmia	P Value ^b
Chronic rhinosinusitis (n = 15)			
Atrophy	0/4 (0)	7/11 (63.6)	.077
Neuropathy	1/4 (25.5)	3/11 (27.3)	1.000
Postviral URI (n = 7)			
Atrophy	1/3 (33.3)	3/4 (75.0)	.486
Neuropathy	2/3 (66.7)	1/4 (25.0)	.486
Trauma (n = 2)			
Atrophy	0/0 (0)	1/2 (50.0)	NA
Neuropathy	0/0 (0)	0/2 (0)	NA
Idiopathic (n = 10)			
Atrophy	0/3 (0)	6/7 (85.7)	.033
Neuropathy	1/3 (33.3)	1/7 (14.3)	1.000

Note:—NA indicates not available.

^a Data are number of patients (%).

^b Fisher exact test.

Threshold-Discrimination-Identification scores of patients with OB atrophy were significantly lower than those of patients without OB atrophy ($P < .05$ for all comparisons, Table 3). When classified according to etiology, OB atrophy was observed in 6 (85.7%) of the 7 patients with idiopathic olfactory dysfunction, whereas OB atrophy was not observed in 3 patients who believed they had olfactory loss but were normosmic according to the olfactory function tests ($P = .033$, Table 4). However, regarding the other etiologies, no significant differences in OB atrophy were noted between patients with normosmia and those with olfactory dysfunction ($P > .05$ for all comparisons). Furthermore, the presence or absence of OB atrophy had no correlation with the age ($P = .743$) or olfactory deficit durations ($P = .652$).

Neuropathy of the OB was detected in 4 (40.0%) of the 10 patients with normosmia and in 5 (20.8%) of the 24 patients with

olfactory dysfunction ($P = .395$). No difference in the presence of OB neuropathy was identified between patients with normosmia and those with olfactory dysfunction when grouped according to etiology ($P > .05$ for all comparisons).

Brain parenchymal lesions were detected in 3 (12.5%) of the 24 patients who had olfactory dysfunction according to the Korean Version of the Sniffin' Sticks II test and OB atrophy on MR images. Focal encephalomalacic changes in the rectus gyrus or frontal lobe and sequelae from hemorrhagic contusions in the bilateral orbitofrontal base may affect olfactory dysfunction.

DISCUSSION

In the present study, we evaluated whether visual analyses of OB atrophy on MR images could serve as an easy and reliable method for diagnosing olfactory dysfunction. Here, we found that ~30% of patients with subjective olfactory loss had normal olfactory function test results and that the subjective severity of olfactory loss in these patients, as represented by the Sino-Nasal Outcome Test and QOD, was similar to that of patients who had hyposmia/anosmia according to the Sniffin' Sticks test. Additionally, the number of patients classified as normosmic according to the olfactory function tests was not different among the various etiology and age groups. These results support additional objective diagnostic methods being required to confirm olfactory loss. OB atrophy on MR images using visual analysis was more frequent in patients with hyposmia/anosmia compared with those with normosmia. Therefore, we suggest that MR imaging evaluations of OB atrophy could be used to objectively diagnose olfactory dysfunction in patients with subjective olfactory loss.

Many previous studies have used MR imaging to assess the OB in patients with olfactory loss because the OB plays an important role in processing olfactory information that is sent between the olfactory receptor neurons and the brain. Several studies have shown that patients with posttraumatic and postviral olfactory dysfunction as well as idiopathic olfactory loss have reduced OB sizes on MR images compared with healthy controls.¹⁹⁻²¹ The depth of the olfactory sulcus, which is located between the gyrus rectus and medial orbital gyrus in the frontal lobe and positioned over the OB and olfactory tract, is considered another relevant parameter for evaluating the olfactory pathway with MR imaging. However, the depth of the olfactory sulcus is not significantly different in patients with idiopathic olfactory loss and those with Parkinson disease compared with healthy controls.^{7,20} Thus, evaluating the OB rather than the olfactory sulcus may be valuable in patients with olfactory dysfunction except for those with congenital anosmia. Unfortunately, the OB volume is not routinely measured in patients with olfactory dysfunction because it requires complex assessment techniques of volumetry; therefore, we hypothesized that visual analyses of OB atrophy or neuropathy on MR images can be practically used as an objective assessment tool in clinical settings for patients with olfactory dysfunction.^{22,23} Our results demonstrated that indeed, OB atrophy was significantly related to decreased olfactory function.

Thin-section coronal T2WI (<2 mm) and 3D images have been highly recommended for the precise anatomic evaluation of the OB and olfactory tract owing to their small sizes.¹⁰ In addition to coronal T2WI at 1.5 mm, we performed high-resolution 3D-

FLAIR and 3D-T2 VISTA with a 0.6-mm section thickness. Using these techniques, we identified OB atrophy in 70.8% of patients with hyposmia/anosmia, as assessed with olfactory function tests, and atrophy was significantly more common in patients with dysfunction than it was in those with normosmia (10.0%). Furthermore, the olfactory function test scores of patients with OB atrophy were significantly lower than those of patients without OB atrophy. Moreover, the detection rate of OB atrophy was not different among the various age and olfactory deficit duration groups. These results suggested that visual analysis of OB atrophy is a useful diagnostic method for patients with subjective olfactory loss regardless of their age and olfactory deficit duration.

Evaluating OB atrophy with MR imaging in patients with idiopathic olfactory loss may help determine whether there is olfactory loss, even though the significance of the absence of atrophy on MR imaging in a patient with subjective symptoms was not identified. Our results showing that there was no difference in OB atrophy between normosmia and hyposmia/anosmia according to the Sniffin' Sticks II test in patients with chronic rhinosinusitis seem to reflect their olfactory deficits possibly being conductive. Because only a few patients had postviral URI and posttraumatic olfactory loss in the present study, it may be difficult to assess the correlation between OB atrophy and the results of olfactory function tests.

The significance of neuropathy (neuromalacic hyperintense changes) of the OB on 3D-FLAIR images has not yet been established in patients with olfactory loss. In our study, neuropathy of the OB was detected not only in patients with hyposmia/anosmia, as assessed with olfactory function tests, but also in patients with normosmia. This result may be because our patients had been experiencing olfactory deficits for >2 months. Further studies are required to determine the prognostic value of neuropathy according to the duration of olfactory loss.

A substantial number of brain lesions that may affect olfactory dysfunction were found in 12.5% of our patients who had hyposmia/anosmia according to the Korean Version of the Sniffin' Sticks II test and OB atrophy on MR images. Two patients with posttraumatic olfactory deficits had focal encephalomalacic changes in the rectus gyrus and frontal lobe, respectively. One patient with idiopathic olfactory loss, though unusual, showed sequelae from a hemorrhagic contusion in the bilateral orbito-frontal base without a history of trauma. This MR imaging finding may have helped this patient receive appropriate counseling because the patient did not link the occurrence of olfactory loss with a significant event.

This study has several limitations. First, our sample size was relatively small, and the data were retrospectively reviewed. Decreased statistical power caused by the sample size might affect the ability to declare statistical significance in our results, such as the relation between the olfactory function tests and the Sino-Nasal Outcome Test-22 (which demonstrated relatively large score differences) or OB atrophy subclassified by etiology (a small number of patients for each subgroup). Further prospective study with a larger population is needed. Second, we could not assess the follow-up data after treatment in patients with OB atrophy or neuropathy due to short-term follow-up. Further studies that include patients with variable deficit-onset times, including sudden olfac-

tory deficits (<4 weeks) and chronic hyposmia/anosmia, should be performed to evaluate the prognostic value of OB atrophy or neuropathy. Nevertheless, our study demonstrates that visual analyses of OB atrophy using MR imaging are closely related to olfactory function.

CONCLUSIONS

The results of the present study show that the detection rate of OB atrophy on MR images was significantly higher in patients with olfactory dysfunction than it was patients with normosmia. Therefore, evaluating OB atrophy with MR imaging may serve as a readily available objective diagnostic method for confirming olfactory dysfunction in patients with subjective olfactory loss.

ACKNOWLEDGMENTS

We thank professor Johannes Frasnelli for providing the Questionnaire of Olfactory Disorders.

REFERENCES

1. Croy I, Nordin S, Hummel T. **Olfactory disorders and quality of life: an updated review.** *Chem Senses* 2014;39:185–94 CrossRef Medline
2. Frasnelli J, Hummel T. **Olfactory dysfunction and daily life.** *Eur Arch Otorhinolaryngol* 2005;262:231–35 CrossRef Medline
3. Croy I, Buschhüter D, Seo HS, et al. **Individual significance of olfaction: development of a questionnaire.** *Eur Arch Otorhinolaryngol* 2010;267:67–71 CrossRef Medline
4. Neuland C, Bitter T, Marschner H, et al. **Health-related and specific olfaction-related quality of life in patients with chronic functional anosmia or severe hyposmia.** *Laryngoscope* 2011;121:867–72 CrossRef Medline
5. Rombaux P, Huart C, Deggouj N, et al. **Prognostic value of olfactory bulb volume measurement for recovery in postinfectious and post-traumatic olfactory loss.** *Otolaryngol Head Neck Surg* 2012;147:1136–41 CrossRef Medline
6. Haehner A, Rodewald A, Gerber JC, et al. **Correlation of olfactory function with changes in the volume of the human olfactory bulb.** *Arch Otolaryngol Head Neck Surg* 2008;134:621–24 CrossRef Medline
7. Wang J, You H, Liu JF, et al. **Association of olfactory bulb volume and olfactory sulcus depth with olfactory function in patients with Parkinson disease.** *AJNR Am J Neuroradiol* 2011;32:677–81 CrossRef Medline
8. Buschhüter D, Smitka M, Puschmann S, et al. **Correlation between olfactory bulb volume and olfactory function.** *Neuroimage* 2008;42:498–502 CrossRef Medline
9. Rombaux P, Duprez T, Hummel T. **Olfactory bulb volume in the clinical assessment of olfactory dysfunction.** *Rhinology* 2009;47:3–9 Medline
10. Duprez TP, Rombaux P. **Imaging the olfactory tract (cranial nerve #1).** *Eur J Radiol* 2010;74:288–98 CrossRef Medline
11. Huart C, Meusel T, Gerber J, et al. **The depth of the olfactory sulcus is an indicator of congenital anosmia.** *AJNR Am J Neuroradiol* 2011;32:1911–14 CrossRef Medline
12. Fokkens WJ, Lund VJ, Mullol J, et al. **European Position Paper on Rhinosinusitis and Nasal Polyps 2012.** *Rhinol Suppl* 2012;23:1–298 Medline
13. Hoekman PK, Houlton JJ, Seiden AM. **The utility of magnetic resonance imaging in the diagnostic evaluation of idiopathic olfactory loss.** *Laryngoscope* 2014;124:365–68 CrossRef Medline
14. Shin DH, Ahn SH, Yang Y, et al. **The effect of sleep disordered breathing on olfactory functions: analysis by Apnea-Hypopnea Index.** *Clin Exp Otorhinolaryngol* 2017;10:71–76 CrossRef Medline
15. Kennedy JL, Hubbard MA, Huyett P, et al. **Sino-Nasal Outcome Test (SNOT-22): a predictor of postsurgical improvement in patients**

- with chronic sinusitis. *Ann Allergy Asthma Immunol* 2013;111:246–51.e2 CrossRef Medline
16. Yang D, Wang J, Ni D, et al. **Reliability and validity of the Chinese version of the Questionnaire of Olfactory Disorders (QOD) when used with patients having olfactory dysfunction.** *Eur Arch Otorhinolaryngol* 2016;273:3255–61 CrossRef Medline
 17. Schneider JF, Floemer F. **Maturation of the olfactory bulbs: MR imaging findings.** *AJNR Am J Neuroradiol* 2009;30:1149–52 CrossRef Medline
 18. Booth TN, Rollins NK. **Spectrum of clinical and associated MR imaging findings in children with olfactory anomalies.** *AJNR Am J Neuroradiol* 2016;37:1541–48 CrossRef Medline
 19. Mueller A, Rodewald A, Reden J, et al. **Reduced olfactory bulb volume in post-traumatic and post-infectious olfactory dysfunction.** *Neuroreport* 2005;16:475–78 CrossRef Medline
 20. Rombaux P, Potier H, Markessis E, et al. **Olfactory bulb volume and depth of olfactory sulcus in patients with idiopathic olfactory loss.** *Eur Arch Otorhinolaryngol* 2010;267:1551–56 CrossRef Medline
 21. Rombaux P, Wetz H, Mouraux A, et al. **Olfactory function assessed with orthonasal and retronasal testing, olfactory bulb volume, and chemosensory event-related potentials.** *Arch Otolaryngol Head Neck Surg* 2006;132:1346–51 CrossRef Medline
 22. Bresciani L, Rossi R, Testa C, et al. **Visual assessment of medial temporal atrophy on MR films in Alzheimer's disease: comparison with volumetry.** *Aging Clin Exp Res* 2005;17:8–13 CrossRef Medline
 23. Gouw AA, van der Flier WM, van Straaten EC, et al. **Reliability and sensitivity of visual scales versus volumetry for evaluating white matter hyperintensity progression.** *Cerebrovasc Dis* 2008;25:247–53 CrossRef Medline

Intravoxel Incoherent Motion MR Imaging in the Differentiation of Benign and Malignant Sinonasal Lesions: Comparison with Conventional Diffusion-Weighted MR Imaging

Z. Xiao, Z. Tang, J. Qiang, S. Wang, W. Qian, Y. Zhong, R. Wang, J. Wang, L. Wu, W. Tang, and Z. Zhang



ABSTRACT

BACKGROUND AND PURPOSE: Intravoxel incoherent motion is a promising method for the differentiation of sinonasal lesions. This study aimed to evaluate the value of intravoxel incoherent motion in the differentiation of benign and malignant sinonasal lesions and to compare the diagnostic performance of intravoxel incoherent motion with that of conventional DWI.

MATERIALS AND METHODS: One hundred thirty-one patients with histologically proved solid sinonasal lesions (56 benign and 75 malignant) who underwent conventional DWI and intravoxel incoherent motion were recruited in this study. The diffusion coefficient (D), pseudodiffusion coefficient (D^*), and perfusion fraction (f) values derived from intravoxel incoherent motion and ADC values derived from conventional DWI were measured and compared between the 2 groups using the Student t test. Receiver operating characteristic curve analysis, logistic regression analysis, and 10-fold cross-validation were performed to evaluate the diagnostic performance of single-parametric and multiparametric models.

RESULTS: The mean ADC and D values were significantly lower in malignant sinonasal lesions than in benign sinonasal lesions (both $P < .001$). The mean f value was higher in malignant lesions than in benign lesions ($P = .003$). Multiparametric models can significantly improve the cross-validated areas under the curve for the differentiation of sinonasal lesions compared with single-parametric models (all corrected $P < .05$ except the D value). The model of $D + f$ provided a better diagnostic performance than the ADC value (corrected $P < .001$).

CONCLUSIONS: Intravoxel incoherent motion appears to be a more effective MR imaging technique than conventional DWI in the differentiation of benign and malignant sinonasal lesions.

ABBREVIATIONS: AUC = area under the curve; D = diffusion coefficient; D^* = pseudodiffusion coefficient; f = perfusion fraction; IVIM = intravoxel incoherent motion; ROC = receiver operating characteristic.

The sinonasal area may contain a wide spectrum of benign and malignant tumors and tumorlike lesions of epithelial, mesenchymal, neural/neuroectodermal, or hematopoietic or-

igins,¹ composing approximately 3% of all head and neck tumors.²⁻⁴ The clinical presentations of sinonasal lesions are often nonspecific.⁵ Patients with malignant sinonasal tumors often have an overall poor prognosis and generally require radiation therapy and chemotherapy as well as surgical resection,⁶ whereas patients with benign lesions, such as polyps, often undergo complete surgical resection or clinical follow-up without surgery.⁷ Thus, the differentiation of benign and malignant sinonasal lesions is of great importance for therapeutic decisions and prognosis. Cross-sectional imaging techniques, such as CT and MR imaging, play an important role in the differentiation of sinonasal lesions. Nevertheless, the morphologic imaging features of benign and malignant sinonasal lesions are often nonspecific and overlap.^{4,8,9}

Conventional diffusion-weighted MR imaging with the measurement of apparent diffusion coefficient values may aid in the discrimination of malignant and benign lesions in the head and neck and the sinonasal area.⁹⁻¹² However, some overlap of ADC values was also observed.^{10,13-15} It has been docu-

Received August 17, 2017; accepted after revision November 14.

From the Departments of Radiology (Z.X., Z.T., W.Q., R.W.), Pathology (S.W.), Radiotherapy (J.W.), and Otolaryngology (L.W.), Eye & ENT Hospital of Shanghai Medical School, Fudan University, Shanghai, P. R. China; Department of Radiology (J.Q., Y.Z.), Jinshan Hospital of Shanghai Medical School, Fudan University, Shanghai, P. R. China; and Siemens Healthcare Ltd (W.T., Z.Z.), Shanghai, P. R. China.

Zebin Xiao, Zuohua Tang, and Jinwei Qiang contributed equally to this study.

This work was supported by the Grant of Science and Technology Commission of Shanghai Municipality (No. 17411962100; 14411962000) and Shanghai Municipal Commission of Health and Family Planning (Grant No. ZK2015A05).

Please address correspondence to Zuohua Tang, MD, PhD, Department of Radiology, Eye & ENT Hospital of Shanghai Medical School, Fudan University, 83 Fenyang Rd, Shanghai, 200031, P. R. China; e-mail: tzh518sunny@163.com; Shuyi Wang, MD, Department of Pathology, Eye & ENT Hospital of Shanghai Medical School, Fudan University, 83 Fenyang Rd, Shanghai, 200031, P. R. China; e-mail: wangshuyi@eent.shmu.edu.cn

Indicates open access to non-subscribers at www.ajnr.org

<http://dx.doi.org/10.3174/ajnr.A5532>

mented that microvascular flow through the complex capillary network generates a “pseudodiffusion” effect known as intravoxel incoherent motion (IVIM).^{13,14} According to IVIM analysis, both tissue diffusivity and microcapillary perfusion can be quantified separately by fitting the MR signal acquired at different b-values to a biexponential model.¹⁵ Consequently, 3 parameters can be obtained from IVIM, including D , D^* , and f , which represent the pure diffusion coefficient, pseudodiffusion coefficient, and perfusion fraction, respectively. Recently, IVIM MR imaging has emerged as a potential new method for the differentiation of head and neck tumors and the prediction of tumor responses to treatment.¹⁶⁻²²

However, to the best of our knowledge, no studies in differentiating benign and malignant sinonasal lesions using IVIM have been performed. In this study, we aimed to investigate IVIM as a tool for distinguishing benign and malignant sinonasal lesions and to compare the differential diagnostic performance of IVIM with conventional DWI in sinonasal lesions.

MATERIALS AND METHODS

Study Population

The institutional review board of Eye & ENT Hospital of Fudan University approved this retrospective study, and the requirement for patient informed consent was waived due to the retrospective nature of this study. One hundred thirty-one consecutive patients with sinonasal solid masses were recruited from May 2015 to March 2017. All masses were confirmed by surgery/biopsy and histopathology. Patients who previously had a history of treatment or recurrence were excluded.

MR Imaging Techniques

MR imaging examinations were performed on a 3T MR imaging scanner (Magnetom Verio; Siemens, Erlangen, Germany) using a 12-channel head coil. Conventional MR images were obtained; then DWI was performed using a single-shot echo-planar imaging sequence with a bipolar scheme along all 3 orthogonal axes to obtain isotropic DWI. Imaging parameters were as follows: TR/TE = 5200/83 ms, number of averages = 2, acquisition matrix = 120 × 120, FOV = 230 mm, slices = 5, slice thickness = 5 mm, parallel imaging acceleration factor = 2. Eleven different b factors ranging from 0 to 1000 s/mm² were used ($b = 0, 50, 100, 150, 200, 250, 300, 350, 400, 800, \text{ and } 1000 \text{ s/mm}^2$). The total scan time was 6 minutes 39 seconds.

Image Processing and Analysis

The conventional monoexponential DWI model is mathematically expressed by the equation $S_b/S_0 = \exp(-b \times \text{ADC})$, where S_b and S_0 are the signal intensity acquired with the diffusion gradient factors of b and 0, respectively. In this study, MR signal intensities of $b=0$ and 1000 s/mm² were used to calculate the ADC.²³ DWI processing was performed on an off-line workstation (Verio; Siemens). The IVIM model is mathematically expressed with the following equation^{13,14}:

$$1) \quad S_b/S_0 = (1 - f) \times \exp(-bD) + f \times \exp[-b(D+D^*)],$$

where S_b and S_0 are the signal intensities in the diffusion gradient factors of b and 0, respectively,^{17,18} f is the perfusion fraction

related to microcirculation, D is the diffusion coefficient representing pure molecular diffusion (the slow component of diffusion), and D^* is the pseudodiffusion coefficient representing incoherent microcirculation within the voxel (perfusion-related diffusion or the fast component of diffusion). Three parameters, D , D^* , and f , can be derived from IVIM by fitting the biexponential curve using a nonlinear least-squares technique. Because D^* is notably greater than D , its influence on signal decay can be neglected when the b-value is $>200 \text{ s/mm}^2$. In that case, Equation 1 can be simplified and the estimation of D can be obtained using only b-values of $>200 \text{ s/mm}^2$, with a simple linear fitting Equation 2:

$$2) \quad S_b/S_0 = \exp(-bD).$$

With the D value determined using Equation 2, f and D^* values can be calculated using a nonlinear regression algorithm based on Equation 1. IVIM processing was conducted by using Matlab (Version 7.9; MathWorks, Natick, Massachusetts).

The ADC value derived from conventional DWI, along with D , D^* , and f values that were derived from IVIM, was measured independently by 2 radiologists (readers 1 and 2 with 10 and 7 years of experience in head and neck imaging, respectively) who were blinded to clinical and histopathologic data. The polygonal ROIs (mean area, $52.93 \pm 37.82 \text{ mm}^2$; range, 26–731 mm²) were drawn along the outer margin of the lesion on the largest slice of the corresponding parameter maps. Obvious necrotic, cystic, calcification, or hemorrhagic regions were avoided to focus on the solid portion of the tumor as much as possible by referring to T2-weighted and contrast-enhanced T1-weighted images. The measurements made by readers 1 and 2 were used to evaluate the interreader reproducibility. To evaluate intrareader reproducibility, these measurements were repeated by reader 1, with a minimum washout period of at least 1 month. The average of the 3 measurement results of readers 1 and 2 was used for the statistical analysis.

Statistical Analysis

All ADC and IVIM parameters of sinonasal lesions are presented as mean \pm SD. The inter- and intrareader reproducibility for ADC and IVIM parameter measurements were evaluated using the intraclass correlation coefficient with 95% confidence intervals. An intraclass correlation coefficient of >0.75 was considered indicative of good agreement.

A simple linear regression analysis was performed to calculate the Pearson correlation coefficient between the patients' ages and conventional DWI and IVIM parameters of the individual lesions. A correlation coefficient (r) of 0.75–1.00 indicated very good-to-excellent correlation; 0.50–0.74, moderate-to-good correlation; 0.25–0.49, fair correlation; and ≤ 0.24 , little or no correlation.

The mean ADC, D , D^* , and f values were compared between benign and malignant sinonasal lesions using the Student t test. The receiver operating characteristic (ROC) analysis curves with 10-fold cross-validation were obtained to determine the optimal cutoff value for significant parameters for differentiating benign and malignant sinonasal lesions. The multivariate logistic regression models, including 2 or 3 of these significant parameters, were

Table 1: Demographics and histology of benign and malignant sinonasal lesions^a

Parameters	Benign Lesions (n = 56)	Malignant Lesions (n = 75)
Mean age (yr)	43.86 ± 14.11	52.27 ± 15.21
Sex (female/male)	24:32	24:51
Histologic subtypes	Inflammatory polyps (28) Inverted papilloma (14) Fibroangioma (5) Spindle cell tumor (4) Schwannoma (2) Ossifying fibroma (2) Enamel cell tumor (1)	Squamous cell carcinoma (23) Olfactory neuroblastoma (13) Malignant melanoma (12) Rhabdomyosarcoma (9) Lymphoma (6) Adenoid cystic carcinoma (5) Undifferentiated carcinoma (2) Osteosarcoma (2) Neuroendocrine carcinoma (2) Malignant fibrohistiocytoma (1)

^aData in parentheses indicate the number of corresponding patients. All inverted papillomas did not have the potential for association with/conversion to squamous cell carcinoma, proven by histopathology.

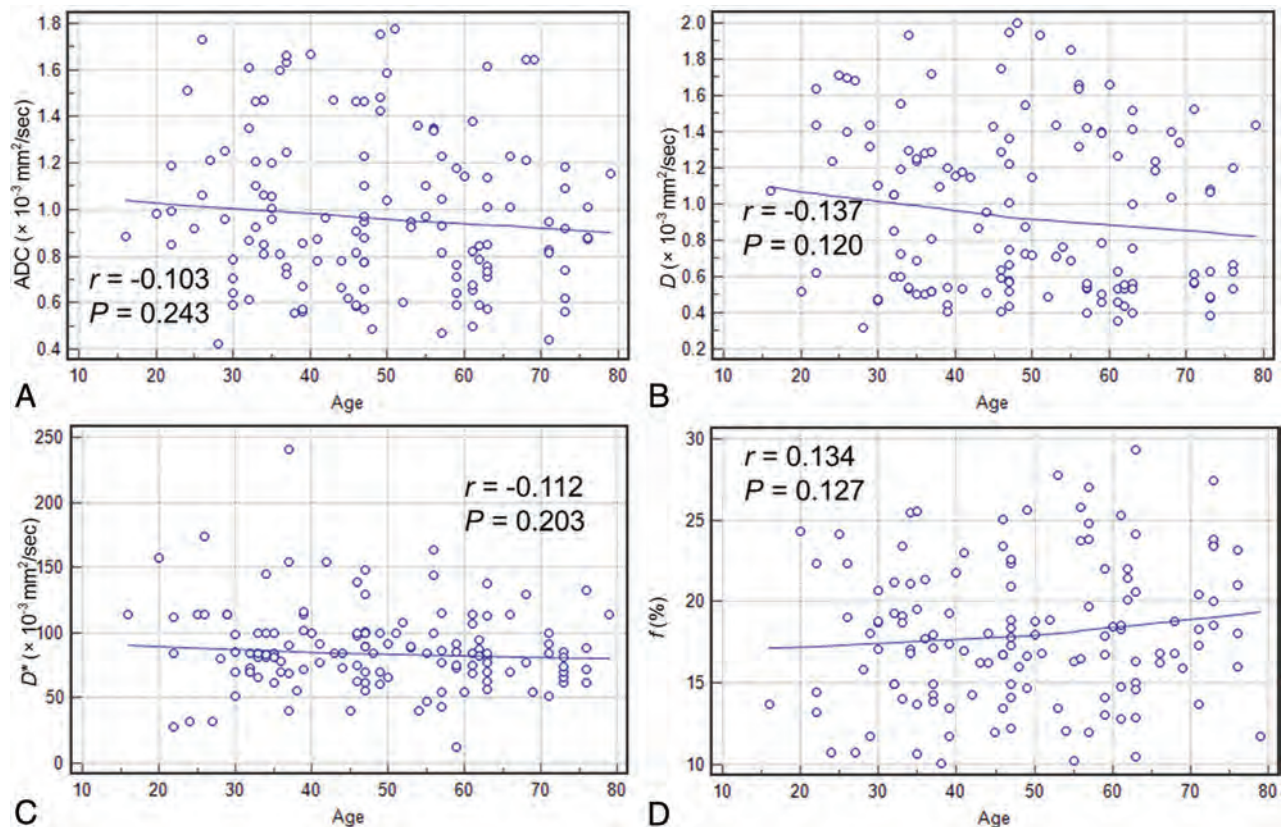


FIG 1. Scatterplots depicting the correlations between the patients' ages and ADC values (A), the patients' ages and *D* values (B), the patients' ages and *D** values (C), and the patients' ages and *f* values (D) for all sinonasal lesions.

generated. For each logistic regression model, cross-validation was performed with a 10-fold procedure. The optimal cutoff value was determined as the point in the upper left-hand corner that maximized the sum of the sensitivity and specificity. The area under the curve (AUC), sensitivity, specificity, accuracy, positive predictive value, and negative predictive value of the single and combined imaging parameters for differential diagnosis were calculated. A Bonferroni correction was used to correct for multiple comparisons.

Statistical analyses were performed in Excel 2013 (Microsoft, Redmond, Washington), MedCalc statistical software (Version 15.2.2; MedCalc Software, Mariakerke, Belgium), and R, Version R 2.15.3 (R Project for Statistical Computing,

<http://www.r-project.org>).²⁴ *P* values < .05 were considered significant.

RESULTS

A total of 131 patients, including 56 patients with benign sinonasal lesions and 75 with malignant sinonasal lesions, were enrolled in this study. Of these patients, 48 were female and 83 were male. The age of patients ranged from 16 to 79 years, with a mean age of 48.67 years. The demographics and histology of benign and malignant sinonasal lesions are summarized in Table 1. Poor correlations were found between the patients' ages and conventional DWI and IVIM parameters, with *r* ranging from -0.103 to 0.137 (all *P* > .05, Fig 1)

Table 2: Inter- and intrareader reproducibility for ADC, *D*, *D*^{*}, and *f* measurements^a

Parameters	ICC	
	Interreader	Intrareader
ADC ($\times 10^{-3}$ mm ² /s)	0.961 (0.913–0.977)	0.954 (0.871–0.980)
<i>D</i> ($\times 10^{-3}$ mm ² /s)	0.942 (0.860–0.986)	0.936 (0.884–0.975)
<i>D</i> [*] ($\times 10^{-3}$ mm ² /s)	0.840 (0.762–0.931)	0.848 (0.766–0.909)
<i>f</i> (%)	0.908 (0.819–0.965)	0.922 (0.835–0.964)

Note:—ICC indicates intraclass correlation coefficient.

^aData in parentheses are 95% confidence intervals.

As shown in Table 2, excellent inter- and intrareader agreement were achieved in the measurement of ADC and IVIM parameters. The mean ADC, *D*, *D*^{*}, and *f* values of benign and malignant sinonasal lesions are shown in Fig 2 and Table 3. The mean ADC and *D* values were significantly lower in malignant sinonasal lesions than in benign sinonasal lesions (both $P < .001$). The mean *f* value of malignant sinonasal masses was higher than that of benign sinonasal masses ($P = .001$). There was no significant difference in the mean *D*^{*} value between the 2 groups ($P > .05$) (Figs 3 and 4).

The diagnostic performance of ADC, *D*, and *f* values for differentiation of benign and malignant sinonasal lesions is demonstrated in Table 4 and Fig 5. From the ROC analysis with 10-fold cross-validation, the largest cross-validated AUC was obtained for *D* compared with ADC and *f* (AUC for *D* versus ADC = 0.899 versus 0.735, corrected $P = .009$; AUC for *D* versus *f* = 0.899 versus 0.656, corrected $P < .0001$; AUC for ADC versus *f* = 0.735 versus 0.656, corrected $P = .08$) in the discrimination of benign and malignant sinonasal lesions. No significant differences were found in the cross-validated AUC among different multiparametric models, including ADC+*D*, ADC+*f*, *D*+*f*, ADC+*D*+*f* (all corrected $P > .05$), and the highest AUC was obtained for the model of ADC+*D*+*f*, followed by the models of *D*+*f*, ADC+*D*, and ADC+*f*. Compared with single-parametric models (except *D*), multiparametric models can significantly improve the cross-validated AUCs for the differentiation of benign and malignant sinonasal lesions (all corrected $P < .05$). Additionally, the combination of *D* and *f* values derived from IVIM can provide a better diagnostic performance than the ADC value (corrected $P < .001$).

DISCUSSION

Our findings showed that quantitative analysis of conventional DWI and IVIM parameters could be helpful in discriminating benign and malignant sinonasal lesions. Additionally, compared with the ADC value derived from conventional DWI, IVIM parameters (especially the combination of *D* and *f* values) can significantly improve the diagnostic performance for differentiating solid sinonasal lesions.

The ADC value quantitating free-water molecule motion within a tissue correlates with tumor cellularity.^{15,23} In the present study, the mean ADC value of malignant sinonasal lesions was significantly lower than that of benign lesions; this finding was in accordance with the results from previous studies.^{9–12,25} Histopathologically, malignancies often exhibit high cellularity, effectively restricting the water molecule diffusion of tumors.²⁵ Moreover, the present patient cohort included 44

patients with small round blue cell tumors, including lymphoma, undifferentiated carcinoma, malignant melanoma, neuroendocrine carcinoma, olfactory neuroblastoma, rhabdomyosarcoma, and so forth. This heterogeneous group of malignant neoplasms shares common histologic characteristics, including a relatively small cell volume, deep nuclear staining, and high tumor nucleus/cytoplasm ratios, resulting in significantly low ADC values.²⁶ Hence, our study revealed that ADC could be a useful imaging parameter for the differentiation of benign and malignant sinonasal lesions. Nevertheless, ADC is derived from conventional DWI with an assumption that the water molecule diffusion is a random motion that follows Gaussian distribution and is calculated by a simple monoexponential decay fitting with 2 b-values. In fact, the measured diffusion signals in living tissues were not simply influenced by the motion of water molecules but also by the perfusion of blood microcirculation at low b-values. Therefore, ADC values obtained from conventional DWI do not exclusively correspond to molecular diffusivity.^{27,28} The IVIM model was recommended to account for molecular diffusion driven by Brownian motion and perfusion-related pseudodiffusion.

IVIM with a biexponential model is a method initially proposed by Le Bihan et al^{13,14} to quantitatively assess the microscopic translational motion that occurs in each image voxel on MR imaging and to distinguish both pure molecular diffusion and capillary perfusion with sufficiently low b-values (< 200 s/mm²). However, the value of IVIM in differentiating benign and malignant sinonasal lesions has not been investigated previously, to our knowledge. Until now, 2 main calculation methods, including a conventional method using a nonlinear, biexponential fitting and a newly simplified method using a linear fitting of a logarithmic transformation, have been applied to produce the final IVIM results.^{29,30}

Recently, Sasaki et al³⁰ reported that the simplified technique could be an alternative to the conventional method in the determination of IVIM parameters for head and neck tumors. Nonetheless, the conventional calculation method could better predict lesion perfusion and diffusion characteristics with fewer artifacts and higher signal-to-noise ratios compared with the simplified technique.³⁰ In addition, the conventional calculation technique using the 2-step fitting with *D* value estimation first was found to best correlate with dynamic contrast-enhanced MR imaging.²⁹ Thus, the conventional method with 2-step fitting was adopted to calculate the IVIM parameters for the differentiation of sinonasal lesions. In this preliminary study, we found that IVIM was a more effective tool than conventional DWI in the differentiation of benign and malignant sinonasal lesions. Additionally, the reproducibility of *D*, *D*^{*}, and *f* values derived from IVIM was excellent; this finding was consistent with that of Jia et al,¹⁸ suggesting that IVIM could also be a reliable method for discerning benign from malignant lesions in the sinonasal area.

Our study showed that the *D* value was significantly lower in malignant sinonasal tumors than in benign lesions. Sumi et al²² reported that the *D* values of malignant salivary gland tumors were significantly different from those of benign tumors. Similar findings were also reported in other malignan-

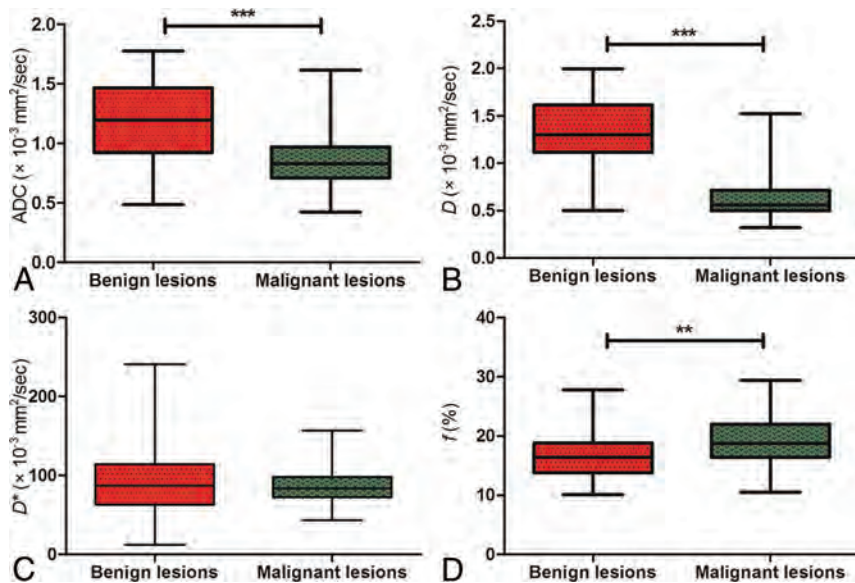


FIG 2. Comparisons of the mean ADC (A), D (B), D^* (C), and f (D) values between benign and malignant sinonasal lesions using the Student t test. Triple asterisks indicate $P < .001$; double asterisks, $P < .01$.

Table 3: Comparisons of ADC, D , D^* , and f values between benign and malignant sinonasal lesions^a

Parameters	Benign Lesions (n = 56)	Malignant Lesions (n = 75)	P Value
ADC ($\times 10^{-3}$ mm ² /s)	1.163 \pm 0.354	0.862 \pm 0.258	<.001
D ($\times 10^{-3}$ mm ² /s)	1.322 \pm 0.347	0.677 \pm 0.299	<.001
D^* ($\times 10^{-3}$ mm ² /s)	90.470 \pm 40.756	86.445 \pm 22.865	.474
f (%)	16.656 \pm 4.274	19.211 \pm 4.066	.001

^aExcept for the P values, data are expressed as the mean \pm SD.

cies in other body organs, such as the breast³¹ and prostate.³² These findings may be explained by hypercellularity in malignant lesions that reduced the microstructure diffusion space of water molecules, resulting in a decrease in the D value. Hence, the D value can be highly valuable for differentiating benign and malignant sinonasal lesions. D^* and f are perfusion-related parameters derived from IVIM, which are significantly correlated with microvessel density, a surrogate marker of angiogenesis.³³ The D^* value is determined as the signal intensity ratios of blood capillaries and is considered linked to perfusion, which, in turn, may be dependent on tumor microvessel density.¹³ Additionally, D^* was reported to be proportional to the mean capillary segment length and average blood velocity; thus, it is reflective of tumor vascularity.¹³ In our present study, we found no significant difference in the D^* value between benign and malignant sinonasal lesions, which was in satisfactory agreement with previous studies.^{34,35} However, our D^* estimation in sinonasal lesions was not consistent with those reported by Kim et al³⁶ for pancreatic pathologies and Sumi et al²² for salivary gland tumors, which may be due to the low signal-to-noise ratio and the relatively poor measurement reproducibility of D^* .³¹ As for the f value, it measures the fractional volume of capillary blood flowing in each voxel and has direct correlations with the extent of normal angiogenesis with intact vessels in terms of basement membrane thickness and pericyte coverage.^{37,38} Therefore, f may be an indicator of vascular permeability. In the current study, we found that the f

value was significantly higher in malignant lesions than in benign sinonasal lesions, a finding in accordance with those in previous studies on head and neck tumors.^{17,19,22,30} With the application of dynamic contrast-enhanced imaging, Xian et al³⁹ found that malignant sinonasal tumors were usually associated with high permeability and high perfusion, which was in good agreement with our results. However, some malignant sinonasal lesions, such as lymphomas, can have a low f value because of low levels of vessel density within scarce amounts of stromal tissue.¹⁷ Moreover, some benign sinonasal lesions can also be associated with a high perfusion level. For example, small vessels with ectasia are frequently observed in the Antoni B areas of schwannomas, resulting in a high f value.¹⁷

Three parameters, ADC, D , and f , were significant for differentiating benign from malignant sinonasal lesions. The ROC analysis with 10-fold cross-validation showed that the cross-validated AUC, sensitivity, specificity, and accuracy levels of the D value were significantly higher than those of the f and ADC values. As previously reported, cellularity and microcirculation influence ADC measurements in a diametrically opposite direction.⁴⁰ However, most malignant tumors had both hypercellularity (low diffusivity) and hypervascularity (high perfusion fraction). D , known as the pure molecular diffusion coefficient, can represent cellularity more precisely, can reduce the bias by avoiding microcirculation contributions,^{13,14} and, therefore, can better differentiate benign and malignant sinonasal lesions. Additionally, the combination of D and f values derived from IVIM can provide a better diagnostic performance than the ADC value, indicating that IVIM could be a more efficient method than conventional DWI for the differentiation of sinonasal lesions.

There are some limitations to our study. First, given the wide variety of histologic types and the small number of each type of benign and malignant sinonasal lesion, selection bias was inevitable, so our findings still need larger prospective studies to further validate them. Additionally, as in previous studies,^{11,12} inflammatory polyps were included in our study. These typically are not a

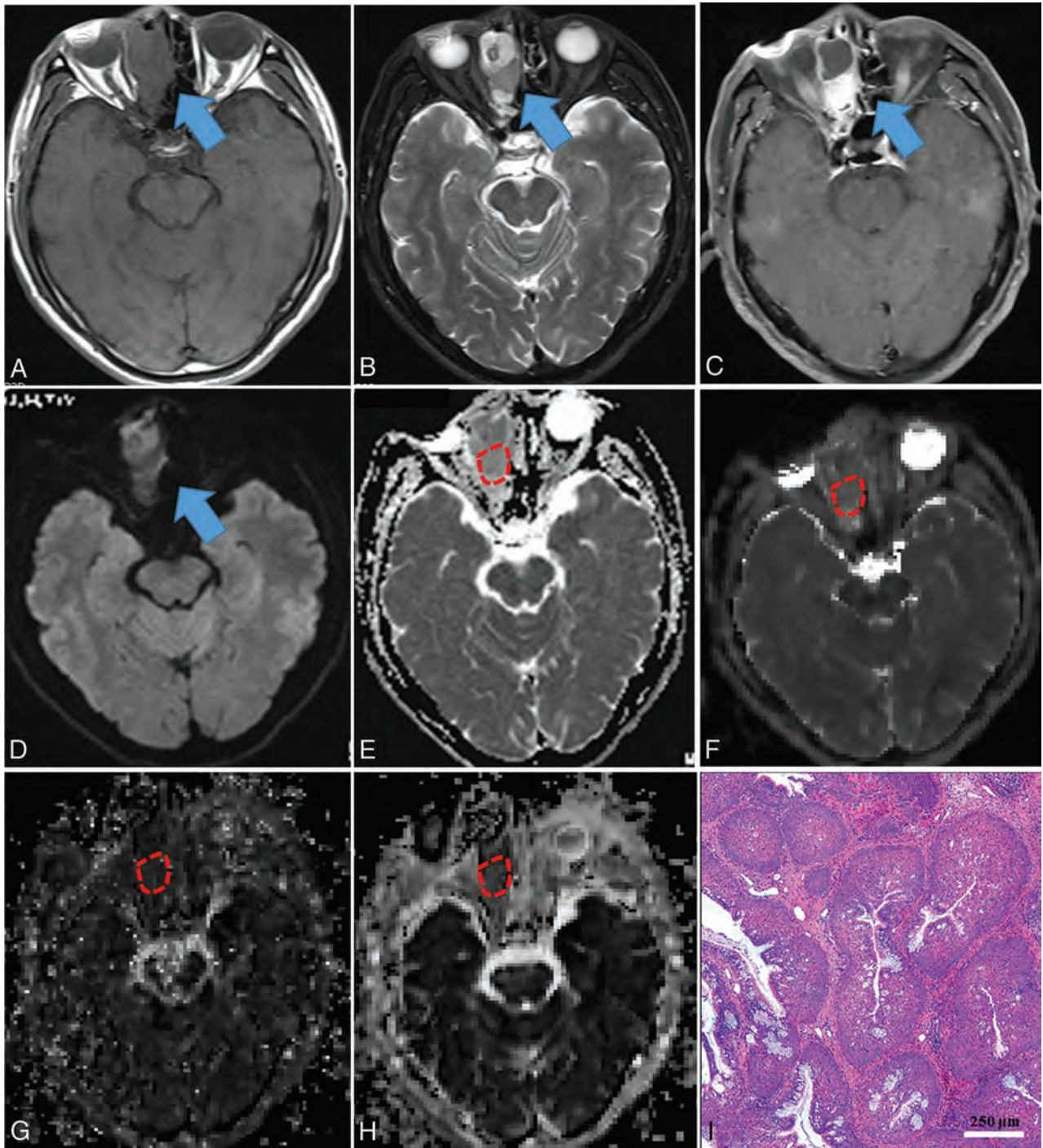


FIG 3. Inverted papilloma in a 71-year-old man. A mass was predominantly located in the right ethmoid sinus with involvement of the right nasal cavity (blue arrow), demonstrating heterogeneous hypo- (necrosis) to isointensity (tumor cells) on T1WI (A), iso- (tumor cells) to hyperintensity (necrosis) on T2WI (B), and heterogeneously intense enhancement on contrast-enhanced T1WI (C), compared with normal-appearing gray matter. The mass showed isointensity on the DWI (blue arrow) (D) compared with normal-appearing gray matter. On the ADC map (E), the mass showed a slightly high signal intensity with an ADC value of $1.425 \times 10^{-3} \text{ mm}^2/\text{s}$ (red polygonal ROI). On IVIM images, the mass appeared obviously iso- to hyperintense on the D map (F) with a D value of $0.871 \times 10^{-3} \text{ mm}^2/\text{s}$ and appeared isointense on the D* (G) and f maps (H) with D* and f values of $61.048 \times 10^{-3} \text{ mm}^2/\text{s}$ and 25.651%, respectively (red polygonal ROIs). Hematoxylin-eosin staining (I) confirmed the mass as an inverted papilloma (original magnification, $\times 100$; scale bar, 250 μm).

diagnostic dilemma because they usually do not demonstrate solid masslike enhancement, bone change, or masquerade as tumors. However, most inflammatory polyps included in our study were hemorrhagic and/or necrotic polyps (19/28), which sometimes may be difficult to discriminate from malignant sinonasal

lesions on conventional CT and MR imaging. Second, the ROI placement for the measurement of conventional DWI and IVIM parameters could not be correlated with fragmental histologic specimens on a site-to-site basis. Third, due to the artifacts from air in the sinuses, there may be some distortions in the measured

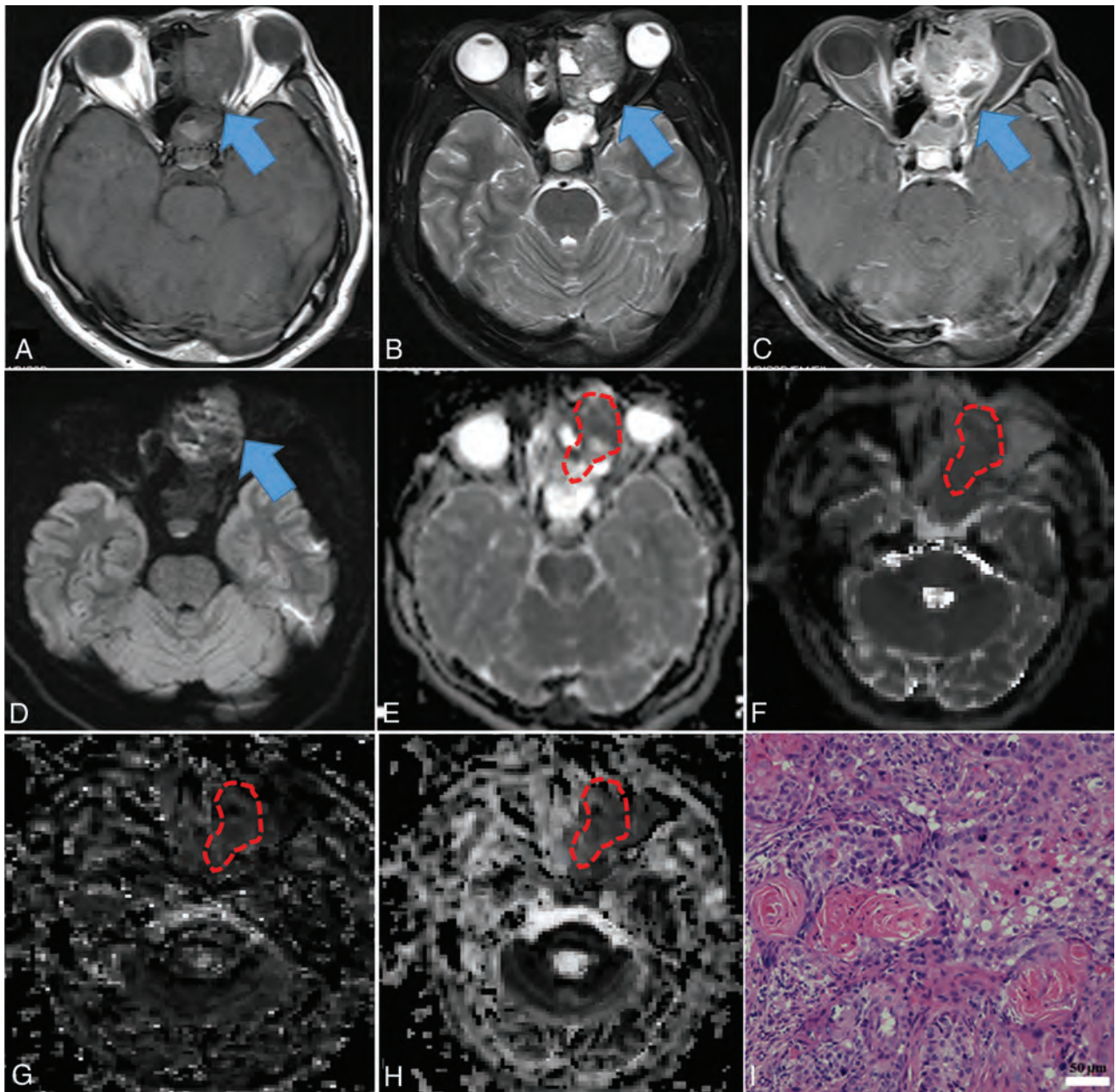


FIG 4. Squamous cell carcinoma in a 53-year-old man. A mass was predominantly located in the left ethmoid sinus with involvement of the ipsilateral orbit, nasal cavity, and sphenoid sinus (blue arrow), demonstrating heterogeneous hypo- (necrosis) to isointensity (tumor cells) on T1WI (A), iso- (tumor cells) to hyperintensity (necrosis) on T2WI (B), and heterogeneously intense enhancement on contrast-enhanced T1WI (C), compared with normal-appearing gray matter. The mass showed heterogeneously hypo- to hyperintensity on the DWI (blue arrow) (D) compared with normal-appearing gray matter. On the ADC map (E), the mass showed hypointensity with an ADC value of $0.872 \times 10^{-3} \text{ mm}^2/\text{s}$ (red polygonal ROI). On IVIM images, the mass appeared dramatically hypointense on the D map (F), with a D value of $0.533 \times 10^{-3} \text{ mm}^2/\text{s}$, hypo- to isointense on the D^* map (G), and iso- to hyperintense on the f map (H), with D^* and f values of $77.473 \times 10^{-3} \text{ mm}^2/\text{s}$ and 22.966%, respectively (red polygonal ROIs). Hematoxylin-eosin staining (I) confirmed the mass as a squamous cell carcinoma (original magnification, $\times 200$; scale bar, 50 μm).

volume that may result in measurement bias. Thus, conventional DWI and IVIM data acquired using readout-segmented echo-planar imaging using parallel imaging and 2D navigator-based reacquisition may be helpful to reduce the artifacts and distortions.^{12,41} Fourth, the value of all these parameters, including ADC, D , D^* , and f , in the differentiations of pathologic types of sinonasal tumors was not evaluated because of the limited number of each type of sinonasal lesion. Finally, because IVIM parameters could be affected by the calculation method, the threshold

values proposed in our study may not be generalizable to other institutions or other methods of IVIM calculation. This issue needs to be investigated in further studies.

CONCLUSIONS

Our preliminary study shows that the ADC value from conventional DWI and the D and f values from IVIM may be helpful for discriminating markers in the differentiation of benign and malignant sinonasal lesions. Furthermore, the combination of

Table 4: Diagnostic performance of single parameters (ADC, D and f) and combined parameters (ADC+ f , ADC+ D , D + f , and ADC+ D + f) for the differentiation of benign and malignant sinonasal lesions using receiver operating characteristic curve analysis with 10-fold cross-validation

	TV	AUC	Cross-Validated AUC	Sensitivity	Specificity	Accuracy	Precision	F Score
ADC	0.919	0.754	0.735	0.800	0.547	0.686	0.684	0.738
D	0.715	0.907	0.899	0.841	0.816	0.831	0.866	0.853
f	16.995	0.676	0.656	0.723	0.472	0.610	0.627	0.723
ADC+ f	—	0.910	0.907	0.857	0.792	0.831	0.857	0.857
ADC+ D	—	0.944	0.914	0.813	0.778	0.797	0.813	0.813
D + f	—	0.938	0.935	0.914	0.813	0.873	0.877	0.895
ADC+ D + f	—	0.951	0.944	0.900	0.833	0.873	0.887	0.894

Note:—TV indicates threshold value.

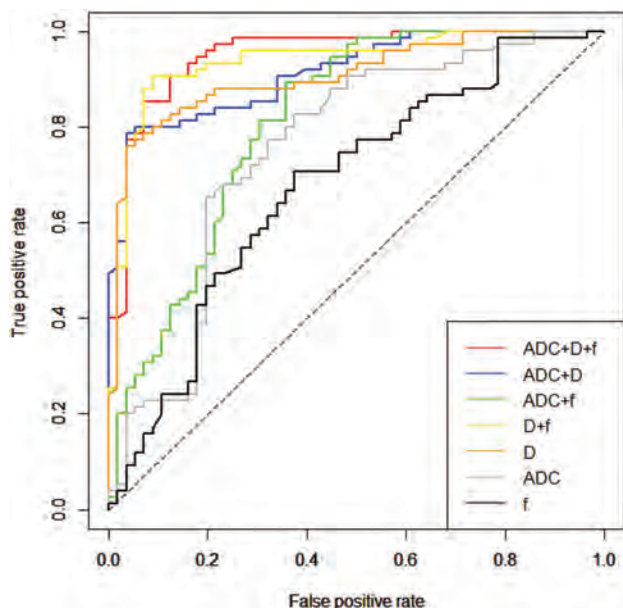


FIG 5. ROC curves with 10-fold cross-validation of single-parameter models (including ADC, D , and f) and multiparametric models (including ADC+ f , ADC+ D , D + f , and ADC+ D + f) in the contrast-enhancing lesions for differentiating benign from malignant sinonasal lesions.

D and f values demonstrates significantly higher sensitivity, specificity, and accuracy than the ADC value, revealing that IVIM appears to be a more valuable tool than conventional DWI for distinguishing benign from malignant sinonasal lesions. Further prospective studies are needed to confirm these findings.

REFERENCES

- Slootweg PJ, Ferlito A, Cardesa A, et al. Sinonasal tumors: a clinicopathologic update of selected tumors. *Eur Arch Otorhinolaryngol* 2013;270:5–20 CrossRef Medline
- Su SY, Kupferman ME, DeMonte F, et al. Endoscopic resection of sinonasal cancers. *Curr Oncol Rep* 2014;16:369 CrossRef Medline
- Eggesbø HB. Imaging of sinonasal tumours. *Cancer Imaging* 2012;12:136–52 CrossRef Medline
- Koeller KK. Radiologic features of sinonasal tumors. *Head Neck Pathol* 2016;10:1–12 CrossRef Medline
- Wang XY, Yan F, Hao H, et al. Improved performance in differentiating benign from malignant sinonasal tumors using diffusion-weighted combined with dynamic contrast-enhanced magnetic resonance imaging. *Chin Med J (Engl)* 2015;128:586–92 CrossRef Medline
- Jégoux F, Metreau A, Louvel G, et al. Paranasal sinus cancer. *Eur Ann Otorhinolaryngol Head Neck Dis* 2013;130:327–35 CrossRef Medline
- Carta F, Blancal JP, Verillaud B, et al. Surgical management of in-

- verted papilloma: approaching a new standard for surgery. *Head Neck* 2013;35:1415–20 CrossRef Medline
- Madani G, Beale TJ, Lund VJ. Imaging of sinonasal tumors. *Semin Ultrasound CT MR* 2009;30:25–38 CrossRef Medline
- Sasaki M, Eida S, Sumi M, et al. Apparent diffusion coefficient mapping for sinonasal diseases: differentiation of benign and malignant lesions. *AJNR Am J Neuroradiol* 2011;32:1100–06 CrossRef Medline
- Sasaki M, Sumi M, Eida S, et al. Multiparametric MR imaging of sinonasal diseases: time-signal intensity curve- and apparent diffusion coefficient-based differentiation between benign and malignant lesions. *AJNR Am J Neuroradiol* 2011;32:2154–59 CrossRef Medline
- White ML, Zhang Y, Robinson RA. Evaluating tumors and tumor-like lesions of the nasal cavity, the paranasal sinuses, and the adjacent skull base with diffusion-weighted MRI. *J Comput Assist Tomogr* 2006;30:490–95 CrossRef Medline
- Wang F, Sha Y, Zhao M, et al. High-resolution diffusion-weighted imaging improves the diagnostic accuracy of dynamic contrast-enhanced sinonasal magnetic resonance imaging. *J Comput Assist Tomogr* 2017;41:199–205 CrossRef Medline
- Le Bihan D. Intravoxel incoherent motion imaging using steady-state free precession. *Magn Reson Med* 1988;7:346–51 CrossRef Medline
- Le Bihan D, Breton E, Lallemand D, et al. MR imaging of intravoxel incoherent motions: application to diffusion and perfusion in neurologic disorders. *Radiology* 1986;161:401–07 CrossRef Medline
- Iima M, Le Bihan D. Clinical intravoxel incoherent motion and diffusion MR imaging: past, present, and future. *Radiology* 2016;278:13–32 CrossRef Medline
- Fujima N, Yoshida D, Sakashita T, et al. Intravoxel incoherent motion diffusion-weighted imaging in head and neck squamous cell carcinoma: assessment of perfusion-related parameters compared to dynamic contrast-enhanced MRI. *Magn Reson Imaging* 2014;32:1206–13 CrossRef Medline
- Sumi M, Nakamura T. Head and neck tumors: assessment of perfusion-related parameters and diffusion coefficients based on the intravoxel incoherent motion model. *AJNR Am J Neuroradiol* 2013;34:410–16 CrossRef Medline
- Jia QJ, Zhang SX, Chen WB, et al. Initial experience of correlating parameters of intravoxel incoherent motion and dynamic contrast-enhanced magnetic resonance imaging at 3.0 T in nasopharyngeal carcinoma. *Eur Radiol* 2014;24:3076–87 CrossRef Medline
- Lai V, Li X, Lee VH, et al. Nasopharyngeal carcinoma: comparison of diffusion and perfusion characteristics between different tumour stages using intravoxel incoherent motion MR imaging. *Eur Radiol* 2014;24:176–83 CrossRef Medline
- Hauser T, Essig M, Jensen A, et al. Prediction of treatment response in head and neck carcinomas using IVIM-DWI: evaluation of lymph node metastasis. *Eur J Radiol* 2014;83:783–87 CrossRef Medline
- Fujima N, Yoshida D, Sakashita T, et al. Prediction of the treatment outcome using intravoxel incoherent motion and diffusional kurtosis imaging in nasal or sinonasal squamous cell carcinoma patients. *Eur Radiol* 2017;27:956–65 CrossRef Medline

22. Sumi M, Van Cauteren M, Sumi T, et al. **Salivary gland tumors: use of intravoxel incoherent motion MR imaging for assessment of diffusion and perfusion for the differentiation of benign from malignant tumors.** *Radiology* 2012;263:770–77 CrossRef Medline
23. Le Bihan D. **Molecular diffusion, tissue microdynamics and microstructure.** *NMR Biomed* 1995;8:375–86 CrossRef Medline
24. Jung Y, Hu J. **A K-fold averaging cross-validation procedure.** *J Non-parametr Stat* 2015;27:167–79 CrossRef Medline
25. Jiang JX, Tang ZH, Zhong YF, et al. **Diffusion kurtosis imaging for differentiating between the benign and malignant sinonasal lesions.** *J Magn Reson Imaging* 2017;45:1446–54 CrossRef Medline
26. Bridge JA, Bowen JM, Smith RB. **The small round blue cell tumors of the sinonasal area.** *Head Neck Pathol* 2010;4:84–93 CrossRef Medline
27. Thoeny HC, De Keyzer F, Boesch C, et al. **Diffusion-weighted imaging of the parotid gland: influence of the choice of b-values on the apparent diffusion coefficient value.** *J Magn Reson Imaging* 2004;20:786–90 CrossRef Medline
28. Padhani AR, Liu G, Koh DM, et al. **Diffusion-weighted magnetic resonance imaging as a cancer biomarker: consensus and recommendations.** *Neoplasia* 2009;11:102–25 CrossRef Medline
29. Suo S, Lin N, Wang H, et al. **Intravoxel incoherent motion diffusion-weighted MR imaging of breast cancer at 3.0 Tesla: comparison of different curve-fitting methods.** *J Magn Reson Imaging* 2015;42:362–70 CrossRef Medline
30. Sasaki M, Sumi M, Eida S, et al. **Simple and reliable determination of intravoxel incoherent motion parameters for the differential diagnosis of head and neck tumors.** *PLoS One* 2014;9:e112866 Medline
31. Liu C, Wang K, Chan Q, et al. **Intravoxel incoherent motion MR imaging for breast lesions: comparison and correlation with pharmacokinetic evaluation from dynamic contrast-enhanced MR imaging.** *Eur Radiol* 2016;26:3888–98 CrossRef Medline
32. Pang Y, Turkbey B, Bernardo M, et al. **Intravoxel incoherent motion MR imaging for prostate cancer: an evaluation of perfusion fraction and diffusion coefficient derived from different b-value combinations.** *Magn Reson Med* 2013;69:553–62 CrossRef Medline
33. Lee HJ, Rha SY, Chung YE, et al. **Tumor perfusion-related parameter of diffusion-weighted magnetic resonance imaging: correlation with histological microvessel density.** *Magn Reson Med* 2014;71:1554–58 CrossRef Medline
34. Wang LL, Lin J, Liu K, et al. **Intravoxel incoherent motion diffusion-weighted MR imaging in differentiation of lung cancer from obstructive lung consolidation: comparison and correlation with pharmacokinetic analysis from dynamic contrast-enhanced MR imaging.** *Eur Radiol* 2014;24:1914–22 CrossRef Medline
35. Iima M, Yano K, Kataoka M, et al. **Quantitative non-Gaussian diffusion and intravoxel incoherent motion magnetic resonance imaging: differentiation of malignant and benign breast lesions.** *Invest Radiol* 2015;50:205–11 CrossRef Medline
36. Kim B, Lee SS, Sung YS, et al. **Intravoxel incoherent motion diffusion-weighted imaging of the pancreas: characterization of benign and malignant pancreatic pathologies.** *J Magn Reson Imaging* 2017;45:260–69 CrossRef Medline
37. Le Bihan D, Turner R. **The capillary network: a link between IVIM and classical perfusion.** *Magn Reson Med* 1992;27:171–78 CrossRef Medline
38. Lewin M, Fartoux L, Vignaud A, et al. **The diffusion-weighted imaging perfusion fraction f is a potential marker of sorafenib treatment in advanced hepatocellular carcinoma: a pilot study.** *Eur Radiol* 2011;21:281–90 CrossRef Medline
39. Xian J, Du H, Wang X, et al. **Feasibility and value of quantitative dynamic contrast enhancement MR imaging in the evaluation of sinonasal tumors.** *Chin Med J (Engl)* 2014;127:2259–64 Medline
40. Liu C, Liang C, Liu Z, et al. **Intravoxel incoherent motion (IVIM) in evaluation of breast lesions: comparison with conventional DWI.** *Eur J Radiol* 2013;82:e782–89 CrossRef Medline
41. Lu P, Sha Y, Wan H, et al. **Assessment of nonarteritic anterior ischemic optic neuropathy with intravoxel incoherent motion diffusion-weighted imaging using readout-segmented echo-planar imaging, parallel imaging, and 2D navigator-based reacquisition.** *J Magn Reson Imaging* 2017;46:1760–66 CrossRef Medline

Imaging of Anaplastic Thyroid Carcinoma

S. Ahmed, M.P. Ghazarian, M.E. Cabanillas, M.E. Zafereo, M.D. Williams, T. Vu, D.F. Schomer, and J.M. Debnam

ABSTRACT

SUMMARY: Anaplastic thyroid carcinoma is fatal if unresectable. However, improved survival has been reported after gross total resection and multimodality therapy. In this report, we describe the contrast-enhanced high-resolution CT characteristics of anaplastic thyroid carcinoma in 57 patients. Anaplastic thyroid carcinoma presented as a large neck mass with necrosis in 82% of cases. The tumors demonstrated common extrathyroidal extension (91%). Sixty-two percent of tumors demonstrated calcification. Visceral space invasion involved the esophagus (62%), trachea (57%), and larynx (29%). Carotid artery encasement was present in 42%, and 43% involved the internal jugular vein. Sixty-three percent had lateral compartment lymphadenopathy; 58% of these nodes were necrotic, and 11% were cystic. No metastatic nodes had calcification. Central compartment lymphadenopathy was seen in 56% of cases, and lateral retropharyngeal lymphadenopathy was detected in 12%. Knowledge of these imaging features aids in guiding the approach to the initial tissue diagnosis with either fine-needle aspiration or core biopsy, assessing the feasibility of surgical resection, and determining prognosis.

ABBREVIATIONS: ATC = anaplastic thyroid carcinoma; CECT = contrast-enhanced CT; DTC = differentiated thyroid cancer

Anaplastic thyroid carcinoma (ATC) accounts for 1%–2% of all thyroid malignancies, but results in over 50% of deaths from thyroid cancer.^{1–3} Despite modern therapies, it remains a highly aggressive disease with one of the worst prognoses among all malignancies. Historically, mean survival was approximately only 5 months,⁴ and 1-year survival was 20%, with 2-year survival at approximately 10%.⁵ With recent advances in multidisciplinary care, median survivals have improved, though most patients do not achieve ultimate cure of their disease.⁶ Women are affected slightly more than men at a ratio of 1.5:1, with a peak incidence in the sixth and seventh decades of life.^{7,8} ATC is known to arise through 2 mechanisms: de novo or from dedifferentiation of well-differentiated thyroid cancer.^{9,10}

ATC is characterized by local invasiveness and extensive ne-

crisis.¹¹ The typical presentation is that of a rapidly enlarging neck mass, often in older patients, prompting contrast-enhanced CT (CECT) evaluation.¹² Doubling time for ATC tumor volume can be as low as 1 week.^{1,13} Symptoms of mass effect upon the trachea and larynx are usually seen at initial presentation. Direct invasion of adjacent structures, including muscle, trachea, larynx, esophagus, and recurrent laryngeal nerve, is common. In addition, nodal metastases are seen in up to 40% of patients at diagnosis.¹⁴ Distant metastases are present in 43% of patients upon presentation, with the most common locations being the lung (78%), adrenals (24%), liver (20%), and brain (18%).¹⁴ Of identifiable causes, death is most commonly the result of advanced pulmonary metastatic disease (35%), followed by airway compromise (16%), tumor-related hemorrhage (14%), and cardiac failure (11%).⁸

In distinction to differentiated thyroid cancer (DTC) and medullary thyroid cancer, all cases of ATC are staged by the American Joint Committee on Cancer TNM system as stage IV disease because of its aggressive nature and poor prognosis.^{4,8} Stage IVA denotes primary tumor without extrathyroidal extension and is considered resectable disease. Stage IVB denotes tumor extension beyond the thyroid without distant metastasis and may or may not be resectable depending on the extent of local invasion. Stage IVC indicates distant metastatic disease. Given improved survival with early multimodality treatment⁶ and increased use of head and neck imaging, it is important for radiologists to be familiar with the imaging features of ATC to avoid delays in diagnosis. In

Received August 4, 2017; accepted after revision October 22.

From the Departments of Diagnostic Radiology (S.A., T.V., D.F.S., J.M.D.), Endocrine Neoplasia (M.E.C.), Head and Neck Surgery (M.E.Z.), and Pathology (M.D.W.), University of Texas MD Anderson Cancer Center, Houston, Texas; and Department of Diagnostic and Interventional Imaging (M.P.G.), University of Texas Houston Medical School, Houston, Texas.

This work was supported by The University of Texas MD Anderson Cancer Center's Cancer Center Support Grant CA16672.

Paper previously presented at: Annual Meeting of the American Roentgen Ray Society, April 17–22, 2016; Los Angeles, California, and Annual Meeting of the American Society of Neuroradiology, May 23–26, 2016; Washington, DC.

Please address correspondence to Salmaan Ahmed, MD, Department of Diagnostic Radiology, 1400 Pressler St, Unit 1482, Houston, TX 77030; e-mail: salmaan.ahmed@mdanderson.org

<http://dx.doi.org/10.3174/ajnr.A5487>

addition, defining the extent of disease, including local invasion and metastatic adenopathy, is critical for appropriate management of the patient.

The imaging literature on ATC is limited, with most reports from before the advent of multidetector CT.^{15,16} To our knowledge, the single article in the radiology literature describing the imaging findings of ATC with multidetector CT included only 9 cases and did not address the frequency of organ invasion, vascular encasement, and cervical lymphadenopathy.¹⁷ Therefore, the purpose of our study was to accurately describe the CECT features of ATC at presentation in a large number of patients presenting to a tertiary cancer referral center.

MATERIALS AND METHODS

Under an institutional review board–approved protocol, the institutional data base was queried for patients with the diagnosis of anaplastic thyroid cancer between June 2004 and February 2017. Patients without CECT imaging before any therapy for ATC or those with suboptimal image quality were excluded. Fifty-seven patients with biopsy-proved ATC and CECT before therapy were included in this retrospective review. Patients underwent imaging on a 4–16-detector LightSpeed CT scanner (GE Healthcare, Milwaukee, Wisconsin), with axial 1.25–3 mm collimation at 120 kVp and 160–400 mA, after injection of 125 mL of Omnipaque 350 (GE Healthcare) at 3 mL/s with a 90-second delay.

Two neuroradiologists (S.A. and either J.M.D. or T.V.), each with a Certificate of Added Qualification and subspecialty interest in head and neck imaging, reviewed all CECT images by consensus. Images were evaluated for the presence of the following: 1) extent of tumor involvement within the thyroid; 2) size of tumor (anteroposterior and transverse dimensions in the axial plane); 3) margins; 4) extrathyroidal extension; 5) tumor morphology; 6) presence of calcifications; 7) esophageal invasion; 8) tracheal invasion; 9) laryngeal invasion; 10) carotid encasement; 11) internal jugular vein involvement; and 12) intrathoracic extension. The presence of central compartment, lateral compartment, and lateral retropharyngeal lymphadenopathy was documented. Lateral and central compartment lymphadenopathy were assessed for calcification, necrosis, and cystic change.

RESULTS

Of the 207 patients with the diagnosis of ATC, 60 patients had pretherapy imaging. Three of the 60 patients were excluded for poor image quality. Of the 57 patients reviewed in our study, 30 patients were men and 27 patients were women. The patient ages ranged between 21 and 82 years (mean, 64 years; median, 65 years). The mean size of the primary tumor was 5.1 × 4.5 cm with a median size of 5.0 × 4.5 cm (anteroposterior × transverse). Figure 1 shows the baseline imaging characteristics of the primary tumor in our patient population, and representative images from

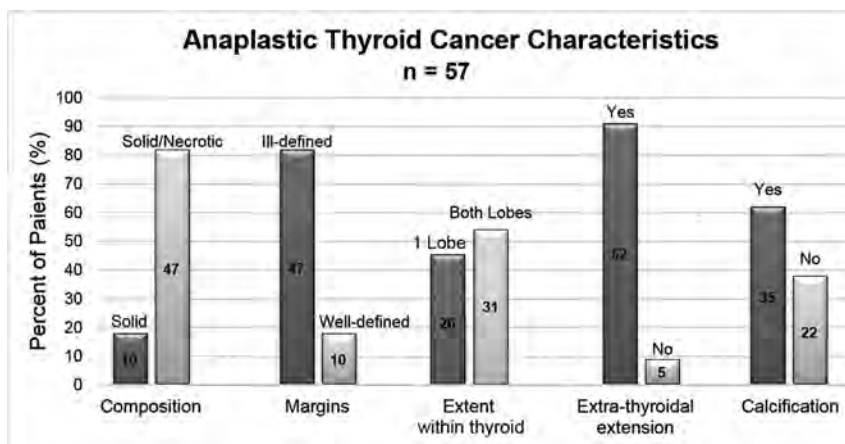


FIG 1. Anaplastic thyroid carcinoma characteristics.

1 of our study patients are shown in Fig 2. The tumor involved 1 lobe of the thyroid in 26 patients (46%), and both lobes were involved in 31 patients (54%). Tumor margins were ill-defined in 47 patients (82%) and well-defined in 10 patients (18%).

Extrathyroidal extension of the tumor was present in 52 of 57 patients (91%). The tumor morphology was mixed solid and necrotic in 47 patients (82%), with the remainder being solid. No lesions were purely cystic. Calcification was present in 62% of cases (35/57). Of those tumors with calcification, coarse calcification was the most com-

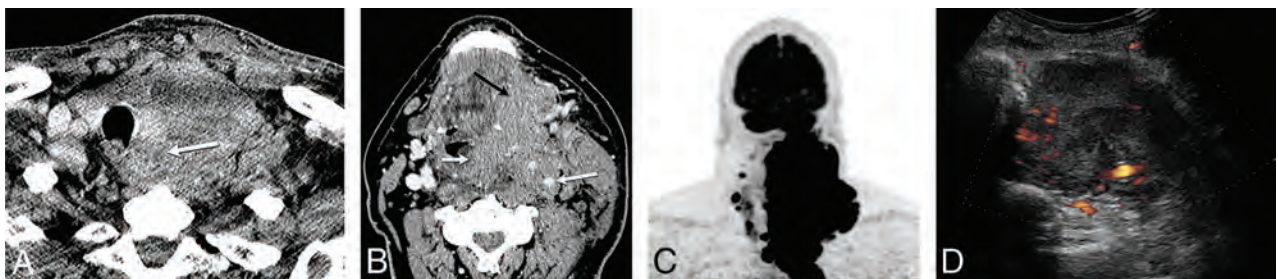


FIG 2. A 60-year-old man with history of neck pain for 1 month and neck CT demonstrating a large left neck mass biopsied as anaplastic thyroid cancer, stage IVC. A, CECT demonstrates a heterogeneously enhancing solid tumor involving the left thyroid lobe and isthmus, with extension to the tracheoesophageal groove and esophageal invasion (arrow). B, Tumor encases the internal carotid artery (large white arrow), and there is direct extension to the prevertebral space, supraglottis (small white arrow), oropharynx, and floor of mouth (black arrow). C, FDG-PET shows intense radiotracer uptake within the left neck tumor with extension to the mediastinum, and there, nodal metastasis to the right neck. D, Pretreatment sonography with Doppler demonstrates a hypoechoic, solid, diffusely infiltrative mass involving the left lobe with increased vascular flow.

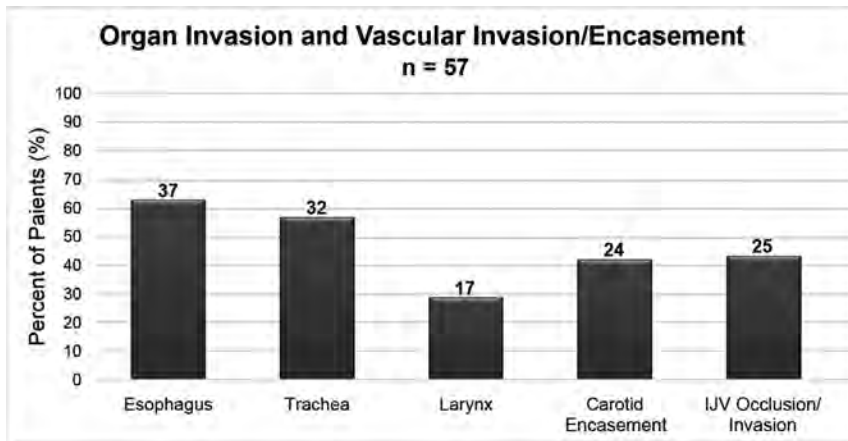


FIG 3. Anaplastic thyroid carcinoma propensity for organ invasion and vascular involvement.

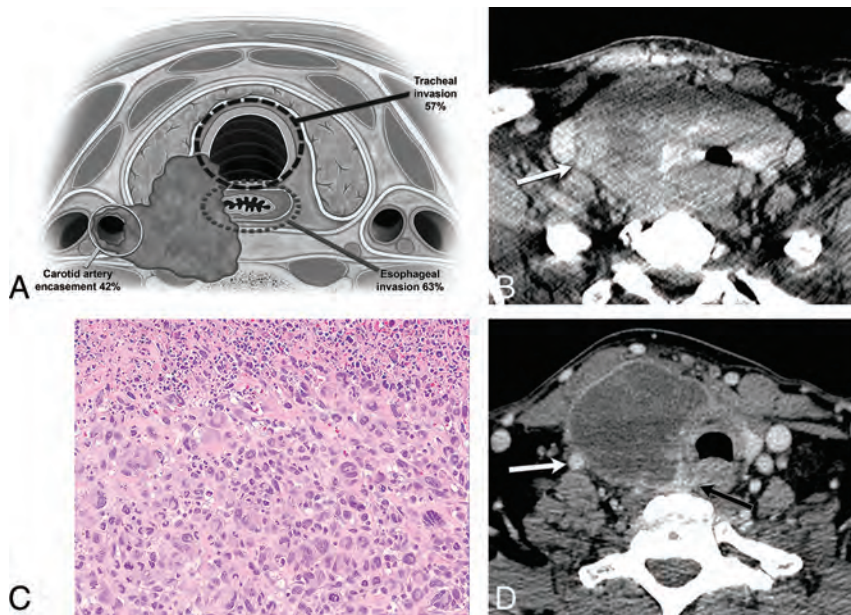


FIG 4. A 60-year-old man with enlarging right neck mass and hoarseness for 2 months with core biopsy demonstrating ATC, stage IVC. *A*, Graphic demonstrating the critical areas of evaluation to characterize the local invasiveness of an aggressive thyroid mass. *B*, Solid, heterogeneously enhancing right lobe tumor invades the trachea and esophagus, with leftward displacement of the midline structures, and encasement of the right ICA (arrow). *C*, Histologic features show enlarged, pleomorphic giant cells with hyperchromatic nuclei growing in sheets consistent with ATC. Necrosis with inflammation is common in these tumors as seen in the upper portion of this picture (hematoxylin-eosin tissue section at 200 \times magnification). *D*, After systemic therapy, the tumor mass has significantly decreased in size, with increased central necrosis, and improved overall local invasiveness. The right ICA is no longer encased (white arrow), and the tumor is now separable from the esophagus (black arrow).

mon (20/57), followed by punctate/stippled calcification (19/57) and 5 cases of eggshell calcification (some tumors had more than 1 type of calcification).

Figure 3 shows the frequency of direct organ invasion and vascular involvement by ATC. The organ with the highest propensity for invasion was the esophagus (63%), followed by the trachea (57%) and the larynx (29%). Vascular involvement by the primary tumor was also commonly present, with carotid artery encasement in 42% of cases and internal jugular vein involvement in 43%. Direct intrathoracic extension of ATC was present in almost half the cases (24/57).

Lateral compartment lymphadenopathy was seen in 63% of our cases, and these metastatic nodes were frequently necrotic (58%), but none contained calcification. Cystic nodes were uncommon (11%). Central compartment lymphadenopathy was seen in 56% of cases; 59% of these nodes were necrotic, and only 3 nodes had calcification (9%), with 2 being cystic (6%). Lateral retropharyngeal adenopathy was seen in 7 patients (12%).

DISCUSSION

Although ATC carries a dismal prognosis, improved survival can be achieved in select cases with a gross total resection in combination with chemotherapy/targeted therapy and radiation therapy. Therefore, precise tumor localization is imperative in determining and assessing treatment options. The primary factors that limit the possibility of meaningful surgery for a patient with ATC are carotid artery encasement (42% in our study), significant laryngeal and tracheal (57% and 29% in our study) or esophageal involvement (63% in our study), significant mediastinal extension, or significant regional or distant metastases. Although laryngotracheal and esophageal resections may be considered for less biologically aggressive tumors, these more complex surgeries and reconstructions are rarely attempted for patients with ATC because of the morbidity of the surgery in the setting of an overall very poor prognosis. Carotid encasement, which was present in 42% of our cases, would be considered inoperable. Similarly, reporting vascular involvement is also critical for the oncologist to counsel patients because this radiographic finding indicates the potential for local hemorrhage and death. Figure 4 demonstrates the typical imaging appearance of ATC at presentation in a patient who was initially deemed inoperable. After positive response to chemoradiation therapy, the carotid encasement and deep organ invasion were significantly improved. In a retrospective review of 121 patients with ATC, age <60 years, tumor size <7 cm, and less extensive disease at presentation were independently associated with decreased disease-related mortality.¹⁸ Increased survival is associated with surgical resection when feasible, younger age, smaller tumor size, higher dose of radiation therapy, absence of distant metastases at presentation, coexistence of papillary thyroid cancer, and management by using multimodal therapy.^{5,19} A retro-

appearance of ATC at presentation in a patient who was initially deemed inoperable. After positive response to chemoradiation therapy, the carotid encasement and deep organ invasion were significantly improved. In a retrospective review of 121 patients with ATC, age <60 years, tumor size <7 cm, and less extensive disease at presentation were independently associated with decreased disease-related mortality.¹⁸ Increased survival is associated with surgical resection when feasible, younger age, smaller tumor size, higher dose of radiation therapy, absence of distant metastases at presentation, coexistence of papillary thyroid cancer, and management by using multimodal therapy.^{5,19} A retro-

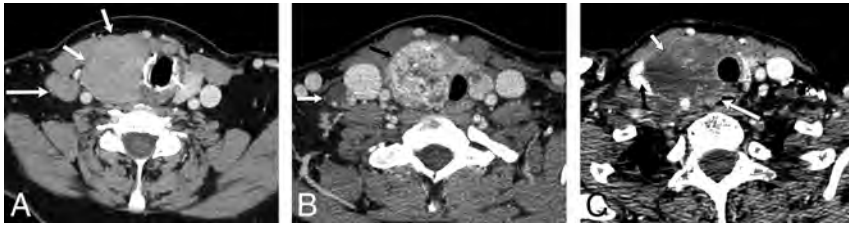


FIG 5. A, Lymphoma: CECT demonstrates a homogeneously enhancing mass diffusely enlarging the right thyroid lobe (*small arrows*) without calcification or necrosis. There is displacement of midline structures without organ invasion. Enlarged right level IV node (*large arrow*) enhances homogeneously without calcification, necrosis, or cystic change. B, Papillary thyroid carcinoma: CECT demonstrates a heterogeneously enhancing right thyroid lobe mass (*black arrow*) with foci of calcification and without necrosis, displacing the midline structures toward the left without organ invasion. Metastatic right level IV node (*white arrow*) demonstrates calcification and cystic change. C, Anaplastic thyroid carcinoma: CECT demonstrates a necrotic right thyroid lobe mass (*small white arrow*) directly invading the esophagus (*large white arrow*) and internal jugular vein (*black arrow*), and there is encasement of the common carotid artery.

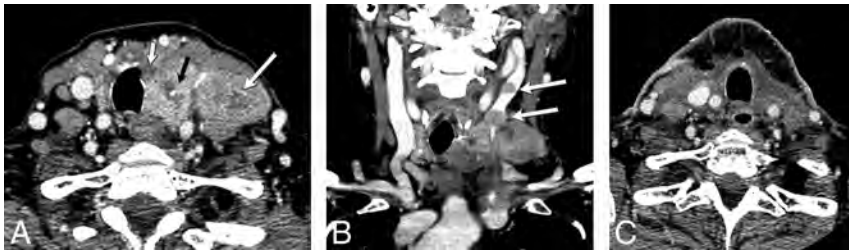


FIG 6. A 64-year-old woman with fine-needle aspiration of left level IV node demonstrating anaplastic thyroid carcinoma, stage IVB. Patient subsequently underwent thyroidectomy, and surgical pathology demonstrated anaplastic thyroid carcinoma arising within papillary thyroid carcinoma. A, Preoperative CECT demonstrates heterogeneously enhancing nodule within the left thyroid lobe with calcification likely corresponding to the pre-existing papillary thyroid carcinoma (*black arrow*). Necrotic tumor within the anteromedial aspect of the left lobe (*small white arrow*) may be invading the trachea and likely corresponds to the anaplastic component seen at final pathology. Metastatic left level IV node demonstrates a necrotic focus (*large white arrow*). B, There is tumor thrombus within the internal jugular vein (*arrows*). C, Patient underwent total thyroidectomy and bilateral neck dissection, including resection of the left internal jugular vein.

spective review by Mohebbati et al⁹ showed a 1-year survival of 54% with gross total resection of the primary tumor versus 28% with gross residual and 8% with no surgery.

When encountering a large thyroid mass, the primary concern remains DTC, which represents >90% of all thyroid cancers. The differential diagnosis also includes ATC and thyroid lymphoma (particularly when the presentation is a rapidly growing neck mass), and other primary thyroid malignancies (poorly differentiated thyroid carcinoma or medullary thyroid cancer), and less commonly metastasis to the thyroid. Sonography is the preferred initial technique for evaluating a neck mass of thyroid origin; however, patients with a rapidly enlarging neck mass and symptoms that might include hoarseness and dysphagia (as seen in ATC) frequently undergo initial evaluation with CECT. Sonography, however, is useful in guiding percutaneous biopsy for rapid diagnosis. The sonographic appearance of ATC is nonspecific and typically reveals a large, heterogeneous, hypoechoic, solid mass with vascularity.¹¹ Accurate diagnosis of ATC can be achieved with fine-needle aspiration in 84% of cases.²⁰ However, at our institution, core biopsy is preferred because of the extensive necrosis typically seen with ATC and also to facilitate adequate tissue for molecular testing.⁴ Molecular testing, though not recommended in professional guidelines at this time, has gained critical

importance in ATC recently. This is because of the recent finding of a basket trial with a BRAF/MEK inhibitor combination (dabrafenib/trametinib) with very high initial response rate in BRAF-mutated ATC. A high index of suspicion for ATC when encountering a rapidly enlarging thyroid mass in an older person, and proceeding with a core biopsy aimed at solid non-necrotic areas, improves diagnostic material to triage patients earlier for therapy. At our institution, core biopsy of suspected ATC or thyroid lymphoma is performed under ultrasound guidance by using a 19-gauge introducer needle and a 20-gauge biopsy gun.

In addition to high-quality CECT of the neck, the initial staging work-up for ATC would also include whole body imaging with PET-CT to exclude distant metastatic disease, brain MR imaging, and chest CT.^{2,11} Figure 1 demonstrates the typical CT imaging features of ATC at presentation, including a large necrotic mass involving both lobes of the thyroid with poorly defined margins, extrathyroidal extension, and local invasion. These imaging features are uncommon in DTC and raise the concern for a higher-grade thyroid carcinoma (poorly differentiated or anaplastic). Figure 5 illustrates the differentiating CT features of papillary thyroid cancer, lymphoma, and ATC in patients with thyroid masses

of similar size at presentation. DTC is most commonly seen on CECT as a solid, homogeneous, hypoattenuating nodule. Calcifications may be seen in both papillary thyroid cancer (32%) and ATC (62% in our cohort).²¹ Thyroid lymphoma typically presents with a rapidly enlarging anterior neck mass and symptoms of mass effect, similar to ATC. Differentiation of lymphoma from ATC is important for both prognosis and treatment implications, and when this rare entity is suspected, flow cytometry can be performed on a fresh fine-needle aspiration sample for diagnosis. Ishikawa et al¹⁵ described 3 features on CT that differentiated primary thyroid lymphoma from ATC with statistical significance. These included the presence or absence of calcification and necrosis and heterogeneous or homogeneous attenuation.^{15,21} ATC contained calcification and necrosis and had heterogeneous attenuation. Thyroid lymphoma, in contrast, was homogeneous without calcification or necrosis.¹⁵ Our findings in ATC (Figs 2 and 3) align with those described in ATC by Kim.²¹ Core biopsy is helpful in the characterization of both ATC and lymphoma.

Metastatic lymphadenopathy from ATC is frequently necrotic, and nodal necrosis was present in 58% of cases in our study. Lymphadenopathy from DTC can be homogeneously enhancing and solid or cystic. Cystic nodes were uncommon in our

study of ATC and were likely related to metastasis from coexisting DTC. DTC lymph nodes are rarely necrotic.²¹ Thus, it is important for biopsy purposes to target a viable tumor focus, but because ATC and papillary thyroid cancer may coexist²² (Fig 6), the lesions with higher-grade imaging features would be preferentially selected for biopsy. If a lymph node is biopsied and initial fine-needle aspiration triage indicates DTC in a patient with CECT imaging of concern for ATC, another biopsy of the thyroid mass would be indicated. Alternatively, if lymph node biopsy returns ATC, no additional sampling of the thyroid mass would be necessary.

CONCLUSIONS

The presence of a rapidly enlarging necrotic thyroid mass should raise concern for ATC, particularly when there is local organ invasion and necrotic cervical lymphadenopathy. Awareness of these imaging features of ATC allows for radiographic distinctions to favor ATC over a well-differentiated thyroid carcinoma or thyroid lymphoma and potentially expedite diagnosis. The frequent local and regional imaging findings, in particular the tumor extent and association with critical structures in the neck, emphasize the role for high-quality CECT imaging. Knowledge of these imaging features will aid in guiding the approach to initial tissue diagnosis with either fine-needle aspiration or core biopsy, assessing if surgical resection is feasible, and determining prognosis.

Disclosures: Maria E. Cabanillas—UNRELATED: Consultancy: Eisai, LOXO, Blueprint; Grants/Grants Pending: Eisai, Kura, Genentech*. *Money paid to the institution.

REFERENCES

1. Are C, Shaha AR. **Anaplastic thyroid carcinoma: biology, pathogenesis, prognostic factors, and treatment approaches.** *Ann Surg Oncol* 2006;13:453–64 CrossRef Medline
2. Bogsrud TV, Karantanis D, Nathan MA, et al. **18F-FDG PET in the management of patients with anaplastic thyroid carcinoma.** *Thyroid* 2008;18:713–19 CrossRef Medline
3. Ragazzi M, Ciarrocchi A, Sancisi V, et al. **Update on anaplastic thyroid carcinoma: morphological, molecular, and genetic features of the most aggressive thyroid cancer.** *Int J Endocrinol* 2014;2014:790834 CrossRef Medline
4. Smallridge RC, Ain KB, Asa SL, et al. **American Thyroid Association guidelines for management of patients with anaplastic thyroid cancer.** *Thyroid* 2012;22:1104–39 CrossRef Medline
5. Smallridge RC, Copland JA. **Anaplastic thyroid carcinoma: patho-**

- genesis and emerging therapies.** *Clin Oncol (R Coll Radiol)* 2010;22:486–97 CrossRef Medline
6. Rao SN, Zafereo M, Dadu R, et al. **Patterns of treatment failure in anaplastic thyroid carcinoma.** *Thyroid* 2017;27:672–81 CrossRef Medline
7. Aschebrook-Kilfoy B, Ward MH, Sabra MM, et al. **Thyroid cancer incidence patterns in the United States by histologic type, 1992–2006.** *Thyroid* 2011;21:125–34 CrossRef Medline
8. Neff RL, Farrar WB, Kloos RT, et al. **Anaplastic thyroid cancer.** *Endocrinol Metab Clin North Am* 2008;37:525–38, xi CrossRef Medline
9. Mohebbati A, Dilorenzo M, Palmer F, et al. **Anaplastic thyroid carcinoma: a 25-year single-institution experience.** *Ann Surg Oncol* 2014;21:1665–70 CrossRef Medline
10. Haddad RI, Lydiatt WM, Ball DW, et al. **Anaplastic thyroid carcinoma, version 2.2015.** *J Natl Compr Canc Netw* 2015;13:1140–50 CrossRef Medline
11. Hahn SY, Shin JH. **Description and comparison of the sonographic characteristics of poorly differentiated thyroid carcinoma and anaplastic thyroid carcinoma.** *J Ultrasound Med* 2016;35:1873–79 CrossRef Medline
12. Cabanillas ME, McFadden DG, Durante C. **Thyroid cancer.** *Lancet* 2016;388:2783–95 CrossRef Medline
13. Ain KB. **Anaplastic thyroid carcinoma: a therapeutic challenge.** *Semin Surg Oncol* 1999;16:64–69 CrossRef Medline
14. Kelil T, Keraliya AR, Howard SA, et al. **Current concepts in the molecular genetics and management of thyroid cancer: an update for radiologists.** *Radiographics* 2016;36:1478–93 CrossRef Medline
15. Ishikawa H, Tamaki Y, Takahashi M, et al. **Comparison of primary thyroid lymphoma with anaplastic thyroid carcinoma on computed tomographic imaging.** *Radiat Med* 2002;20:9–15 Medline
16. Takashima S, Morimoto S, Ikezoe J, et al. **CT evaluation of anaplastic thyroid carcinoma.** *AJR Am J Roentgenol* 1990;154:1079–85 CrossRef Medline
17. Lee JW, Yoon DY, Choi CS, et al. **Anaplastic thyroid carcinoma: computed tomographic differentiation from other thyroid masses.** *Acta Radiol* 2008;49:321–27 CrossRef Medline
18. Kim TY, Kim KW, Jung TS, et al. **Prognostic factors for Korean patients with anaplastic thyroid carcinoma.** *Head Neck* 2007;29:765–72 CrossRef Medline
19. Smallridge RC, Marlow LA, Copland JA. **Anaplastic thyroid cancer: molecular pathogenesis and emerging therapies.** *Endocr Relat Cancer* 2009;16:17–44 CrossRef Medline
20. Us-Krasovec M, Golouh R, Auersperg M, et al. **Anaplastic thyroid carcinoma in fine needle aspirates.** *Acta Cytol* 1996;40:953–58 CrossRef Medline
21. Kim DW. **Computed tomography features of papillary thyroid carcinomas.** *J Comput Assist Tomogr* 2014;38:936–40 CrossRef Medline
22. Molinaro E, Romei C, Biagini A, et al. **Anaplastic thyroid carcinoma: from clinicopathology to genetics and advanced therapies.** *Nat Rev Endocrinol* 2017;13:644–60 CrossRef Medline

Multiparametric Analysis of Permeability and ADC Histogram Metrics for Classification of Pediatric Brain Tumors by Tumor Grade

S. Vajapeyam, D. Brown, P.R. Johnston, K.I. Ricci, M.W. Kieran, H.G.W. Lidov, and T.Y. Poussaint



ABSTRACT

BACKGROUND AND PURPOSE: Accurate tumor grading is essential for treatment planning of pediatric brain tumors. We hypothesized that multiparametric analyses of a combination of permeability metrics and ADC histogram metrics would differentiate high- and low-grade tumors with high accuracy.

MATERIALS AND METHODS: DTI and dynamic contrast-enhanced MR imaging using T1-mapping with flip angles of 2°, 5°, 10°, and 15°, followed by a 0.1-mmol/kg body weight gadolinium-based bolus was performed on all patients in addition to standard MR imaging. Permeability data were processed and transfer constant from the blood plasma into the extracellular extravascular space, rate constant from the extracellular extravascular space back into blood plasma, extravascular extracellular volume fraction, and fractional blood plasma volume were calculated from 3D tumor volumes. Apparent diffusion coefficient histogram metrics were calculated for 3 separate tumor volumes derived from T2-FLAIR sequences, T1 contrast-enhanced sequences, and permeability maps, respectively.

RESULTS: Results from 41 patients (0.3–16.76 years of age; mean, 6.22 years) with newly diagnosed contrast-enhancing brain tumors (16 low-grade; 25 high-grade) were included in the institutional review board–approved retrospective analysis. Wilcoxon tests showed a higher transfer constant from blood plasma into extracellular extravascular space and rate constant from extracellular extravascular space back into blood plasma, and lower extracellular extravascular volume fraction ($P < .001$) in high-grade tumors. The mean ADCs of FLAIR and enhancing tumor volumes were significantly lower in high-grade tumors ($P < .001$). ROC analysis showed that a combination of extravascular volume fraction and mean ADC of FLAIR volume differentiated high- and low-grade tumors with high accuracy (area under receiver operating characteristic curve = 0.918).

CONCLUSIONS: ADC histogram metrics combined with permeability metrics differentiate low- and high-grade pediatric brain tumors with high accuracy.

ABBREVIATIONS: AROC = area under receiver operating characteristic curve; DCE-MRI = dynamic contrast-enhanced MR imaging; FL = 3D tumor volume from T2-FLAIR images; EES = extracellular extravascular space; K_{ep} = rate constant from EES back into blood plasma; K^{trans} = transfer constant from blood plasma into EES; PG = 3D tumor volume from T1-contrast-enhanced images; ROC = receiver operating characteristic; v_e = extracellular extravascular volume fraction; v_p = fractional blood plasma volume

Primary brain tumors have an incidence rate of 5.67 per 100,000¹ in children younger than 19 years of age and remain the most common cause of disease-related death in children. Accurate assessment of tumor grade is critical for diagnosis and treatment planning, especially with recent advances in

genomic and molecular subtyping of tumors and targeted treatments for different subtypes. Conventional MR imaging remains the technique of choice for diagnosis and treatment; however, advanced imaging techniques such as perfusion and diffusion imaging have also proved useful for physiologic characterization of tumors.

Dynamic contrast-enhanced MR imaging (DCE-MRI) provides information on the vessel permeability and microvasculature in brain tumors and has been used extensively in adults in

Received August 18, 2017; accepted after revision October 30.

From the Departments of Radiology (S.V., D.B., P.R.J., T.Y.P.) and Pathology (H.G.W.L.), Boston Children's Hospital, Boston, Massachusetts; Cancer Center (K.I.R.), Massachusetts General Hospital, Boston, Massachusetts; Division of Pediatric Oncology (M.W.K.), Dana-Farber Boston Children's Cancer and Blood Disorders Center, Boston, Massachusetts; and Harvard Medical School (S.V., M.W.K., H.G.W.L., T.Y.P.), Boston, Massachusetts.

Paper previously presented at: Annual Meeting of the American Society of Neuroradiology and the Foundation of the ASNR Symposium, April 22–27, 2017; Long Beach, California.

Please address correspondence to Sridhar Vajapeyam, PhD, Department of Radiology, 300 Longwood Ave, Boston, MA 02115; e-mail: sridhar.vajapeyam@childrens.harvard.edu

<http://dx.doi.org/10.3174/ajnr.A5502>

tumor grading,²⁻⁵ but less frequently in children.^{6,7} DTI provides information about tumor cellularity and is useful for characterization of tissue, tumor grading, tumor response to treatment, and distinction of tissue types.⁸ ADC histogram analysis provides a comprehensive analysis of the volumetric diffusion characteristics of the tumor and has been used to predict survival in both adults^{9,10} and children.¹¹

We retrospectively analyzed DCE-MR imaging and DTI data from children presenting with a brain mass during 3 years at Boston Children's Hospital and examined the permeability and ADC histogram metrics as predictors of tumor grade. We hypothesized that a combination of DCE-MR imaging and ADC histogram metrics would improve the accuracy of tumor grading on MR imaging.

MATERIALS AND METHODS

Subjects

Children who presented with a brain mass from 2013 to 2017 who had DCE-MR imaging and DTI studies were included. The study was performed with the approval of the institutional review board of the Dana Farber Cancer Institute.

MR Imaging Acquisition

All MR imaging studies were performed on a 3T scanner (Skyra; Siemens, Erlangen, Germany). Standard MR imaging in all patients consisted of sagittal T1, axial T2, precontrast axial T2-FLAIR, axial DTI (TR = 6500 ms, TE = 88 ms, slice thickness = 2 mm, b-values of 0 and 1000 s/mm², 30 gradient directions), and postcontrast T1 images. All patients underwent a DCE-MR imaging protocol as follows: 1) variable flip angle echo-spoiled gradient-echo T1-mapping sequences using flip angles of 15°, 10°, 5°, and 2°; TR = 5 seconds; TE = minimum; FOV = 240 mm; section thickness = 5 mm; and 2) DCE-MR imaging sequence consisting of 50 phases, 7 seconds apart, flip angle = 15°, TR = 4 seconds, TE = minimum. FOV, section thickness, and scan locations were identical to those in the T1-mapping sequences. A single bolus of gadobutrol (0.1-mL/kg body weight) was injected 20 seconds after the start of scanning at an injection rate of 2 mL/s.

DCE-MR Imaging Postprocessing

DCE-MR images were transferred to a VersaVue workstation (In vivo, Gainesville, Florida) for automated processing using OmniLook software. Voxelwise T1 maps were generated from the variable flip angle images, and the 2-compartment Tofts model¹² was used to generate voxelwise values of the pharmacokinetic parameters, namely the transfer constant from the blood plasma into the extracellular extravascular space (K^{trans}), rate constant from extracellular extravascular space back into blood plasma (K_{ep}), extracellular extravascular volume fraction (v_e), and fractional blood plasma volume (v_p).

The model of Weinmann et al¹³ was used for blood plasma concentration. ROIs were drawn on each section of the tumor around contrast-enhancing portions of the tumor by an imaging data analyst or by a PhD scientist and verified by a Certificate of Added Qualification–certified neuroradiologist, and the mean (over voxels) and SDs of each of the variables were recorded. Only enhancing tumors were included in the analysis.

ADC Histogram Analysis

Due to their superior anatomic contrast, axial B0 images from the DTI sequence were registered to the axial T2-FLAIR images using the mutual information algorithm in FSL (<http://www.fmrib.ox.ac.uk/fsl>)¹⁴ and the same transformation matrix used on the ADC maps to register them to the T2-FLAIR images. Axial postcontrast images were also separately registered to T2-FLAIR using the same methodology. 3D ROIs comprising the 3D tumor volume from T2-FLAIR images (FL) and the 3D tumor volume from T1-contrast-enhanced images (PG) were automatically generated using the thresholding feature in Fiji (<http://fiji.sc/>),¹⁵ an Open Source (<https://opensource.org/>) distribution of Java modules along with ImageJ software (National Institutes of Health, Bethesda, Maryland). The ADC values of the voxels in the 3D tumor volume from T2-FLAIR images (FL), and PG ROIs were then used to generate the FL and PG ADC volumes, respectively. These volumes were thresholded using a uniform range of 600–2600 × 10⁻⁶ mm²/s to automatically exclude cyst, necrosis, and hemorrhage. FL and PG ADC histograms were then generated using a uniform bin width of 7.8 mm²/s to facilitate comparison of shape descriptors of the histograms. Histogram metrics used for statistical analysis were the number of peaks (unimodal or bimodal), mean, SD, skewness, and kurtosis of these histograms. In the case of tumors showing bimodal ADC histograms, the lower peak was measured for mean and SD, and skewness and kurtosis were not recorded.

DCE-MR imaging and ADC histogram analyses were blinded to tumor grading results.

Statistical Methods

Low- and high-grade tumor groups were compared for permeability variables and ADC histogram metrics using the Wilcoxon test and *t* test using the NPARIWAY and *t* test procedures of SAS (SAS Institute, Cary, North, Carolina).¹⁶ Corresponding to the *t* test, estimates and 95% confidence intervals for the difference between means were calculated.

Receiver operating characteristic (ROC) curves and their areas (AROC) were estimated for highly statistically significant variables in the permeability set (v_e , K^{trans} , K_{ep}), ADC histogram set (FL_ADC_mean, PG_ADC_mean), and the 6 pairs of variables comprising 1 variable from each set. Focus was on the v_e and FL_ADC_mean pair because these variables and their relationship were considered the most stable.

The ROC curve shows the trade-off between the true-positive rate (classifying the tumor of a patient with a high-grade tumor as high-grade) and false-positive rate (classifying the tumor of a patient with a low-grade tumor as high-grade). The AROC estimates the average true-positive rate over all possible false-positive rates and is also an estimate of the probability of correctly classifying a random pair of patients, 1 from the low-grade group and 1 from the high-grade group.

In addition to point estimates, Wald-based tests (corresponding to the null hypothesis that the true AROC is 0.5) and 95% confidence intervals for the AROC were calculated. All estimates, confidence intervals, and tests were nonparametric and were calculated using the LOGISTIC procedure of SAS.

Table 1: Group comparisons: low- versus high-grade tumor

Variable	Low-Grade (Mean)	High-Grade (Mean)	Mean Diff	Mean SE	Lower 95% CL	Upper 95% CL	P Value (T Test)	χ^2 (Wilcoxon)	P Value (Wilcoxon)
K^{trans} (min^{-1})	0.14	1.50	1.36	0.45	0.46	2.27	.004	16.72	<.001
K_{ep} (min^{-1})	1.18	8.85	7.67	1.99	3.64	11.70	<.001	18.98	<.001
v_e	0.22	0.13	-0.09	0.02	-0.13	-0.05	<.001	13.41	<.001
v_p	0.05	0.05	0.00	0.01	-0.02	0.02	.764	0.23	.630
FL_ADC_mean ($\times 10^{-6}$ mm^2/s)	1458	1022	-436	84.47	-607	-265	<.001	15.65	<.001
FL_ADC_SD ($\times 10^{-6}$ mm^2/s)	336.8	285.0	-51.8	36.01	-125	21.06	.158	.56	.454
FL_ADC_skew	0.45	1.24	0.80	0.26	0.27	1.32	.004	7.55	.006
FL_ADC_kurt	1.28	1.97	0.70	0.73	-0.79	2.18	.347	1.58	.208
PG_ADC_mean ($\times 10^{-6}$ mm^2/s)	1472	1066	-406	100.7	-610	-203	<.001	11.70	<.001
PG_ADC_SD ($\times 10^{-6}$ mm^2/s)	261.0	308.4	47.46	40.47	-34.4	129.3	.248	1.93	.165
PG_ADC_skew	0.69	1.30	0.61	0.30	0.01	1.21	.047	2.26	.133
PG_ADC_kurt	2.51	2.31	-0.20	0.93	-2.09	1.70	.835	0.34	.560

Note:—Diff indicates difference; SE, standard error; CL, confidence limit; skew, skewness; kurt, kurtosis.

RESULTS

Sixty-three patients were identified. Six patients had final diagnoses that were not brain tumors, 10 had nonenhancing tumors and were excluded from DCE-MR imaging analysis, and 6 patients were excluded due to motion or susceptibility artifacts. The remaining 41 patients were included.

Twenty-three children were boys, and 18, girls (age range, 0.30–16.76 years; median age, 4.76 years; mean age, 6.22 years). There were 31 infratentorial and 10 supratentorial tumors, and all except 2 were newly diagnosed.

Forty patients had enhancing biopsy-confirmed tumors, and 1 had a diffuse midline glioma located in the pons presumed to be high-grade. World Health Organization grades 1–2 were considered low-grade, whereas grades 3–4 were considered high-grade. Of these tumors, 16 were confirmed low-grade (7 pilocytic astrocytomas, 5 low-grade gliomas, 1 mature teratoma, 1 atypical meningioma, 1 low-grade ganglioglioma, and 1 low-grade mixed germ cell tumor). Twenty-five tumors were high-grade (12 medulloblastomas, 4 glioblastomas, 4 anaplastic ependymomas, and 1 each of atypical teratoid/rhabdoid tumor, embryonal tumor not otherwise specified, choroid plexus carcinoma, embryonal tumor with rhabdoid features, and diffuse midline glioma). Not all final diagnoses were given as the World Health Organization 2016 classification because some cases did not fit well into this classification at the time of diagnosis.

Molecular subtyping was successful in 11 of the 12 patients with medulloblastoma, yielding 3 sonic hedgehog/SHH-activated, 2 wingless/WNT-activated, and 6 classified as group 3 or 4.

There was no statistically significant difference in mean ages between the low-grade (mean, 7.28 years; median, 5.31 years) and the high-grade cohort (mean, 5.54 years; median, 4.57 years) ($P = .552$).

Group comparisons of all permeability and ADC histogram variables are shown in Table 1. Of the pharmacokinetic variables analyzed, K^{trans} and K_{ep} were significantly higher in high-grade tumors compared with low-grade tumors ($P < .001$), and v_e was significantly lower in the high-grade group ($P < .001$).

Of the ADC histogram metrics analyzed, the mean ADC of the T2-FLAIR tumor volume (FL_ADC_mean) and the PG tumor volume (PG_ADC_mean) were significantly higher for low-grade tumors (Fig 1) compared with high-grade tumors ($P < .001$) (Fig 2). Low-grade tumors also showed a tendency for lower

skewness for T2-FLAIR tumor volume (FL_ADC_skew, $P = .006$). None of the other variables showed statistically significant group differences between low- and high-grade tumors. Six high-grade tumors showed bimodal T2-FLAIR ADC histograms, and 4 showed bimodal PG ADC histograms, while all the ADC histograms for low-grade tumors had just a single peak.

No group differences were found among the molecular subtypes in the medulloblastoma cohort ($P \geq .294$).

ROC analysis of the 5 highly statistically significant variables (K^{trans} , K_{ep} , v_e , FL_ADC_mean, and PG_ADC_mean) showed that all displayed high sensitivity and specificity in discriminating low- and high-grade tumors, with AROC values above 0.82 ($P < .001$) as seen in Table 2. AROC values for v_e and FL_ADC_mean were 0.843 and 0.870, respectively, while the AROC estimate for the 2-variable combination of these metrics was 0.918 (Fig 3). Focus was on this pair because the individual variables and their relationship were considered the most stable.

The Spearman correlation between v_e and FL_ADC_mean across the 41 tumors was 0.49 ($P = .001$). Correlation within the low- and high-grade groups was not significant.

DISCUSSION

Multiparametric imaging of pediatric brain tumors provides physiologic information beyond standard MR imaging. Koob et al⁷ recently reported increased accuracy in differentiating grades I and IV pediatric brain tumors using a combination of diffusion and DSC perfusion metrics. Similarly, Morana et al¹⁷ showed improved prognostic capability by combining DWI, arterial spin-labeling, and PET data in pediatric diffuse astrocytic tumors. Other studies have demonstrated the advantage of combinations of DWI, DSC perfusion, MR spectroscopy, and PET data in studying pediatric brain tumors.^{18–20} To our knowledge, this is the first study to demonstrate a multiparametric approach using DCE and ADC histogram metrics in pediatric brain tumors.

While DSC and arterial spin-labeling perfusion metrics have been reported for pediatric brain tumor grading,^{21–23} there are fewer studies using DCE-MR imaging.⁶ Our results show that among the DCE-MR imaging parameters, K^{trans} , K_{ep} , and v_e all successfully distinguished low- and high-grade tumors, and this result is consistent with our report from a smaller cohort.⁶ High-grade tumors exhibited higher values of K^{trans} and K_{ep} , indi-

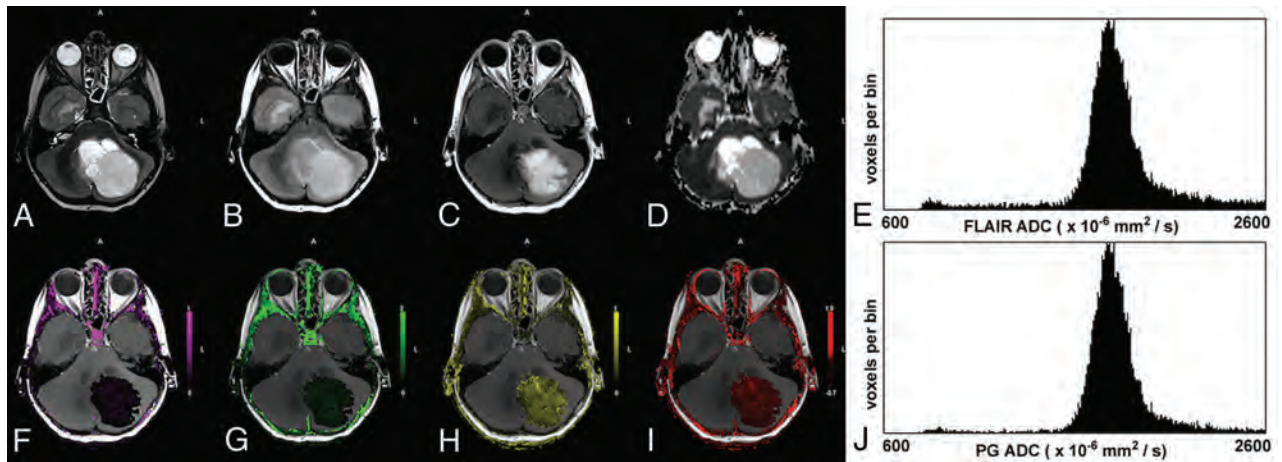


FIG 1. A 6-year-old boy with a low-grade pilocytic astrocytoma. The upper row shows the T2-weighted image (A), T2-FLAIR image (B), post-contrast T1-weighted image (C), ADC map (D), and the ADC histogram of the FLAIR tumor volume (E), respectively. The lower row shows the K^{trans} map (F), K_{ep} map (G), v_e map (H), v_p map (I), and the ADC histogram of the enhancing tumor volume (J), respectively. The enhancing tumor volume was defined as the nodular enhancement of the solid component for pilocytic astrocytomas. Note the low K^{trans} and K_{ep} and the high v_e values in this low-grade tumor. The mean ADC of the FLAIR tumor volume is $1821 \times 10^{-6} \text{ mm}^2/\text{s}$ and $1808 \times 10^{-6} \text{ mm}^2/\text{s}$ for the enhancing tumor volume.

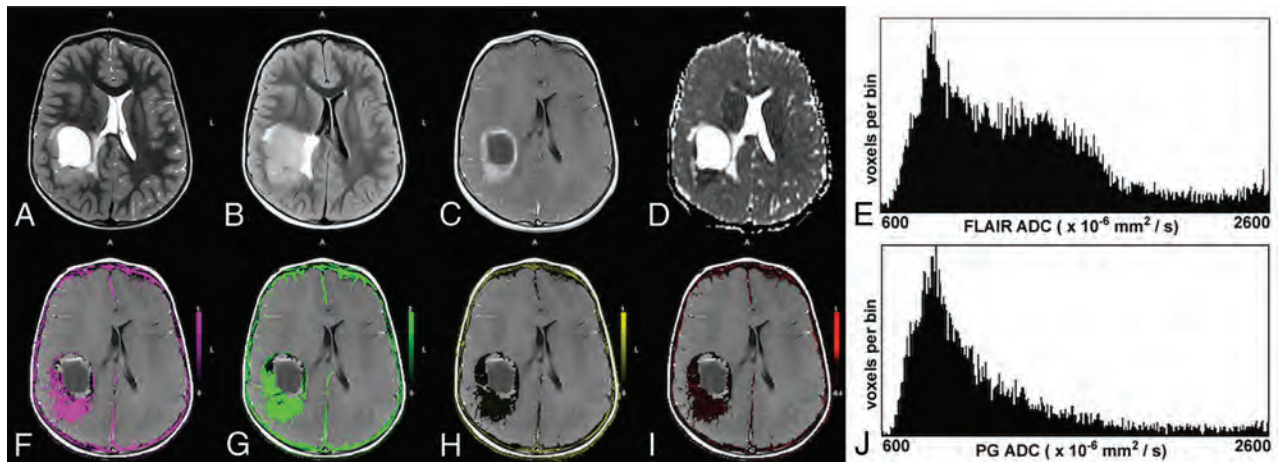


FIG 2. A 5-year-old boy with parietal anaplastic ependymoma. The upper row shows the T2-weighted image (A), T2-FLAIR image (B), post-contrast T1-weighted image (C), ADC map (D), and the ADC histogram of the FLAIR tumor volume (E), respectively. The lower row shows the K^{trans} map (F), K_{ep} map (G), v_e map (H), v_p map (I), and the ADC histogram of the enhancing tumor volume (J), respectively. Note the high K^{trans} and K_{ep} and the lower v_e values in this high-grade tumor. The histogram of the FLAIR tumor volume is bimodal. The mean ADC of the lower peak of the FLAIR tumor volume is $867 \times 10^{-6} \text{ mm}^2/\text{s}$ and $1262 \times 10^{-6} \text{ mm}^2/\text{s}$ for the enhancing tumor volume.

Table 2: Predictors of AROC

Predictor	AROC	SE	95% Lower CL	95% Upper CL	T Value	P Value
K^{trans}	0.883	0.052	0.781	0.984	7.40	<.001
K_{ep}	0.908	0.047	0.815	1.0	8.59	<.001
V_e	0.843	0.066	0.713	0.972	5.19	<.001
FL_ADC_mean	0.870	0.055	0.762	0.978	6.74	<.001
PG_ADC_mean	0.820	0.066	0.691	0.949	4.86	<.001
$V_e + \text{FL_ADC_mean}$	0.918	0.043	0.834	1.0	9.81	<.001

Note:—CL indicates confidence limit.

cating leaky vessels. This finding is consistent with the angiogenesis seen in high-grade tumors caused by neoangiogenic proteins such as vascular endothelial growth factor. Our finding of lower v_e in high-grade tumors differs from reports in adult glioblastomas,^{3,24,25} likely due to the multiple different high-grade tumor types in children. Jensen et al,²⁶ however, found that adult patients with gliomas with lower v_e in peritu-

moral edema had significantly shorter overall survival rates, supporting our hypothesis that lower v_e corresponds to a higher grade and more aggressive tumor.

Of the ADC histogram metrics we tested, FL_ADC_mean and PG_ADC_mean showed significant differences between low- and high-grade tumors, with lower ADC corresponding to

high-grade tumors. Lower ADC indicates high tumor cellularity and has been associated with shorter survival as well.⁹⁻¹¹ ADC histogram skewness and kurtosis did not show the same significant differences. Although the number of ADC histograms with bimodal peaks was too small for statistical analysis (6 for FL_ADC_mean and 4 for PG_ADC_mean), all tumors exhibiting bimodal peaks were high-grade. High-grade tumors often yield bi-

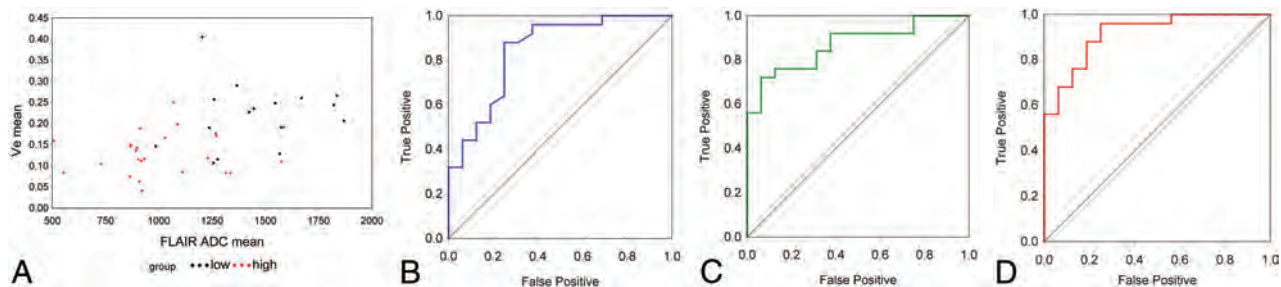


FIG 3. A, Scatterplot of v_e versus FL_ADC_mean for all 41 cases analyzed. High-grade tumors are shown in red, and low-grade, in black. B, ROC curve for v_e (AROC = 0.843). C, ROC curve for FL_ADC_mean (AROC = 0.870). D, ROC curve when v_e and FL_ADC_mean are combined (AROC = 0.918). Note the improved accuracy shown for the multiparametric predictor, reflected in the increased AROC.

modal ADC distributions due to the presence of peritumoral edema.^{9–11}

We did not detect any group differences among the molecular subtypes of medulloblastoma, which may be due to the small sample size. Recent studies have reported other distinguishing MR imaging features of some of these subtypes,^{27–29} and a larger future sample size may show differences in permeability and ADC histogram metrics among the subtypes. We would postulate that the group 3 tumors, which are ill-defined and have the poorest prognosis,³⁰ would have high K^{trans} and K_{ep} and low v_e with low mean ADC histogram values.

Because v_e is a measure of the extracellular extravascular space and ADC is also indicative of extracellular space, we tested for a correlation between ADC and v_e . ADC and v_e were highly correlated across the entire cohort ($P = .001$). Although a previous study was unable to find voxelwise correlations between v_e and ADC in adult gliomas,³¹ our findings suggest a link between the mean values in pediatric brain tumors, possibly due to the different tumor types seen in children.

Permeability metrics assess tumor microvasculature, whereas ADC histogram metrics assess tumor cellularity. We hypothesized that these modalities may provide complementary information to assist in tumor grading and tested combinations of permeability and ADC variables as predictors of tumor grade using ROC curves. A combination of v_e and FL_ADC_mean showed a higher AROC (0.918) compared with v_e (0.843) or FL_ADC_mean (0.870) alone. Thus, multiparametric analysis may yield the best predictors of tumor grade in pediatric brain tumors.

One limitation of the study is the relatively small number and heterogeneity of tumors studied. Larger numbers of individual tumor types are necessary to validate these findings across all tumor types. The addition of PET¹⁹ and MR spectroscopy^{7,18} has also shown promise and may benefit future analyses. Future prospective work could include other multiparametric approaches incorporating ADC histogram and T1 permeability to differentiate molecular and genomic subtypes of pediatric brain tumors.

CONCLUSIONS

The permeability metrics K^{trans} , K_{ep} , and v_e and the ADC histogram metrics FL_ADC_mean and PG_ADC_mean were able to distinguish low- and high-grade pediatric brain tumors with a high degree of accuracy. A multiparametric approach combining permeability and ADC histogram metrics improves the accuracy of pediatric brain tumor grading with high sensitivity and specificity.

Disclosures: Tina Young Poussaint—UNRELATED: Grants/Grants Pending: Pediatric Brain Tumor Consortium Neuroimaging Center, Comments: National Institutes of Health grant with subcontract*; Royalties: Springer Science for a book. *Money paid to the institution.

REFERENCES

- Ostrom QT, Gittleman H, Xu J, et al. **CBTRUS Statistical Report: Primary Brain and Other Central Nervous System Tumors Diagnosed in the United States in 2009–2013.** *Neuro Oncol* 2016;18:v1–v75 CrossRef Medline
- Falk A, Fahlström M, Rostrup E, et al. **Discrimination between glioma grades II and III in suspected low-grade gliomas using dynamic contrast-enhanced and dynamic susceptibility contrast perfusion MR imaging: a histogram analysis approach.** *Neuroradiology* 2014;56:1031–38 CrossRef Medline
- Li X, Zhu Y, Kang H, et al. **Glioma grading by microvascular permeability parameters derived from dynamic contrast-enhanced MRI and intratumoral susceptibility signal on susceptibility weighted imaging.** *Cancer Imaging* 2015;15:4 CrossRef Medline
- Roberts HC, Roberts TP, Ley S, et al. **Quantitative estimation of microvascular permeability in human brain tumors: correlation of dynamic Gd-DTPA-enhanced MR imaging with histopathologic grading.** *Acad Radiol* 2002;9:S151–55 CrossRef Medline
- Zhang N, Zhang L, Qiu B, et al. **Correlation of volume transfer coefficient K^{trans} with histopathologic grades of gliomas.** *J Magn Reson Imaging* 2012;36:355–63 CrossRef Medline
- Vajapeyam S, Stamouliis C, Ricci K, et al. **Automated processing of dynamic contrast-enhanced MRI: correlation of advanced pharmacokinetic metrics with tumor grade in pediatric brain tumors.** *AJNR Am J Neuroradiol* 2017;38:170–75 CrossRef Medline
- Koob M, Girard N, Ghattas B, et al. **The diagnostic accuracy of multiparametric MRI to determine pediatric brain tumor grades and types.** *J Neurooncol* 2016;127:345–53 CrossRef Medline
- Poussaint TY, Rodriguez D. **Advanced neuroimaging of pediatric brain tumors: MR diffusion, MR perfusion, and MR spectroscopy.** *Neuroimaging Clin N Am* 2006;16:169–92, ix CrossRef Medline
- Pope WB, Qiao XJ, Kim HJ, et al. **Apparent diffusion coefficient histogram analysis stratifies progression-free and overall survival in patients with recurrent GBM treated with bevacizumab: a multicenter study.** *J Neurooncol* 2012;108:491–98 CrossRef Medline
- Rahman R, Hamdan A, Zweifler R, et al. **Histogram analysis of apparent diffusion coefficient within enhancing and nonenhancing tumor volumes in recurrent glioblastoma patients treated with bevacizumab.** *J Neurooncol* 2014;119:149–58 CrossRef Medline
- Poussaint TY, Vajapeyam S, Ricci KI, et al. **Apparent diffusion coefficient histogram metrics correlate with survival in diffuse intrinsic pontine glioma: a report from the Pediatric Brain Tumor Consortium.** *Neuro Oncol* 2016;18:725–34 CrossRef Medline
- Tofts PS. **Modeling tracer kinetics in dynamic Gd-DTPA MR imaging.** *J Magn Reson Imaging* 1997;7:91–101 CrossRef Medline
- Weinmann HJ, Laniado M, Mützel W. **Pharmacokinetics of GdDTPA/dimeglumine after intravenous injection into healthy volunteers.** *Physiol Chem Phys Med NMR* 1984;16:167–72 Medline

14. Jenkinson M, Beckmann CF, Behrens TE, et al. **FSL**. *Neuroimage* 2012;62:782–90 CrossRef Medline
15. Schindelin J, Arganda-Carreras I, Frise E, et al. **Fiji: an open-source platform for biological-image analysis**. *Nat Methods* 2012;9:676–82 CrossRef Medline
16. SAS/STAT 14.1 User's Guide. July 2015. <http://support.sas.com/documentation/cdl/en/statug/68162/HTML/default/viewer.htm#titlepage.htm>. Updated November 2, 2015
17. Morana G, Piccardo A, Tortora D, et al. **Grading and outcome prediction of pediatric diffuse astrocytic tumors with diffusion and arterial spin labeling perfusion MRI in comparison with 18F-DOPA PET**. *Eur J Nucl Med Mol Imaging* 2017;44:2084–89 CrossRef Medline
18. Tzika AA, Astrakas LG, Zarifi MK, et al. **Multiparametric MR assessment of pediatric brain tumors**. *Neuroradiology* 2003;45:1–10 CrossRef Medline
19. Zukotynski KA, Fahey FH, Vajapeyam S, et al. **Exploratory evaluation of MR permeability with 18F-FDG PET mapping in pediatric brain tumors: a report from the Pediatric Brain Tumor Consortium**. *J Nucl Med* 2013;54:1237–43 CrossRef Medline
20. Tensaouti F, Ducassou A, Chaltiel L, et al; radiotherapy committee of the French Society for Childhood Cancer (SFCE). **Prognostic and predictive values of diffusion and perfusion MRI in paediatric intracranial ependymomas in a large national study**. *Br J Radiol* 2016; 89:20160537 CrossRef Medline
21. Ho CY, Cardinal JS, Kamer AP, et al. **Relative cerebral blood volume from dynamic susceptibility contrast perfusion in the grading of pediatric primary brain tumors**. *Neuroradiology* 2015;57:299–306 CrossRef Medline
22. Ho CY, Cardinal JS, Kamer AP, et al. **Contrast leakage patterns from dynamic susceptibility contrast perfusion MRI in the grading of primary pediatric brain tumors**. *AJNR Am J Neuroradiol* 2016;37: 544–51 CrossRef Medline
23. Yeom KW, Mitchell LA, Lober RM, et al. **Arterial spin-labeled perfusion of pediatric brain tumors**. *AJNR Am J Neuroradiol* 2014;35: 395–401 CrossRef Medline
24. Abe T, Mizobuchi Y, Nakajima K, et al. **Diagnosis of brain tumors using dynamic contrast-enhanced perfusion imaging with a short acquisition time**. *Springerplus* 2015;4:88 CrossRef Medline
25. Choi HS, Kim AH, Ahn SS, et al. **Glioma grading capability: comparisons among parameters from dynamic contrast-enhanced MRI and ADC value on DWI**. *Korean J Radiol* 2013;14:487–92 CrossRef Medline
26. Jensen RL, Mumert ML, Gillespie DL, et al. **Preoperative dynamic contrast-enhanced MRI correlates with molecular markers of hypoxia and vascularity in specific areas of intratumoral microenvironment and is predictive of patient outcome**. *Neuro Oncol* 2014;16: 280–91 CrossRef Medline
27. Perreault S, Ramaswamy V, Achrol AS, et al. **MRI surrogates for molecular subgroups of medulloblastoma**. *AJNR Am J Neuroradiol* 2014;35:1263–69 CrossRef Medline
28. Lastowska M, Jurkiewicz E, Trubicka J, et al. **Contrast enhancement pattern predicts poor survival for patients with non-WNT/SHH medulloblastoma tumours**. *J Neurooncol* 2015;123:65–73 CrossRef Medline
29. Yeom KW, Mobley BC, Lober RM, et al. **Distinctive MRI features of pediatric medulloblastoma subtypes**. *AJR Am J Roentgenol* 2013; 200:895–903 CrossRef Medline
30. Ramaswamy V, Northcott PA, Taylor MD. **FISH and chips: the recipe for improved prognostication and outcomes for children with medulloblastoma**. *Cancer Genet* 2011;204:577–88 CrossRef Medline
31. Mills SJ, Soh C, Rose CJ, et al. **Candidate biomarkers of extravascular extracellular space: a direct comparison of apparent diffusion coefficient and dynamic contrast-enhanced MR imaging-derived measurement of the volume of the extravascular extracellular space in glioblastoma multiforme**. *AJNR Am J Neuroradiol* 2010;31: 549–53 CrossRef Medline

Prenatal Factors Associated with Postnatal Brain Injury in Infants with Congenital Diaphragmatic Hernia

R. Radhakrishnan, S.L. Merhar, W. Su, B. Zhang, P. Burns, F.Y. Lim, and B.M. Kline-Fath

ABSTRACT

BACKGROUND AND PURPOSE: Approximately 60% of infants with congenital diaphragmatic hernia have evidence of brain injury on postnatal MR imaging. It is unclear whether any brain injury is present before birth. In this study, we evaluated fetal MR imaging findings of brain injury and the association of congenital diaphragmatic hernia severity with postnatal brain injury.

MATERIALS AND METHODS: Fetal MR imaging and postnatal brain MR imaging were retrospectively evaluated in 36 cases of congenital diaphragmatic hernia (from 2009 to 2014) by 2 pediatric neuroradiologists. Brain injury on postnatal MR imaging and brain injury and congenital diaphragmatic hernia severity on fetal MR imaging were recorded. Correlations between brain abnormalities on fetal and postnatal brain MR imaging were analyzed. Postnatal brain injury findings correlating with the severity of congenital diaphragmatic hernia were also assessed.

RESULTS: On fetal MR imaging, enlarged extra-axial spaces (61%), venous sinus distention (21%), and ventriculomegaly (6%) were identified. No maturational delay, intracranial hemorrhage, or brain parenchymal injury was identified on fetal MR imaging. On postnatal MR imaging, 67% of infants had evidence of abnormality, commonly, enlarged extra-axial spaces (44%). Right-sided congenital diaphragmatic hernia was associated with a greater postnatal brain injury score ($P = .05$). Low observed-to-expected lung volume was associated with postnatal white matter injury ($P = .005$) and a greater postnatal brain injury score ($P = .008$). Lack of liver herniation was associated with normal postnatal brain MR imaging findings ($P = .03$).

CONCLUSIONS: Fetal lung hypoplasia is associated with postnatal brain injury in congenital diaphragmatic hernia, suggesting that the severity of lung disease and associated treatments affect brain health as well. We found no evidence of prenatal brain parenchymal injury or maturational delay.

ABBREVIATION: CDH = congenital diaphragmatic hernia

As many as 60% of infants with congenital diaphragmatic hernia (CDH) show evidence of brain injury on MR imaging performed before discharge from the neonatal intensive care unit.¹⁻⁶ We and other investigators have shown that postnatal factors in the neonatal intensive care unit, including the use of

extracorporeal membrane oxygenation, the need for inotropes, lack of oral feeding at discharge, and placement of a gastrostomy tube before hospital discharge are associated with evidence of brain injury on MR imaging.^{1,6,7} In addition, a large diaphragmatic defect, persistent pulmonary hypertension, and the presence of liver herniation into the chest are associated with a greater degree of brain injury postnatally.⁵ Despite evidence of postnatal brain injury in these infants, the presence and extent of brain injury in utero are unclear. Prior work by Danzer et al³ suggested brain maturational delay in infants with CDH. However, this finding has not been reported in other studies, and we found no evidence of delayed maturation on postnatal brain MR imaging in our prior study of infants with CDH.¹

Evaluating fetal brain MRIs in this population could provide more information on the timing of injury and the possibility of in utero onset of maturational delay. Understanding the association of lung MR imaging biomarkers of CDH severity with brain in-

Received July 11, 2017; accepted after revision October 30.

From the Department of Radiology (R.R.), Riley Hospital for Children at Indiana University, Indianapolis, Indiana; Perinatal Institute (S.L.M.), Division of Neonatology, Division of Biostatistics and Epidemiology (B.Z.), Fetal Care Center (P.B., F.Y.L.), and Department of Radiology (B.M.K.-F.), Cincinnati Children's Hospital Medical Center, Cincinnati, Ohio; and Department of Mathematics (W.S.), University of Cincinnati, Cincinnati, Ohio.

Paper previously presented at: Annual Meeting of the American Society of Neuro-radiology and the Foundation of the ASNR Symposium, April 22-27, 2017; Long Beach, California.

Please address correspondence to Rupa Radhakrishnan, MD, Riley Hospital for Children at Indiana University, 705 Riley Hospital Dr, Indianapolis, IN 46032; e-mail: rupa.rad@gmail.com; @RadRupa

<http://dx.doi.org/10.3174/ajnr.A5500>

jury could also provide valuable information when counseling parents. The goal of our study was to evaluate the presence of prenatal brain injury on fetal MR imaging in infants with CDH and the association of CDH severity assessed on fetal MR imaging with postnatal brain injury. We hypothesized that infants with CDH would have no evidence of prenatal brain injury and that CDH severity would correlate with later brain injury.

MATERIALS AND METHODS

Patient Selection

This retrospective review was approved by the institutional review board of Cincinnati Children's Hospital Medical Center. We identified infants with CDH born between 2009 and 2014 who had postnatal MR imaging of the brain and fetal MR imaging available for review. This cohort overlaps that in our previous study¹ but is not identical. If the infant had >1 fetal MR imaging performed, both examinations were reviewed, but the most recent fetal MR imaging was used for statistical analysis. Fetuses with prenatally diagnosed CDH referred to our institution typically have undergone fetal MRIs at least once in the early third trimester to estimate lung volumes. Frequently, a second trimester fetal MR imaging is performed at the time of referral as a part of the routine diagnostic work-up to aid patient counseling.

Image Review

Fetal imaging and postnatal brain MR imaging were reviewed by 2 pediatric neuroradiologists (R.R., B.M.K.-F.) at separate time points and blinded to the postnatal brain imaging outcome. Fetal MR imaging was performed at 1.5T, on either a Signa (GE Healthcare, Milwaukee, Wisconsin) or an Ingenia (Philips Healthcare, Best, the Netherlands) system. Fetal MRIs included T2 single-shot fast-spin-echo images of the brain in 3 planes: axial, sagittal, and coronal (interleaved slices without a gap, 3-mm thickness at <24 weeks' gestation, and 4-mm thickness at >24 weeks' gestation). At least 2 stacks in each plane were obtained to the radiologist's satisfaction. The smallest FOV possible was used. T1-weighted imaging of the fetal brain and body was performed at a slice thickness of 5 mm. Diffusion imaging was performed intermittently before but routinely after 2012.

Findings recorded on the fetal MR imaging were germinal matrix hemorrhage, the presence of restricted diffusion when performed, ventriculomegaly, and enlarged extra-axial spaces. Enlargement of the extra-axial spaces was determined when the distance between the inner margin of the calvaria and the frontal or parieto-occipital region was greater than the values for gestational age.^{8,9} Ventriculomegaly was diagnosed when the maximum width of the lateral ventricles at the level of the atrium measured >10 mm.¹⁰ The presence of maturational delay, engorged dural venous sinuses, and parenchymal signal abnormality was recorded by a senior neuroradiologist (B.M.K.-F.). Brain maturation was assessed comprehensively on T2-weighted images by comparison with a published and widely used timeline of brain development, germinal matrix involution, myelination, and cortical infolding/sulcation.¹¹ Brain maturation was dichotomously graded as normal or delayed. Figure 1 highlights a few of the maturational changes that were assessed.



FIG 1. A, Coronal T2-weighted image of a fetus with CDH at 24 weeks demonstrating expected maturation with the presence of the interhemispheric and Sylvian fissure (*dashed arrow*), but with an otherwise smooth appearance of the frontal lobes. There is expected visualization of the migrating neurons as evidenced by alternating dark and bright bands in the cerebral parenchyma (*arrows*) corresponding, from inside out, to the ventricular zone/germinal matrix, periventricular fiber rich zone, intermediate zone, subplate zone, and cortical plate. B, Coronal T2-weighted image of a 32-week fetus with CDH showing age-appropriate maturation with the presence of the superior and inferior frontal sulci (*arrows*) and the inferior temporal sulcus (*dashed arrow*). The 5 layer pattern of migration is no longer present.

Postnatal imaging was performed on a 1.5T MR imaging scanner (Signa or Ingenia) or a 3T MR imaging scanner (Achieva; Philips Healthcare), or a small-bore-extremity 1.5T MR imaging scanner adapted for neonatal imaging in the neonatal intensive care unit. Postnatal imaging sequences used were T1-weighted (sagittal volume-gradient T1 or sagittal and axial spin-echo T1), axial and coronal T2-weighted, axial susceptibility-weighted and axial diffusion-weighted imaging, or diffusion tensor imaging in 12–15 directions. Postnatal brain MRIs were reviewed independently by 2 pediatric neuroradiologists (B.M.K.-F. and R.R.), blinded to fetal imaging and clinical factors except gestational age at time of imaging. Conflicts were resolved by consensus. A composite postnatal brain injury score was obtained to include ventriculomegaly; extra-axial space enlargement; injury to the cortex, white matter, and basal ganglia; and intraventricular, parenchymal, and cerebellar hemorrhage on a system modified by previous work by Danzer et al^{3,12} and Tracy et al¹⁵ and published by our group (Table 1).¹ Markers of CDH severity, including lung volumes, side of CDH, the presence of intrathoracic liver, and the presence of congenital heart disease (from the patient's chart) were recorded.

Lung-volume measurements were performed by specifically trained image analysis technologists in a prospective fashion using a free-standing Vitrea workstation (Vital Images, Minnetonka, Minnesota). In our institution, lung volumes are typically measured on coronal T2-weighted images. We assessed 2 commonly used measures of severity of lung hypoplasia:

Percentage Predicted Lung Volume = Total Lung Volume/Predicted Lung Volume × 100, as described by Barnewolt et al,¹³ where Predicted Lung Volume = Total Thoracic Volume – Mediastinal Volume.

Observed-To-Expected Lung Volume = Total Lung Volume/Expected Lung Volume, where Expected Lung Volume = 0.0033 × (Gestational Age in Weeks)^{2.86} based on the formula by Rypens et al.¹⁴

The size of the diaphragmatic defect was assessed on the basis of surgical notes, classified according to the Congenital Diaphragmatic Hernia Study Group classification from A to D, with A

Table 1: Postnatal brain injury scoring system^a

MRI Finding	MRI Score				
	0	1	2	3	4
Ventriculomegaly	<10 mm	10–15 mm	>15 mm	Obstructive	
Extra-axial spaces	<5 mm	5–10 mm	>10 mm		
Intraventricular hemorrhage	None	Grade 1	Grade 2	Grade 3	Grade 4
Parenchymal hemorrhage (not grade 4 intraventricular hemorrhage)	Absent	Present			
Cerebellar hemorrhage	None	<3 foci, <5-mm size	>3 foci or >5-mm size		
White matter injury	None	<3 foci, unilateral	>3 foci or bilateral	Multiregional	
Cortical injury	None	Single	Multiple	Extensive	
Basal ganglia injury	None	Single	Multiple	Extensive	

^a Postnatal brain injury graded on a published scale.¹

being a small defect and D reflecting diaphragmatic agenesis.¹⁵ For our analysis, we dichotomized the diaphragmatic defect size, with A or B being small and C or D being a large defect.

Statistical Analysis

Descriptive statistics were performed to describe the characteristics of the prenatal and postnatal variables. Total injury scores were compared among different levels of categoric variables using 1-way ANOVA. The relationship among categoric variables was assessed by a χ^2 test or Fisher exact test. The Pearson correlation was used to evaluate the correlation among continuous variables. Associations between prenatal antecedents, such as the presence of brain injury and the severity of diaphragmatic hernia, and postnatal brain injury findings were analyzed using multivariate linear regression models. The association between any brain injury and the risk factors was assessed using logistic regression models. All analyses were performed with SAS, Version 9.4 (SAS Institute, Cary, North Carolina). $P < 0.05$ was considered statistically significant.

RESULTS

Fifty-six infants with CDH had postnatal imaging, of whom 36 infants (17 girls) had fetal MRIs and were included in the study. Sixty-two fetal MRIs had been performed on these 36 infants. Twenty-six infants had 2 fetal MRIs, and 10 had 1 fetal MRI. Fetal MRI was performed between 20 and 36 weeks' postmenstrual age. Thirty-five infants had at least 1 fetal MRI in the third trimester, and only 1 infant had a single fetal MRI in the second trimester.

On fetal MR imaging, enlarged extra-axial spaces were the most common brain finding, seen in 22/36 MRIs (Fig 2). Other less common findings were the presence of venous sinus distention (Fig 3) and ventriculomegaly (Table 2). Ventriculomegaly was mild, seen only on the early MR imaging in 2 infants and resolved on the subsequent third trimester MR imaging. There were no cases of maturational delay, intracranial hemorrhage, or brain parenchymal injury identified on fetal MR imaging. Findings related to CDH severity are listed in Table 3.

On postnatal MR imaging, 24/36 infants had findings of brain injury (Table 4). The average brain injury score was 1.8 ± 1.8 . The most common postnatal MR imaging finding was enlarged extra-axial spaces. Postnatal enlargement of extra-axial spaces was associated with a larger defect size ($P = .003$), right diaphragmatic hernia ($P = .026$), lower percentage predicted lung volume ($P = .02$), and enlarged extra-axial spaces on the last fetal MR imaging ($P = .02$).

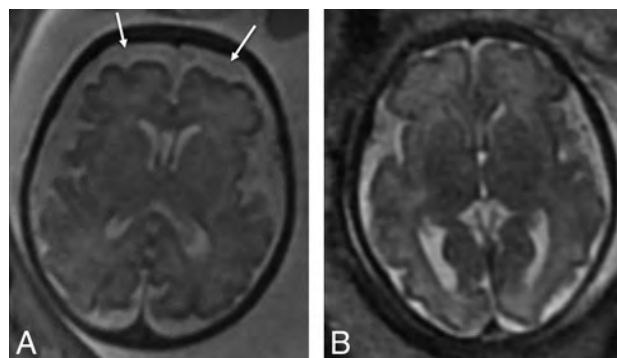


FIG 2. Axial T2-weighted images of two 32-week fetuses with CDH with enlarged extra-axial spaces as marked by *arrows* (A) and normal extra-axial spaces (B).

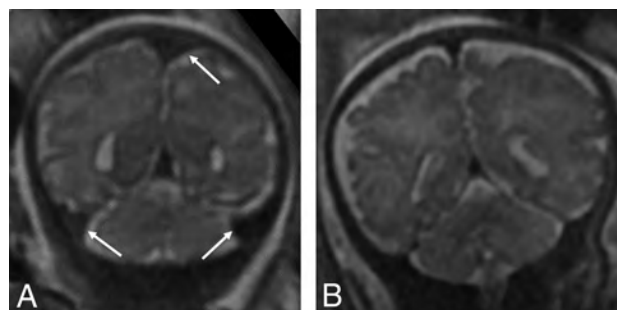


FIG 3. Coronal T2-weighted images of a 34-week fetus with CDH (A) with engorged dural venous sinuses (*arrows*) and a comparison 34-week fetus without CDH (B) without dural venous sinus engorgement.

Table 2: Brain injury on fetal MRI

Pattern of Injury ^a	No. (%)
Enlarged extra-axial spaces	22 (61)
Venous sinus distention	9 (21)
Ventriculomegaly	2 (6)
Germinal matrix hemorrhage	None
Diffusion abnormalities	None
Parenchymal abnormalities	None
Delayed sulcation	None

^a $n = 36$.

Right-sided CDH was significantly associated with postnatal ventriculomegaly (OR, 7.67; 95% CI, 1.36–43.14; $P = .02$) and a greater postnatal brain injury score (mean, 2.5 ± 2 for right-sided CDH versus mean, 1.54 ± 1.73 for left CDH, $P = .05$). Low observed-to-expected lung volume was associated with postnatal white matter injury ($P = .005$). Lack of liver herniation was asso-

ciated with normal postnatal brain MR imaging findings ($P = .03$).

The postnatal brain injury score was almost moderately correlated (Pearson correlation coefficient = -0.44 , $P = .008$) with fetal observed-to-expected lung volume (Fig 4).

DISCUSSION

Our data show that prenatal imaging assessment of the severity of congenital diaphragmatic hernia is associated with brain injury on postnatal predischarge MR imaging. We also show that most fetuses had enlarged extra-axial spaces on the MR imaging performed in late gestation. The cause of this abnormality is unclear, and none of the factors of the severity of congenital diaphragmatic hernia (side, size of defect, percentage predicted lung volume, observed-to-expected fetal lung volume) correlated with this

finding. It is possible that the presence of some degree of venous hypertension due to mass effect by the congenital diaphragmatic hernia and resultant alterations in CSF dynamics might play a role in the presence of this finding prenatally. In a study by Tracy et al,⁵ in fetuses with CDH, there were only 2 fetuses with enlarged extra-axial spaces, one of which had normalized in the third trimester. It is surprising that the incidence of enlarged extra-axial spaces in their study differed substantially from ours, and this may relate to methods of measurement of extra-axial space enlargement. As mentioned in the “Materials and Methods” section, we based our measurements on previously published criteria by Watanabe et al.⁹ The same measurement was also used in another study of fetuses with congenital heart disease, in which the authors found enlarged extra-axial spaces and mild ventriculomegaly as the most common abnormality, seen in 70%.⁸ The enlargement of the extra-axial spaces in the congenital heart disease study was attributed to a combination of delayed maturation and altered CSF dynamics.⁸ However, in our cohort of fetuses with CDH, we did not find any sulcation delay, and we propose some degree of venous sinus hypertension due to intrathoracic mass effect affecting CSF resorption as a cause of the enlarged extra-axial spaces.

Another finding that would support central venous compression in the chest from the diaphragmatic hernia would be the prominent dural sinuses, which we identified in 9 fetuses. We realize that while there are no specific measures of fetal dural venous sinus distention, this specific finding was graded in a blinded fashion by an expert fetal neuroimager (B.M.K.-F.) with 12 years’ experience. In spite of lack of strict objective criteria, dural venous sinus engorgement has also been suggested by other fetal imaging colleagues in informal discussion. Most interesting, the presence of dural venous sinus distention did not correlate with postnatal evidence of brain injury; therefore, the clinical implication of this finding is unclear. It is possible that we failed to demonstrate significant correlations with postnatal brain injury due to the small sample size. Future investigations that would help to better understand venous flow and CSF dynamics could be

directed at measurement of central venous pressures on echocardiograms in fetuses and infants with CDH.

The transient mild ventriculomegaly that we identified in 2 fetuses in the third trimester is of uncertain etiology. Tracy et al⁵ did not identify ventriculomegaly in their cohort of fetuses with CDH. This may, therefore, be an incidental finding.

We identified significant relationships of the severity of lung hypoplasia with postnatal brain injury. The severity of lung hypoplasia is known to be associated with postnatal pulmonary artery hypertension,¹⁶ greater use of extracorporeal membrane oxygenation, and greater neonatal mortality.¹⁷ Spaggiari et al¹⁶ specifically found that observed to expected total lung volume obtained by MR imaging and intrathoracic liver were associated with pul-

Table 3: Findings related to CDH severity on fetal MRI

CDH Severity Markers ^a	
Mean (range) of percentage predicted lung volume	23.4% (11.7%–64%)
Mean (range) of observed-to-expected lung volume (o/e TLV)	0.44 (0.19–0.69)
No. of infants with right-sided diaphragmatic hernia	10 (28%)
No. of infants with liver herniation into chest	19 (53%)
No. of infants with large diaphragmatic defect	21 (58%)

Note:—o/e TLV indicates observed to expected total lung volume.

^a $n = 36$.

Table 4: Findings of brain injury on postnatal MRI

Pattern of Injury ^a	No. (%)
Enlarged extra-axial spaces	16 (44)
Intraventricular hemorrhage	7 (19)
Ventriculomegaly	6 (17)
Cerebellar hemorrhage	6 (17)
White matter injury	6 (17)
Parenchymal hemorrhage	2 (6)

^a $n = 36$.

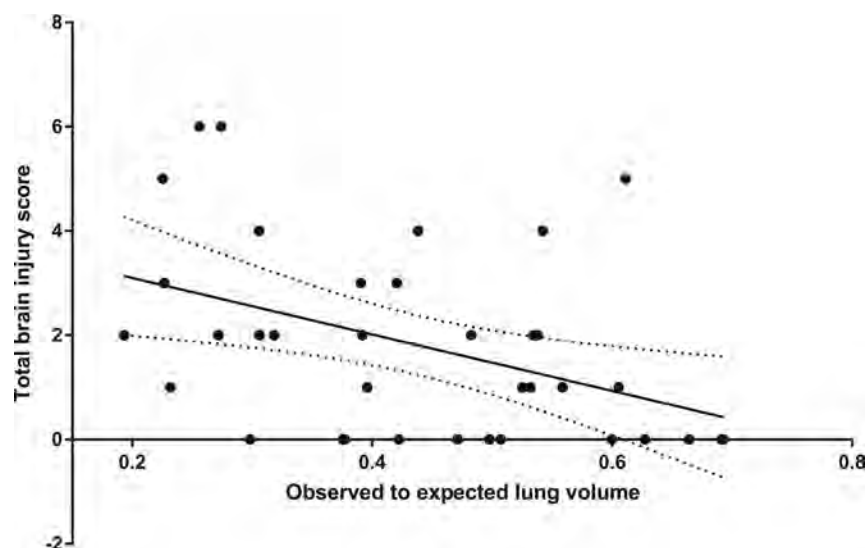


FIG 4. Postnatal brain injury score correlated negatively with observed to expected total lung volume on the latest fetal MR imaging (Pearson correlation coefficient = -0.44 , $P = .008$).

monary artery hypertension, but not right CDH.¹⁶ This information would aid in prenatal counseling because the risk of brain injury may also be increased in severe lung hypoplasia.

Other important information gained from this study is the relative timing of brain injury in infants with CDH. Lack of brain parenchymal injury prenatally and evidence of brain parenchymal injury after a CDH operation suggest that brain injury likely occurs after birth in these infants as they transition out of fetal circulation. Furthermore, in a series of infants with CDH, Tracy et al⁵ showed that the findings of the first postnatal head sonography before surgical correction of CDH were usually normal; this result would indicate that most brain parenchymal injury occurred later in the neonatal period, possibly during the time in the neonatal intensive care unit or the operation. In addition, the use of extracorporeal membrane oxygenation may also be a postnatal contributing factor for brain injury as we identified in our previous neonatal study. This timeline for the occurrence of brain injury in CDH could aid in developing appropriate guidelines for neuroprotective neonatal and surgical care at the time of greatest vulnerability to injury.

Due to the retrospective nature of the study, we were not able to control for other factors unrelated to CDH that might have played a role in the fetal imaging findings in these infants. Detailed maternal history was not always available for review. The size of the fetal brain is much smaller than the neonatal brain, and subtle abnormalities may not be perceptible at this stage with routine anatomic MR imaging. Diffusion tensor imaging may provide additional details on microstructural brain injury in these fetuses with CDH. Due to our small sample size, we may have failed to demonstrate other significant associations between the severity of CDH and prenatal and postnatal brain injury. However, we attempted to reduce bias and improve confidence in our findings by blinded review of fetal and postnatal brain MR imaging findings, as well as CDH severity. Our data show that postnatal brain injury is related to the severity of lung hypoplasia in CDH identified prenatally. The timing of major parenchymal brain injury is likely perinatal or neonatal, and not prenatal.

CONCLUSIONS

We provided a detailed assessment of the association of prenatal brain MR imaging findings and CDH severity with postnatal MR imaging evidence of brain injury. Enlarged extra-axial spaces in the third trimester were found to be the most common abnormality prenatally. Postnatal brain injury was influenced by a measure of prenatal pulmonary hypoplasia (o/e TLV). Absence of maturational delay or major parenchymal injury on fetal MR imaging suggests that these forms of brain injury are likely related to perinatal/early neonatal events rather than in utero injury.

Disclosures: Stephanie Merhar—UNRELATED: Grants/Grants Pending: KL2, Comments: 5KL2TR001426–03, KL2 award for neuroimaging and motor outcomes, Principal Investigator, Merhar; Travel/Accommodations/Meeting Expenses Unrelated to Activities Listed: Pediatrix meeting, Orlando Florida, February 2017. Beth Kline-Fath—UNRELATED: Payment for Lectures Including Service on Speakers Bureaus: Applied Radiology Webinar, Comments: \$1500.

REFERENCES

1. Radhakrishnan R, Merhar S, Meinen-Derr J, et al. **Correlation of MRI brain injury findings with neonatal clinical factors in infants with congenital diaphragmatic hernia.** *AJNR Am J Neuroradiol* 2016;37:1745–51 CrossRef Medline
2. Hunt RW, Kean MJ, Stewart MJ, et al. **Patterns of cerebral injury in a series of infants with congenital diaphragmatic hernia utilizing magnetic resonance imaging.** *J Pediatr Surg* 2004;39:31–36 CrossRef Medline
3. Danzer E, Zarnow D, Gerdes M, et al. **Abnormal brain development and maturation on magnetic resonance imaging in survivors of severe congenital diaphragmatic hernia.** *J Pediatr Surg* 2012;47:453–61 CrossRef Medline
4. Ahmad A, Gangitano E, Odell RM, et al. **Survival, intracranial lesions, and neurodevelopmental outcome in infants with congenital diaphragmatic hernia treated with extracorporeal membrane oxygenation.** *J Perinatol* 1999;19(6 Pt 1):436–40 CrossRef Medline
5. Tracy S, Estroff J, Valim C, et al. **Abnormal neuroimaging and neurodevelopmental findings in a cohort of antenatally diagnosed congenital diaphragmatic hernia survivors.** *J Pediatr Surg* 2010;45:958–65 CrossRef Medline
6. Danzer E, Hedrick HL. **Neurodevelopmental and neurofunctional outcomes in children with congenital diaphragmatic hernia.** *Early Hum Dev* 2011;87:625–32 CrossRef Medline
7. Danzer E, Gerdes M, Bernbaum J, et al. **Neurodevelopmental outcome of infants with congenital diaphragmatic hernia prospectively enrolled in an interdisciplinary follow-up program.** *J Pediatr Surg* 2010;45:1759–66 CrossRef Medline
8. Brossard-Racine M, du Plessis AJ, Vezina G, et al. **Prevalence and spectrum of in utero structural brain abnormalities in fetuses with complex congenital heart disease.** *AJNR Am J Neuroradiol* 2014;35:1593–99 CrossRef Medline
9. Watanabe Y, Abe S, Takagi K, et al. **Evolution of subarachnoid space in normal fetuses using magnetic resonance imaging.** *Prenat Diagn* 2005;25:1217–22 CrossRef Medline
10. Wax JR, Bookman L, Cartin A, et al. **Mild fetal cerebral ventriculomegaly: diagnosis, clinical associations, and outcomes.** *Obstet Gynecol Surv* 2003;58:407–14 Medline
11. Kline-Fath BM. **Fetal magnetic resonance imaging: normal brain imaging.** In: Kline-Fath BM, Bulas DJ, Bahado-Singh R, eds. *Fundamental and Advanced Fetal Imaging: Ultrasound and MRI.* Philadelphia: Wolters Kluwer; 2015
12. Danzer E, Gerdes M, D'Agostino JA, et al. **Longitudinal neurodevelopmental and neuromotor outcome in congenital diaphragmatic hernia patients in the first 3 years of life.** *J Perinatol* 2013;33:893–98 CrossRef Medline
13. Barnewolt CE, Kunisaki SM, Fauza DO, et al. **Percent predicted lung volumes as measured on fetal magnetic resonance imaging: a useful biometric parameter for risk stratification in congenital diaphragmatic hernia.** *J Pediatr Surg* 2007;42:193–97 CrossRef Medline
14. Rypens F, Metens T, Rocourt N, et al. **Fetal lung volume: estimation at MR imaging—initial results.** *Radiology* 2001;219:236–41 CrossRef Medline
15. Tsao K, Lally KP. **The Congenital Diaphragmatic Hernia Study Group: a voluntary international registry.** *Semin Pediatr Surg* 2008;17:90–97 CrossRef Medline
16. Spaggiari E, Stirnemann JJ, Sonigo P, et al. **Prenatal prediction of pulmonary arterial hypertension in congenital diaphragmatic hernia.** *Ultrasound Obstet Gynecol* 2015;45:572–77 CrossRef Medline
17. Büsing KA, Kilian AK, Schaible T, et al. **MR relative fetal lung volume in congenital diaphragmatic hernia: survival and need for extracorporeal membrane oxygenation.** *Radiology* 2008;248:240–46 CrossRef Medline

T2 Relaxometry MRI Predicts Cerebral Palsy in Preterm Infants

L.-W. Chen, S.-T. Wang, C.-C. Huang, Y.-F. Tu, and Y.-S. Tsai



ABSTRACT

BACKGROUND AND PURPOSE: T2-relaxometry brain MR imaging enables objective measurement of brain maturation based on the water-macromolecule ratio in white matter, but the outcome correlation is not established in preterm infants. Our study aimed to predict neurodevelopment with T2-relaxation values of brain MR imaging among preterm infants.

MATERIALS AND METHODS: From January 1, 2012, to May 31, 2015, preterm infants who underwent both T2-relaxometry brain MR imaging and neurodevelopmental follow-up were retrospectively reviewed. T2-relaxation values were measured over the periventricular white matter, including sections through the frontal horns, midbody of the lateral ventricles, and centrum semiovale. Periventricular T2 relaxometry in relation to corrected age was analyzed with restricted cubic spline regression. Prediction of cerebral palsy was examined with the receiver operating characteristic curve.

RESULTS: Thirty-eight preterm infants were enrolled for analysis. Twenty patients (52.6%) had neurodevelopmental abnormalities, including 8 (21%) with developmental delay without cerebral palsy and 12 (31.6%) with cerebral palsy. The periventricular T2-relaxation values in relation to age were curvilinear in preterm infants with normal development, linear in those with developmental delay without cerebral palsy, and flat in those with cerebral palsy. When MR imaging was performed at >1 month corrected age, cerebral palsy could be predicted with T2 relaxometry of the periventricular white matter on sections through the midbody of the lateral ventricles (area under the receiver operating characteristic curve = 0.738; cutoff value of >217.4 with 63.6% sensitivity and 100.0% specificity).

CONCLUSIONS: T2-relaxometry brain MR imaging could provide prognostic prediction of neurodevelopmental outcomes in premature infants. Age-dependent and area-selective interpretation in preterm brains should be emphasized.

ABBREVIATIONS: BSID-II = Bayley Scales of Infant and Toddler Development, 2nd ed; BSID-III = Bayley Scales of Infant and Toddler Development, 3rd ed; CP = cerebral palsy; DD = delayed development; ROC = receiver operating characteristic curve

Preterm infants are at high risk of cognitive and behavior problems. It remains a challenging issue in 50%–60% of extremely preterm infants despite the advances in neonatal critical care.¹ Although late preterm infants born between 33 and 37 weeks of gestational age are considered low-risk, the

neurodevelopmental scales still fall behind compared with term controls.²

MR imaging is considered a good tool for early diagnosis of brain injury in prematurity, but the conventional qualitative approach remains subjective.^{3,4} The incidence of macroscopic cystic-necrotic periventricular leukomalacia has markedly declined, and new forms of microscopic focal or diffuse nondestructive white matter injury are emerging.⁵ However, this microscopic necrosis and gliosis is not readily detected by conventional MR imaging.⁶

T2 relaxometry, also called T2 mapping, is a quantitative T2-weighted MR imaging that demonstrates the physical properties of brain-water, enabling objective measurement of tissue characteristics based on the water-macromolecule ratio in white matter. In very preterm infants, T2 relaxometry has been applied to discriminate diffuse excessive high signal intensity in white matter at term-equivalent age.⁷ However, the changes of T2 relaxometry in preterm periventricular WM injury and

Received July 12, 2017; accepted after revision October 30.

From the Departments of Pediatrics (L.-W.C., C.-C.H., Y.-F.T.) and Diagnostic Radiology (Y.-S.T.), National Cheng Kung University Hospital, College of Medicine, National Cheng Kung University, Tainan, Taiwan; Institutes of Clinical Medicine (L.-W.C.) and Gerontology (S.-T.W.), College of Medicine, National Cheng Kung University, Tainan, Taiwan; and Department of Pediatrics (C.-C.H.), Taipei Medical University, College of Medicine, Taipei, Taiwan.

This work was supported by National Cheng Kung University Hospital-10403006.

Please address correspondence to Yi-Shan Tsai, MD, Department of Diagnostic Radiology, National Cheng Kung University Hospital, College of Medicine, National Cheng Kung University, 138 Sheng-Li Rd, Tainan City 70403, Taiwan; e-mail: crevice123@hotmail.com

Indicates open access to non-subscribers at www.ajnr.org

<http://dx.doi.org/10.3174/ajnr.A5501>

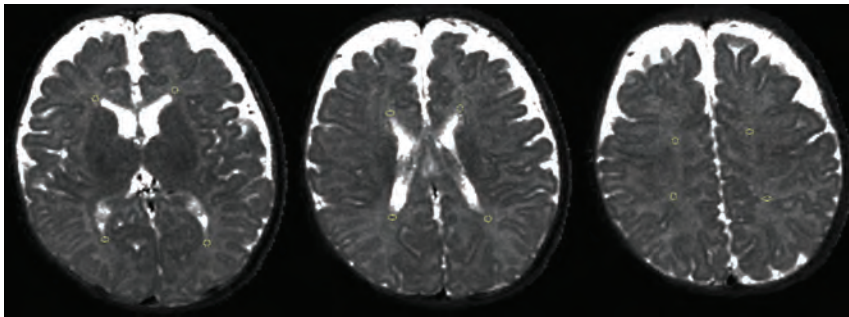


FIG 1. Manually drawn periventricular white matter on 3 axial sections through the frontal horns, midbody of the lateral ventricles, and centrum semiovale. The circular ROI area is 5–8 mm². The 4 T2-mapping values of each section are averaged for calculation.

further correlation to neurodevelopmental outcomes have not been established.^{4,7}

In contrast to the physiologic decrease of cerebral water in healthy infants, WM injury leading to delayed myelination and tissue destruction may present with free water retention and prolong the T2 value on brain MR imaging.⁸ Our study hypothesizes that there are distinct patterns of T2 relaxometry according to the neurodevelopmental status. Furthermore, this study provides a model of outcome prediction with T2-relaxometry brain MR imaging in premature infants.

MATERIALS AND METHODS

Participants

From January 1, 2012, to May 31, 2015, preterm infants (born at <37-week gestational age) who underwent T2-relaxometry brain MR imaging at younger than 1 year of age were included. The demographic data and clinical indications of brain MR imaging were retrospectively reviewed. We excluded patients with major neurologic underlying diseases, such as congenital cerebral malformation, hypoxic-ischemic encephalopathy, shaken baby syndrome, and neonatal/infantile epilepsy. Patients who had neurodevelopmental follow-up for >12 months in the hospital were enrolled for analysis. The institutional review board of National Cheng Kung University Hospital approved the study.

Neuroimaging Studies

The patients were scanned on an Achieva 1.5T MR imaging scanner (Philips Healthcare, Best, the Netherlands). The infants were swaddled and administered oral chloral hydrate (50 mg per kilogram) before MR imaging. The pulse sequences included axial T1WI, axial T2WI, FLAIR, DWI, and T2 relaxometry. T2 relaxometry was performed using an ultrafast turbo gradient spin-echo sequence (TSE factor, 5; TR/TE, 3500/20, 40, 60, 80, 100 ms; twenty-eight 4-mm-thick axial sections without a slice gap; FOV, 200 × 200 mm²; matrix, 224 × 200; voxel size, 0.9 × 1 mm; bandwidth, 73.7 Hz/pixel; acquisition time 4 minutes 50 seconds).

Three sections of periventricular white matter, including axial sections through the frontal horns, midbody of the lateral ventricles, and centrum semiovale, were selected for analyses (Fig 1).^{9,10} A circular ROI with 5- to 8-mm² area was positioned for measurement. For sections through the frontal horns and midbody of the lateral ventricles, ROIs were placed over the periventricular white matter of the anterior and posterior ventricular poles. For the

centrum semiovale, ROIs were placed over 2 sites in each hemisphere. The 4 T2-mapping values of each section were averaged. When there were cystic lesions in the periventricular white matter, the ROIs were placed over the nearby parenchymal tissue rather than the fluid component within the cysts. The measurements were performed twice by 1 pediatric neurologist and once by 1 radiologist, generating intrarater and interrater reliabilities. Data of the 3 measurements were averaged for final analyses.

Neurodevelopmental Outcomes

Neurodevelopmental evaluations were performed at the outpatient clinics by pediatric neurologists, who decided the eligibility for tests with the Bayley Scales of Infant and Toddler Development, 2nd ed (BSID-II) or 3rd ed (BSID-III). Delayed development (DD) was defined with a motor or language scale of <70 with the BSID-II or a cognitive, motor, or language scale of <85 with the BSID-III.¹¹ Cerebral palsy (CP), apart from the pure DD, was defined as severe impairment of motor function with spasticity due to nonprogressive disturbances in the brain.¹²

Statistical Analysis

The T2-quantification values of periventricular white matter in relation to age were fitted with semi-log plots and further analyzed with restricted cubic spline regression in preterm infants with normal development, DD without CP, and CP. The comparison between the CP and non-CP groups was performed with the χ^2 test for categorical variables and the Mann-Whitney *U* test for numeric variables, evaluating the differences in average attenuation values and the adjusted attenuation values. To predict CP with T2 relaxometry, we assessed the logistic regression with the backward selection method and the receiver operating characteristic (ROC) curve.¹³ Cut-point estimation, 95% confidence interval, and areas under the ROC curve were calculated. Sensitivities and specificities at cutoff points were determined with the Youden index. The level of significance was set at $P < .05$. The intrarater reliability was represented with the intraclass correlation, which was rated as fair at 0.40–0.59, good at 0.60–0.74, and excellent when >0.74.¹⁴ The interrater reliability was represented with the interrater agreement κ coefficient and was defined as moderate at 0.41–0.60, good at 0.61–0.80, and very good at 0.81–1.00.¹⁵

Statistical analysis was performed using commercially available software (MedCalc for Windows, Version 14.8.1; MedCalc Software, Mariakerke, Belgium.) The age-versus-T2-quantification graphs and semi-log lines were plotted with GraphPad Prism 5 software (GraphPad Software, San Diego, California). Restricted cubic spline regression and prediction models of CP were performed with SAS statistical software (SAS Institute, Cary, North Carolina).

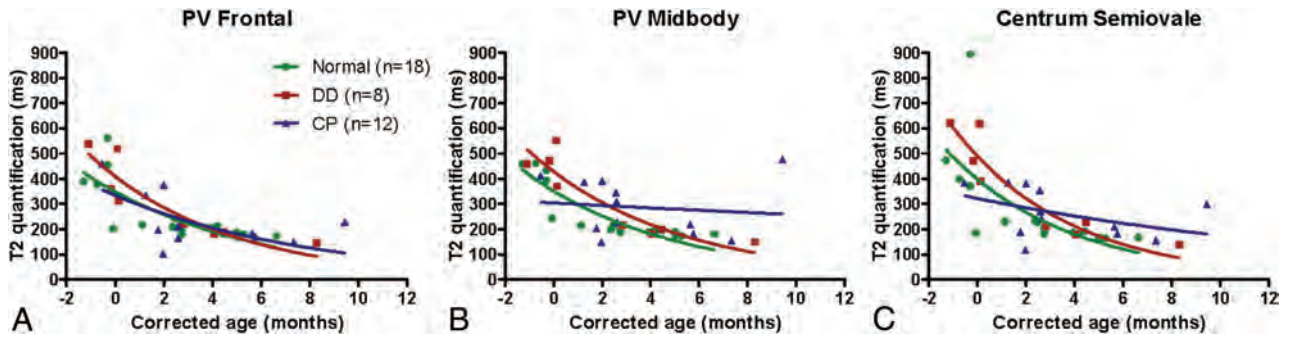


FIG 2. T2-relaxation values versus age among patients with normal development, delayed development without cerebral palsy, and cerebral palsy. T2 quantification in periventricular white matter declines with age. Periventricular white matter through sections of the frontal horns of the lateral ventricles (A), midbody of the lateral ventricles (B), and centrum semiovale (C). DD indicates delayed development (without cerebral palsy); PV, periventricular.

RESULTS

During the study period, 57 preterm infants underwent 60 brain MR imaging examinations with T2 relaxometry before 1 year of age. For patients who had >1 brain MR imaging, only the first study was analyzed. Nineteen patients were excluded because of congenital cerebral malformation ($n = 6$), neonatal/infantile epilepsy ($n = 5$), loss to follow-up ($n = 4$), hypoxic-ischemic encephalopathy ($n = 2$), shaken baby syndrome ($n = 1$), and poor imaging quality ($n = 1$). Thus, 38 patients were enrolled for analysis.

The average gestational age was 31.8 ± 3.4 weeks (range, 24.0–37.0 weeks), and the mean birth weight was 1675.7 ± 771.4 g (range, 505–3554 g). Among the 38 preterm infants, 7 were girls and 31 were boys. Five patients had brain MR imaging due to CNS symptoms, and the other 33 patients without clinical symptoms had brain MR imaging for abnormalities on screening brain sonography. CNS symptoms included isolated seizure ($n = 2$), CNS infection ($n = 1$), facial palsy ($n = 1$), and precocious puberty ($n = 1$). Abnormalities on screening brain sonography included persistent periventricular hyperechogenicity ($n = 18$), periventricular leukomalacia ($n = 7$), ventriculomegaly ($n = 6$), porencephalic cyst ($n = 1$), and absence of the septum pellucidum ($n = 1$).

Neurodevelopment was followed for a mean of 31.7 ± 9.9 months (range, 12.0–50.2 months). Among the 38 patients, 29 were evaluated with the BSID-III, and 3, with the BSID-II. The BSID examinations were performed at a mean age of 21.1 ± 7.1 months; (range, 7.0–34.0 months). The remaining 6 patients, for whom BSID tests were not arranged, were confirmed as having normal neurodevelopmental statuses by pediatric neurologists during scheduled visits. Among the 38 patients, 20 (52.6%) had developmental disorders, including 8 (21%) with pure DD without CP and 12 (31.6%) with CP.

Brain MR imaging was performed at a mean of 2.8-month corrected age, ranging from 1.3 months before term to 9.4 months of age. The intrarater correlation coefficients corresponding to periventricular white matter ranged from 0.73 to 0.78, indicating good-to-excellent intraobserver reliability. The interrater agreement coefficients among regions of white matter ranged from 0.57 to 0.73, suggesting moderate-to-good reliability between the 2 observers.

The age-dependent curve of T2-relaxometry values versus corrected age is shown in Fig 2. In infants with normal neurode-

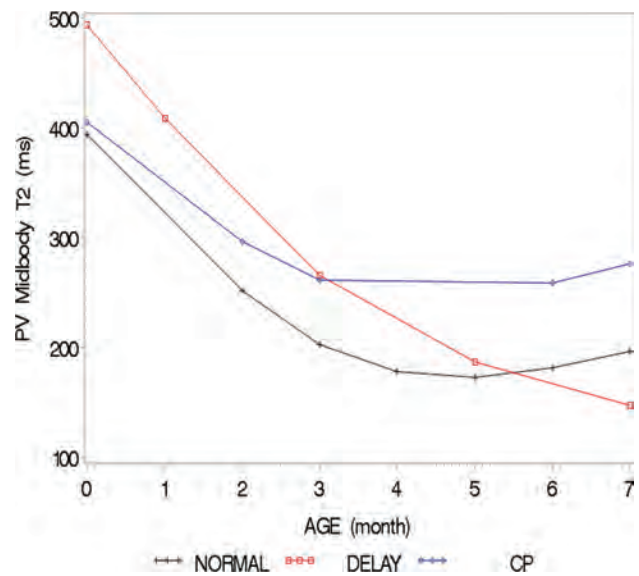


FIG 3. Restricted cubic spline regression analysis of T2 relaxometry versus age in the midbody periventricular white matter. T2-quantification values in relation to age are curvilinear, linear, and flat among normal development (black line), delayed development (red line), and cerebral palsy (blue line) in preterm infants, respectively. PV indicates periventricular.

velopment and patients with DD, T2-relaxometry values decreased with age. However, the T2-quantification values in the CP group did not show a rapid decline, especially in the periventricular white matter around the midbody of the lateral ventricles and centrum semiovale. Further analysis with restricted cubic spline regression showed that T2 relaxation values at the periventricular white matter in relation to age were curvilinear in normal development, linear in DD, and flat in CP (Fig 3).

For age-specific analysis of CP prediction, patients were reclassified into 2 groups according to MR imaging before or after 1-month corrected age (Table).^{16,17} There was only 1 patient who developed CP among the 10 neonates who underwent MR imaging examinations before 1 month of age. T2 mapping had no statistically significant impact on prediction of CP in this group. Twenty-eight patients had MR imaging performed after 1-month corrected age (mean corrected age of MR imaging, 4.2 ± 2.1 months), and there were 11 patients diagnosed with CP. There was no difference in sex, gestational age, birth body weight, and

Demographic data of birth history, birth condition, and T2 relaxometry values at 3 different sections of periventricular white matter^a

	≤1 m/o CGA at MRI (n = 10)		>1 m/o CGA at MRI (n = 28)		P Value
	Non-CP	CP	Non-CP	CP	
No.	9	1	17	11	
Sex, M/F	9:0	1:0	12:5	9:2	.823
GA (wk)	32.3 ± 3.1	37.0	31.9 ± 3.4	30.9 ± 3.6	.397
BBW (gm)	1586.6 ± 746.4	2160	1863.3 ± 862.8	1411.1 ± 675.0	.158
DOIC (+) (No.)	4/9	0	9/17	1/8	.137
PROM (+) (No.)	2/9	0	5/17	1/8	.673
1st Apgar ^b score	4.6 ± 2.5	9	4.9 ± 2.4	6.3 ± 1.5	.217
2nd Apgar ^b score	6.7 ± 2.2	10	7.7 ± 2.1	8.2 ± 0.8	.800
CGA at MRI (mo)	-0.4 ± 0.5	-0.5	4.0 ± 1.7	3.9 ± 2.7	.410
PV frontal	412.5 ± 116.5	458.8	194.8 ± 24.1	211.1 ± 79.7	.814
PV midbody	426.4 ± 85.2	410.8	191.3 ± 16.9	226.8 ± 110.6	.036 ^c
Centrum semiovale	491.3 ± 201.0	382.6	186.9 ± 28.0	252.8 ± 92.5	.086

Note:—m/o indicates month old; CGA, corrected gestational age; GA, gestational age; BBW, birth body weight; DOIC, delay of initial crying; PROM, premature rupture of membrane; PV, periventricular.

^aData are mean ± SD unless otherwise indicated.

^bThe Apgar score is an assessment of overall newborn well-being.

^cP value < .05.

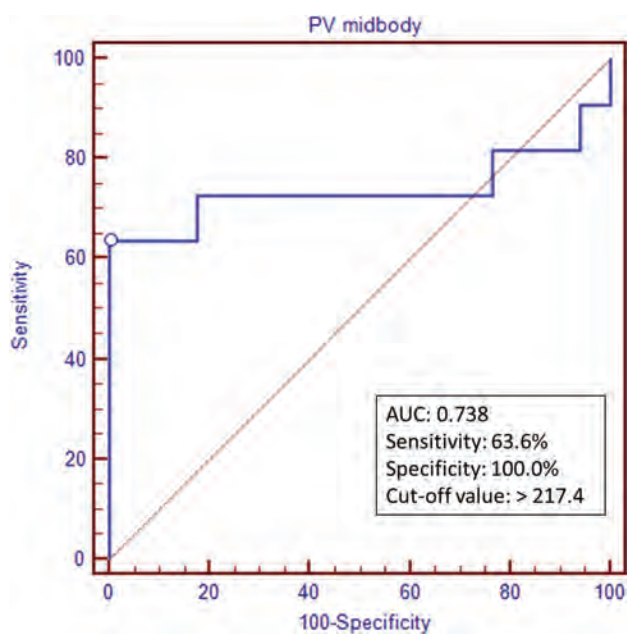


FIG 4. Receiver operating characteristic curves of T2 relaxometry on the sections through the midbody of the lateral ventricles.

birth condition between the patients with and without CP in this group. The periventricular T2-relaxometry value around the midbody of the lateral ventricles was significantly higher in patients with CP ($P = .036$). The area under the ROC curve for predicting CP with T2-relaxation values in the midbody periventricular white matter was 0.738 (95% CI, 0.538–0.885) with ROC analysis. The sensitivity and specificity for diagnosing CP using the optimized cutoff point of the T2 relaxometry value (>217.4) were 63.6% and 100%, respectively (Fig 4).

DISCUSSION

With the advances of neonatal intensive care, macroscopic cystic periventricular leukomalacia has been replaced by other forms of white matter lesions, including microscopic necrosis and diffuse white matter injury, both of which are prone to be underestimated in conventional qualitative MR imaging.¹⁸ T2 relaxometry is a fast scan to quantify tissue characteristics, providing an objec-

tive measurement of the watery contents of the brain.⁴ Our study found that white matter maturation patterns were different depending on the neurologic outcomes because T2 relaxometry showed curvilinear decline in preterm infants with normal development, linear decline in those with DD, and was flat in those with CP.

T2-relaxation values descended rapidly in the first few months due to the fast myelination process during the first year of life.^{19,20} This rapid decline of T2 relaxometry observed in normal brain maturation corresponded to the curvilinear decline in our preterm infants with normal development. In this study, the altered T2 relaxometry patterns in the CP group illustrated slower decline of T2 quantification, with relatively lower T2 values in the early stage of WM injury and higher T2 values in the later stage.

The T2-relaxation values in periventricular WM in 2.4T MR imaging ranged from 214 to 247 ms when healthy premature infants were scanned at 37 weeks of postconceptional age, suggesting the watery characteristics of brain tissue in premature infants at the perinatal stage.²¹ In our study of infants with CP, the damaged WM revealed lower T2 relaxation than the normal watery WM in the neonatal period and higher T2 relaxation values than the normal myelinated WM in later infancy. Previous animal studies found that T2WI hypointensity in the early stage of cerebral WM injury was related to pathologic microcysts and diffuse noncystic gliosis, and our observation of lower T2 values at the early stage of WM injury in infants with CP may reflect the pathologic changes.^{22,23}

During a normal developmental process, the anterior caps and posterior periventricular bands in the deep white matter around the lateral ventricles are associated with the denseness of migrating neurons and white matter fibers converging from different regions of the hemisphere.²⁴ The T2WI signals could vary according to the neuronal cells and fiber composition; however, all these caps and periventricular bands should not be obvious after 40 weeks of gestational age.^{10,25} Furthermore, the brain free water in the deep cerebral white matter starts to decrease physiologically after 1 month of life.¹⁷ As a result, to diminish the effects of caps/periventricular bands and water decline interferences, we regrouped the patients according to MR imaging before or after 1-month corrected age for analysis of CP prediction.

In our observation, T2-relaxation values of the midbody periventricular white matter could predict CP when MR imaging was performed after 1-month corrected age. In preterm infants, T2 relaxometry of >217.4 predicted CP with 63.6% sensitivity and 100.0% specificity. When predicting outcomes with the signals on T2-quantification MR imaging, infants' ages should be considered cautiously. Although not a very early neuroimaging indicator compared with other studies using term-equivalent age MR imaging,³ our T2-quantification model could still enhance the clinical judgment in high-risk preterm infants because the diagnosis of cerebral palsy might sometimes be equivocal before 18 months of age.¹²

The study was limited by the retrospective design and small sample size. Prediction of outcomes with MR imaging before 1-month corrected age could not be achieved because of the small study population. In the study, only preterm infants who had clinical indications for brain MR imaging were included; thus, there was selection bias resulting in the higher rates of CP and DD in our series.¹² The significance of T2 quantification in preterm cerebral development should be further verified through universal studies in both high- and low-risk preterm infants. The tools of developmental evaluation in the study included BSID-II and BSID-III. Although there was discrepancy between the 2 editions, the correlation of BSID-II and BSID-III in preterm infants has been addressed in other investigations.¹¹ The analyses of developmental performance with categoric outcomes further excluded the direct comparison between BSID-II and BSID-III scores.

In our work, T2 relaxometry was estimated with 5 TEs (20, 40, 60, 80, 100 ms); however, the maximum TE of 100 ms may not be long enough for accurate measurements in premature infants' brains. The value for the T2 relaxometry would be underestimated when using few echoes and an insufficient TE. For better estimation, previous studies suggested that 32 echoes with multi-exponential fits were optimal to define the T2-decay curve; however, the long scanning time may be a restriction for young infants.^{26,27} The precision of T2-relaxometry measurements could be diminished due to partial volume effects because the spatial resolution was limited in the study. The T2-quantification values might be expanded because of mixed periventricular white matter and adjacent CSF within the ROIs. Early quantitative MR imaging in thin slices with autocalculation computer programs may provide more precise prediction than the results in our study.^{3,28} However, the simple manual measurement of T2 relaxometry in specific white matter areas could still be useful clinically.

Our study focused on the neuroimaging-neurodevelopmental correlations, and the clinical events regarding the perinatal complications were not analyzed. Further comprehensive studies of T2-quantification MR imaging in a large population of preterm infants could provide more illustrative information on the interaction of perinatal clinical events, neuroimaging variations, and long-term neurobehavioral outcomes.

CONCLUSIONS

T2-relaxometry brain MR imaging could be of prognostic value in preterm infants. The maturation patterns of periventricular white matter differed according to neurodevelopmental outcomes. T2 relaxation values over the midbody periventricular white matter

at >1 -month corrected age could predict CP. T2-relaxometry brain MR imaging provides neuroimaging-outcome correlation among preterm infants, especially when interpreted with age-specific and area-selective considerations.

ACKNOWLEDGMENTS

We thank Mr Feng-Mao Chiu, the clinical MR imaging application specialist of Philips Healthcare, for the support in the simulation model in T2-estimation accuracy.

REFERENCES

1. Kidokoro H, Anderson PJ, Doyle LW, et al. **Brain injury and altered brain growth in preterm infants: predictors and prognosis.** *Pediatrics* 2014;134:e444–53 CrossRef Medline
2. Romeo DM, Brogna C, Sini F, et al. **Early psychomotor development of low-risk preterm infants: influence of gestational age and gender.** *Eur J Paediatr Neurol* 2016;20:518–23 CrossRef Medline
3. Plaisier A, Raets MM, Ecury-Goossen GM, et al. **Serial cranial ultrasonography or early MRI for detecting preterm brain injury?** *Arch Dis Child Fetal Neonatal Ed* 2015;100:F293–300 CrossRef Medline
4. He L, Parikh NA. **Atlas-guided quantification of white matter signal abnormalities on term-equivalent age MRI in very preterm infants: findings predict language and cognitive development at two years of age.** *PLoS One* 2013;8:e85475 CrossRef Medline
5. Ment LR, Hirtz D, Hüppi PS. **Imaging biomarkers of outcome in the developing preterm brain.** *Lancet Neurol* 2009;8:1042–55 CrossRef Medline
6. Pierson CR, Folkerth RD, Billiards SS, et al. **Gray matter injury associated with periventricular leukomalacia in the premature infant.** *Acta Neuropathol* 2007;114:619–31 CrossRef Medline
7. Hagmann CF, De Vita E, Bainbridge A, et al. **T2 at MR imaging is an objective quantitative measure of cerebral white matter signal intensity abnormality in preterm infants at term-equivalent age.** *Radiology* 2009;252:209–17 CrossRef Medline
8. Ashikaga R, Araki Y, Ono Y, et al. **Appearance of normal brain maturation on fluid-attenuated inversion-recovery (FLAIR) MR images.** *AJNR Am J Neuroradiol* 1999;20:427–31 Medline
9. He L, Parikh NA. **Automated detection of white matter signal abnormality using T2 relaxometry: application to brain segmentation on term MRI in very preterm infants.** *Neuroimage* 2013;64:328–40 CrossRef Medline
10. Maalouf EF, Duggan PJ, Rutherford MA, et al. **Magnetic resonance imaging of the brain in a cohort of extremely preterm infants.** *J Pediatr* 1999;135:351–57 CrossRef Medline
11. Moore T, Johnson S, Haider S, et al. **Relationship between test scores using the second and third editions of the Bayley Scales in extremely preterm children.** *J Pediatr* 2012;160:553–58 CrossRef Medline
12. Spittle AJ, Orton J. **Cerebral palsy and developmental coordination disorder in children born preterm.** *Semin Fetal Neonatal Med* 2014;19:84–89 CrossRef Medline
13. Steyerberg EW, Vickers AJ, Cook NR, et al. **Assessing the performance of prediction models: a framework for traditional and novel measures.** *Epidemiology* 2010;21:128–38 CrossRef Medline
14. Fleiss, JL. *Statistical Methods for Rates and Proportions.* 2nd ed. New York: Wiley; 1981
15. Altman DG. *Practical Statistics for Medical Research.* London: Chapman and Hall/CRC; 1990
16. Welker KM, Patton A. **Assessment of normal myelination with magnetic resonance imaging.** *Semin Neurol* 2012;32:15–28 CrossRef Medline
17. Murakami JW, Weinberger E, Shaw DW. **Normal myelination of the pediatric brain imaged with fluid-attenuated inversion-recovery (FLAIR) MR imaging.** *AJNR Am J Neuroradiol* 1999;20:1406–11 Medline
18. Back SA. **Brain injury in the preterm infant: new horizons for**

- pathogenesis and prevention. *Pediatr Neurol* 2015;53:185–92 CrossRef Medline
19. Ding XQ, Kucinski T, Wittkugel O, et al. **Normal brain maturation characterized with age-related T2 relaxation times: an attempt to develop a quantitative imaging measure for clinical use.** *Invest Radiol* 2004;39:740–46 CrossRef Medline
 20. Leppert IR, Almlı CR, McKinstry RC, et al; Brain Development Cooperative Group. **T(2) relaxometry of normal pediatric brain development.** *J Magn Reson Imaging* 2009;29:258–67 CrossRef Medline
 21. Ferrie JC, Barantin L, Saliba E, et al. **MR assessment of the brain maturation during the perinatal period: quantitative T2 MR study in premature newborns.** *Magn Reson Imaging* 1999;17:1275–88 CrossRef Medline
 22. Riddle A, Dean J, Buser JR, et al. **Histopathological correlates of magnetic resonance imaging-defined chronic perinatal white matter injury.** *Ann Neurol* 2011;70:493–507 CrossRef Medline
 23. Jeon TY, Kim JH, Yoo SY, et al. **Neurodevelopmental outcomes in preterm infants: comparison of infants with and without diffuse excessive high signal intensity on MR images at near-term-equivalent age.** *Radiology* 2012;263:518–26 CrossRef Medline
 24. Childs AM, Ramenghi LA, Evans DJ, et al. **MR features of developing periventricular white matter in preterm infants: evidence of glial cell migration.** *AJNR Am J Neuroradiol* 1998;19:971–76 Medline
 25. Girard N, Raybaud C, Poncet M. **In vivo MR study of brain maturation in normal fetuses.** *AJNR Am J Neuroradiol* 1995;16:407–13 Medline
 26. Whittall KP, MacKay AL, Graeb DA, et al. **In vivo measurement of T2 distributions and water contents in normal human brain.** *Magn Reson Med* 1997;37:34–43 CrossRef Medline
 27. Whittall KP, MacKay AL, Li DK. **Are mono-exponential fits to a few echoes sufficient to determine T2 relaxation for in vivo human brain?** *Magn Reson Med* 1999;41:1255–57 Medline
 28. Sled JG, Nossin-Manor R. **Quantitative MRI for studying neonatal brain development.** *Neuroradiology* 2013;55(suppl 2):97–104 CrossRef Medline

Expression Changes in Lactate and Glucose Metabolism and Associated Transporters in Basal Ganglia following Hypoxic-Ischemic Reperfusion Injury in Piglets

Y. Zheng and X.-M. Wang



ABSTRACT

BACKGROUND AND PURPOSE: The neonatal brain has active energy metabolism, and glucose oxidation is the major energy source of brain tissue. Lactate is produced by astrocytes and released to neurons. In the central nervous system, lactate is transported between neurons and astrocytes via the astrocyte-neuron lactate shuttle. The aim of this study was to investigate the regulatory mechanisms of energy metabolism in neurons and astrocytes in the basal ganglia of a neonatal hypoxic-ischemic brain injury piglet model.

MATERIALS AND METHODS: A total of 35 healthy piglets (3–5 days of age; 1.0–1.5 kg) were assigned to a control group ($n = 5$) or a hypoxic-ischemic model group ($n = 30$). The hypoxic-ischemic model group was further divided into 6 groups according to the ^1H -MR spectroscopy and PET/CT scan times after hypoxia-ischemia (0–2, 2–6, 6–12, 12–24, 24–48, and 48–72 hours; $n = 5/\text{group}$). ^1H -MR spectroscopy data were processed with LCModel software. Maximum standard uptake values refer to the maximum standard uptake values for glucose (or FDG). The maximum standard uptake values of the basal ganglia-to-occipital cortex ratio were analyzed. The expression levels of glucose transporters and monocarboxylate transporters were detected by immunohistochemical analysis.

RESULTS: Lactate levels decreased after an initial increase, with the maximal level occurring around 2–6 hours following hypoxia-ischemia. After hypoxia-ischemia, the maximum standard uptake values of the basal ganglia and basal ganglia/occipital cortex initially increased then decreased, with the maximum occurring at approximately 6–12 hours. The lactate and glucose uptake (basal ganglia/occipital cortex maximum standard uptake values) levels were positively correlated. The expression levels of glucose transporter-1 and glucose transporter-3 were positively correlated with the basal ganglia/occipital cortex. The expression levels of monocarboxylic acid transporter-2 and monocarboxylic acid transporter-4 were positively correlated with lactate content.

CONCLUSIONS: The results indicate that lactate and glucose transporters have a synergistic effect on the energy metabolism of neurons and astrocytes following hypoxic-ischemic reperfusion brain injury.

ABBREVIATIONS: ANLS = astrocyte-neuron lactate shuttle; BG = basal ganglia; GLUT = glucose transporter; HI = hypoxic-ischemic; MCT = monocarboxylic acid transporter; OC = occipital cortex; SUV_{max} = maximum standard uptake values

Recent studies of the astrocyte-neuron lactate shuttle (ANLS) suggest that lactate is generated and released by astrocytes in the process of glucose metabolism and is further taken up and metabolized by neurons as an oxidizing substrate in energy me-

tabolism in the brain.^{1,2} Lactate metabolism provides adenosine triphosphate to neurons under hypoxic conditions.³ The ANLS requires monocarboxylic acid transporters on the plasma membranes of both neurons and astrocytes for transfer of lactate, pyruvate, and other monocarboxylic acids, as well as acetoacetic acid, β -hydroxybutyric acid, and so forth.⁴ Astrocytes and neurons express different monocarboxylate transporter (MCT) subtypes, because astrocytes primarily express MCT-4 and neurons primarily express MCT-2.⁵ Lactate and its transporters play important roles in cell metabolism under hypoxic-ischemic conditions.² The transport and uptake of lactate between astrocytes and neurons are mediated by MCTs. Briefly, lactate is transported out of astrocytes by membrane-bound MCT-4 and gathers in the extracellular compartment. Neurons then take up lactate through membrane-bound MCT-2, which is then converted to acetone by

Received May 9, 2017; accepted after revision October 30.

From the Department of Radiology, Shengjing Hospital of China Medical University, Shenyang, PR China.

This study was supported by the National Natural Science Foundation of China (No. 30570541, 30770632, 81271631) and the Outstanding Scientific Fund of Shengjing Hospital (No. 201402).

Please address correspondence to Xiaoming Wang, MD, Department of Radiology, Shengjing Hospital of China Medical University, No. 36, Sanhao St, Heping District, Shenyang 110004, PR China; e-mail address: wangxm024@163.com; @little_yangyang

Indicates open access to non-subscribers at www.ajnr.org

<http://dx.doi.org/10.3174/ajnr.A5505>

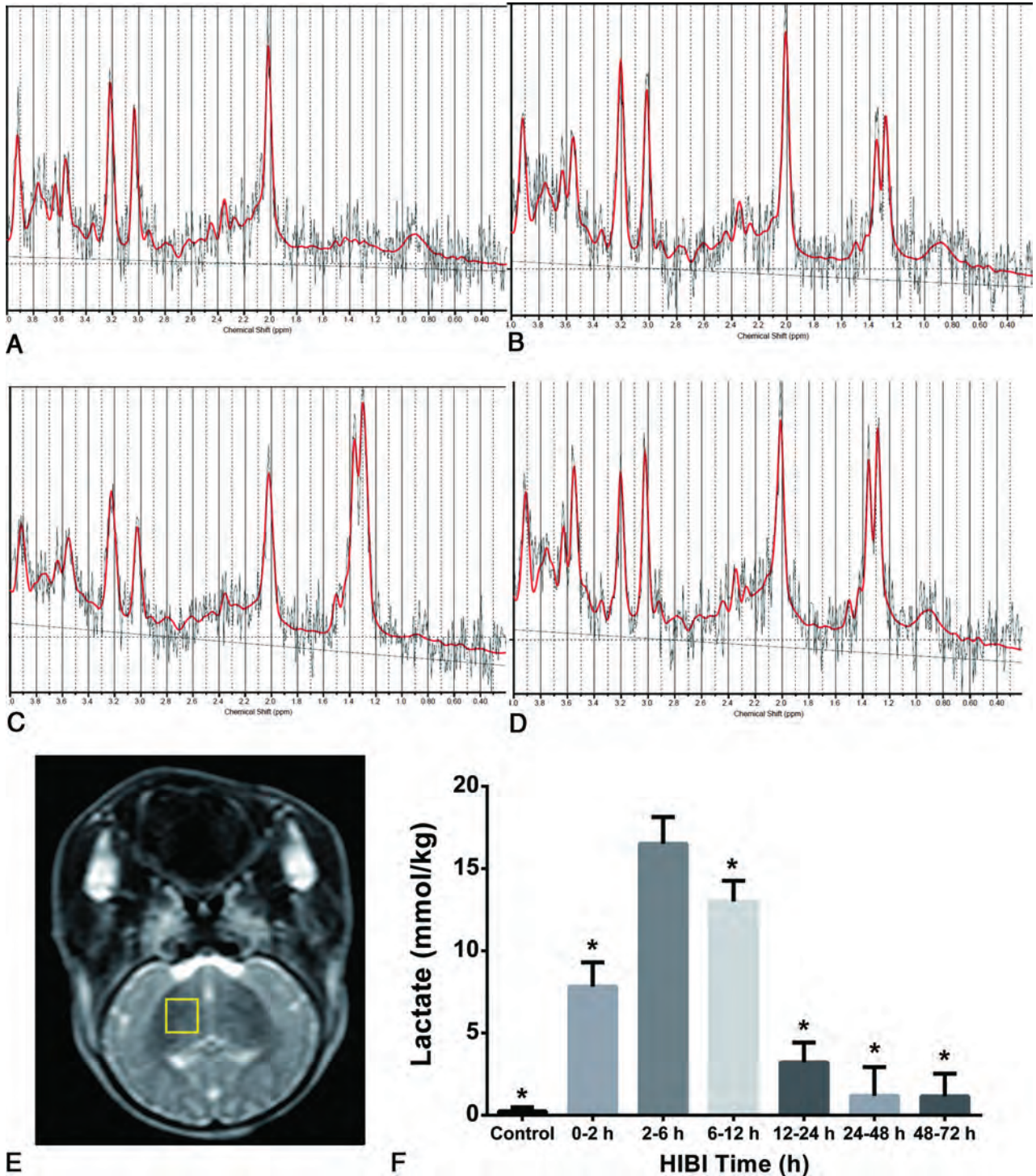


FIG 1. Changes in ^1H -MR spectroscopy spectra and lactate content in the BG within 72 hours after HI. ^1H -MR spectroscopy spectra of the right BG of the control and HI model groups at 0–2, 2–6, and 6–12 hours after HI are shown as A–D (lactate peak is located at 1.33 ppm). The lactate peak in the control group is low and flat (A) and peaked at 2–6 hours after HI (C). ROI selection (E): right BG (yellow solid red). The change in lactate content after HI is shown in F (we calibrated the results, assuming 80% brain-water content, 100% visibility of water signal, and 55.5 mol/L). The asterisk represents a statistical difference compared with the 2- to 6-hour time point. HIBI indicates hypoxic-ischemic brain injury.

lactate dehydrogenase, and acetone is then metabolized aerobically via the citric acid cycle to produce energy.^{5–9}

Moreover, lactate is closely associated with glucose metabolism, but a correlation with dynamic metabolic changes remains unclear. In vivo glucose metabolism in the brain is evaluated by [^{18}F] fluorodeoxyglucose imaging. In this study, ^1H -MR spec-

troscopy in combination with [^{18}F] FDG imaging was used to observe changes in lactate and glucose levels at different time points after hypoxic-ischemic (HI) in a piglet model. Histologic analysis demonstrated the existence of a mutual regulatory mechanism of energy metabolism in astrocytes and neurons after HI.

Levels of lactate, SUV_{max}, MCTs, and GLUTs in the control and HI model groups^a

Parameter	Control (n = 5)	HI Model Group (n = 5/Group)					
		0–2 hr	2–6 hr	6–12 hr	12–24 hr	24–48 hr	48–72 hr
Lactate	0.24 ± 0.25	7.82 ± 1.48 ^b	16.51 ± 1.62 ^b	13.01 ± 1.25 ^b	3.21 ± 1.21 ^b	1.18 ± 1.74	1.23 ± 1.40
BG/OC	0.99 ± 0.01	1.08 ± 0.04 ^b	1.17 ± 0.06 ^b	1.23 ± 0.02 ^b	1.16 ± 0.03 ^b	1.04 ± 0.04 ^b	0.96 ± 0.01
MCT-2	0.19 ± 0.00	0.21 ± 0.01 ^b	0.22 ± 0.01 ^b	0.24 ± 0.01 ^b	0.27 ± 0.01 ^b	0.21 ± 0.01 ^b	0.19 ± 0.00
MCT-4	0.21 ± 0.01	0.24 ± 0.01 ^b	0.25 ± 0.01 ^b	0.26 ± 0.01 ^b	0.27 ± 0.01 ^b	0.25 ± 0.02 ^b	0.22 ± 0.02
GLUT-1	0.14 ± 0.02	0.16 ± 0.04	0.20 ± 0.05 ^b	0.25 ± 0.01 ^b	0.24 ± 0.03 ^b	0.18 ± 0.05	0.15 ± 0.05
GLUT-3	0.13 ± 0.00	0.13 ± 0.01	0.16 ± 0.01 ^b	0.22 ± 0.06 ^b	0.18 ± 0.01 ^b	0.14 ± 0.01 ^b	0.14 ± 0.01

^a Data are mean ± SD.

^b *P* < .05 versus the control group.

MATERIALS AND METHODS

Experimental Animals

A total of 35 healthy Yorkshire or Large White piglets (3–5 days of age; 1.0–1.5 kg) were randomly divided into 7 groups of 5 piglets each: a control group and 6 HI model groups. All animal experiments satisfied the standards of the Regulations for the Administration of Affairs Concerning Experimental Animals and Measures for the Administration of Licenses Concerning Experimental Animals.

Establishment of the HI Model

Control Group. Room temperature was maintained at 28°C–30°C. The animals were injected intramuscularly with 0.6 mL/kg of Su-Mian-Xin (Veterinary Research Center, Jilin University, Changchun, China).¹⁰ Each animal was mechanically delivered 100% oxygen with a TKR-200C small animal ventilator (Jiangxi TELI Anesthesia & Respiration Equipment, Nanchang City, China) using a 2.5-mm-diameter endotracheal tube. The parameters of the ventilator were the following: inspiration-to-expiration ratio, 1:1.5; respiratory rate, 30 breaths/min; pressure, 0.05–0.06 MPa. A hand-held TUFFSAT Pulse Oximeter (GE Healthcare, Milwaukee, Wisconsin) was used to monitor heart rate and oxygen saturation. After the neck skin was disinfected with iodophor, the jugular vein was catheterized and an operation was performed to free the bilateral common carotid arteries. Then, the incisions were sutured, and the animals were placed in an incubator to maintain body temperature.

Model Groups. During the first stage, animals in the model groups underwent the same procedures as those in the control group. In the second stage, following 30 minutes of stabilization, artery clamps were used to block the bilateral common carotid arteries. Simultaneously, the oxygen concentration administered by mechanical ventilation was decreased to 6% (mixed in 94% nitrogen; Dalian Special Gases, Dalian City, China), which was maintained for 40 minutes and then increased to 100%. Both clamps on the bilateral common carotid arteries were then removed, blood flow was recovered, and the incisions were sutured. Oxygen saturation and heart rate were monitored throughout the procedure. Mechanical ventilation was stopped after spontaneous breathing was restored.

There were 7 groups (*n* = 5 piglets each): a control group and 6 model groups. The 6 HI model groups were based on PET/CT and MR spectroscopy scanning times after hypoxia-ischemia (0–2, 2–6, 6–12, 12–24, 24–48, and 48–72 hours). The model group was standardized, in which case, the HI time and surgical procedure of each neonate piglet in the model group were the same. The piglets in the control group underwent the same operation without HI process.

According to the preoperative, operative, and postoperative monitoring of the hypoxic-ischemic brain injury model, partial pressure of carbon dioxide in arterial blood was maintained in the range of 4.5–6.5 kPa, and partial pressure of oxygen in arterial blood, in the range of 8–13 kPa.¹¹

After completion of PET/CT and MR spectroscopy at the designated time points, the piglets were immediately injected with anesthetics. After the reaction disappeared (ie, loss of pain reflex because of excessive anesthetic), the skull was opened along the sutura cranium, and the spinal cord was cut at the medulla. The whole brain was collected along with the cerebellum after the piglet was decapitated.

¹H-MR Spectroscopy Scanning and Data Processing

¹H-MR spectroscopy scans were performed of control group and at 0–2, 2–6, 6–12, 12–24, 24–48, and 48–72 hours after HI.

MR imaging was performed with an Achieva 3T TX system (Philips Healthcare, Best, the Netherlands) equipped with a pencil beam, second-order shim. Body coil emission and 8-channel sensitivity encoding head coil reception were used. ¹H-MR spectroscopy was implemented with a point-resolved spectroscopy single-voxel sequence with the following scanning parameters: TR/TE, 2000/37 ms; average number of signals, 64; and VOI, 10 × 10 × 10 mm. The right basal ganglia (BG) was chosen as the ROI. Shimming and water suppression were automatically performed by the scanner. ¹H-MR spectroscopy results were analyzed using the LCModel software package (<http://www.lcmodel.com/>).¹²

PET/CT Studies

PET/CT scans were performed of control group and at 0–2, 2–6, 6–12, 12–24, 24–48, and 48–72 hours after HI.

PET Reagents

[¹⁸F] FDG was synthesized using the MINitrac positron-emitting isotope production system (GE Healthcare) and a TracerLab MX-FDG synthesizer (GE Healthcare). High-performance liquid chromatography used for quality control showed that the radioactive purity of [¹⁸F] FDG was >99%.

Functional Imaging

[¹⁸F] FDG (3.7 MBq/kg; injection dose, 3.7–5.55 MBq) was administered to the experimental animals in the model groups via the jugular vein at different time points after HI. Feeding was stopped 6 hours before administration to maintain low levels of blood glucose. The radioactivity of the syringe before and after injection was measured. PET/CT scanning (Discovery Elite PET/CT system; GE Healthcare) was performed 50 minutes after

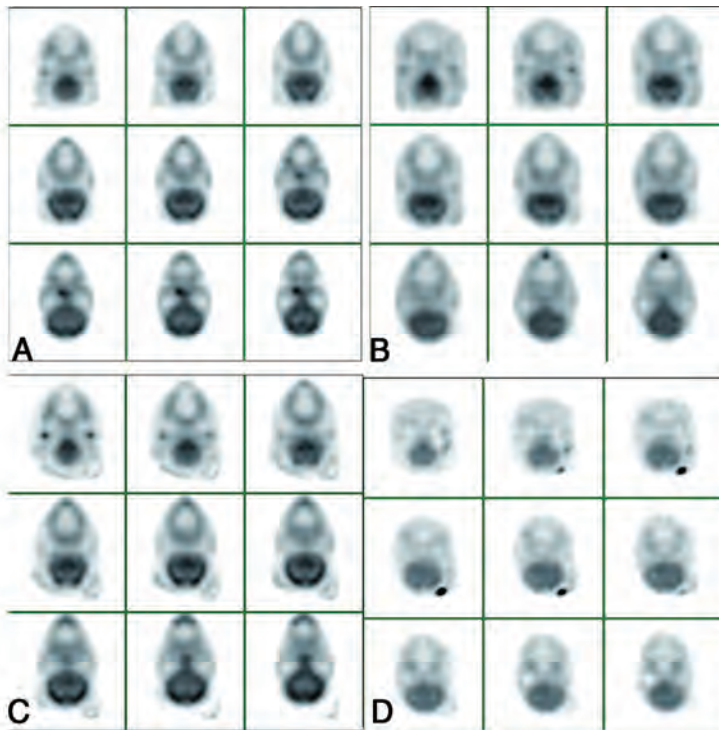


FIG 2. [^{18}F] FDG PET/CT images in the control group (A) and the time points of 6–12, 12–24, and 48–72 hours in the HI model groups (B–D). Changes in the SUV_{max} of the basal ganglia and BG/OC ratio of the BG in the control and HI model groups (E–F). The BG and OC of the control group (A) are clearly visible on [^{18}F] FDG PET/CT images. [^{18}F] FDG uptake was symmetrically distributed. At 6–12 hours after HI, the BG/OC ratio of the HI groups was greater than that of the control group (B). At 12–24 hours after HI, the BG/OC ratio in the BG was decreased compared with 6–12 hours (C). The BG/OC ratio was further decreased after 48–72 hours, and the BG and cortex showed less clearance (D). The SUV_{max} of the basal ganglia and BG/OC ratio peaked at 6–12 hours after HI. The *hashtag* represents a statistical difference compared with the 6- to 12-hour time points (E–F). Changes in lactate levels and the BG/OC ratio after HI (G). The left vertical axis represents the lactate content, and the right vertical axis represents the BG/OC ratio (G, the *circle* represents the average value of lactate content; the *diamond* represents the average value of BG/OC). Spearman correlation analysis showed that the lactate content was positively correlated with the BG/OC ratio ($r = 0.74, P < .001$; H). HIBI indicates hypoxic-ischemic brain injury.

injection of the imaging agent. The PET slice thickness was 3.25 mm. CT scanning parameters included the following: voltage, 80 kV; current, 50 mA; slice thickness, 3.25 mm. A 3D model was used in PET scanning.

Image Processing

PET/CT raw data were processed with Volume Viewer software on an AW4.6 workstation (GE Healthcare). The bilateral BG and occipital cortex (OC) on the same side were selected as the ROI. The size of the ROI of the BG was normalized to 1.0×1.0 cm, and that of the OC, to 0.5×0.5 cm. The ROI was placed on the BG and the OC by reference to the CT images by 2 experienced radiologists. Maximum standard uptake values (SUV_{max}) of the BG/OC ratios were determined. The SUV_{max} of the BG and BG/OC ratio reflects the uptake of [^{18}F] FDG in the BG.

Histologic Examination and Immunohistochemical Analyses

The fixed brain tissue was sliced in the coronal plane into 4-mm-thick sections. Slices containing the BG and hippocampus were used for immunohistochemical staining of MCT-2, MCT-4, glucose transporter-1 (GLUT-1), and GLUT-3 using antibodies purchased from Abcam (Bristol, England).

Statistical Analyses

All statistical analyses were performed with SPSS Software for Windows (Version 17.0; IBM, Armonk, New York). Data are presented as the mean \pm SD. Analysis of variance was used to analyze the data with equal variance followed by post hoc analysis with the least significant difference test. Spearman rank correlation analyses were conducted, and correlation coefficients and boxplot data were used. A P value $< .05$ was considered statistically significant.

RESULTS

Change in Lactate in the BG across Time after HI

^1H -MR spectroscopy showed that after HI, the lactate concentration increased first and then decreased but was still

slightly higher than that of the control group at 48–72 hours (Fig 1 and Table).

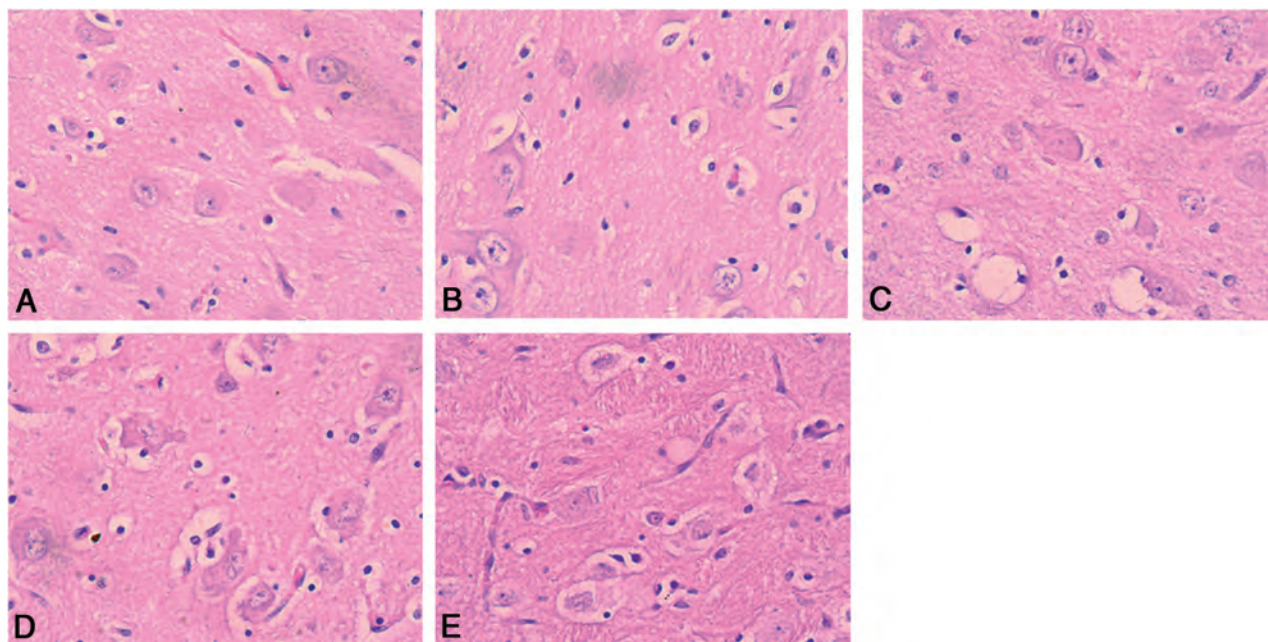


FIG 3. H&E staining of the BG in the control and HI model groups. A–E, H&E-stained images of the control group and the 6-, 24-, 48-, and 72-hour time points of the HI model groups. Compared with the control group (A), we observed the following apparent pathologic changes: swelling in some astrocytes (B), many astrocytes and some neurons apparently swollen with visible vacuoles and karyopyknosis (C), and astrocytes apparently swollen and necrotic. Neurons also showed swelling and necrosis (D), the neuronal membranes were damaged, and nuclei were swollen and weakly stained. These observations were made at $\times 400$ magnification (E).

PET/CT Results

The radioactivity concentration was symmetrically distributed between the left and right hemispheres of the control group. The bilateral BG and OC were clearly visible and showed increased glucose metabolic activity, with radioactivity sparsely distributed in the white matter (Fig 2). There were significant differences in the SUV_{max} of the BG and BG/OC between 6 and 12 hours and other time points ($P < .01$). The OC and BG were still visible at 12–48 hours after HI. At 48–72 hours, the brain structures were less clear, and decreased metabolism was noted throughout the whole brain.

Histologic Findings

H&E Staining and Expression Levels of MCT-2 and MCT-4 in the BG after HI. H&E staining of the control group showed that the neurons were neatly arranged with intact cell morphology, abundant neuron plasma, and clear nucleoli. At 6 hours after HI, some glial cells were swollen with pale cytoplasm and intact neurons. At 24 hours after HI, a large portion of the glial cells was swollen with condensed nucleoli and the neurons were swollen and round with pale cytoplasm and bubbles. At 48 hours after HI, the glial cells were swollen and degraded, and the neurons were swollen with scattered visible neuronal necrosis. At 72 hours after HI, the neuronal cell membranes were broken and nuclei were swollen and pale. At different time points after HI, the astrocytes and neurons had sustained different degrees of damage (Fig 3).

After HI, the expression of both MCT-2 and MCT-4 in the BG initially increased and then peaked at 12–24 hours (Fig 4). There were significant differences in MCT-2 and MCT-4 expression levels at 12–24 hours, compared with the control group and the other HI model groups ($P < .01$).

Expression Levels of GLUT-1 and GLUT-3 in the BG after HI. The expression levels of GLUT-1 and GLUT-3 increased just after HI and peaked at 12–24 hours. The expression levels of both were significantly different at 12–24 hours after HI from the other time points ($P < .01$). GLUT-1 expression decreased after 12–24 hours, as did GLUT-3 expression (Fig 5).

DISCUSSION

The results showed that lactate levels had peaked at 2–6 hours after HI and glucose peaked at 6–12 hours. The expression levels of the MCTs and GLUTs increased after HI (peak at 12–24 hours) and then decreased, and the study showed that astrocytes and neuronal damage after HI were not synchronized. Astrocytes damage occurred earlier and was more severe than neuronal damage; these findings were consistent with those of our previous study.^{10,13}

It is likely more advantageous to detect lactate using 1H -MR spectroscopy at the 3T field strength with a long TE of 288 ms because lipid T2 is short and the TE of the lipid signal declines; these features greatly distinguish lactate and lipid peaks. In 1.5T field strength, a long TE of 144 ms usually shows an inverted lactate peak, which is therefore also easy to separate from the lipid peak. However, if a long TE (144 ms) is used with 3T, false-negative results may occur.¹⁴ In the present study, the use of a short TE (37 ms) led to overlap of the lactate and lipid peaks, but use of LCMoDel separated the overlapped lactate and lipid signals and thus can still ensure the accuracy of the results.

In this study, the lactate content peaked at 2–6 hours and then gradually decreased. Several studies have shown that the increase in lactate concentration lasted for some time after HI.¹⁵ Pellerin et al¹⁶ proposed the ANLS hypothesis, which states that lactate, as a

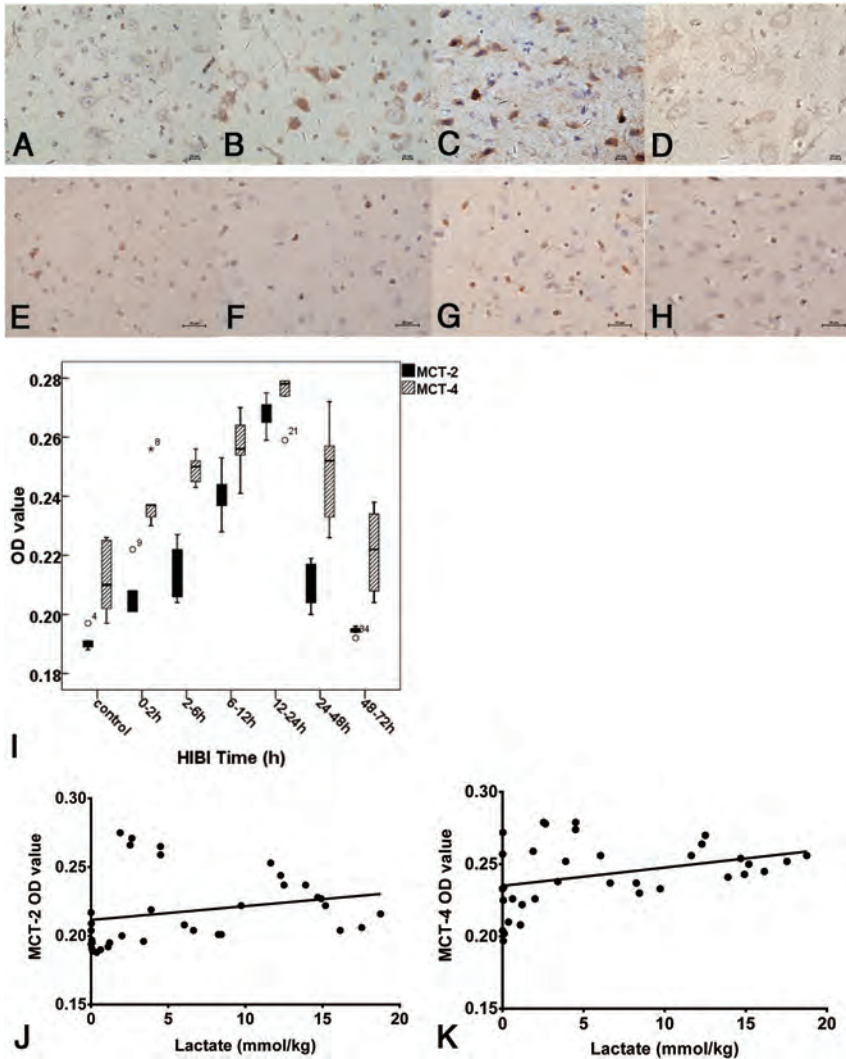


FIG 4. Expression levels of MCT-2 and MCT-4 in the BG in the control and HI model groups (A–H) and change in expression levels of MCT-2 and MCT-4 in the BG after HI (I) and correlation with lactate content (J and K). A–D, MCT-2 expression in the control group and at 6, 24, and 48 hours after HI in the HI model groups. MCT-2 was mainly stained brown in the membrane of the neurons (A). Compared with the control group (A), MCT-2 staining at 6 and 24 hours after HI (B and C) was darker and greater numbers of positive cells were observed. MCT-2 expression was reduced at 48 hours (D). E–H, MCT-4 expression in the BG of the control group and at 6, 24, and 48 hours after HI in the model groups. MCT-4 was mainly expressed in the membranes of astrocytes (E). MCT-4 staining was darker at 6 and 24 hours after HI (F and G), compared with the control group (E). MCT-4 expression was reduced at 48 hours after HI (H). The expression levels of MCT-2 and MCT-4 were highest at 12–24 hours (I). Expression levels of MCT-2 and MCT-4 were positively correlated with the lactate level (J and K): MCT-2 ($r = 0.47$), MCT-4 ($r = 0.38$).

substrate of energy metabolism in neurons, was preferable to glucose as an energy source of neurons.¹⁷ In the current study, the regulation mechanism of lactate and glucose after HI was investigated on the basis of the ANLS hypothesis. A high concentration of lactate or hypoxia can induce activation of glycolytic enzymes^{18,19} and further upregulate MCTs. Immunohistochemical analyses showed that after HI, the expression levels of MCT-2 and MCT-4 also increased, peaked around 12–24 hours, and then decreased. MCT-4 is primarily expressed in astrocytes and has a relatively low affinity for lactate, which facilitates the release of lactate, while MCT-2 is primarily expressed in neurons and has a high affinity for lactate; thus, characteristic kinetics are favorable for the uptake of lactate.²⁰

anaerobic metabolism is limited, the uptake and use of glucose by the brain are enhanced to supplement the energy shortage caused by HI. Therefore, an increase in lactate content is accompanied by an increase in glucose uptake.

Within 24 hours after HI, increased glucose uptake can temporarily supplement energy deficiencies, the glucose uptake is closely correlated with the upregulation of GLUTs at this stage. Immunohistochemical analyses showed that GLUT-1 and GLUT-3 synthesis increased after HI, peaked at 12–24 hours, and then decreased after 24 hours. Because GLUT-1 is mainly expressed in vascular endothelial cells, its increase helps transport glucose into the extracerebral space via the blood-brain barrier and increases glucose levels in the brain.²⁹ GLUT-3 is mainly ex-

Studies have shown that neurons can preferentially use lactate released from astrocytes. At normal physiologic concentrations of extracellular glucose and lactate, 79% of the energy produced in neurons is from lactate and 21% is from glucose. Moreover, neurons can more rapidly use glucose and lactate than astrocytes,^{21,22} and histologic results also confirmed that neurons are damaged after astrocytes are damaged.¹⁰ Therefore, as an energy substrate of aerobic metabolism after HI, lactate has an important role in the protection of neurons after HI.^{23–25}

After HI, the energy produced by lactate metabolism is not sufficient to maintain the normal physiologic activity of neurons. The increased expression levels of GLUT-1 and GLUT-3 and the increased use of glucose constitute a protective cellular response. The increase in lactate and glucose can temporarily compensate for the lack of energy in the brain in response to the needs of anaerobic solution.^{18,26}

HI promotes abnormal glucose metabolism and is closely associated with brain cell necrosis.²⁷ A decrease in the uptake of [¹⁸F] FDG, to a certain degree, often implies irreversible brain injury.²⁸ The results of the present study indicated that following HI, glucose metabolism increased and the BG/OC ratio with lactate content peaked at around 6–12 hours. Glucose metabolism then decreased with time, and the uptake of [¹⁸F] FDG in the whole brain decreased up to 48–72 hours following HI. Lactate and glucose are critical for energy metabolism and interact closely with one another. After HI, glycolysis produces lactate; and because the energy generated from anaerobic

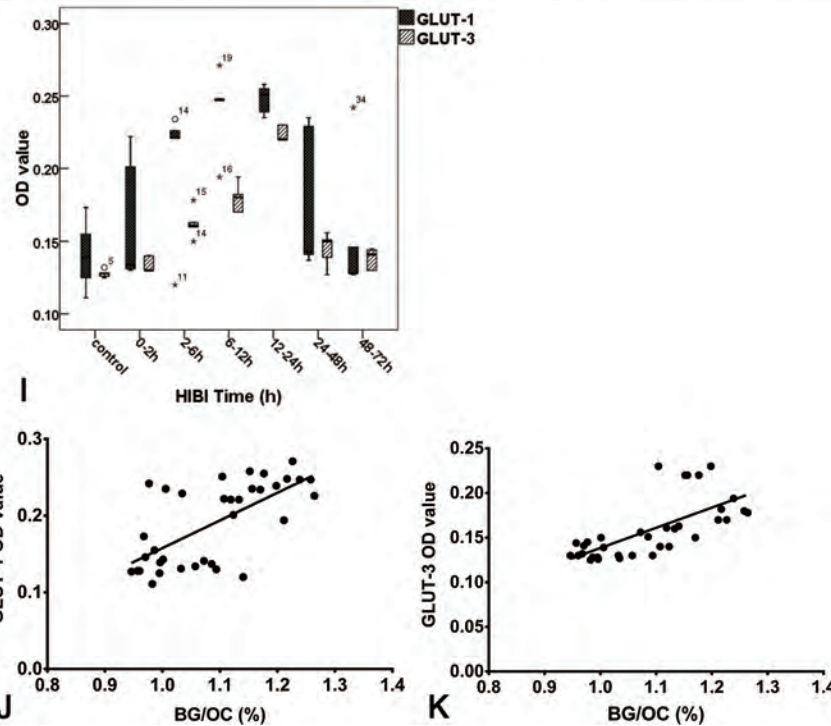
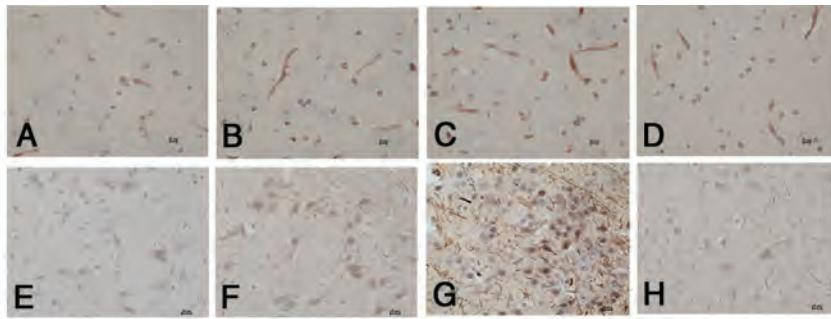


FIG 5. Expression levels of GLUT-1 and GLUT-3 in the BG in control and HI model groups (A–H), immunohistochemical staining of GLUT-1 and GLUT-3 in the BG within 72 hours after HI (I), and correlation with BG/OC (J and K). A–D, GLUT-1 expression in the control group and at 6, 24, and 48 hours after HI in the HI model groups. GLUT-1 was mainly expressed in vascular endothelial cells (positive staining is shown as dark brown, rod-shaped structures) and astrocytes (A). Positively stained endothelial cells and astrocytes increased at 6 and 24 hours (B and C) and decreased at 48 hours (D) after HI. E–H, GLUT-3 expression in the control group and at 6, 24, and 48 hours after HI in the HI model groups. GLUT-3 was mainly expressed in neurons (E). The staining of the neuronal membrane was darker at 6 and 24 hours after HI (F and G). The staining lightened, and positively stained cells decreased at 48 hours after HI (H). GLUT-1 and GLUT-3 expression levels were highest at 12–24 hours (I). Spearman correlation analysis showed that the expression levels of GLUT-1 and GLUT-3 were positively correlated with the BG/OC ratio (J and K): GLUT-1 ($r = 0.64$); GLUT-3 ($r = 0.75$).

pressed in neurons, and the upregulation of GLUT-3 promotes the transport of glucose from the extracerebral space into neurons. This increased glucose uptake improves energy metabolism. Upregulation of both GLUT-1 and GLUT-3 molecules temporarily supplements the energy deficiency and the demands of anaerobic glycolysis under HI conditions.¹⁸ At 48 hours after HI, astrocytes showed swelling and degeneration, while swelling and scattered necrosis of neurons was also observed. Up to 72 hours, many neurons were necrotic. Expression levels of GLUT-1 and GLUT-3 decreased after 24 hours. This decrease in GLUTs weakens the capacity to transport glucose, which reduces the uptake of [¹⁸F] FDG.

Immediately after HI, lactate production increased. The ANLS

model can reflect lactate and hypoxia stimulation of MCTs and GLUTs. Up to the later stages of HI, necrosis of neurons and astrocytes disrupts coordination of the neuronal network and causes energy exhaustion. This series of changes in biochemical processes, including lactate, glucose, and associated transporters, coregulate energy metabolism after HI.^{30,31}

The size, cardiovascular system, and brain maturity of neonate piglets and neonate children are highly similar. Therefore, the neonate piglet hypoxic-ischemic brain injury model and hypoxic ischemic encephalopathy are also similar.³² The success rate of modeling using piglets born within 24 hours is low with high mortality. Piglets at 3–5 days of age can guarantee the success rate and meet the perinatal/neonatal brain requirements. Older neonate piglets do not meet the perinatal requirement but are more like older neonate children. Kyng et al³³ used Danish Landrace piglets within 24 hours after birth, while neonate Yorkshire or Large White piglets 3–5 days of age were used in the present study. In this model, the bilateral internal carotid arteries were blocked and supplied with low oxygen concentrations. During the experiment, 2 piglets died, one due to excessive anesthesia and a second due to excessive blood loss. Nonetheless, this model is highly reproducible, with a high success rate and low mortality. Reperfusion was simulated during recovery of the blood supply, which is conducive to a reperfusion study.^{34–36} However, different anesthetics and anesthesia methods have different effects on neonatal brain injury. Using halothane to anesthetize animals may increase the degree of brain injury in the model.³⁷ Propofol has a neuroprotective effect, which can reduce the degree of brain damage.^{38,39} In this study, Sumianxin was used as an anesthetic, and has the advantage of an effective anesthesia with smooth induction and recovery. The anesthesia time of Sumianxin is short and thus can reduce its impact on the model.¹⁹

CONCLUSIONS

These results suggest that lactate and glucose transporters have coordinated regulation of energy metabolism following HI.

REFERENCES

1. Itoh Y, Esaki T, Shimoji K, et al. Dichloroacetate effects on glucose and lactate oxidation by neurons and astroglia in vitro and on glu-

- cose utilization by brain in vivo. *Proc Natl Acad Sci U S A* 2003;100:4879–84 CrossRef Medline
2. Bouzat P, Oddo M. **Lactate and the injured brain: friend or foe?** *Curr Opin Crit Care* 2014;20:133–40 CrossRef Medline
 3. Genc S, Kurnaz IA, Ozilgen M. **Astrocyte-neuron lactate shuttle may boost more ATP supply to the neuron under hypoxic conditions—in silico study supported by in vitro expression data.** *BMC Syst Biol* 2011;5:162 CrossRef Medline
 4. Halestrap AP, Price NT. **The proton-linked monocarboxylate transporter (MCT) family: structure, function and regulation.** *Biochem J* 1999;343(Pt 2):281–99 Medline
 5. Hertz L, Dienel GA. **Lactate transport and transporters: general principles and functional roles in brain cells.** *J Neurosci Res* 2005;79:11–18 CrossRef Medline
 6. Chiry O, Fishbein WN, Merezhinskaya N, et al. **Distribution of the monocarboxylate transporter MCT2 in human cerebral cortex: an immunohistochemical study.** *Brain Res* 2008;1226:61–69 CrossRef Medline
 7. Amaral AI, Teixeira AP, Martens S, et al. **Metabolic alterations induced by ischemia in primary cultures of astrocytes: merging 13C NMR spectroscopy and metabolic flux analysis.** *J Neurochem* 2010;113:735–48 CrossRef Medline
 8. Pellerin L, Bouzier-Sore AK, Aubert A, et al. **Activity-dependent regulation of energy metabolism by astrocytes: an update.** *Glia* 2007;55:1251–62 CrossRef Medline
 9. Pellerin L, Magistretti PJ. **How to balance the brain energy budget while spending glucose differently.** *J Physiology* 2003;546(Pt 2):325 CrossRef Medline
 10. Wang XY, Wang HW, Fu XH, et al. **Expression of N-methyl-d-aspartate receptor 1 and its phosphorylated state in basal ganglia of a neonatal piglet hypoxic-ischemic brain injury model: a controlled study of (1)H MRS.** *Eur J Paediatr Neurol* 2012;16:492–500 CrossRef Medline
 11. Broad KD, Fierens I, Fleiss B, et al. **Inhaled 45–50% argon augments hypothermic brain protection in a piglet model of perinatal asphyxia.** *Neurobiol Dis* 2016;87:29–38 CrossRef Medline
 12. Provencher SW. **Automatic quantitation of localized in vivo 1H spectra with LCModel.** *NMR Biomed* 2001;14:260–64 CrossRef Medline
 13. Wang H, Wang X, Guo Q. **The correlation between DTI parameters and levels of AQP-4 in the early phases of cerebral edema after hypoxic-ischemic/reperfusion injury in piglets.** *Pediatr Radiol* 2012;42:992–99 CrossRef Medline
 14. Lange T, Dydak U, Roberts TP, et al. **Pitfalls in lactate measurements at 3T.** *AJNR Am J Neuroradiol* 2006;27:895–901 Medline
 15. Thoren AE, Helps SC, Nilsson M, et al. **The metabolism of C-glucose by neurons and astrocytes in brain subregions following focal cerebral ischemia in rats.** *J Neurochem* 2006;97:968–78 CrossRef Medline
 16. Pellerin L, Pellegrini G, Bittar PG, et al. **Evidence supporting the existence of an activity-dependent astrocyte-neuron lactate shuttle.** *Dev Neurosci* 1998;20:291–99 CrossRef Medline
 17. Cater HL, Chandratheva A, Benham CD, et al. **Lactate and glucose as energy substrates during, and after, oxygen deprivation in rat hippocampal acute and cultured slices.** *J Neurochem* 2003;87:1381–90 CrossRef Medline
 18. Espinoza-Rojo M, Iturralde-Rodriguez KI, Cháñez-Cárdenas ME, et al. **Glucose transporters regulation on ischemic brain: possible role as therapeutic target.** *Cent Nerv Syst Agents Med Chem* 2010;10:317–25 CrossRef Medline
 19. Zheng Y, Wang XM. **Measurement of lactate content and amide proton transfer values in the basal ganglia of a neonatal piglet hypoxic-ischemic brain injury model using MRI.** *AJNR Am J Neuroradiol* 2017;38:827–34 CrossRef Medline
 20. Bergersen LH. **Is lactate food for neurons? Comparison of monocarboxylate transporter subtypes in brain and muscle.** *Neuroscience* 2007;145:11–19 CrossRef Medline
 21. Gao C, Zhou L, Zhu W, et al. **Monocarboxylate transporter-dependent mechanism confers resistance to oxygen- and glucose-deprivation injury in astrocyte-neuron co-cultures.** *Neurosci Lett* 2015;594:99–104 CrossRef Medline
 22. Bouzier-Sore AK, Voisin P, Canioni P, et al. **Lactate is a preferential oxidative energy substrate over glucose for neurons in culture.** *J Cereb Blood Flow Metab* 2003;23:1298–306 CrossRef Medline
 23. Moxon-Lester L, Sinclair K, Burke C, et al. **Increased cerebral lactate during hypoxia may be neuroprotective in newborn piglets with intrauterine growth restriction.** *Brain Res* 2007;1179:79–88 CrossRef Medline
 24. Ogawa M, Watabe H, Teramoto N, et al. **Understanding of cerebral energy metabolism by dynamic living brain slice imaging system with [18F]FDG.** *Neurosci Res* 2005;52:357–61 CrossRef Medline
 25. Berthet C, Lei H, Thevenet J, et al. **Neuroprotective role of lactate after cerebral ischemia.** *J Cereb Blood Flow Metab* 2009;29:1780–89 CrossRef Medline
 26. Royer C, Lachuer J, Crouzoulon G, et al. **Effects of gestational hypoxia on mRNA levels of Glut3 and Glut4 transporters, hypoxia-inducible factor-1 and thyroid hormone receptors in developing rat brain.** *Brain Res* 2000;856:119–28 CrossRef Medline
 27. Hardy OT, Hernandez-Pampaloni M, Saffer JR, et al. **Diagnosis and localization of focal congenital hyperinsulinism by 18F-fluorodopa PET scan.** *J Pediatr* 2007;150:140–45 CrossRef Medline
 28. Thorngren-Jerneck K, Ley D, Hellstrom-Westas L, et al. **Reduced postnatal cerebral glucose metabolism measured by PET after asphyxia in near term fetal lambs.** *J Neurosci Res* 2001;66:844–50 CrossRef Medline
 29. Vemula S, Roder KE, Yang T, et al. **A functional role for sodium-dependent glucose transport across the blood-brain barrier during oxygen glucose deprivation.** *J Pharmacol Exp Ther* 2009;328:487–95 CrossRef Medline
 30. Brown AM, Ransom BR. **Astrocyte glycogen and brain energy metabolism.** *Glia* 2007;55:1263–71 CrossRef Medline
 31. Mehta SL, Manhas N, Raghuram R. **Molecular targets in cerebral ischemia for developing novel therapeutics.** *Brain Res Rev* 2007;54:34–66 CrossRef Medline
 32. Buckley NM. **Maturation of circulatory system in three mammalian models of human development.** *Comp Biochem Physiol A Comp Physiol* 1986;83:1–7 Medline
 33. Kyng KJ, Skajaa T, Kerrn-Jespersen S, et al. **A piglet model of neonatal hypoxic-ischemic encephalopathy.** *J Vis Exp* 2015:e52454 CrossRef Medline
 34. Roohey T, Raju TN, Moustogiannis AN. **Animal models for the study of perinatal hypoxic-ischemic encephalopathy: a critical analysis.** *Early Hum Dev* 1997;47:115–46 CrossRef Medline
 35. Zhang YF, Wang XY, Guo F, et al. **Simultaneously changes in striatum dopaminergic and glutamatergic parameters following hypoxic-ischemic neuronal injury in newborn piglets.** *Eur J Paediatr Neurol* 2012;16:271–78 CrossRef Medline
 36. Zhang YF, Wang XY, Cao L, et al. **Effects of hypoxic-ischemic brain injury on striatal dopamine transporter in newborn piglets: evaluation of 11C-CFT PET/CT for DAT quantification.** *Nucl Med Biol* 2011;38:1205–12 CrossRef Medline
 37. Thoresen M, Simmonds M, Satas S, et al. **Effective selective head cooling during posthypoxic hypothermia in newborn piglets.** *Pediatr Res* 2001;49:594–99 CrossRef Medline
 38. Lingwood BE, Dunster KR, Healy GN, et al. **Cerebral impedance and neurological outcome following a mild or severe hypoxic/ischemic episode in neonatal piglets.** *Brain Res* 2003;969:160–67 CrossRef Medline
 39. Björkman ST, Foster KA, O'Driscoll SM, et al. **Hypoxic/ischemic models in newborn piglet: comparison of constant FiO2 versus variable FiO2 delivery.** *Brain Res* 2006;1100:110–17 CrossRef Medline

Using Correlative Properties of Neighboring Pixels to Improve Gray-White Differentiation in Pediatric Head CT Images

T.P. Madaelil, A. Sharma, C. Hildebolt, and M. Parsons

ABSTRACT

BACKGROUND AND PURPOSE: A lower radiation dose can have a detrimental effect on the quality of head CT images. The aim of this study performed in a pediatric population was to test whether an image-processing algorithm (Correlative Image Enhancement) based on the correlation among intensities of neighboring pixels can improve gray-white differentiation in head CTs.

MATERIALS AND METHODS: Sixty baseline head CT images with normal findings obtained from scans of 30 children were processed using Correlative Image Enhancement to produce corresponding enhanced images. Gray-white differentiation in baseline and enhanced images was assessed quantitatively by calculating the contrast-to-noise ratio and conspicuity in equivalent ROIs in gray and white matter. Two masked readers rated the images for visibility of gray-white differentiation on a 5-point Likert scale. Differences in both quantitative and qualitative measures of gray-white differentiation between baseline and enhanced images were tested for statistical significance. *P* values < .05 were considered significant.

RESULTS: Image processing resulted in improvement in the contrast-to-noise ratio (from 1.86 ± 0.94 to 2.26 ± 1.00 , *P* = .02) as well as conspicuity (from 37.28 ± 11.56 to 46.4 ± 11.5 , *P* < .001). This was accompanied by improved subjective visibility of gray-white differentiation as reported by both readers (*P* < .01).

CONCLUSIONS: Image processing using Correlative Image Enhancement had a beneficial effect on quantitative measures of gray-white differentiation. This translated into improved perception of gray-white differentiation by readers. Further studies are needed to assess the effect of such image processing on the detection of disease processes using head CTs.

ABBREVIATIONS: CIE = Correlative Image Enhancement; CNR = contrast-to-noise ratio; GWD = gray-white differentiation; SI = signal intensity

Differentiation of gray and white matter on head CTs is important in the recognition of normal structures as well as identification of pathologic changes within brain parenchyma.¹⁻³ Accordingly, it has long been used as a measure of the diagnostic quality of head CT images.³ The ease of gray-white differentiation is adversely affected by the presence of noise, which, while being inherent in the process of image generation, can be particularly prominent when images are acquired at a lower radiation dose. This is the case with pediatric head CTs, which, in response to increased awareness and concern about radiation-induced harm, are often acquired using aggressive dose reduction.⁴⁻⁹ A number

of optimization techniques have been developed that aim to maintain diagnostic quality while reducing radiation exposure.¹⁰⁻¹⁷ Many of these strategies such as tube current modulation or use of iterative reconstruction techniques are applicable at the level of image generation or reconstruction at the scanner.^{10,11,15-17} In addition, some image postprocessing techniques have been proposed that can improve gray-white differentiation on head CT images after they have been generated.¹³

Correlative Image Enhancement (CIE, patent pending) is an image-processing algorithm that aims to increase the conspicuity of details of interest within digital images by targeted noise reduction and contrast optimization.¹⁸⁻²⁰ Using both qualitative and quantitative measures such as conspicuity and contrast-to-noise ratio (CNR), we aimed to test whether CIE improved gray-white differentiation (GWD) in pediatric head CT images with normal findings.

MATERIALS AND METHODS

This retrospective, institutional review board–approved, Health Insurance Portability and Accountability Act–compliant study was ap-

Received June 2, 2017; accepted after revision October 30.

From the Department of Interventional Neuroradiology (T.P.M.), Emory University Hospital, Atlanta, Georgia; and Mallinckrodt Institute of Radiology (A.S., C.H., M.P.), Washington University School of Medicine, Washington University, St. Louis, Missouri.

Please address correspondence to Thomas P. Madaelil, MD, Interventional Neuroradiology, Emory University Hospital, 1364 Clifton Rd, NE, Suite AG21, Atlanta, GA 30322; e-mail: Thomas.madaelil@emory.edu

<http://dx.doi.org/10.3174/ajnr.A5506>

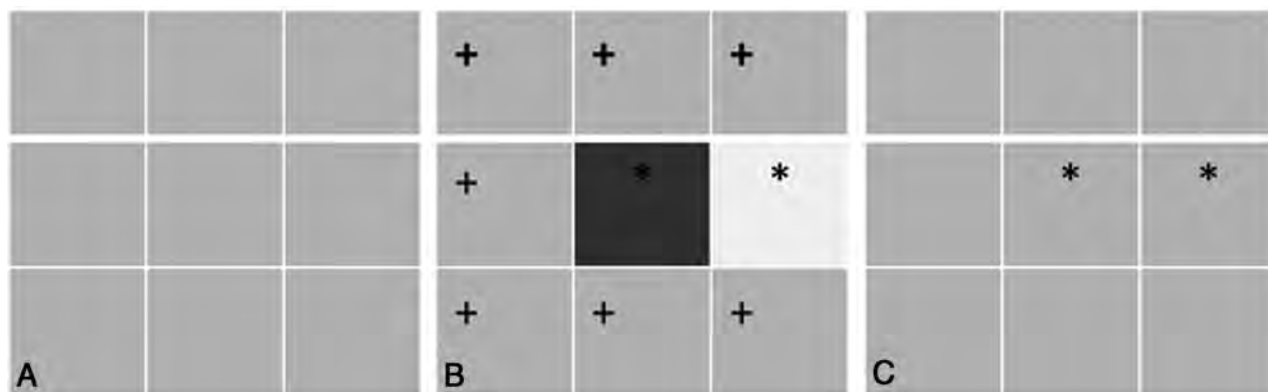


FIG 1. These images represent 9 contiguous pixels representing the same structure that spans these pixels. In an ideal noise-free image (A), these 9 pixels would have identical intensities. The presence of noise that invariably accompanies digital images causes intensities of some of these pixels to be higher or lower than expected (B). Modifying the intensities of pixels (*asterisk*) on the basis of the preponderance of intensities (*plus sign*) in their neighboring pixels can mitigate the effect of noise (C).

proved by the institutional review board at Washington University in Saint Louis with a waiver of consent for using existing data.

Patient and Image Selection

We identified head CTs of 30 children (17 males, 13 females; mean age, 7.5 ± 5.6 years) performed during 1 month in 2014, and with normal findings. These included 15 children scanned with our routine “low-dose” head CT protocol with aggressive dose reduction (100 kV[peak], 89 ± 16 mA, 137 ± 27 mGy \times cm dose-length product) and 15 children scanned with our “standard” protocol with less aggressive dose reduction (100 kVp, 302 ± 72 mA, 486 ± 121 mGy \times cm dose-length product). At our institution, all head CTs of children are acquired using a low-dose protocol except for patients with head trauma and those in the intensive care unit. All scans had been performed with an FOV range of 150–230 mm and slice thickness of 4 mm. From each study, we selected 2 images, one across the basal ganglia and the other through the centrum semiovale. These 60 baseline images were converted into Portable Network Graphics format for processing.

Image Processing

Image processing was performed by one of the coauthors using CIE, an algorithm developed by him, within Matlab (MathWorks, Natick, Massachusetts) to generate corresponding enhanced images. This coauthor did not participate in subsequent image or statistical analysis. The algorithm modified the intensity of each pixel in the image on the basis of its intensity and that of its neighboring pixels relative to a threshold intensity defined by the user. This threshold was chosen at a level in-between the intensities of normal-appearing white matter and gray matter. This process aimed to simultaneously correct the variations in the pixel intensities induced by noise (Fig 1) and to exaggerate the difference between the intensities of pixels around the chosen threshold. The enhanced images thus created were saved as individual files in Portable Network Graphics format. The size of baseline and enhanced images was identical.

Quantitative Image Review

All baseline and enhanced images were converted into DICOM format using the JPEG to DICOM plugin for Osirix Lite (Pixmeo,

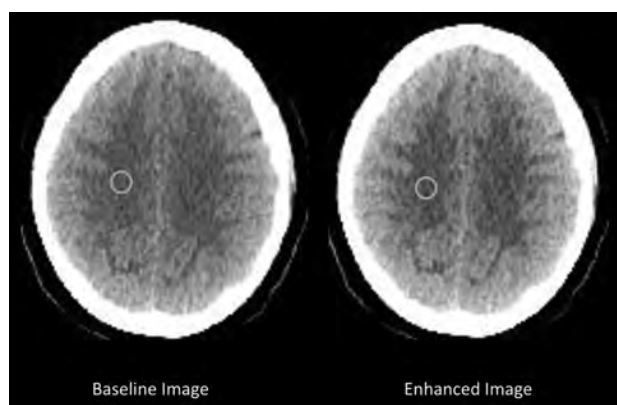


FIG 2. Axial head CT image across the centrum semiovale before (baseline image) and after (enhanced image) processing with CIE, with equivalent ROIs used to measure gray and white matter intensities. These measurements were used to calculate the conspicuity of gray matter and CNR between gray and white matter.

Bernex, Switzerland) for quantitative analysis. Means (SI) and SDs of the gray matter (gm) and the white matter (wm) intensities were measured from equivalent ROIs in the baseline and enhanced images (Fig 2). These measurements were then used to calculate gray matter conspicuity and the CNR between gray and white matter using the following formulae:

$$\text{Conspicuity} = \text{SI}_{\text{gm}} - \text{SI}_{\text{wm}}/\text{SI}_{\text{gm}}$$

$$\text{CNR} = \text{SI}_{\text{gm}} - \text{SI}_{\text{wm}}/\text{Noise}$$

$$\text{Noise} = \sqrt{[(\text{SD}_{\text{gm}})^2 + (\text{SD}_{\text{wm}})^2]}.$$

For images obtained at the ganglionic level, GM was sampled in the putamen and white matter in the frontal lobe. For the supra-ganglionic images, GM was sampled along the cerebral convexity and the white matter within the centrum semiovale.

Qualitative Image Review

Two blinded readers (a board-certified neuroradiologist with 10 years of practice experience and a neuroradiology fellow) who did not participate in the image processing rated the ease of perception of GWD in each image on a predefined 5-point scale ranging from 1 (imperceptible GWD) to 5 (very easily perceptible GWD).

Readers also rated the presence of artifacts within the image on a 3-point scale (1, artifacts making the image nondiagnostic; 2, some artifacts but the image is still diagnostic; 3, no artifacts present). Images were presented to the readers in fixed display settings that were identical for baseline and enhanced images.

Statistical Analysis

We analyzed the baseline data to assess the association between the qualitative measure of GWD (mean GWD ratings provided by 2 readers) and quantitative measures (conspicuity and CNR) using regression analysis. As part of this analysis, residuals were assessed for normality with the Shapiro-Wilk W test. If residuals were normally distributed (Shapiro-Wilk W , P value $> .05$), least-squares regression analysis was used to determine the product-moment correlation coefficient (r) and the coefficient of determination (r^2). If residuals were non-normally distributed (Shapiro-Wilk W , $P \leq .05$), the Spearman ρ rank correlation coefficient was calculated.

To test the effect of image processing on conspicuity and CNR, we tested differences between variables on baseline and enhanced images for normality with the Shapiro Wilk W test, and equality of variances was tested with the F test. If data distributions were normal (Shapiro-Wilk W , P value $> .05$) and variances were equal (F test, P value $> .05$), the 2-tailed t test was used. If either or both of the data distributions were non-normally distributed (Shapiro-Wilk W , P value $\leq .05$) and/or variances were not equal (F test, P value $\leq .05$), the 2-tailed Mann-Whitney U test was used. Because most comparisons involved non-normally distributed data, boxplots of results were used to illustrate differences.

To assess the effect of image processing on the qualitative perception of GWD, we subtracted baseline GWD and artifact ratings from corresponding enhanced ratings. Positive numbers indicated beneficial effects of image enhancement, and negative numbers indicated detrimental effects of image enhancement. The normality of the data distributions for differences in ratings was tested with the Shapiro-Wilk W test, and all distributions were non-normal ($P < .05$); therefore, minimum, maximum, and median values plus 25th and 75th quantiles (quartiles) were used for descriptive statistics. In addition, the number of positive and negative differences was determined. The 1-sample, signed rank test (2-tailed, with a test value of zero) was used to assess the probability of obtaining the observed differences (or more unlikely differences) if the null hypothesis that there was no difference between baseline and enhanced images was true.

The effect of image processing was also assessed for subgroups with 2 distinct radiation levels used.

$P \leq .05$ was considered statistically significant. Statistical analyses were performed with JMP Pro Statistical Software, Release 12.0.1 (SAS Institute, Cary, North Carolina) and MedCalc Statistics for Biomedical Research, Version 17.2, (MedCalc Software, Ostend, Belgium; <https://www.medcalc.org>; 2017).

RESULTS

Correlation between Qualitative and Quantitative Measures of GWD

At baseline, gray matter conspicuity was 37.3 ± 11.6 with a baseline CNR between gray and white matter of 1.9 ± 0.9 . The mean GWD rating assigned by 2 readers on baseline images was 3.2 ± 0.9 . A positive correlation was observed between the mean GWD

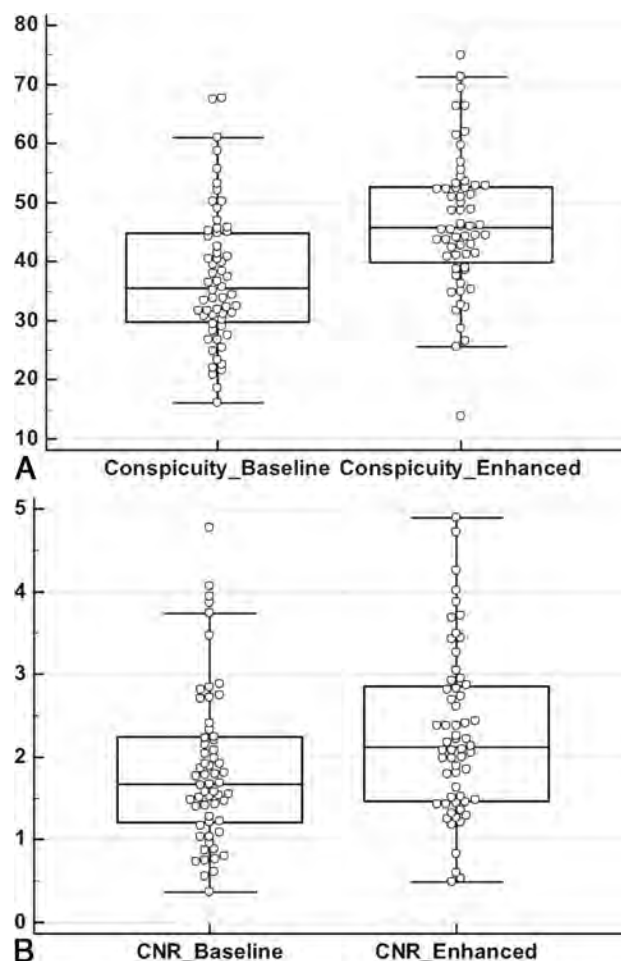


FIG 3. Boxplots showing the distribution of gray matter conspicuity (A) and CNR between gray and white matter (B) in 60 paired head CT images with normal findings before (baseline) and after (enhanced) processing with CIE. Both of these quantitative measures of gray-white differentiation demonstrated significant improvement following image processing ($P < .001$ for conspicuity; $P = .015$ for CNR).

rating and both conspicuity ($r = 0.29$; 95% confidence limits, 0.035, 0.50; $r^2 = 0.08$; $P = .027$) and CNR ($\rho = 0.54$; 95% confidence limits, 0.33, 0.70; $P < .001$).

Effect of Image Processing on Quantitative Measures of GWD

Image processing resulted in a significant ($P < .001$) increase in the gray matter conspicuity from a value of 37.3 ± 11.6 on baseline images to 46.4 ± 11.5 on enhanced images (Fig 3A). Similarly, the CNR between gray and white matter on the enhanced images (2.3 ± 1.0) represented a significant increase from the corresponding baseline value of 1.9 ± 0.9 (Fig 3B, $P = .02$).

For patients scanned using standard protocol, conspicuity increased from 38.3 ± 12.3 at baseline to 47.5 ± 11.2 ($P < .001$) on enhanced images, and CNR increased from 2.3 ± 1.0 at baseline to 2.8 ± 0.9 ($P = .024$) on enhanced images. For the subgroup scanned with the low-dose protocol, there was significant improvement ($P = .003$) in conspicuity from a baseline value of 36.3 ± 10.9 to 45.4 ± 11.9 on enhanced images. While CNR increased by 24% from a baseline value of 1.4 ± 0.6 to 1.7 ± 0.7 on enhanced images, differences did not reach significance ($P = .058$).

CIE: Effect on Qualitative GWD Rating

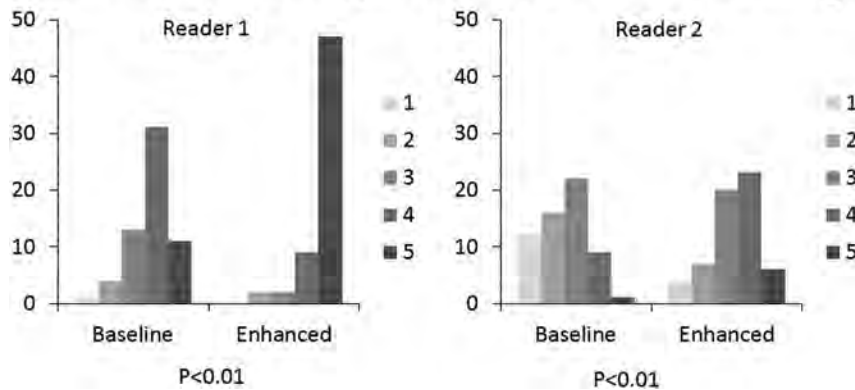


FIG 4. Clustered columns showing the distribution of qualitative GWD ratings assigned by 2 blinded radiologists to baseline and enhanced images on a 5-point Likert scale ranging from 1 (imperceptible GWD) to 5 (very easily perceptible GWD). The vertical axis shows the percentage of all cases assigned a given GWD rating. A favorable shift toward higher GWD ratings was seen with image processing for both radiologists ($P < .01$).

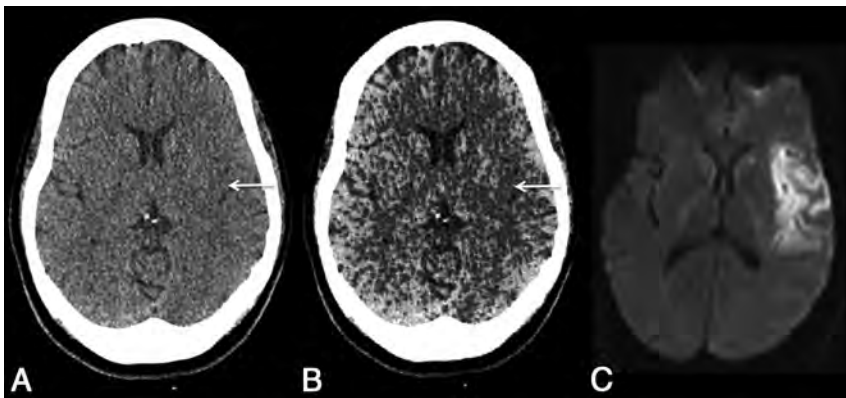


FIG 5. Axial head CT image across the insula obtained within 3 hours of stroke onset before (A) and after (B) processing with CIE. Note that improved gray-white differentiation following image processing makes it easier to perceive the loss of normal gray matter density in the insula (arrow), corresponding to the infarction proved on subsequent DWI (C).

Effect of Image Processing on Qualitative Perception of GWD

Reader 1 assigned a median GWD rating of 4 to baseline images (range, 1–5; 25th quartile 3; 75th quartile 4) and a median GWD rating of 5 to enhanced images (range, 2–5; 25th quartile 5; 75th quartile 5). For reader 2, the median baseline GWD rating was 3 (range 1–5; 25th quartile 2; 75th quartile 3) and the median enhanced GWD rating was 3 (range, 1–5; 25th quartile 3; 75th quartile 4). For both readers, these ratings constituted a significant improvement in the GWD rating following image processing (Fig 4, $P < .01$). Improvement in the GWD rating was observed for images obtained with standard protocol and for images obtained with low-dose protocol ($P < .01$ for each reader in each group). There was no difference in the artifact ratings of baseline and enhanced images assigned by either reader ($P = .11$ for reader 1 and $P > .99$ for reader 2).

DISCUSSION

Increasing recognition of the adverse effects of radiation has prompted efforts to reduce the radiation dose used to obtain diagnostic CT scans, especially in the pediatric population.^{9,21–23} A

lower signal-to-noise ratio, resulting from a reduction in the radiation dose,²¹ can, however, adversely affect the visibility of gray-white matter differentiation on pediatric head CTs. By demonstrating an objective improvement in CNR and the conspicuity of GWD, our results indicate that image processing using CIE may help in mitigating some of the detrimental effects of the lower radiation dose on head CT. The beneficial effect of this image processing was observed even in scans that were obtained with an aggressive dose-reduction protocol. Our results are similar to those of Bier et al,¹³ who achieved improvement in GWD in adult head CTs using a different image-processing algorithm based on the frequency-selective nonlinear blending. Both studies are also similar in demonstrating that such improvement in GWD can be achieved without inducing any appreciable artifacts. These image-processing algorithms are, however, dissimilar in that CIE, being based on the continuity of structures, is technique-neutral and has been used both for enhancing CT and MR images.²⁰

Radiologists routinely adjust the window and level of digital radiologic images to optimize the contrast needed for easy visualization of details of interest such as GWD.^{24–27} Such contrast optimization, however, does not affect the relative intensity values assigned to individual pixels on the Hounsfield unit scale and would not be expected to improve the inherent CNR between gray and white matter.

On the other hand, our image-processing algorithm improved the GWD by modifying relative assigned values of individual pixel intensity for pixels representing gray and white matter as indicated by improved CNR. The image algorithm used by Bier et al¹³ appears to have a similar effect because they described the signal intensity (SI) of cortical gray matter after image processing as approximately 60, a level that would not be expected for normal gray matter on the Hounsfield unit scale. While previous authors described this newly assigned intensity level in terms of Hounsfield units, it may not be appropriate because the newly assigned intensities may not align with the expected value of certain tissues on the Hounsfield unit scale.

Both quantitative measures of GWD correlated with and translated into easier perception of GWD by both readers (Fig 4). This may indicate that the beneficial effects of this tool may help readers of different experience levels. Given the subjective nature of the GWD rating scale, one reader rated the images more critically than the other (Fig 4). These differences could either represent an actual difference in the ease of GWD perception between readers or differences in the

expectation of best possible GWD achievable on head CT images. While we are not able to postulate the exact cause for these differences, improved GWD perception was noted for each reader irrespective of their baseline ratings. Improved perception of GWD can be expected to be helpful for diagnosing diseases in which it is lost (such as ischemic infarction, encephalitis) as well as for diseases in which gray matter is unduly thickened (such as malformations of cortical development).^{1,2,28-31} Using the same image-processing algorithm that improved GWD on head CT images with normal findings, previous investigators were able to improve the accuracies of radiologists in diagnosing acute infarction and encephalitis on head CTs.^{13,30,32} Further studies are needed to test whether improved gray-white differentiation afforded by CIE on head CT images can translate into similar improved sensitivity for the detection of disease processes such as ischemic infarcts (Fig 5).

In this feasibility study, the readers were not able to adjust the window or level of the images. It is likely that the ability to optimize window settings would have allowed radiologists to improve the visibility of GWD in baseline images. However, improvement in objective, quantitative measures indicates a favorable effect of CIE beyond what would be achievable by window and level adjustments. Furthermore, enhanced images generated with this image-processing algorithm could also be subject to further optimization using window and level adjustment tools. While the algorithm was applied to only 2 images from each patient's scan, we expect similar results if this algorithm were to be applied to the entire set of images in head CT.

CONCLUSIONS

Image processing using an algorithm based on correlative properties of contiguous pixels improved the CNR between normal gray and white matter in head CTs of children. This benefit was also observed for scans obtained using a low radiation dose. Further studies are needed to see whether these results can translate into better detection of disease processes.

Disclosures: Aseem Sharma—UNRELATED: Consultancy: Biomedical Systems, Comments: As a consultant, I serve as an independent reviewer for imaging studies performed for research by third parties; RELATED: The algorithms used in this study were co-invented by me. I have applied for a patent (pending) for these algorithms and founded a company (Correlative Enhancement LLC) with the aim of future commercialization of the IP. I am the sole proprietor of the company, and since the inception of the company until now (including the time during which I processed the images for this study), this company has not received funding from any external source. While I used the algorithms to process the images for this study, I did not participate in image review, image analysis, or the subsequent statistical analysis.

REFERENCES

1. Truwit CL, Barkovich AJ, Gean-Marton A, et al. **Loss of the insular ribbon: another early CT sign of acute middle cerebral artery infarction.** *Radiology* 1990;176:801–06 CrossRef Medline
2. Moulin T, Cattin F, Crépin-Leblond T, et al. **Early CT signs in acute middle cerebral artery infarction: predictive value for subsequent infarct locations and outcome.** *Neurology* 1996;47:366–75 CrossRef Medline
3. Weinstein MA, Duchesneau PM, MacIntyre WJ. **White and gray matter of the brain differentiated by computed tomography.** *Radiology* 1977;122:699–702 CrossRef Medline
4. Brenner DJ, Hall EJ. **Computed tomography: an increasing source of radiation exposure.** *N Engl J Med* 2007;357:2277–84 CrossRef Medline
5. Pearce MS, Salotti JA, Little MP, et al. **Radiation exposure from CT scans in childhood and subsequent risk of leukaemia and brain tumours: a retrospective cohort study.** *Lancet* 2012;380:499–505 CrossRef Medline
6. Palmer E. **Image Gently Think A-Head Campaign focuses on pediatric head CT protocols.** *Radiol Technol* 2017;88:446–47 Medline
7. Frush DP, Lungren MP. **The Image Gently Think A-Head Campaign: keep calm and image gently.** *J Am Coll Radiol* 2017;14:301–02 CrossRef Medline
8. Applegate KE, Cost NG. **Image Gently: a campaign to reduce children's and adolescents' risk for cancer during adulthood.** *J Adolesc Health* 2013;52(5 Suppl):S93–97 CrossRef Medline
9. Goske MJ, Applegate KE, Boylan J, et al. **The 'Image Gently' campaign: increasing CT radiation dose awareness through a national education and awareness program.** *Pediatr Radiol* 2008;38:265–69 CrossRef Medline
10. McCollough CH, Primak AN, Braun N, et al. **Strategies for reducing radiation dose in CT.** *Radiol Clin North Am* 2009;47:27–40 CrossRef Medline
11. Wu TH, Hung SC, Sun JY, et al. **How far can the radiation dose be lowered in head CT with iterative reconstruction? Analysis of imaging quality and diagnostic accuracy.** *Eur Radiol* 2013;23:2612–21 CrossRef Medline
12. Bodelle B, Wichmann JL, Scholtz JE, et al. **Iterative reconstruction leads to increased subjective and objective image quality in cranial CT in patients with stroke.** *AJR Am J Roentgenol* 2015;205:618–22 CrossRef Medline
13. Bier G, Bongers MN, Ditt H, et al. **Enhanced gray-white matter differentiation on non-enhanced CT using a frequency selective non-linear blending.** *Neuroradiology* 2016;58:649–55 CrossRef Medline
14. Löve A, Siemund R, Höglund P, et al. **Hybrid iterative reconstruction algorithm in brain CT: a radiation dose reduction and image quality assessment study.** *Acta Radiol* 2014;55:208–17 CrossRef Medline
15. Greess H, Wolf H, Baum U, et al. **Dose reduction in computed tomography by attenuation-based on-line modulation of tube current: evaluation of six anatomical regions.** *Eur Radiol* 2000;10:391–94 CrossRef Medline
16. Mulkens TH, Bellinck P, Baeyaert M, et al. **Use of an automatic exposure control mechanism for dose optimization in multi-detector row CT examinations: clinical evaluation.** *Radiology* 2005;237:213–23 CrossRef Medline
17. Graser A, Wintersperger BJ, Suess C, et al. **Dose reduction and image quality in MDCT colonography using tube current modulation.** *AJR Am J Roentgenol* 2006;187:695–701 CrossRef Medline
18. Sharma A, Goyal M, Miller-Thomas M, et al. **Feasibility of improving detection of early ischemic infarction on head CT using continuity-based correlative enhancement.** In: *Proceedings of the Radiological Society of North America 2015 Scientific Assembly and Annual Meeting*, Chicago, Illinois. November 29 to December 4, 2015. <http://archive.rsna.org/2015/15010218.html>. Accessed March 6, 2016
19. Sharma A, JP, Warren LA, Parsons MS, et al. **Feasibility of using continuity-based correlative enhancement for improving recognition of structural details based on gray-white differentiation in head CT images.** In: *Proceedings of the Radiological Society of North America 2015 Scientific Assembly and Annual Meeting*, Chicago, Illinois. November 29 to December 4, 2015. <http://archive.rsna.org/2015/PediatricRadiology.pdf>. Accessed March 6, 2016
20. Parsons M, Sharma, A, Mhapsekar, R, et al. **Image processing to improve visualization of mesial temporal sclerosis on MRI.** In: *Proceedings of the Radiological Society of North America 2016 Scientific Assembly and Annual Meeting*, Chicago, Illinois. November 27 to December 2, 2016. archive.rsna.org/2016/16018969.html. Accessed March 20, 2017
21. Frush DP. **Justification and optimization of CT in children: how are we performing?** *Pediatr Radiol* 2011;41(Suppl 2):467–71 CrossRef Medline
22. Goske MJ, Applegate KE, Boylan J, et al. **The Image Gently Campaign: working together to change practice.** *AJR Am J Roentgenol* 2008;190:273–74 CrossRef Medline

23. Hall EJ. **Lessons we have learned from our children: cancer risks from diagnostic radiology.** *Pediatr Radiol* 2002;32:700–06 CrossRef Medline
24. Lev MH, Farkas J, Gemmete JJ, et al. **Acute stroke: improved nonenhanced CT detection—benefits of soft-copy interpretation by using variable window width and center level settings.** *Radiology* 1999; 213:150–55 CrossRef Medline
25. Kuo R, Cheng SJ, Huang JK, et al. **Promotion of residents' diagnostic accuracy of early ischemic infarct on nonenhanced brain computed tomography with a modified window setting.** *Neurologist* 2010;16: 306–07 CrossRef Medline
26. Arsava EM, Saarinen JT, Unal A, et al. **Impact of window setting optimization on accuracy of computed tomography and computed tomography angiography source image-based Alberta Stroke Program Early Computed Tomography Score.** *J Stroke Cerebrovasc Dis* 2014;23:12–16 CrossRef Medline
27. Sahi K, Jackson S, Wiebe E, et al. **The value of “liver windows” settings in the detection of small renal cell carcinomas on unenhanced computed tomography.** *Can Assoc Radiol J* 2014;65:71–76 CrossRef Medline
28. Sanelli PC, Sykes JB, Ford AL, et al. **Imaging and treatment of patients with acute stroke: an evidence-based review.** *AJNR Am J Neuroradiol* 2014;35:1045–51 CrossRef Medline
29. Abdel Razek AA, Kandell AY, Elsorogy LG, et al. **Disorders of cortical formation: MR imaging features.** *AJNR Am J Neuroradiol* 2009;30: 4–11 Medline
30. Bongers MN, Bier G, Ditt H, et al. **Improved CT detection of acute herpes simplex virus type 1 encephalitis based on a frequency-selective nonlinear blending: comparison with MRI.** *AJR Am J Roentgenol* 2016;207:1082–88 CrossRef Medline
31. Tomura N, Uemura K, Inugami A, et al. **Early CT finding in cerebral infarction: obscuration of the lentiform nucleus.** *Radiology* 1988; 168:463–67 CrossRef Medline
32. Bier G, Bongers MN, Ditt H, et al. **Accuracy of non-enhanced CT in detecting early ischemic edema using frequency selective nonlinear blending.** *PLoS One* 2016;11:e0147378 CrossRef Medline

Looking Deep into the Eye-of-the-Tiger in Pantothenate Kinase–Associated Neurodegeneration

J.-H. Lee, A. Gregory, P. Hogarth, C. Rogers, and S.J. Hayflick



ABSTRACT

BACKGROUND AND PURPOSE: A detailed delineation of the MR imaging changes in the globus pallidus in pantothenate kinase–associated neurodegeneration will be helpful for diagnosis and monitoring of patients. The aim of this study was to determine the morphologic spectrum of the “eye-of-the-tiger” sign and the topographic pattern of iron deposition in a group of patients with pantothenate kinase–associated neurodegeneration.

MATERIALS AND METHODS: Seventy-four MR imaging scans from 54 individuals with *PANK2* mutations were analyzed for signal patterns in the globus pallidus. Sixteen SWI data from 15 patients who underwent 1.5T ($n = 7$), 3T ($n = 7$), and 7T ($n = 2$) MR imaging were included to visualize the iron topography.

RESULTS: The linear hyperintensity alongside the medial border of the globus pallidus was the earliest T2 signal change. This finding was evident before SWI changes from iron deposition became visible. T2WI performed in early childhood mostly showed isolated hyperintense signal. In adult patients, marked signal reduction within an earlier hyperintense center resulting from iron accumulation led to the loss of signal difference between the central and surrounding areas. Signal hypointensity on SWI progressed from the medial to the lateral portion of the globus pallidus with increasing age. The fiber connections between the medial globus pallidus and the anteromedial aspect of the substantia nigra and subthalamic nucleus were markedly hypointense on SWI.

CONCLUSIONS: In pantothenate kinase–associated neurodegeneration, the globus pallidus MR imaging changes using SWI develop as region-specific and age-dependent phenomena. Signal inhomogeneity was observed across the globus pallidus in pantothenate kinase–associated neurodegeneration and should be considered when determining the concentration of iron.

ABBREVIATIONS: PKAN = pantothenate kinase–associated neurodegeneration; GP = globus pallidus; SN = substantia nigra; STN = subthalamic nucleus

Neurodegeneration with brain iron accumulation is a heterogeneous group of genetic diseases that shares the feature of basal ganglia iron accumulation.¹ The diagnosis of neurodegeneration with brain iron accumulation is suspected by combining

clinical features and MR imaging evidence of iron accumulation in the brain.¹ The most common neurodegeneration with brain iron accumulation disorder is pantothenate kinase–associated neurodegeneration (PKAN), caused by a mutations in the *pantothenate kinase 2 (PANK2)* gene.¹

PKAN is usually suspected when the “eye-of-the-tiger” sign on T2WI is present.^{2,3} It comprises a central region of signal hyperintensity, reflecting gliosis and edema, and surrounding hypointensity caused by iron accumulation in the globus pallidus (GP).^{4,5} However, this specific MR imaging sign for PKAN may be absent in early disease stages.³ Isolated GP hyperintensity on T2WI may predate the appearance of surrounding hypointensity related to iron accumulation.³ Additionally, it appears to change with time, obscuring an initially hyperintense center by the accumulation of iron.⁶ The eye-of-the-tiger sign has been reported to occur as an imaging phenocopy in other conditions, such as neuroferritinopathy, carbon monoxide intoxication, multiple system atrophy, and corticobasal degeneration, and in healthy adults.^{3,5,7,8} A

Received August 20, 2017; accepted October 31.

From the Departments of Molecular and Medical Genetics (J.-H.L., A.G., P.H., C.R., S.J.H.), Neurology (P.H., S.J.H.), and Pediatrics (S.J.H.), Oregon Health & Science University, Portland, Oregon; and Department of Neurology (J.-H.L.), Pusan National University Yangsan Hospital, Medical Research Institute, Pusan National University School of Medicine, Yangsan, South Korea.

Jae-Hyeok Lee and Susan J. Hayflick contributed equally to this work.

Please address correspondence to Jae-Hyeok Lee, MD, PhD, Department of Neurology, Pusan National University Yangsan Hospital, Pusan National University School of Medicine, Beomo-ri, Mulgum-eup, Yangsan, Gyeongsangnam-do 626–770, Republic of Korea; e-mail: jhlee.neuro@pusan.ac.kr; Susan Hayflick, MD, Departments of Molecular & Medical Genetics, Neurology, and Pediatrics, Oregon Health & Science University, Portland, OR 97239; e-mail: hayflick@ohsu.edu

 Indicates article with supplemental on-line table.

 Indicates article with supplemental on-line photos.

<http://dx.doi.org/10.3174/ajnr.A5514>

detailed delineation of the radiographic changes in the GP in PKAN, especially early in the disease, will be helpful for the diagnostic evaluation.

In most cases of PKAN, iron accumulation is limited to the GP and substantia nigra (SN), even in advanced stages.^{1,2,4} The detection of iron depends on the MR imaging sequence used.⁴ SWI has shown higher sensitivity for visualization of brain iron than conventional techniques, including T2WI.⁹ Previous SWI studies demonstrated iron-related signals in the GP and SN.^{10,11} SWI also showed marked hypointense tracts connecting the GP and SN.^{10,11} However, their anatomic delineation and clinical significance have not yet been determined.

The aim of this study was to delineate the topographic spectrum of the eye-of-the-tiger sign and pathologic iron accumulation using SWI in individuals with PKAN across the life span and their disease course. On the basis of this analysis, we propose a definition of the eye-of-the-tiger sign that is specific to PKAN.

MATERIALS AND METHODS

Brain MR imaging scans of patients with PKAN were obtained from the Oregon Health & Science University and Pusan National University Yangsan Hospital using protocols approved by the respective institutional review boards. Seventy-four MR imaging scans were collected on 54 patients with PKAN (mean age at first MR imaging, 13.4 years; range, 9 months ~ 76 years) with *PANK2* mutations from 49 families. Serial MR imaging scans were available for 14 patients: 9 patients with 2 serial scans and 5 patients with 3 serial scans (mean time between scans, 2.08 years; range, 9 months ~ 5 years). MR imaging was performed with 1.5T ($n = 51$), 3T ($n = 21$), and 7T ($n = 2$) scanners. Two siblings underwent both 3T and 7T MR imaging at the same time point. T2WIs were available for all subjects; the corresponding axial T1WIs were available in 48 MR images from 41 subjects.

To identify the eye-of-the-tiger sign on axial T2WI, we selected 2 consecutive images at the level of and just above the level of the anterior commissure (On-line Fig 1). The presence of a visible round hyperintense center in the anteromedial aspect of the GP at the level of the anterior commissure was considered a key component of the eye-of-the-tiger sign. We divided typical cases with the round hyperintense center into 2 groups according to the surrounding signal intensity. The signal intensity of the surrounding GP area was scored as isointense or hypointense relative to adjacent internal capsule (On-line Fig 1).³ The MR imaging findings were classified as “atypical” in the cases with marked signal reduction within an earlier hyperintense center, which led to the obscuring or loss of signal difference between the central and surrounding areas.

Among 54 patients with PKAN, 16 SWI data from 15 patients who underwent MRI at 1.5T ($n = 7$), 3T ($n = 7$), and 7T ($n = 2$) were analyzed to determine the topography of iron accumulation (On-line Table). One patient had 2 serial SWIs at 3T (patient 9). SWI findings of 2 siblings have already been published (patients 7 and 13).¹⁰ We evaluated the following demographic and clinical data: sex; age at clinical evaluation and MR imaging with SWI acquisition; age at onset; family history; clinical features; clinical subtype (classic or atypical based on age at onset and rate of disease progression according to the criteria of Hayflick et al²); and

PANK2 mutation data (NM_153638.2). SWI sequences were defined as those with low flip angles acquired with a gradient-echo technique designed to accentuate susceptibility effects (TR, 27–50 ms; TE, 20–40 ms; flip angle, 12°–15°; slice thickness, 2.0–3.0 mm). SWI was created by combining the magnitude and phase images. SWI was viewed in the axial and coronal planes using the open-source OsiriX Imaging Software (<http://www.osirix-viewer.com>), which provided multiplanar reconstruction views. SWI was used to identify the subthalamic nucleus (STN) and SN. In coronal SWI, the SN lies inferior and medial to the STN.¹² T2- and T2*-weighted sequences were excluded from the analysis because they were not sufficiently sensitive to visualize the signal changes in the SN and STN in detail for the determination of iron topography. Five age- and sex-matched healthy individuals served as controls at each field strength (1.5T and 3T).

Because this was a retrospective study, the scans were obtained on different MR imaging scanners with corresponding sequence parameters. Field strength and sequence parameters were taken into account in determining normal-versus-abnormal signal intensity characteristics. T2 or T1 signal intensity in the GP was compared with that in the adjacent normal-appearing white matter. The globus pallidus becomes hypointense with respect to white matter around the end of the first decade of life.¹³ The signal changes associated with myelination on T1WI and T2WI were considered when evaluating MR imaging scans obtained during infancy and early childhood. All MR images were anonymized without clinical information and presented randomly during the interpretation. To ensure consistency, the same rater (J.-H.L.) rated the MR images. They were then reviewed by the second rater (S.J.H.) to provide independent validation of the results. Any discrepancy between raters was resolved by consensus.

RESULTS

The Eye-of-the-Tiger Sign on T2WI and T1WI

On T2WI, the eye-of-the-tiger sign with the hyperintense round center was observed in 47 MRIs (63.5% of all MRIs) from 42 patients. Among them, 15 MRIs (mean age at MR imaging, 4.7 years; range, 3~7 years) from 13 patients were found to have an isolated T2-hyperintense center without surrounding hypointensity (Fig 1). At a higher resolution, these hyperintense centers were not confined to the anterior GP but extended to the posterior GP at the level just above the anterior commissure (On-line Fig 1). The posteroinferior portion of the GP appeared isointense. Thirty-two images from 30 patients (mean age at MR imaging, 15.1 years; range, 3~45) showed surrounding hypointensity related to excessive iron accumulation. The surrounding areas of hypointensity tended to increase in size and decrease in signal intensity with age (Fig 1).

None of 12 MR imaging scans from 8 patients younger than 3 years of age had a typical eye-of-the-tiger sign. The round hyperintense center in the anteromedial GP was observed at older than 3 years of age. Seven MRIs from 6 patients (mean age at MR imaging, 2.15 years; range, 22 months ~ 3 years) showed linear T2-hyperintensity that streaked along the medial border of the GP (Fig 2). In 4 of those 6 patients, the round hyperintense centers were visualized in the follow-up scans.

Eleven patients presented with atypical imaging features in

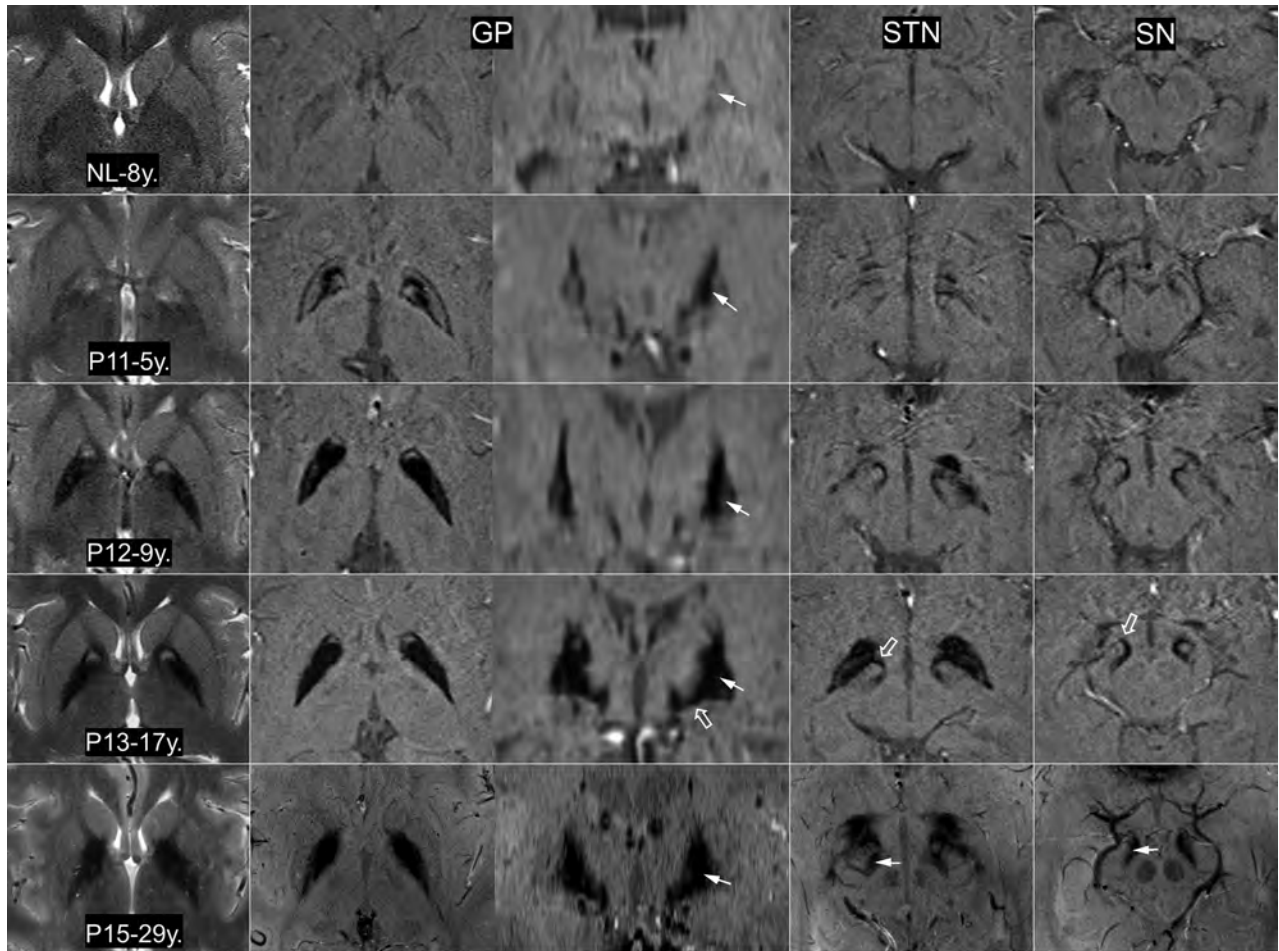


FIG 1. The eye-of-the-tiger sign on T2WI and iron topography on SWI at 3T MR imaging (NL, P11, P12, P13) and 7T MR imaging (P15). On T2WI, the round hyperintense center is reduced in size with extension of the surrounding hypointensity. A noticeable difference in signal hypointensity between the medial and lateral segments of the globus pallidus tends to be obscured with increasing age (*arrows*). The reduction of signal intensity in both the subthalamic nucleus and substantia nigra (P15, *arrow*) tends to be proportional to that of the GP. The fiber connections of the medial GP with the SN and STN are dramatically visualized (P13, *open arrow*). NL indicates healthy control; P11/P12/P13/P15, the number of patients in the On-line Table; y., years of age.

their 13 MR imaging scans (mean age at MR imaging, 27.1 years; range, 5~76 years). All of them showed marked signal reduction without clearly visible round hyperintensity in the GP (Fig 3). The dark streak between the medial and lateral segments of the GP extended anteriorly into the hyperintense center. In cases without a hyperintense center, hyperintense streaking was frequently observed in the central region.⁶ Three patients did not show any hyperintense focus within the GP. In these cases, T2-hypointensity almost always extended into the genu of the internal capsule (Fig 3). Bilateral GP calcification was observed in 3 among 7 patients who underwent brain CT. In 1 patient at 5 years of age, the hyperintense center was obscured probably by calcification (Fig 3). The dark streak was observed within the hyperintense center in the other patient at 4 years of age.

Signal changes were commonly observed on T1WI. There were 48 of these MRIs reviewed. The region of T2-hyperintensity appeared hypointense on T1WI in 25 MRIs (52%) from 24 patients (mean age at MR imaging, 12.6 years; range, 4~76 years) (On-line Fig 2). Thirty-two MRIs (66%) from 30 patients (mean age at MR imaging, 15.9 years; range: 4~76 years) showed T1-hyperintensity in the region of T2-hypointensity.

Iron-Related Hypointense Signal on SWI

The clinical and imaging features from 15 patients with SWI are summarized in the On-line Table. In our case series, signal hypointensity on SWI with an isolated T2-hyperintense center was first detected in a 3-year-old patient (Fig 2). In a patient with serial MRIs, SWI hypointensity was not evident at 22 months of age. The follow-up SWI at 4 years of age showed the typical pattern of iron deposition accompanied by the appearance of an isolated T2-hyperintense center in the GP. In patients with isolated T2-hyperintensity, SWI showed marked iron-related hypointense signal contiguous with the medial aspect of the GP (On-line Fig 3). There was a noticeable difference in signal intensity between the medial and lateral segments of the GP (Fig 1). SWI signal hypointensity was greatest medially. This SWI signal difference across the GP tended to be obscured and lost as the surrounding T2-hypointensity became more evident. The reduction of signal intensity in both the STN and SN tended to be proportional to that of the GP (Fig 1). SWI showed marked hypointense tracts connecting the medial portion of the GP and the STN. The hypointense connecting tracts ran medially through the crus cerebri from the pars reticulata of the SN. They were more prominent in

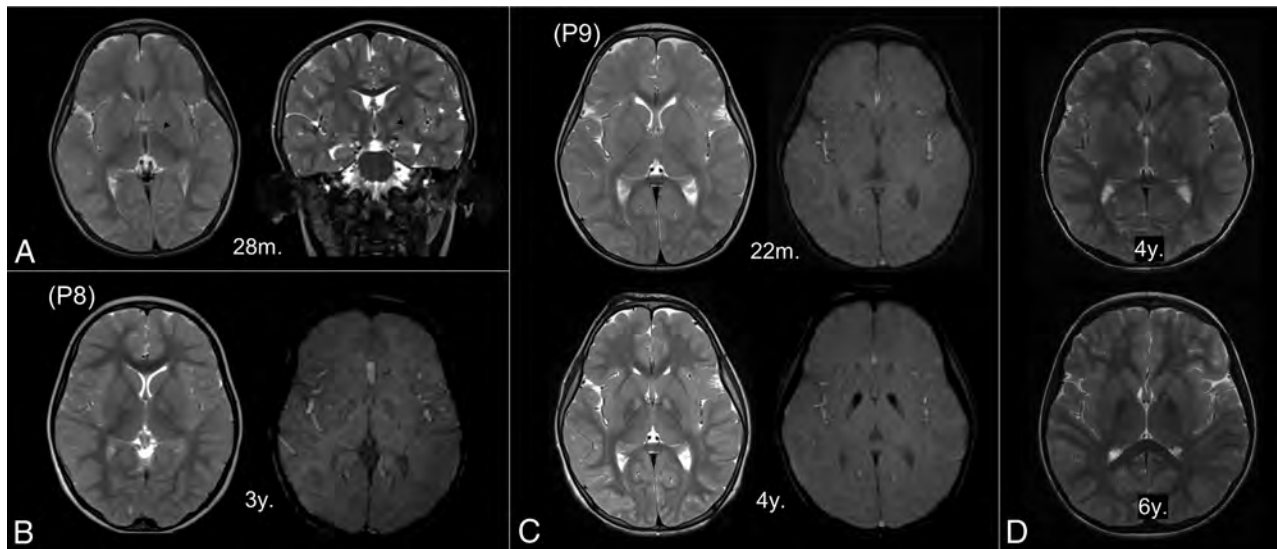


FIG 2. Early MR imaging changes in the globus pallidus. The linear T2-hyperintensity that streaks along the medial border of the GP is the earliest T2 change (A, arrowhead). The round center in the anteromedial aspect is first observed at 3 years of age (B, left). Subtle hypointensity is also detected on the susceptibility-weighted image (B, right). In patients with serial MRIs (C and D), iron-related hypointensity becomes definitely evident by 4 years of age with the appearance of an isolated T2-hyperintense center (C). The surrounding areas decrease in signal intensity with age (D). P8 and P9 indicate the number of patients in the On-line Table; m., months of age; y., years of age.

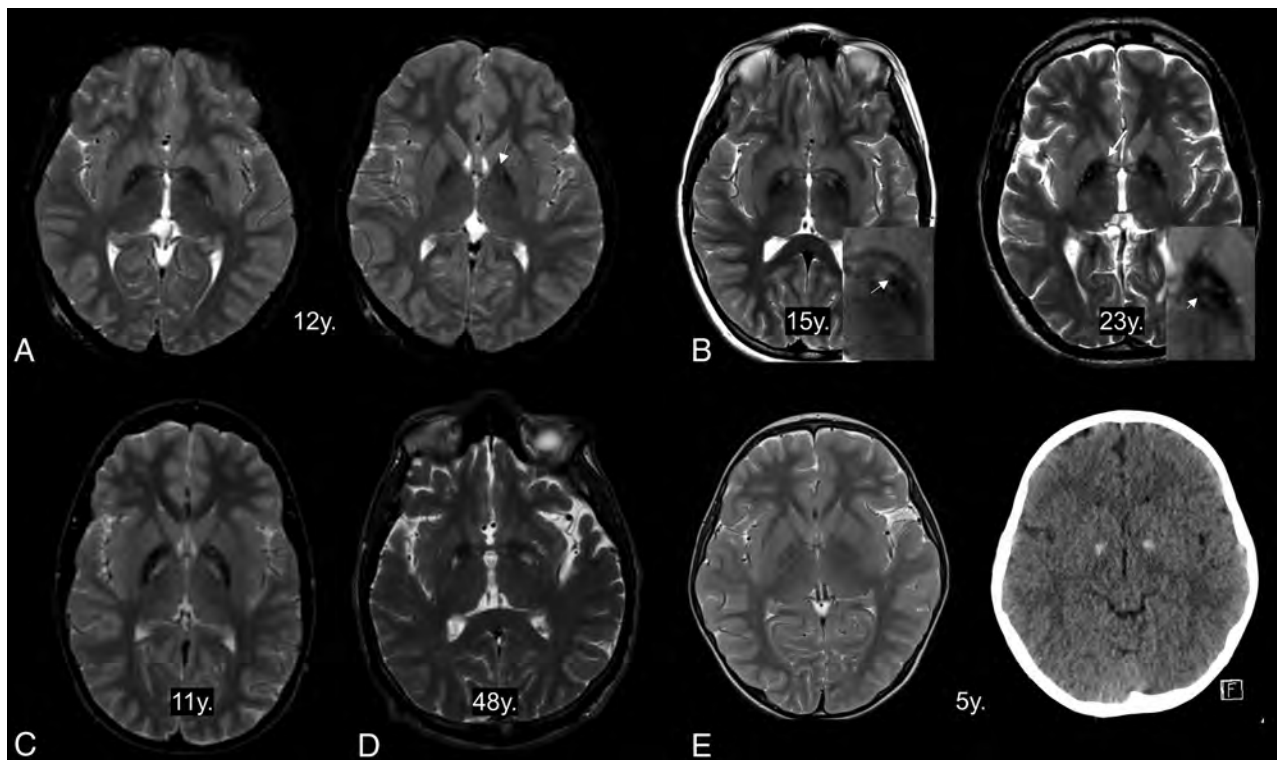


FIG 3. Atypical features of the eye-of-the-tiger sign. The hyperintense area in the anteromedial globus pallidus has totally disappeared at the anterior commissural level (A, left) but is partly visible at just above that level (A, right, arrow). The dark streaks extend into the hyperintense centers (B, left, arrow). The remaining component of hypointensity is observed as hyperintense stripes (B, right, short arrow). T2-hyperintensity extends into the genu of the internal capsule (B, right, long arrow). The hyperintense areas are unusually located in the whole medial GP (C) and posterior GP (D). The hyperintense center is obscured in a patient with GP calcification (E). y. indicates years of age.

the rostral and anterior portions of the SN. All hypointense areas showed similar tendencies toward decreasing signal intensity with age. MR imaging with a higher field strength provided better spatial and contrast resolution. Two siblings underwent 7T MR imaging, which showed iron deposition in the SN and STN and their connecting tracts more clearly.

DISCUSSION

In this study, we demonstrated a wide morphologic spectrum of the eye-of-the-tiger sign and the characteristic pattern of iron deposition using SWI. However, this study is limited by a retrospective collection of cases, simple visual assessment without quantitation, and intersite or interscanner variability in the MR

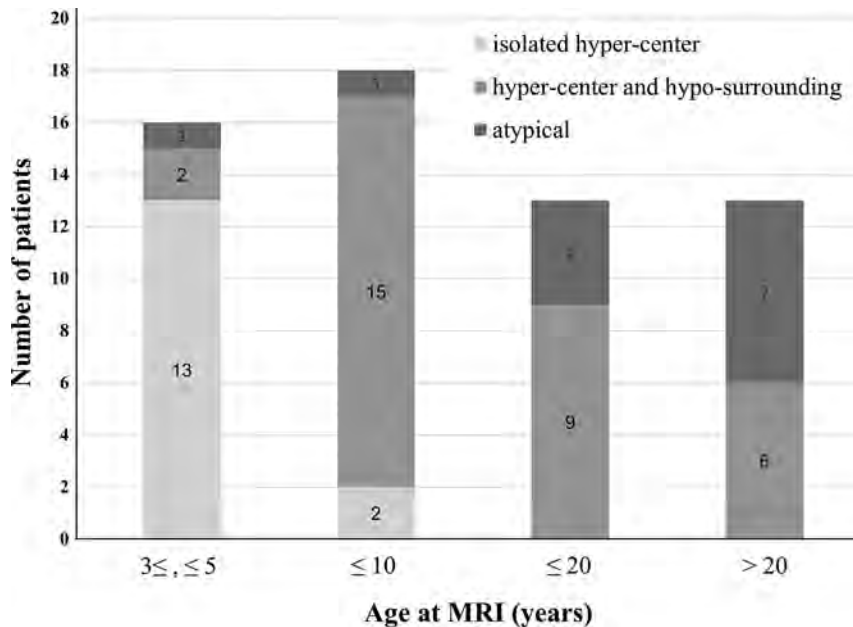


FIG 4. Graph shows the age distribution of the eye-of-the-tiger sign classified into 3 categoric patterns. “Hyper-center” indicates T2-hyperintense center of the GP; “hypo-surrounding,” the surrounding area with T2-hypointensity; atypical, atypical features.

imaging sequence parameters. Despite these limitations, important conclusions can be drawn from this large series.

The MR imaging signal pattern in the GP was found to differ within subjects as their age increased and disease advanced, as well as across subjects depending on the extent of surrounding hypointensity resulting from iron accumulation. The typical eye-of-the-tiger sign with surrounding hypointensity was observed in only about half of the patients. T2WI performed in early childhood mostly showed the round center without surrounding hypointensity (Fig 4). In adult patients older than 20 years of age, the hyperintense center was often condensed, streaked, or entirely lost, presumably due to increased iron accumulation. With the increase and extension of iron deposition, the hyperintense center varied in shape from small round to streaked. In addition to the effects from iron, the T2-hyperintense area of the sign was probably obscured by diamagnetic calcium deposits in some cases.¹⁴

The isolated hyperintense center on T2WI of the GP has been described as the earliest MR imaging change in patients with PKAN.³ Additionally, we found it present as a linear T2-hyperintense signal that streaks along the medial border of the GP in children younger than 3 years of age. This finding was evident before SWI changes from iron deposition became visible. The current understanding of PKAN pathogenesis and the sequence of cellular changes supports tissue edema and gliosis arising from the primary metabolic insult and preceding the accumulation of iron.¹⁵ Notably, in the early change, the posteroinferior portion of the GP appeared iso-intense or without signal changes, suggesting less tissue damage from a primary metabolic insult. The efficacy of deep brain stimulation from previous reports also suggests that this area may retain greater preservation of functional activity than the anteromedial region of the GP.¹⁶

The detection of the eye-of-the-tiger sign can be influenced by MR imaging acquisition settings, such as axis plane or thickness. The T2-hyperintense center in the anteromedial region is typi-

cally visible at the level of anterior commissure. The sensitivity for detecting the sign depends on the MR imaging sequences. Signal changes reflecting gliosis or iron deposits were also observed on T1WI, though the sensitivity of T1WI was much lower than that of T2WI. SWI clearly depicted the increase and extension of iron deposition in the white matter, small structures such as the STN and SN, and the corresponding area of T2-hyperintensity. Even in cases of isolated T2-hyperintense centers, SWI showed the specific pattern of iron deposition. This is because SWI is less affected by factors such as myelin loss and changes in water concentration than other conventional sequences using T2 methods.⁹

In PKAN, the signal hypointensity on SWI progressed from the medial to the lateral portion of the GP with increasing age and advancing disease. Although rigorous serial follow-up data are lacking, topographic spreading of

iron deposition does not clearly correlate with the duration or severity of disease symptoms.^{3,6} Our observations are most consistent with age-related patterns of iron deposition. In previous investigations using in vivo MR imaging, iron deposition increased with age in the GP, occurring first in the internal GP and progressing from the medial to the lateral aspect during normal brain development and aging.¹⁷ The region-specific pattern of iron deposition in normal aging can be enhanced and observed in pathologic conditions, such as parkinsonian variant multisystem atrophy, in which iron deposits mostly in the posterolateral part of the putamen are in line with the aging pattern.^{18,19}

The ability to quantify the iron content in the GP of patients with PKAN would help to understand disease progression and possibly monitor treatment response as disease-modifying agents are developed. There have been attempts to quantify iron stores in vivo in patients with PKAN, in which the surrounding hypointense area of the GP was usually used to determine the concentration of iron.^{11,20,21} However, most studies, including clinical trials of the iron-chelating drug deferiprone in PKAN, used single or 2 consecutive, manually drawn ROIs of the 2D images without delineating the exact boundaries of the GP.^{22,23} Signal inhomogeneity across the GP observed in this study should be considered when determining the concentration of iron.

Involvement of the SN and STN in previous studies may have been underestimated due not only to less sensitive sequences for the detection of iron but also less spatial resolution to discriminate among structures.^{3,7} SWI dramatically visualizes the paramagnetic signals from iron deposition around the fiber connections of the GP with the SN and STN. The findings of increasing iron deposition along these tracts in proportion to GP iron content, with a trend toward higher levels in their rostral connection to the GP, may suggest an underlying spreading process.²⁴ The damage to white matter tracts could represent neural network dysfunction. Similar paramagnetic susceptibility was detected in

the pallidoreticular pathways after carbon monoxide intoxication and was related to worse neuropsychiatric performance and a greater likelihood of parkinsonism.²⁵ In a previous diffusion tensor imaging study of PKAN, the alterations in white matter integrity were more widespread, affecting mainly the connections between the basal ganglia and the frontal regions.²⁶ However, the correlation of white matter damage with clinical parameters in patients with PKAN has not been fully elucidated.

CONCLUSIONS

The eye-of-the-tiger sign specific for PKAN was better defined using SWI in combination with T2WI. The morphology of the sign was found to differ depending on the extent of iron accumulation. Iron-related SWI changes in the GP develop as region-specific and age-dependent phenomena, which may contribute to the better understanding of the disease process in PKAN.

ACKNOWLEDGMENTS

We thank the Advanced Imaging Research Center and the Oregon Opportunity partnership for advancing biomedical research. The AIRC helped us obtain the 7T MRI data.

REFERENCES

- Hogarth P. **Neurodegeneration with brain iron accumulation: diagnosis and management.** *J Mov Disord* 2015;8:1–13 CrossRef Medline
- Hayflick SJ, Westaway SK, Levinson B, et al. **Genetic, clinical, and radiographic delineation of Hallervorden-Spatz syndrome.** *N Engl J Med* 2003;348:33–40 CrossRef Medline
- Hayflick SJ, Hartman M, Coryell J, et al. **Brain MRI in neurodegeneration with brain iron accumulation with and without PANK2 mutations.** *AJNR Am J Neuroradiol* 2006;27:1230–33 Medline
- Kruer MC, Hiken M, Gregory A, et al. **Novel histopathologic findings in molecularly-confirmed pantothenate kinase-associated neurodegeneration.** *Brain* 2011;134:947–58 CrossRef Medline
- Amaral LL, Gaddikeri S, Chapman PR, et al. **Neurodegeneration with brain iron accumulation: clinicoradiological approach to diagnosis.** *J Neuroimaging* 2015;25:539–51 CrossRef Medline
- Delgado RF, Sanchez PR, Speckter H, et al. **Missense PANK2 mutation without “eye of the tiger” sign: MR findings in a large group of patients with pantothenate kinase-associated neurodegeneration (PKAN).** *J Magn Reson Imaging* 2012;35:788–94 CrossRef Medline
- McNeill A, Birchall D, Hayflick SJ, et al. **T2* and FSE MRI distinguishes four subtypes of neurodegeneration with brain iron accumulation.** *Neurology* 2008;70:1614–19 CrossRef Medline
- Sethi KD, Mehta SH, Morgan JC. **Defining the eye-of-the-tiger sign.** *JAMA Neurol* 2015;72:606 CrossRef Medline
- Haacke EM, Cheng NY, House MJ, et al. **Imaging iron stores in the brain using magnetic resonance imaging.** *Magn Reson Imaging* 2005;23:1–25 CrossRef Medline
- Lee JH, Park J, Ryu HS, et al. **Clinical heterogeneity of atypical pantothenate kinase-associated neurodegeneration in Koreans.** *J Mov Disord* 2016;9:20–27 CrossRef Medline
- Szumowski J, Bas E, Gaarder K, et al. **Measurement of brain iron distribution in Hallervorden-Spatz syndrome.** *J Magn Reson Imaging* 2010;31:482–89 CrossRef Medline
- Lenglet C, Abosch A, Yacoub E, et al. **Comprehensive in vivo mapping of the human basal ganglia and thalamic connectome in individuals using 7T MRI.** *PLoS One* 2012;7:e29153 CrossRef Medline
- Barkovich AJ. *Pediatric Neuroimaging.* 4th ed. Philadelphia: Lippincott Williams & Wilkins; 2005:17–75
- Wu YW, Hess CP, Singhal NS, et al. **Idiopathic basal ganglia calcifications: an atypical presentation of PKAN.** *Pediatr Neurol* 2013;49:351–54 CrossRef Medline
- Meyer E, Kurian MA, Hayflick SJ. **Neurodegeneration with brain iron accumulation: genetic diversity and pathophysiological mechanisms.** *Annu Rev Genomics Hum Genet* 2015;16:257–79 CrossRef Medline
- Castelnaud P, Cif L, Valente EM, et al. **Pallidal stimulation improves pantothenate kinase-associated neurodegeneration.** *Ann Neurol* 2005;57:738–41 CrossRef Medline
- Aquino D, Bizzi A, Grisoli M, et al. **Age-related iron deposition in the basal ganglia: quantitative analysis in healthy subjects.** *Radiology* 2009;252:165–72 CrossRef Medline
- Harder SL, Hopp KM, Ward H, et al. **Mineralization of deep gray matter with age: a retrospective review with susceptibility-weighted MR imaging.** *AJNR Am J Neuroradiol* 2008;29:176–83 CrossRef Medline
- Lee JH, Baik SK. **Putaminal hypointensity in the parkinsonian variant of multiple system atrophy: simple visual assessment using susceptibility-weighted imaging.** *J Mov Disord* 2011;4:60–63 CrossRef Medline
- Dezortova M, Herynek V, Krssak M, et al. **Two forms of iron as an intrinsic contrast agent in the basal ganglia of PKAN patients.** *Contrast Media Mol Imaging* 2012;7:509–15 CrossRef Medline
- Dusek P, Tovar Martinez EM, Madai VI, et al. **7-Tesla magnetic resonance imaging for brain iron quantification in homozygous and heterozygous PANK2 mutation carriers.** *Mov Disord Clin Pract* 2014;1:329–35
- Cossu G, Abbruzzese G, Matta G, et al. **Efficacy and safety of deferiprone for the treatment of pantothenate kinase-associated neurodegeneration (PKAN) and neurodegeneration with brain iron accumulation (NBIA): results from a four years follow-up.** *Parkinsonism Relat Disord* 2014;20:651–54 CrossRef Medline
- Zorzi G, Zibordi F, Chiapparini L, et al. **Iron-related MRI images in patients with pantothenate kinase-associated neurodegeneration (PKAN) treated with deferiprone: results of a Phase II pilot trial.** *Mov Disord* 2011;26:1756–59 CrossRef Medline
- Peckham ME, Dashtipour K, Holshouser BA, et al. **Novel pattern of iron deposition in the fascicula nigrale in patients with Parkinson’s disease: a pilot study.** *Radiol Res Pract* 2016;2016:9305018 CrossRef Medline
- Chang CC, Chang WN, Lui CC, et al. **Clinical significance of the pallidoreticular pathway in patients with carbon monoxide intoxication.** *Brain* 2011;134:3632–46 CrossRef Medline
- Stoeter P, Roa-Sanchez P, Speckter H, et al. **Changes of cerebral white matter in patients suffering from pantothenate kinase-associated neurodegeneration (PKAN): a diffusion tensor imaging (DTI) study.** *Parkinsonism Relat Disord* 2015;21:577–81 CrossRef Medline

Sonographic Development of the Pericallosal Vascularization in the First and Early Second Trimester of Pregnancy

B. De Keersmaecker, H. Pottel, G. Naulaers, and L. De Catte



ABSTRACT

BACKGROUND AND PURPOSE: Anomalies of the corpus callosum are rare. Routine scanning in midtrimester of the pregnancy often fails to identify defective development. The purpose of the study was to identify the pericallosal artery and all its main branching arteries during early gestation from the first trimester onward, to measure the length of the pericallosal artery during its development, and to establish a normal vascular map for each week of development.

MATERIALS AND METHODS: We performed a single-center prospective, longitudinal clinical study in 15 patients between 11 and 22 weeks of gestation. The origin and course of the different blood vessels were identified.

RESULTS: There was a linear association among gestational age, the biparietal diameter, and the length of the pericallosal artery. The curvature of the developing pericallosal artery increases linearly with the gestational age and biparietal diameter, and 4 variations of branching of the callosomarginal artery were observed.

CONCLUSIONS: The pericallosal artery and its branches can be identified and measured from 11 weeks on, and the pericallosal artery takes its characteristic course. A defective course or an abnormal biometry of the pericallosal artery could be an early sonographic marker of abnormal development of the corpus callosum.

ABBREVIATIONS: BPD = biparietal diameter; CC = corpus callosum; CMA = marginal callosal artery; L1 and L2 = the anterior and distal part of the pericallosal artery to the highest point

The development of the corpus callosum (CC) starts with the formation of the genu during the eleventh week of gestation and progresses in an anterior-to-posterior direction with the development of the body and splenium.¹ Finally, the most anterior part, the rostrum, is formed.^{2,3} More recent neuroimaging studies have shown callosal connections originating more centrally in the hippocampal primordium near and superior to the anterior commissure.⁴ The expansion of the lobes makes the anterior border of the CC move progressively forward to coincide with the enhanced anterior curvature of the cingulate gyrus.³ Finally, the rostrum and the genu connect the frontal lobes, the body of the CC joins the posterior part of

the frontal lobes and the parietal lobes, and the splenium unites the temporal and occipital lobes.

Traditionally in the second trimester of pregnancy, the fetal brain is examined in 3 axial planes.^{5,6} Absence of the cavum septi pellucidi, an interruption of the cerebral falx, and absence of a transverse hypoechoic communication between the 2 frontal hemispheres are indirect sonographic signs of absence of the CC.

Because anomalies of the CC are rare (0.3%–0.7% to 2%–3%), their detection in a nonselected population remains difficult.^{7,8} Furthermore, routine axial scanning planes fail to identify defective development of the CC before midgestation.^{5,6,9} However, direct and complete visualization of the CC and pericallosal arteries can be established in the sagittal plane from 18 weeks on,¹⁰ though the fetal position, maternal obesity, and oligohydramnios may limit an optimal view in a sagittal plane.

High-resolution transvaginal sonography probes allow examining the central nervous system and diagnosing pathologic conditions at aneuploidy screening at 11–14 weeks.^{11–15} Nevertheless, in a retrospective analysis of >45,000 pregnancies scanned between the eleventh and thirteenth week of gestation, none of the 10 cases of agenesis of the corpus callosum were either suspected or diagnosed.¹⁶

Received August 15, 2017; accepted after revision October 30.

From the Department of Fetal Medicine (B.D.K.), Universitaire Ziekenhuizen Leuven, Leuven, Belgium; Department of Obstetrics and Gynaecology (B.D.K.), AZ Groeninge, Kortrijk, Belgium; Department of Public Health and Primary Care (H.P.), Katholieke Universiteit Leuven, Leuven, Belgium; and Departments of Women and Child (G.N.) and Fetal Medicine (L.D.C.), University Hospitals Leuven, Leuven, Belgium.

Please address correspondence to Luc De Catte, MD, University Hospitals Leuven, Department of Fetal Medicine, Leuven, BE; e-mail: luc.decatte@uzleuven.be

Indicates open access to non-subscribers at www.ajnr.org

<http://dx.doi.org/10.3174/ajnr.A5562>

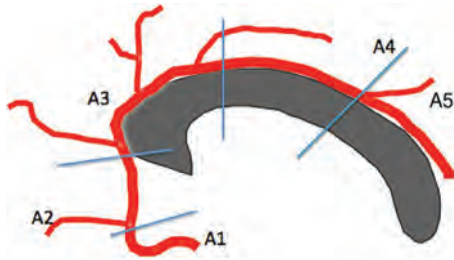


FIG 1. A1 is the segment originating from the internal carotid artery and extending to the anterior communicating artery. A2 extends from the anterior communicating artery to a region between the rostrum and genu. The A3 segment courses around the genu to the rostral part of the body. A4 and A5 segments are the continuation of the pericallosal artery.

The CC is lined by the pericallosal arteries, which branch distally from the anterior cerebral artery. These vessels are divided into 5 segments as presented in Fig 1.

Power Doppler flow demonstrates the normal distribution of the pericallosal artery and its variant branching at the twentieth-week sonographic examination and more recently even at the end of the first trimester.¹⁷

The sensitivity of screening for fetal CC agenesis using indirect sonographic signs such as an abnormally shaped or absent cavum septi pellucidi (or ventriculomegaly/colpocephaly from midgestation onward) is poor^{5,6} and is not applicable in the first trimester. Furthermore, dysgenesis of the CC could escape detection because most of the aforementioned signs are lacking.¹⁷

Aim

In the absence of specific screening tools for and direct visualization of the developing CC before midgestation, we hypothesized that the progressive development of the pericallosal vascularization precedes callosal development and might therefore act as a marker for the early callosal development.

The blood supply of the corpus callosum is ensured by 2 arterial systems. The carotid system supplies the pericallosal artery. A part of the splenium is supplied by the vertebrobasilar system by its terminal branches. These systems give rise to perforating arteries that ensure the intrinsic vascularization of the corpus callosum, creating a system of regular stitches around the fibers of the corpus callosum.^{41,42,43} The formation of the corpus callosum is associated with medial and upward rotation of the cingulate gyrus, with consequent formation of the cingulate sulcus. When the CC does not form, the cingulate gyri do not rotate and are small due to hypoplasia of the cingulum, and the medial hemisphere sulci radiate to the third ventricle. An abnormal pattern might be an early indirect sonographic marker.

Therefore, dysgenesis of the corpus callosum could be reflected by a misshapen or abnormal course of the pericallosal arteries and their branches.¹⁸⁻²⁰ With this study, we aimed to document the normal longitudinal development and variants of the pericallosal vasculature from 11 to 22 weeks of gestation using power Doppler flow and high-frequency sonography probes.

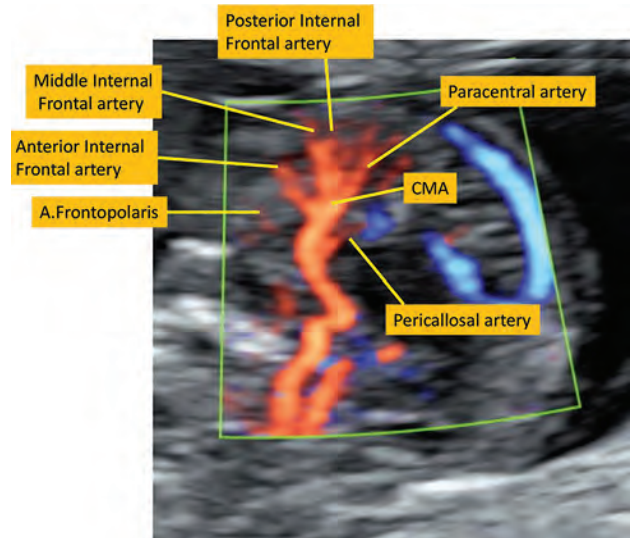


FIG 2. The callosomarginal artery is the largest branch of the pericallosal artery. The main branches are the frontopolar artery (A. Frontopolaris), the anterior internal frontal artery, the middle internal frontal artery, the posterior internal frontal artery, and the paracentral artery. They may arise from the pericallosal artery or the CMA.

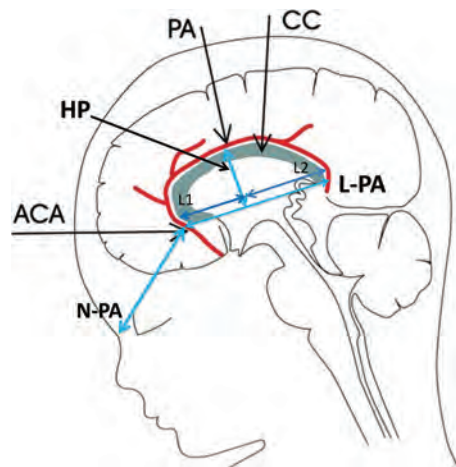


FIG 3. N-PA indicates the distance between the frontonasal junction and the origin of the pericallosal artery; L-PA, the length of the pericallosal artery: a straight line connecting the most anterior and posterior part of this artery; HP, the highest point of the curvature of the pericallosal artery perpendicular to L-PA line; L1, the anterior part of the L-PA distance to the HP; L2, the posterior part of the L-PA distance to the HP; ACA, anterior cerebral artery.

MATERIALS AND METHODS

We performed a single-center prospective, clinical study including 15 patients referred for sonographic examination at 11–13 weeks of gestation. Patients were eligible in case of a viable singleton pregnancy with a low first-trimester aneuploidy risk ($<1/1000$), no subsequent chromosomal abnormalities or growth restriction, and no sonographic evidence of fetal anomalies. Gestational age was determined by an early dating scan.²¹

Patients younger than 18 years of age or with multiple pregnancies were excluded. Eligible patients were invited for a weekly or biweekly follow-up scan by a single Fetal Medicine Foundation–certified operator up to 22 weeks of gestation, the

time at which the fully developed corpus callosum could be identified by sagittal scanning of the fetal brain.

All patients underwent a second-trimester sonography by another sonographer who demonstrated a normal corpus callosum in a midsagittal view.

Transabdominal sonography was performed with a Voluson E8 Expert, (GE Healthcare, Milwaukee, Wisconsin) with a transabdominal RAB 4–8 D transducer (GE Healthcare).

Number of observations in relation to gestational age. Mean length of the pericallosal artery (millimeter) in relation to gestational age (\pm SD)

Gestational Age (wk)	Fetuses (No.)	Mean Length of Pericallosal Artery (mm)	SD
11	3	4.43	0.78
12	13	4.1	0.44
13	10	6.3	1.22
14	11	6.96	0.66
15	5	7.75	1.08
16	11	9.68	1.48
17	9	12.34	2.19
18	9	13.15	1.7
19	7	15.66	1.43
20	9	16.82	1.8
21	2	20.55	2.86
22	1	18.43	0.36

A complete fetal biometry and a first-trimester aneuploidy screening were performed. The midsagittal plane used for identifying the nasal bone and nuchal translucency served as a template for the high-definition power color Doppler investigation of the pericallosal region in accordance with the as low as reasonably achievable principles. Settings were the following: harmonics-high, speckle reduction imaging II 3, frequency mid, wall motion filter low, pulse rate frequency 0.6 kHz, persistence high).

The thermal and mechanical indices were kept below 1 for safety reasons according to the recommendations of the Bio-Effects and Safety Committee of the International Society of Ultrasound in Obstetrics and Gynecology.²² The origin and the course of the frontopolar artery, the ramus anterior, the ramus medianus, the ramus posterior, the callosomarginal artery, the paracentral artery, and the precunealis were identified (Fig 2). Corresponding images and clips were digitally stored.

To define the natural course of the pericallosal arteries in relation to the fetal head, we measured the distance between the frontonasal junction and the origin of the pericallosal artery in a sagittal plane. The length of the pericallosal artery was measured by drawing a straight line connecting the most anterior to most posterior part of this artery as visualized by color Doppler flow at 94 different time points. The mean and the fifth and ninety-fifth percentiles were calculated for the length

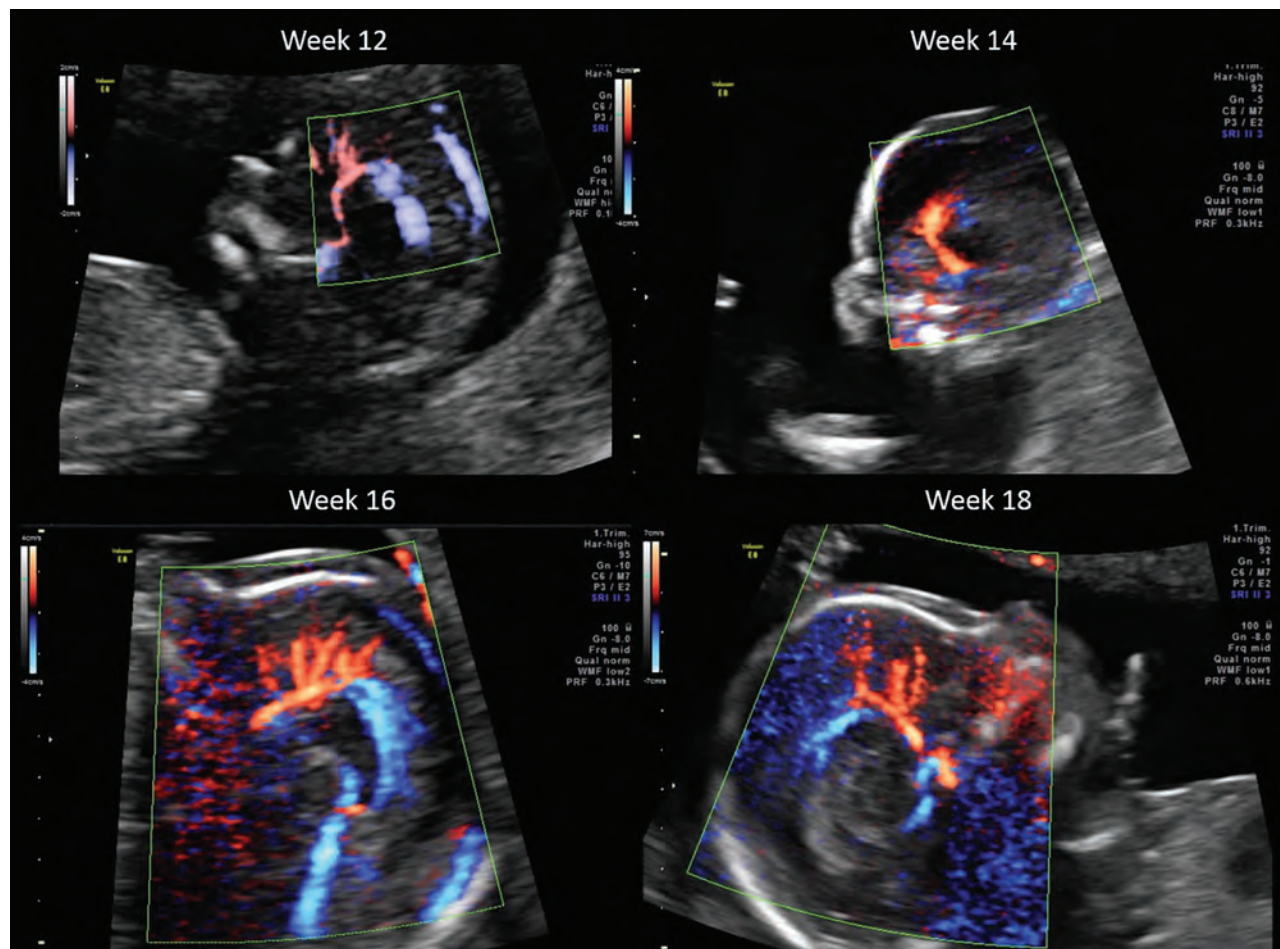


FIG 4. The different branches of the pericallosal arteries at week 12, week 14, week 16 and week 18, respectively.

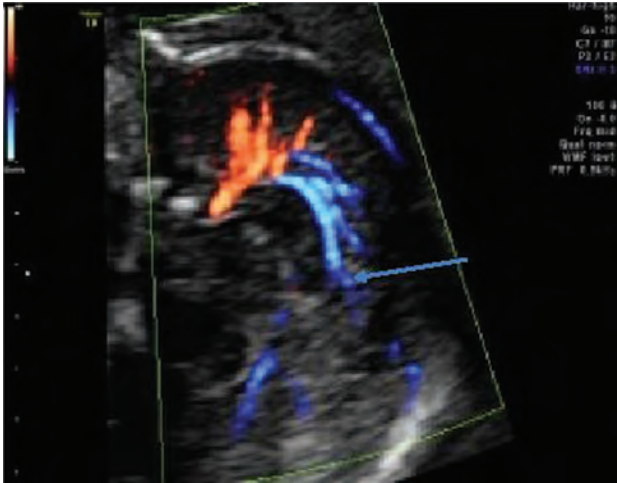


FIG 5. The precuneal artery (arrow) can be observed from 16 weeks onward, and this artery was visible in midtrimester in 80% of our fetuses.

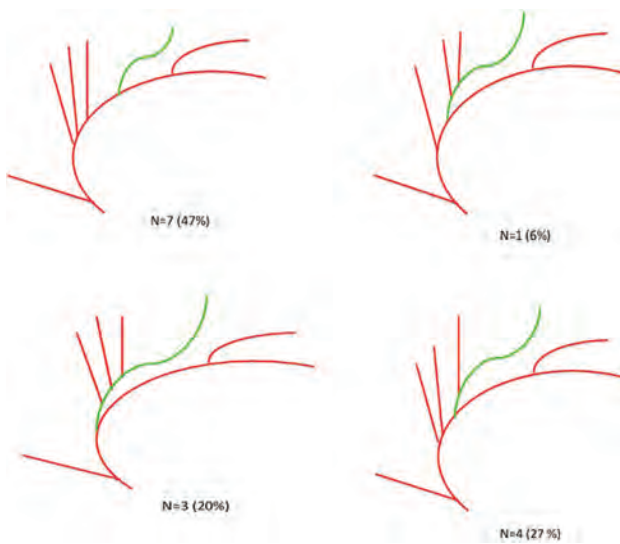


FIG 6. Variants of the callosomarginal artery.

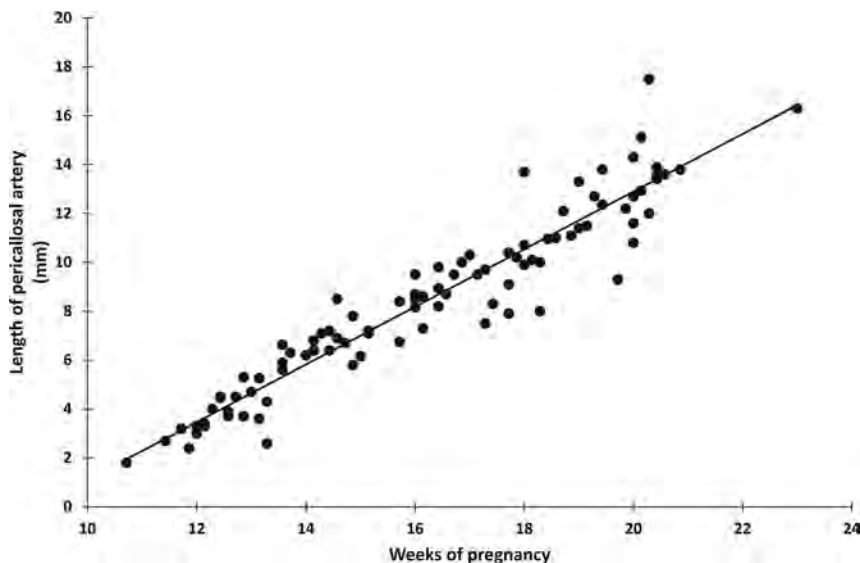


FIG 7. Linear correlation between the developing pericallosal artery and gestational age ($n = 94$) ($r = 0.951$) ($P < .0001$).

of the pericallosal artery in relation to gestational age and biparietal diameter (BPD).

We defined the rounded course of the pericallosal artery by measuring the distance between the highest point of the curvature of the pericallosal artery perpendicular to the straight line connecting the most anterior to most posterior part of this artery as visualized by color Doppler flow. Subsequently, the length of the pericallosal artery distance was divided into L1 and L2, the anterior and distal part of the pericallosal artery to the highest point (Fig 3). Each measurement was performed 3 times and averaged. Mean values for the highest point, L1 and L2, with the fifth and ninety-fifth percentiles, were calculated for each gestational week.

To study the natural variation in the course and the origin of the marginal callosal artery (CMA), we constructed a diagram of the vascular development. The distances between the origins of the different branches of the pericallosal artery were measured for each gestational week. The assessment of the variants in the origin of the CMA was performed according to the Fisher classification.²³

Normal fetal development was confirmed by systematic evaluation of the fetal anatomy and biometry (biparietal diameter, occipitofrontal diameter, head circumference, abdominal circumference, and femur length) and the presence of a normally developed corpus callosum and pericallosal artery at the second-trimester sonography by another independent Fetal Medicine Foundation operator. The pericallosal artery and its branches were reassessed on the anonymized stored images at 3 and 6 months to calculate the interobserver variability.

Statistical analysis was performed with SAS 9.3 (SAS Institute, Cary, North Carolina). Descriptive statistics are presented as mean (\pm SD) or median (percentiles), depending on the normality of the data. Frequency tables with the Fisher exact test were used to compare independent proportions. Linear regression between variables was performed, and the Pearson correlation coefficient was reported, together with its 95% confidence interval.

Statistical significance was considered at the .05 significance level. Bland-Altman plots were used to evaluate the intraobserver variability. The study was approved by the ethics board of the University Hospital Leuven, Belgium, and all participating patients consented.

RESULTS

All 15 consenting and participating patients completed the study. A total of 94 transabdominal observations were performed, with a median of 7 sonography scans per patient (range, 3–8). One patient was seen on 3 occasions in early pregnancy. Further management of her pregnancy occurred in another center. However, sonographic evaluation in the third trimester did not reveal CNS abnormalities in any of these patients (Table and Fig 4).

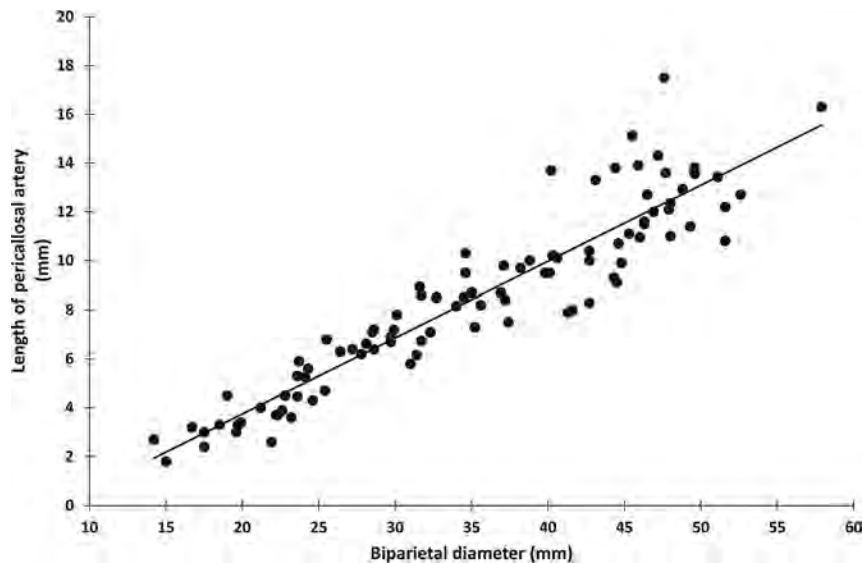


FIG 8. Linear correlation between the developing pericallosal artery and BPD ($n = 94$) ($r = 0.932$) ($P < .0001$).

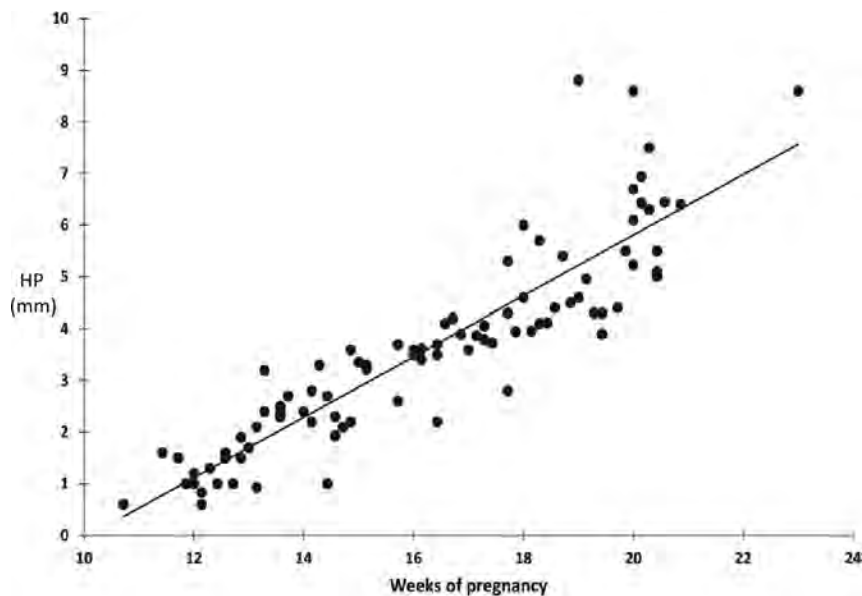


FIG 9. Height of the slope (millimeters) in relation to gestational age ($n = 94$) ($r = 0.904$) ($P < .0001$). HP indicates highest point.

All patients delivered at term (mean, 39 weeks 1/7 days). The mean maternal age was 31.2 ± 4.4 years, and the mean body mass index in this selected group of 15 patients was 24.3 ± 3.2 . The mean BMI allowed a successful visualization of the blood vessels. In 8/15 patients, the placenta was localized anteriorly. The pericallosal vasculature was assessed in short scanning episodes for an additional total scanning time of <60 seconds in all cases. The anterior part of the pericallosal artery could be observed in a sagittal plane from a crown-rump length of >36 mm (corresponding to 10 5/7 weeks of gestation).

In 4 of 15 patients with a sonogram at 11.0–11 6/7 weeks of gestation, the presence of a pericallosal artery could be demonstrated. At 12.0–12 6/7 weeks of pregnancy, the anterior part of the pericallosal artery was visualized in all but 1 patient (14/15).

The anterior internal frontal artery, the middle internal frontal artery, and the posterior internal frontal artery were detected in 93.33% (14/15), 66.66% (10/15), and 26.66% (4/15) of patients, respectively.

From 13 to 13 6/7 weeks onward, the anterior internal frontal artery was seen in all cases (14/14). The middle internal frontal artery and posterior internal frontal artery were seen in 85.7% (12/14) and 75% (9/12), respectively. At 14–14 6/7 weeks, the middle internal frontal artery was depicted in all cases and the posterior internal frontal artery was seen in 78.57% (11/14). All the branches were demonstrated from 15 completed weeks onward in all patients. The precuneal artery (Fig 5) was observed from 16 weeks onward in 46.6% ($n = 7$) and by 20 weeks in 73.3% ($n = 11$). In 20% of the cases ($n = 3$), the middle and posterior internal frontal arteries were connected by a common trunk, the most common variant.

Variations of branching of the callosomarginal artery come in 4 different types, of which the CMA starting from the A1 and the A4 segment was not observed. From the CMA, 6 (40%) started in the A2 segment and 8 (53.3%) originated in the A3 segment. In 3 cases (20%), the CMA branched before the ramus anterior; in 1 case (6%), between the ramus anterior and ramus medianus; in 4 cases (27%), between the ramus medianus and posterior; and in 7 cases (47%), after the ramus posterior (Fig 6).

We found a strong linear correlation ($P < .0001$ in all cases) between the length of the developing pericallosal artery and gestational age ($n = 94$) ($r = 0.951$) (Fig 7), BPD ($n = 94$) ($r = 0.932$) (Fig 8), head circumference ($n = 94$) ($r = 0.937$), femur length ($n = 94$) ($r = 0.933$), and crown-rump length ($n = 23$) ($r = 0.796$).

The distance from the nasofrontal junction to the origin of the pericallosal artery and the curvature of the developing vasculature documents its spatial development and that of the future CC. Between 12 and 22 weeks of gestation, the origin of the pericallosal artery distance increased linearly with gestational age ($r = 0.905$) and the BPD ($r = 0.867$).

The curvature of the developing pericallosal vasculature was defined by the highest point (Fig 9), L1 (Fig 10), and L2 (Fig 11), all of which increased linearly with gestational age ($r = 0.904$; 0.935, and 0.944, respectively) and the BPD ($r = 0.873$; 0.926;

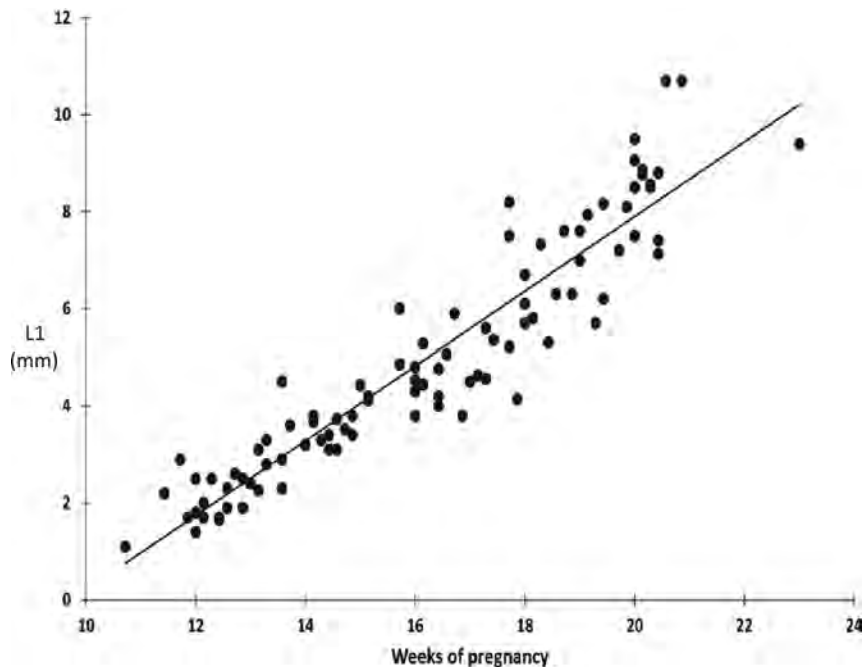


FIG 10. Increasing slope of the pericallosal artery (millimeters) in relation to gestational age. ($n = 94$) ($r = 0.935$) ($P < .0001$).

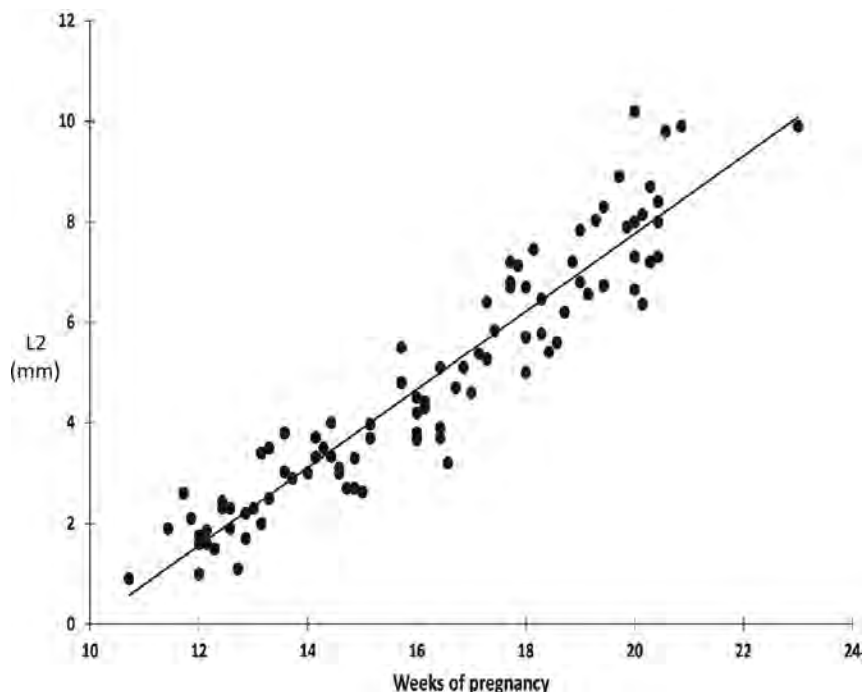


FIG 11. Decreasing slope of the pericallosal artery (millimeters) in relation to gestational age ($n = 94$) ($r = 0.944$) ($P < .0001$).

0.913). The highest point/L1 ratio, representing the slope of the anterior part of the pericallosal artery and hence the developing CC, decreased slightly throughout the investigated timeframe.

We measured the distances between the different developing branches across time. The frontopolar artery and the ramus anterior, the ramus anterior and the ramus medianus, the ramus medianus and the ramus posterior, the ramus posterior and the callosomarginal artery, the callosomarginal artery and the para-

central artery, and the paracentral artery and precuneal artery illustrate the proportional growth of the pericallosal blood vessels. Intraobserver variations of the length of the pericallosal artery and the distances between the origins of the different branches were not statistically significant.

DISCUSSION

Agensis and dysgenesis of the corpus callosum are the more frequent central nervous system malformations associated with variable prognosis. In association with chromosomal abnormalities, genetic syndromes, and central nervous system and non-CNS abnormalities, the prognosis is invariably poor.²⁴ Isolated complete agensis, however, seems to have a better prognosis than a partial or hypoplastic corpus callosum.¹⁹ A recent meta-analysis of 27 studies on the outcome shows a higher proportion of chromosomal anomalies, more gross and fine motor control affection, and a higher percentage of epilepsy in the partial agensis group compared with the complete agensis of the CC group.⁴⁰ Today, diagnosis relies on a midtrimester sonographic examination potentially revealing ≤ 1 of the associated signs such as mild ventriculomegaly, colpocephaly, absent cavum septi pellucidi, upward displacement of the third ventricle, teardrop configuration of the lateral ventricles, or cystic dilation of the third ventricle.^{25,26} However, these signs might be subtle or missing.^{27,28} The presence of a normal CC and its biometry has been assessed by transabdominal and transvaginal 2D and 3D sonography and with fetal MR imaging from 18 weeks onward.^{10,17,29-33}

Indirect appreciation of the developing CC will be seen by demonstration of the pericallosal artery and its branches. Recently, color Doppler mapping documented the modified arterial vascular supply with loss of the semicircular loop in CC agensis (Fig 12).²⁵ In a partial agensis of the CC, the paracentral artery follows the anterior part of the CC but loses its normal course when the CC vanishes. At this level, the artery moves in an upward and posteriorly oblique direction (Fig 13).^{19,20} The corpus callosum formation is associated with a medial and upward rotation of the cingulate gyrus, with consequent formation of the cingulate sulcus. In cases of an absent CC, the cingulate gyri do not rotate and are small due to hypoplasia. In

cases of partial agenesis, we expect therefore a shorter length of the pericallosal artery as well as a different branching pattern and course. Knowledge of the development and variations in the different branches may enhance the diagnosis of partial agenesis of the corpus callosum.

In the first trimester, the midsagittal plane of the fetal head allows investigating the nasal bone and the nuchal translucency as screening markers for Down syndrome and the intracranial translucency for the detection of open neural tube defects.^{34,35} Adding power color Doppler flow in fetuses at rest for short time intervals, respecting thermal index and mechanic index, shows the developing pericallosal vasculature and its variants³⁶⁻³⁸ in the first trimester either with 2D or 3D sonography.

Most first-trimester studies document either the presence or the course and/or length of the pericallosal artery only. In a cross-sectional study including 80 patients attending for first-trimester aneuploidy screening, chorionic villus sampling, or amniocentesis, a reference range of the length of the pericallosal artery was

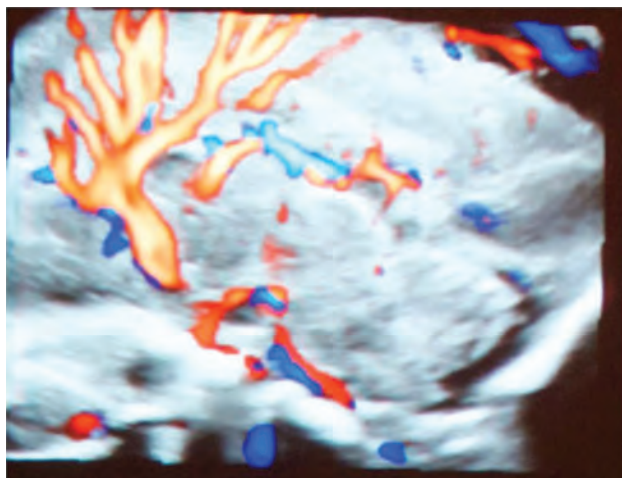


FIG 12. Pericallosal artery and branches in agenesis of the corpus callosum.

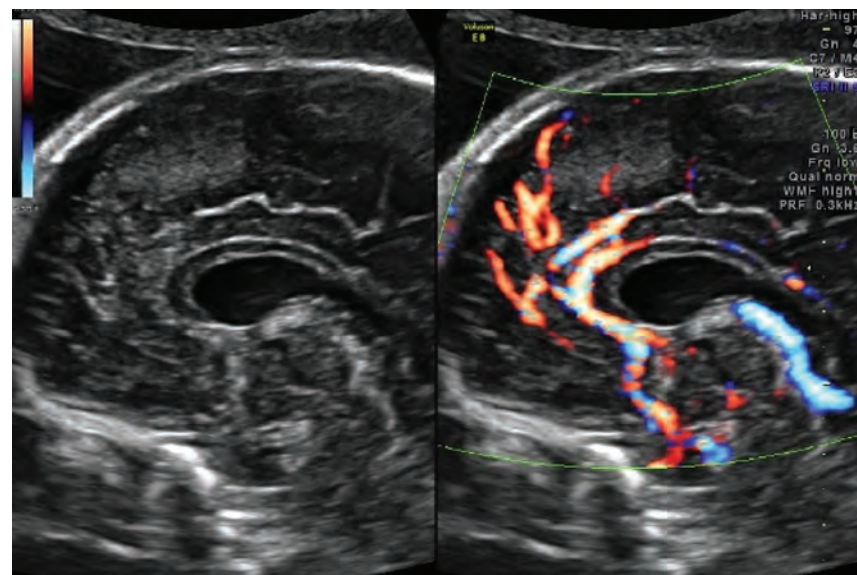


FIG 13. Aberrant pattern of the pericallosal artery and its branches in partial agenesis of the corpus callosum.

provided from 14 weeks onward in relation to BPD and gestational age.³⁶ In agreement with Pati et al,³⁶ we also detected a high linear correlation (>0.9) between the length of the pericallosal artery and gestational age and the BPD, respectively. However, in that study, the developing vascular map was not analyzed. Conturso et al³⁸ viewed the pericallosal arteries in healthy fetuses at 11–13 weeks of gestation in 70 cases using 3D technology in the first trimester of pregnancy.

Diaz-Guerrero et al³⁷ evaluated 150 fetuses between 11 and 14 weeks and failed to visualize the pericallosal artery in only 6 cases. Subsequently, 2 of these 6 cases were diagnosed with agenesis of the corpus callosum in association with a chromosomal abnormality. In the 4 other fetuses, the pericallosal artery was not seen due to the fetal position and excessive fetal movement.³⁷ However, in addition to the biometry of the pericallosal artery, we favor evaluating the morphology of the vasculature of the pericallosal artery and its branches because it might enhance the diagnosis of complete agenesis as well as dysgenesis of the CC. This evaluation has already been described in the second trimester of pregnancy.²⁰ Therefore, detailed knowledge of the arterial supply of the corpus callosum might distinguish normal variants from deteriorated vascularization associated with abnormal development of the CC.^{17,39}

Limitations of our study are the small number of healthy subjects, therefore the lack of an unhealthy case, and an average body mass index of 24, which does not always represent the general population.

CONCLUSIONS

In a population of healthy fetuses, the pericallosal artery and its branches can be consistently identified and measured from 11 weeks on. A defective course or an abnormal biometry of the pericallosal artery could be an early sonographic marker for identifying abnormal development of the corpus callosum. Further prospective evaluation of the vascularization and biometry of the pericallosal artery in the late first trimester is needed for proof of this concept.

ACKNOWLEDGMENTS

We sincerely thank the patients for the participation in this study.

REFERENCES

1. Rakic P, Yakovlev P. **Development of the corpus callosum and cavum septi in man.** *J Comp Neurol* 1968;132:45–72 CrossRef Medline
2. Hansen PE, Ballesteros MC, Soila K, et al. **MR imaging of the developing brain, I: prenatal development.** *Radiographics* 1993;13:21–36 CrossRef Medline
3. Bull J. **The corpus callosum.** *Clin Radiol* 1967;18:2–18 CrossRef Medline
4. Raybaud C. **The corpus callosum, the other great forebrain commissures and the septum pellucidum: anatomy, development and malformation.** *Neuroradiology* 2010;S2:447–77 CrossRef Medline

5. Pilu G, Hobbins J. **Sonography of the fetal cerebrospinal anomalies.** *Prenat Diagn* 2002;22:321–30 CrossRef Medline
6. Reece EB, Goldstein I. **Three-level view of fetal brain imaging in the prenatal diagnosis of congenital anomalies.** *J Matern Fetal Med* 1999;8:249–52 Medline
7. Dobyns W. **Absence makes the search growth longer.** *Am J Hum Genet* 1996;58:7–16 Medline
8. Salomon L, Alfirevic Z, Berghella V, et al; ISUOG Clinical Standards Committee. **Practice guidelines for performance of the routine mid-trimester fetal ultrasound scan.** *Ultrasound Obstet Gynecol* 2011;37:116–26 CrossRef Medline
9. Rossi A, Prefumo F. **Accuracy of ultrasonography at 11–14 weeks of gestation for detection of fetal structural anomalies: a systematic review.** *Am J Obstet Gynecol* 2013;207:1160–67 CrossRef Medline
10. Achiron R, Achiron A. **Development of the human corpus callosum: a high-resolution, cross-sectional sonographic study.** *Ultrasound Obstet Gynecol* 2001;18:343–47 CrossRef Medline
11. Fong K, Toi A, Salem S, et al. **Detection of fetal structural abnormalities with US during early pregnancy.** *Radiographics* 2004;24:157–74 CrossRef Medline
12. Sepulveda W, Dezerega V, Be C. **First-trimester sonographic diagnosis of holoprosencephaly: value of the “butterfly” sign.** *J Ultrasound Med* 2004;23:761–65; quiz 766–67 CrossRef Medline
13. Sepulveda W, Lutz I, Be C. **Holoprosencephaly at 9 weeks and 6 days in a triploid fetus: two- and 3-dimensional sonographic findings.** *J Ultrasound Med* 2007;26:411–14 CrossRef Medline
14. van Zählen-Sprock R, van Vugt J, van Geyn H. **First and early second trimester diagnosis of anomalies of the central nervous system.** *J Ultrasound Med* 1995;14:603–10 Medline
15. Engels A, Joyeux L, Brantner C, et al. **Sonographic detection of central nervous system defects in the first trimester of pregnancy.** *Prenat Diagn* 2016;36:266–73 CrossRef Medline
16. Syngelaki A, Chelemen T, Dagklis T, et al. **Challenges in the diagnosis of fetal non-chromosomal abnormalities at 11–13 weeks.** *Prenat Diagn* 2011;31:90–102 CrossRef Medline
17. Pashaj S, Merz E. **Prenatal demonstration of normal variants of the pericallosal artery by 3D ultrasound.** *Ultraschall Med* 2014;35:129–36 CrossRef Medline
18. Shinar S, Har-Toov J, Lerman-Sagie T, et al. **A thick corpus callosum in the second trimester can be transient and of uncertain significance.** *Ultrasound Obstet Gynecol* 2016;48:452–457 CrossRef Medline
19. Ghi T, Carletti A, Contro E, et al. **Prenatal diagnosis and outcome of partial agenesis and hypoplasia of the corpus callosum.** *Ultrasound Obstet Gynecol* 2010;35:35–41 CrossRef Medline
20. Volpe P, Paladini D, Resta M, et al. **Characteristics, associations and outcome of partial agenesis of the corpus callosum in the fetus.** *Ultrasound Obstet Gynecol* 2006;27:509–16 CrossRef Medline
21. Pexters A, Daemen A, Bottomley C, et al. **New crown-rump length curve based on over 3500 pregnancies.** *Ultrasound Obstet Gynecol* 2010;35:650–55 CrossRef Medline
22. Salvesen K, Lees C, Abramowicz J, et al. **Safe use of Doppler ultrasound during the 11 to 13 + 6-week scan: is it possible?** *Ultrasound Obstet Gynecol* 2011;37:625–28 CrossRef Medline
23. Fisher CM. **The circulus of Willis: anatomical variations.** *Vas Dis* 1965;2:99–105
24. Pisani F, Maria Edgarda B, Giovanni P, et al. **Prenatal diagnosis of agenesis of corpus callosum: what is the neurodevelopmental outcome?** *Pediatr Int* 2006;48:298–304 CrossRef Medline
25. Pilu G, Sandri F, Perolo A, et al. **Sonographic fetal agenesis of the corpus callosum: a survey of 35 cases.** *Ultrasound Obstet Gynecol* 1993;3:318–29 CrossRef Medline
26. Gupta J, Lilford R. **Assessment and management of fetal agenesis of corpus callosum.** *Prenat Diagn* 1995;15:302–12 Medline
27. Paladini D, Pastore G, Cavallaro A, et al. **Agenesis of the fetal corpus callosum: sonographic signs change with gestational age.** *Ultrasound Obstet Gynecol* 2013;42:687–90 CrossRef Medline
28. Malinger G, Lev D, Oren M, et al. **Non-visualization of the cavum septi pellucidi is not synonymous with agenesis of the corpus callosum.** *Ultrasound Obstet Gynecol* 2012;40:165–70 CrossRef Medline
29. Bennett G, Bromley B, Benacerraf BR. **Agenesis of the corpus callosum: prenatal detection usually is not possible before 22 weeks of gestation.** *Radiology* 1996;199:447–50 CrossRef Medline
30. Chasen S, Birnholz J, Gurewitsch E, et al. **Antenatal growth of the corpus callosum.** *Am J Obstet Gynecol* 1997;176:S66 CrossRef Medline
31. Harreld J, Bhore R, Chason D, et al. **Corpus callosum length by gestational age as evaluated by fetal MR imaging.** *AJNR Am J Neuroradiol* 2011;32:490–94 CrossRef Medline
32. Malinger G, Zakut H. **The corpus callosum: normal fetal development as shown by transvaginal sonography.** *AJR Am J Roentgenol* 1993;161:1041–43 CrossRef Medline
33. Araujo Júnior E, Visentainer M, Simioni C, et al. **Reference values for the length and area of the fetal corpus callosum on 3-dimensional sonography using the transfrontal view.** *J Ultrasound Med* 2012;31:205–12 CrossRef Medline
34. Nicolaidis KH. **Screening for fetal aneuploidies at 11 to 13 weeks.** *Prenat Diagn* 2011;31:7–15 CrossRef Medline
35. Chaoui R, Benoit B, Mitkowska-Wosniak H, et al. **Assessment of intracranial translucency (IT) in the detection of spina bifida at 11 to 13 week scan.** *Ultrasound Obstet Gynecol* 2009;34:249–52 CrossRef Medline
36. Pati M, Cani C, Bertucci E, et al. **Early visualization and measurement of the pericallosal artery: an indirect sign of corpus callosum development.** *J Ultrasound Med* 2012;31:231–37 CrossRef Medline
37. Díaz-Guerrero L, Guigni-Chalraud G, Soso-Olavarría A. **Assessment of pericallosal arteries by color Doppler ultrasonography at 11–14 weeks: an early marker of fetal corpus callosum development in normal fetuses and agenesis in cases with chromosomal anomalies.** *Fetal Diagn Ther* 2013;34:85–89 CrossRef Medline
38. Conturso R, Contro E, Bellusi F, et al. **Demonstration of the pericallosal artery at 11–13 weeks of gestation using 3D ultrasound.** *Fetal Diagn Ther* 2015;37:305–09 CrossRef Medline
39. Cavalcanti D, Albuquerque F, Silva B, et al. **The anatomy of the callosomarginal artery: applications to microsurgery and endovascular surgery.** *Neurosurgery* 2010;66:602–10 CrossRef Medline
40. D’Antonio F, Pagani G, Familiari A, et al. **Outcomes associated with isolated agenesis of the corpus callosum: a meta-analysis.** *Pediatrics* 2016;138. pii: e20160445 CrossRef Medline
41. Kakou M, Velut S, Destrieux C. **Arterial and venous vascularization of the corpus callosum [in French].** *Neurochirurgie* 1998;44(1 suppl): 31–37 Medline
42. Wahl M, Strominger Z, Jeremy R, et al. **Variability of homotopic and heterotypic callosal connectivity in partial agenesis of the corpus callosum: a 3T diffusion tensor imaging and Q-ball tractography study.** *AJNR Am J Neuroradiol* 2009;30:382–89 CrossRef Medline
43. Nakata Y, Barkovich A, Wahl M, et al. **Diffusion abnormalities and reduced volume of the ventral cingulum bundle in genesis of the corpus callosum: a 3T imaging study.** *AJNR Am J Neuroradiol* 2009;30:1142–48 CrossRef Medline

Spinal Arteriovenous Vascular Malformations in Patients with Neural Tube Defects

E. Giordan, C. Bortolotti, G. Lanzino, and W. Brinjikji



ABSTRACT

BACKGROUND AND PURPOSE: Neural tube defects, such as tethered cord, intradural lipoma, or myelomeningocele may coexist with spinal vascular malformations. The coexistence of these 2 rare entities is suggestive of a causal relationship between them, which may lead to further understanding of their pathogenesis. We present a series of 6 patients with epidural spinal arteriovenous fistulas associated with neural tube defects.

MATERIALS AND METHODS: We retrieved cases of spinal vascular malformations associated with neural tube defects seen at our institution. The clinical presentation, MR imaging/MRA and angiographic imaging, treatment outcomes, and long-term neurologic outcomes were analyzed. Descriptive statistical analyses are reported.

RESULTS: Six patients with epidural arteriovenous fistulas and neural tube defects were included in this study. The mean age at presentation was 42 years, and the most common presenting symptoms were lower extremity weakness followed by sensory disturbances and bladder/bowel dysfunction. In most cases (5/6), the fistulas were located at the sacral level. All cases were fed by the lateral sacral artery (6/6). Four patients had prior spine surgery, but the fistula was in the operative bed in 2 cases. All fistulas were extradural with secondary intradural venous drainage. Five patients underwent transarterial embolization with Onyx, and 1 patient had a treatment-related complication.

CONCLUSIONS: It is conceivable that there is a pathophysiologic link between neural tube defects and development of spinal vascular malformations. Delayed neurologic deterioration or high conus signal in a patient with a neural tube defect should suggest the possibility of such an association.

Neural tube defects are relatively uncommon abnormalities of spinal cord and spinal column formation. They occur consequent to failure or improper fusion of the neural tube during embryologic development. Spinal epidural arteriovenous fistulas or malformations are rare entities, which have been sporadically associated with neural tube defects, though a formal association between the 2 conditions has not yet been established. The coexistence of 2 uncommon conditions (ie, neural tube defect and spinal vascular malformation) in the same patient may suggest a causal relationship rather than mere coincidence. We present the first series of spinal epidural arteriovenous fistulas associated with neural tube defects along with an extensive review of the litera-

ture. On the basis of this association, we suggest that these 2 rare entities could share a common pathophysiologic origin.

MATERIALS AND METHODS

Patient Selection

We retrospectively reviewed all cases of spinal vascular malformations associated with neural tube defects evaluated at the Mayo Clinic. Selection criteria included patients with lipomeningocele, myelomeningocele, dermoid cyst, neuroenteric cyst, tethered cord, intradural lipoma, and diastematomyelia with a coexisting epidural, dural, or intradural arteriovenous fistula or malformation. Patients who underwent a prior spinal surgery for spina bifida repair were included in the study.

Image Analysis

MR imaging and angiographic findings were reviewed by a neuroradiologist. All patients underwent spinal MR imaging and conventional spinal angiography. The presence of flow voids, increased T2 hyperintensity, or spinal cord enhancement was documented. Selective spinal angiography was performed in all cases to identify the fistulous point, feeder location and number, and venous

Received June 6, 2017; accepted after revision October 30.

From the Departments of Neurologic Surgery (E.G., G.L.) and Radiology (G.L., W.B.), Mayo Clinic, Rochester, Minnesota; and Department of Neurosurgery (C.B.), Istituto di Ricovero e Cura a Carattere Scientifico Istituto delle Scienze Neurologiche di Bologna, Bologna, Italy.

Please address correspondence to Giuseppe Lanzino, MD, Mayo Clinic, 200 1st St SW, Rochester, MN 55905; e-mail: lanzino.giuseppe@mayo.edu; @wbrinjikji

Indicates article with supplemental on-line table.

<http://dx.doi.org/10.3174/ajnr.A5498>

Summary of cases of spinal epidural arteriovenous fistula and neural tube defects

Case No.	Age (yr), Sex	Fistula Location	Presentation				Length of Clinical FU (mo)	Long-Term Outcome	Prior Surgery (Type of Surgery)	Associated NTD
			Sensory Symptoms	Bladder Dysfunction	Bowel/Sexual Dysfunction	Motor Symptoms				
1	46, M	S	Y	Y	N	N	2	Unchanged	N	TC + IL
2	44, F	L4	Y	N	N	Y	3	Worsened	Y (MMC repair)	MMC
3	65, F	S	Y	Y	Y	Y	4	Improved	Y (laminectomy)	TC + DS
4	64, M	S	Y	Y	Y	Y	3	Improved	N	TC + IL
5	57, F	S	Y	Y	Y	Y	NA	NA	Y (MMC repair)	MMC
6	64, F	S	Y	N	N	Y	6	Improved	Y (laminectomy)	TC

Note:—N indicates no; Y, yes; NA, not applicable/not defined; NTD, neural tube defect; TC, tethered cord; IL, intrathecal lipoma; MMC, myelomeningocele; DS, diastematomyelia; FU, follow-up; S, sacrum.

draining pattern. Postoperative MRA or DSA was performed in all patients undergoing treatment, to assess AVF obliteration. Postoperative imaging follow-up ranged from 2 to 14 months.

Data Collection

The study sample was collected by reviewing the surgical and radiologic data base. Patient history, clinical examination, radiologic findings, and follow-up information were obtained from digital records. Both the modified Rankin Scale and the Aminoff Motor Disability Scale scores were determined retrospectively. The timing and presence of any spine operation were documented. Fistulas were considered possibly related to a prior operation if the fistula was in the operative bed. In cases of patients who had an operation and development of a fistula at a distant location (ie, lower sacral fistula following lumbar laminectomies and so forth), the fistula was not thought to be related to the prior surgery. Lesions were considered “missed” on imaging if there was clear MR imaging evidence of a fistula and the patient was treated for a different disease entity (ie, transverse myelitis, degenerative disease, neuropathy, and so forth). MR imaging evidence of a fistula included high T2 cord signal in the presence of flow voids with or without cord enhancement.

Statistical Analysis

No formal statistical comparisons were performed. Descriptive results are presented as mean \pm SD for continuous variables and number (percentage) for categorical variables. All data analyses were performed using the statistical software package JMP 13.0 (SAS Institute, Cary, North Carolina).

RESULTS

Baseline Patient Characteristics and Clinical Presentation

Six patients included in this series had neural tube defects associated with spinal vascular malformations. In all cases, the malformations were classified as epidural fistulas (Table). Two patients were men and 4 were women. The mean age at presentation was 56.6 years. The coexistence of tethered cord and intradural lipoma was found in 4 cases (cases 1, 2, 4, and 5). One patient had a disorder of cord formation with partial diastematomyelia with a tethered cord, while 2 had myelomeningoceles.

Clinical presentations included the following: 1) sensory changes in 6 patients, 2) bladder/bowel dysfunction in 4 patients, and 3) progressive motor weakness in 5. All patients experienced some degree of neuropathic pain, sometimes bilateral with an ascending distribution. Symptom duration ranged from 1 to 12 months.

Delayed Diagnosis and Prior Treatment

In 3 cases, the vascular malformations were missed at first imaging, with a consequent delay in recognition ranging from 2 months to 2 years. The average time from symptom manifestation to diagnosis was 8 months. Two patients in this series had undergone myelomeningocele repair during childhood and presented decades later with an epidural AVF. Two additional patients underwent laminectomies before diagnosis of the fistula, which were remote from the site of the fistula. In 1 of these 2 patients, there was clear imaging evidence of an underlying vascular malformation before the laminectomy.

Imaging Findings

Enlarged vascular structures and flow voids were detected on MR imaging on the surface of the lower spinal cord in all patients. Five patients had T2 signal changes in the conus. Cord enhancement was detected in 3 patients.

Epidural arteriovenous fistulas were located at the sacral level in all patients except for 1 case in which it was located at the L4 level. Fistulas were fed by 1 vessel in 4 patients and by 2 separate arterial feeders in 2 patients. In all patients, the arterial feeder was the lateral sacral artery arising off the internal iliac artery, 4 from the left and 2 from the right. In 2 patients, both lateral sacral arteries fed the fistula. In all cases, while the actual arteriovenous shunt was extradural, secondary intradural venous drainage was present. None of the patients had a history of spinal hemorrhage.

Treatment and Outcomes

Five patients underwent transarterial embolization of the epidural fistula with Onyx (Covidien, Irvine, California). Postoperative MRA or DSA was performed in all cases within 24 hours to confirm closure of the fistula. One patient had a spinal cord infarct and consequent severe paraparesis due to embolization of an arterial feeder, which also supplied the anterior spinal artery. In 1 patient, symptoms were mild and not ascribable to the arteriovenous shunt; therefore, no invasive treatment was recommended.

Clinical and imaging follow-up ranged from 2 to 14 months. Four patients clinically improved with regression of sensory symptoms after treatment. However, recovery of bladder and/or bowel function was slower compared with other motor and/or sensory neurologic symptoms. One patient did not recover urinary function completely. Following treatment, both the modified Rankin Scale and Aminoff Motor Disability Scale scores improved in 3 patients, were stable in 1, and worsened in the patient who had a complication. Follow-up MR imaging showed



FIG 1. A, Sagittal T2-weighted spine MR imaging showing tethering of the spinal cord (lower arrowheads). Note the conus tip at the L4–L5 level and flow voids throughout the spinal canal, most prominent in the sacral canal (arrowheads), extending superiorly to approximately the T2 level. B, Right internal iliac artery angiogram demonstrates an arteriovenous shunt in the spinal canal of the sacrum (black arrow). The feeding artery enters through the left S4 neural foramen. C, Left internal iliac artery angiogram demonstrates an additional feeder to the arteriovenous shunt (lower black arrow). Intradural draining veins (upper black arrow) are visible. D, Angiogram obtained following embolization demonstrates a large cast of Onyx extending from the site of fistula to the coronal venous plexus.

resolution of T2 hyperintensity in 5 cases. Spinal cord enhancement decreased in 2.

Case Examples

Case 1. This 46-year-old man presented with a 2-decade history of back pain and bladder dysfunction following a motor vehicle collision (Fig 1). He had no history of an operation. Spine MR imaging showed tethering of the spinal cord, with the tip of the

with mild atrophy in the left upper cord (T3–T4). Signs of previous L2 laminectomy for spina bifida correction were recognized along with a prominent fatty placode in the posterior cord at the L4–5 level, which was tethered to the conus. MRA showed prominent tortuous dilated veins from the sacrum to the foramen magnum.

The patient underwent DSA with injection of the right internal iliac artery, which demonstrated an epidural spinal arteriovenous fistula fed by a branch of the lateral sacral artery. The fistula was

conus at the L4–L5 level. An intradural lipoma was identified posteriorly in the sacral canal, extending from S3 to S4, with cutaneous components from L3 to S4. There was mild displacement of the left S3 and S4 nerve roots. Enhancing vascularity throughout the spinal canal extended superiorly to the T2 level with numerous pial vessels along the posterior surface of the spinal cord.

Due to MR imaging findings consistent with a spinal vascular malformation, conventional spinal angiography was performed, which demonstrated an epidural arteriovenous fistula fed by a lateral sacral artery branch, which coursed through the left S4 neural foramen with a large draining vein coursing superiorly up into the thoracic region as well as some supply from the right lateral sacral artery.

The patient underwent embolization of the vascular malformation with Onyx 18. Postoperative angiography demonstrated complete obliteration of the fistula. Spinal MRA/MR imaging performed 2 months later did not show any evidence of residual fistula, and all T2 cord changes resolved. The patient reported decreased back pain following embolization, denying any new weakness, numbness, or bowel and bladder changes.

Case 2. This 44-year-old woman had a history of spina bifida surgery (L2–S1 laminectomy) when she was 10 years of age (Fig 2). The patient presented with a 3-year history of burning pain with progressive numbness ascending from her feet to thighs. The pain worsened with walking or lying in bed. Neurologic examination documented decreased temperature, pinprick, and touch sensation. The patient underwent spinal MR imaging, which demonstrated an unusual C1–C2 anomaly with absence of the odontoid process. Tortuous surface vascularity extended from the conus and along the entire dorsal thoracic cord

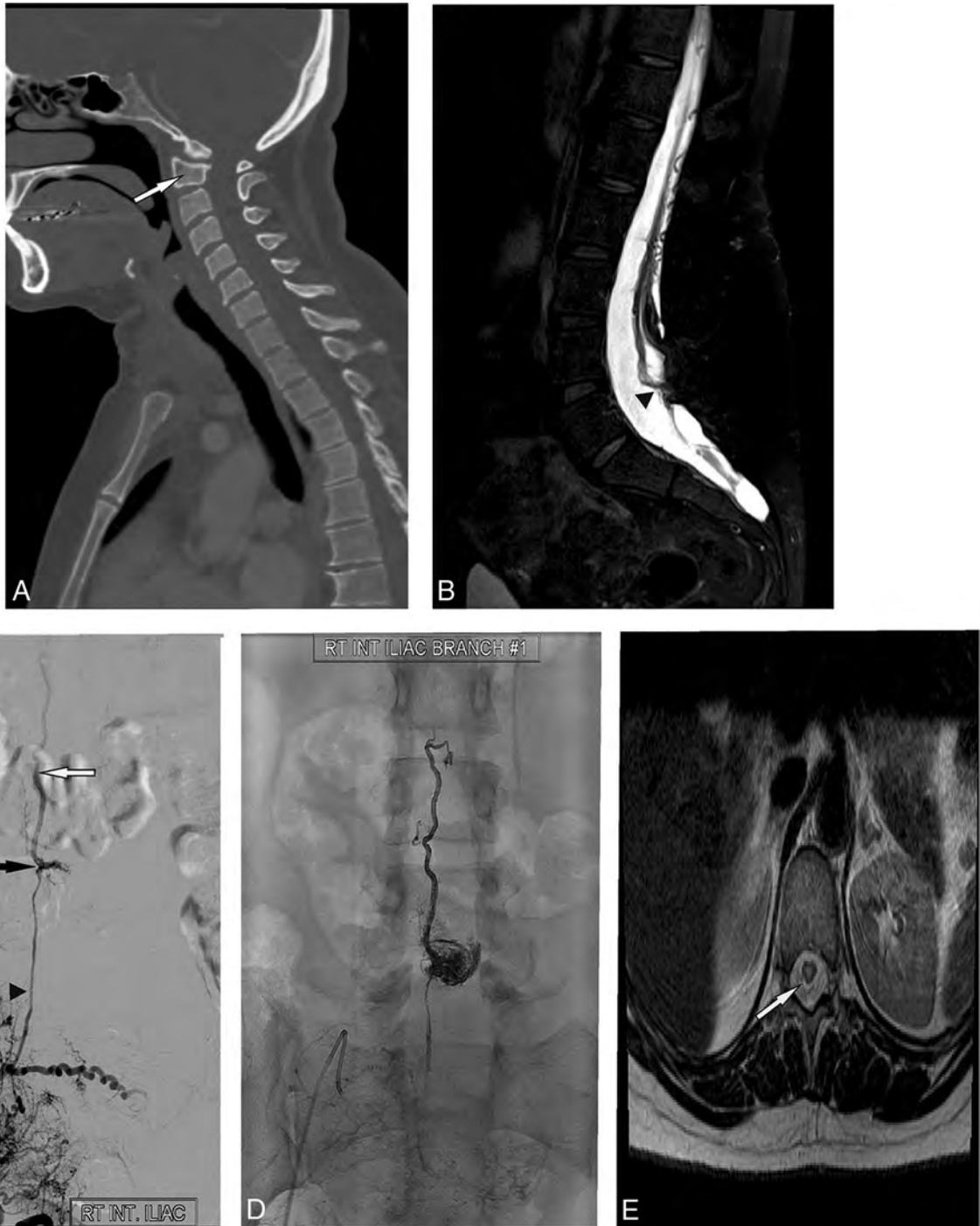


FIG 2. A, Sagittal noncontrast CT demonstrates the absence of the odontoid process (*white arrow*). B, Sagittal T2-weighted MR imaging of the lumbar spine shows tortuous dilated veins throughout the spinal canal. There is also a fatty placode in the posterior thecal sac at L4–5 (*arrowhead*), with conus tethering extending to the placode. C, Selective angiogram of the right lateral sacral artery (*arrowhead*) arising from the right internal iliac artery demonstrates an epidural spinal fistula (*lower black arrow*) with intradural venous drainage (*upper white arrow*) along the coronal venous plexus. D, Post-Onyx embolization x-ray image demonstrates an Onyx cast including the feeding artery, arteriovenous connection, and intradural draining vein. E, Axial T2-weighted MR imaging demonstrates myelomalacia of the central conus (*arrow*), consistent with cord infarction.

located at L4–5 in the region of the fatty placode. A large epidural vein ascended from this level and then coursed intradurally. The patient then underwent embolization with 3 mL of Onyx 18. Postoperative MRA showed a decreased tortuous dilated vein within the spinal canal.

The patient had a spinal cord infarction that led to postoperative lower extremity bilateral paresis. In retrospect, the arterial feeder to

the fistula also supplied a small anterior spinal artery. The patient was admitted for a short rehabilitation in which she experienced progressive improvement of her weakness. Spinal MRA 3 months later showed that embolization resulted in significantly decreased vascularity within the spinal canal with nearly imperceptible flow voids. After 12 months, the patient continues to have significant diffuse pain and impaired mobility due to lower extremity weakness.

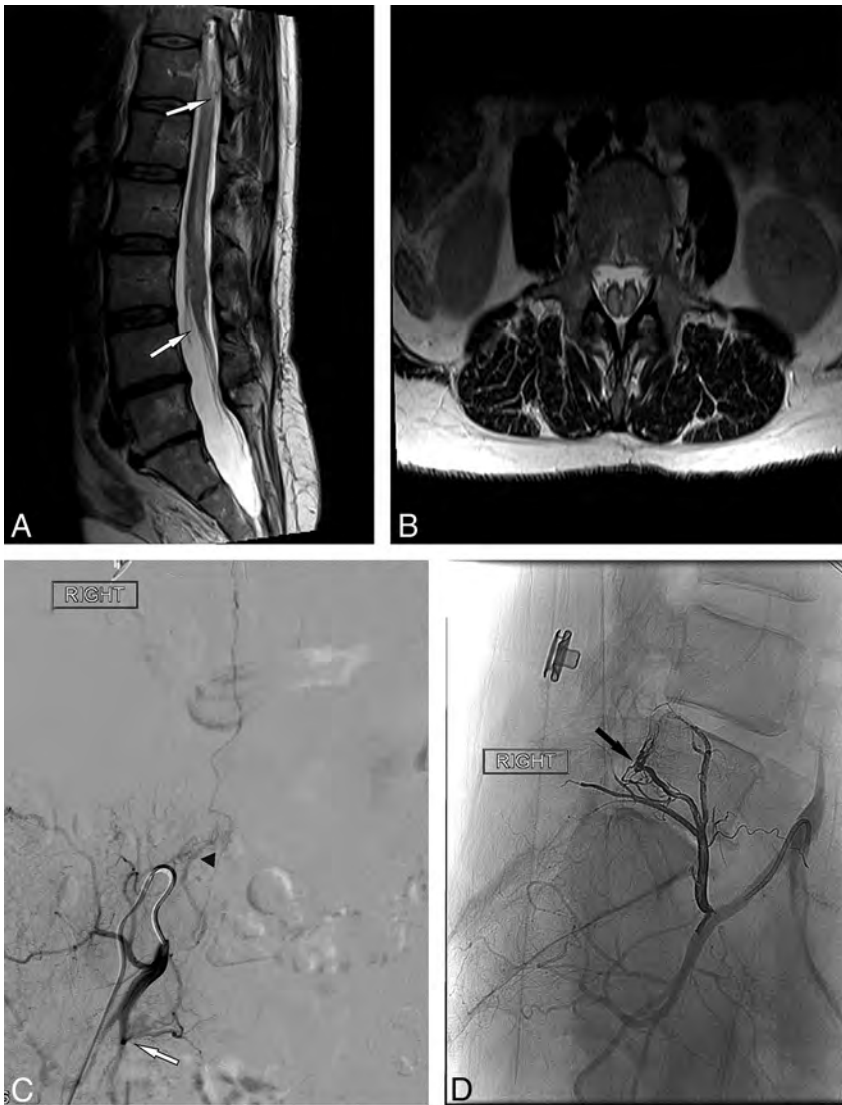


FIG 3. A, Sagittal T2-weighted MR imaging demonstrates tethering of the spinal cord with the tip of the conus at the L3–4 interspace (*white arrow*) before surgical release. There is high T2 signal of the cord and a faintly visualized flow void (*upper white arrow*). B, Axial T2-weighted MR imaging shows partial diastematomyelia in the lumbar spine without evidence of a fibrous band or bony spur/bar. High cord signal is present in both hemicords. C, Right internal iliac artery spinal angiogram demonstrates an epidural fistula arising from the right lateral sacral artery (*white arrow*) with an intradural draining vein (*arrowhead*). D, Post-Onyx embolization angiogram demonstrates an Onyx cast in the ventral epidural space of L5 (*black arrow*).

Case 3. This 65-year-old woman presented with stuttering/fluctuating lower extremity weakness with associated bladder hesitancy and bowel constipation (Fig 3). Spinal MR imaging at presentation demonstrated a thickened and congested spinal cord with the conus lying at the L3–L4 level. MR imaging showed some cord tethering along with partial diastematomyelia at L2–L3. On the basis of these imaging findings, which were obtained without contrast, the patient underwent laminectomy for cord untethering. Postoperatively, the patient declined to the point that she was no longer able to ambulate. A further MR imaging of the cervical and thoracic spine showed progression of the T2 signal abnormality and swelling within the central thoracic cord. On the basis of these findings, she was given a diagnosis of transverse myelitis and started on corticosteroids.

She then came to our institution for a second opinion. Spinal angiography confirmed an epidural fistula arising from the right

lateral sacral artery. The feeding artery entered through the right L5 neural foramen with the epidural draining vein coursing down to the S1 nerve root sleeve. The patient underwent transarterial embolization of the feeding artery with Onyx 18. Follow-up angiography of the right internal iliac artery, left common iliac artery, middle sacral artery, and bilateral L3 lumbar arteries demonstrated no residual fistula. The patient's motor and sensory symptoms improved at 9 months, while impaired bladder control persisted. Spinal MRA and MR imaging performed at 10 months showed no residual fistula and significant improvement in long-segment cord edema.

DISCUSSION

Our case series of 6 patients with neural tube defects and associated spinal vascular malformations demonstrated several interesting findings. In all cases, the fistula associated with the neural tube defect was extradural and had secondary intradural venous drainage. The main arterial feeder was the lateral sacral artery in all 6 cases, and all fistulas were in the sacral or lower lumbar region. In 2 cases, it is conceivable that the fistula was a delayed complication of myelomeningocele repair performed at a young age; however, in the other 4 cases, the fistula was not associated with prior surgery. Because these fistulas were extradural and anatomically associated with the neural tube defect, our findings suggest that the association between the 2 pathologic conditions may share a causal relationship rather than representing a mere coincidence. The findings from our study are clinically relevant because they highlight the importance of carefully studying the spinal vascularity in patients with neural tube defects who develop myelopathic symptoms during adulthood.

Spinal vascular malformations associated with neural tube defects are uncommon, but several single case reports have been reported suggesting a possible causal relationship. In our review of the literature, we found 17 adults and 3 pediatric patients with a combination of spinal vascular malformation and neural tube defects (On-line Table).^{1–21} In accordance with our experience, these lesions were discovered, in most cases, during midadulthood with symptoms often attributable to both the arteriovenous fistula and tethered cord. Misdiagnosis and delay in symptom recognition were common, as demonstrated in our case series. Clinical presentations included sensory changes in 76% of pa-

tients, bladder/bowel dysfunction in 67% of patients, and motor weakness in 80%. Symptom duration was variable, ranging from 1 to 72 months. Arteriovenous fistulas were located at the sacral level in 29% of cases and at the lower lumbar levels in 57%. Thirty-eight percent of vascular malformations were classified as spinal dural fistulas, whereas 62% were intradural arteriovenous fistulas or malformations. Only 1 case of extradural vascular malformation was documented, though the lower incidence of epidural shunts in the earlier reports may be related to less familiarity with this condition, which is diagnosed with much more frequency today due to advances in imaging and better understanding of the pathologic shunts.²² In 60% of patients, the feeder was the lateral sacral artery arising off the internal iliac artery, while the anterior spinal artery fed the malformation in 20%. In most cases, intradural venous drainage was documented. None of the patients presented with hemorrhage. Surgical treatment was the preferred technique in 43% of reported cases, with embolization in 29%. In the remaining third, a combined approach was chosen.

Some authors argue that the coexistence of neural tube defect and vascular malformation is the result of incomplete regression of mesenchymal tissue during the embryonic period. A premature disjunction of the neural ectoderm from the cutaneous ectoderm allows migration of the periaxial mesoderm into the developing neural tube. This mesenchyme migration could prevent adequate closure of the neural tube.⁵ While the pluripotent mesoderm primarily develops into fat, it may also develop into other tissues, including striated muscle, cartilage, fibrous bands, and blood vessels. Some authors argue that a failure to form the capillary component of the mesoderm might lead to the formation of a direct arteriovenous shunt.¹¹ Other authors believe that mesenchymal cells forming the primordial vascular plexus are involved in the pathogenesis of arteriovenous fistulas with lipomyelomeningocele or lipoma. Vascular differentiation in fat tissue is suppressed by neural crest cells under normal conditions of development. However, if the neural crest cells are defective, inhibition fails and a lipoma may arise forming an AVM secondarily.¹⁰ It is speculated that the lipoma itself and its tethering effect further impair the venous drainage, resulting in venous hypertension and development of fistula-related symptoms.

While in 4 of our patients the epidural fistula was not associated with a prior surgery, in 2 patients, the fistula was diagnosed decades after surgical myelomeningocele repair. It is also conceivable that in these cases, the epidural fistula formed because of microvascular trauma during the reparative surgery, and the slow progressive hemodynamic changes associated with the low-pressure direct arteriovenous shunt may have only manifested clinically several years later. Such an association between surgery and extradural fistulas has been described.^{6,22} Some authors believe that AVF formation following spinal surgery is improbable and that a congenital association is more likely.¹⁴ However, any hypotheses regarding the pathogenesis of post-neural tube defect repair AVFs are purely speculative, especially given the paucity of cases in the literature. In cases in which the symptomatology worsens after surgical correction of a neural tube defect, careful study of the spinal vascularity is important.³ For example, in 1 case in our series, a patient presented with a myelopathy and MR imaging evidence of a spinal vascular malformation associated

with a tethered cord and had exacerbation of the myelopathy following the untethering procedure. It was at that point that the fistula was discovered.

An epidural arteriovenous fistula associated with a neural tube defect can have important treatment implications as well. As demonstrated in our series, all patients with such malformations had lateral sacral artery feeders. Thus, when inspecting MR imaging before angiography, identification of a lumbar or sacral neural tube defect should prompt the angiographer to inspect these arteries first, possibly saving time during the spinal angiographic procedure. In 2 cases, we found that an anterior spinal artery arose from the lateral sacral artery. This is a relatively rare occurrence. Prior cadaveric studies suggest that the presence of an anterior spinal artery arising at the sacral level is <3%.²³ This is important because failure to identify an anterior spinal artery arising from such a low level can have disastrous consequences as demonstrated in case 2.

Limitations

Our study has limitations. This was a small case series on a rare entity; thus, no statistical comparisons were made. Preoperative imaging was not available for the 2 patients who were treated in childhood for their myelomeningoceles; thus, we are unable to determine whether the fistulas in these cases were present before the operation. This study was a retrospective chart review, so it is prone to various forms of bias, including selection bias. Last, there is a wide range in the amount of posttreatment follow-up the patients received.

CONCLUSIONS

In this report, we present the first series of epidural arteriovenous fistulas associated with neural tube defects. The rare concurrence of neural tube defects with spinal vascular malformations is something that should be considered when evaluating a patient with a neural tube defect and myelopathy. The pathophysiology of these entities is still a matter of debate, with most authors speculating that these lesions form due to a defect in migration of embryologic layers during neural tube formation. However, due to the paucity of cases reported in literature and the small size of this case series, all hypotheses are purely speculative. Nevertheless, the increasingly reported association between 2 uncommon pathologic conditions raises the strong possibility of a causal relationship between the two. When one evaluates these patients, attention should be paid to identifying the anterior spinal artery arising from a low-lying artery such as the lateral sacral artery.

Disclosures: Giuseppe Lanzino—UNRELATED: Consultancy: Medtronic/Covidien*. Waleed Brinjikji—UNRELATED: Consultancy: Cerenovus; Employment: Marblehead Medical LLC. Comments: chief executive officer. *Money paid to the institution.

REFERENCES

1. Chanthanaphak E, Pongpech S, Jiarakongmun P, et al. **Filum terminale arteriovenous fistulas: the role of endovascular treatment.** *J Neurosurg Spine* 2013;19:49–56 CrossRef Medline
2. Chatkupt S, Ruzicka PO, Lastra CR. **Myelomeningocele, spinal arteriovenous malformations and epidermal nevi syndrome: a possible rare association?** *Dev Med Child Neurol* 1993;35:737–41 Medline
3. Cheung AC, Kalkanis SN, Ogilvy CS. **Paraplegia after tethered cord surgery: an uncommon combined anomaly of spinal arteriovenous**

- fistula and sacral lipoma: case report.** *Neurosurgery* 2005;57:E598; discussion E598 CrossRef Medline
4. Djindjian M, Ayache P, Brugieres P, et al. **Sacral lipoma of the filum terminale with dural arteriovenous fistula: case report.** *J Neurosurg* 1989;71:768–71 CrossRef Medline
 5. Erdogan C, Hakyemez B, Arat A, et al. **Spinal dural arteriovenous fistula in a case with lipomyelodysplasia.** *Br J Radiol* 2007;80:e98–100 Medline
 6. Gross BA, Du R. **Spinal pial (type IV) arteriovenous fistulae: a systematic pooled analysis of demographics, hemorrhage risk, and treatment results.** *Neurosurgery* 2013;73:141–51; discussion 151 CrossRef Medline
 7. Hurst RW, Bagley LJ, Marcotte P, et al. **Spinal cord arteriovenous fistulas involving the conus medullaris: presentation, management, and embryologic considerations.** *Surg Neurol* 1999;52:95–99 CrossRef Medline
 8. Kendall BE, Logue V. **Spinal epidural angiomatous malformations draining into intrathecal veins.** *Neuroradiology* 1977;13:181–89 CrossRef Medline
 9. König M, Hentsch A, Schmieder K, et al. **Extraspinal dural arteriovenous fistula in a patient with lipomyelodysplasia: value of MRI and MRA.** *Neuroradiology* 1999;41:579–83 CrossRef Medline
 10. Krisht KM, Karsy M, Ray WZ, et al. **Extraspinal type I dural arteriovenous fistula with a lumbosacral lipomyelomeningocele: a case report and review of the literature.** *Case Rep Neurol* 2015;2015:526321 CrossRef
 11. Lee JH, Chung CK, Choe G, et al. **Combined anomaly of intramedullary arteriovenous malformation and lipomyelomeningocele.** *AJNR Am J Neuroradiol* 2000;21:595–600 Medline
 12. Lim SM, Choi IS, David CA. **Spinal arteriovenous fistulas of the filum terminale.** *AJNR Am J Neuroradiol* 2011;32:1846–50 CrossRef Medline
 13. Macht S, Chapot R, Bieniek F, et al. **Unique sacral location of an arteriovenous fistula of the filum terminale associated with diastematomyelia and lowered spinal cords.** *Neuroradiology* 2012;54:517–19 CrossRef Medline
 14. Mavani SB, Nadkarni TD. **Tethered cord due to caudal lipomeningocele associated with a lumbar dural arteriovenous fistula.** *J Neurosurg Spine* 2014;21:489–93 CrossRef Medline
 15. Rajeev K, Panikar D. **Dural arteriovenous fistula coexisting with a lumbar lipomeningocele: case report.** *J Neurosurg Spine* 2005;3:386–89 CrossRef Medline
 16. Rice JF, Jelsma RK. **Combined arteriovenous malformation and intramedullary lipoma: surgery and embolotherapy.** *AJNR Am J Neuroradiol* 1986;7:171–73 Medline
 17. Sato M, Takigawa T, Shiigai M, et al. **Spinal dural arteriovenous fistula with lipomyelodysplasia.** *Neurol Med Chir (Tokyo)* 2013;53:107–09 Medline
 18. Srinivasan A, Roy NK, Ghuman MS, et al. **Spinal dysraphism masking the presentation of spinal dural arteriovenous fistula: a serendipitous development or a congenital predisposition to an early-onset variant of spinal dural arteriovenous fistula?** *Neurol India* 2016;64:1380–81 CrossRef Medline
 19. Tubbs RS, Oakes WJ. **Lipomyelomeningocele and arteriovenous malformation: case reports and a review of the literature.** *Childs Nerv Syst* 2006;22:628–31 CrossRef Medline
 20. Weon YC, Chung JI, Roh HG, et al. **Combined spinal intramedullary arteriovenous malformation and lipomyelomeningocele.** *Neuroradiology* 2005;47:774–79 CrossRef Medline
 21. Wortsman J, Chui M, Gray T, et al. **Spinal meningeal AVM supplied from the internal iliac artery associated with tethered cord syndrome in an adult: case report.** *J Can Assoc Radiol* 1983;34:323–25 Medline
 22. Nasr DM, Brinjikji W, Clarke MJ, et al. **Clinical presentation and treatment outcomes of spinal epidural arteriovenous fistulas.** *J Neurosurg Spine* 2017;26:613–20 CrossRef Medline
 23. Kroszczynski AC, Kohan K, Kurowski M, et al. **Intraforaminal location of thoracolumbar anterior medullary arteries.** *Pain Med* 2013;14:808–12 CrossRef Medline

Celebrating 35 Years of the AJNR

March 1983 edition

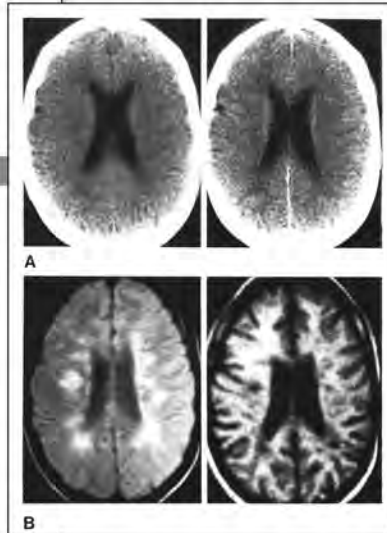
NMR Demonstration of Cerebral Abnormalities: Comparison with CT

Michael Brant-Zawadzki^{1,2}
 Peter L. Davis^{1,3}
 Lawrence E. Crooks^{1,3}
 Catherine M. Mills^{1,3}
 David Norman^{1,3}
 Thomas H. Newton^{1,3}
 Phil Sheldon^{1,3}
 Leon Kaufman^{1,3}

Sixty-eight patients with a wide spectrum of brain pathology were imaged with both computed tomography (CT) using a G.E. 8800 scanner and nuclear magnetic resonance (NMR) imaging with a 3.5 kG prototype device. NMR was more advantageous in the detection and/or characterization of pathology in 26 of the 58 patients, especially when demyelination was part of the disease process or when the lesion was obscured on CT by beam-hardening artifact. Punctate foci of calcification identified on CT were not detected on NMR, but larger calcifications were seen. NMR was sensitive to detection of both normal and abnormal vascular structures. The ability of NMR to differentiate among different pathologic entities remains to be fully evaluated. NMR currently complements CT in the evaluation of many disease entities and may actually replace CT in some. The full future potential of NMR and its role with respect to CT has only begun to be elucidated.

The rapid development of nuclear magnetic resonance (NMR) imaging is documented by many recent reports, several of which include representative clinical material [1-6]. Clinical studies have begun to clarify the future role of NMR. However, current NMR equipment is far from standardized. Both hardware and imaging technique differ substantially among the imagers now being used. Certain techniques are already proving more useful than others in delineating pathology [7-9]. Because of the rapidly changing technology, clinical efficacy questions regarding NMR are still somewhat premature. Comparison studies with CT must be evaluated with the understanding that one is comparing the technologies at very different stages of maturity.

The impressive quality of the few images already published has fueled increasing interest in the diagnostic impact of NMR. The intent of this communication is to summarize initial experience at the University of California, San Francisco, in NMR imaging of patients with a broad spectrum of cerebral disease and to compare the results with CT. Ultimately the utility of NMR and its role with respect to CT must await determination of the optimal imaging techniques within each disease category, but sufficient results have already been obtained to illustrate the clinical usefulness of NMR in selected cases even in its current state of development and to indicate fertile areas of further investigation in order to better



This article appears in the March/April 1983 issue of AJNR and the May 1983 issue of AJR.
 Received September 17, 1982; accepted after revision November 15, 1982.
 Presented at the XI Symposium Neurodiagnostic, Washington, DC, October 1982.
 The work was supported in part by General Electric, Milwaukee, Wis., and by U.S. Public Health Service grant CA 32650 (National Cancer Institute).
¹ Department of Radiology, University of California, San Francisco, CA 94143.
² Department of Radiology, San Francisco General Hospital, Room 1005G, 1001 Potrero Ave, San Francisco, CA 94110. Address reprint requests to M. Brant-Zawadzki.
³ Radiologic Imaging Laboratory, University of California, San Francisco, South San Francisco, CA 94060.
 AJNR 4:117-124, March/April 1983
 0195-9106/83/040117-08\$02.00
 © American Roentgen Ray Society

Digital Subtraction Angiography with Intravenous Injection: Assessment of 1,000 Carotid Bifurcations

Gary W. Wood^{1,2}
 Robert F. Lukin¹
 Thomas A. Tomnick¹
 Alan Chambers¹

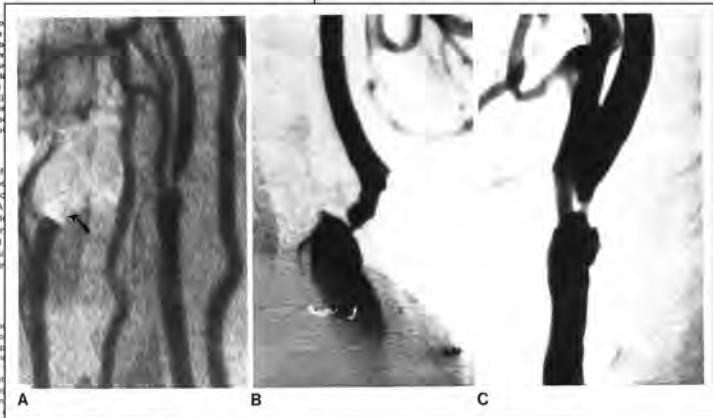
Digital subtraction angiography formed on 500 consecutive artery bifurcations. Diagnosed 625 internal, and 904 external carotid arteriography angiograms with diagnostic quality 95 internal, and 79 of 91 carotid occlusion (14 of 14) with clinically significant stenosis was defined as a percentage of specificity, and accuracy of 94%.

Several clinical trials of digital subtraction angiography (DSA) with intravenous contrast injection have been reported [1-5]. Clinical acceptance anticipates results of DSA study was designed to determine diagnostic quality external disease can be obtained degree of carotid stenosis and (3) the utility of DSA in disease.

Subjects and Methods

The steady population on Cincinnati Medical Center for standard carotid arteriography carotid bifurcations, anatomic correlation purposes alone of all cases were outpatient clinic and telemedicine clinical follow-up, and contrast.

A commercially available examination, and a prototype system has undergone technical testing in the University of Wisconsin, Madison, and operational characteristics have been described [6]. Serial imaging at one frame/second with four summations/frame was used for neck examinations using radiographic technique of 65-75 kVp and 200-300 mA. The system employs a dual mode 5 or 9 inch (12.7 or 22.9 cm) cesium-iodide image intensifier with a Plumbicon camera. Digital conversion and processing occur instantly with real-time display and postprocessing ability on a 256 x 512 matrix with resolution of 8 bits. Performance specifications include 1% contrast resolution and a 650:1 system signal-to-noise ratio. A 16 gauge, 30.5 cm, straight, end-hole catheter (Intracath, Demerit) placed in the



This article appears in the March/April 1983 issue of AJNR and the May 1983 issue of AJR.
 Received April 14, 1982; accepted after revision September 24, 1982.
 Presented at the XI Symposium Neurodiagnostic, Washington, DC, October 1982.
 Department of Radiology, University of Cincinnati Medical Center, 234 Goodenow St., Cincinnati, OH 45267. Address reprint requests to R. F. Lukin.
¹ Present address: Department of Radiology, Albany Medical Center, Albany, NY 12208.
 AJNR 4:125-129, March/April 1983
 0195-9106/83/040125-05\$02.00
 © American Roentgen Ray Society

Concerns about a New Preterm MR Imaging Scoring System

We have read with interest the recently published article by George et al.¹ Because more centers are performing brain MR imaging in preterm infants before term-equivalent age (TEA), there is indeed a need for a robust and validated scoring system for both documenting injury and help in predicting outcomes. Most of us are using either the score of Woodward et al² or that of Kidokoro et al³ when assessing the MR imaging performed at TEA, but these scoring systems cannot be used before 36 weeks' postmenstrual age (PMA).

In the article by George et al,¹ 83 preterm infants were studied at a mean PMA of 32 weeks. The scoring system appears easy to use, and 20 MRIs were scored initially by a neurologist with additional training in radiology and subsequently by a radiologist, with overall good interrater reproducibility (intraclass correlation coefficient [ICC], 0.82–0.97) but a low score for cortical gray matter (0.08; ICC, 0.00–0.63). The T2-weighted MR images provided in the supplemental file are of excellent quality. However, we do not agree with the interpretation given to some of them and would like to bring this to the attention of the readers of this journal.

In Fig 2, the image shown is scored as an example of grade 2 white matter injury (WMI). However, the symmetric smooth-walled cysts adjacent to the ventricles are typical of subependymal pseudocysts (SEPs), also referred to as connatal cysts, and they are not in the white matter. They are not uncommon and are sometimes mistaken for cystic periventricular leukomalacia (c-PVL).^{4,5} There are several publications that help us make the distinction between SEPs and c-PVL.^{6,7} First, SEPs are already present at birth and readily visible on cranial sonography; they are below the roof of the lateral ventricles (Fig 1); they are most often seen directly adjacent to the ventricles in the frontal lobe; and the walls of the cysts are smooth and when several are present, they look like a string of beads on a parasagittal view. Distinguishing these cysts from c-PVL or other cysts within the white matter is generally not difficult, and it is very important because the neurodevelopmental outcome of infants with SEPs is almost uniformly within the normal range, as reported by several groups, except when these cysts

are markers for an underlying problem (eg, cytomegalovirus [CMV] or a metabolic or other rare disorder).^{6,8–11}

Another matter of debate is shown in Figs 11, 12, and 14, where germinal matrix hemorrhages are scored as deep gray matter injury. Again, we do not agree with the interpretation given and consider that these images show hemorrhage within the germinal matrix rather than injury being primarily in the central gray nuclei. It is possible that there is injury directly to the gray matter or poor secondary growth, but it is not shown in these images. A similar issue is seen in Fig 7 where low signal is seen on the margin of the ventricle rather than being primarily in the white matter.

In this study of George et al¹ the number of infants with a grade 2 cystic WMI score, a deep gray matter injury score, or a linear WM injury score is limited to 1, 8, and 7, respectively. Because these numbers are small, we do not know whether they have much of an impact on the use of their score. We do, however, think that one should be aware of these diagnostic discrepancies. We are especially concerned that SEPs are still being misinterpreted as cystic WMI because only infants with the latter type of injury have an adverse outcome, unless the SEPs are markers for an underlying problem that needs specific investigation that may otherwise not be performed if the cysts are interpreted as c-PVL.

Disclosures: Linda de Vries—UNRELATED: Employment: consultant neonatologist University Medical Center Utrecht; Payment for Lectures Including Service on Speakers Bureaus: neonatal sonography course, Comments: This course runs every year in London, and an honorarium is provided. I am a faculty of IpoKrates and receive an honorarium for lectures*; Royalties, Comments: I am a coauthor of 2 books for which I receive royalties, *Atlas of Amplitude Integrated EEGs in the Neonate* (ISBN-13:9781841846491) and *An Atlas of Neonatal Brain Sonography* (ISBN: 978-1-898683-56-8). Frances Cowan—UNRELATED: Employment: part-time perinatal neurologist, Chelsea and Westminster Hospital, London, UK; Payment for Lectures Including Service on Speakers Bureaus, Comments: I speak at an annual neonatal sonography course and receive an honorarium. *Money paid to the institution.

REFERENCES

1. George JM, Fiori S, Fripp J, et al. **Validation of an MRI brain injury and growth scoring system in very preterm infants scanned at 29- to 35-week postmenstrual age.** *AJNR Am J Neuroradiol* 2017;38:1435–42 CrossRef Medline
2. Woodward LJ, Anderson PJ, Austin NC, et al. **Neonatal MRI to predict neurodevelopmental outcomes in preterm infants.** *N Engl J Med* 2006;355:685–94 CrossRef Medline
3. Kidokoro H, Anderson PJ, Doyle LW, et al. **Brain injury and altered**

- brain growth in preterm infants: predictors and prognosis. *Pediatrics* 2014;134:e444–53 CrossRef Medline
4. Al Rifai MT, Al Tawil KI. The neurological outcome of isolated PVL and severe IVH in preterm infants: is it fair to compare? *Pediatr Neurol* 2015;53:427–33 CrossRef Medline
 5. Brun N, Robitaille Y, Grignon A, et al. Pyruvate carboxylase deficiency: prenatal onset of ischemia-like brain lesions in two sibs with the acute neonatal form. *Am J Med Genet* 1999;84:94–101 Medline
 6. Rademaker KJ, De Vries LS, Barth PG. Subependymal pseudocysts: ultrasound diagnosis and findings at follow-up. *Acta Paediatr* 1993;82:394–99 CrossRef Medline
 7. Malinge G, Lev D, Ben Sira L, et al. Congenital periventricular pseudocysts: prenatal sonograph-c appearance and clinical implications. *Ultrasound Obstet Gynecol* 2002;20:447–51 CrossRef Medline
 8. Cevy-Macherel M, Forcada Guex M, Bickle Graz M, et al. Neurodevelopment outcome of newborns with cerebral subependymal pseudocysts at 18 and 46 months: a prospective study. *Arch Dis Child* 2013;98:497–502 CrossRef Medline
 9. Larcos G, Gruenewald SM, Lui K. Neonatal subependymal cysts detected by sonography: prevalence, sonographic findings, and clinical significance. *AJR Am J Roentgenol* 1994;162:953–56 CrossRef Medline
 10. Ramenghi LA, Domizio S, Quartulli L, et al. Prenatal pseudocysts of the germinal matrix in preterm infants. *J Clin Ultrasound* 1997;25:169–73 Medline
 11. Leijser LM, de Vries LS, Rutherford MA, et al. Cranial ultrasound in metabolic disorders presenting in the neonatal period: characteristic features and comparison with MR imaging. *AJNR Am J Neuroradiol* 2007;28:1223–31 CrossRef Medline

● L.S. de Vries

Department of Neonatology
University Medical Center, Utrecht University
Utrecht, the Netherlands

● F.M. Cowan

Neonatal Department
Chelsea and Westminster Hospital
Imperial College
London, UK

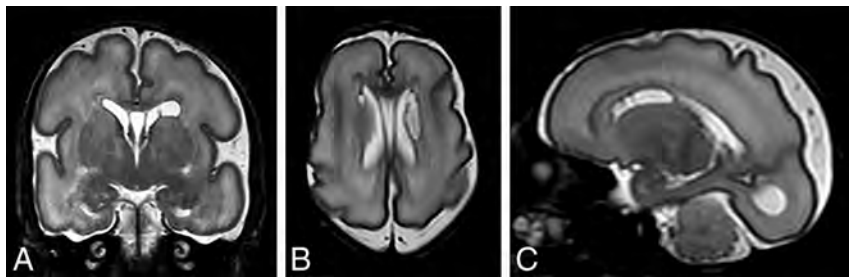


FIG 1. T2-weighted coronal (A), axial (B), and parasagittal (C) MR images showing smooth-walled subependymal cysts, mainly sited directly adjacent to the anterior ventricular margins.

REPLY:

We thank Professors Linda de Vries and Frances Cowan for their interest in our recent publication, “Validation of an MRI Brain Injury and Growth Scoring System in Very Preterm Infants Scanned at 29- to 35-Week Postmenstrual Age.”¹ In their correspondence, the authors expressed concern about our example presented in On-line Fig 2, which they said we presented as “grade 2 white matter injury (WMI).” They correctly pointed out that the example shows connatal cysts and not cystic periventricular leukomalacia (PVL), an observation with which we entirely agree. They were concerned that connatal cysts are “still being misinterpreted as cystic WMI.”

We would like to confirm that nowhere in our publication or on-line material have we called this example in On-line Fig 2, WMI. We have not labeled it cystic PVL or inferred that in the text or on-line material. The exact descriptions in the text are “white matter abnormality,” “cystic degeneration,” or “cystic lesion.” In On-line Tables 1 and 2, this scoring category is called “cerebral WM, cystic lesion.” The scoring system was descriptive and not interpretive—that is, if a cyst was observed, then it was scored without interpretation of the pathogenesis or etiology. This descriptive approach was undertaken to improve the reproducibility of the scoring system, especially in cases in which the pathogenesis or etiology of a lesion was unclear. We agree that it is of paramount importance that clinicians do not interpret our example as cystic PVL; thus, we have amended the caption of On-line Fig 2 to “Bilateral connatal cysts, classified as cerebral WM, cystic lesion, focal bilateral, score 2 (axial T2)” to ensure the utmost clarity.

The authors also commented on On-line Figs 11, 12, and 14, in which they suggest that “germinal matrix hemorrhages are scored as deep gray matter injury.” We agree that germinal matrix hemorrhages are evident in these images; however, from the available images, we think that a secondary involvement of the deep GM (head of caudate) is very likely and, in any case, cannot be excluded, hence our scoring of the images of these subjects as focal bilateral deep GM signal abnormality. An additional coronal image that relates to On-line Fig 12 is included here as On-line Fig 12B, to demonstrate caudothalamic groove germinal matrix hemorrhages, in which extension into the adjacent caudate head is likely. The deep GM subscale score demonstrated strong associations with both motor and cognitive outcomes in our article.

We include 2 additional images from the same subject used in On-line Fig 7, to clarify the involvement of WM in addition to the germinal matrix hemorrhage in this case. We believe that signal abnormality from the additional T1 images supplied, despite the low quality, can support the presence of linear hyperintensity involving the white matter next to the more evident germinal matrix hemorrhage, along with a slightly enlarged ventricle.

We are not presenting this scoring system as a diagnostic tool but rather as an assessment in which our methodology has demonstrated predictive validity. Compared with MR imaging at term-equivalent age in preterm infants, certain features are specific to the earlier imaging time point, such as hemorrhagic lesions, which present unique challenges to scoring. Our choice of

being very sensitive in our scoring may have led to a tendency to overestimate germinal matrix hemorrhages populating part of the putamen and caudate, for example. We believe this is better than the alternative of potentially underestimating the impact of germinal matrix hemorrhages on adjacent tissue structures. We think that our approach is sensitive and descriptive in a new and challenging area and an important first step in developing robust and validated MR imaging scoring tools for use in this population.

REFERENCE

1. George JM, Fiori S, Fripp J, et al. **Validation of an MRI brain injury and growth scoring system in very preterm infants scanned at 29- to 35-week postmenstrual age.** *AJNR Am J Neuroradiol* 2017;38:1435–42
CrossRef Medline

● **J.M. George**

Queensland Cerebral Palsy and Rehabilitation Research Centre
Centre for Children's Health Research
Faculty of Medicine, University of Queensland
Brisbane, Australia

● **S. Fiori**

Department of Developmental Neuroscience
Stella Maris Scientific Institute
Pisa, Italy

● **J. Fripp**

● **K. Pannek**

Health and Biosecurity
The Australian e-Health Research Centre
Commonwealth Scientific and Industrial Research Organisation
Brisbane, Australia

● **J. Bursle**

Department of Medical Imaging
Royal Brisbane and Women's Hospital
Brisbane, Australia

● **R.X. Moldrich**

Centre for Clinical Research
Faculty of Medicine, University of Queensland
Brisbane, Australia

● **A. Guzzetta**

Department of Developmental Neuroscience
Stella Maris Scientific Institute
Pisa, Italy

● **A. Coulthard**

Department of Medical Imaging
Royal Brisbane and Women's Hospital
Brisbane, Australia

Discipline of Medical Imaging

University of Queensland

Brisbane, Australia

● **R.S. Ware**

Menzies Health Institute Queensland
Griffith University
Brisbane, Australia
Queensland Centre for Intellectual and Developmental Disability
University of Queensland
Brisbane, Australia

● **S.E. Rose**

Health and Biosecurity
The Australian e-Health Research Centre
Commonwealth Scientific and Industrial Research Organisation
Brisbane, Australia

● **P.B. Colditz**

Centre for Clinical Research
Faculty of Medicine, University of Queensland
Brisbane, Australia

Perinatal Research Centre

Royal Brisbane and Women's Hospital

Brisbane, Australia

● **R.N. Boyd**

Queensland Cerebral Palsy and Rehabilitation Research Centre
Centre for Children's Health Research
Faculty of Medicine, University of Queensland
Brisbane, Australia

Spinal Angiogram: A Treacherous Criterion Standard...



We read with great interest the article recently published in the *American Journal of Neuroradiology* by Barreras et al¹ entitled, “Analysis of 30 Spinal Angiograms Falsely Reported as Normal in 18 Patients with Subsequently Documented Spinal Vascular Malformations.” This very valuable article for the interventional neuroradiology and neurosurgical communities presents the causes of false-negative digital subtraction angiography findings for the depiction of spinal dural arteriovenous fistulas (SDAVFs). The authors found that the most frequent reason for missing a SDAVF on spinal DSA (sDSA) was misinterpretation of abnormal findings documented on the DSA (55.6%), followed by nonexploration of the ROI (29.6%), and, finally, inadequate opacification of the artery supplying the fistula (nonselective injection) (14.8%).

We congratulate the authors for their effort in seeking the reasons for false-negative DSA findings in the diagnosis of SDAVF and for emphasizing the need for a rigorous protocol for spinal DSA. While spinal DSA is the criterion standard examination for the diagnosis of SDAVF,² it remains an operator-dependent examination, which can lead to false-negative results in a substantial number of cases due to potentially avoidable operator-related misinterpretations. Missing a SDAVF on DSA has a great impact on a patient’s outcome because it may delay the treatment, thus reducing the chance of recovery.

In addition to the recommendations suggested by the authors (adoption of rigorous technical and training standards and second opinion reviews), we would like to share our experience and insist on the need for full spinal DSA, which includes systematically (from top to bottom and bilaterally) the following: costocervical trunks, vertebral arteries, intercostal arteries, lumbar arteries, medial sacral artery, iliolumbar arteries, and lateral sacral arteries (superior and inferior). We insist that all these arteries must be catheterized as selectively as possible. For instance, for the lateral sacral arteries, the catheterization of the internal iliac artery is not sufficient because proximal injection may lead to poor opacification of the lateral sacral arteries (Fig 1). In the article of Barreras et al,¹ most of the missed fistulas (52.9%) were at or

below the L4 level, which confirms the need for a complete spinal DSA, including the lower spinal supplies.

Additionally, a cervical myelopathy may be observed in the case of an intracranial AVF with perimedullary venous drainage.³ Thus, a cerebral DSA with internal and external carotid artery catheterization and opacification should be performed secondarily in case of a negative sDSA finding.

In most cases of missed SDAVFs in the article of Barreras et al,¹ the fistula was documented on the DSA but misinterpreted. Some conditions may enhance the quality of the images acquired during the sDSA, such as the intravenous injection of hyoscine or glucagon to reduce peristalsis-related artifacts or performing the sDSA with the patient under general anesthesia with provoked apnea during the runs to reduce the patient’s motion artifacts.

A peculiar anatomic variation may also be responsible for a false-negative sDSA performed for SDAVF: a separate origin of the dorsospinal branch from the segmental artery on the aorta.⁴ Indeed, the dorsospinal branch (which usually gives rise to the radiculomeningeal branches) may not arise from the segmental artery but instead originate from the aorta. This anatomic variation can be suspected when no physiologic blush of the vertebral body is seen during the selective injection of the segmental artery (because the branches feeding the ipsilateral hemivertebral body are supplied by the dorsospinal trunk).

Furthermore, the catheterization of the origin of the segmental artery may be responsible for vasospasm. In case of a low-flow fistula, this spasm may reduce the flow toward the fistula, which could be responsible for the nonvisualization of the SDAVF.

Moreover, we stress that metachronous double dural AVFs,⁵ even if rare, may be observed. Thus, clinical recurrence after SDAVF treatment with negative sDSA findings at the SDAVF site should suggest performing a complete sDSA, looking for a second fistula.

Finally, the authors do not mention the potential of noninvasive/semi-invasive techniques such as time-resolved MR angiography⁶ or intra-aortic CT angiography (IA-CTA).⁷ These techniques potentially provide an overall examination of the whole spinal cord supply in a single acquisition. They may be valuable in patients with atheromatous vessels with stenosis at the origin of the intercostal/lumbar arteries, leading to difficult stable catheterization and thus to poor vessel opacification (Fig 2). However,

Indicates article with supplemental on-line video.

<http://dx.doi.org/10.3174/ajnr.A5470>

while time-resolved MRA is sensitive for the depiction of SDAVFs (sensitivity as high as 81%⁶), the spatial resolution of this examination is limited and the precise location of the shunt point cannot be evaluated on time-resolved MRA in some cases.⁸ Concerning IA-CTA, despite its potential for the depiction of SDAVFs (sensitivity of 90%⁷) and the valuable information it provides regarding the location of the shunt point and its relationship with the bone landmarks, this examination may also provide false-negative results, mainly for SDAVFs supplied by branches from the internal iliac arteries, due to the incomplete opacification of the latter vessels by the contrast material injected directly in the aorta (Fig 1).

In conclusion, interventional neuroradiologists and neurologists should keep in mind that a single negative spinal DSA finding is not enough to rule out a spinal vascular malformation and therefore should be repeated with enhanced acquisition protocol if the clinical presentation is strongly suggestive of a SDAVF.

Disclosures: Frédéric Clarençon—UNRELATED: Payment for Lectures Including Service on Speakers Bureaus: Balt Extrusion, Medtronic. David Grabli—UNRELATED: Board Membership: AbbVie, Zambon; Employment: Assistance Publique-Hôpitaux de Paris; Grants/Grants Pending: Assistance Publique-Hôpitaux de Paris, Institut National de la Santé et de la Recherche Medicable, France Parkinson*; Payment for Lectures Including Service on Speakers Bureaus: Novartis, Merz, Pharma AbbVie, Teva; Travel/Accommodations/Meeting Expenses Unrelated to Activities Listed: AbbVie, Merz Pharma. Nader-Antoine Sourour—UNRELATED: Consultancy: Medtronic, MicroVention; Stock/Stock Options: Medina. *Money paid to the institution.

REFERENCES

- Barreras P, Heck D, Greenberg B, et al. **Analysis of 30 spinal angiograms falsely reported as normal in 18 patients with subsequently documented spinal vascular malformations.** *AJNR Am J Neuroradiol* 2017;38:1814–19 CrossRef Medline
- Koch C. **Spinal dural arteriovenous fistula.** *Curr Opin Neurol* 2006; 19:69–75 CrossRef Medline
- Cognard C, Gobin YP, Pierot L, et al. **Cerebral dural arteriovenous fistulas: clinical and angiographic correlation with a revised classification of venous drainage.** *Radiology* 1995;194:671–80 CrossRef Medline
- Chiras J, Merland JJ. **The dorsospinal artery: a little known anatomical variant—its importance in spinal angiography.** *J Neuroradiol* 1979;6:93–100 Medline
- Rizvi T, Garg A, Mishra NK, et al. **Metachronous double spinal dural arteriovenous fistulas: case report and review of the literature.** *J Neurosurg Spine* 2006;4:503–05 CrossRef Medline
- Saïndane AM, Boddu SR, Tong FC, et al. **Contrast-enhanced time-resolved MRA for pre-angiographic evaluation of suspected spinal dural arterial venous fistulas.** *J Neurointerv Surg* 2015;7:135–40 CrossRef Medline
- Clarençon F, Di Maria F, Sourour NA, et al. **Evaluation of intra-aortic CT angiography performances for the visualisation of spinal vascular malformations' angioarchitecture.** *Eur Radiol* 2016;26:3336–44 CrossRef Medline
- Lindenholz A, Terbrugge KG, van Dijk JM, et al. **The accuracy and utility of contrast-enhanced MR angiography for localization of spinal dural arteriovenous fistulas: the Toronto experience.** *Eur Radiol* 2014;24:2885–94 CrossRef Medline

● F. Clarençon

● E. Shotar

Department of Neuroradiology

Pitié-Salpêtrière Hospital, Assistance Publique-Hôpitaux de Paris
Paris, France

Paris VI University, Pierre et Marie Curie

Paris, France

● A.-L. Boch

Department of Neurosurgery

Pitié-Salpêtrière Hospital, Assistance Publique-Hôpitaux de Paris
Paris, France

● C. Rolla-Bigliani

● A. Al Raasi

Department of Neuroradiology

Pitié-Salpêtrière Hospital, Assistance Publique-Hôpitaux de Paris
Paris, France

● D. Grabli

Paris VI University, Pierre et Marie Curie

Paris, France

Department of Neurology

Pitié-Salpêtrière Hospital, Assistance Publique-Hôpitaux de Paris
Paris, France

● S. Vicart

Department of Neurology

Pitié-Salpêtrière Hospital, Assistance Publique-Hôpitaux de Paris
Paris, France

● N.-A. Sourour

Department of Neuroradiology

Pitié-Salpêtrière Hospital, Assistance Publique-Hôpitaux de Paris
Paris, France

● J. Chiras

Department of Neuroradiology

Pitié-Salpêtrière Hospital, Assistance Publique-Hôpitaux de Paris
Paris, France

Paris VI University, Pierre et Marie Curie

Paris, France



FIG 1. A 56-year-old man presenting with a progressive paraparesis lasting for a few months. Spinal cord MR imaging, sagittal T2-weighted imaging (A), and contrast-enhanced T1WI (B) demonstrate T2 hyperintensity involving the thoracolumbar spinal cord and the conus medullaris (A, white arrows), which may be suggestive of a SDAVF. However, no perimedullary vein enhancement on contrast-enhanced T1WI is seen (B). A first digital subtraction angiography was performed with a negative result for SDAVF (not shown). However, the internal iliac arteries were not catheterized during this first spinal DSA. A second sDSA was performed 3 months after the first one (C). The right internal iliac artery was catheterized, but too proximally. The sDSA findings were interpreted as normal. A second look revealed a possible fistula fed by the right superior lateral sacral artery (LSA) (C, arrow). D and E, Right internal iliac artery DSA in an anteroposterior projection. D, Early phase. E, Late phase, large FOV. The tip of the catheter is located close to the origin of the right LSA. The presence of a SDAVF is confirmed, fed by the right superior LSA (D, white arrow). The shunt point is located along the right S1 nerve root (asterisk) with low-flow ascending venous drainage (D and E, black arrows). Note the pre-anastomosis between a branch of the LSA (D, black arrowhead) and the medial sacral artery (D, white arrowheads).



FIG 2. A 76-year-old man who had a previous embolization with coils and Onyx (Covidien, Irvine, California) for a right T7 SDAVF. Recurrence of the clinical symptoms (gait disturbance) was observed >1 year after the endovascular treatment. The spinal cord MR imaging (not shown) was suggestive of a recurrence of the fistula. An sDSA was performed (A) and confirmed the recurrence of the fistula (*asterisk* indicates the shunt point; *black arrows*, descending venous drainage), which was fed by the contralateral intercostal artery (left T7) via the retrocorporeal network (A, *white arrows*). The patient was referred for surgery for the treatment of this recurrence. After surgical treatment, the patient experienced a slight clinical worsening (ataxia). Within the 2 months after the surgical treatment, the patient continued to experience gradual clinical worsening (worsening of the ataxia with walking being impossible). A full sDSA was scheduled to rule out a recurrence of the SDAVF. The selective injection of the left T7 intercostal artery showed no residual fistula (B). The right T6 intercostal artery could not be catheterized selectively due to ostium stenosis, and the injection was performed in front of the origin of the intercostal artery (C, early phase; D, late phase). The sDSA findings were thus interpreted as normal. A spinal cord MR imaging was performed the day after the sDSA (E, sagittal T2WI; F, sagittal contrast-enhanced T1WI) and showed postoperative changes associated with spinal cord hyperintensity, suggestive of venous edema (E, *white arrows*). Equivocal posterior perimedullary serpiginous T2 hypointensities (E, *arrowhead*) presenting a doubtful enhancement were also seen (F, *arrowheads*), possibly corresponding to perimedullary vein dilations. Time-resolved MR angiography (Time Resolved Imaging of Contrast Kinetics, TRICKS; GE Healthcare, Milwaukee, Wisconsin), sagittal acquisition (G, early phase; H, late phase). Abnormal early perimedullary vein enhancement was seen (H, *white arrows*) at the midthoracic level, suggestive of sAVF recurrence (On-line Video). A new sDSA was performed with the patient under general anesthesia. Selective catheterization of the right T6 intercostal artery (I, early phase; J, late phase) confirmed the recurrence of the spinal DAVF with early opacification of dilated perimedullary veins (I and J, *black arrows*).

Beware of Multiphase CTA Interpretation

We read with interest the recent article by Byrne et al,¹ which describes the “delayed vessel sign” as a reliable indicator of vessel occlusion. This is very useful, especially when trying to diagnose an embolic occlusion of a distal vessel.

According to the authors, the delayed vessel sign “refers to the presence of an artery distal to the point of occlusion/stenosis that is absent or poorly opacified on the initial angiographic phase but becomes more opacified on the delayed phases, appearing denser than the equivalent vessel on the opposite side.”

This interpretation, however, is incorrect in certain circumstances. When a distal vessel is occluded due to an embolus, the opacification of that vessel up to the embolus is delayed because there is a column of blood that slows down the transit of contrast up to the point of occlusion. It is different from the “clot outline sign,”² described in the “Discussion,” which is instead related to the antegrade opacification distal to a partially occlusive state.

Thus, even though in some cases, retrograde filling of the vessel past its point of occlusion is clearly demonstrated (the sample case on Fig 2), in others (Fig 1), the delayed opacification is instead clearly related to the alternative concept explained above. Indeed, in Fig 1, notice how, in the delayed late phase (Fig 1C), the contrast has slightly progressed more distally compared with part B of same figure, confirming that we are not looking at retrograde opacification but, instead, at delayed antegrade opacification

proximal to the clot because there has been antegrade advancement of a column of contrast in between these 2 phases. The interpretation in this perspective now leads to a diagnosis of the point of occlusion at a more distal location than the erroneous interpretation of the authors. Also, this different interpretation, in some patients, may lead to a different evaluation of the collateral state and may eventually have a different prognostic predictive value.

This comment is about an alternative additional explanation of the findings and not the role of this technique, which, again, we find very useful and for which we thank the authors.

Disclosures: Eytan Raz—UNRELATED: Consultancy: Covidien; Royalties: Springer; Stock/Stock Options: Penumbra and Stryker.

REFERENCES

1. Byrne D, Sugrue G, Stanley E, et al. **Improved detection of anterior circulation occlusions: the “delayed vessel sign” on multiphase CT angiography.** *AJNR Am J Neuroradiol* 2017;38:1911–16 [CrossRef](#) [Medline](#)
2. Christoforidis GA, Mohammad Y, Avutu B, et al. **Arteriographic demonstration of slow antegrade opacification distal to a cerebrovascular thromboembolic occlusion site as a favorable indicator for intra-arterial thrombolysis.** *AJNR Am J Neuroradiol* 2006;27:1528–31 [Medline](#)

✉ E. Raz

✉ M. Shapiro

Radiology Department, Neurointerventional Radiology Section
New York University Langone Medical Center
New York, New York

<http://dx.doi.org/10.3174/ajnr.A5499>

REPLY:

We thank Drs Raz and Shapiro for their interest in our study¹ and appreciate the opportunity to address their comments.

While delayed antegrade filling is a potential mechanism for the delayed vessel sign on multiphase CT angiography, we think that retrograde filling is by far the most common mechanism of delayed enhancement. In our article, we assessed maximum pial collateral enhancement and found that it correlated with the phase of appearance of the delayed vessel sign, which we believe supports this interpretation. In addition, one of the most useful aspects of identifying the delayed vessel is that the precise site of occlusion is nearly always identified by tracing back along the delayed vessel until enhancement abruptly decreases, again suggesting delayed retrograde opacification.

We realize that it is difficult for readers to evaluate the relatively small printed figures from the multiphase CTA study demonstrated in Fig 1 of our article, but we strongly believe that it supports a retrograde mechanism of delayed enhancement. All 3 parts of Fig 1 are from the same intracranial level. If you closely examine the indicated delayed vessel in part C, it is subtly proximal to the delayed vessel in part B (ie, retrograde filling). We have

reviewed the actual DICOM dataset and confirmed that there is proximal occlusion to the delayed vessel in this patient (and a subtle focal hyperdense vessel at the occlusion on the noncontrast CT).

We acknowledge that an antegrade opacification mechanism, due to advancement of a column of contrast between phases proximal to an occlusion, should be considered when the delayed vessel sign is encountered; however, we do not think it is a commonly encountered scenario.

REFERENCE

1. Byrne D, Sugrue G, Stanley E, et al. **Improved detection of anterior circulation occlusions: the “delayed vessel sign” on multiphase CT angiography.** *AJNR Am J Neuroradiol* 2017;38:1911–16 [CrossRef](#) [Medline](#)

D. Byrne

Department of Radiology
Mater Misericordiae University Hospital
Dublin, Ireland

P.J. MacMahon

Department of Radiology
Mater Misericordiae University Hospital
Dublin, Ireland
School of Medicine
University College Dublin
Dublin, Ireland

<http://dx.doi.org/10.3174/ajnr.A5511>